ORNL/TM-11239

ornl

OAK RIDGE NATIONAL LABORATORY

MARTIN MARIETTA

Ceramic Technology for Advanced Heat Engines Project Semiannual Progress Report for October 1988 Through March 1989

Prepared for
U.S. Department of Energy
Assistant Secretary for
Conservation and Renewable Energy
Office of Transportation Systems
Advanced Materials Development Program

CERAMIC TECHNOLOGY FOR ADVANCED HEAT ENGINES

OPERATED BY
MARTIN MARIETTA ENERGY SYSTEMS, INC.
FOR THE UNITED STATES
DEPARTMENT OF ENERGY

ORNL/TM-11239

Metals and Ceramics Division

CERAMIC TECHNOLOGY FOR ADVANCED HEAT ENGINES PROJECT SEMIANNUAL PROGRESS REPORT FOR OCTOBER 1988 THROUGH MARCH 1989

D. R. Johnson
Project Manager

Date Published: August 1989

NOTICE: This document contains information of a preliminary nature. It is subject to revision or correction and therefore does not represent a final report.

Prepared for
U.S. Department of Energy
Assistant Secretary for Conservation and Renewable Energy
Office of Transportation Systems
Advanced Materials Development Program
EE 04 00 00 0

Prepared by the
OAK RIDGE NATIONAL LABORATORY
Oak Ridge, Tennessee 37831-6285
operated by
MARTIN MARIETTA ENERGY SYSTEMS, INC.
for the
U.S. DEPARTMENT OF ENERGY
under Contract DE-AC05-84OR21400

REPORTS PREVIOUSLY ISSUED

ORNL/TM-9325	Period March 1983-September 1983
ORNL/TM-9466	Period October 1983-March 1984
ORNL/TM-9497	Period April 1984-September 1984
ORNL/TM-9673	Period October 1984-March 1985
ORNL/TM-9947	Period April 1985-September 1985
ORNL/TM-10079	Period October 1985-March 1986
ORNL/TM-10308	Period April 1986-September 1986
ORNL/TM-10469	Period October 1986-March 1987
ORNL/TM-10705	Period April 1987-September 1987
ORNL/TM-10838	Period October 1987-March 1988
ORNL/TM-11116	Period April 1988-September 1988

Research sponsored by the U.S. Department of Energy, Assistant Secretary for Conservation and Renewable Energy, Office of Transportation Systems, as part of the Ceramic Technology for Advanced Heat Engines Project of the Advanced Materials Development Program, under contract DE-AC05-84OR21400 with Martin Marietta Energy Systems, Inc.

CONTENTS

CERAMIC TECHNOLOGY FOR ADVANCED HEAT ENGINES PROJECT SEMIANNUAL PROGRESS REPORT FOR OCTOBER 1988 THROUGH MARCH 1989

SUMMARY

The Ceramic Technology For Advanced Heat Engines Project was developed by the Department of Energy's Office of Transportation Systems (OTS) in Conservation and Renewable Energy. This project, part of the OTS's Advanced Materials Development Program, was developed to meet the ceramic technology requirements of the OTS's automotive technology programs.

Significant accomplishments in fabricating ceramic components for the Department of Energy (DOE), National Aeronautics and Space Administration (NASA), and Department of Defense (DoD) advanced heat engine programs have provided evidence that the operation of ceramic parts in high-temperature engine environments is feasible. However, these programs have also demonstrated that additional research is needed in materials and processing development, design methodology, and data base and life prediction before industry will have a sufficient technology base from which to produce reliable cost-effective ceramic engine components commercially.

An assessment of needs was completed, and a five-year project plan was developed with extensive input from private industry. The objective of the project is to develop the industrial technology base required for reliable ceramics for application in advanced automotive heat engines. The project approach includes determining the mechanisms controlling reliability, improving processes for fabricating existing ceramics, developing new materials with increased reliability, and testing these materials in simulated engine environments to confirm reliability. Although this is a generic materials project, the focus is on the structural ceramics for advanced gas turbine and diesel engines, ceramic bearings and attachments, and ceramic coatings for thermal barrier and wear applications in these engines. This advanced materials technology is being developed in parallel and close coordination with the ongoing DOE and industry proof-of-concept engine development programs. To facilitate the rapid transfer of this technology to U.S. industry, the major portion of the work is being done in the ceramic industry, with technological support from government laboratories, other industrial laboratories, and universities.

This project is managed by ORNL for the Office of Transportation Systems, Heat Engine Propulsion Division, and is closely coordinated with complementary ceramics tasks funded by other DOE offices, NASA, DoD, and industry. A joint DOE and NASA technical plan has been established, with DOE focus on automotive applications and NASA focus on aerospace applications. A common work breakdown structure (WBS) was developed to facilitate coordination. The work described in this report is organized according to the following WBS project elements:

0.0 Management and Coordination

1.0 Materials and Processing

- 1.1 Monolithics
- 1.2 Ceramic Composites
- 1.3 Thermal and Wear Coatings
- 1.4 Joining

2.0 Materials Design Methodology

- 2.1 Modeling
- 2.2 Contact Interfaces
- 2.3 New Concepts

3.0 Data Base and Life Prediction

- 3.1 Structural Qualification
- 3.2 Time-Dependent Behavior
- 3.3 Environmental Effects
- 3.4 Fracture Mechanics
- 3.5 NDE Development

4.0 Technology Transfer

This report includes contributions from all currently active project participants. The contributions are arranged according to the work breakdown structure outline.

0.0 PROJECT MANAGEMENT AND COORDINATION

D. R. Johnson
Oak Ridge National Laboratory

Objective/scope

This task includes the technical management of the project in accordance with the project plans and management plan approved by the Department of Energy (DOE) Oak Ridge Operations Office (ORO) and the Office of Transportation Systems. This task includes preparation of annual field task proposals, initiation and management of subcontracts and interagency agreements, and management of ORNL technical tasks. Monthly management reports and bimonthly reports are provided to DOE; highlights and semiannual technical reports are provided to DOE and program participants. In addition, the program is coordinated with interfacing programs sponsored by other DOE offices and federal agencies, including the National Aeronautics and Space Administration (NASA) and the Department of Defense (DoD). This coordination is accomplished by participation in bimonthly DOE and NASA joint management meetings, annual interagency heat engine ceramics coordination meetings, DOE contractor coordination meetings, and DOE Energy Materials Coordinating Committee (EMaCC) meetings, as well as special coordination meetings.

1.0 MATERIALS AND PROCESSING

INTRODUCTION

This portion of the project is identified as project element 1.0 within the work breakdown structure (WBS). It contains four subelements: (1) Monolithics, (2) Ceramic Composites, (3) Thermal and Wear Coatings, and (4) Joining. Ceramic research conducted within the Monolithics subelement currently includes work activities on green state ceramic fabrication, characterization, and densification and on structural, mechanical, and physical properties of these ceramics. Research conducted within the Ceramic Composites subelement currently includes silicon carbide and oxide-based composites, which, in addition to the work activities cited for Monolithics, include fiber synthesis and characterization. Research conducted in the Thermal and Wear Coatings subelement is currently limited to oxide-base coatings and involves coating synthesis, characterization, and determination of the mechanical and physical properties of the coatings. Research conducted in the Joining subelement currently includes studies of processes to produce strong stable joints between zirconia ceramics and iron-base alloys.

A major objective of the research in the Materials and Processing project element is to systematically advance the understanding of the relationships between ceramic raw materials such as powders and reactant gases, the processing variables involved in producing the ceramic materials, and the resultant microstructures and physical and mechanical properties of the ceramic materials. Success in meeting this objective will provide U.S. companies with new or improved ways for producing economical, highly reliable ceramic components for advanced heat engines.

1.1 MONOLITHICS

1.1.1 Silicon Carbide

Turbomilling of SiC Whiskers and SiC Whisker/Alumina Composites
D. E. Wittmer (Southern Illinois University)

Objective/Scope

The purpose of this work is to investigate the turbomilling process as a means of improved processing for SiC whisker-ceramic matrix composites, and to design and fabricate prototype turbomilling units.

Technical Progress

During this reporting period the three prototype turbomills were completed, and two of the turbomills were delivered to ORNL. Installation and calibration of the torque/h.p./r.p.m. sensors will be completed when the proper electrical services are installed at ORNL.

As reported previously, the turbomilling trials of silicon carbide whiskers in alumina and silicon nitride matrices were competed ahead of schedule and the results reported in the last semi-annual report. Delay in the preparation of the final report was approved by the project monitor to allow for the addition of test data detained by equipment problems at ORNL.

Due to the success of this program, additional funding was requested to support Phase II of this work. Contract negotiations are in progress and the award is anticipated to be finalized in April. Phase II is divided into 3 major tasks:

Task 1. Beneficiation of SiC whiskers.

Task 2. Development of aspect ratio reduction parameters.

Task 3. Improved dispersion of particulate matrices.

Task 1. Beneficiation of SiC Whiskers

During this phase of the project, SiC whiskers will be processed in the turbomill to develop improved beneficiation techniques. It intended in this task to study the influence of the density of the milling media on the beneficiation process and fracture behavior of the whiskers by using dense silicon nitride or PSZ beads for high density media and a polymer bead (such as delrin, teflon, or other tough polymer) for low density media.

Several small batches of SiC whiskers will be processed by turbomilling with the solids loading, fraction of milling media and turbomilling speed determined through the use of an experimental design matrix. Sedimentation techniques will be utilized to separate the longer whiskers from whisker fragments and impurities and remove the soluble impurities.

The as-received SiC whiskers will be analyzed for free carbon, free Si, presence of unreacted silica, and chemical composition by standard

analytical techniques to produce a baseline chemical composition. Selected products from the sedimentation process will also be analyzed, ie. the supernatant liquid for dissolved and ultra-fine saturated impurities, the resultant coarse whisker fraction and fine fraction chemical composition, surface area and particle sizes for coarse and fine fractions, and morphology. A portion of the beneficiated SiC whiskers will then be heat treated in vacuum or other appropriate atmosphere for comparison with the untreated virgin whiskers, and the untreated beneficiated whiskers. The information and products of this task will also be utilized in the development of other tasks as discussed in the additional tasks.

Task 2. Development of Aspect Ratio Reduction Parameters.

The SiC aspect ratio will be determined as a function of turbomilling parameters from the information generated during Task 1. During this task a model will be developed, based on the mathematical relationship between average surface area, average particle size and measured whisker diameters, to determine the average aspect ratio for the SiC products produced in Task 1. This calculated data will then be compared to the aspect ratio as viewed by SEM and optical methods.

The effect of turbomilling on the whiskers/ceramic matrix composites will also be determined during this task. Whiskers developed as products of Task 1 will be dispersed in the matrix material selected by the Company. The whisker volume loading will be varied from 15 vol.% to 40 vol.% for the matrix material(s) to be specified later by the company. It is anticipated that silicon nitride will be one of the specified matrix materials. During turbomilling processing, samples will be pulled by syphon at selected time intervals and measured for particle size distribution, surface area and aspect ratio. The results shall be monitored by density and fracture results for hot-pressed and/or HIPed and/or sintered samples.

Task 3. Improved Dispersion of Particulate Matrices.

In conjunction with Task 2, Task 3 will investigate the dispersion of the matrix material(s) specified by the Company by the turbomilling process, prior to the introduction of the SiC whiskers to the matrix. Slurry pH, solids loading, coarse:fine ratio, type and amount of dispersant and other turbomilling parameters will be adjusted and monitored to develop optimized conditions for dispersing the selected matrix material(s). Once these conditions have been identified, SiC whiskers from Task 1 at whisker loadings from 15 vol.% to 40 vol.% will be added, following the dispersion step. During this step it will be necessary to develop techniques to uniformly flocculate the resultant whisker/particulate dispersion to avoid separation upon mill discharge. The slurries produced in this task will then be vacuum assisted, pressure cast into disks for the preparation of test samples. Isopressing of the dry preforms may be required to enable densification. The results shall again be monitored by density and fracture results for hot-pressed and/or HIPed and/or sintered samples.

During this reporting period, Task 1 and 2 were initiated and some preliminary results are being prepared for presentation at the 91st Annual American Ceramic Society Meeting, Indianapolis, IN, April 23-27, 1989. The turbomilling parameters investigated were:

MILLING MEDIA
--200 g of 3 mm Plastic (4200 beads)
--200 g of 3 mm PSZ (316 beads)

MILLING TIME
--120 min for Plastic Media
-- 60 min for PSZ Media
--Samples Pulled Every 15 min

MILLING SPEED--800 r.p.m. or 1200 r.p.m.

WHISKER LOADING LEVEL--200 g or 300 g

1 liter Distilled, Deionized Water

Status of Milestones

Phase I:

Design, fabrication, and testing of prototype turbomills. Completed.	Nov. 1988
Dispersion and homogenization of SiCw/alumina matrix composites. Completed.	Nov. 1988
Dispersion and homogenization of SiCw/silicon nitride matrix composites. Completed.	Nov. 1988
Final report, approved new milestone date.	June 1989

Phase II:

Milestone chart to be produced after contract negotiations are completed.

Presentations and Publications

D. E. Wittmer and W. Trimble, "Ceramic Composites Processed by Turbomilling", Proceedings of the 3rd International Symposium on Ceramic Materials for Engines, Las Vegas, N.V. November 27-30, 1988, in press.

Presentations and Publications (continued)

D. E. Wittmer and W. Trimble, "Fracture Behavior of SiCw Reinforced Ceramic Matrix Composites", Ceramic Engineering and Science Proceedings, Vol. 9, 1989, in press.

D. E. Wittmer, "Processing of Ceramic Whisker Reinforced Ceramic Matrix Composites", Proceedings of the Joint Conference on Advanced Ceramic Materials, April 4-5, 1989, Materials Technology Center, Southern Illinois University, Carbondale, IL.

Reinforcements for High Temperature Ceramics

Christos I. Kyriacou (Keramont Corporation)

Objective/scope

The production of TiB_2 whiskers; consolidation of composites of SiC matrix with TiB_2 whiskers, and testing of composite properties in air above 1200°C.

Technical progress

The research to be carried out on this contract has three main objectives as they are defined in the objective/scope section above. Work on the contract until now has focussed on designing and building the pilot facility. Research until now has focussed on the development and optimization of TiB_2 whisker growth.

The whiskers are produced by the reduction of the metal halides of titanium and boron. Two possible reaction routes were investigated:

$$TiCl_4 + 2BBr_3 + 5H_2 \rightarrow TiB_2 + 6HBr + 4HCl \qquad [1]$$

$$H(1400°K) = +177.457 \text{ kJ/mole}, \quad G°(1400°K) = -80.317 \text{ kJ/mole}$$

$$TiCl_4 + 2BCl_3 + 5H_2 \rightarrow TiB_2 + 10\ HCl \qquad [2]$$

$$H(1400°K) = +335.987 \text{ kJ/mole}, \quad G°(1400°K) = -29.363 \text{ kJ/mole}$$

The reaction route [2] is the most commonly used in the formation of TiB_2. Previous work done on TiB_2 utilized the reaction route [2] for the formation of coatings[1] and whiskers[2]. From thermodynamic analysis of the two reaction routes, the maximum theoretical yield of formation of the TiB_2 is 73.9% from reaction [1] and 46.5% from reaction [2]. The production of TiB_2 is thermodynamically favored by reaction route [1], giving a larger theoretical yield by a factor of 2. The reaction route [1] was chosen for the research to be carried out in this contract and the formation of TiB_2 whiskers.

The optimum conditions for the formation of TiB_2 from reaction route [1] was further investigated by thermodynamic equilibrium analysis as a function of gas composition and temperature. The optimum theoretical yield of TiB_2 was found at a ratio of [B/(B + Ti)] of 2/3. The theoretical yield of TiB_2 was found to increase sharply with decrease in the [Halogen/(Halogen + H)] ratio or increasing dilution of the gases with excess hydrogen. The concentration of products and by-products from the reaction as a function of temperature is shown in Figure 1. The mass balance for the reaction as obtained from thermodynamic analysis is shown in Table 1.

Table 1. Thermodynamic equilibrium Composition of the reactants and products.

FURNACE INPUT

SPECIES	MOLE FRACTION	MASS FRACTION
$TiCl_4$	0.0769	0.2668
$BBr_3(g)$	0.1538	0.7048
$H_2(g)$	0.7692	0.0284

FURNACE OUTPUT

SPECIES	MOLE FRACTION	MASS FRACTION
$TiCl_3(g)$	0.00217	0.0074
$TiCl_4(g)$	0.00464	0.0195
$BCl_3(g)$	0.01372	0.0355
HCl(g)	0.18837	0.1518
HBr(g)	0.38168	0.6827
$H_2(g)$	0.35210	0.0157
$TiB_2(s)$	0.05682	0.0873

VOLUME FRACTION = MOLE FRACTION (ASSUME IDEAL GAS LAW)

T = 1400°K B/B+Ti = 2/3 HALOGEN/HALOGEN+HYDROGEN = 1/3

THEORETICAL YIELD = 73.9%

If the deposition rate of TiB_2 is controlled, other variables can be monitored to study the effect of the experimental parameters on the growth and morphology of the whiskers. Such parameters are supersaturation, gas composition, gas flow velocity, type of substrate, furnace geometry, etc.

The second most important parameter for the growth of the whiskers we believe to be the catalyst which at the liquid state will grow a needle shape single crystal of TiB_2 through a Vapor-Liquid-Solid (VLS) growth mechanism[3,4]. Previous work at Keramont indicated that a catalyst of Au-Pd was able to produce TiB_2 whiskers via the VLS growth mechanism. The Au-Pd catalyst however, becomes an extremely high cost factor for the production of whiskers. Other catalyst systems are being examined to evaluate the effect of the catalyst on the growth of TiB_2 whiskers by the VLS mechanism.

Experimental Apparatus

The formation of TiB_2 whiskers is being carried out in a quartz tube furnace 3 inches in diameter, 30 inches long. The whisker are grown on a substrate which is resistance heated to about 1200°C. Two type of substrates are being examined, graphite and quartz. The precursor gases of titanium chloride ($TiCl_4$, purity 99.9%), and boron bromide (BBr_3, purity 99.99%) are transferred from commercial containers into saturation vessels. The vessels are maintained at a temperature corresponding to a certain vapor pressure of the liquids. The vapors are then carried into the reaction furnace by a saturated hydrogen steam. The feed gas composition is controlled by the precursor gas saturation temperature and the hydrogen flow rate. The overall experimental apparatus is shown in Figure 2. The exhaust gases composed mainly of HBr and HCl are neutralized with caustic soda and the remaining hydrogen is burned. The reactivity of the gases and the efficiency of the reaction is monitored by a mass spectrometer. A series of experiments is being carried out to optimize the quality and increase the yield of the whiskers. The experiments have begun recently and no conclusive results can be published at this time.

Status of milestones

The schedule of the main milestones is as follows:

i) August 30, 1989: Production of TiB_2 whiskers.
ii) October 30, 1989: Consolidation of SiC matrix with TiB_2 whiskers.
iii) November 30, 1989: Testing of composite properties.

The schedule of the milestones is proceeding as planned.

Publications

None

References

1. S. Motojima et al, "Chemical Vapor Growth of Titanium Diboride Whiskers" Bulletin of the Chemical Society of Japan, Vol 48 (41), 1975.

2. T. M. Besmann and K. E. Spear "Analysis of the Chemical Vapor Deposition of Titanium Diboride" J. Electrochem. Soc. Solid-State Science and Technology, Vol 124, No. 5, (1977).

3. E. I. Givargizov, Current Topics in Material Science, Volume 1, Chapter 3. Edited by E. Kaldis. North-Holland Publishing Company, 1978.

4. R. S. Wagner, Whisker Technology, Chapter 3. Edited by A. P. Levitt. Wiley-Interscience Inc.

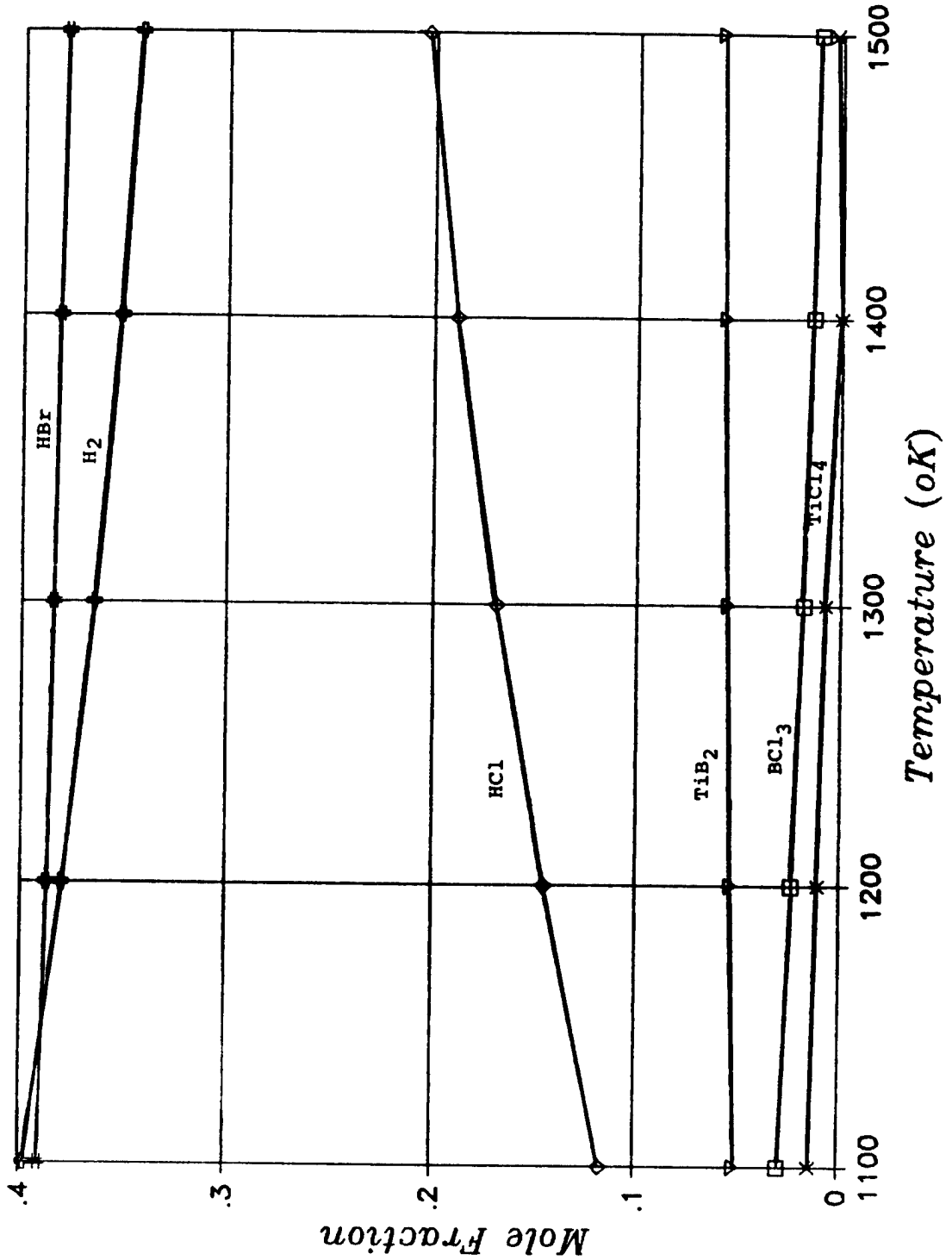

Figure 1. Equilibrium concentration of gases as a function of temperature. Gas input $TiCl_4$: BBr_3: H_2 = 0.0769: 0.1538: 0.7692. B/(B + Ti) = 2/3, Hal/(Hal + H) = 1/3.

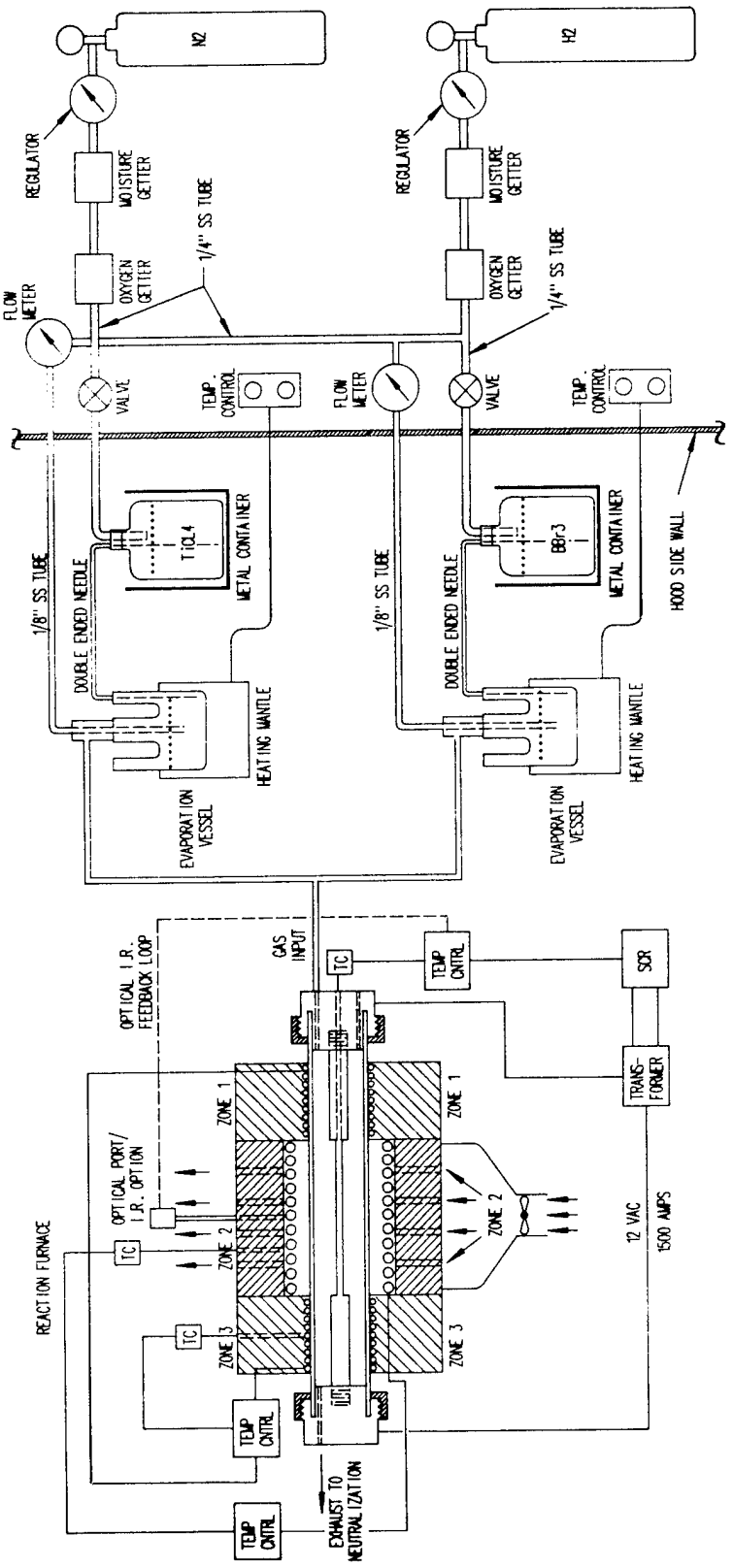

Figure 2. The pilot facility for the production of TiB_2 whiskers.

1.1.2 Silicon Nitride

Sintered Silicon Nitride
George Gazza (U.S. Army Materials Technology Laboratory)

Objective/scope

The program is concentrating on sintering compositions in the Si_3N_4-Y_2O_3-SiO_2 system using a two-step sintering method where the nitrogen gas pressure is raised to 7-8 MPa during the second step of the process. During the sintering, dissociation reactions are suppressed by the use of high nitrogen pressure and cover powder of suitable composition over the specimen. Variables in the program include the sintering process parameters, source of starting powders, milling media, time, and specimen composition. Resultant properties determined are room temperature modulus of rupture, high temperature stress-rupture, oxidation resistance, and fracture toughness. Successful densification of selected compositions with suitable properties will lead to densification of injected molded or slip cast components for engine testing.

Technical progress

An investigation of slip casting methods for composition No. 39 (85.8m/o silicon nitride-4.73m/o yttria-9.47m/o silica), is being carried out in order to minimize "green" body agglomerates to reduce pore formation during sintering and develop complex shape forming casting process (Fig. 1) to produce disc shaped specimens. The base composition with and without Mo2C is milled in aqueous solution with stearic acid and a 3-5% methocel or XUS 40303.00 binder (Dow Chemical Co., Midland, MI). The XUS binder is dissolved in hot water prior to adding to the slip. The slip is placed in a flask and stir blended under vacuum to remove entrapped air. The slip is pressure cast, dried, and subjected to an organics burnout treatment prior to sintering. The use of Darvan C (R. T. Vanderbuilt Co., Norwalk, CT), glycerine and lignosols as dispersants are also being studied.

In addition to in-house slip casting studies, a slip cast body of composition No. 39 was produced outside of MTL. Slips used to form the casting exhibited a low viscosity of approximately 30 cps measured at 50 rpm with a Brookfield viscometer. Solids loading was 50w/o at a pH of approximately 10.20. The slip was deaired prior to casting. Thusfar, slip cast "green" body densities have not increased beyond density levels produced by cold pressing of powder compacts. Also, considerable cracking occurs as the slip casts body size increases. It is believed that this is due to the relatively narrow particle size distribution of the Toyo-Soda powder used for the study. The elimination of surface impurities, such as retained Cl from a precursor of the synthesis process, will be attempted by prefiring the silicon nitride powder in a nitrogen atmosphere at approximately 1200°C prior to mixing with other compositional components and slip casting. Although "green" densities of the slip cast bodies are similar to those produced

by cold pressing, it is not known at this time whether the pores in the slip cast material are finer and more uniformly distributed than in the cold pressed specimens. Further efforts will concentrate on pressure slip casting which appears to produce improved bodies with reduced tendency to crack. Sintering of pieces from cracked bodies at 1940-1950°C resulted in high density specimens, 3.27-3.29g/cc.

Specimens will be produced in simple geometric shapes, such as disc and bars, to study the process and for evaluation of mechanical behavior after sintering the "green" bodies. NDE techniques will also be used to examine "green" specimens for identification of flaws which may be carried into the densified specimens to serve as fracture origins.

Powder of composition No. 39 was also obtained from a spray drying process where only soft agglomerated are expected to form. A dispersant was added to the powder during a preliminary milling process and was not removed prior to sintering. Higher weight loss values (5%) than usual were noted and some surface cracks formed on the compact during sintering. Further compacts will be sintered after an initial burnout treatment.

Specimens of composition No. 39 containing 1m/o Mo2C in the as-sintered condition and after stress-rupture testing (900°C for 150 hours under 300 MPa stress, then raised to 1250°C for 162 hours under 400 MPa stress) were sent to ORNL for examination by STEM. Results of the analytical microscopy by L. Allard and T. Nolan indicated that the specimens were comprised of beta silicon nitride grains with interconnecting single crystal boundary regions (Figure 2a). Particles of Mo_5Si_3, as shown in Figure 2b, were dispersed throughout the microstructure. Figures 2b and 3 both show cavities formed in the microstructure which developed during stress-rupture testing. The boundary regions were found to consist of Y and Si (Fig. 4). Mo was not detected in these areas. Analysis of the Mo_5Si_3 particles (Fig. 5) indicated a small amount of Fe present.

Established milestones

A. Evaluate slip casting methods for compositions of interest. Focus on pressure slip casting techniques. Re-examine sintering of silicon nitride containing N-apatite as the boundary phase (May 1, 1989).

B. Determine strength and intermediate temperature stability of sintered specimens containing the N-apatite. Generate "green" bodies of silicon nitride with pyrosilicate or N-apatite grain boundary phases using established slip casting procedures (July 1, 1989).

C. Complete data base of properties using sintered specimens from slip cast bodies. Complete microstructural examination of sintered specimens. Write final report (September 30, 1989).

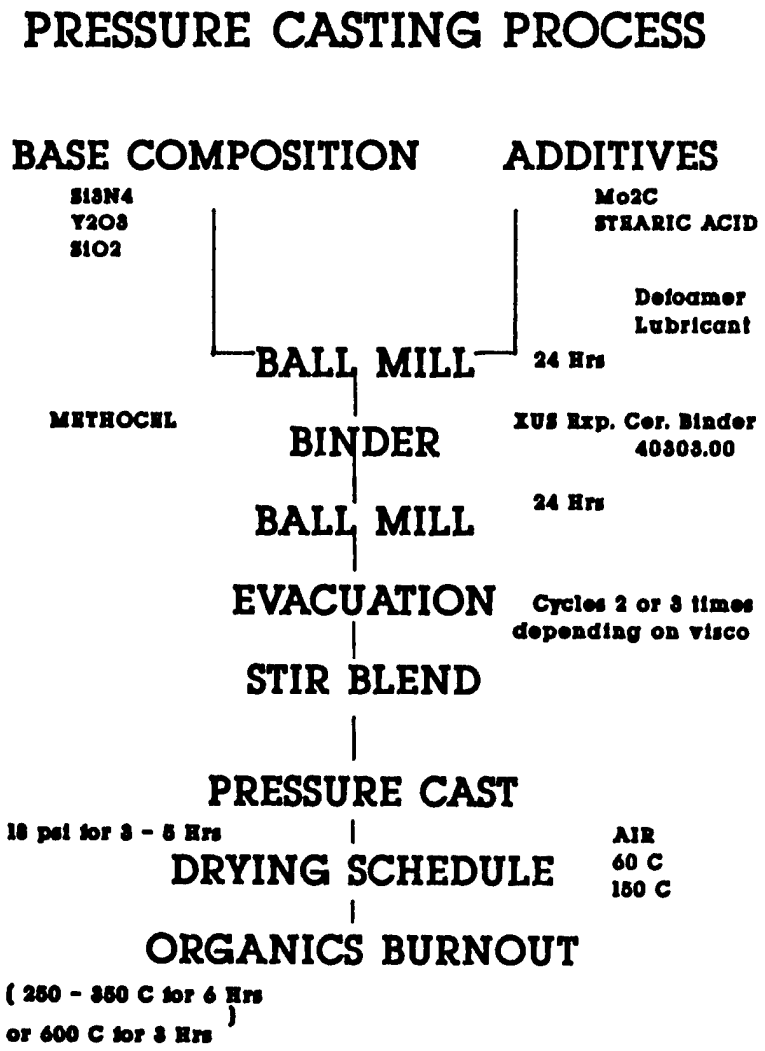

Fig. 1. Flow chart of pressure casting method for Si_3N_4-Y_2O_3-SiO_2 composition.

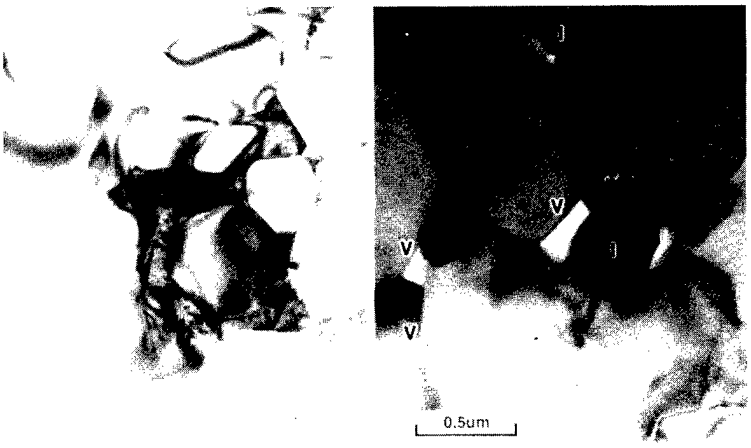

AS-SINTERED (a) vs. STRESS RUPTURE TESTED (b)

Note voids (V) in boundary regions of the tested specimen. Results of electron diffraction and x-ray elemental analysis of inclusions (I) are consistent with a Mo_5Si_3 phase.

Fig. 2. Stem micrograph of (a) as-sintered specimen and (b) stress-rupture tested specimen.

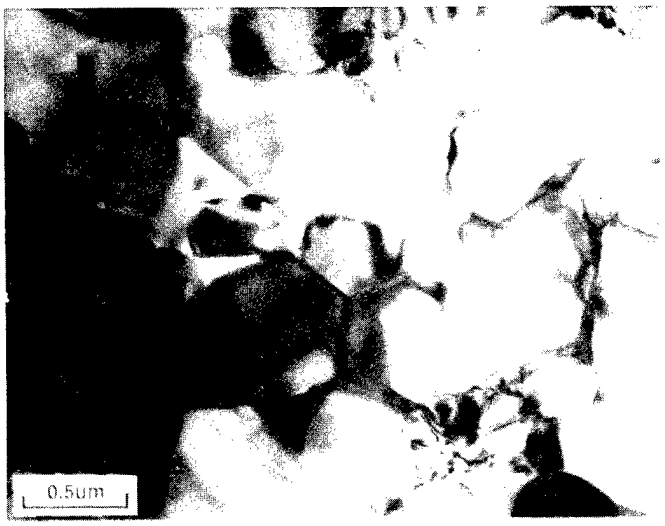

MICROSTRUCTURE TYPICAL OF THE STRESS RUPTURE SPECIMEN.
Note voids in several locations.

Fig. 3. Microstructure of stress-rupture tested specimen.

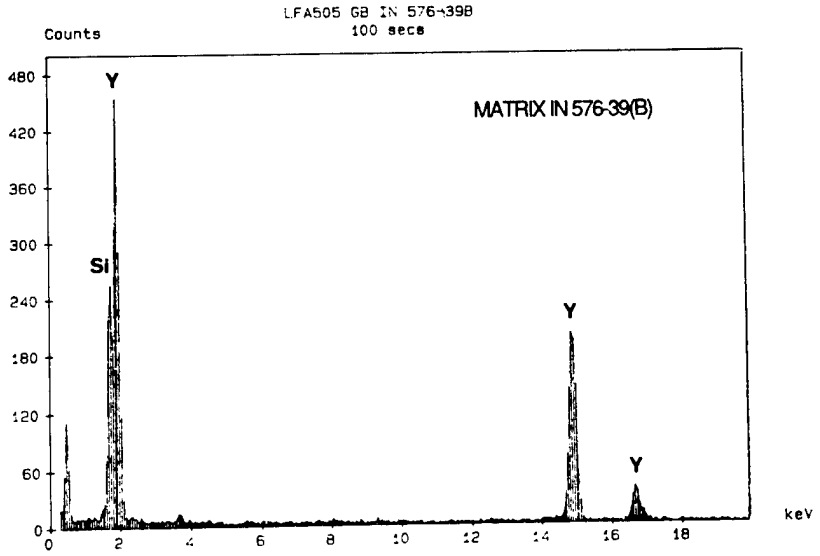

Fig. 4. EDXA of boundary region in sintered specimens.

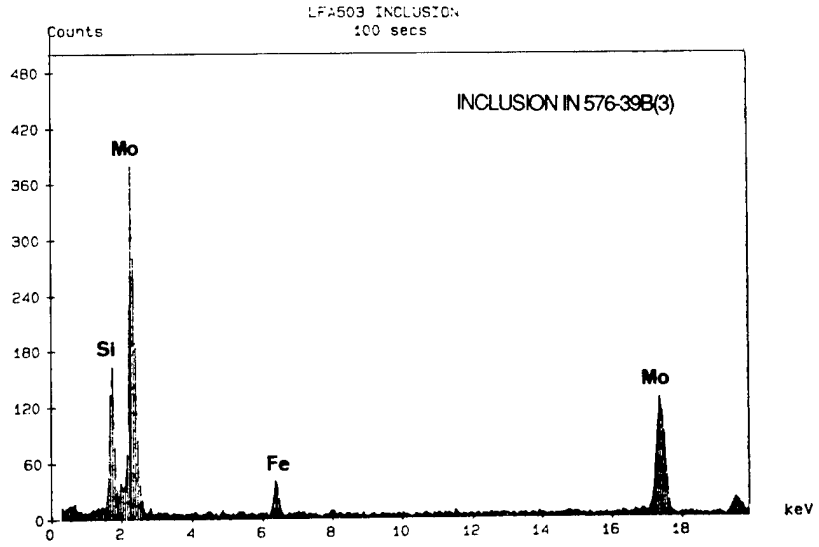

Fig. 5. EDXA of Mo_5Si_3 particle.

Synthesis of High Purity Sinterable Si_3N_4 Powders

G. M. Crosbie, J. M. Nicholson, R. L. Predmesky, E. D. Stiles, and E. L. Cartwright (Ford Motor Company)

Objective/scope

The goal of this task is to achieve major improvements in the quantitative understanding of how to produce sinterable Si_3N_4 powders having highly controlled particle size, shape, surface area, impurity content and phase content. Through the availability of improved powders, new ceramic materials are expected to be developed to provide reliable and cost-effective structural ceramics for application in advanced heat engines.

Of interest to the present powder needs is a silicon nitride powder of high cation and anion purity without carbon residue.

The process study is directed towards a modification of the low temperature reaction of $SiCl_4$ with liquid NH_3 which is characterized (1) by absence of organics (a source of carbon contamination); (2) by pressurization (for improved by-product extraction efficiency); and (3) by use of a non-reactive gas diluent for $SiCl_4$ (for reaction exotherm control).

In the "further development" phase begun October 1987, our goal is to test for unique properties of the ceramics sintered from the low carbon powders, before committing to a pilot plant of the 110 L scale designed. In view of powder quantities needed to allow tests of the ceramics, the major task is to design and implement a scaled-up version of the silicon nitride synthesis processing equipment to produce greater amounts of powders with high cation and anion purity and low carbon residue.

Technical progress

Introduction

Silicon nitride based ceramics are often considered to represent the toughest of the high-temperature (above 1000°C) monolithic ceramics intended for advanced heat engine use. Also, due to a desirable combination of lower temperature properties (wear resistance, low density, high hardness, and toughness), the nitride ceramics are already finding commercial applications in certain passenger vehicles.

Ceramic reliability and cost depend on powder qualities and subsequent processing. Because powders can limit the capability to achieve unique sintered properties and to fabricate complex shapes, the availability of appropriate powders is critical to advanced ceramics research. In the case of silicon nitride ceramics, the powder purity is especially important, since a low solubility in silicon nitride for many impurities leads to high concentrations of those impurities in grain boundary phases. Also, carbon residues (which are found in some otherwise high purity powders) are considered to be detrimental to second phase oxynitride development, thermal stability, and mechanical properties.

Previous work

The primary points of reference for the previous process work are the 1986 and 1987 Automotive Technology Development Contractors' Meeting proceedings papers[1,2] and the previous semiannual reports.[3,4]

In the previous lab demonstration work, we prepared a novel process flowsheet for preparation of Si_3N_4 with a block flow diagram and a mathematical model of mass and heat balances for the "vapor chloride-liquid ammonia" process. We observed that the cooling from latent heat of vaporization of NH_3 more than offsets the heat of reaction at 0°C and 75 psig.

Powder characteristics met or were approaching target values. Key results were achieved in the areas of phase and microstructure, and carbon purity. Si_3N_4 powder was produced with phase content, particle size and shape which are close to those characteristics considered desirable for pressureless sinterability.

Specifically, the powder derived by thermal decomposition of an intermediate imide product (from reaction of $SiCl_4$ with liquid NH_3 0°C and 75 psig) was principally alpha silicon nitride (as determined by x-ray diffraction, which has little sensitivity to amorphous phases) with crystallite size of 0.2 to 0.3 micron and primarily equiaxed particle shape.

The process was identified to have features which are important for scale-up. Key features of near-neutral heat balance and liquid-like materials handling were demonstrated.

Also, improvements were achieved in yield, laboratory production rate, cation purity, and alpha/beta ratios.

In the extension period work, we prepared a pilot plant design for the "vapor chloride-liquid ammonia" process, carried out additional process development including the "liquid chloride-liquid ammonia" direct reaction, campaigned runs to test process stability, carried out sintering tests, and reported on a new analytical method for discriminating amorphous and crystalline phases in silicon nitride powders.

Previous pre-pilot plant work

In the "further development" phase begun in the previous period, we increased reactor volume, took steps to improve quality of sealing of vessels and piping, and incorporated direct mechanical agitation while under pressure. By this means, we have equipment to produce 100 g lots of powder (by liquid-liquid and vapor-liquid routes) for sintering tests and characterization of the sintered materials.

Through joint work with an engineering firm, the 4 L scale skid-mounted imide reactor system was installed in a dynamometer test cell and pressure tested to 225 psig (1.65 MPa absolute) with nitrogen in March 1988.

We found evidence for rapid rinsing out of the chloride by-product with the use of agitation. We installed additional subsystems to the prepilot plant, found high oxygen contents in initial nitride powders produced, and extended transient flow modeling of the saturator.

Summary of current period work

Although we still have not achieved a powdermaking run processed entirely through the dedicated pre-pilot plant equipment, the quality of x-ray diffraction result for a February 1989 batch justified extensive characterization, which we report here. Even with discounting of 5% for surface adsorbed oxygen, the powder has 4.5% oxygen contamination.

The properties of Batch 5437-23 (liquid-liquid rxn.) are as follows:

CHEMICAL		PHYSICAL	
	wt.%		
Carbon	0.1	BET Surface Area	39 m^2/g
Nitrogen	33.3		
Oxygen	9.8	$Diameter_{50,sed}$	1.9 μm
Aluminum	0.59		
Iron	0.21	Mass finer than 1 μm	41.4%
Calcium	0.05		
		XRD: alpha/ (alpha + beta)	92%

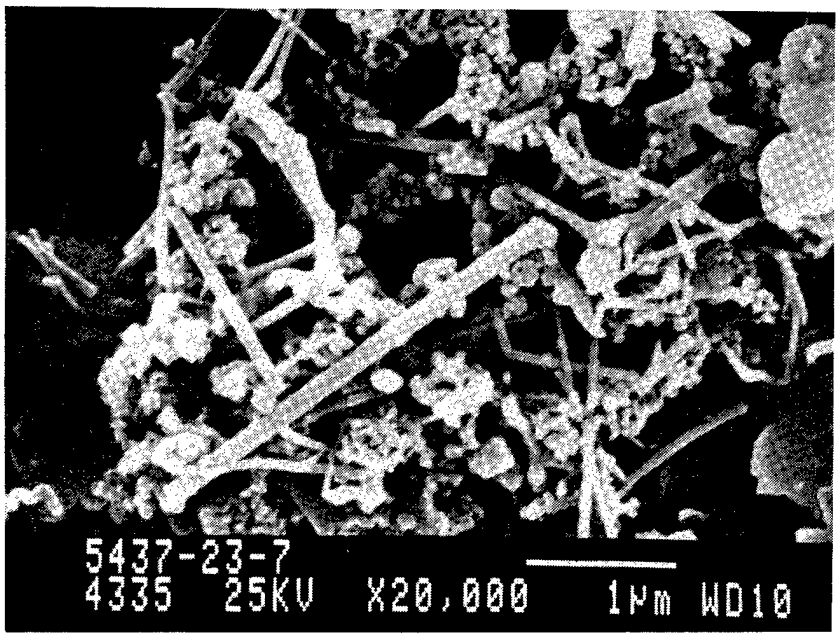

Fig. 1. Scanning electron micrograph of Batch 5437-23. Crystallites smaller than 0.1 μm are seen as well as substantial fiber content. Dispersion procedure: (1) The powder was mixed into a solution of 2-ethyl 1-hexanol + 2% sulfonated mineral oil [Twitchell 8262 Base, Emery Industries, Inc., 4900 Este Ave., Cincinnati, Ohio 45232]; (2) the resulting slurry was dispersed into n-hexanes in an ultrasonic bath; (3) a drop was applied to a carbon planchet with the excess hexane-rich suspension wicked out of the observation area with lens tissue. Photograph courtesy of W. T. Donlon and Y. T. Lu.

Process development

Due to the large driving force for reaction of water with ammonia and for reactions of oxygen and water with the intermediate imide to form silica, the strategy we have followed (in the 500 mL scale apparatus) was to do all processing in a closed system of pipes and vessels.

What stands in the way of completing a run with the dedicated equipment (with all anaerobic transfers) is the decomposition furnace. Although rated for 1800°C use, the heating elements (bars of $LaCrO_3$) distorted and showed signs of incipient melting at 1420°C (at the heater bars). When contact occurred with the decomposition tube, perforation occurred and the amorphous silicon nitride inside turned to sand.

To further eliminate oxygen and water contamination sources, we successfully introduced "sniffing" type helium leak detection in this period. This sensitivity to leaks led to several changes: the change of material in the decomposition vessel seal, re-orienting a backwards pipe section, and change of the material in all VCR fittings from PTFE to an elastomer. Leaks in these areas would certainly contribute to O content.

In an unusual application of the method, we carried out the helium leak detection with the system cold and full of ammonia. Subsystems which were tight at room temperature became leaky after chilling. The line from the reactor to the condenser was rebuilt with an all-welded design.

No runs were made in March 1989 during the delays waiting to put new heating elements into the furnace and to rebuild lines.

Three runs were completed in the December 1988-January 1989 period. In the last of the three runs, a 38 g batch (largest yet!) was produced with a tap density of 0.4 g/cm^3 (promising for subsequent processing) with strong alpha-Si_3N_4 signal in XRD pattern, but unfortunately also oxynitride and bulk oxygen content. An attempt in the middle run to reduce oxygen by use of a N_2 - 4% H_2 gas mixture led to reductions of both nitrogen and oxygen content (with some visual evidence that the imide was reduced to silicon metal around 500°C).

Infant furnace heater element failures (and uncontrolled room temperatures and air-flow rates) have affected peak temperatures, in turn, requiring manual transfer to another furnace to complete the decomposition (first and third runs).

In one run in the October-November 1988 period, we produced 67 g of the intermediate product. Chemical analysis showed that only about 50% of the chloride was removed by rinsing. The loss of ammonia with a leak at the bottom valve contributed to the incomplete Cl removal. Also, lower ambient temperatures are now seen to lead to lower quantities of NH_3 transferred (at a fixed pressure differential), as evidenced by the total NH_3 actually used falling short by about 40% from that previously loaded. Reloading NH_3 by mass, not volume, is suggested for cooler ambient temperatures.

Equipment and process modifications

Based on a vendor's analysis (and our own analysis) of a few valve failures, we specified and installed a new type of valve on the lines used for piping solids-containing intermediate imide products.

Leaks arose in the ram-type valve at the bottom of the reactor. The ram was resurfaced, new teflon O-rings installed, and a supporting fixture was placed underneath to limit side-loading of the ram upon pneumatic actuation.

Fixes which had been made in previous months to the bottom valve and slurry handling valves continued to perform satisfactorily.

The cleanout sequence was revised to include a hot water rinse, an alcohol rinse, and a 45°C vacuum "bake-out." The run start-up routine now includes dumping of the first load of ammonia, as was suggested during a site visit.

Transient flow modeling

As reported in the previous semi-annual report, a technical report was prepared by L.-F. Chen of the Control Systems Department (Ford Research) to describe the modeling of flow transients for the saturator that has been built for use with the pre-pilot plant. In previous laboratory demonstration tests of the "vapor $SiCl_4$ - liquid NH_3" process, flow transients have caused clogging when the vapor repeatedly supersaturates at the reactor entry during operation.

Initial modeling results showed that supersaturations can readily occur with less than 2 psig drops in system backpressure, when no flow restrictions are present. With sharp flow restrictions, the transient supersaturation can be suppressed in the initial design. However, the sharp restrictions are not desirable as they represent points for clogs to form.

A more complex transient flow model was generated with an additional balanced volume to provide symmetrical flows during pressure transients. In this case, no sharp flow restrictions were necessary. With the added volume, the response to a pressure drop was a simple relaxation, rather than an overshoot. This more complex version was used to show that supersaturations could be avoided without sharp flow constrictions as long as appropriate volume parameters were chosen. This meets the modeling milestone for the saturator.

In order to experimentally verify the state-space model of transient flows in the saturator, we have implemented and instrumented the balanced flow saturator design adjacent to the process apparatus. The flowmeters and other hardware for the balanced flow design have been installed and have been electrically connected to the data acquisition system. Following discussions, pressure sensors and flow constrictions were located at critical points upstream and downstream of the mixing point. The pressure sensor signals were calibrated with the data acquisition system.

Status of milestones

This two-year follow-on contract was initiated October 1, 1987 for the "Further Development of Synthesis of High-Purity Sinterable Silicon Nitride (Si_3N_4) Powders for Application in Ceramic Technology for Advanced Heat Engines Project." Key 1988 milestones were completed on schedule: commissioning of scaled-up equipment and the modeling of saturator transient performance.

Although the 1989 milestones are on schedule, the furnace problems have slowed production of lots of powder for sintering tests. A three-month extension has been agreed upon.

Publications

G. M. Crosbie, R. L. Predmesky, J. M. Nicholson, and E. D. Stiles, "Prepilot Scale Synthesis of Silicon Nitride Under Pressure," *Bull. Am. Ceram. Soc.*, 68 [5] 1010-14 (1989).

K. R. Carduner, R. O. Carter III, M. J. Rokosz, C. R. Peters, G. M. Crosbie, and E. D. Stiles, "Silicon-29 Magic Angle Spinning Nuclear Magnetic Resonance of Sintered Silicon Nitride Ceramics," in press, *Chemistry of Materials*, June 1989.

G. M. Crosbie, J. M. Nicholson, and E. D. Stiles, "Sintering Factors for a Dry-Milled Silicon Nitride-Yttria-Alumina Composition," *Bull. Am. Ceram. Soc.*, 68 [6] in press, June 1989.

K. R. Carduner and G. R. Hatfield, "Solid State NMR: Applications in High Performance Ceramics," accepted for publication, *J. Mater. Sci.*

G. M. Crosbie, J. M. Nicholson, R. L. Predmesky, E. D. Stiles, "Pre-Pilot Synthesis of Low-Carbon Si_3N_4," manuscript submitted to DKG for publication in the proceedings the Second International Conference on Ceramic Powder Processing Science, October 12-14, 1988, at Berchtesgaden (Bavaria), Fed. Rep. of Germany.

G. M. Crosbie, J. M. Nicholson, R. L. Predmesky, and E. D. Stiles, "Synthesis of Low-Carbon Si_3N_4: Pre-Pilot Study," presented at the 91st Annual Meeting of the American Ceramic Society, April 23-27, 1989, Indianapolis, Indiana.

G. M. Crosbie, ORNL Foreign Trip Report, ORNL/FTR-3107, October 31, 1988.

References

1. G. M. Crosbie, "Silicon Nitride Powder Synthesis," pp. 255-265 in *Proc. of the 24th Automotive Technology Development Contractors' Coordination Meeting, Soc. of Automotive Engineers*, Warrendale, Pa., 1987 (P-197).

2. G. M. Crosbie, J. M. Nicholson, R. L. Predmesky, and E. D. Stiles, "Silicon Nitride Powder Synthesis Program," pp. 127-135 in *Proc. of the 25th Automotive Technoloqv Develooment Contractors' Coordination Meeting, Soc. of Automotive Engineers*, Warrendale, Pa., 1988 (P-209).

3. G. M. Crosbie, "Synthesis of High Purity Sinterable Si_3N_4 Powders," pp. 17-23 in *Ceramic Technology for Advanced Heat Engines Project Semiannual Report for October 1986 through March 1987*, ORNL/TM-10469, Oak Ridge National Laboratory, Oak Ridge, Tenn., August 1987.

4. G. M. Crosbie, J. M. Nicholson, R. L. Predmesky, and E. D. Stiles, "Synthesis of High Purity Sinterable Si_3N_4 Powders," pp. 20-27 in *Ceramic Technology for Advanced Heat Engines Project Semiannual Report for April Through September 1988*, ORNL/TM-11116, Oak Ridge National Laboratory, Oak Ridge, Tenn., March 1989.

Microwave Processing of Silicon Nitride
H. D. Kimrey and M. A. Janney (Oak Ridge National Laboratory)

Objective/scope

The objective of this research is to identify those aspects of microwave processing of silicon nitride that might (1) accelerate densification, (2) permit sintering of high density with much lower levels of sintering aids, (3) lower the sintering temperature, or (4) produce unique microstructures.

Technical progress

An annealing study of dense silicon nitride was initiated in the 2.45-GHz microwave furnace. The experiments are to determine if (1) the room-temperature mechanical properties can be enhanced, and (2) if the refractoriness of the grain boundaries can be enhanced by a microwave anneal. Samples were obtained from GTE and were of a PY6 composition. The samples had a cross-sectional shape of a thunderbird and were cut into approximately 30-g pieces. The samples were annealed with a dummy piece of the same composition so that the thermocouple would be effectively inside the sample. The insulation scheme developed last year was used with the packing powder containing 2 wt % yttria to reduce yttria migration. Ten anneals were performed during the reporting period. These are shown in Table 1 along with the annealing conditions.

Table 1. Time and temperature parameters for microwave annealing samples.

Sample number SNA8900X-Y	Anneal temperature (°C)	Anneal time (h)
5-B	1629	2
3-B	1698	2
5-A	1696	5
5-C	1680	10
2-C	1765	1
1-B	1750	2
3-D	1748	5
1-C	1800	2
3-A	1800	5
2-A	1800	6

The specimens were machined into bars for flexural strength testing. Figure 1 is a Weibull plot of flexure strength using the four-point bend method for five of the samples. The inner and outer spans were 6.35 mm (0.25 in.) by 12.7 mm (0.4 in.) respectively. The load rate was 1.27 mm/min (0.05 in./min). The test bars were nominally

2.79 mm (0.110 in.) by 3.05 mm (0.120 in.) in cross section by 19.05 mm (0.750 in.) in length. The average strength of the as-received material was about 730 MPa (106 ksi), similar to quoted values. Inspection of the fracture surfaces on a number of broken bars under a stereo microscope revealed a large number of dark spots. A spot of this type is usually the fracture origin in these samples. In all cases the microwave annealed samples have reduced strength. Each of the samples analyzed thus far has been overfired. The lowest temperature/shortest time sample is SNA89002-C. This sample was annealed at 1765°C for 1 h. The strength was reduced by roughly 10% with the distribution in strengths being significantly tighter. Scanning electron microscope examination was done on the as-received material and the 1765°C, 1-h sample. The microstructure of the as-received sample consisted of silicon nitride, yttrium silicate glass, and possibly, silicon oxynitride. The annealed sample had porosity that correlated with the disappearance of the yttrium silicate glass phases in the as-received sample. One might conclude the migration of yttrium from the sample is associated with the formation of the porosity. Along with the formation of porosity, we noted a 0.5% linear expansion of the sample and a 1% weight loss.

Publications

None

Milestones

On schedule

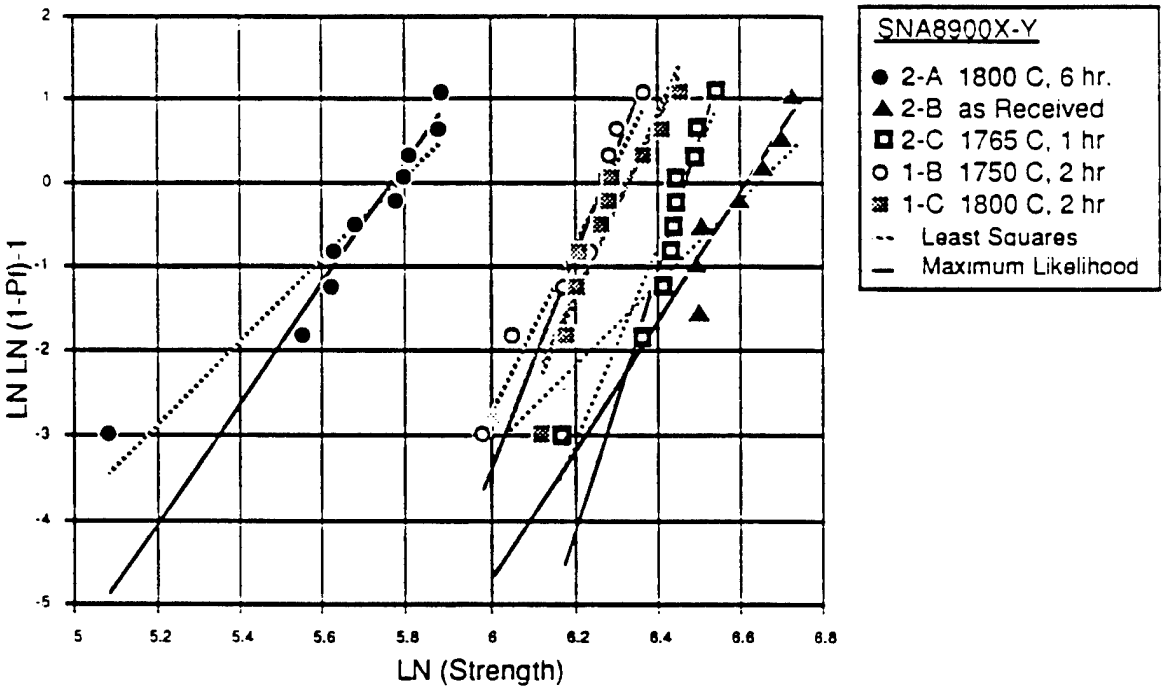

Fig. 1. Weibull plot of microwave-annealed GTE PY6 silicon nitride.

Silicon Nitride Milling Characterization

S. G. Malghan
(National Institute of Standards and Technology)

Objective/Scope

Ceramics have been successfully employed in engines on a demonstration basis. The successful manufacture and use of ceramics in advanced engines depends on the development of reliable materials that will withstand high, rapidly varying thermal stress loads. Improvement in the starting ceramic powders is a critical factor in achieving reliable ceramic materials for engine applications. Milling of powders is an integral unit operation in the manufacture of silicon nitride components for advanced energy applications. The production and use of these powders require the use of efficient milling techniques and understanding of characteristics of the milled powders in a given environment. High energy attrition milling appears to offer significant advantages over conventional tumbling and attrition mills.

The objectives of this project are to: (1) develop fundamental understanding of surface chemical changes taking place when silicon nitride powder is attrition milled in aqueous environment, and (2) demonstrate the use of high energy attrition milling for silicon nitride powder processing, by developing measurement techniques and data on the effect of milling variables on the resulting powder. This study will provide data and models for effective application of high energy attrition milling to industrial processing of silicon nitride powder. It also will provide recommended procedures for physical and surface chemical characterization of powders and slurries involved in the milling process.

Technical Progress

The technical progress covered in this report includes descriptions of selection criteria of milling system and powder, characterization of starting powder, and procedure for size distribution determination.[1]

Milling System and Powder Selection- A horizontal ceramic mill in which all wetted parts are constructed of silicon nitride was selected, based on initial criteria that silicon nitride powder

---

[1] Certain commercial equipment, instruments and materials may be identified in this report in order to adequately specify the experimental procedure. Such identification does not imply recommendation or endorsement by the National Institute of Standards and Technology, nor does it imply that the materials or equipment identifies are necessarily the best available for the purpose.

milling will be conducted in a high energy attrition milling system and contamination from milling will be minimized. In this mill, the milling media are agitated with discs that push them against the product flow, eliminating dead areas in the milling chamber. In addition, power input to this milling system is expected to be in the range of 1-2 kw per liter of mill volume. This mill is expected to be in operation in the third quarter 1989. In the mean time, search for HIP'd silicon nitride media of 0.5 to 1.0 mm diameter is in progress.

Discussions with some of the major silicon nitride powder users in the US indicate that the use of UBE powder could benefit directly or indirectly their efforts in processing of these powders. Hence UBE powders are being used in this project.

Characterization of Starting Powder- Since initial milling tests are planned with SN E-3 powder from UBE, more effort has been devoted to characterize the same. Determination of size distribution of this powder by X-ray sedimentation using Sedigraph (Micromeritics Inst. Corp.) showed that suspension preparation procedure had a major effect on variability of the size distribution data. Basic surface properties of the SN E-3 powder in aqueous suspensions were determined by electrokinetic sonic amplitude (ESA) measurements using Matec's ESA system. These data indicate that reproducibility of ESA and isoelectric point (IEP) measurements are excellent. The IEP data of 2 to 10 % (v/v) powder in aqueous environment were in the range of pH = 5.0 to 5.2. Ageing of aqueous suspensions for four hours had no effect on the surface properties of this powder.

Procedure for Size Distribution Determination- A statistical design study for identification of effects of suspension preparation parameters has been underway using UBE's SN E-10 silicon nitride powder. Out of three replicate series of experiments planned, two series have been completed. These data indicate that reproducibility of experimental data are far better at shorter ultrasonication times and lower power inputs. The ultrasonication time and power input can change the entire size distribution curve and shift d_{50} from 0.54 to 0.74 micron. A shift of this magnitude is considered to be significant.

Status of Milestone

Task 5. Subtasks 5.1.2 and 5.1.3 are behind schedule due to delay in ordering the attrition mill and long lead time required by the manufacturer of this mill. Once the mill arrives, additional effort will be provided to get back on schedule.

1.1.4 Processing of Monolithics

Improved Processing

R. L. Beatty, R. A. Strehlow, and O. O. Omatete (Oak Ridge National Laboratory)

Objective/scope

The objective of this project is to determine and develop the reliability of selected advanced ceramic processing methods. This project is to be conducted on a scale that will permit the potential for manufacturing use of candidate processes to be evaluated.

Technical progress

Gel-casting of silicon nitride

Work was begun to develop methods of gel-casting silicon nitride formulations in addition to continuing some work with alumina. We recognize that several of the steps of the process for alumina will need to be altered to use silicon nitride. The first objective in the development of the process for silicon nitride is to develop a preparation with a castable formulation at 50% volumetric loading.

Because a silicon nitride formulation includes other components, it is necessary to pre-mix the several powders. Because mixing may be difficult at the desired high volumetric loadings of more than 50% for the silicon nitride, a concentration step has been added for these initial silicon nitride studies in order to obtain sinterable samples. These preparations are being conducted concurrently with the studies on the dispersion and rheology of the mixtures. We expect to be able to delete these steps subsequently. The additions to the process are:

1. wet milling of the blended silicon nitride formulation at 30-40% solids with monomer, and

2. vacuum concentrating the mixture to the desired range of greater than 50% volumetric loading.

Several castings having 50 vol % loadings have been made and are in various stages of drying at this time. We are using a scanning laser microscope to determine the size distribution as powders are mixed and dispersants are incrementally added. The speed of size analysis with this device (typically less than a minute per determination) permits rapid measurement to be made of particle size distribution. This is expected to decrease markedly the necessary time for dispersant studies.

Gel-casting of alumina

A milestone specifying the preparation of eight alumina plates and the writing of a letter report was met.

The technical objectives of this project are to develop measures of reliability for the processing of structural or engineering ceramics and then to use these measures in an efficiently designed experimental approach. Both systematic variation of process parameters and incremental improvements are to be evaluated. The milestone represented a demonstration of the ability to prepare a number of plate specimens, each of which could provide several tensile samples. Eleven specimens were documented. Two of the plate specimens were prepared during test and development of the final test composition. The other nine were prepared using that composition during subsequent tests. The original innovation had used an alumina powder with a mean particle size that was larger than that of our chosen silicon nitride material (0.5 μm). Accordingly, although two plates had been made earlier with the original formulation, they were not suitable for tensile testing.

The formulation uses an RC-HP fine-grained dry-ball-milled alumina powder and is prepared at a 52 vol % particle loading in the slurry. After mixing and vacuum de-airing, the material has reached a concentration of 54.3% loading. The slip is then cast, gelled, and dried. We expect that higher loadings are possible and will yield an improved product in subsequent development. The sintered densities of the product specimens using an air sintering furnace were 3.95 g/cm^3.

The dimensional changes were measured for two of the parts. The linear shrinkage on gelling from the as-cast solids level of 54.3% is 3.5%, which corresponds to a solids loading in the gelled green body of about 61%. It is likely that re-entrant mold designs would require this level of loading in the cast formulation. The linear shrinkage was 18.2–18.4%. The values for straightness (mm/mm) were determined for two specimens and found to be 0.3–0.5%.

Both the isotropy of the shrinkage and the value for straightness are gratifying results. The process is capable of making products with controlled dimensions, including tensile test specimens. Ongoing efforts will be directed toward the preparation of silicon nitride specimens similar to the alumina ones reported here.

Drying studies

Drying is a critical unit operation in the process. Programmers have been acquired for the drying ovens to obtain better data and control for this operation. The gelled body is normally dried slowly and with attention to humidity and temperature control, because too much residual moisture can lead to flaws that fragment the part during final processing steps. Earlier tests showed that a drying rate of as much as 10°C per hour to 100°C followed by a hold of 1–3 days was satisfactory for the 9-mm-thick specimen plates. Because this schedule has not yet been optimized, drying studies were begun. Data on readsorption showed that, even over periods of hundreds of hours, dried castings do not reabsorb significant amounts of moisture. This is taken to mean that no unusual storage conditions are required for products at this stage of the process.

Several large-form alumina castings were made in the shape of a 6.35-cm (2.50-in.) cube along with other specimens as part of the drying program. Drying data were obtained on eight specimens. Initial analysis showed two constant rate drying periods in the early stages of drying, to a loss of 15% of the contained moisture.

Dispersant studies and analysis of particulate size in casting slips

The size and number density of the largest agglomerates in a casting can limit the quality and acceptability of produced parts. Studies have begun using a scanning laser microscope to assess the size distribution of particles in the casting slips at different stages in the slip preparation as well as to assess dispersant activity for the powders.

Although the procedure used calls for ball-milling for several hours, there remained a significant population of larger agglomerates in the mix when it was cast. Addition of a small amount of additional dispersant, in this case Darvan®-C, significantly reduced the population of larger particles as shown in Fig. 1. Even though the addition of dispersant was made at a low shear rate, there was a significant decrease in the number of particles in the large size range. The measured decrease of these larger particles shows that we have not yet optimized either the quantity of dispersant or the milling procedure. The use of this particle size measurement technique is being explored as a prospective in-process test method.

Status of milestones

January 31, 1988, milestone completed. Others are on schedule.

Publications

None.

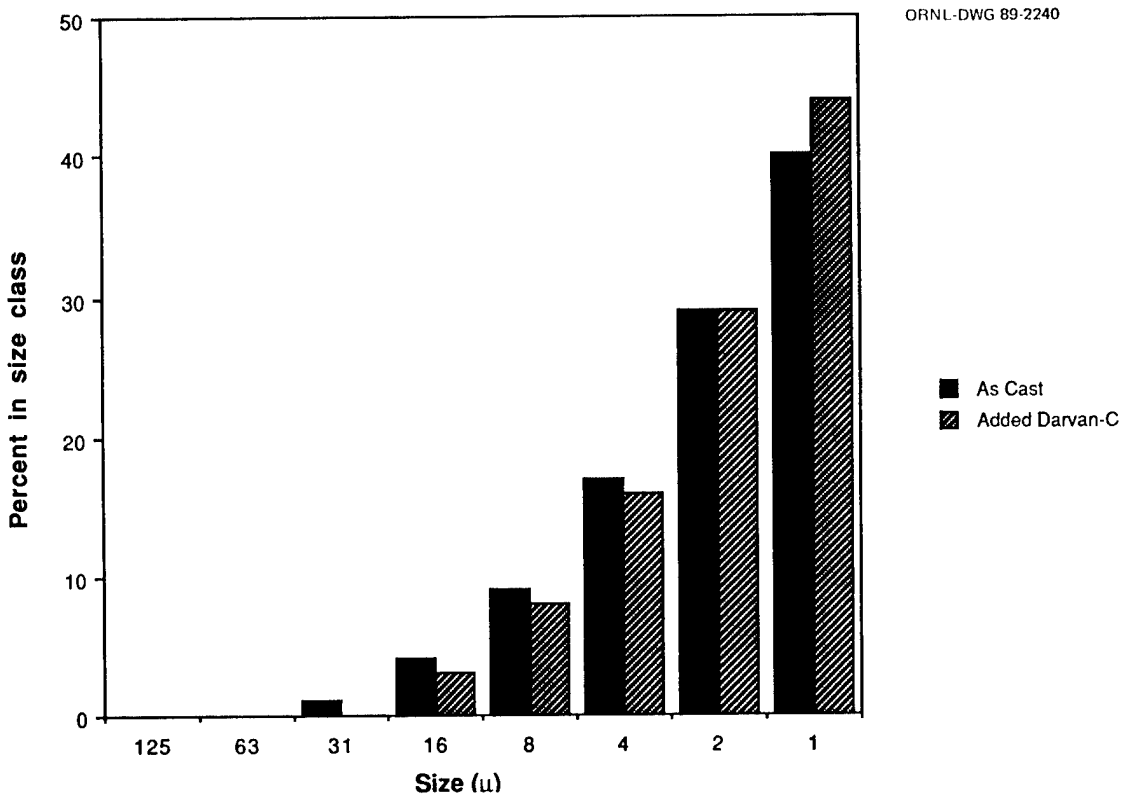

Fig. 1. Size distribution of ball-milled gel-casting alumina mixture showing the effect of additional dispersant.

1.2 CERAMIC COMPOSITES

1.2.2 Silicon Nitride Matrix

SiC-Whisker-Toughened Silicon Nitride

H. Yeh, E. Solidum (Garrett Ceramic Component Division),
K. Karasek, S. Bradley (Engineered Materials Research Center), and
J. Schienle (Garrett Auxiliary Power Division)

Objective/scope

The objective of this program (Phase II) is to maximize the toughness in a high strength, high temperature SiC whisker/Si_3N_4 matrix material system that can be formed to shape by slip casting and densified by a method amenable to complex shape mass production. The ASEA glass encapsulation hot isostatic pressing (HIP) technique shall be used for densification throughout the program.

The program is divided into four technical tasks with multiple iterations of process development and evaluation. Parametric studies shall be conducted to optimize processing steps developed in the Phase I effort, guided by established analytical and NDE techniques. The four technical tasks are: Task 1 - Selection of SiC whiskers, Task 2 - Baseline Casting Process, Task 3 - Parametric Densification Study, and Task 4 - Effect of Specimen Size and Shape.

The technical effort was initiated in May 1988. During this reporting period (Oct.'88-Mar '89), Task 1 effort was completed and Task 2 effort was initiated. Task 2 is scheduled to be completed at the end of June 1989.

Technical progress

TASK 1 - Selection of Whisker

The purpose of this task was to select a SiC whisker (SiC_w) as the reinforcement in GN-10 Si_3N_4 matrix, prior to the start of the process optimization and property evaluation studies to be conducted under Tasks 2 through 4.

The most direct method to evaluate the effectiveness of a reinforcing whisker is to measure the mechanical properties of a composite containing the whiskers. Composite billets (approximately 2 1/2" Dia. x 3" Ht.) containing 20 wt.% SiC_w were formed by a baseline slip casting process and densified to full density using the ASEA glass encapsulated HIP technique. The densified composite billets were subsequently machined into test

bars and other samples for characterization.

Four types/versions of whiskers were selected for evaluation in two stages. Based on the mechanical properties, microstructure and processing data, one type/version whiskers was selected for use under Tasks 2-4 (see Dec. '88-Jan.'89 bi-monthly).

At the start of Phase II, two types of whiskers, Tateho 1S-105 and American Matrix Inc. SiC_w (designated as AM5) appeared to be very promising and were available in commercial production quantities. Thus, these two whiskers were initially selected for evaluation (referred as Stage 1) under this task. The results indicated that the AM5 whisker is better; however, the AM5 composite exhibited a cracking problem during densification. It was attributed to the high surface oxygen content of the as-supplied whiskers.

Consequently, it was decided to evaluate the behavior of AM5 whiskers after an acid etching treatment to reduce surface oxygen. A sufficient quantity of AM5 whiskers was HF-etched for this purpose at Allied-Signal using a procedure established by T. Tiege (see Oct.-Nov. '88 Bi-Monthly Report). This version of whisker is designated as AM5E in the subsequent discussion. It was also decided to evaluate Advanced Composite Materials Corporation (ACMC) SC-9 SiC whisker in parallel with AM5E evaluation. This effort is referred as State 2 whisker evaluation. ACMC whiskers are not commercially available. Matrix powders were supplied to ACMC for them to blend 20wt.% SC-9 whiskers into the matrix powder; after blending the composite blend was returned to Garrett Ceramic Components Division for processing. A sample representing the whiskers used in the blend was shipped to us along with the blend as a reference. This ACMC whisker is designated as AC3 in the subsequent discussions.

The results of the first stage whisker evaluation (Tateho and AM5) were reported in the last semi-annual report. The following is a summary of the 2nd Stage whisker evaluation efforts and the justifications for selecting HF-etched American Matrix SiC whisker for the remainder of this program.

A. Whisker and Whisker-Powder Blend Characterization

1. Whisker Morphology

The morphology of the AC3 and AM5E whiskers were examined by scanning transmission electron microscopy (STEM) (Figure 1). The AC3 SiC whiskers were generally fairly straight and had smooth surfaces. Diameters ranged from 0.2 μm to 1μm with the average being about 0.5 μm. Whisker lengths varied from 5 μm to over 100 μm. Some debris was noted. The HF etched AM5E whiskers appears to

have slightly sharpened surface morphology than those of the AM5 whiskers.

2. Surface Chemistry X-ray Photoelectron Spectroscopy

The AC3, AM5, and AM5E SiC whiskers were analyzed by X-ray photoelectron spectroscopy (XPS). The energy scale was calibrated by setting the binding energy of the first carbon peak at 282.40 eV.

The results are listed in Table I along with those from a previous set of whiskers from ACMC (AC2). The major concern is the surface oxygen content -- which is usually indicative of surface SiO_2 -- such as that exhibited by the AM5 whiskers. The SiO_2 and SiC can react at high temperature, yielding SiO and CO gases. As a result, the whiskers degrade, while the sample and encapsulating glass can crack. Both the AM5E and AC3 exhibited surface oxygen levels which were low enough to be acceptable, although the AC3 was a little higher than expected (particularly in comparison with the earlier AC2).

The surface impurity levels do not appear to be any immediate cause for concern. The F impurity on the AM5E whiskers probably results from the HF acid etch. It is not clear what effect, if any, this would have upon the processing or properties. Ca, which appears on the AC3, AM5, and AM5E, is not expected to have much effect. The effect of the N or Al impurities is also not known. The Fe level on the AC3 is similar to the level measured on prior lots of ACMC whiskers, and it has proved to be acceptable.

3. Length Distribution

SiC whisker length distributions were measured for the AC3 and AM5 whiskers prior to blending and the AC3 and AM5E whiskers in whisker-powder blends. The analysis on the etched/cleaned American Matrix whiskers (AM5E) prior to blending was not conducted, since it was assumed that this step would not substantially change the length distribution from that of the as-received whiskers (AM5).

A comparison between AM5 and AC3 whiskers indicated that the AC3 whiskers have more whiskers which are slightly longer than the AM5 whiskers. The difference is not, however, very large. The comparison between the 20 wt% SiC Whisker - GN-10 Si_3N_4 blends for the AM5 and AC3 whiskers showed even a smaller difference than in the as-received whiskers.

4. X-ray Diffraction (XRD) of AC3 Blend

The blending of the AC3 whiskers with GN-10 Si_3N_4 powder was performed at ACMC. The blend was analyzed by XRD in an effort to spot any impurities that might have been introduced. The powder contained α-Si_3N_4, Y_2O_3, a minor amount of β-Si_3N_4. It was difficult to discern the presence of β-SiC, since the peaks overlapped the Si_3N_4 peaks. No impurities were detected. In particular, no crystalline Al_2O_3 was seen because Al_2O_3 media were suspected to be used in blending the mixture.

5. Bulk Carbon Level of Whisker - Si3N4 Powder Blends

The bulk carbon (C) levels of the whisker - powder blends were measured as a check of SiC levels. These data are listed in Table II. Assuming a 29±1 wt.% C level in the starting SiC whiskers and taking the Si_3N_4 and sintering aid powders into account, this C level can be converted into an equivalent SiC whisker content. These values are also given in Table II. Considering the uncertainty level, both composites have whisker levels which fall at the nominal 20 wt.% level.

B. Composite Fabrication

Composite billets containing 20% HF-etched AM whiskers (AM5E) and 20% ACMC SC-9 whiskers (AC3), respectively, were slip cast using the established procedures. The later was custom blended at ACMC. Table III lists some of the processing data. There was no significant difference between the processing behavior of the etched AM whiskers (AM5E) and the as-supplied AM whiskers (AM5) which were processed previously. Billets of each composite were densified by the glass encapsulation HIP process. The densities were 3.275 g/cc for the AM5E composite and 3.279 g/cc for the ACMC composite, respectively. Two billets of each composite were HIP'ed in the same run. One billet of each composite cracked during HIP'ing. The uncracked ones were machined into test bars for characterization. The AM5E composite exhibited a lower tendency to cracking than AM5 composite did under first stage evaluation. This is attributed to the reduced surface S_iO_2 levels discussed earlier.

C. Mechanical Properties

Ten MOR bars of each composite were tested in four-point bending at room temperature. The test parameters and results are shown in Table IV. The test results for Tateho whisker and "as-received" American Matrix whisker (AM5) reinforced GN-10 composites, which were reported in the last semi-annual

report are also included in Table IV for comparison.

The composite reinforced with AM5E whiskers exhibited a flexural strength of 92.5 ksi compared to 94.9 ksi for the composite reinforced with AM5. Since the average strengths were close, the acid-etching step converting AM5 to AM5E does not appear to affect composite strength. The ACMC whisker (AC3) composite had an average strength of 89.1 ksi. The scatter in strength data for the ACMC whisker composite was unusually high, ranging from 65.4 ksi to 117.9 ksi.

The fracture surfaces were examined at 40X using a binocular microscope. The AM5E composite exhibited both surface and internal fracture origins, which is similar to that observed previously for GN-10 reinforced with whiskers. All AC3 composite fractures originated from the surface.

The five K_{IC} bars of each composite were notched (Chevron) at the mid-span and subsequently tested at room temperature in three-point bending. The test parameters and toughness results are shown in Table V. The first stage evaluation test results reported previously are included in Table V for comparison. The toughness of acid-etched American Matrix and ACMC whisker composites were virtually the same, 6.31 $ksi*in^{1/2}$ and 6.39 $ksi*in^{1/2}$, respectively. The toughness of the acid-etched American Matrix whisker (AM5E) composite is slightly higher than that measured previously for "as-received" American matrix whisker (AM5) reinforced GN-10 (6.02 $ksi*in^{1/2}$), but the small increase could be due to batch-to-batch differences since the composites were not co-processed.

D. Microstructure

Polished cross-sections of composites reinforced with AM5E and AC3 whiskers were prepared to evaluate whisker distribution and orientation. Representative microstructures for the composites are shown in Figures 2 through 4. Both composites exhibit good whisker dispersion, although the AM5E composite exhibits some preferred orientation along the test bar length. Previously, similar observations were made for GN-10 composites containing AM5 whiskers. The AC3 whisker composites exhibited no evidence of preferred orientation. Small dark specks are present throughout the AC3 whisker composite microstructure. These are believed to be associated with porosity.

Scanning Electron Microscopy (SEM) analysis was performed on the fracture surfaces of the above two composite systems. Figures 5 and 6 show typical fracture origins for AM5E whisker composite. Figure 5 shows an agglomerate-type defect in a specimen which exhibited a 97.5 ksi strength. Figure 6 shows

a surface fracture origin in an 87.6 ksi sample. Energy Dispersive X-Ray (EDX) analysis revealed no contaminants or concentrations of sintering aids at the fracture origins, indicating good sintering aids distribution.

Figures 7 and 8 illustrate typical failure origins in AC3 whisker composite. In Figure 7, the fracture origin of this low strength specimen (62.5 ksi) was a cluster of small pores located near the specimen surface. Figure 8 shows surface failure origin of an 84.6 ksi specimen; the origin appears to be finer grained than the surrounding matrix. Again, EDX analysis revealed no contaminants or concentrations of sintering aids at the fracture origins.

The SEM microstructure of the fractured AM5E and AC3 whisker composites appear similar with respect to toughening. The fracture surfaces of both composites contain whisker fractures below the matrix fracture plane which suggests the whiskers may have failed independently of the matrix and bridged the crack (Figure 9).

Scanning transmission electron microscopy (STEM) revealed some similarities and some differences between AC3 and AM5E composite. The average matrix grain size and grain aspect ratio were virtually identical. However, the volume fractions of SiC whiskers in the areas examined by STEM were 15.0% for the AC3 composite compared to 20.6% for the AM5E composite. Some whisker degradation products were observed with the AC3 composite. The grain-boundary-phase volume fraction was slightly higher for the AC3 composite. Some degradation products were observed in the AC3 composite. The AM5E whiskers tended to be somewhat oriented in the composite in agreement with the optical microscopy results discussed above. Grain-boundary-pocket compositions were different for the two composites. Grain boundaries were always non-crystalline. In both samples there were micron-size areas lacking grain boundary phase.

However the carbon content analysis results presented earlier showed that the SiC_w whisker contents of both composites were in general agreement with the batched (20%). The low SiC whisker content detected by STEM probably was caused by whisker degradation due to surface SiO_2 content and potential uneven distribution of SiC whisker.

E. Conclusion

On comparing the MOR and toughness test results listed in Table IV and Table V, respectively, the "as-received" American Matrix, (AM5) "etched" American Matrix (AM5E), and ACMC (AC3) whisker composites were close with respect to room temperature

strength and fracture toughness; the Tateho whisker composite exhibited lower strength and toughness. Based on these results, the "etched" American Matrix whisker composite appears to be the best whisker candidate for the remainder of the program. This conclusion is based on a slightly higher K_{IC} than for the "as-received" American Matrix whisker composite (6.31 ksi*in$^{1/2}$ compared to 6.02 ksi*in$^{1/2}$) and less scatter in strength data relative to the ACMC whisker composite (92.5 + 9.8 ksi compared to 89.1 + 18.8 ksi).

From processing point of view, there are additional reasons for recommending the etched American Matrix whisker. Both versions of American Matrix whiskers are available commercially, while the ACMC whiskers are only available as a blend. Therefore, using either version of the American Matrix whiskers allows us more control on processing. Between the two versions of American Matrix whiskers, the etched one exhibited a lower tendency to cracking during densification than the un-etched. It should be noted that both versions of American matrix whisker composites exhibited a tendency of whisker alignment in the casting direction, while the ACMC composite did not. We believe that the whisker alignment tendency could be minimized through processing optimization.

TASK 2 - BASELINE CASTING PROCESS

The objective of this task is to develop a green forming process from powder preparation through slip casting, for composites containing 10, 20, 30 and 40 Wt % SiC whiskers. The matrix material is Garrett Ceramic Components' GN-10 Si_3N_4 formulation and the whisker is HF-etched American Matrix SiC. The optimized green composites shall be used for investigation under Task 3 Parametric Densification studies. Under this task, detailed characterizations shall be performed on the starting materials (matrix powders and whiskers), and in-process materials (slips, castings, etc.) by NDE and destructive techniques.

To maintain consistency in whisker properties a lot of 13-kg American Matrix SiC whiskers (designated as AM7) has been purchased for this program. This lot of whiskers has been HF-etched and then Argon thermal treated to reduce the surface SiO_2 layer (at American Matrix) as recommended by Task 1 results. A lot of 50 kg of Si_3N_4 powder was also purchased for this program in order to minimize potential lot-to-lot variations in Si_3N_4 powders. Similarly, a sufficient amount of sintering and materials were also set aside from the same lot for this program.

A. Whisker Analysis

A sample was taken from the lot of HF-etched American Matrix SiC whiskers (AM7) for XPS and other analyses. The XPS

results are listed in Table VI. For comparison, the XPS results of two other versions of American Matrix SiC whiskers analyzed under Task 1 (AM5 and AM5E) are also listed in Table VI. The results of other types of analyses on AMT analyses shall be presented in the next report.

Clearly, the HF etch has removed most of the surface SiO_2. The AM7 major-component-surface chemistry is fairly similar to that of the AM5E; it does not at all resemble that of the un-etched AM5 whiskers which is dominated by SiO_2.

Considering the surface impurity levels of AM7, the Ca is the one major surprise. The high level, however, is not expected to cause problems. Fe appears to be low enough to avoid concern about it catalyzing degradation. The F level is much higher than on the AM5E whiskers. It is not clear why this is the case, although some of the fluorine may be tied-up with the Ca. We have not been able to determine any positive or negative effects of fluorine in the composites so far.

B. Processing

Due to the HF-etching and washing/infiltration procedures performed on the whiskers at American Matrix Inc. prior to shipping to Garrett Ceramic Components, it was found that the whiskers do not contain any detectable undesired foreign substance; therefore, not requiring any further washing/cleaning. A series of sedimentation experiments were performed to determine the feasibility of reducing the whisker length distribution with a reasonable yield. It was found that the length distribution is already too narrow to be further reduced with a good yield. Thus, it was decided that the whiskers in the as-received state shall be used under this task.

The composite slips were prepared by blending the matrix GN-10 Si_3N_4 slip the appropriate amounts of SiC whiskers, water and deflocculant. The GN-10 slip was prepared following the procedures established under the ATTAP subcontract at GCCD (NASA/DOE DEN3-335 Subcontract 1774888). The solid contents and SiC whisker loading of the composite slip is controlled by the solid contents of the GN-10 and the amounts of SiC whisker and water. Table VII lists the properties of the composite slips.

The composite slip was then cast under pressure into a mold with four (4) cavities, each measured 2"x3". After casting, the composite plates were dried. Composite plates containing 10, 20, 30 and 40% SiC have been made. These plates will be inspected visually and by X-ray microfocus and will be sectioned for microstructural analysis.

The rectangular mold is selected over the cylindrical one that was previously used under Phase I and also Task 1 of Phase II. This change in mold geometry is in an attempt to minimize/ eliminate whisker re-orientation during casting. The thickness of the plates are typically 1/2"-3/4", while the height of the cylindrical billets are 3"-3 1/2". The casting time for the cylindrical billets is typically 5 hours, while for the plates is one hour.

Status of milestones

The milestones are on schedule.

Publications/presentations

A summary report entitled "Development of Silicon Carbide Whisker Reinforced Silicon Nitride Formed by Slip Casting", co-authored by H.C. Yeh, J.L. Schienle, K.R. Karasek, and S.A. Bradley, was presented by H.C. Yeh at Contractor's Coordination Meeting, October 22-24, 1988.

K.R. Karasek presented a paper (co-authored by S.A. Bradley, J.T. Donner, and H.C. Yeh) entitled "Characterization of Recent SiC Whiskers," at the 13th Annual Conference on Composites and Advanced Ceramics in Cocoa Beach, FL, on January 17, 1988.

Table I

X-ray Photoelectron Spectroscopy Surface Chemistry Data for SiC Whiskers

Atomic % (Binding Energy in eV)

	AC3*	AC2#	AM5E	AM5§
Si 2p	29.6(100.6)	33.5(100.4)	29.4(100.4)	15.9(100.5)
Si 2p	7.7(102.2)	6.0(101.9)	6.0(101.9)	17.3(103.2)
Si 2p			3.2(103.1)	
C 1s	26.5(282.4)	32.8(282.4)	28.8(282.4)	13.6(282.4)
C 1s	11.2(283.8)	5.8(284.0)	9.4(284.0)	2.8(283.9)
C 1s		2.6(286.0)		1.9(285.3)
O 1s	13.8(531.0)	1.2(529.9)	16.3(531.9)	8.1(531.3)
O 1s	7.5(532.1)	13.5(531.8)		37.5(532.4)
N 1s	2.2(397.1)	4.6(397.0)¥	3.7(397.5)	
N 1s	0.9(399.1)			
Ca 2p3	0.5(347.3)		0.9(348.3)	1.7(347.9)
Fe 2p3	0.2(711.0)			
F 1s			1.5(685.5)	
Al 2p			0.8(73.7)	

* Received from Advanced Composite Materials Co., Greer, SC in December 1989.

\# Received from Advanced Composite Materials Co., Greer, SC in middle to late 1986.

§ Received from American Matrix, Inc., Knoxville, TN in March 1988.

¥ Value taken from broad energy survey scan rather than high resolution scan; therefore, the accuracy will not be as high as for the other values shown.

Table II

Whisker - Si_3N_4 Powder Blend Bulk C Content Data

Whisker Used in Blend	C Wt.% in Blend	Equivalent SiC Wt.%
ACMC AC3	5.1±0.3	18±2
American Matrix AM5	6.2±0.3	21±2

TABLE III - COMPOSITE PROCESSING DATA

	COMPOSITE SLIP			
SiC_W Loading WT %	% Solids	Viscosity (cp)	pH	Green Density (g/cc)
20% Acid-etched American Matrix	69.0	127	9.88	1.95
20% ACMC SC-9	70.0	1600	10.43	1.65

Table IV

MOR Test Results For Si_3N_4 Composites Containing Different SiC Whiskers

SiC Whisker	MOR ksi (MPa)
"as-received" American Matrix	94.9 ± 8.1 (654 ± 56)
"acid-etched" American Matrix	92.5 ± 9.8 (638 ± 68)
ACMC	89.1 ± 18.8 (614 ± 130)
Tateho	78.2 ± 6.3 (539 ± 43)

Test Dimensions (nominal)
Width: 0.250 inch (6.35 mm)
Thickness: 0.125 inch (3.175 mm)
Length : 2.0 inch (50.8 mm)

Test Parameters (four point bending)
Outer Span: 1.50 inch (38.1 mm)
Inner Span: 0.75 inch (19.05 mm)
Crosshead Speed: 0.02 inch/minute (0.51 mm/minute)

Table V

K_{IC} Test Results

SiC Whisker	Fracture Toughness ksi*in$^{1/2}$ (MPa*m$^{1/2}$)
"as-received" American Matrix	6.02 ± 0.17 (6.62 ± 0.19)
"acid-etched" American Matrix	6.31 ± 0.32 (6.94 ± 0.65)
ACMC	6.39 ± 0.23 (7.02 ± 0.25)
Tateho	5.34 ± 0.26 (5.87 ± 0.29)

Test Dimensions (nominal)

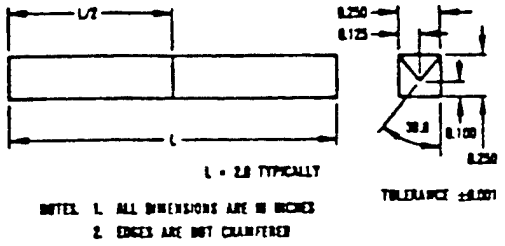

Test Parameters (three point bending)

Span: 1.50 inch (38.1 mm)

Crosshead Speed: 0.0005 inch/minute (0.0127 mm/minute)

Table VI

X-ray Photoelectron Spectroscopy Surface Chemistry Data for SiC Whiskers

	Atomic % (Binding Energy in eV)		
	AM7[1]	AM5E	AM5[2]
Si 2p	31.7(100.5)	29.4(100.4)	15.9(100.5)
Si 2p	2.7(102.2)	6.0(101.9)	17.3(103.2)
Si 2p		3.2(103.1)	
C 1s	29.2(282.4)	28.8(282.4)	13.6(282.4)
C 1s	4.6(284.4)	9.4(284.4)	2.8(283.9)
C 1s	1.1(290.2)		1.9(285.3)
O 1s	18.0(531.7)	16.3(531.9)	8.1(531.3)
O 1s			37.5(532.4)
N 1s	2.2(397.8)	3.7(397.5)	
Ca 2p3	5.5(347.5)	0.9(348.3)	1.7(347.9)
Fe 2p3	0.3(711.9)		
F 1s	4.7(684.5)[3]	1.5(685.5)	
Al 2p		0.8(73.7)	

1- Received from American Matrix, Inc., Knoxville, TN in March 1989

2- Received from American Matrix, Inc., Knoxville, TN in March 1988

3- Value taken from broad energy survey scan rather than high resolution scan; therefore, the accuracy will not be as high as for the other values shown.

Table VII - Composite Slip Properties

Wt%SiC_w	% Solids	Viscosity (cps)	pH	Sp. Gravity (g/cc)
10	74	363	10.38	2.01
20	70.1	691	10.25	1.90
30	64.6	1068	10.17	1.76
40	59.2	2684	10.28	1.66

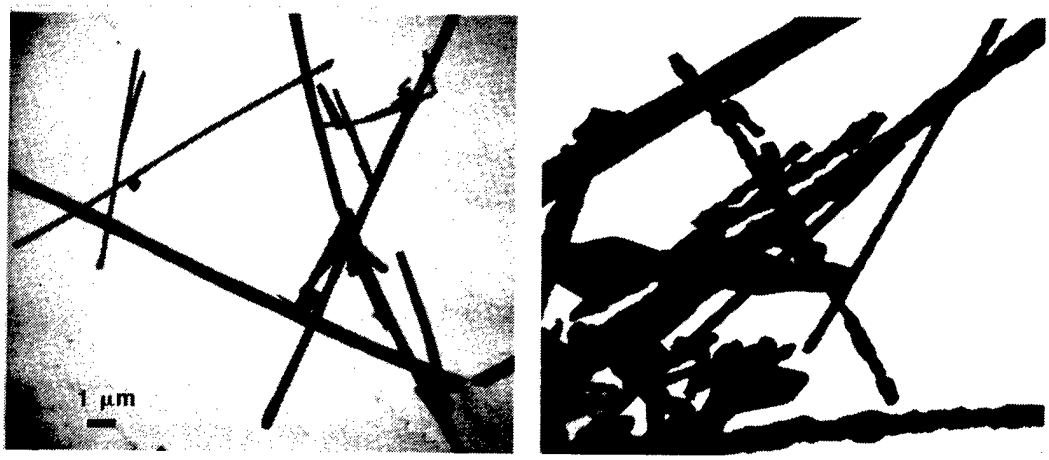

Figure 1 - AMC AC3 (left) and American Matrix AM5E (right) SiC whiskers.

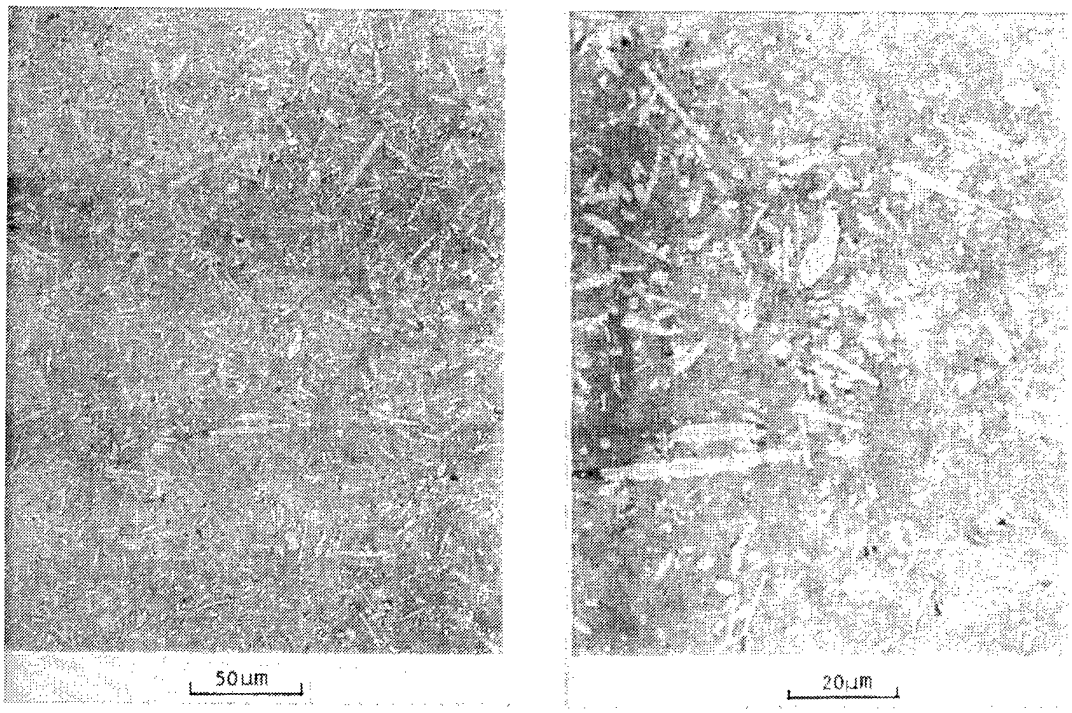

Figure 2 - The American Matrix whiskers (AM5E) are well dispersed in the densified composite. (Polished Section Parallel to test bar length).

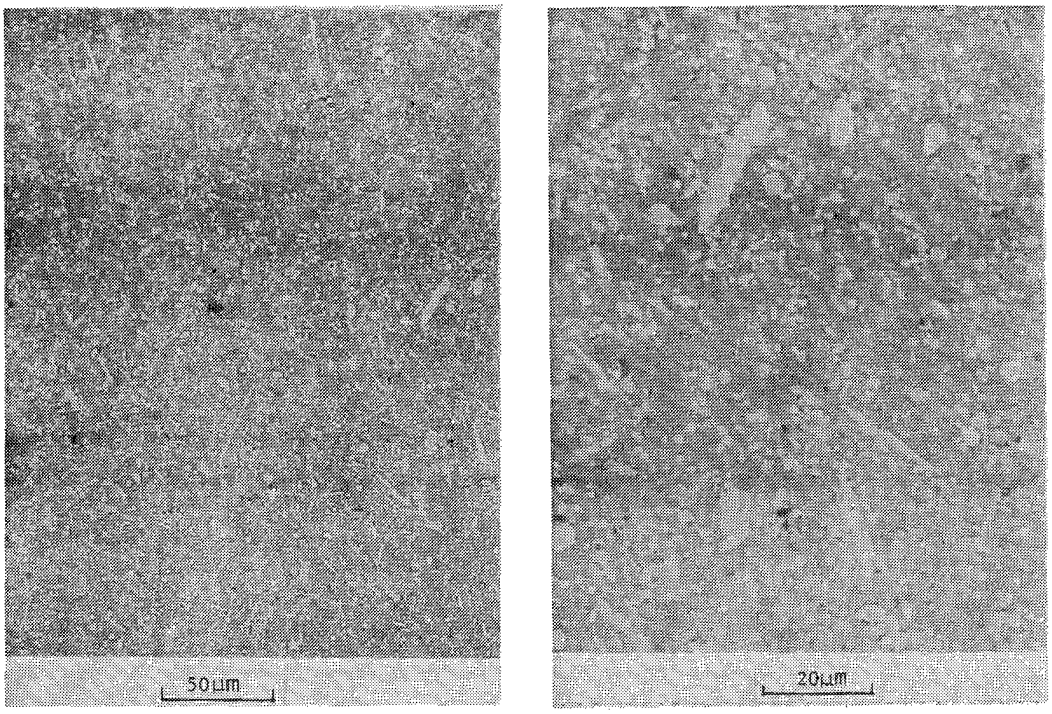

Figure 3 - Few American matrix whiskers (AM5E) lie in the plane of the test bar cross-section suggesting preferred orientation (polished section Transverse to test bar length), compared with Figure 2.

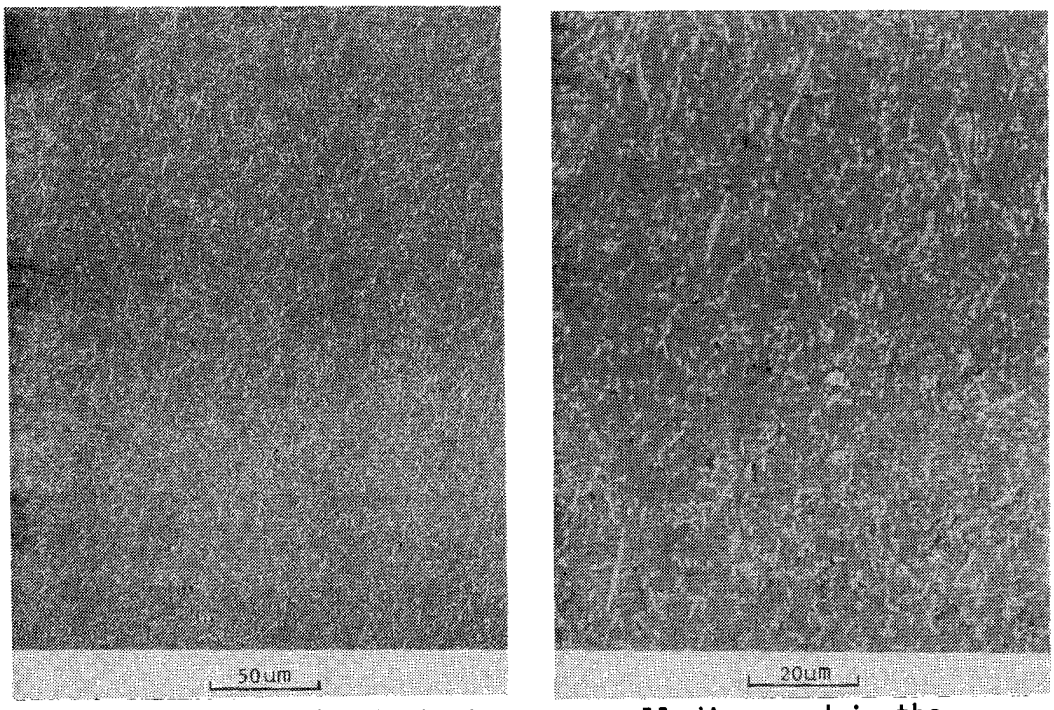

Figure 4 - The ACMC (AC3) whiskers are well dispersed in the densified composite showing no preferred orientation.

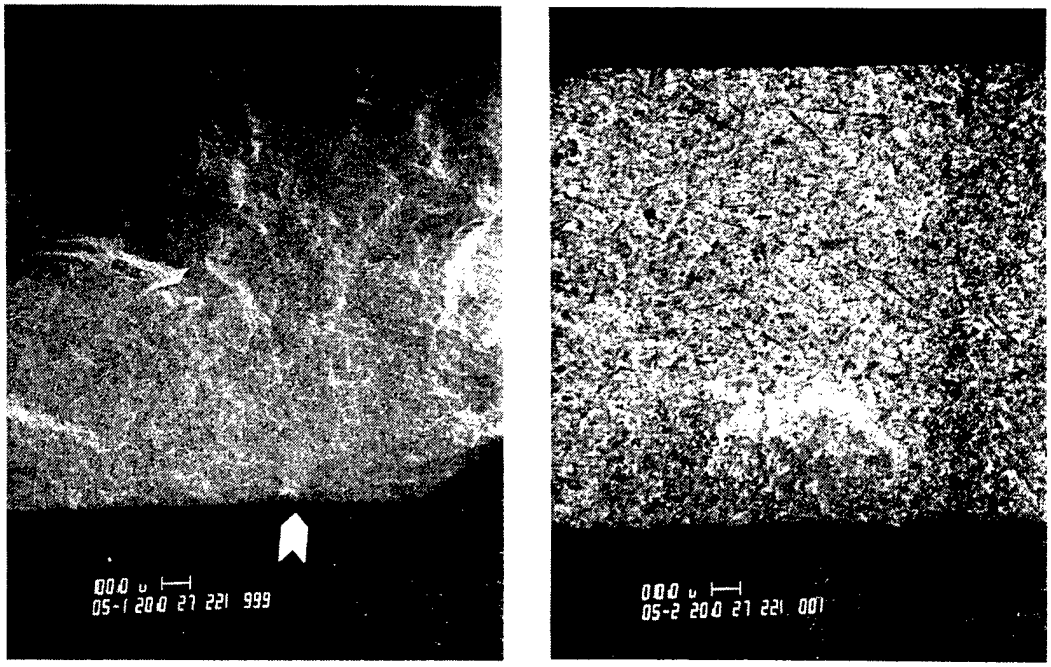

Figure 5 - American Matrix whisker reinforced composite which failed from sub-surface agglomorate type defect.

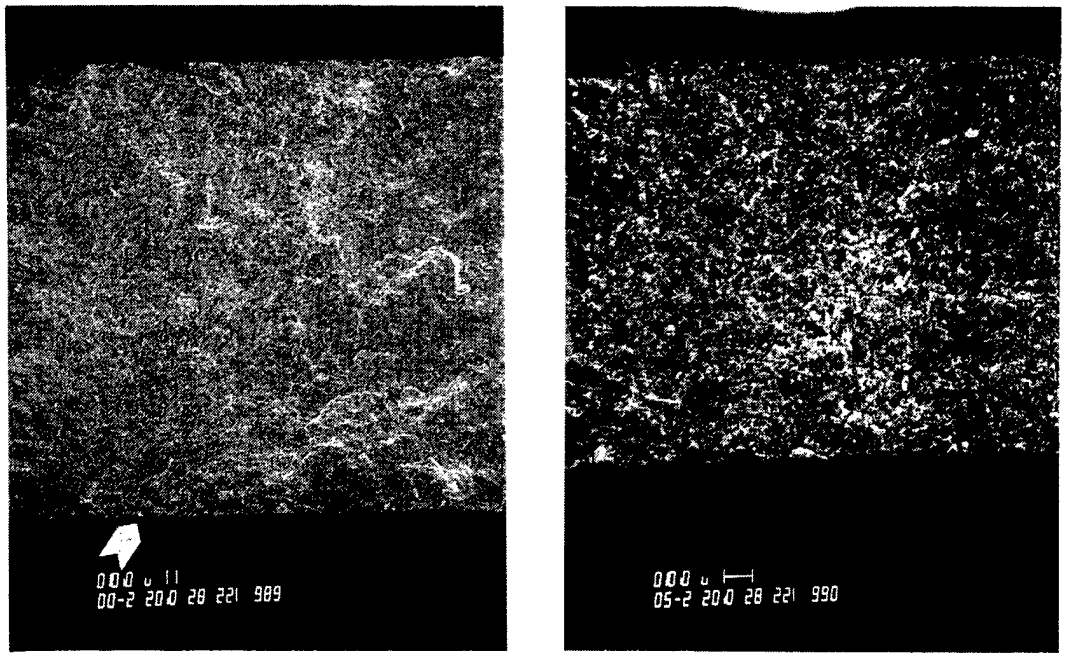

Figure 6 - Tensile surface fracture origin in American Matrix whisker reinforced composite.

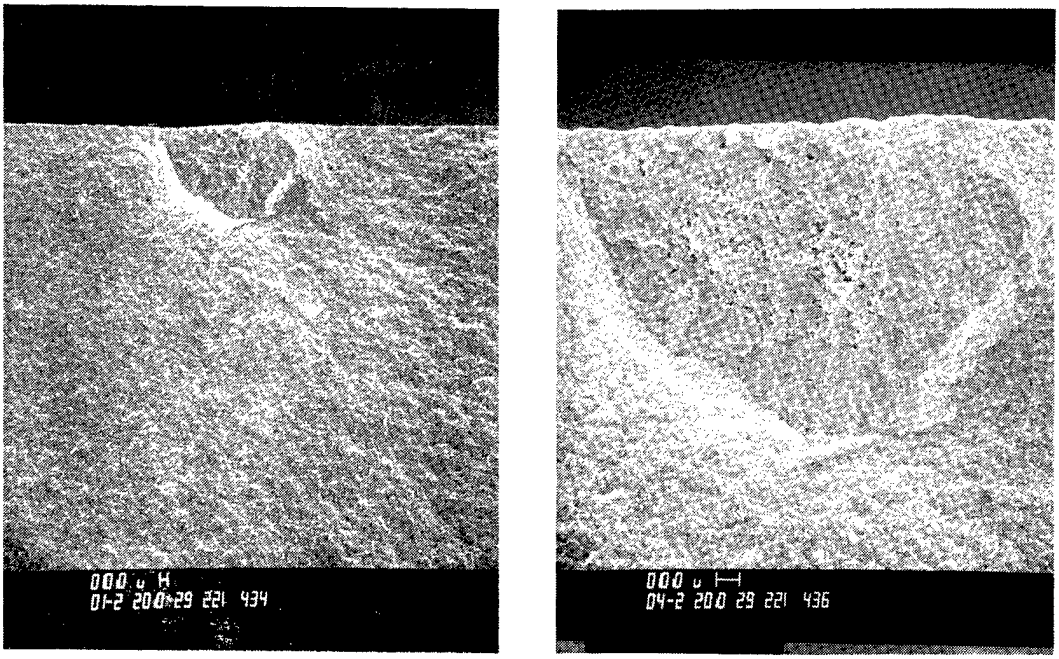

Figure 7 - ACMC whisker reinforced composite which failed at pore cluster near specimen surface.

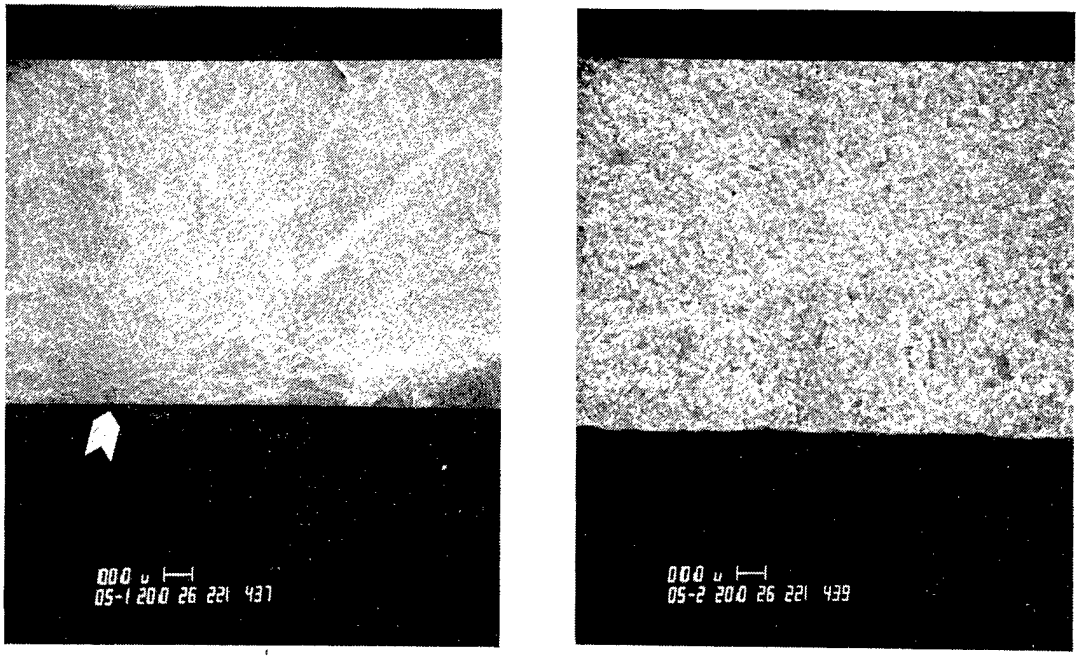

Figure 8 - Tensile Surface Fracture Origin in ACMC whisker reinforced Composite.

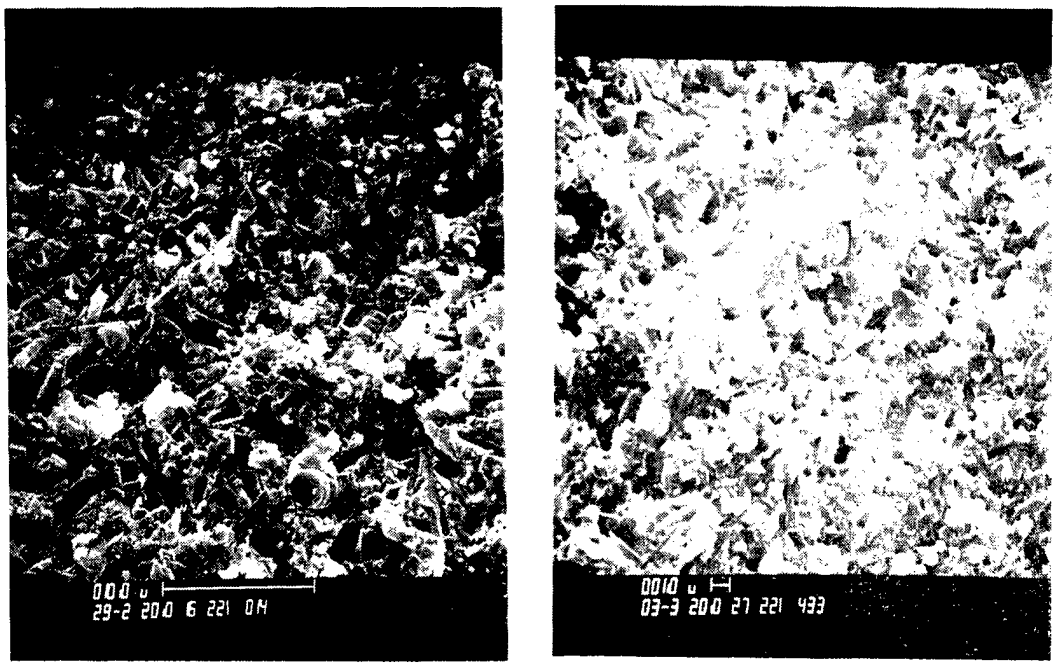

Figure 9 - Whisker pullout sockets on American Matrix whisker (left and ACMC whisker (right) reinforced composites, suggest crack Bridging Toughening Mechanism.

Ceramic Matrix Composites - GTE Laboratories Incorporated

Objective/Scope

The objective of the proposed effort is to study the effect of sintering aids on microstructure and properties of Si_3N_4-SiC(w) composites and utilize the results obtained to design and synthesize an advanced composite of improved properties. It is also an objective of this effort to refine forming and consolidation processes and develop technology for prototype part fabrication.

Technical Progress

Material Development

Efforts to microstructurally tailor silicon nitride ceramics have focused on annealing as a means of modifying the intergranular glass phase through devitrification. Monolithic materials were prepared with 8.8 v/o of Y_2O_3, MgO or CeO_2 sintering aid added to [1.5 w/o Al_2O_3 + balance Si_3N_4 (Ube E-10)]. Bodies were hot pressed in BN-coated graphite dies in an argon atmosphere. Baseline materials were hot pressed at 1725°C/34.4 MPa for 90 minutes. Annealing was incorporated into subsequent runs by cooling to the annealing temperature from the hot pressing temperature at 60°C/min: i.e. the ceramic was hot pressed and annealed in a single cycle without cooling to room temperature prior to the annealing step. Initial characterization is reported in Table 1. The applied annealing schedule had no effect on the room temperature modulus of rupture of AY6 or AC8, while the MOR of the annealed magnesia-containing material, AM4, increased by thirty percent (30%) relative to its counterpart produced by the standard 90-minute hot pressing schedule. Phase analyses of the MgO-containing materials by XRD of powdered broken MOR bars were inconclusive. Beta Si_3N_4 was the major phase. A secondary crystalline phase was indicated by the presence of several reflections, but could not be identified.

Table 1: Characterization of Si_3N_4 Ceramics

Material	Densification Schedule	Density (% Theo.)	Rm. Temp MOR (MPa)	1200°C MOR (MPa)	Linear Response To Failure at 1200°C
AY6	A	99.6	1052±80	773±70	Yes
	B	99.5	991±91	652±50	Yes
AM4	A	98.6	646±97	617±11	No
	B	98.6	838±86	515±7	No
AC8	A	98.4	1006±88	503±12	Yes
	B	98.5	937±124	509±8	Yes

A ≡ 1725°C/90 min hot press
B ≡ 1725°C/90 min hot press → cool 60°C/min → anneal 1200°C/240 min.
AY6 ≡ 6.0 w/o Y_2O_3 + 1.5 w/o Al_2O_3 + Bal. Si_3N_4
AM4 ≡ 4.4 w/o MgO + 1.5 w/o Al_2O_3 + Bal. Si_3N_4
AC8 ≡ 8.3 w/o CeO_2 + 1.5 w/o Al_2O_3 + Bal. Si_3N_4

Evaluation of the mechanical property data for AY6+30 v/o SiC(w) composite materials reflects improvements gained as a result of changes in the silicon nitride raw material as well as the hot pressing and hot isostatic pressing (HIP) schedules. Modifications of the hot pressing and HIPing schedules of UBE Si_3N_4-based materials to higher temperatures were implemented to yield increased matrix grain size, leading to improved fracture toughness (Table 2). The observed improvements in strength are attributed to the increased fracture toughness.

Table 2: Room Temperature Mechanical Property Data for AY6+30 v/o SiC whisker Composites Prepared with Silar SC-9* SiC Whiskers and Different Silicon Nitrides by Hot Pressing (HP) and Injection Molding (IM) and Hot Isostatic Pressing (HIP)

Material	Process	K_{IC} ($MPa \cdot m^{1/2}$)	MOR (MPa)
SN502 Si_3N_4	Hot Pressed	6.4 ± 0.5	975 ± 39
(Temp ≈1725°C)	IM/HIP	4.2	818 ± 112
UBE** Si_3N_4	Hot Pressed	7.3 ± 0.6	1043 ± 50
(Temp ≈1800°C	IM/HIP	6.9 ± 0.4	1143 ± 48

*Advanced Composite Materials Corporation, Greer, SC
**AY6 prepared using 80% E-03 and 20% E-10 grades UBE Si_3N_4

Strength (four-point MOR) measurements at elevated temperature for the Si_3N_4-SiC(w) composites prepared with UBE Si_3N_4 show essentially the same behavior as previously observed for composites prepared with SN502 Si_3N_4. Table 3 shows average values measured at 1200°C and 1400°C of both hot pressed and injection molded-HIPed composite material prepared with UBE Si_3N_4. These data are comparable to those previously obtained for composites prepared from SN502.

At 1200°C, there was essentially no difference in the strength of the materials. Plastic deformation (nonlinear force-time response) was not observed. At the 1400°C test temperature, UBE Si_3N_4-based composites exhibit slightly higher strength values. At the higher temperature, the data shows nonlinear deformation of the UBE Si_3N_4-based samples at approximately 230 MPa, while those prepared with SN502 Si_3N_4 yield a lower stress level (≈144 MPa). This behavior appears to be related to the lower SiO_2 content of the UBE powder. The reduced amount of SiO_2 leads to a reduction of the amount and a change in composition of the intergranular glass phase.

Table 3: Room and Elevated Temperature MOR Data for Hot-Pressed and Injection Molded and HIPed AY6+30 v/o SiC(w) Composites Prepared with Different Silicon Nitride Materials

Material	Process	Average MOR (MPa) 25°C	1000°C	1200°C	1400°C
SN-502 Si_3N_4 Silar SC-9 SiC(w)	Hot Pressed	975±39(5)**	819±64(3)	597±26(3)	257±25(3)
UBE* Si_3N_4	Hot Pressed	1043±50(5)	-	618±27(3)	407±62(3)
Silar SC-9 SiC(w)	IM/HIPed	1195±71(7)	-	616±105(3)	386±58(3)

*AY6 prepared using 80% E-03 and 20% E-10 graded UBE Si_3N_4

**( ) number of test specimens

High Temperature Properties

Since it is known that at 1200°C subcritical crack growth can contribute to the catastrophic failure of Si_3N_4 ceramics containing Y_2O_3 and Al_2O_3 sintering aids, additional elevated temperature testing has been performed. A Si_3N_4-AY6 monolithic material was precracked with a Knoop indentation and subjected to static loading at 1200°C. Failure was observed within 20 min after the application of a 206.7 MPa stress. Examination of the fractured surface of the indented AY6 bend bar revealed extensive slow crack growth prior to the onset of fast fracture. A precracked sample of a composite containing 30 v/o SiC whisker reinforcement responded to the imposed stress for over 400 hours in a manner analogous to that observed for standard, i.e., unindented, samples of this material. Similar tests conducted with indented and standard bend bars of composites with whisker additions of 10 v/o and 20 v/o exhibited the same behavior (Figure 1). At the three volume concentrations of SiC whisker additions examined, the indented samples had approximately the same steady state creep rates as standard bend bars, in spite of the presence of large surface flaws on the tensile faces (Table 4). The data also show that in bending at 1200°C with an applied stress of 206.7 MPa, the steady state creep rate of the AY6-based composites decreased with increasing content of whisker additions.

Subsequent to these creep tests, the indented composite samples were broken in flexure at room temperature and the fracture surfaces examined. The surface oxide scale developed during the tests was clearly visible. Subcritical crack growth was not observed for any of the AY6-SiC whisker composites.

Table 4: Steady-State Creep Rates Obtained from Figure 1

Material	Sample Type	Normalized Creep Rate
AY6 + 10 v/o SiCW	Standard	10.4
	Indented	10.1
AY6 + 20 v/o SiCW	Standard	6.1
	Indented	5.1
AY6 + 30 v/o SiCW	Standard	1.0
	Indented	1.0
AY6	Indented	Fractured in 20 min

Subcritical crack growth resistance was evaluated further. Empirical observations of fracture data have defined the relationship:

$$V = AK_1^N \qquad (1)$$

where: N = crack velocity exponent
V = crack velocity
A = const.
K_I = applied stress intensity

Based on this relationship, (equation (1), fracture mechanics analysis leads to

$$\sigma_f = C\,\dot{\sigma}^{\left(\frac{1}{N+1}\right)} \qquad (2)$$

where: σ_f = fracture strength
C = const.
$\dot{\sigma}$ = stress rate
N = crack velocity exponent

The exponent N is a measure of a material's resistance to subcritical crack growth, a higher N value indicating increased resistance.

Four materials (Table 5) were evaluated.

Table 5: Virtual Binder Phase Composition of Silicon Nitride-Based Ceramics Evaluated in the Present Study

Material	Sintering Aid Content (w/o of Composition) Al_2O_3	Y_2O_3	SiO_2*	$SiO_2/Al_2O_3+Y_2O_3$
AY6	1.50	6.00	2.60	0.35
AY6 + 30 v/o SiCP (8 μm)	1.05	4.23	2.00	0.38
AY6 + 30 v/o Si_3N_4	1.05	4.25	2.66	0.50
AY6 + 30 v/o SiCW	1.05	4.25	2.82	0.53

*Based on O_2 analysis of Si_3N_4 and SiC powders

The latter three material powders were prepared by dispersing either SiC or α-Si_3N_4 in the preblended AY6 powder. This results in a change in the amounts of sintering aids (i.e. the Y_2O_3 and Al_2O_3 additives and the SiO_2 obtained from the surfaces of the SiC and Si_3N_4 powders) contained within those bodies.

Modulus of rupture tests at 1200°C (four-point loading) were conducted at different applied stressing rates by varying the testing machine crosshead speed. Preliminary testing of precracked (30N Knoop indentation) monolithic Si_3N_4 at 1200°C substantiated the fracture mechanics premise and showed that fracture stress increased, and the bend bars fractured at a constant K_I, and the amount of subcritical crack growth prior to fast fracture decreased as stressing rate was increased (Table 6).

Table 6: Strength and Subcritical Crack Growth of Precracked Monolithic AY6 at 1200°C

Stress Rate $MPa \cdot sec^{-1}$	MOR (MPa)	Growth of Indentation Crack	Calculated* 1200°C K_{IC} $(MPa \cdot m^{1/2})$
1.9	302	109%	5.40
21.2	320	74%	5.35
208.4	350	55%	5.40

$$*K_{IC} = \frac{M\sigma(\pi a)^{1/2}}{\Phi}$$

M = 1.03
σ = MOR
a = crack size
Φ = elliptic integral to account for crack shape

The data for the four materials evaluated are shown in Figure 2, and the crack velocity exponents are given in Table 7.

Table 7: Crack Velocity Exponent Data at 1200°C

Material	Crack Velocity Exponent, N*
AY6	5
AY6 + 30 v/o SiCP	14
AY6 + 30 v/o SiCw	18
AY6 + 30 v/o Si_3N_4	21

$$*\sigma_f = C\dot{\sigma}^{\left(\frac{1}{N+1}\right)}$$

The data show that the resistance to subcritical crack growth at 1200°C of the monolithic AY6-Si_3N_4 is substantially less than that of the AY6-30 v/o SiC whisker composite. However, the value for the reduced sintering aids monolith, i.e. AY6 + 30 v/o Si_3N_4, is coincident with that for the whisker-containing composite. Additionally, the crack velocity exponent obtained for the AY6-30 v/o SiC particulate composite is similar to that of both the AY6-SiC whisker and the AY6-Si_3N_4 materials. These observations indicate that the reduction of the glass content of these materials is the

primary reason for increasing the subcritical crack growth resistance. Although the morphology of the SiC dispersoid has little apparent effect on N at low crack velocity, it does strongly influence the fast fracture high crack velocity behavior, i.e. modulus of rupture, once the flaw reaches critical size.

Constant compressive stress creep experiments have been performed at North Carolina State University. Stresses were increased in 50 MPa increments over the range of 50 to 350 MPa. Experiments to obtain the activation energy of creep were performed at constant stresses. The temperature was raised incrementally by 25°C over a range of 1470 to 1670K.

Figure 3 shows the steady-state creep rate as a function of stress for four different temperatures. At 1200°C the stress exponent, n, is 0.87 over the entire stress range tested. Above this temperature, the stress exponents show a marked increase at stress levels greater than 225 MPa. For example, at 1300°C the stress exponent is 0.43 at low stresses but increases to 1.01 above the break. To understand the cause of this change in stress dependence, the effect of glass devitrification on the kinetics of creep has been studied. Previous work has shown that annealing increases the relative amount of devitrified glass in the grain boundary phase.

To determine the effect of devitrification on creep behavior, two creep runs were performed. The first was performed at 1350°C in the stress range of 50 to 350 MPa following a 4-hour anneal at the same temperature. The second experiment was performed at the same conditions but following a 50-hour anneal at 1350°C. The second experiment produced stress exponents very similar to the values of the first. However, there was a decrease in creep rate at all conditions. This suggests that, while devitrification plays a role in the rate of deformation, it may not be responsible for the observed change in stress exponent at high stresses. Measurements at even longer times of anneal are currently being carried out to determine the time necessary to achieve a stable microstructure. Recent data has shown that the change in stress exponent occurs at approximately 1% strain in all samples. Therefore, the total strain may play a key role in the kinetic behavior of this material.

Process Development

Research during this reporting period on injection molding of whisker-reinforced materials concentrated on the binder removal process. This work was based on the assumption that silicon nitride-based materials reinforced with whiskers would be able to withstand higher stresses encountered during a rapid binder removal cycle better than monolithic silicon nitride. It should therefore be possible to accelerate binder removal cycles for injection-molded, whisker-reinforced materials.

As an initial evaluation, two accelerated binder removal cycles were evaluated. Figure 4 shows the time temperature cycles used, normalized against a standard binder removal cycle. The first cycle used the same atmosphere as the stan-

dard cycle but was shortened by 42%. The second cycle used an air atmosphere and was 66% shorter than the standard cycle.

Two injection-molded test bars of AY6 + 30 volume % SiC whiskers were included in each binder removal cycle for each of the four gate configurations evaluated previously for injection molding (semiannual report, Oct. 1988). In addition, two injection-molded bars of monolithic AY6 were also included as controls.

After the first binder removal cycle, one of the monolithic control samples had fractured in multiple pieces, and the other showed numerous surface cracks. The whisker-containing samples all remained intact with only two bars showing signs of surface-connected damage after the burnout process.

For the second cycle, examination of the whisker-containing samples by x-radiography revealed some internal cracking apparent after binder removal, particularly in gate types 3 and 4 (semiannual report, Oct. 1988). These gate types tend to produce the greatest number of fold lines during the injection process, and it is believed that these fold line regions developed into cracks during binder removal. Examination of radiographs of similar samples after a standard binder removal show the same degree of internal cracks for gate types 3 and 4.

One of the control samples used in the second cycle also fractured into multiple pieces, while the second control AY6 bar showed three externally connected hairline cracks.

All the SiC whisker-containing samples in the second cycle remained intact, but 6 of the 8 bars showed surface-connected cracking. As was observed in the first cycle, gate types 3 and 4 showed the greatest number of cracks after the second cycle. These cracks also tended to be associated with fold lines.

The radiographic results of the second cycle have not yet been determined, but it is believed that the results will be similar to those discussed for the first cycle with only a slight increase in damage severity.

The summary of data to date supports the premise that whisker-containing material can withstand severe binder removal schedules.

Another aspect of the current work includes optimization of forming by injection molding. Based on analyses of whisker orientation in injection molded parts, a new gating configuration was developed for the fabrication of CATE axial turbine blades from whisker-containing composites. The gate modification work concentrates on minimizing distortion in the airfoil section, which typically is not machined after densification.

Test Method Development

In compliance with the desire to standardize MOR within the DOE heat engine program, a new four-point loading fixture has been fabricated. The spans of this fixture conform to MIL-STD-1942(MR) configuration B (quarter point loading with outer span = 40 mm and load point diameter = 4.5 mm). Results using this fixture were

compared to MOR values obtained using the standard GTEL fixture (outer span = 22.0 mm, inner span = 9.8 mm, load point diameter = 6.1 mm). Room temperature MOR was conducted at a crosshead speed of 4.95 mm/min, which corresponds to calculated strain rates of $5.7 \times 10^{-3}min^{-1}$ and $7.4 \times 10^{-3}min^{-1}$ for the MIL-Std. and GTEL Std. fixtures, respectively. Initially, a ceramic with a high Weibull modulus, GTE Wesgo AL995 Al_2O_3, (M = 22) was used to compare the fixtures. The results (Table 8) show that both fixtures yield statistically identical results at room temperature. Further evaluation employing lower Weibull modulus test materials and high temperature testing is in progress.

Table 8: Comparison of Test Fixtures

Fixture	Room Temperature MOR of AL995[x]
MIL-STD-B	244±6 MPa
GTEL-STD	239±11 MPa

[x]average of ten bend bars

Status of Milestones

Program execution is on schedule.

Communications/Visits/Travel

J.G. Baldoni attended the 3rd International Symposium on Ceramic materials and Components for Engines (Las Vegas, NV, 11/27-30/88. A paper titled "Creep and Crack Growth Resistance of Silicon Nitride Composites by J.G. Baldoni and S.T. Buljan was presented and will be published in the conference proceedings.

H. Kim attended the Conference on Composite Materials at Cocoa Beach, FL, 1/16-20/89.

Problems Encountered

None.

Publications

None.

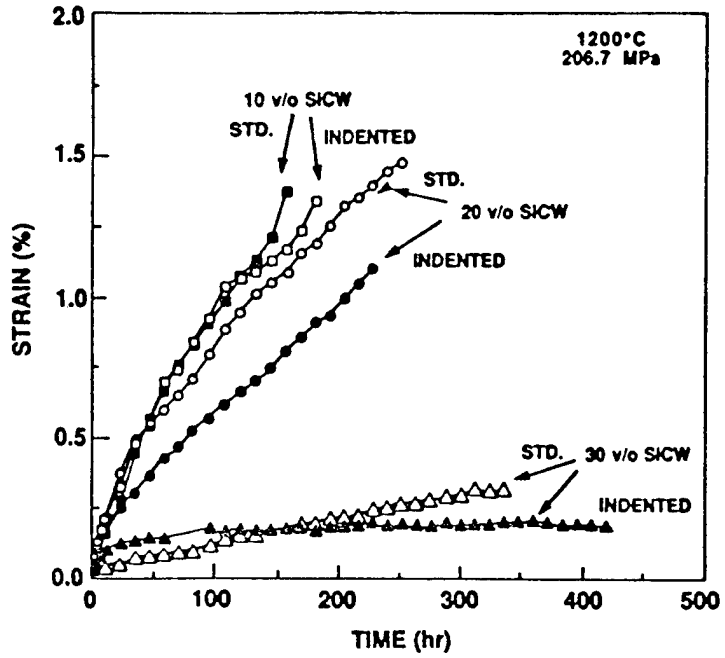

Figure 1. Comparison of precracked and standard bend bar subjected to creep at 1200°C

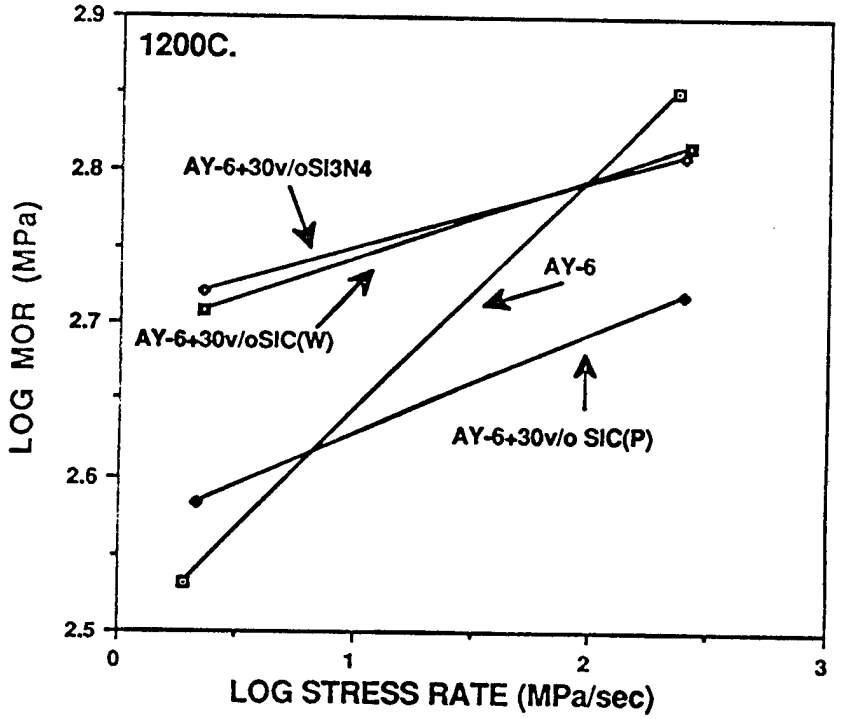

Figure 2. Effect of stressing rate on the strength of four silicon nitride-based ceramics

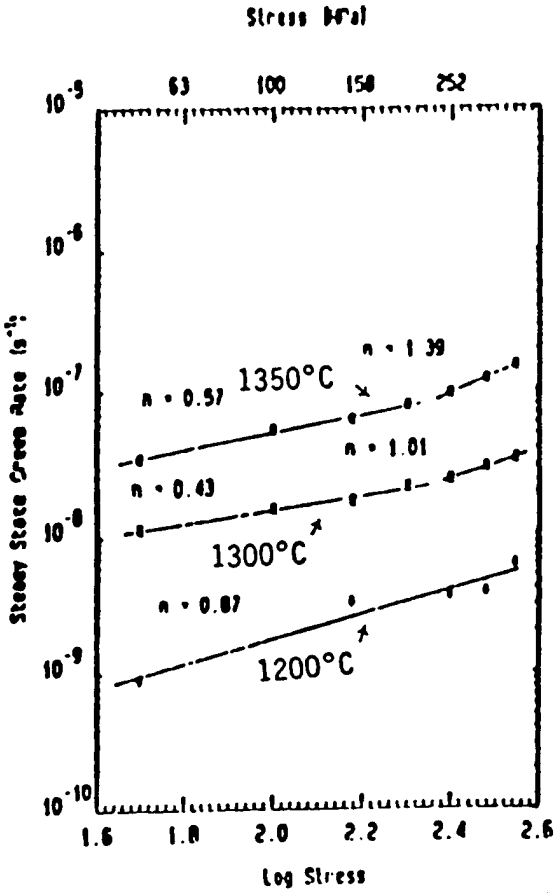

Figure 3. Steady-state creep rate versus stress for 30 vol. % SiC whisker-reinforced Si_3N_4

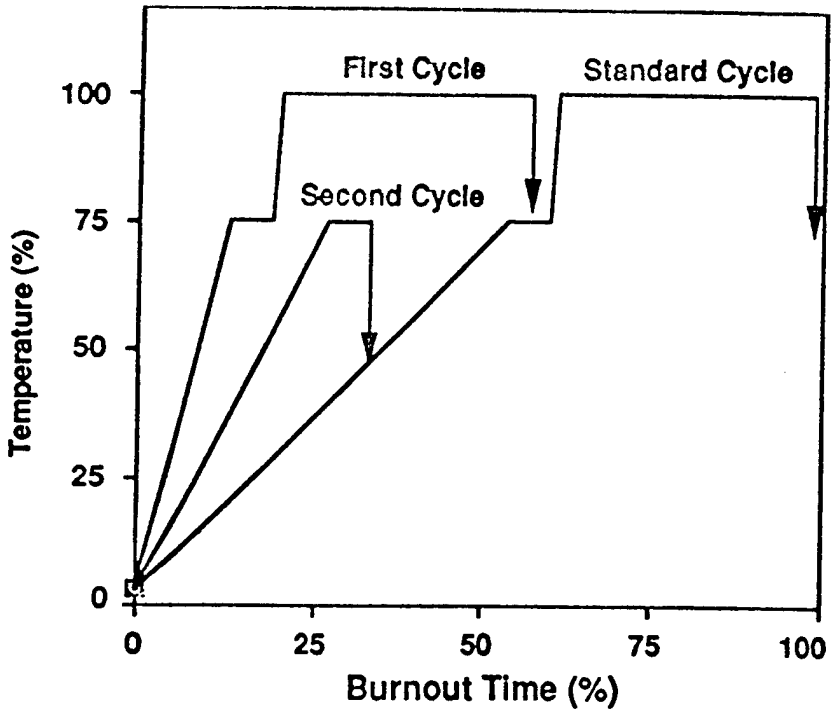

Figure 4. Comparison of experimental burnout cycles with the standard cycle for injection-molded materials

Material Development in the Si_3N_4/SiC(w) System Using Glass Encapsulated HIPing - Phase II

Normand D. Corbin, Glenn J. Sundberg, Kerry N. Siebein, Vimal K. Pujari, Guilio A.Rossi, Jeffrey S. Hansen, Janet L. Hammarstrom, and Craig A. Willkens.
(Norton Company)

Objective/scope

This two year program is to develop fully dense Si_3N_4 matrix SiC whisker composites which show enhanced properties over monolithic Si_3N_4 materials. Materials will be processed using an RBSN approach followed by high pressure glass encapsulation HIPing. The primary goal is to develop a composite with a fracture toughness >10 $MPa(m)^{.5}$ and capable of operating up to 1400°C.

Studies will be conducted to tailor the whisker/matrix interface and determine the optimum whisker morphology for fracture toughness improvements. The effect of forming on whisker orientation, fracture toughness, and shape distortion will also be addressed.

Technical progress

1.0 EVALUATION PROCEDURES

Procedures for analytical evaluations and mechanical property determinations have previously been described in detail.(1) Flexural strength is determined using the U.S. Army recommended procedures for a cross-section of 3 mm x 4 mm.(2) Fracture toughness is determined by either an indentation method (3), a controlled flaw method (4), or by a chevron notch method (5), depending on material availability.

As previously detailed (6) a technique was developed for determining the surface composition of individual SiC whiskers by Scanning Auger Microanalysis (SAM). This method was used to evaluate additional whisker materials.

Chevron Notch Fracture Toughness Testing - Room temperature and high temperature fracture toughness measurements of various composites and monoliths were measured using the Chevron Notch technique previously described (5). The specimen geometry was a 3 mm x 4 mm x 50 mm test bar, the chevron notch geometry had an $alpha_0$ = 0.55 and $alpha_1$ = 1.0. The test was performed on an

Instron 4206 testing machine, the loading rate was 0.012 mm/min. A 5 mm upper span and a 40 mm lower span were used. Chevron Notch test results were determined using both the Straight Through Crack Approximation (STCA) (7) and the Bluhm Slice Model (8). There was good agreement between the results calculated with both models. The results presented were calculated using the Bluhm Slice Model.

Room Temperature Toughness Comparisons - A composite and a monolith material were prepared using a HIPed SRBSN approach for evaluation of room temperature fracture toughness by several methods. This task was initiated to determine the effect of test method on fracture toughness. As shown in Table 1 there is a significant variability in toughness depending on the test method. This data demonstrates that great care should be exercised in comparing fracture toughness values from different analysis methods. In lieu of a standard testing procedure, it is recommended that the fracture toughness of a readily available material which has been extensively evaluated in the literature (for example NC-132) be tested along with composites. This will aid in comparisons between different techniques by supplying a normalization factor.

2.0 REINFORCEMENTS

Dispersion Behavior - The dispersion character of American Matrix SiC whiskers (9) was determined by relative acoustophoretic mobility (RAM) (10) (comparable to zeta potential analysis). Of particular interest was the effect of trace surface impurities and a silica layer on the isoelectric point. Results from four experiments are illustrated in Figure 1. Figure 1a shows that as received SiC(w) in deionized water at pH~6 possess a negative surface charge. An acid titration decreases the negative charge until the isoelectric point (IEP) of ~ 3.2 is reached. Below this point, the whiskers become positively charged. This behavior is similar to that for SiO_2 which has an IEP of 2.0. The reverse (base) titration shows a marked hysteresis when returning to a pH of ~ 6.0. This phenomenon is better illustrated in Figure 1b where the whiskers were soaked at low pH overnight. Upon reverse titration the surface charge does not change and remains positive even at high pH. This procedure has been shown to dissolve many surface impurities from the whiskers. Table 2 lists the concentration of ions present in the effluent from HNO_3 washing of these SiC whiskers. Our experience

TABLE 1 Comparison of Fracture Toughness Values as Determined by Different Methods

Material	Room Temperature Fracture Toughness ($MPa\sqrt{m}$)				
	IN[C]	CF[D]	CN[E]	CN[F]	DCB[G]
MONOLITH (A)	3.9±.1	4.2±.3	4.6±.1	---	4.9
COMPOSITE (B)	4.2±.1	5.2±.2	5.4±.1	4.6	6.4
NC-132	3.5±.1	4.6±.1	---	4.3	---

A) 4 w/o Y_2O_3 in HIPed SRBSN (Norton Product 3X015)

B) 4 w/o Y_2O_3 in HIPed SRBSN matrix, 30v/o SiC(w), random orientation (Product 7X014)

C) Indentation method; Anstis et al, 10kg indent, measured at 400X magnification

D) Controlled flaw method; Chantikul et al, 10kg indent, MIL-STD-1942 bar

E) Chevron Notch; Courtesy N.Shaw, NASA Lewis Research Center

F) Chevron Notch; determined at Norton Company

G) Double Cantilever Beam; Courtesy A.H.Heuer, Case Western Reserve

with SiC powders has indicated that the presence of Ca^{++} and Mg^{++} ions (hydroxides having IEPs ~ 12.5) result in RAM behavior which is characteristic of the data in Figures 1a and 1b. Thus, these ionic impurities control the whisker dispersion behavior.

The curves in Figures 1c and 1d show the effect of a surface silica layer on SiC. The whiskers in Figure 1c were oxidized in air at 1000°C for 1 hour prior to analysis. The resulting IEP in the acid titration has shifted downward to ~ 2.7, closer to the IEP of silica (~ 2.0). The curve in Figure 1d represents data from an HF cleaned AMI whisker.(11) This process will remove a SiO_2 layer. The IEP value of 4.5, is considerably higher than "as-received" whiskers suggesting the removal of the silica layer. For both traces a marked hysteresis occurs upon increasing pH. As with the "as-received" whiskers ionic impurities have a strong influence on their dispersion behavior.

TABLE 2 Concentration of Ions Detected by Atomic Absorption Spectrophotometry in Effluent from Acid Soak of American Matrix SiC Whiskers

Fe	45ppm	Ca	420ppm
Cr	10ppm	Mg	124ppm
Ni	100ppm	Al	180ppm

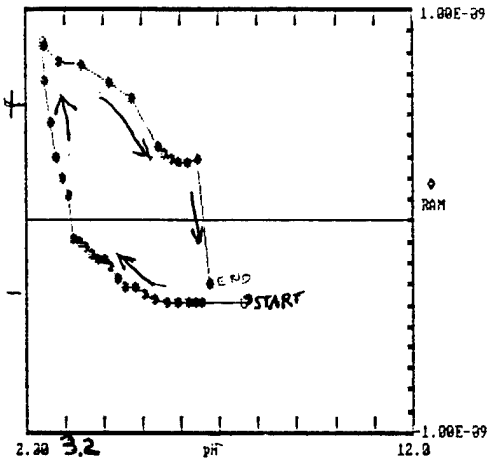

a) As received AMI whiskers, Acid-Base Titration

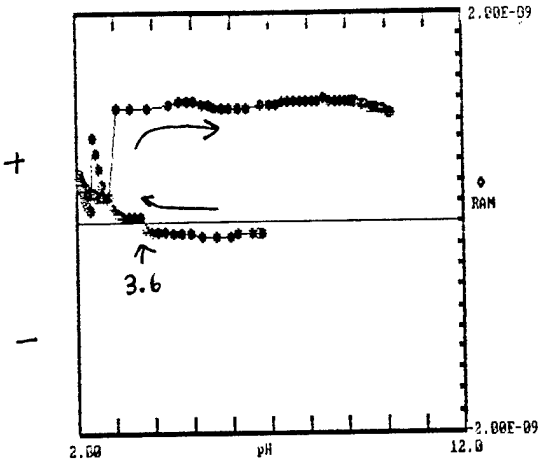

b) As received AMI whiskers Acid Titration and 24 hr acid soak followed by base Titration

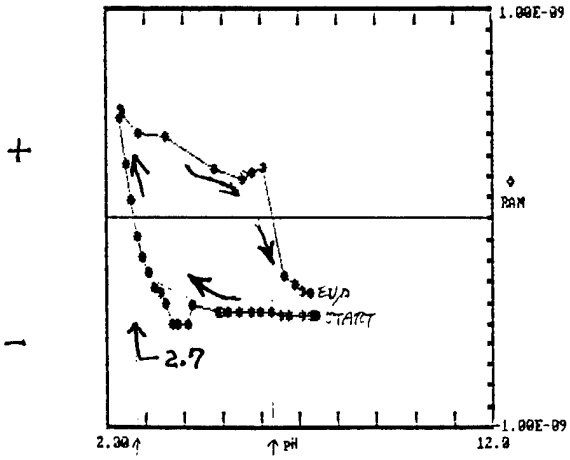

c) Oxidized AMI whiskers, Acid-Base Titration

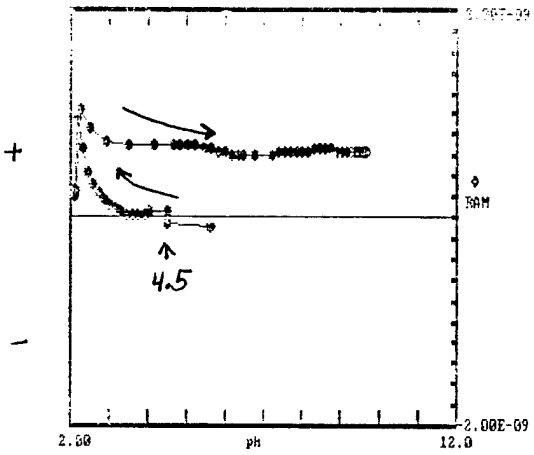

d) HF cleaned AMI whiskers, Acid Titration and 24 hr acid soak followed by base Titration

Figure 1 Relative Acoustophoretic Mobility (RAM) vs. Ph for SiC Whiskers

3.0 FORMING

An extrusion die and an injection mold have been prepared to fabricate composites with uniaxially aligned whiskers into 3 mm x 4 mm x 50 mm test bars. Prior to this, only substandard size bars could be molded or extruded. Fully dense extruded material has been successfully prepared into 3 mm x 4 mm x 50 mm bars. This was accomplished by extruding oversized rods and machining to the required dimensions after HIPing.

4.0 INTERFACE

Boron Nitride - Boron nitride coatings are being applied to SiC grain (~ 100μm) and SiC whiskers at Norton Company. The grain is used to develop the BN coating process and determine BN reactivity in Si_3N_4. During this contract period the reactivity of BN coatings in Si_3N_4 was evaluated. In addition, BN coated SiC whiskers and composites with BN coated whiskers were evaluated.

Composites were prepared utilizing boron nitride coated SiC grain (~ 2μm thick coating). The composition and structure of the coatings were previously described.(5) The grain was incorporated into both a Si_3N_4 matrix and an SRBSN matrix and then HIPed to full density to compare the effect of different processing on the resulting interface structure. Evaluation of the interface after HIPing was conducted by optical microscopy on polished specimens. The results showed that the BN interface was deteriorated as a result of the RBSN process. The coating is no longer continuous on the grains and appears to migrate into the matrix. The cause for this is unclear but may be a result of the oxygen content (~ 7 atomic %) of the coating being in the form of B_2O_3 which would melt and flow at typical nitridation temperatures (~ 1400°C). These results demonstrate the need for protective overcoatings to limit degradation of BN when the composite undergoes a nitridation step. Protective coatings are under development. The material prepared with Si_3N_4 powder did not show interface deterioration as with RSBN. The coating remained on the SiC grain and was of uniform thickness. It should be noted that when BN is present at the interface debonding occurs when an indentation crack interacts with the interface. This is clearly demonstrated in Figure 2 where cracks interact with coated and uncoated grains.

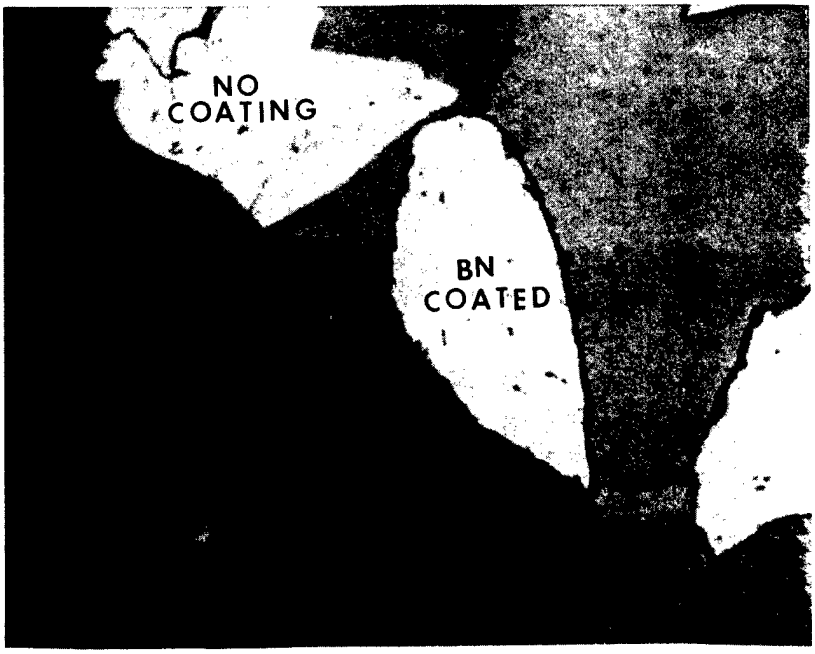

Figure 2 Crack interactions with BN coated and uncoated SiC grain in Si_3N_4

A BN coating was applied to American Matrix SiC whiskers. Hexagonal BN (PDF#34-421) was detected by XRD. Auger analysis (Figure 3) shows the coating to be stoichiometric BN and contain 10-15 atomic percent carbon. TEM reveals the coating to be ~ 150-300nm thick, crystalline, and to contain a whiskery (or platey) morphology oriented perpendicular to the whisker surface (Figure 4). The "as-coated" whiskers were bonded together by the BN coating. Prior to blending with matrix materials the whiskers were ground in a mortar and pestle to break up the agglomerates. After deagglomeration the material was evaluated by optical microscopy. The whisker morphology of the SiC was still apparent.

The coated SiC whiskers were blended (~ 15 wt%) with Si_3N_4 powder (4 wt%, Y_2O_3) and HIPed to determine the survivability of thin (~ 200 nm) coatings during processing. The interface was evaluated by TEM to determine morphology and crystallinity. In most cases the BN remained at the SiC whisker/matrix interface but it was also present in the matrix. Its presence in the matrix is attributed to grinding of the whiskers prior to their blending with Si_3N_4 where the coating could break away from the whisker surface. The BN had a layered structure ranging from 5-10 nm thick. Figure 5 is a bright field transmission electron micrograph of the BN. The structure

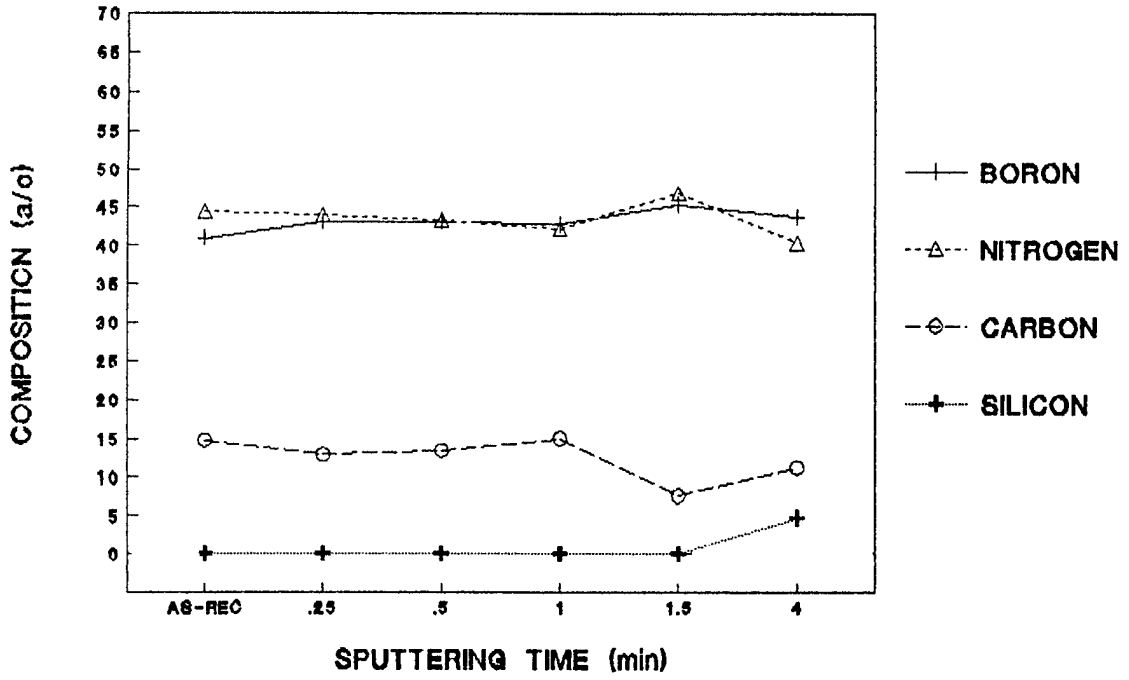

Figure 3 Auger electon spectroscopy of BN Coating on SiC whiskers applied by CVD at Norton Company

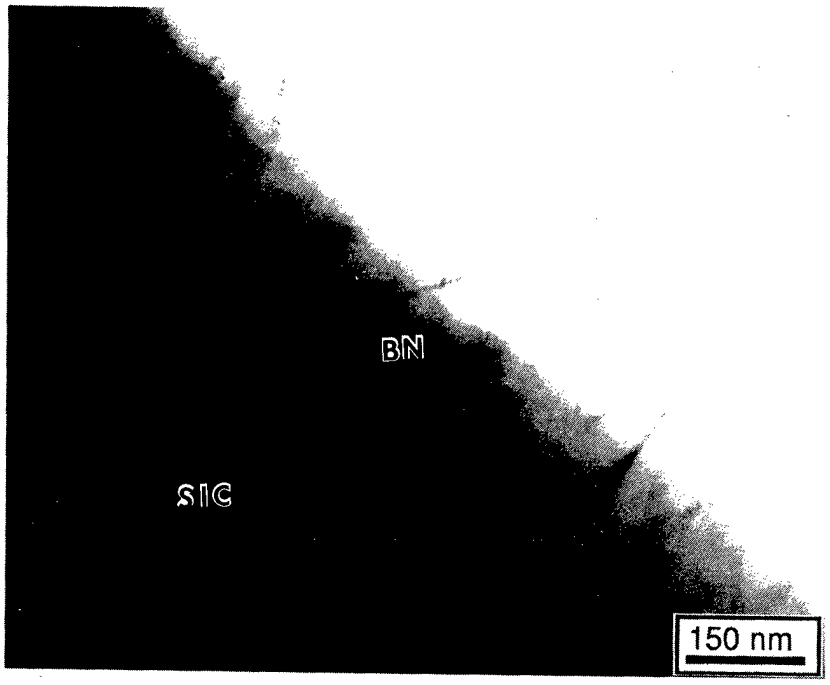

Figure 4 TEM Micrograph of the BN coating on a SiC whisker applied by CVD at Norton Company

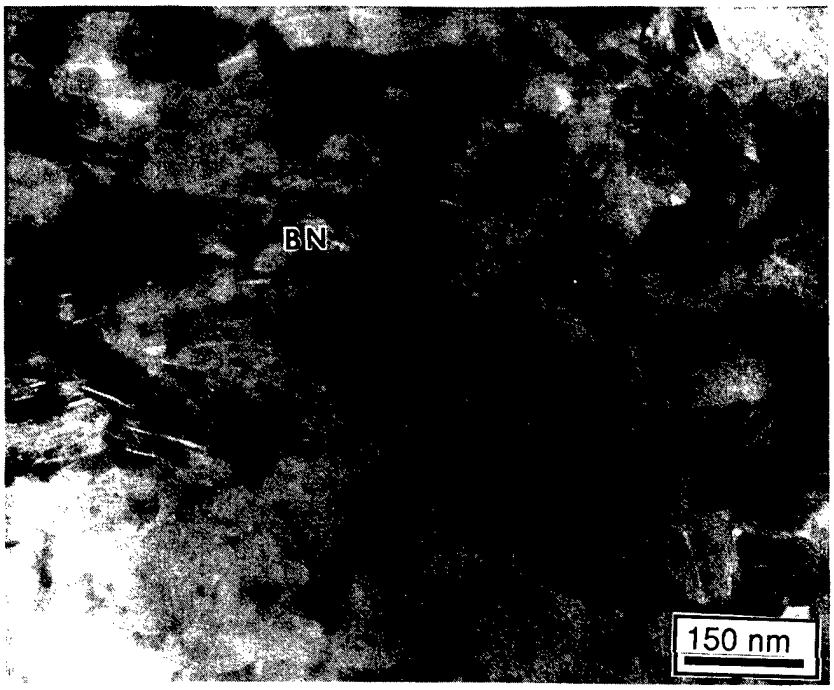

Figure 5 Bright field transmission electron micrograph of the BN coating. The layers of BN are approximately 5-10 nm thick and are not densely packed.

is a mix of microcrystalline and amorphous BN. The thickness of the BN interface varied greatly and the coating was not continuous. The coating thickness ranges from 0 nm to over 3.0 microns. Figure 6 is a bright field transmission electron micrograph of the whisker BN interface. The BN coating is approximately 50-75 nm thick in this area. In most areas the coating did not appear well bonded to the whiskers nor was it fully dense; that is it contained voids between the layers.

Figure 7 is a photomicrograph of the interaction of a crack with a BN coated whisker in the HIPed material. The BN interface allows debonding to occur at the interface. This debonding should improve fracture toughness by promoting crack bridging and whisker pullout. Materials for fracture toughness evaluation are being prepared.

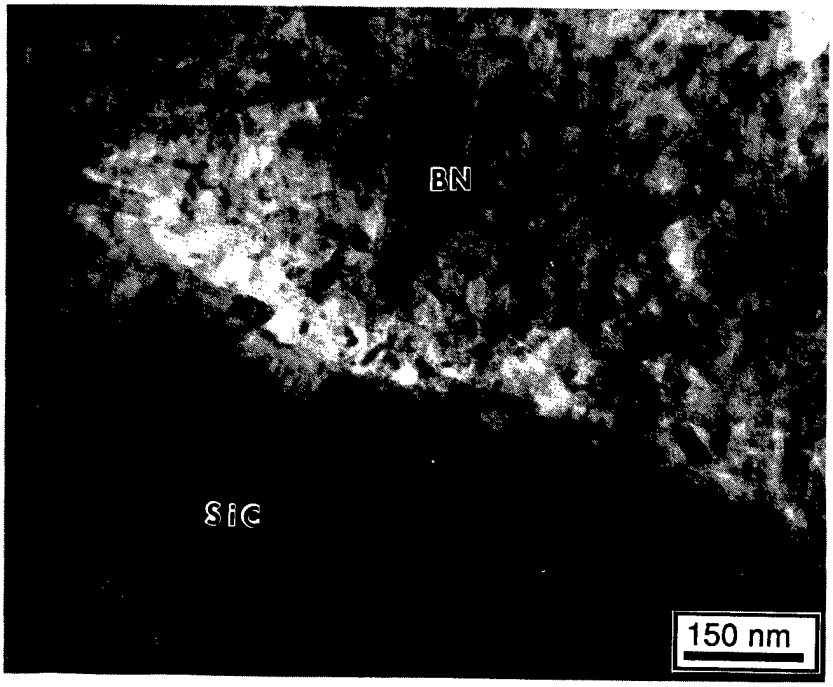

Figure 6 Bright field micrograph of the BN coated a whisker/ matrix interface. The coating is approximately 50 nm thick in this area.

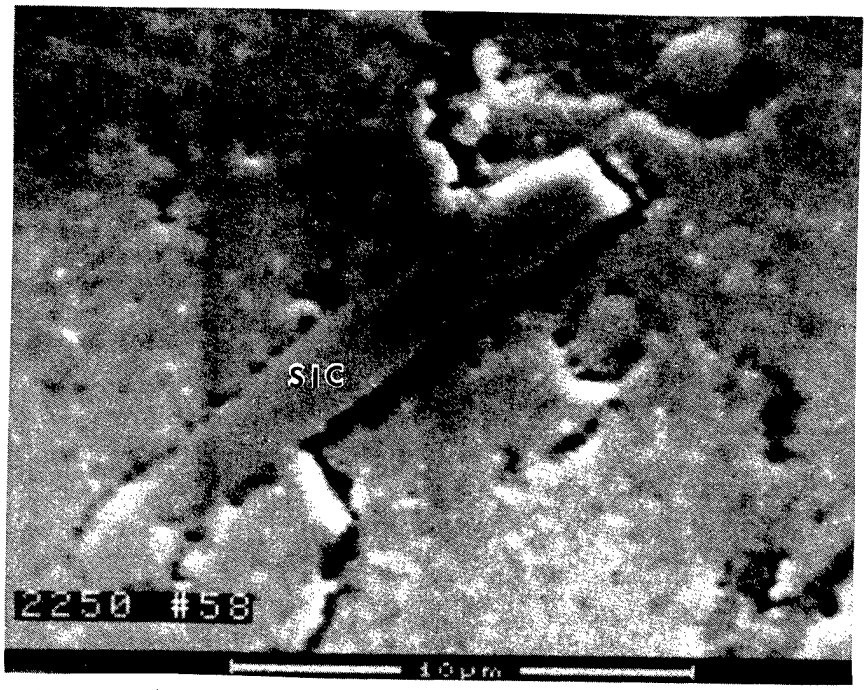

Figure 7 Evidence of debonding in the HIP'ed composite reinforced with BN coated SiC whiskers.

Carbon - As previously reported (5) Auger analysis of SiC whiskers prepared at ACMC (12) shows a carbon surface. TEM examination revealed a continuous and amorphous surface coating ranging in thickness from ~ 2-4 nm. These whiskers were incorporated into a Si_3N_4/4 wt% Y_2O_3 matrix at a 30 volume percent loading, injection molded to uniaxially align the whiskers, and HIPed to full density using the ASEA glass encapsulation method. The controlled flaw fracture toughness for this material was 6.9 MPa$\sqrt{m}$. TEM analysis was conducted to determine if the carbon coating on the whiskers remains in the processed composite. The carbon layer was not observed. The carbon may have dissolved into the glassy phase, although the mechanism of carbon loss is unconfirmed. The interface thickness between SiC and Si_3N_4 was ~ 2-4 nm. It is expected that a portion of this boundary contains the intergranular glassy phase, which typically forms a thermodynamically stable, continuous grain boundary film.(13)

A limited number of carbon coated Tokai whiskers (Grade 300C) were examined by TEM to determine the thickness of the carbon layer on the whiskers. The amorphous carbon coating on the as-received whiskers was continuous and approximately 3.5 nm thick. The whiskers were predominantly alpha SiC and contain many inclusions. Metal beads were present at the ends of the whiskers. A composite prepared from Si_3N_4 powder and 4 wt%, Y_2O_3 with 30 vol% of these whiskers was examined using TEM to determine if the carbon coating was present after composite processing. The interface between the SiC whisker and the Si_3N_4 matrix did contain carbon (Figure 8), although the carbon layer appeared to be between 30 to 120 nm thick. The discrepancy between carbon layer thickness in the composite relative to the as-received whiskers is suspected to be due to a variable coating thickness between the as-received whiskers. Fewer whiskers in the composite were examined than in the as-received state and the preliminary TEM analysis must not be considered a statistically representative sample. The carbon coating had a layered, crystalline appearance after processing, similar to graphite. The carbon coating was discontinuous around the whiskers and large regions of the coating were present within the matrix. The coating did not appear well bonded to either the whiskers or the matrix. The graphitization of the carbon layer during densification had also been observed when these whiskers were incorporated into a spinel matrix.(14)

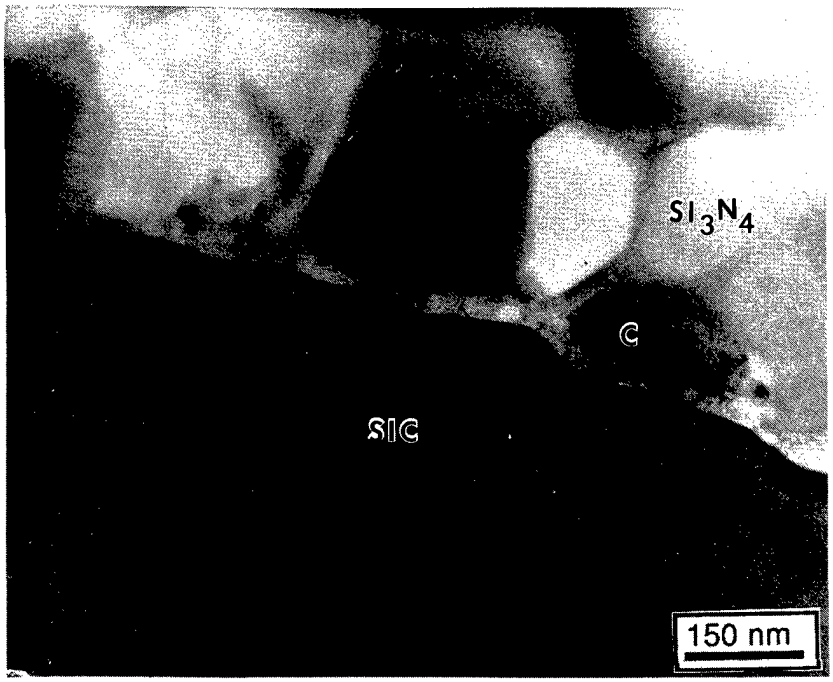

Figure 8 Bright field transmission electron micrograph of the carbon coated Tokai SiC whisker/4 wt% Y_2O_3-Si_3N_4 interface.

Oxide - The application of a Norton proprietary oxide coating to American Matrix Inc. SiC whiskers was accomplished using a solution/reprecipitation method. The coating was examined by TEM. A bright field micrograph of the coated whisker is presented in Figure 9. The coating is microcrystalline, continuous, and ranges from 10 nm to 20 nm thick.

A Si_4N_4 (4 wt % Y_2O_3) matrix was reinforced with 20 volume % of these whiskers. The composite was injection molded to uniaxially align the whiskers and HIPed to full density using the ASEA process. The controlled flaw fracture toughness for this material is 6.8 MPa$\sqrt{m}$. The resulting interface between Si_3N_4 and the SiC whiskers was evaluated by TEM. The coating is not present on the whiskers after densification. It must have dissolved into the glassy phase during processing. No effect of the coating on increasing the interface thickness in the composite was observed. A thin film, approximately 1 nm to 2 nm thick, was present between adjacent Si_3N_4 grains and between SiC whiskers and Si_3N_4 grains. The glassy phase appeared to segregate to large pockets at multigrain junctions.

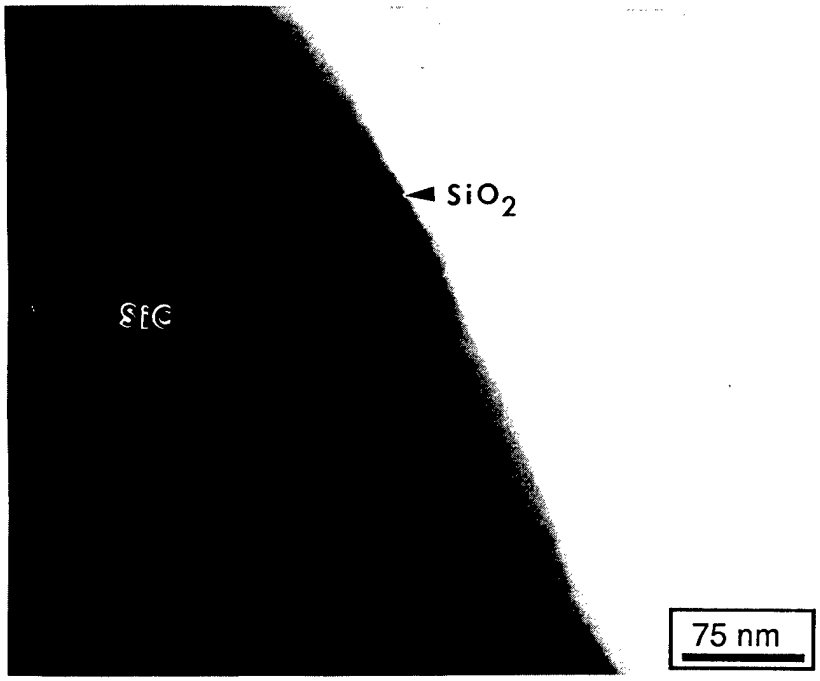

Figure 9 Bright field electron micrograph showing the oxide coating applied by a solution method on a SiC whisker.

The observations of the grain boundary thicknesses in the composite specimen agree with values observed experimentally in a wide number of ceramics. A previous study by D. R. Clark (15) concluded that there is an equilibrium thickness for the intergranular film in polycrystalline ceramics. The equilibrium thickness for siliceous films in hot pressed Si_3N_4 is on the order of a few silica tetrahedra, approximately 1 nm to 2 nm.(15) The dielectric constants of the grain determine the thickness of the intergranular phase, therefore it was expected that the grain boundary thicknesses would be different between two Si_3N_4 grains and between a Si_3N_4 grain and SiC. However, in the composite speciman the thickness of the grain boundaries between the two were similar.

Interfacial Stresses - Multiphase materials are known to develop residual stresses as a result of differtial thermal expansion mismatch between the matrix and reinforcement phase. The presence of these stresses has been used to explain fracture toughness variations in Si_3N_4 monoliths with different secondary phases.(16) Experimental qualification of these stresses are difficult but have been obtained for the Al_2O_3/SiC(w) system by an x-ray diffraction method.(17) Different models exist to calculate the anticipated residual stresses in various composite systems. Recent work by Hsueh et.al. (18) have incorporated the presence of an interfacial film between the SiC(w) and Al_2O_3 and mullite matrices. A cylinder composite model was used to determine the residual stress which developed upon cooling. The interfacial stress generated during cooling decreased as the thermal expansion coefficient of the film increased for the case of SiC whiskers in Al_2O_3. In this case the thermal expansion of the matrix is greater than SiC. When the thermal expansion of the whisker is greater than the matrix (for example Mullite/SiCw) the opposite is observed. Interfacial stresses decrease as the thermal expansion coefficient of the film decreases. This later case is comparable to SiC whisker in Si_3N_4.

Similar calculations were performed at Norton Company to estimate the residual stresses in the Si_3N_4/SiC(w) system. A composite cylinder model containing an intergranular phase between the Si_3N_4 and SiC (Figure 10) was selected. Stresses were calculated by finite element analysis methods. End effects were not considered in these calculations. The material properties and geometry constraints are listed in Table 3. The effect of intergranular phase thickness and intergranular phase coefficient of thermal expansion (CTE) on the maximum principle tensile stress within the system is exhibited in Figure 11. Interfacial tensile stresses greater than 800 MPa can occur within the intergranular phase when the intergranular phase has a CTE $\geq 7.0 \times 10^{-6}$. It should be noted that secondary phases with CTE's above 7.0×10^{-6} are known to appear in Si_3N_4 materials. For example, Y_2SiO_5 11.4×10^{-6} (001 direction (19)), and $Y_5(SiO_3)_3N$ 8.2×10^{-6} (bulk (20)). The maximum principle tensile stress occurs in the SiC whisker rather than in the intergranular phase at low CTE values for the intergranular phase. There was little effect of changing the intergranular phase thickness from 10 nm to 50 nm.

TABLE 3 Material Properties and Geometry Contraints Used for the Calculation of the Residual Stresses

Materials Properties

Si_3N_4: E = 300 GPa, Poisson ratio = 0.3, CTE = 3.5 x $10^{-6}/^{o}C$

SiC: E = 440 GPa, Poisson ratio = 0.3, CTE = 4.5 x $10^{-6}/^{o}C$

Inter Granular Phase: E = 186 GPa, Poisson ratio = 0.3, CTE = 3.0 - 12.0 x $10^{-6}/^{o}C$

Geometric Conditions

30 volume percent SiC

SiC diameter = 0.5 um

Change in Temperature = 1000°C

Intergranular Phase Thickness = 10 nm, 50 nm

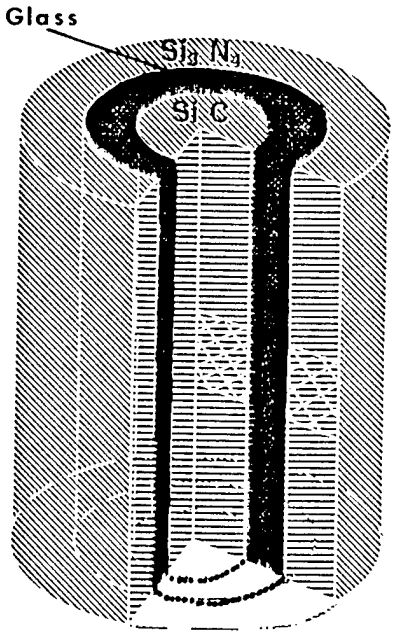

Figure 10 The composite cylinder model used to determine residual stress from thermal expansion mismatch.

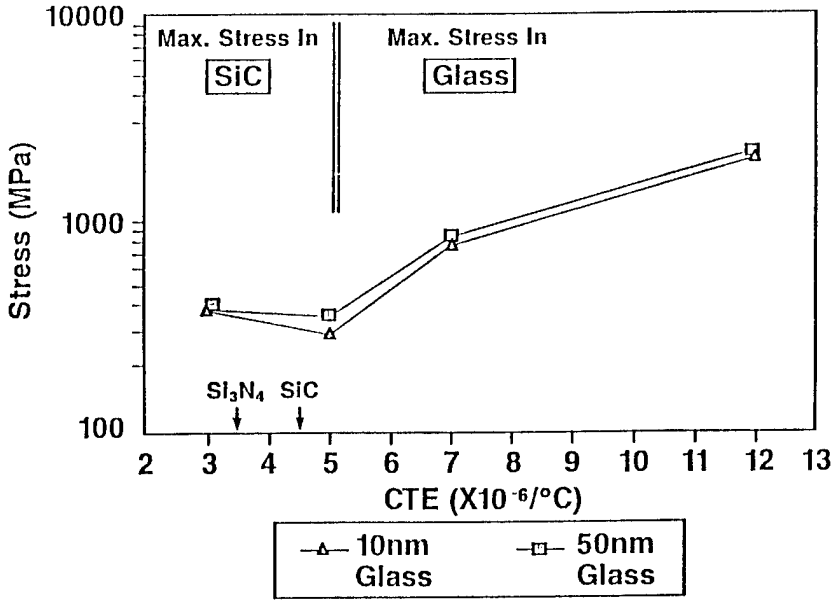

Figure 11 Maximum residual tensile stress as a function of intergranular phase thermal expansion coefficient and thickness of the intergranular phase.

5.0 PROPERTY PROGRESS

High Temperature Strength - Our experience has shown that the impurity content of Si_3N_4 materials has a significant effect on high temperature (>1300°C) mechanical properties. As compared to Si_3N_4 the SiC whiskers contain relatively high impurity contents. A study was initiated to determine if these impurities are affecting high temperature properties.

Involved were a standard purity and high purity matrix; a standard purity SiC whisker (Tateho T44), a high purity SiC whisker (Tokai) and a high purity SiC particulate (see Table 4). It should be noted that there is considerable lot-to-lot variation in the purity of SiC whiskers and we have chosen specific lots to conduct this evaluation. The particulate possessed a 2μm average particle size.

The mechanical property results are compared in Table 5. The composite 1370°C fast fracture strength was more influenced by the purity of the matrix than the reinforcement. When the high purity matrix was used a strength of 544 MPa (~80 ksi) was obtained. The standard matrix

produced composites of ~ 415 MPa (~ 60 ksi) independent of reinforcement purity. A similar trend is observed when comparing the high purity monolith to the standard grade. It has been previously observed in the Tateho product that inclusions are concentrated within the whisker core.(21) In this location impurities would be less likely to diffuse into the matrix and modify the high temperature properties. This may be the reason that there were no observed differences as a result of the reinforcement phase used. The importance of the matrix purity on composite properties is most likely a result of its prominence (70-80 w/o) in the composite. It should be noted that the monolith strengths are higher than the composite with the corresponding matrix (634 vs. 544, high purity and 517 vs. ~ 410, Std purity).

Preliminary stress rupture life at 1370°C shows both the monolith and composite exceeded 200 hrs at 200-250 MPa. There were no dramatic differences between composite, and monolith, or between purity levels. The fracture toughness of the composite made with SiC was 20% higher than that of the composites made with SiC particulate (5.3 vs. 4.4). This is consistent with the work of Faber and Evans showing whisker morphologies to being more effective than particulates in toughening (22).

Elevated Temperature Toughness - The fracture toughness to 1370°C was determined on selected materials using a chevron notch method. (See Table 6) For this analysis we included a hot pressed Si_3N_4 with 1 wt%, MgO (NC-132) as a reference material. This material is reported to have a room temperature toughness of 4.7 MPa$\sqrt{m}$ by a chevron notch method.(23) Our result is 8.5% lower. The other samples consist of a monolith representative of the composite matrix, a composite with uncoated SiC whiskers, and a composite with carbon coated whiskers. The toughest specimen (2197 #50) exhibited whisker pullout on the fracture surface as shown in Figure 12. This sample uses AMI SiC whiskers which were treated at Norton Company to produce a thin carbon layer at the surface. The room temperature toughness of this sample is 26% higher than the composites without a carbon surface (5.8 vs. 4.6). This improvement in toughness is observed to 1370°C. The NT-154 monolith fracture toughness is essentially identical to the composite with uncoated SiC whiskers (7X014) further demonstrating the need for interface modification for toughness improvements.

TABLE 4

Impurity Contents of SiC Whiskers and Matrix Materials*

(ppm)

	Lot	Fe	Ca	Al
Tateho T44	11/86	340	810	3100
Tokai	7/87	63	26	46
Nissorundum	GMF5H2	17	1	30
High Purity Matrix*	--	90	18	30
Std. Purity Matrix*	--	260	33	130

*HIP SRBSN (4% Y_2O_3) matrix

TABLE 5

Properties of Materials Evaluated to Determine the Effect of Impurities

SAMPLE Matrix (c)	Reinforcement	Code	CFT (a)	1370 C Strength (b)
High Purity	--	2154M-43	5.4±.2	92±5 (634±34)
Standard	--	3XO15	4.2±.2	75±9 (517±62)
High Purity	20% Standard (Tateho T44)	2154C-43	5.3±.3	79±4 (544±28)
Standard	30% Standard (Tateho T44)	7X014	5.2±.1	61±3 (421±21)
Standard	30% High Purity (Tokai 7/87)	2206-51	5.3±.1	59±2 (407±14)
Standard	30% High Purity (SiC Powder)	2207-51	4.4±.2	61±1 (421±7)

a) control flaw fracture toughness in $MPa\sqrt{m}$

b) 4 point specimen MIL-STD 1942 3x4mm in Ksi (MPa)

c) HIP SRBSN (4% Y_2O_3) matrix

TABLE 6

Chevron Notch Toughness Results

Material Code	Matrix+ Composition	30 v/o SiC Whisker	RT	1000°C	1200°C	1370°C
NC132	Si_3N_4 + 1% MgO	---	4.3	---	3.91	---
NT154	Si_3N_4 + 4% Y_2O_3	---	4.7	4.1	3.74	4.07
7X014	SRBSN + 4% Y_2O_3	Tateho	4.6	---	3.9	4.1
2197#50	Si_3N_4 + 4% Y_2O_3	C-Coated AMI SiCw*	5.8	5.2	5.6	4.7

Specimen cross-section is 3 mm x 4 mm

* Coating applied at Norton Company

+ Si_3N_4 = use of Si_3N_4 powder precursor

SRBSN = use of Si powder precursor followed by nitridation step

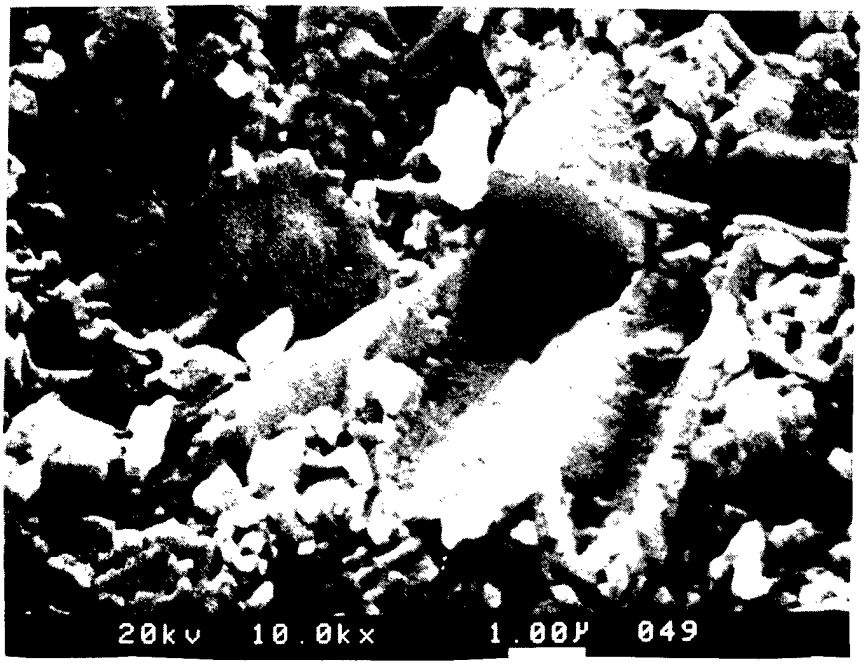

Figure 12 Secondary electron image of the fracture surface of a 30 vol% AMI SiC whisker reinforced 4 wt% Y_2O_3-Si_3N_4 chevron notch bar.

6.0 SUMMARY

Stoichiometric BN has been deposited on AMI SiC whiskers by CVD. The BN coated SiCw have been incorporated into a 4 wt% Y_2O_3-Si_3N_4 matrix and HIP'ed to full density. The BN interface was present after densification and during crack interaction provided debonding of whiskers from the matrix.

The chevron notch toughness of a carbon coated AMI SiC whisker reinforced 4 wt% Y_2O_3-Si_3N_4 composite was on average 30% greater than the unreinforced monolith from 22 to 1200°C.

The mean room temperature controlled flaw toughness of SiO_2 and C coated AMI SiC whisker reinforced 4 wt% Y_2O_3-Si_3N_4 composites were 6.8 MPa$\sqrt{m}$.

Status of milestones

All Milestones are on schedule.

Publications

1. C.A. Willkens et al, "The Influence of Microstructure Orientation on the Fracture Toughness of Si_3N_4 Based Materials," *Cer. Eng. and Sci. Proc.*, Vol. 9, No. 9-10, p.1367 (1988).

2. N.D. Corbin et al, "The Influence of Reinforcement Orientation on the Toughness of Si_3N_4 Matrix Composites," in the *Proceedings of Whisker and Fiber Toughened Ceramics*, Ed. R. Bradley, D. Clark, D. Larsen, J. Stiegler, ASM International, p.131 (1988).

3. N.D. Corbin et al, "Material Development in the Silicon Nitride-Silicon Carbide Whisker System," to be published in the *Proceedings of the 26th Automotive Technology Development Contractors' Coordination Meeting October 1988*, Society of Automotive Engineers Inc. Warrendale, PA.

References

1. N. D. Corbin and C. A. Willkens, "Development of Toughened Si_3N_4 Composites by Glass Encapsulated Hot Isostatic Pressure Final Report," ORNL/SUB/86-95906/1.

2. MIL-STD-1942 (MR), Flexural Strengths of High Performance Ceramics at Abient Temperature, November 21, 1983.

3. G. Antis, et al, *Journal of the American Ceramic Society*, Vol. 64, #9, p. 533-543, September 1981.

4. Chantikul, et al, *Journal of the American Ceramic Society*, Vol. 64, #9, p. 539-543, September 1981.

5. N. D. Corbin, et al, *Ceramic Technology for Advanced Heat Engines Project Semiannual Progress Report for April 1988 to September 1988*.

6. N. D. Corbin, et al, *Ceramic Technology for Advanced Heat Engines Project Semiannual Progress Report for October 1987 1988 to March 1988*, ORNL/TM-10838, p.39-59.

7. D. Munz, J. L. Shannon, R. T. Bubsey, *Int. J. of Fracture*, Vol. 16, p.R137-R142 (1980).

8. J. Bluhm, *Eng. Frac. Mech*, Vol. 2, Pergamon Press, Great Britain, p.593-604 (1978).

9. American Matrix Inc., Knoxville, TN, Generation 4 Grade 1A SiC Whisker.

10. Pen Kem Inc., Bedford Hills, New York, Model 700 Acoustophoretic Analyzer.

11. American Matrix Inc., Knoxville, TN, HF washed SiC Whisker, No. 3580.

12. Advanced Composites Materials Corporation, Greer, SC.

13. D. R. Clarke, Colloque C4, supplement au n 4. Tome 46, C4-51-C4-59, avril 1985.

14. M. Yamamoto et al, *Conference Proceedings of Whisker and and Fiber Toughened Ceramics*," Published by ASM International, Edited by R. A. Bradley, D. E. Clark, D. C. Larsen, J. O. Stiegler, p.73-79 (1988).

15. D. R. Clarke, *J. Am. Ceram. Soc.* 70(1), 15-22 (1987).

16. D. J. Kim, P. Greil, G. Petzow, *Advanced Ceramic Materials* 2 (4) 822-26 (1987).

17. P. Predecki, A. Abuhosan, C. S. Barnett, To be published in *Advances in X-ray Analysis*.

18. C. Hsueh, P. F. Becher, P. Angelini, *J. Am. Ceram. Soc.* 71(11) 929-33 (1988).

19. H. M. O'Bryan, P. K. Gallagher, G. W. Berkstresser, *J. Am. Ceram. Soc.* 71(1) C42-C43 (1988).

20. R. R. Wills, S. Holmquist, J. M. Wimmer, J. A. Cunningham, *J. Mat. Sci.* (11) 1305-1309 (1976).

21. P. Pirouz et al, *Interfaces in Polymer, Ceramic, and Metal Matrix Composites*, Elsevier Press, New York, Editor H. Ishida, p.141-153 (1988).

22. K. T. Faber, A. G. Evans, *Acta metall*, Vol. 31, No. 4, p.565-576 (1983).

23. J. A. Salem, J. L. Shannon, *J. Mat. Sci.* (22), 321-324 (1987).

Pressureless Sintering of Si_3N_4/SiC Whisker Composites

S. D. Nunn and T. Y. Tien (University of Michigan)

Objective/scope

Compositional evaluation has been continued in an effort to achieve the highest possible densities while increasing the SiC whisker content in Si_3N_4 matrix composites using yttrium aluminum garnet (YAG) as a liquid phase sintering aid. Additionally, preliminary test measurements have been made to determine the mechanical properties of the sintered ceramic composites.

Technical progress

Sintering aid additions

Compositions consisting of a β-Si_3N_4 matrix reinforced with SiC whiskers and containing YAG as a sintering aid were prepared and sintered. The processing procedure is shown in the flow diagram in Fig. 1. The individual processing steps have been described in detail in an earlier report.[1] The amount of SiC whisker addition varied from 0 to 40 wt.% and the YAG addition was also varied. The compositions evaluated are shown in Tables 1 and 2.

Four-point bend testing

Specimens for four-point bend testing were machined from the sintered ceramic composite samples. The test specimens were rectangular bars 2-mm wide by 1.5-mm thick by 19-mm long. All surfaces of the bars (except the ends) were ground in a direction parallel to the length of the bar. The tensile surface was later polished to remove the machining marks. The four-point bend test fixture was self-aligning and had an inner span of 4 mm and an outer span of 13.5 mm. The fracture strength and toughness were measured in a mechanical testing machine using a crosshead speed of 0.13 mm/min (0.005 in/min).

For the fracture toughness measurements, a controlled flaw consisting of a Vicker's diamond point indent using a 20 kg load was made in the tensile surface of the test bar at the midpoint of the inner span. K_{IC} was then calculated using the equation reported by Chantikul et al.[2]

Results and discussion

Sintering aid addition - Some properties of the sintered composites which are related to the sinterability of the different compositions are shown in Table 1. The variation of the theoretical density of the samples with the whisker content is shown graphically in Fig. 2.

For the samples listed in Table 1 as SCW0 through SCW30, the Si_3N_4-to-YAG ratio was held constant while the whisker content was varied from 0 to 30 wt.%. As a result, the wt.% of YAG sintering aid in the overall composition was decreased as the whisker content was increased. As shown by the plot of the open circles in Fig. 2, this resulted in a sharp drop in density for the samples with greater than 10 wt.% SiC whiskers.

The wt.% of the YAG addition in samples SCW20-2 and SCW30-2 was held constant at the same level in the overall composition as for the sample with 0% whiskers. In these samples, the SiC whiskers replaced an equivalent wt.% of the Si_3N_4 matrix. With the increased amount of sintering aid additive (over SCW20 and SCW30), these samples sintered to higher densities as shown by the closed circles in Fig. 2.

The amount of sintering aid was increased further in SCW30-3 and SCW40 resulting in the densities shown by the open squares in the figure.

Four-point bend testing - Listed in Table 2 are the fracture strength and fracture toughness values for several composite compositions measured in four-point bending. The fracture strengths are on the high end of the range of values reported by other workers for hot-pressed composites.[3-6] The relatively high values may, in part, be due to the small size of the test bars. The fracture toughness values (except for sample 5) lie in the middle of the range of values reported for hot-pressed composites made with commercially available whiskers.[4-6]

Summary

1. Sintering evaluations show that for sintered composites of a Si_3N_4 matrix reinforced with SiC whiskers, the amount of YAG added as a liquid phase sintering aid must be increased as the whisker content is increased if high densities are to be obtained.

2. Preliminary tests of sintered Si_3N_4/SiCw composites to determine the fracture strength and fracture toughness measured in four-point bending show values in the same range as those reported for hot-pressed composites.

References

1. S. D. Nunn and T. Y. Tien, "Pressureless Sintering of Si_3N_4/SiC Whisker Composites," Semi-annual report submitted to ORNL under Contract No. SC-19X-SA125C, April 1988.

2. P. Chantikul et al., "A Critical Evaluation of Indentation Techniques for Measuring Fracture Toughness: II, Strength Method," *J. Am. Ceram. Soc.*, **64** [9] 539-543 (1981).

3. P. D. Shalek, et al., "Hot-Pressed SiC Whisker/Si_3N_4 Matrix Composites," *Am. Ceramic. Soc. Bull.*, **65** [2] 351-56 (1986).

4. T. N. Tiegs and J. W. Geer, "Dispersion Toughened Oxide Composites," CTAHE Bi-monthly report to DOE, August 1988.

5. R. Lundberg, et al., "SiC-Whisker-Reinforced Si_3N_4 Composites," *Am. Ceram. Soc. Bull.*, **66** [2] 330-333 (1987).

6. S. T. Buljan, et al., "Si_3N_4-SiC Composites," *Am. Ceram. Soc. Bull.*, **66** [2] 347-352 (1987).

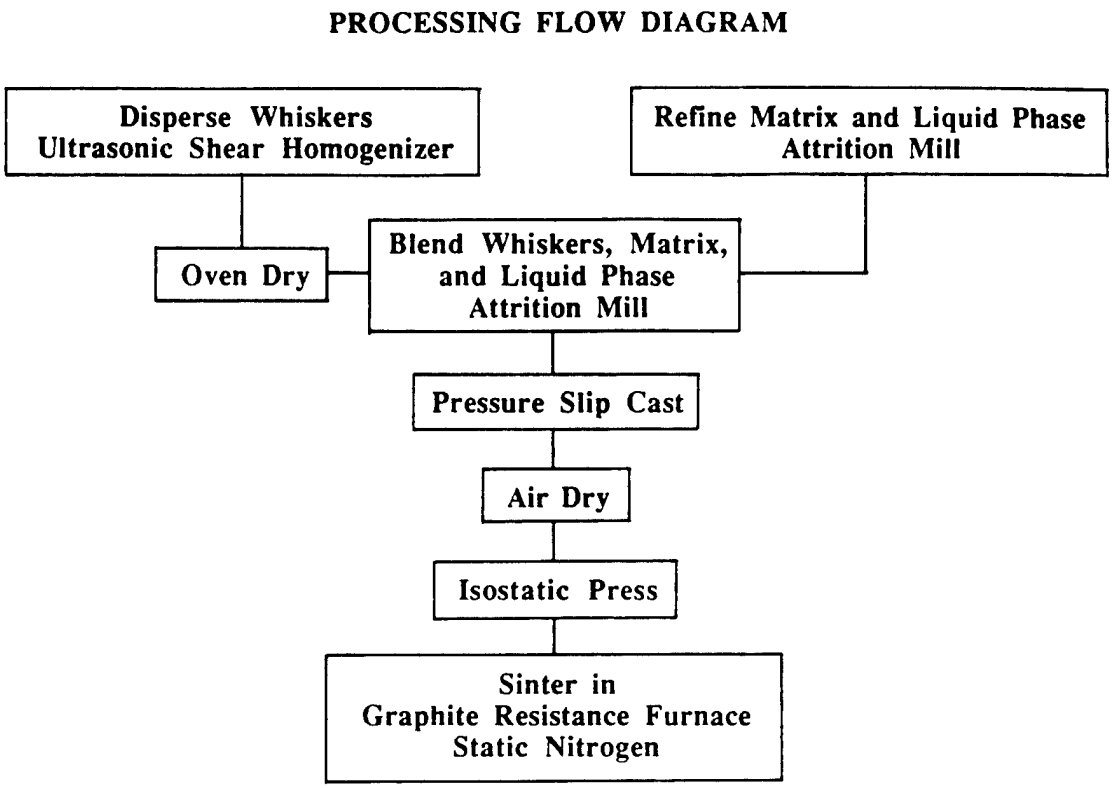

Figure 1. Processing flow diagram for the blending and sintering of SiC whisker reinforced Si_3N_4 ceramic composites.

Table 1. Composition and sintered density of composite samples.

	Composition			Sintered Density		
	Si3N4 (wt.%)	YAG (wt.%)	SCw (wt.%)	Bulk Density (gm/cc)	Th. Density (%)	Open Porosity (vol.%)
SCW0	84.46	15.54	0.00	3.25	97	0
SCW10	76.02	13.98	10.00	3.21	96	0
SCW20	67.56	12.44	20.00	2.88	87	8.6
SCW30	59.12	10.86	30.00	2.39	72	25.1
SCW20-2	64.46	15.54	20.00	3.22	96	0
SCW30-2	54.46	15.54	30.00	3.08	92	1.8
SCW30-3	52.50	17.50	30.00	3.17	94	0
SCW40	41.00	19.00	40.00	3.02	89	3.5

Si3N4 - H. C. Starck, LC12 Lot S-8584A
YAG - 3Y2O3 5Al2O3
Al2O3 - Malakoff Industries, Inc., RC-HP DBM Lot BM-2194
Y2O3 - Morton Thiokol, Inc., 87829 Lot I17G
SiC Whiskers - Tateho Chemical Industries, SCW#1-S Lot 245

Table 2. Composition and properties of composite samples.

	Composition			Sintered Properties			
	Si3N4 (wt.%)	YAG (wt.%)	SCw (wt.%)	Bulk Density (gm/cc)	Th. Density (%)	Fracture Strength (MPa)	Frac. Toughness (MPa m)
1	95.00	5.00	0.00	3.05	94	920	5.6
2	75.50	14.50	10.00	3.27	98	973	6.4
3	64.00	16.00	20.00	3.19	95	984	5.9
4	52.50	17.50	30.00	3.17	94	894	6.7
5	41.00	19.00	40.00	3.02	89	569	3.8

Si3N4 - H. C. Starck, LC12 Lot S-8584A
YAG - 3Y2O3 5Al2O3
Al2O3 - Malakoff Industries, Inc., RC-HP DBM Lot BM-2194
Y2O3 - Morton Thiokol, Inc., 87829 Lot I17G
SiC Whiskers - Tateho Chemical Industries, SCW#1-S Lot 245

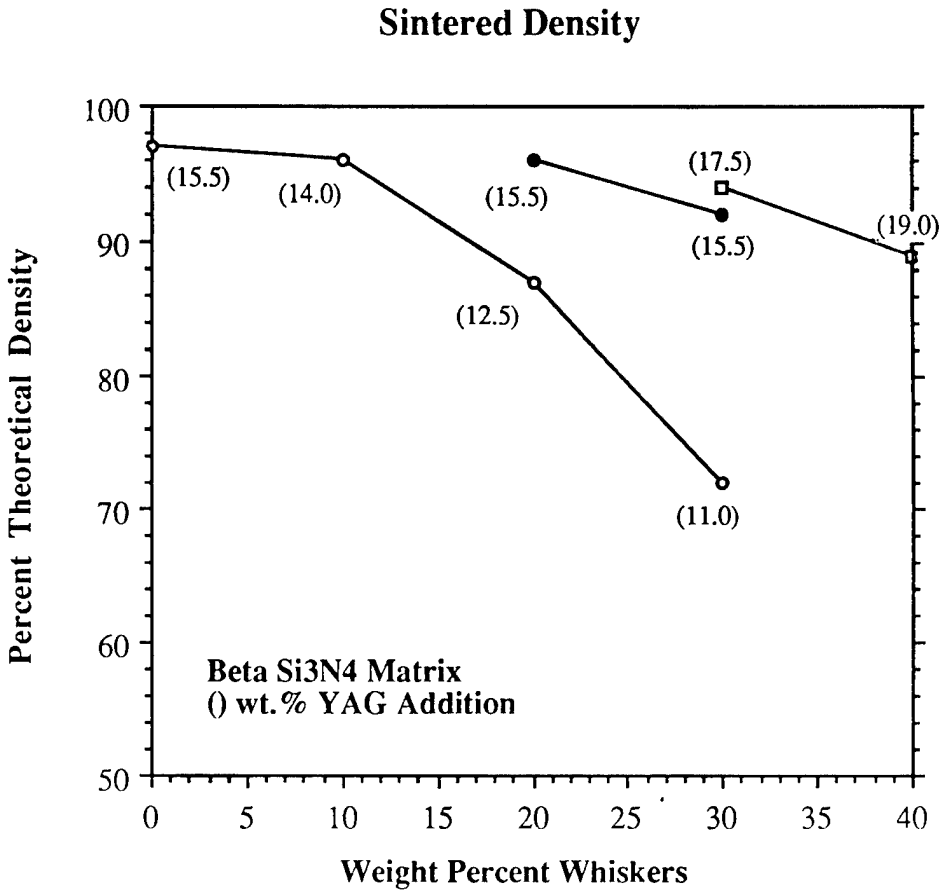

Figure 2. Sintered density of SiC whisker reinforced Si_3N_4 ceramic composites containing varying amounts of whiskers and liquid phase sintering aid (YAG).

1.2.3 Oxide Matrix

Dispersion Toughened Ceramic Composites

T. N. Tiegs, M. K. Ferber, W. H. Elliott, Jr., P. A. Menchhofer, J. W. Geer, P. D. Tennis, and S. M. Leahy (Oak Ridge National Laboratory)

Objective/scope

This work involves development and characterization of SiC whisker reinforced ceramic composites for improved mechanical performance. To date, most of the work has dealt with alumina as the matrix because it was deemed a promising material for initial study. However, an effort in SiC whisker reinforced-sialon is in progress with emphasis on pressureless sintering and control of the whisker-matrix interface properties. In addition, studies of whisker growth processes were initiated which will attempt to improve the mechanical properties of SiC whiskers by reducing their flaw sizes.

Technical progress

Hot-pressed sialon-SiC whisker composites

Sialon-SiC whisker composites were fabricated using both pre-reacted sialon powder and unreacted starting powders (silicon nitride, aluminum nitride and alumina). For both types of matrices, yttria and alumina sintering aids were added at a 3:5 ratio to form yttrium aluminum garnet ($3Y_2O_3$-$5Al_2O_3$ or YAG) during fabrication. Composite densification by hot-pressing with 20 vol % SiC whiskers as a function of the YAG content is shown in Fig. 1. For the pre-reacted powders, with no sintering aid present, densification of the powder-whisker mixtures did not occur to any extent. However, with as little as 0.5 wt % YAG present, densities >95% T.D. were readily obtained. On the other hand, the composites from the unreacted powders showed densification with or without sintering aid. This indicates that some amount of liquid phase is necessary to promote particle-whisker rearrangement during fabrication. The liquid phase can either be from the sintering aids added or from transient liquid phases which result from the reaction of the starting matrix powders. The microstructure of the composites showed no apparent whisker degradation.

The results on the fracture toughness are summarized in Fig. 2. They show good fracture toughness >6 $MPa\sqrt{m}$ for the sialon composites containing 0.5 and 2 wt % YAG and using pre-reacted sialon powders. Examination of the fracture surfaces from all the samples reveals two levels of crack-whisker interaction based on the relative amounts of liquid phase present during densification. At the high liquid phase contents, the fracture surface was relatively smooth, indicating minimal crack-whisker interactions and consequently poor toughening. In contrast, the composites with the low levels of liquid phase showed rough surfaces and easily observed whiskers, indicating extensive interactions and interfacial debonding. The flexural strength (Fig. 3) also showed a dependence on the liquid phase content analogous to the one observed with the fracture toughness.

Methods to increase the crack-whisker interaction, and hence the fracture toughness for the sialon matrix composites, include whisker coatings and crystallization of the glassy grain boundary phases. Carbon has been shown to increase the level of debonding and thus the fracture toughness in alumina matrix composites. The effect of a whisker carbon coating on the fracture toughness of a sialon matrix composite containing a large amount of liquid phase is shown in Fig. 4. While the increase is not dramatic, it still indicates that coatings may offer a means to improve the interface debonding in the sialon composites. To determine the effect of crystallizing the glassy grain boundary phases, composite materials were heat-treated at 1400°C for 8 h. A comparison of the indent fracture toughnesses before and after heat treatment is shown in Fig. 5. Evidently, crystallization helps to improve the crack-whisker interaction and the fracture toughness.

Sintered sialon-SiC whisker composites

Like the hot-pressed materials, sialon-SiC whisker composites were fabricated using both pre-reacted sialon powder and unreacted starting powders. Densification as a function of the YAG content is shown in Fig. 6. As before, a correlation of increasing density with increasing amounts of liquid phase is evident.

The mechanical properties of the sintered composites with densities >95% T.D. is summarized in Fig. 7. The results show decreasing strength and toughness with increasing Al:Si ratios.

Hot-pressed silicon nitride-SiC whisker composites

Previous results reported last reporting period showed that the liquid phases present during fabrication have more effect at controlling the whisker-matrix interface bonding than the initial whisker surface chemistry. Like the sialon matrix composites discussed above, carbon coated whiskers were examined to determine their ability to increase matrix-whisker debonding and improve toughness. The results are summarized in Fig. 8. Also included is a composite with surface-modified whiskers for comparison. As shown, no improvement in toughness was observed for the composites containing the carbon-coated whiskers.

Other whisker characteristics of interest are effects of diameter and aspect ratio on the fracture toughness. A plot of the toughness as a function of average whisker diameter shows increasing K_{IC} with increasing diameters (Fig. 9). Similar results have been observed in alumina matrix composites.[1] To determine the effect of aspect ratio on toughness, whiskers were milled with Teflon media for various times and the reduction in lengths determined by scanning electron microscopy. Those results are shown in Fig. 10 and indicate essentially no change in fracture toughness for a reduction in aspect ratio from ~30:1 for the as-received whiskers to ~12:1 for milled whiskers.

SiC whisker analysis

Research into the mechanisms responsible for the observed toughening behavior in the composite materials shows that crack-whisker interaction resulting in crack bridging is the major toughening

process.[1] For this mechanism to operate, debonding along the crack-whisker interface must occur during crack propagation and allow the whiskers to bridge the crack in its wake. Micromechanical modeling and available experimental evidence indicates that the composite toughness K_{IC} (composite), can be described as the sum of the matrix toughness, K_{IC} (matrix), and a contribution due to whisker toughening, ΔK_{IC} (whisker reinforcement). In other words,

$$K_{IC}\ (\text{composite}) = K_{IC}\ (\text{matrix}) + \Delta K_{IC}\ (\text{whisker reinforcement}). \quad (1)$$

The derived relationship for the increase in fracture toughness due to whisker reinforcement, ΔK_{IC} [whisker reinforcement], is given below:

$$\Delta K_{IC}\ (\text{w.r.}) = \sigma_f\{V_f \cdot r/[3 \cdot (1 - \nu^2)] \cdot E_c/E_w \cdot \gamma_m/\gamma_i\}^{1/2}, \quad (2)$$

where

ΔK_{IC} (w.r.) = increase in fracture toughness due to whisker reinforcement
σ_f = fracture strength of whiskers
V_f = volume fraction of whiskers
r = whisker radius
ν = Poisson's ratio for whiskers
E = Young's modulus for composite (c) and whiskers (w)
γ = fracture energy for matrix (m) and matrix-whisker interface (i)

As given, composite fracture toughness will increase with increasing (1) whisker strength, (2) volume fraction of whiskers, (3) ratio of Young's modulus of the composite to that of the whisker, (4) whisker diameter and (5) ratio of the interfacial energies of the matrix and the matrix-whisker interface. In addition, the strength of the whiskers is directly related to the increase in composite fracture toughness, whereas the other parameters have a square-root dependence. Considering many of the parameters are essentially fixed in a narrow range, either by matrix selection (E_c), whisker selection (E_w,ν) or processing considerations (V_f), to increase composite toughness by whisker reinforcement significantly, improvements in whisker strength are necessary.

Using the above relationship and the observed increase in fracture toughness for hot-pressed alumina and silicon nitride matrix composites, the strength of some current commercial SiC whiskers can be calculated. A summary of the calculations is given in Table 1. It should be noted that the whisker strength calculated for the Los Alamos National Laboratory (LANL) whiskers is essentially the same value obtained by direct mechanical measurements (8.6 GPa vs 8.4 GPa).[2] Thus, we are confident that the strengths that we calculate from composite fracture toughness data are reasonable values. However, some error is assuredly introduced because of whisker orientation, variations in whisker size and surface chemistry, and matrix properties, such as grain size. To minimize these variations, processing of the composites within each of the two matrix sets was intentionally kept the same. As shown in Table 1, the observed whisker strengths vary from 4.1 to 8.6 GPa. It is

interesting to note that the vapor-liquid-solid (VLS) growth whiskers from LANL exhibited the highest strength in comparison to the other whiskers derived from the carbothermic reduction of silica.

Using the Griffith relationship of flaw size as a function of strength and fracture toughness, the flaw sizes can be estimated in the current commercial SiC whiskers. The fracture toughness of the whisker was taken from a literature value if K_{IC} = 3.23 MPa$\sqrt{m}$.[3] As shown in Table 1, the estimated flaw sizes can be quite large in comparison to the size of the whiskers themselves.

Extensive investigations by transmission electron microscopy (TEM) of the flaws in SiC whiskers derived from rice-hulls have been described in previous papers.[4-6] The defects were described as small, partially crystalline inclusions (approximately 0.01 μm diam) containing calcium, manganese and oxygen concentrated in a whisker core region. Similar observations have been made on whiskers not derived from rice hulls.[15]

Obviously, these inclusions are nowhere near the flaw size estimated by Eq. (2) and shown in Table 1. However, examination of TEM photographs[4-6] reveals that, while the inclusions themselves are too small, the accumulation of the small inclusions in the core region is precisely in the appropriate range. In other words, the core regions probably act as the strength-limiting flaws in those SiC whiskers.

Other more obvious strength-limiting internal flaws observed in commercial SiC whiskers include voids or holes. Defects of this type have been documented by other researchers.[7-9] Again the size of these voids are in the correct range of 0.2-0.3 μm estimated by Eq. (2) for this type of whiskers.

Another strength-limiting defect associated with the whiskers is surface roughness which is sometimes referred to as "bamboo structure." Previous work on Si, SiC, Al_2O_3 and B_4C whiskers showed that surface roughness leads to stress concentrations and a reduction of observed strength.[10,11] The magnitude of the stress concentration factor at the surface roughness steps is related to the step height, the step angle, and the root radius of the step. Applying the same methods of the present SiC whiskers, we can calculate stress concentration factors as high as approximately 1.6 and 1.9 (Table 2). The other whiskers in the present study have step heights <0.01 μm and would not exhibit an observed strength decrease.[5,12] Using these calculated stress concentration factors, corrected whisker strengths and flaw sizes can then be estimated (Table 2). The whisker strength for the American Matrix, Inc., material now is in the range of strength associated with the other whiskers derived from carbothermic reduction of silica. Interestingly, the corrected strength of the LANL whiskers are in the same strength range observed for VLS growth whiskers from the early 1970s[13] and observed for the intrinsic strength of LANL whiskers.[14]

References

1. P. F. Becher, C. H. Hsueh, P. Angelini, and T. N. Tiegs, "Toughening Behavior in Whisker Reinforced Ceramic Matrix Composites," *J. Am. Ceram. Soc.* **71**(12), 1050-61 (1988).

2. J. J. Petrovic, J. V. Milewski, D. L. Rohr, and F. D. Gac, "Tensile Mechanical Properties of SiC Whiskers," *J. Mater. Sci.* **20**, 1167-77 (1985).

3. J. J. Petrovic and R. B. Roof, "Fracture Toughness of a β-SiC Whisker," *J. Am. Ceram. Soc.* **67**(10), C219-20 (1984).

4. S. R. Nutt, "Defects in Silicon Carbide Whiskers," *J. Am. Ceram. Soc.* **67**(6), 428-31 (1985).

5. S. R. Nutt, "Microstructure and Growth Model for Rice-Hull Derived SiC Whiskers," *J. Am. Ceram. Soc.* **71**(3), 149-56 (1988).

6. L. F. Allard, T. A. Nolan and M. H. Rawlins, Oak Ridge National Laboratory, "Ultrastructure of Silicon Carbide Whiskers," unpublished results (1989).

7. M. Martin, H. Yeh, and J. Schienle, "Whisker Toughened Si_3N_4 Composite," pp. 327-31 in *Proc. Auto. Tech. Contractors' Coord. Meeting*, 24th, 1986, Vol. P-197, Society of Automotive Engineers, Inc., Warrendale, PA (1987).

8. H. Yeh, J. Schienle, K. Karasek and S. Bradley, *Development of Ceramic Matrix Composites for Application in the Ceramic Technology for Advanced Heat Engines*, ORNL/Sub/85-22008/1 (1988).

9. N. D. Corbin and C. A. Wilkins, *Development of Toughened Si_3N_4 Composites by Glass Encapsulated Hot Isostatic Pressure*, ORNL/Sub/86-95906/1 (1988).

10. R. L. Mehan and J. A. Herzog, "Mechanical Properties of Whiskers," pp. 157-95 in *Whisker Technology*, ed. A. P. Levitt, Wiley, New York (1970).

11. D. M. Marsh, "Stress Concentrations at Steps on Crystal Surfaces and Their Role in Fracture," pp. 119 in *Fracture of Solids* ed. D. G. Drucker and J. J. Gilman, Interscience, New York (1963).

12. L. F. Allard, P. Pendelton, and J. S. Brinen, "Structure and Chemistry of Silicon Carbide Whisker Surfaces," pp. 472-73 in *Proc. 44th Annual Meeting Electron Microscopy Soc. Am.*, G. W. Bailey, ed., San Francisco Press, San Francisco, CA (1986).

13. A. J. G. Op het Veld and J. D. B. Weldkamp, "Mechanical and Microscopical Investigation of SiC Whiskers," pp. 269-81 in *Fibre Science and Technology (2)*, Elsevier Publ. Co., England (1970).

14. J. J. Petrovic and R. C. Hoover, "Tensile Fracture Behavior of Long SiC Whiskers," *J. Mater. Sci.* 22(2), 517-22 (1987).

Status of milestones

All milestones are on schedule.

Publications

T. N. Tiegs, "SiC Whisker-Reinforced Sialon Composites: Effect of Sintering Aid Content," to be published in Proceedings of 13th Annual Conference on Composites and Advanced Ceramics, January 15-18, 1989, Cocoa Beach, FL.

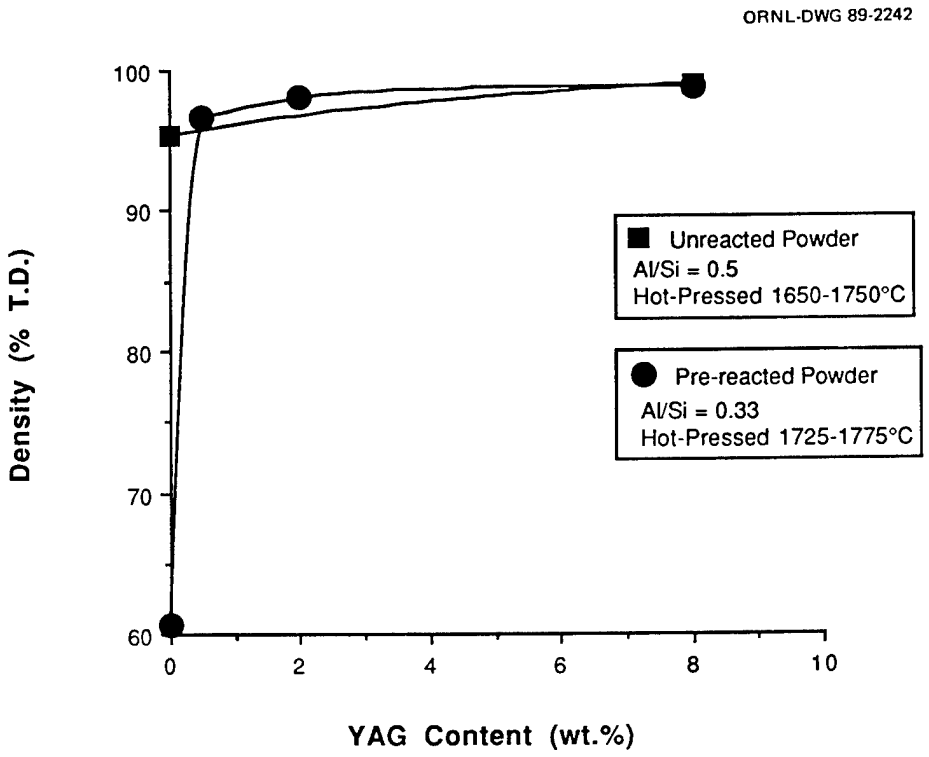

Fig. 1. Effect of YAG content on hot-pressing densification of sialon-20 vol % SiC whisker composites.

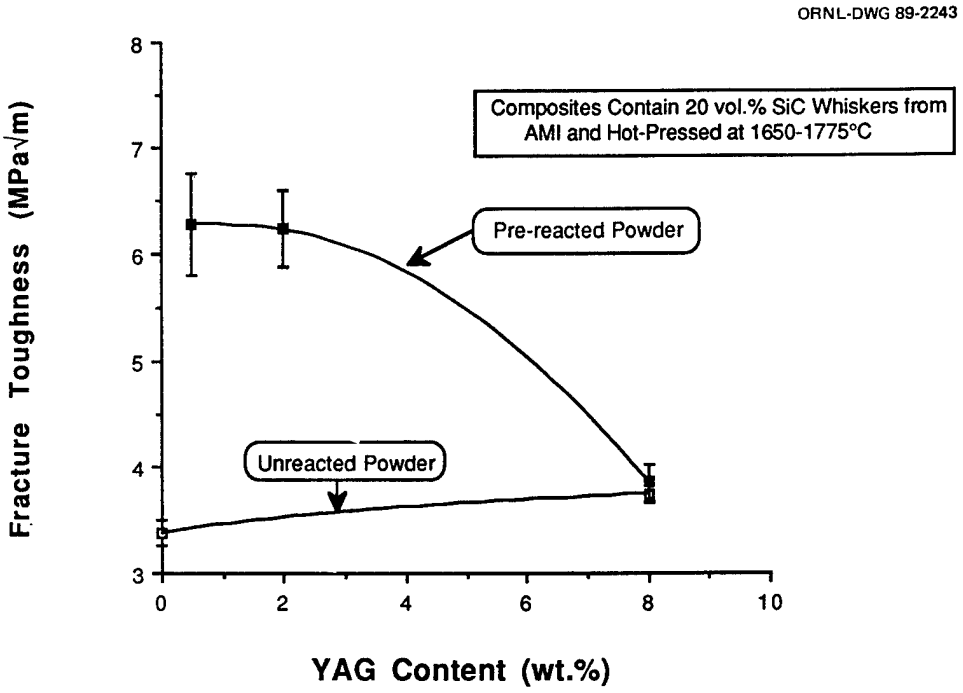

Fig. 2. Effect of YAG content on fracture toughness of sialon-20 vol % SiC whisker composites.

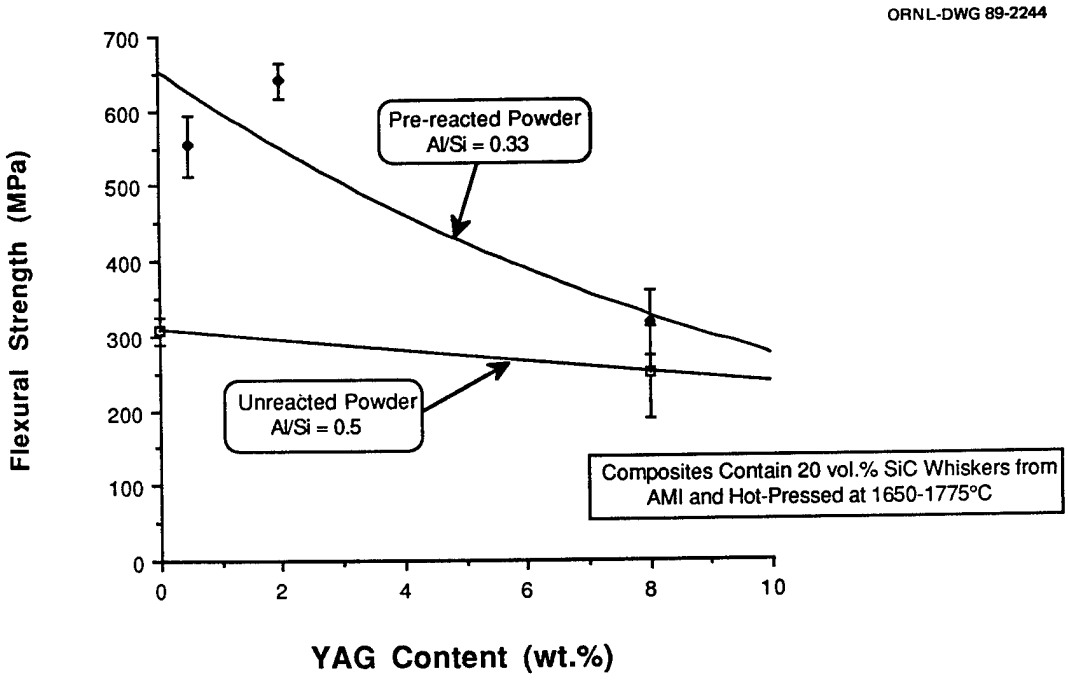

Fig. 3. Effect of YAG content on flexural strength of sialon-20 vol % SiC whisker composites.

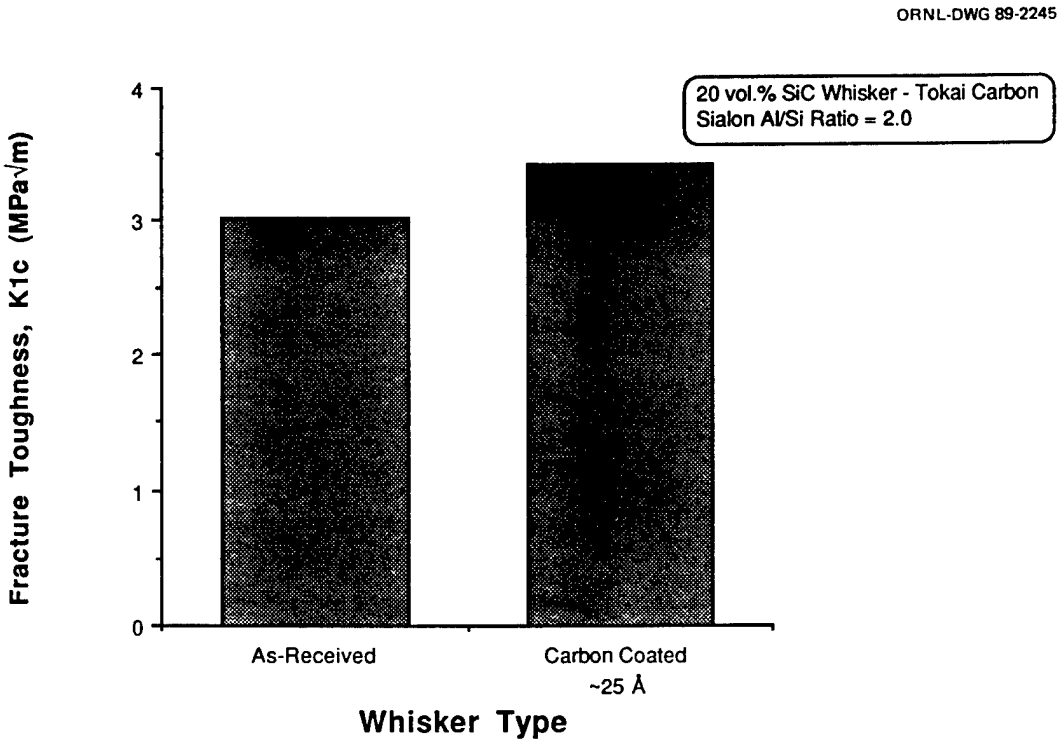

Fig. 4. Effect of whisker carbon coating on the fracture toughness of sialon-20 vol % SiC whisker composites.

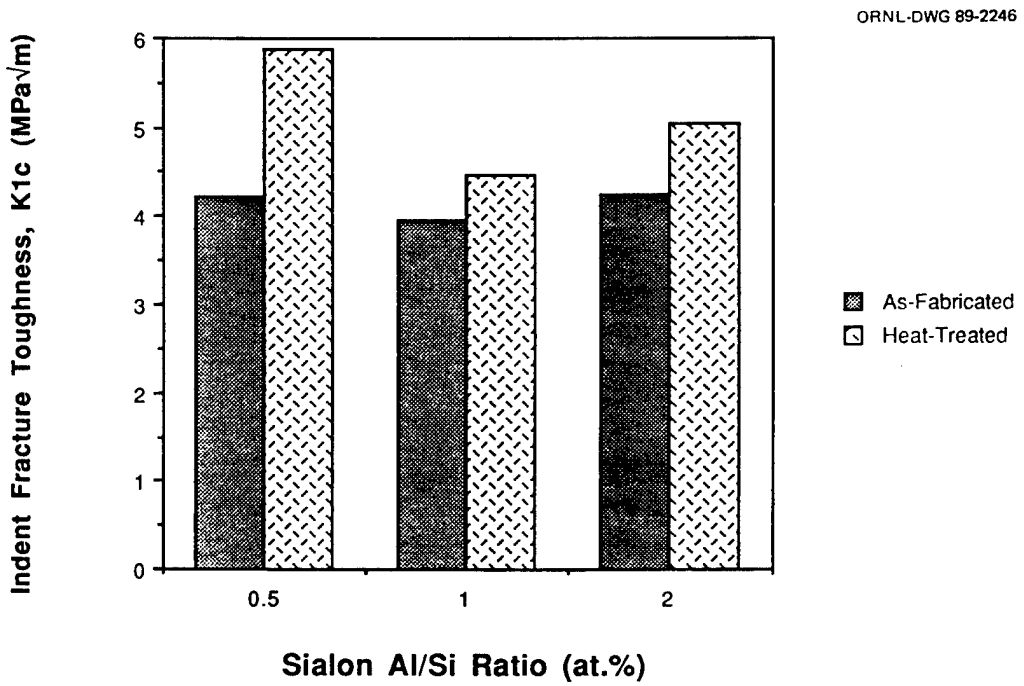

Fig. 5. Effect of heat treatment to crystallize glassy grain boundary phases on the fracture toughness of sialon-20 vol % SiC whisker composites.

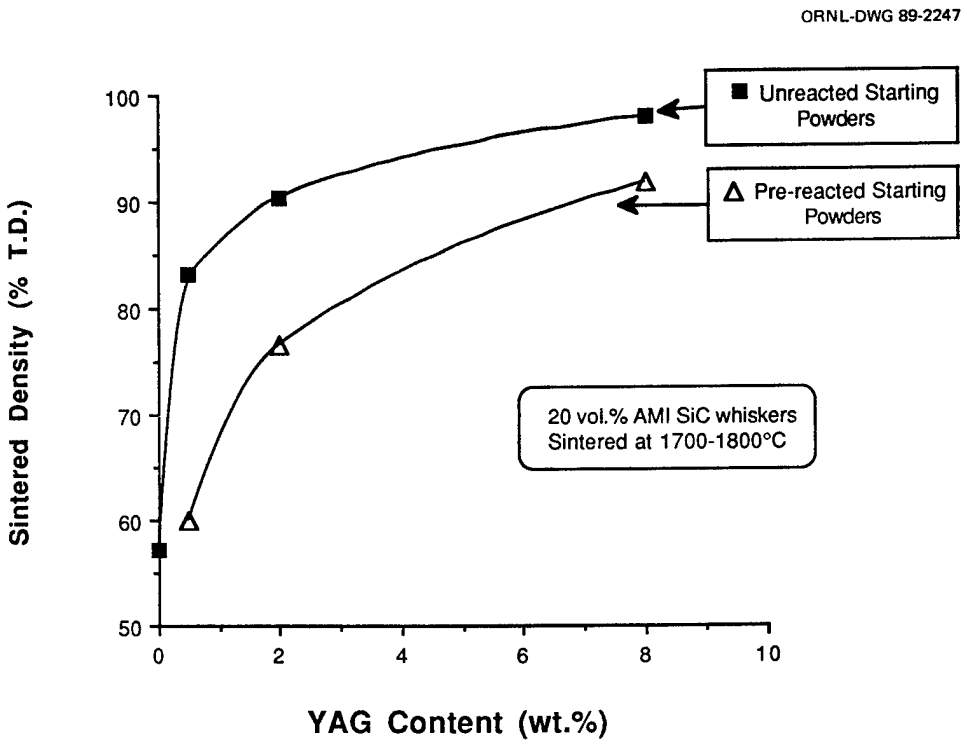

Fig. 6. Densification of sialon-20 vol % SiC whisker composites by pressureless sintering as a function of sintering aid content and starting powders.

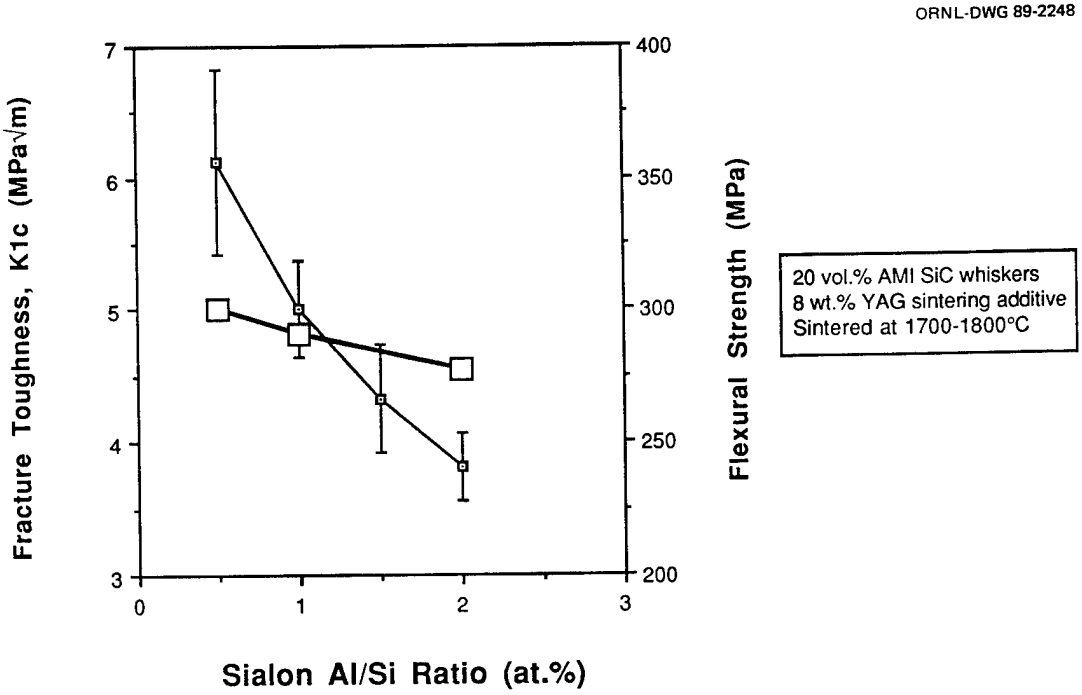

Fig. 7. Fracture toughness and flexural strength of pressureless sintered sialon-20 vol % SiC whisker composites as a function of sialon composition.

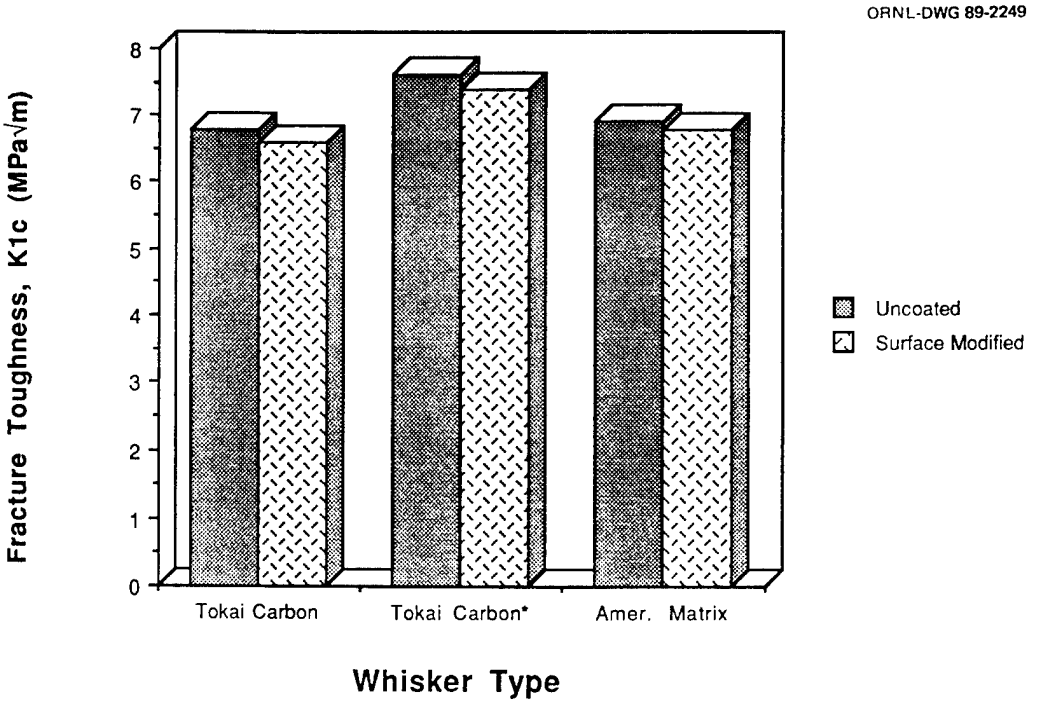

Fig. 8. Effect of whisker carbon coating on the fracture toughness of silicon nitride - 6% yttria-2% alumina-20 vol % SiC whisker composites. The whiskers from Tokai Carbon have approximately 25 Å carbon on surfaces. The whiskers from American Matrix were heat-treated in Ar-4% H_2 to develop a carbon-rich surface.

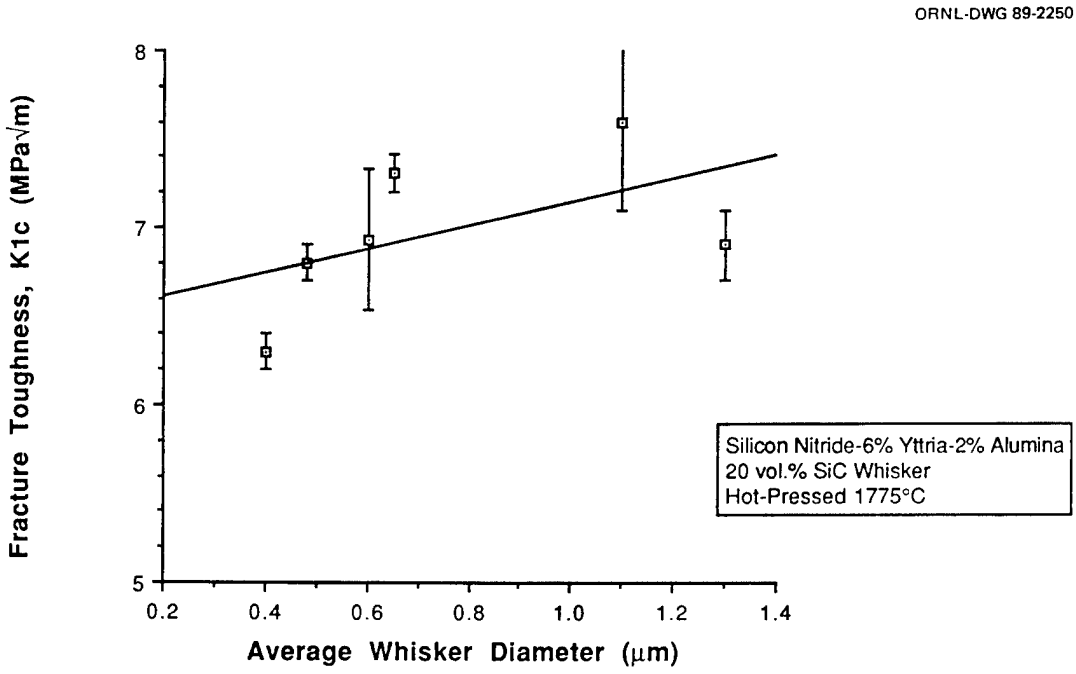

Fig. 9. Effect of whisker diameter on fracture toughness of silicon nitride - 6% yttria-2% alumina-20 vol % SiC whisker composites.

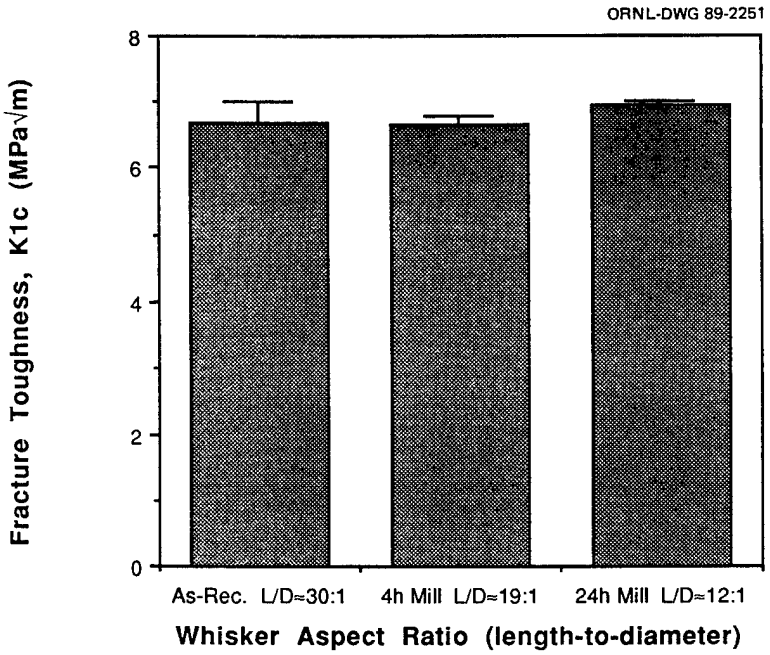

Fig. 10. Effect of whisker aspect ratio on fracture toughness of silicon nitride - 6% yttria-2% alumina-20 vol % SiC whisker composites.

Table 1. Calculated strength of selected SiC whiskers[a] and an estimated flaw size[b]

Whisker source	Average whisker radius (μm)	Alumina matrix[c] Observed ΔK_{IC} (MPa$\sqrt{m}$)	Alumina matrix[c] Calculated σ_f (GPa)	Silicon nitride matrix[d] Observed ΔK_{IC} (MPa$\sqrt{m}$)	Silicon nitride matrix[d] Calculated σ_f (GPa)	Estimated flaw size range (μm)
ARCO[e]	0.35	5.7	7.9	N.D.	N.D.	0.11-0.20
ARCO[f]	0.35	4.5	6.3	3.3	6.7	0.15-0.31
AMI[g]	0.65	4.0	4.1	3.0	4.1	0.39-0.74
Tateho[h]	0.20	3.4	6.3	2.3	6.2	0.17-0.32
Tokai[i]	0.25	3.9	6.4	2.8	6.7	0.15-0.30
LANL[j]	0.40	6.6	8.6	N.D.	N.D.	0.09-0.17
Huber[k]	0.25	3.9	6.4	N.D.	N.D.	0.16-0.30

[a]Based on Eq. (2) in text. From Appendix B of ref. 1, $(\gamma_m/\gamma_i) = 5$ for alumina matrix and $(\gamma_m/\gamma_i) = 3$ for the silicon nitride matrix. Surface chemistry similar for all SiC whiskers listed. Young's modulus for alumina composites, E_c = 395 GPa, for the silicon nitride composites, E_c = 320 GPa, and the SiC whiskers, E_w = GPa.

[b]Using Griffith relationship correlating flaw size to strength and toughness; $c = (A \cdot K_{IC}/A\sigma_f)^2$, where c is the flaw size, A is a geometric constant (0.8–1.1), K_{IC} is the whisker fracture toughness from ref. 3 (3.23 MPa$\sqrt{m}$), and σ_f is the whisker strength.

[c]Fracture toughness of alumina matrix, K_{IC} = 2.5 MPa$\sqrt{m}$.

[d]Fracture toughness of silicon nitride matrix, K_{IC}' = 4.0 MPa$\sqrt{m}$.

[e]ARCO Chemical Co. (present name - Advanced Composites Materials Corp.), Greer, SC; Grade SD-9, received 2/84.

[f]ARCO Chemical Co. (present name - Advanced Composites Materials Corp.), Greer, SC; Grade SC-9, received 9/85.

[g]American Matrix Inc., Knoxville, TN; Grade 1, received 6/88.

[h]Tateho Chemical Industries, Japan; Grade SCW-1S, received 1/86.

[i]Tokai Carbon Co., Japan; Grade Tokawhisker, received 3/86.

[j]Los Alamos National Laboratory, Los Alamos, NM; Grade 3,4 A+B, received 10/84.

[k]Huber Corp., Borger, TX; Grade 7117; received 12/86.

Table 2. Corrected strengths for SiC whiskers exhibiting surface roughness

Whisker source	Approximate roughness step height (μm)	Calculated stress concentration factor[a]	Corrected whisker strength (GPa)
AMI[b]	0.2	1.5	6.2
LANL[c]	0.45	1.9	16.3

[a]Based on Fig. 6.30 of Ref. 1, where the root radius, r = 30 Å and the step angle, θ = 20°.

[b]American Matrix, Inc., Knoxville, TN; Grade 1, received 6/88.

[c]Los Alamos National Laboratory, NM, Grade 3,4 A+B, received 10/84.

Processing of Sinterable Transformation Toughened Ceramics for Application in Ceramic Technology for Advanced Heat Engine Project

E. Lilley and G. A. Rossi (Norton Company)

Objective/scope:

The objective of Phase IIA is to optimize the properties of two classes of transformation toughened ceramics, which were already studied in Phase I of this contract. These ceramics are Y-TZP (Y_2O_3 stabilized Tetragonal Zirconia Polycrystals) and Ce-ZTA (CeO_2-ZrO_2 toughened Al_2O_3).

For the Y-TZP materials, one of the main efforts will be to study the low temperature degradation and understand how it is affected by microstructure and composition. In the case of the Ce-ZTA ceramics, the main goal is to optimize the high temperature mechanical properties by minimizing the flaw size and controlling the microstructures.

Technical progress

1. Y-TZP

1.1 Mechanical Properties Development

One of the goals of this work is to evaluate the mechanical properties of Y-TZP materials produced from melted and rapidly cooled powders. Strength and toughness are being measured in the temperature range from room temperature to 700°C which is expected to be the range of practical importance for these zirconia ceramics. Here we report on the K_{IC} measurements done on double torsion specimens using three specimens at each temperature. The results are plotted for MG-008 (4.7 w/o yttria), our most commonly studied material in this program. For comparison, the results on higher yttria material MG014 (5.4 w/o) from the Phase I of this study are also presented. The measurements show respectable toughness at temperatures up to 500°C ($K_{IC} \geq 5$) (see Fig. 1). Moreover, there is very little difference between the MOR for the two different yttria concentrations, which is surprising.

MOR measurements are being performed at 300, 500, and 700°C on both the Y-TZP's and the Ce/Y-TZP's used in the low temperature degradation studies.

1.2 Low Temperature Degradation Studies

Further studies have been made at 250°C in atmospheric pressure nitrogen which had been bubbled through water at room temperature in addition to the ones reported earlier on MG-008. MG-024/sintered containing 5.27 w/o yttria and MG-026/S containing 5.52 w/o yttria were exposed for times up to 2400 hours and the results plotted in Fig. 2. There is a clear trend showing that higher yttria samples transformed from tetragonal to monoclinic more slowly than the lower yttria samples. This same trend has been observed in the literature for fine grain size Y-TZP's made from very fine chemically derived powders. The addition of ceria in the melt to a material like MG-008 further improves the resistance to low temperature degradation. The 2 w/o CeO_2 addition material only forms 8% monoclinic after 100 hours, whereas 4 w/o CeO_2 shows zero monoclinic after 1000 hours. There appears to be little effect of HIPing over sintering in this set of experiments on surface monoclinic formations.

All the samples measured in Fig. 2 except MG008/S/XT-1300 were polished before any exposure at 250°C. By careful polishing the materials always had zero monoclinic at time t=o. This 0% monoclinic has been plotted for convenience in Fig. 2 at 0.1 hours because it is a semi-log plot. There is, in fact, a difference in behavior between polished and machined surfaces which is highlighted in Fig. 3. The rate of formation of the monoclinic phase is slower for the machined than for the polished samples. This can be explained as follows: When the tetragonal grains transform to monoclinic, they undergo a small (~4%) volume change which puts the transformed surface layer under compression. In the case of the machined bars (Samuel et al.) [1] showed that the deformed surface is already under compression with a thickness of about 30 microns. During low temperature degradation the pre-existing compressive stress will act to further constrain the transformation so that it proceeds more slowly than in the polished case and it reaches a lower limiting monoclinic % plateau.

The third line on Fig. 3 is for a machined MOR bar heated at 1300°C for 1 hour before testing. The recent work of Whalan et al. [2] has shown that Y-TZP ceramics can undergo surface recrystallization. At 1300°C a grain size of about 0.2 micron was produced on the surface. Since the tetragonal --> monoclinic transformation is strongly grain size dependent it is expected, and confirmed in Fig. 3 that this treatment would slow down the rate of low temperature degradation.

Although the formation of surface monoclinic during exposure at different temperatures and its measurements by XRD gives us an impression of the degradation, it is the depth of the transformation zone which is most revealing. The rate of growth of the thickness of the monoclinic layer is related to the formation of the monoclinic phase on the surface as observed by XRD, i.e. the XRD occurs primarily from the first 5 micron regions due to absorption. Ideally no monoclinic would form on the surface and there would then be no reaction layer. When there is a reaction layer it is most easily measured by fracturing a bar and looking at the cross section in an optical microscope. With proper illumination the monoclinic zone can often be seen quite clearly as in Fig. 4. This particular sample of MG-008 was held at 250°C for 2000 hours and has formed a layer of about 100 micron thickness. On the other hand, it is not always possible to discern the reaction zone in some of the fine grain zirconias made from chemically derived powders, especially if the reaction zone thickness is less than 10 microns. The Raman microprobe, with resolution less than 5 microns, should then be used. Such measurements have been made in this work at the Ceramic Center at the University of Rutgers.

The depth of the transformed monoclinic layers has been measured for several different materials for different exposure times at 250°C and the results plots in Fig. 5. There appears to be somewhat less degradation in the HIPed bars than in the sintered bars. Most striking is the reduction in thickness of the transformed layer as the zirconias have increasing yttria contents i.e. MG-008 4.7, MG-024 5.2 and MG-026 5.5 w% yttria.

The second test that we have employed involves holding samples in water in a closed system at 120°C for different times. Some of these results are presented in Fig. 6. For the MG-008 there is a large difference between the monoclinic depth formed on sintered samples as opposed to HIPed ones. The slower growth rate in HIPed materials also shows in the MG-024 finer grain size and in the MG-026 material but only clearly at longer times. The accuracy of our measurements is, however, limited when the transformed zone is less than 10 microns thick. The best result here is for MG-026 which has formed a monoclinic layer of only 10 microns after 1000 hours at 120°C in water.

An intriguing question is, what effect do the transformed microcracked layers have on the strength of the zirconia? At 250°C we have found that MG-008 sintered that the strength declined only about 10%, and was still ~150 ksi, after 4000 hours. The high strength HIPed material decreased in strength somewhat faster but tended to plateau at about the same strength level as the sintered material. The situation at 120°C in water is slightly different. The MOR does not dramatically change

with time as shown in Fig. 7, except perhaps for MG-008/S which loses ~25% of its strength in 250 hours but then levels off.

Samples of commercial Nilcra material are included in this study for comparison. These magnesia stabilized zirconias appear to undergo no loss in strength but then their MOR's are much lower.

References

[1] R. Samuel, S. Chandrasekar, T. N. Farris, and R. H. Licht, "Grinding Forces and Energy for Brittle Materials", to be published in the Journal of the American Ceramic Society.

[2] P. J. Whalan, F. Reidinger and R. F. Antrim, Journal of American Ceramic Society, 72, 319-321 (1989).

2. Ce-ZTA CERAMICS

The previous semiannual report had shown that the composition 40 w/o (16 w/o CeO_2-ZrO_2)/60 w/o Al_2O_3 abbreviated as Z16CE60A, exhibited the best mechanical properties and therefore was chosen for further optimization. Since the microstructure had shown clusters of CeO_2-ZrO_2 grains, resulting from imperfect mixing of the CeO_2-ZrO_2 and Al_2O_3 powders, it was decided to make the same composition by melting the three oxides and quenching the melt to produce a rapidly solidified crude. This technique is expected to produce excellent microstructural homogeneity.

The rapidly solidified (R/S) crude was made at Norton's PMI in Manchester, NH with a proprietary technology. However, the actual composition came out higher in CeO_2 and Al_2O_3, i.e. 38 w/o (18.5 w/o CeO_2-ZrO_2)/62 w/o Al_2O_3, abbreviated as Z18.5CE62A. This crude was used to produce the powder for the fabrication of the Ce-ZTA ceramics.

In the following section the results of the characterization of the crude, of the powder made by vibratory milling and of the ceramics will be presented.

For comparison purposes, ceramics of composition Z16CE60A were also made with the Moffatt's coacervation technique [1], using a R/S Z16CE powder and Sumitomo AKP-30 Al_2O_3. These ceramics were characterized for microstructure and strength and the fracture surface of bend bars was also analyzed by fractography by SEM.

2.1 Crude Characterization

The R/S crude was characterized for BET area, density by He pycnometry and X-ray diffraction. A BET area of 0.02 m^2/g was measured, which seems to indicate absence of open microporosity. The density by He pycnometry was found to be 3.68 g/cm^3, which is 79% of the theoretical density (TD = 4.67 g/cm^3) calculated from the densities of t-CeO_2-ZrO_2 (6.30 g/cm^3) and of alpha-Al_2O_3 (3.98 g/cm^3). The lower density is due mainly to the fact that Al_2O_3 is non crystalline, as shown by XRD; another reason might be the possible presence of closed porosity.

The XRD pattern of the crude (Fig. 8) shows only the peaks of t-ZrO_2. However, if the crude is calcined at high temperature, the "amorphous" Al_2O_3 is transformed into crystalline transitional phases and eventually into alpha- Al_2O_3.

2.2 Powder Characterization

Two batches of powders were prepared by vibratory milling in water, the first batch by milling the as-received crude and the second one by milling the crude calcined at high temperature. The first billets made with the powder obtained from the uncalcined crude cracked upon firing, because the powder contained an excessive amount of moisture. Therefore the powder was calcined and crack-free billets were fabricated. Most of the billets, however, were made using the powder obtained from the calcined crude. The particle size distribution (PSD) curve of this powder, obtained after vibratory milling in water for 96 hours, is shown in Fig. 9. The powder appears to be finer than 2 um, about 65% being submicron.

2.3 Processing/Shape Forming/Firing

The Ce-ZTA billets were made by die pressing followed by CIPing and also by pressure casting of aqueous slurries, unfiltered or filtered through a 5 um filter. Two types of billets were made, either square (5x5 cm) or rectangular (8.8x3.8 cm) in shape, the latter for the double torsion test for K_{IC}. The billets were fired at 1600°C for different times in order to study the microstructure/property relationship.

2.4 Characterization of the Ceramics

The Ce-ZTA ceramics were characterized for density (Archimedes method), phase content by XRD, microstructure by SEM, strength and fracture toughness. Fractography was also performed on selected broken MOR bars to identify the fracture origin. Table 1 shows the physical properties and Table 3 the mechanical properties for these materials.

Table 1

MATERIAL	PROCESSING SHAPE FORM'G.	FIRING CONDITIONS	FIRED DENSITY	% m-ZrO_2 GROUND	% m-ZrO_2 ANNEAL
Z18.5CE62A (uncalcined crude)	DP/CIP	1600/1	4.65	N/A	<5
Z18.5CE62A (calcined crude)	DP/CIP	1600/1	4.71	40	4
"	DP/CIP	1600/3	4.68	46	17
"	DP-CIP	1600/6	4.62	58	29
"	PC/UNFILT.	1600/1	4.66	N/A	N/A
"	PC/FILT.	1600/1	4.72	N/A	N/A

Note: DP = die pressing at 70 MPa; CIP = cold isostatic pressing at 210 MPa; PC = pressure casting; anneal = samples annealed at 1000°C/1 hr.

The data of Table 1 shows that an increase in firing time at 1600°C causes some desintering and that the % m-ZrO_2, as expected, increases with aging time, both in the ground and annealed (1000°C) samples, due to coarsening of the microstructure and increased transformability of the t-CeO_2-ZrO_2 grains.

Figs. 10, 11, and 12 show the microstructure of the ceramics fabricated by die pressing/CIPing and fired at 1600°C for 1, 3, and 6 hours. It appears that the microstructure is very uniform, more than in the case of the ceramics previously made using mechanically mixed powders. A small fraction of the CeO_2-ZrO_2 grains appear trapped within the larger Al_2O_3 grains. Image analysis was performed on these microstructures to get the grain size distribution (GSD). Fig. 13 shows the GSD hystograms for CeO_2-ZrO_2 and Fig. 14 for Al_2O_3. The average grain size (AGS) changes with firing time as shown in Table 2.

Table 2

AVERAGE GRAIN SIZE AS FUNCTION OF FIRING TIME AT 1600°C

MATERIAL	CeO_2-ZrO_2 (um)	Al_2O_3 (um)
1600/1	1.19	1.33
1600/3	1.55	1.56
1600/6	1.69	1.93

It appears that the ratio of the average grain sizes does not change appreciably with annealing time.

Table 3 shows the strength and toughness values obtained for the Ce-ZTA ceramics made with the R/S calcined crude, except material #1 which was made with the calcined powder from the as-received crude.

Table 3 shows that the toughness is very good, but the value obtained depends on the technique used. The high value of 13.6 $MPa.m^{\frac{1}{2}}$ was obtained by Dr. P. F. Becher at ORNL on one sample. A DCB K_{IC} measurement will be performed at ORNL on the same material in order to evaluate the R-curve behavior. It is also interesting to note that the strength can be improved by using colloidal consolidation (pressure casting) using a filtered slurry. It is believed possible to attain strength values of 1 GPa in pressureless sintered Ce-ZTA ceramics by an optimized colloidal consolidation method and by appropriate firing/annealing schedules which will optimize the microstructure.

The results of the fractographic analysis of the bend bars machined out of the billets made by pressure casting a filtered slurry are not available yet. Fractography of the ceramics made by DP/CIP has shown the presence of different types of flaws, i.e. pores, agglomerates and inclusions. Figs. 15, 16 and 17 display some examples of these flaws. Fig. 15 shows an elongated pore probably caused by burn out of an organic contaminant (i.e. lint, paper fiber). Fig. 16 shows a high porosity region which could have resulted from the melting of a foreign inclusion (i.e. silicate). Fig. 17 shows, instead, a cluster of larger grains as fracture origin.

2.5 Ce-ZTA Ceramic Made With Moffatt's Technique

The coacervation technique developed by Dr. W. Moffatt at MIT [1] consists in preparing two stable aqueous dispersion of two different powders containing some dissolved PVA, mixing them to form a stable mixed slurry and then cause coacervation by adding a water miscible liquid (i.e. acetone) in which PVA is insoluble. The idea is to prevent phase separation by "freezing in" the homogeneous dispersion of the powders, which otherwise would tend to segregate due to their different density. An additional advantage is the wet processing which prevents the formation of hard agglomerates. Techniques similar to Moffatt's have been recently developed, i.e. the gelling on cooling of ceramic suspensions containing agarose [2] and the gel casting of aqueous suspensions obtained through aqueous polymerization of vinyl monomers, developed at ORNL [3]. The composition Z16CE60A was chosen for the Moffatt technique. The two powders used were R/S, mostly submicron, 16 w/o CeO_2-ZrO_2 and Sumitomo AKP-30 Al_2O_3. The suspensions were not sedimented to eliminate the large agglomerates. A 7.5 cm diameter disc, about 0.6 cm thick, was made by colloid pressing of the coacervate, dried, sintered at 1500°C/3 hr. and HIPed at 1500°C/.75 hrs. HIPing was done to remove the residual porosity. Fig. 18 shows the microstructure of this material, which appear very uniform, almost as nice as that of the ceramic made with the R/S crude shown in Fig. 10. The average RT strength for this material was 889 MPa (8 bars). However, the standard deviation was 45%, which was explained by fractographic analysis. The prevalent fracture origins were found to be either Al_2O_3 or ZrO_2-rich inclusions, probably originating from unbroken agglomerates present in the mixed slurry before coacervation. Figs. 19 and 20 show Al_2O_3-rich and ZrO_2-rich inclusions, respectively, as indicated by SEM/EDS analysis. This result implies that considerable strength improvement can be expected when such agglomerates are removed either by filtration or sedimentation. It is concluded that the Moffatt technique has a considerable potential when properly used and optimized.

REFERENCES

[1] W. C. Moffatt and H. K. Bowen, "Composite Ceramic Production by Precipitation of Polymer Solutions Containing Ceramic Powder", J. Matls. Sci. Letters, Vol. 6, pp. 383-385, 1987.

Table 3

MATERIAL	RT MOR	1000°C MOR	RT K_{IC}	1000°C K_{IC}	REM
Z18.5CE62A S1600/1 DP/CIP	692 (10)	315 (9)	7.0 (5)	3.4 (5)	DT
Z18.5CE62A S1600/1 DP/CIP	634 (10)	---	13.6 (1) 9.6 (1)	---	MCF MI
Z18.5CE62A S1600/3 DP/CIP	689 (10)	---	9.8 (1)	---	MI
Z18.5CE62A S1600/6 DP/CIP	565 (9)	---	9.9 (1)	---	MI
Z18.5CE62A S1600/1 PC/UNFILT.	482 (9)	---	---	---	---
Z18.5CE62A S1600/1 PC/FILT.	799 (10)	---	---	---	---
Z18.5CE62A S1600/1 H1500/.75 DP/CIP	903 (7)	---	---	---	---

Note: S = sintered; H = HIPed; DP = die pressed at 70 MPa; CIP = cold isostatically pressed at 210 MPa; FILT. = slurry filtered through 5 um filter; UNFILT. = unfiltered; DT = double torsion method for K_{IC}; MI = microindentation method for K_{IC} (Palmqvist model); MCF = multiple controlled flaw method for K_{IC}; PC = pressure cast.

[2] A. J. Fanelli and R. D. Silvers, "Process for Injection Molding Ceramic Composition Employing an Agaroid Gel-Forming Material to Add Green Strength to a Preform", U. S. Patent 4,734,237 (Mar. 29, 1988).

[3] M. A. Janney and O. O. Omatete, "Development of an Aqueous Gelcasting System", prepatent information, ORNL.

Status of milestones

All milestones are on schedule.

Publications

A paper titled "CeO_2-ZrO_2 Toughened Al_2O_3 Ceramics of High Strength and Toughness", authors G. A. Rossi and P. J. Pelletier, presented at the Third International Conference on Ceramics for Heat Engines in Las Vegas, NE, in November, 1988, will appear in the Conference Proceedings. Another paper titled "CeO_2-ZrO_2 Toughened Al_2O_3 Ceramics made with Chemically Derived and Rapidly Solidified Powders", author G. A. Rossi, was presented at the 7th SIMCER in Bologna, Italy, in December, 1988 and will be published in the Conference Proceedings.

DOUBLE TORSION K I c FRACTURE TOUGHNESS

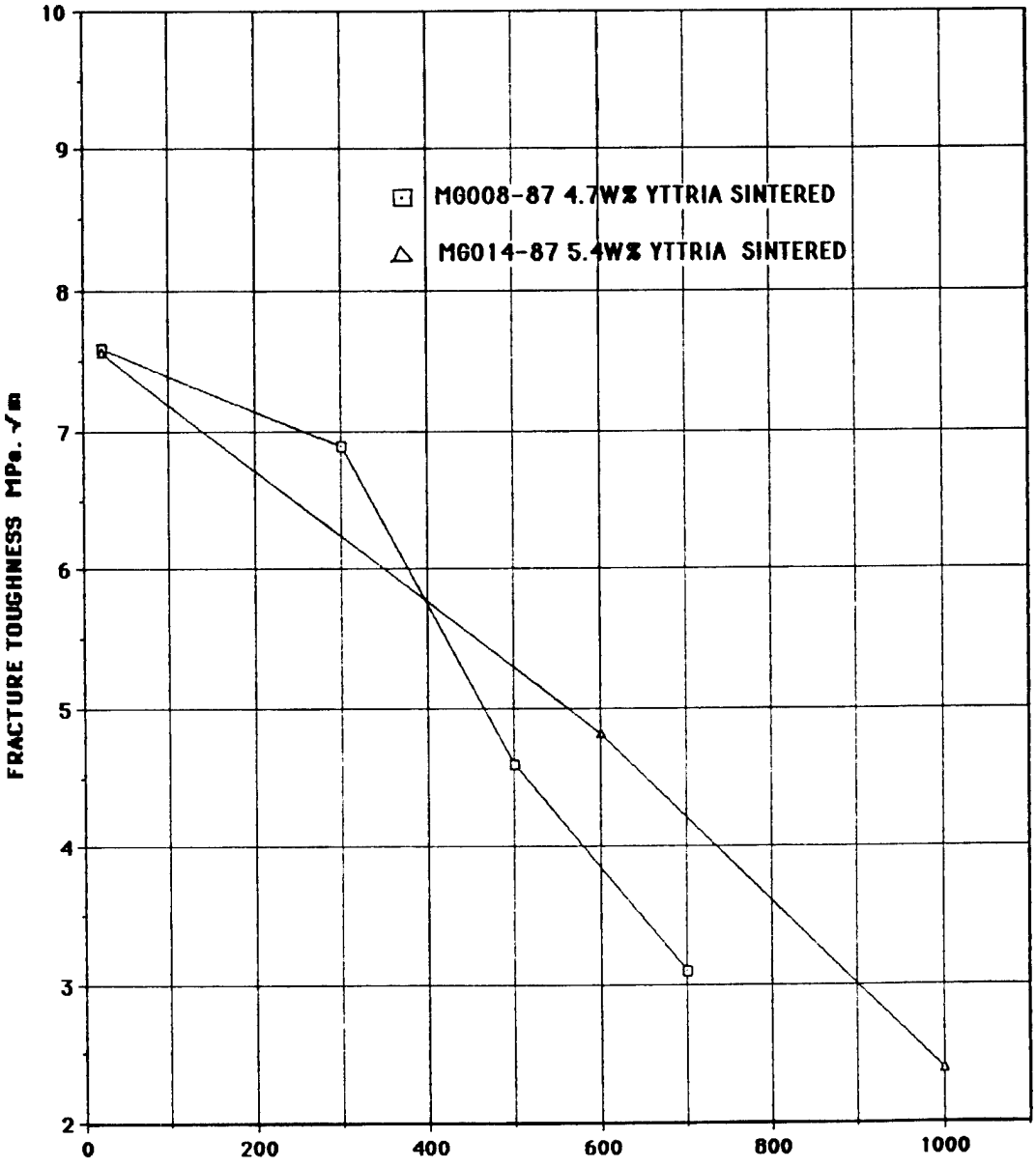

FIGURE 1

AB 2/6/88

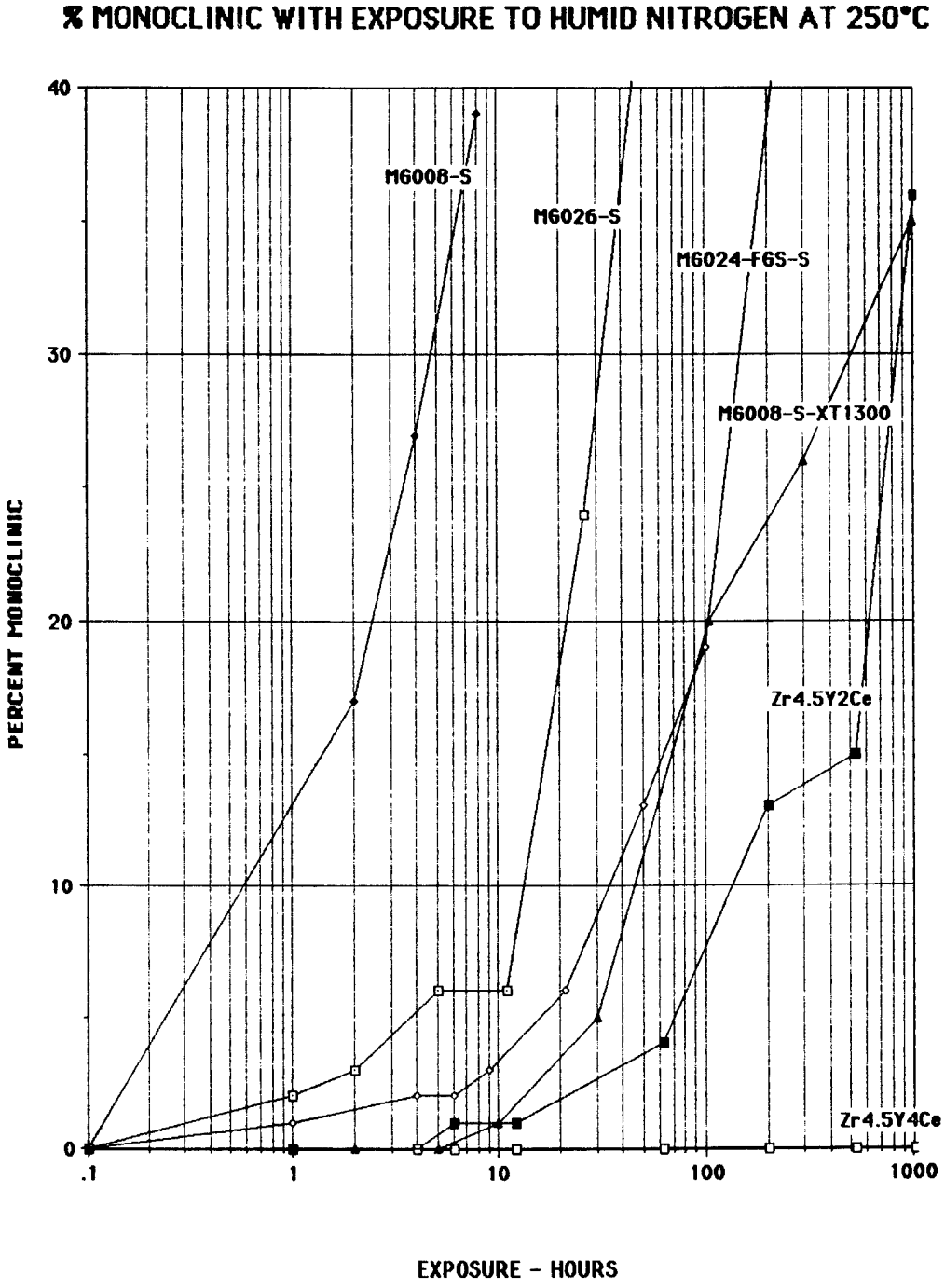

FIGURE 2

AB 2/14/89

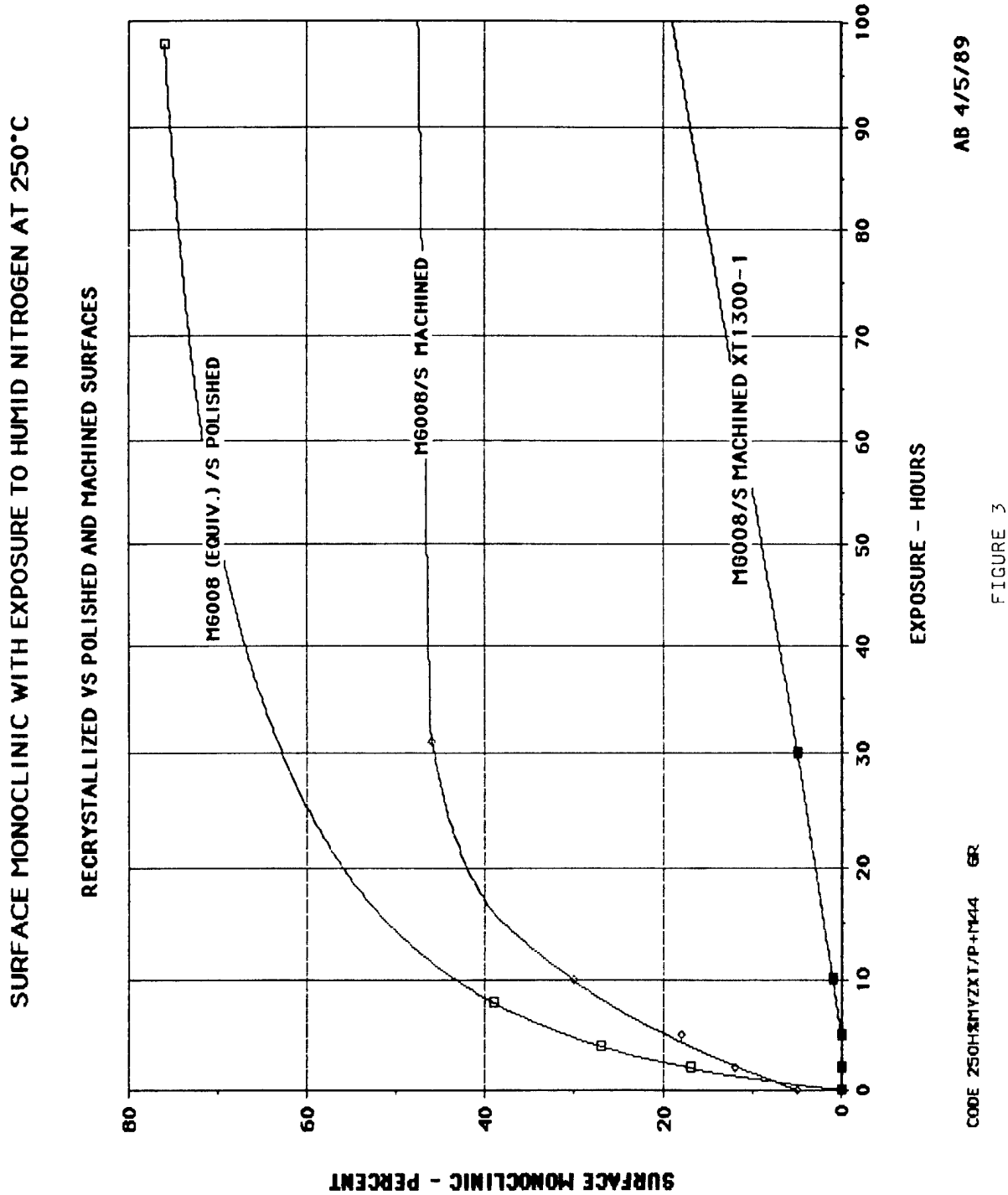
SURFACE MONOCLINIC WITH EXPOSURE TO HUMID NITROGEN AT 250°C
RECRYSTALLIZED VS POLISHED AND MACHINED SURFACES
M6008 (EQUIV.) /S POLISHED
M6008/S MACHINED
M6008/S MACHINED XT1300-1
SURFACE MONOCLINIC - PERCENT
EXPOSURE - HOURS
0
20
40
60
80
0
10
20
30
40
50
60
70
80
90
100
AB 4/5/89

FIGURE 3

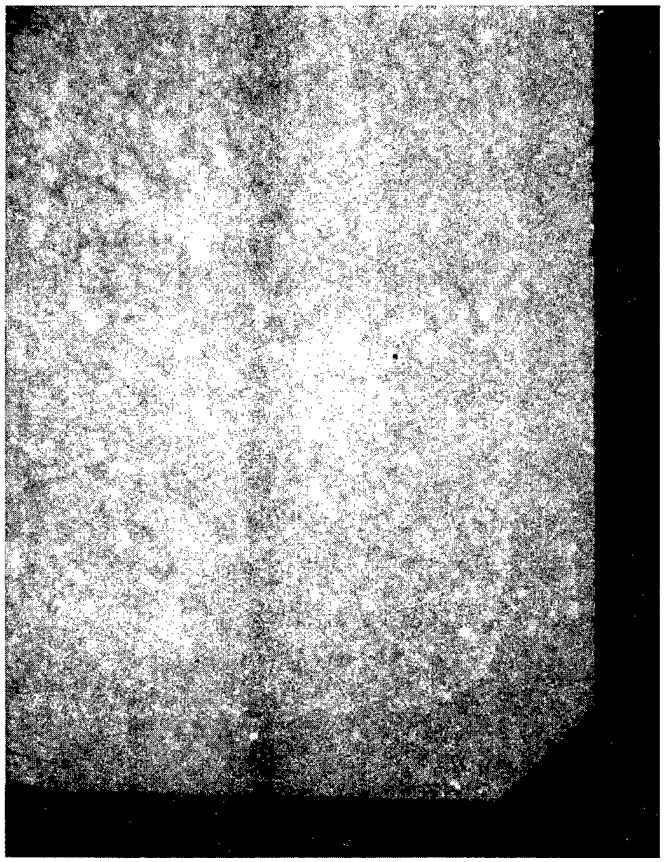

Fig. 4: Optical micrograph of corner of a fractured MOR bar at 100x magnification showing reaction layer due to low temperature degradation at 250°C for 2000 hrs.

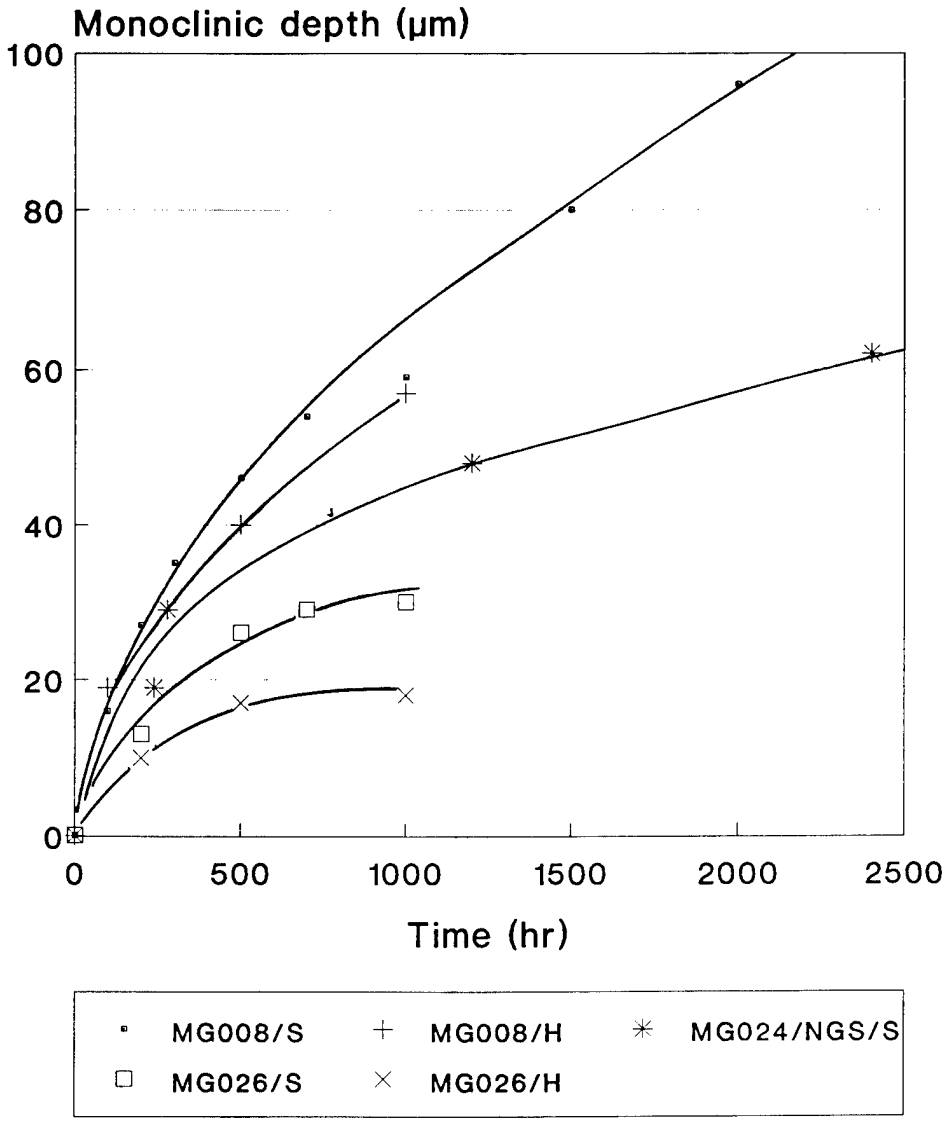

LTD Monoclinic Depth vs. Time
at 250 C/Oven

FIGURE 5

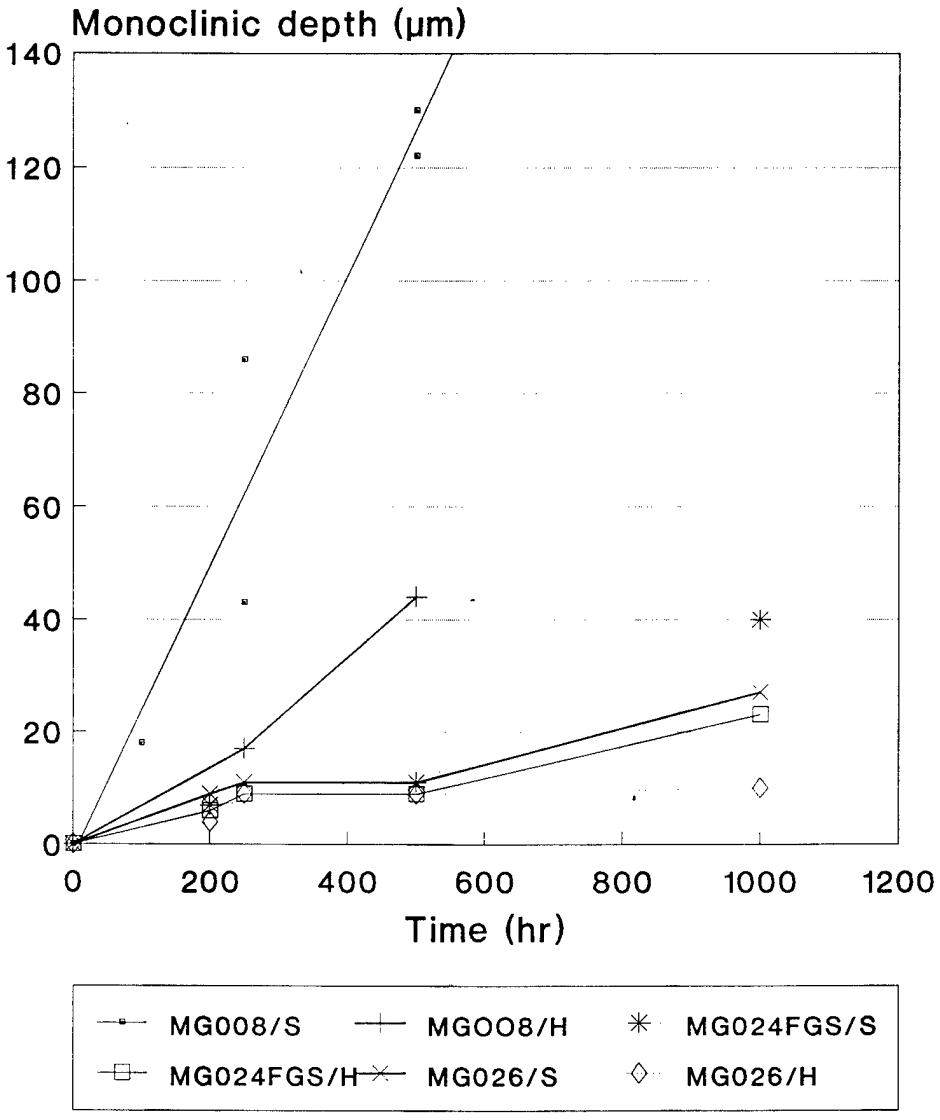

Monoclinic Depth vs. Time
at 120 C/Water

FIGURE 6

FLEXURAL STRENGTH WITH EXPOSURE TO WATER AT 120°C

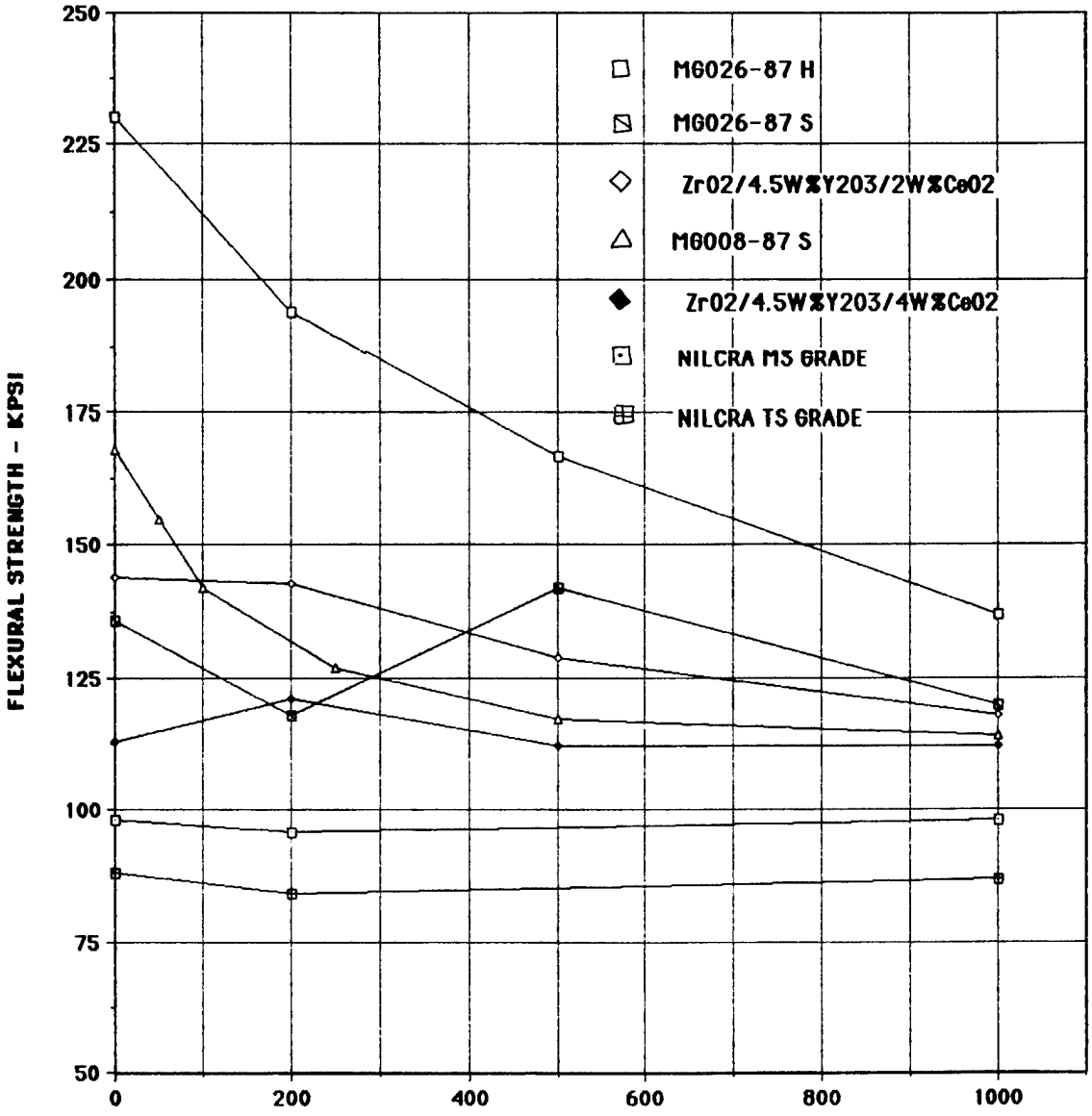

AB 2/7/89

FIGURE 7

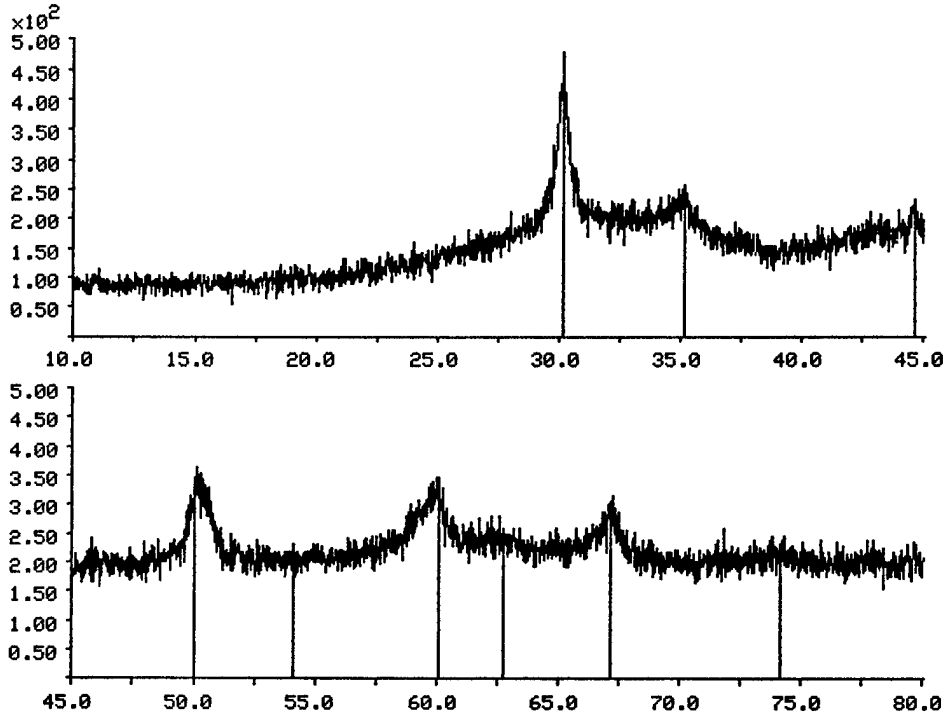

Fig. 8. XRD pattern of Z18.5CE62A crude.

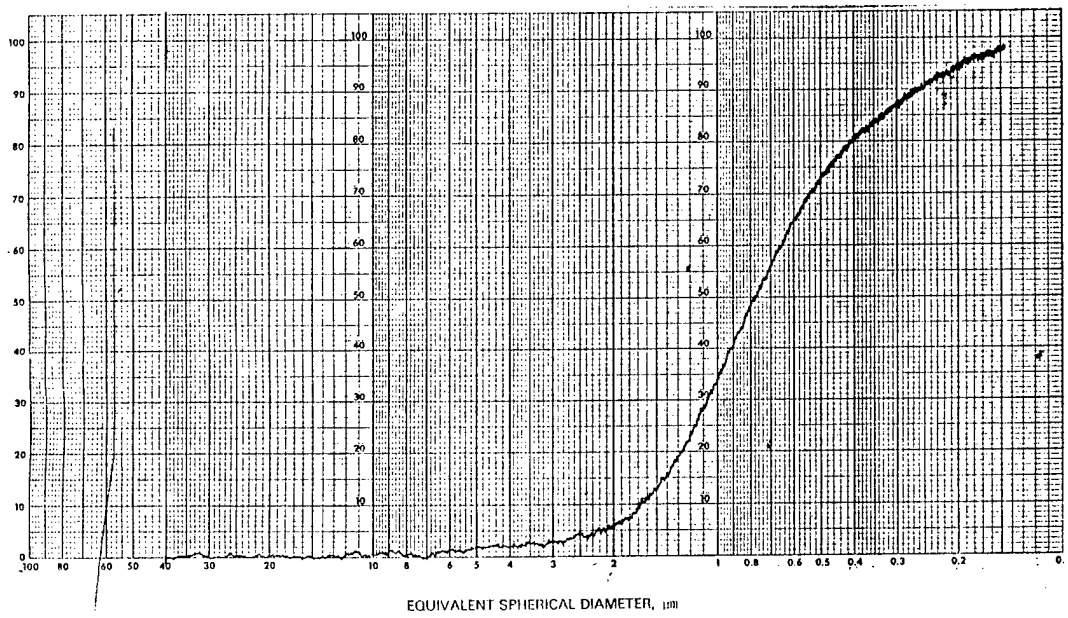

Fig. 9. Particle size distribution of powder obtained by vibratory milling of Z18.5CE62A crude for 96 hrs.

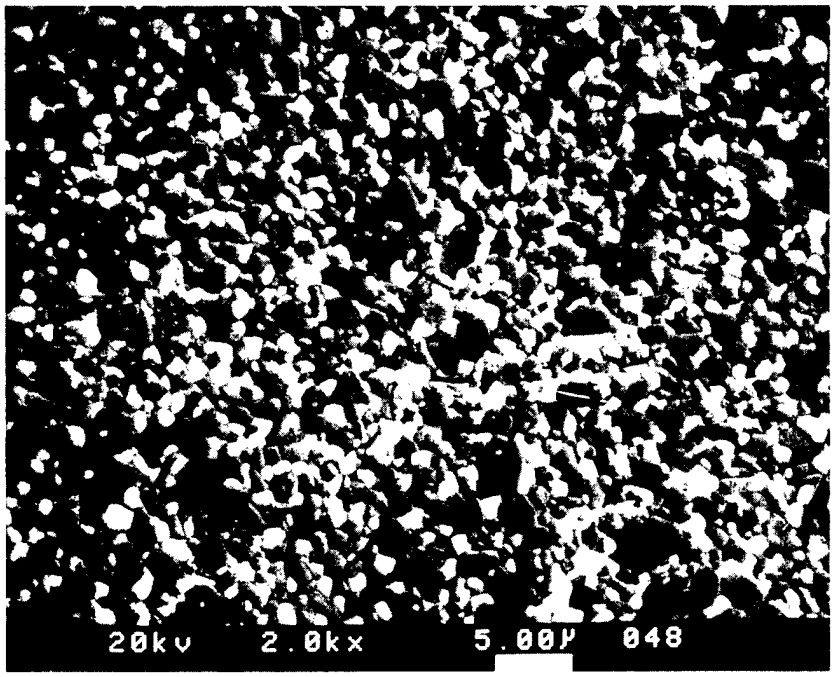

Fig. 10. Microstructure (SEM) of Z18.5CE62A ceramic fired at 1600°C/1 hr.

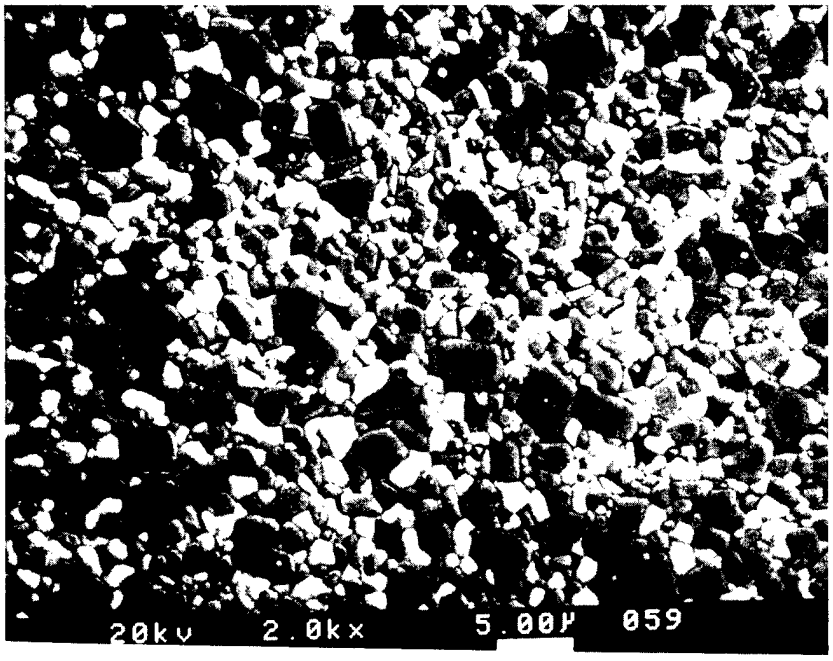

Fig. 11. Microstructure (SEM) of Z18.5CE62A ceramic fired at 1600°C/3 hrs.

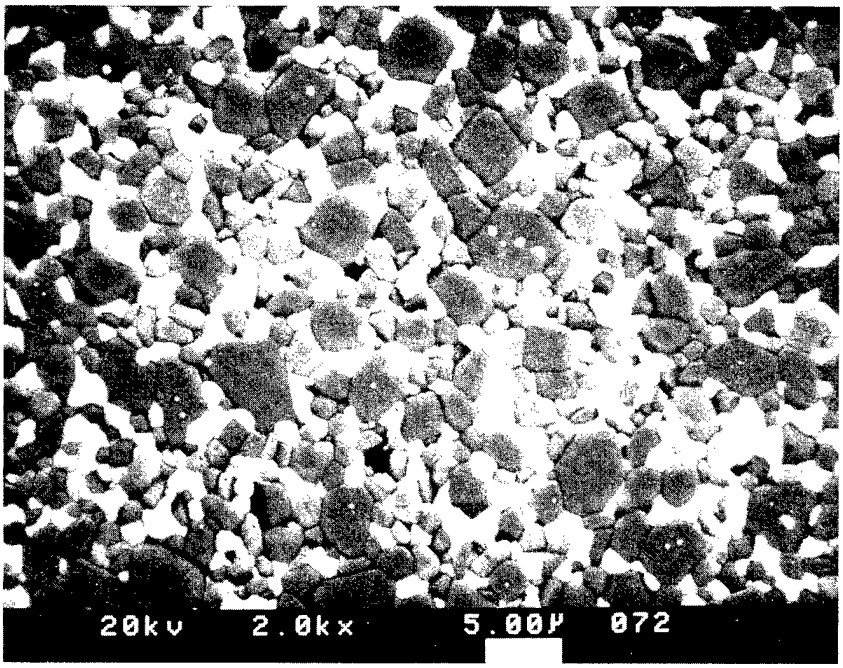

Fig. 12. Microstructure (SEM) of Z18.5CE62A ceramic fired at 1600°C/6 hrs.

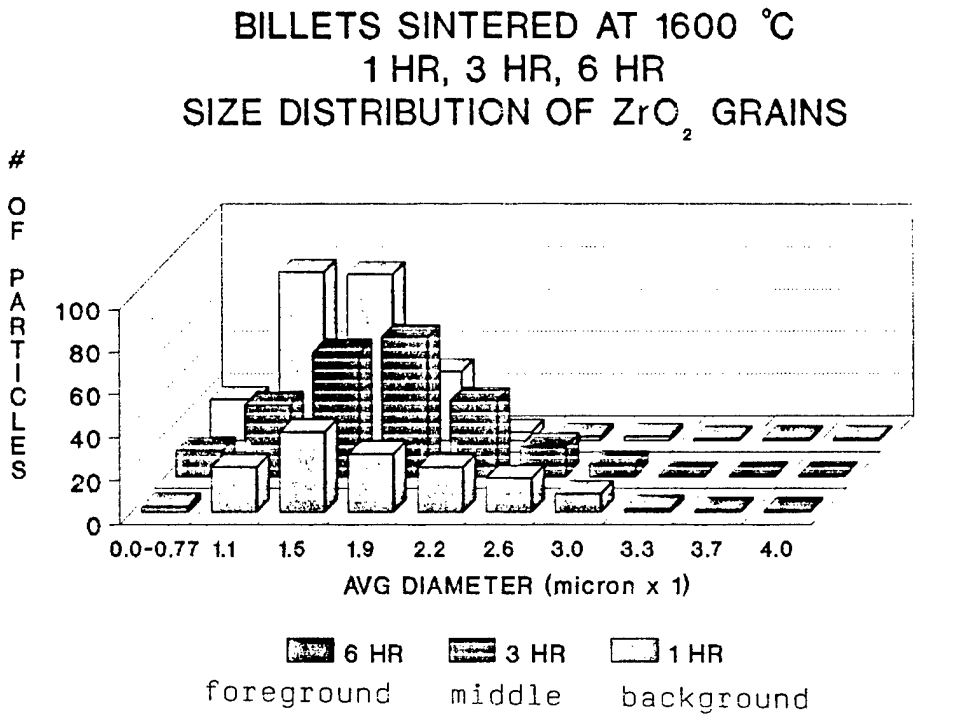

CODE: Z18.5CE62A-FL1050-1600

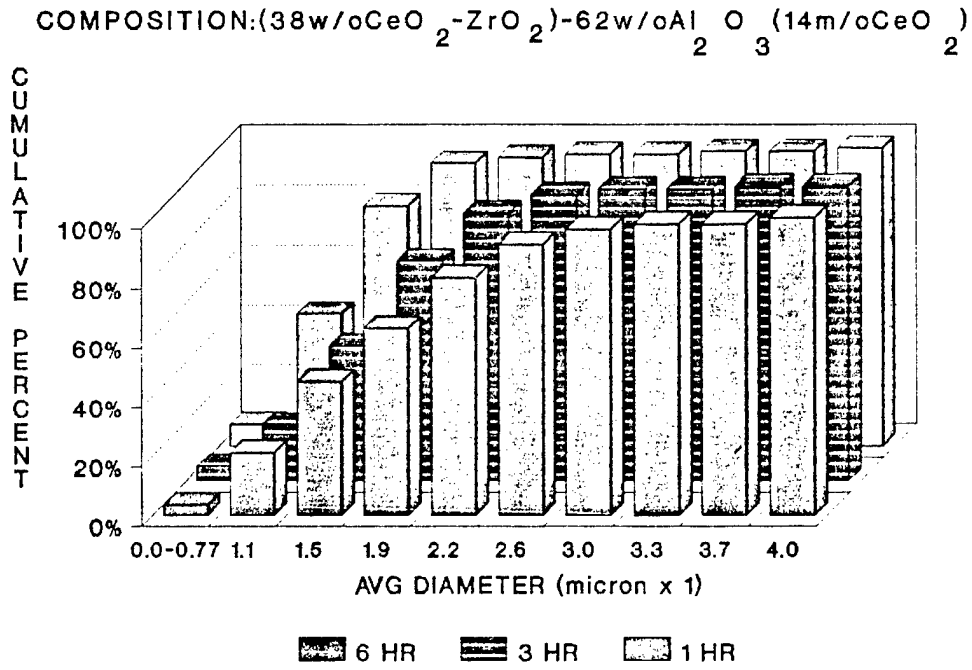

CODE: Z18.5CE62A-FL1050-1600

Fig. 13. Size distribution of CeO_2-ZrO_2 grains in Z18.5CE62A ceramic fired at 1600°C for 1, 3, and 6 hrs.

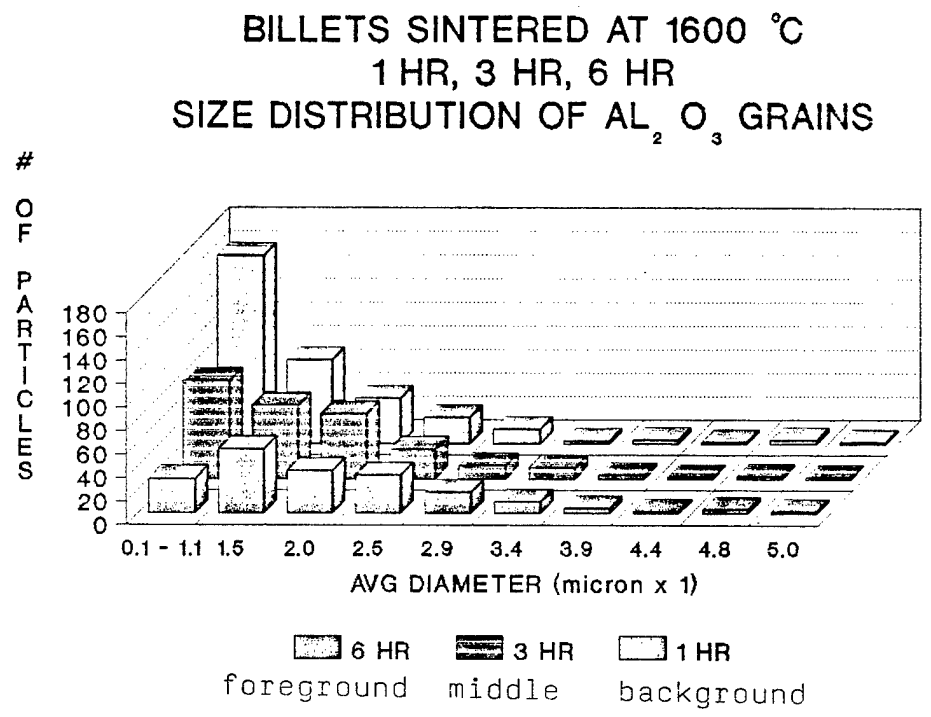

CODE: Z18.5CE62A-FL1050-1600

COMPOSITION:(38w/oCeO$_2$-ZrO$_2$)-62w/oAl$_2$O$_3$(14m/oCeO$_2$)

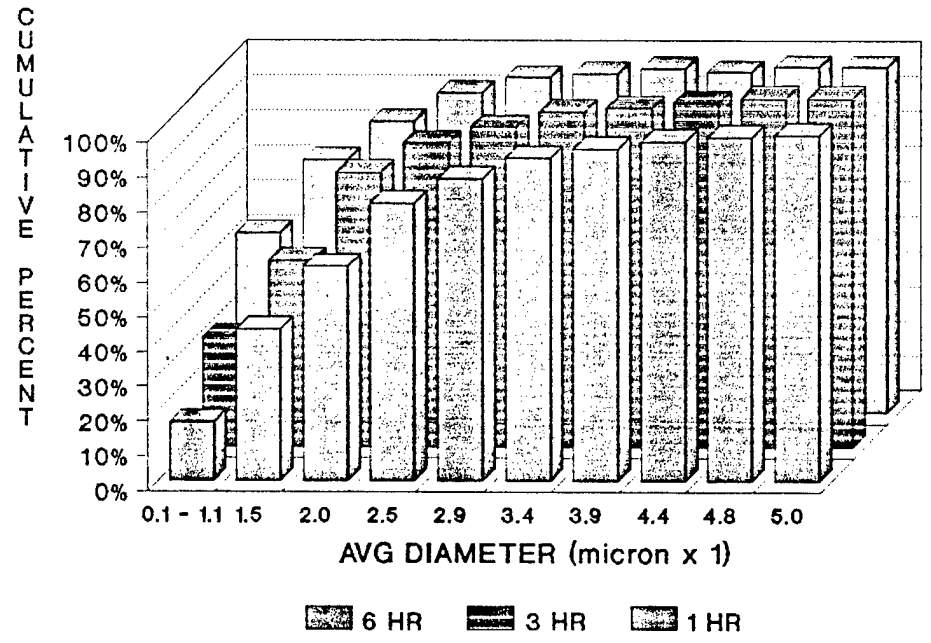

Fig. 14. Size distribution of Al_2O_3 grains in Z18.5CE62A ceramic fired at 1600°C for 1, 3, and 6 hrs.

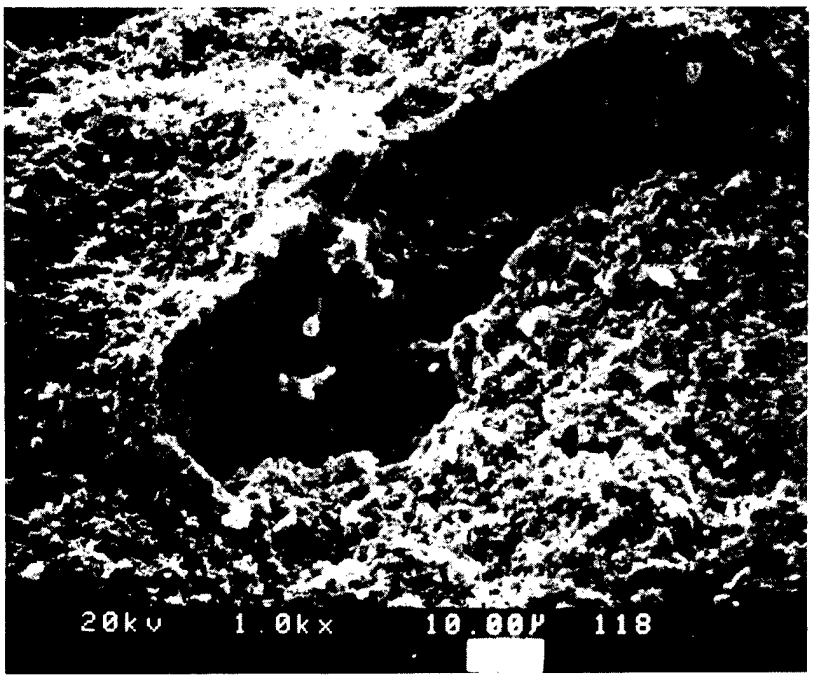

Fig. 15. Fractograph (SEM) showing elongated pore in Z18.5CE62A ceramic fired at 1600°C/1 hr.

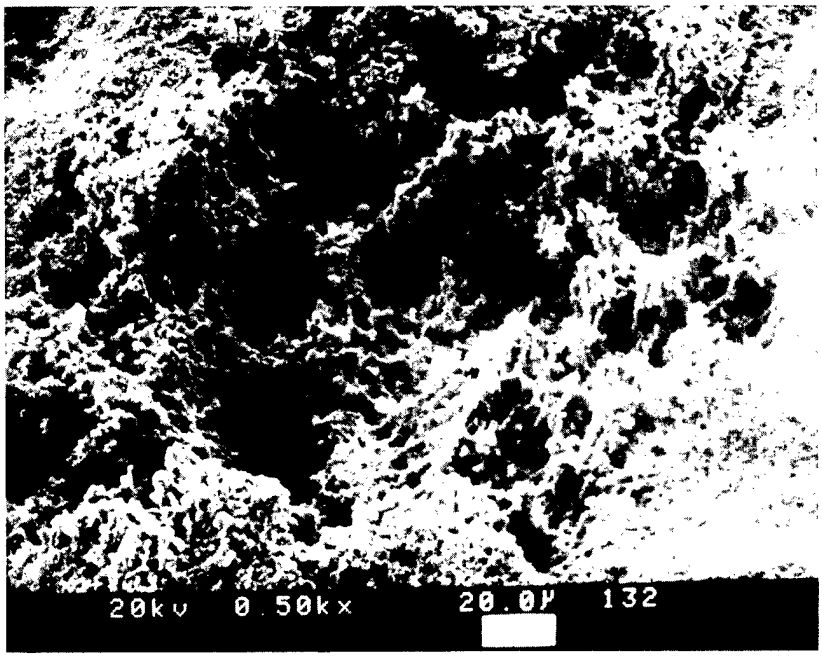

Fig. 16. Fractograph (SEM) showing high porosity region in Z18.5CE62A ceramic fired at 1600°C/1 hr.

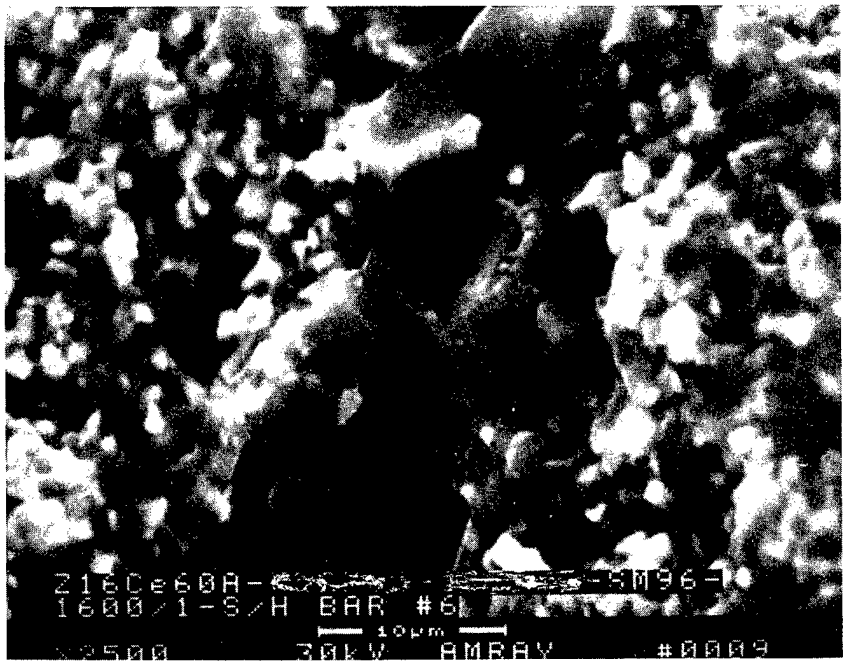

Fig. 17. Fractograph (SEM) showing dense grain cluster in Z18.5CE62A ceramic fired at 1600°C/1 hr.

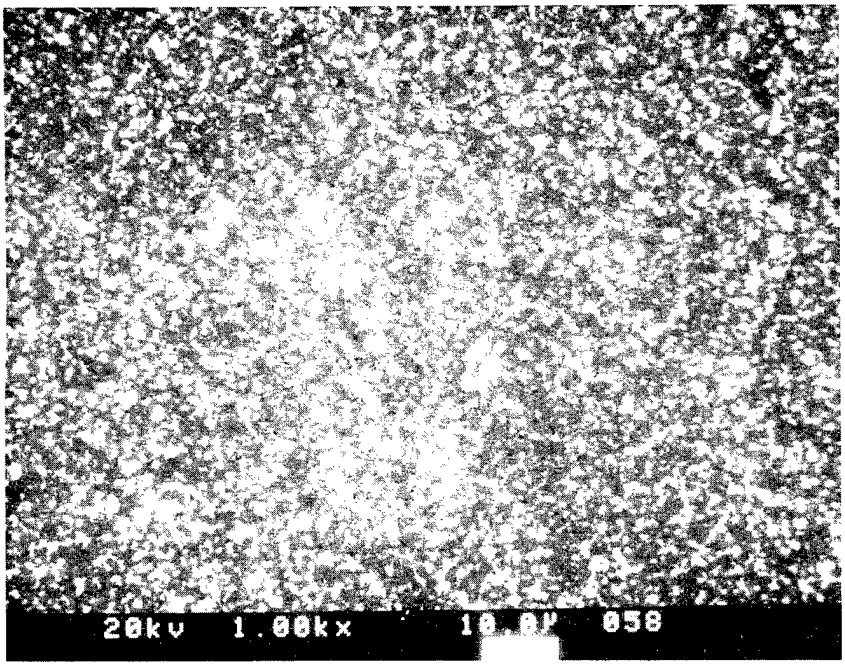

Fig. 18. Microstructure (SEM) of Z16CE60A ceramic made with the Moffatt technique, sintered at 1500°C/3 hrs. and HIPed at 1500°C/.75 hr.

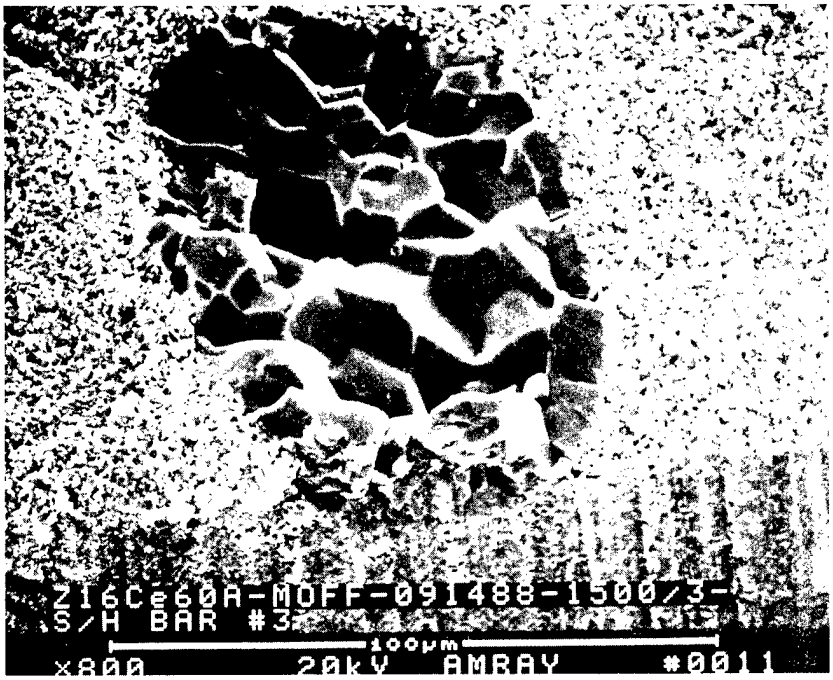

Fig. 19. Fractograph (SEM) of Z16CE60A ceramic made with Moffatt technique, showing Al_2O_3-rich inclusion.

Fig. 20. Fractograph (SEM) of Z16CE60A ceramic made with Moffatt technique, showing ZrO_2-rich inclusion.

Processing and Characterization of Transformation Toughened Ceramics With Strength Retention to Elevated Temperatures

R.A. Cutler, C. B. Brinkpeter, S. L. Bruner and D. W. Prouse (Ceramatec, Inc.), A.V. Virkar and D.K. Shetty (Univ. of Utah)

Objective/scope

Previous work[1] has shown that it is possible to increase the strength of Al_2O_3-ZrO_2 ceramics by incorporating transformation-induced residual stresses in sintered specimens consisting of three layers. The outer layers contained Al_2O_3 and unstabilized ZrO_2, while the central layer contained Al_2O_3 and partially stabilized ZrO_2. When cooled from the sintering temperature, some of the zirconia in the outer layers transformed to the monoclinic form while zirconia in the central layer was retained in the tetragonal polymorph. The transformation of zirconia in the outer layers led to the establishment of surface compressive stresses and balancing tensile stresses in the bulk. In theory, the residual stress will not decrease with temperature until the monoclinic to tetragonal transformation temperature is reached since monoclinic and tetragonal ZrO_2 polymorphs have nearly the same coefficients of thermal expansion.

During the first two years of ORNL funding it was demonstrated that 1) three layer composites could be made with retention of compressive surface stresses to temperatures of 750°C[2,3]; 2) residual stresses could be detected by strength testing[2,3], strain gauge measurements[4], characterization of monoclinic content by x-ray diffraction[2], or indentation/strength measurements[5]; 3) the three layer composites have excellent damage resistance[5]; and 4) significant (300-400 MPa) residual compressive stress which is not transformation-induced can be introduced by grinding monolithic Al_2O_3-15 vol. % ZrO_2(3.0 mol. % Y_2O_3).

The objectives of the present two year subcontract are 1) to increase the use temperature of three-layer composites by substituting HfO_2 for ZrO_2, 2) develop aqueous and nonaqueous slip casting techniques for three layer composites in order to obtain better layer uniformity and to maximize residual compressive stress by optimizing the outer layer thickness, 3) superimpose temperature stresses on transformation-induced stresses in three layer composites, and 4) demonstrate improved thermal shock resistance and damage resistance in optimized composites.

Technical progress

Slip Casting

Surface cracks were eliminated during drying of slip cast monolithic Al_2O_3-15 vol. % ZrO_2(3 mol. % Y_2O_3) plates by increasing the strength of the binder added to the slip.

Densities of 98.8% of theoretical were achieved on sintered monolithic inner layer plates. The plates were subsequently HIPed to greater than 99.8% of theoretical density before slicing the plates into bars for strength testing. The bars were surface ground before testing since previous work[6] showed that substantial residual stresses, which were retained to high temperatures, were introduced during grinding. The strength at room temperature was 893 MPa with a standard deviation of 47 MPa (9 bars tested). The strength at 1000°C was 557 MPa with a standard deviation of 49 MPa (5 bars tested). The strength of the slip cast bars exceeds the strength of the same composition made by dry pressing which was measured at 950°C as 528 MPa with a standard deviation of 21 MPa (3 bars tested)[6].

The strength at 1000°C is close to the milestone of 600 MPa. The retention of 62.4 % of the room temperature strength of the slip cast composite is in good agreement with the results of Tsukuma and Takahata[7] which reported room temperature strength of 1 GPa decreasing to 700 MPa at 1000°C for a similar composition (Al_2O_3-20 wt. % ZrO_2(2 mol. % Y_2O_3)). The relatively high room temperature strength (893 MPa) of the slip cast composite is due in part to surface grinding. As discussed previously[6], there is no indication by x-ray diffraction of tetragonal (t) to monoclinic (m) transformation on sintered, ground or fracture surfaces of this material. It is postulated that residual compressive stress introduced by plastic deformation of the surface during grinding is largely responsible for the large strength increase experienced after grinding[6]. The fact that the strength decreases with increasing temperature suggests that either the residual stresses are relaxed during exposure at 1000°C or that reversible transformation (t-->m-->t) occurs during the loading-unloading process.

Despite the good high temperature strengths achieved for the monolithic composites, these materials do not protect against surface damage due to the thin region which is affected by the grinding stresses. Three-layer composites, on the other hand, give protection against surface flaws[5]. Slip cast three-layer plates developed minor cracks upon drying. A two-layer (Al_2O_3-15 vol. % ZrO_2 outer layer and Al_2O_3-15 vol. % ZrO_2(Y_2O_3) inner layer) cylinder was successfully dried and sintered without cracking. The cylinder was cast in a new mold and the plates in old molds with increased surface roughness. New molds were made to improve the surface finish of the slip cast plates. Additional monolithic inner layer plates, as well as monolithic outer layer and three-layer plates (approximately 65 mm x 65 mm x 7 mm with varying outer layer thicknesses), were cast with improved surface finish.

Monolithic and three-layer Al_2O_3-15 vol. % ZrO_2 composites were slip cast, sintered and HIPed to greater than 99% of theoretical density. The monolithic outer layer (Al_2O_3-15 vol. % ZrO_2), inner layer (Al_2O_3-15 vol. %ZrO_2(3

mol. % Y_2O_3)) and three-layer plates were ground and sliced into bars for strength testing. The monolithic inner layer bars made from the new molds had a mean room temperature strength 975 MPa with a standard deviation of 86.2 MPa (4 bars), slightly improved compared to the strength data discussed above. The monolithic outer layer bars were not as strong, with a mean strength of 732.9 MPa (std. dev. of 78.4 MPa, 6 bars tested). The strength differential between outer and inner layer bars is similar to that obtained on dry pressed bars (Dry pressed and ground bars had strengths of 650 MPa, 806 MPa and 879 MPa for outer, inner and three-layer bars, respectively[6]).

The improvement in strength for slip cast bars, as compared to dry pressed bars, was most apparent for three-layer bars where the uniformity of layers was greatly improved. Three-layer bars where the outer layers were approximately 1/11th the total thickness (thickness of outer layers approximately 450 μm) had a mean strength of 984 MPa (std. deviation of 144.8 MPa, 8 bars tested). The bars which fractured from the tensile surface, as opposed to the chamfer, had a mean strength of 1066.7 (std. dev. of 102.5 MPa, 5 bars). The highest strength in this group was 1213 MPa. Three-layer bars with outer layers 1/17th the total thickness (thickness of outer layers approximately 300 μm) had a mean strength of 1,022.7 (std. dev. of 34.1 MPa, 5 bars tested). This group of bars failed from either inclusions (presumably iron contamination) or chamfers. Two three-layer bars where the outer layer thickness was approximately 125 μm (thickness of outer layer was 1/37th the total thickness), were fractured with strengths of 1053 MPa and 1213 MPa. Both of these bars failed from the chamfer where the inner layer is exposed. While the strength are not a strong function of outer layer thickness, due primarily to the tendency of the bars to fail from the chamfer region (this may be eliminated by putting the bars under triaxial compression), the data show that strength above 1200 MPa is possible with three-layer Al_2O_3-15 vol. % ZrO_2. The strength differential between three-layer and outer layer material is between 289 MPa and 400 MPa. The strength differential achieved with three-layer dry pressed bars was up to 375 MPa.

Three-layer bars with outer layer thicknesses of 300 μm and 125 μm were tested at 1000°C. Three bars with an outer layer thickness of 300 μm had a mean strength of 561 MPa and a standard deviation of 92 MPa (the highest strength bar failed at 667 MPa and the lowest strength bar failed at 499 MPa). One of the bars failed from the chamfer while the other two failed from the tensile surface. Three bars with an outer layer thickness of 125 μm had a mean strength of 584 MPa and a standard deviation of 10 MPa. The mean of all six bars was 577 MPa with a standard deviation of 48 MPa. This clearly demonstrates that the milestone of 600 MPa at 1000°C is feasible. It also suggests that some residual stress has been retained at 1000°C. Testing of the outer layer monolithic

specimens is underway to confirm the retention of some of the room temperature residual stress. The strength differential between three-layer composites and monolithic outer layer bars will give an indication of the strength retention achieved, since failure generally occurred from the tensile surface at 1000°C. High temperature x-ray diffraction will be used to monitor the m-->t transformation which occurs during heating, which is responsible for the decreasing residual stress. The attainment of strength of approximately 575 MPa at 1000°C is significant since the best previous strength of three-layer composites at 1000°C was 325 MPa. The improved uniformity of the outside layer, surface grinding, and improved dispersion of ZrO_2 are believed to be the principal reasons for the significantly improved high temperature strength.

Slip cast three-layer composites continued to show a greater tendency to crack than monolithic plates. The variation of solids content between 65 and 75 wt. % did not affect the tendency to crack or the final density. Controlled humidity drying, using H_2SO_4-H_2O mixtures, showed improvement in limiting cracking during drying. The plates were dried in steps of decreasing humidity (i.e., 100%, 80%, 60%, 40%, 20%, 3% over a 10 day time period). The ability to control humidity and temperature simultaneous and ramp at controlled humidity rates would be ideal for the three-layer composites.

Slip casting using pH to control the dispersion was investigated for the monolithic outer layer composition, which has lower density after sintering and HIPing than the inner layer composition. Slips at pH of 2.5 and 11.5 showed no improvement in density (after sintering) over the same composition cast using the combination of Darvan C (ammonium polyelectrolyte dispersant) and citric acid. Low pH slips degrade plaster molds. Alcohols are also incompatible with plaster molds and poorly dispersed the outer layer composition.

Temperature Stress

Strengthening of three-layer composites based solely on temperature stresses (compressive surface stresses introduced due to differences in thermal expansion mismatch) was made by fabricating bars with outer layers of Al_2O_3-15 vol. % ZrO_2(3 mol. % Y_2O_3) and an inner layer of ZrO_2(3 mol. % Y_2O_3)-40 vol. % Al_2O_3. The powders were dry pressed, sintered and HIPed using similar processing techniques as described previously[2,3]. The expected difference in thermal expansion between the inner and outer layers was 0.9×10^{-6}/°C resulting in a predicted strength increase of 300 MPa for composites where the outer layers were 1/12 the total thickness. The linear thermal expansion mismatch between 25 and 1000°C was measured to be 9.3×10^{-7}/°C, in excellent agreement with the desired expansion differential. Monolithic and three-layer bars were made with strengths as shown in Table 1. The

Table 1
Room Temperature Characterization of Al_2O_3-ZrO_2 Composites Made with Temperature-Induced Stress

Composition	Ground	Density (g/cc)	Strength (MPa) No.[a]	$\bar{x}$[b]	s[c]
Outer[d]	Hand[e]	4.32	5	500	42
Outer	Machine[f]	4.32	5	737	66
Inner[g]	Hand	5.22	5	704	100
Inner	Machine	5.22	4	1076	190
1/12-5/6-1/12[h]	Hand	5.06	5	777	25
1/12-5/6-1/12	Machine	5.06	5	949	62
1/6-2/3-1/6[i]	Hand	4.90	5	703	54
1/6-2/3-1/6	Machine	4.90	5	781	75

a. Number of specimens tested.
b. Mean value.
c. Standard deviation.
d. Monolithic outer layer bars of composition Al_2O_3-15 vol. % ZrO_2(3 mol. % Y_2O_3).
e. Hand ground (chamfered) before HIPing with no other grinding.
f. Machine ground (220 grit wheel at a down feed of 2.5 μm/pass before spark out) after HIPing.
g. Monolithic inner layer bars of composition ZrO_2(3 mol. % Y_2O_3)-40 vol. % Al_2O_3.
h. Three-layer bars where the outer layers are ≈1/12 the total thickness.
i. Three-layer bars where the outer layers are ≈1/6 the total thickness.

strengths of hand ground bars were considerably lower than the strengths of machine ground bars, most likely due to plasticity for bars where the outer layer was Al_2O_3-15 vol. % ZrO_2(3 mol. % Y_2O_3) and due to plasticity and transformation toughening for ZrO_2(3 mol. % Y_2O_3)-40 vol. % Al_2O_3 bars. The strength improvement of 212 GPa, due to temperature stresses, for the three-layer bars is in fair agreement with prediction. Elevated temperature testing of the three-layer temperature stress bars having a room temperature strength of 949±62 MPa was performed at 750°C and 1000°C. The strength at 750°C was 508 MPa with a standard deviation of 70 MPa (3 bars) and strength at 1000°C was 329 MPa (2 bars with individual values of 366 and 297 MPa). All of the bars failed from the tensile surface. This data is difficult to understand based on the strength of the monolithic outer layer of these bars (Al_2O_3-15 vol. % ZrO_2(3 mol. % Y_2O_3)) and thermal expansion behavior, as discussed above. Failure from within the tensile region does not explain the data due to the low tensile stresses predicted at 750 and 1000°C. Further work is underway to understand these data.

Al_2O_3-HfO_2 Compositions

Al_2O_3-15 vol. % HfO_2, Al_2O_3-15 vol. % HfO_2(4 mol. % Y_2O_3) and HfO_2(4 mol. % Y_2O_3) compositions were dry pressed, sintered and HIPed using hafnia powders received from Teledyne Wah Chang Albany. X-ray diffraction showed that the sintering temperature of 1600°C was not high enough to fully convert the monolithic $HfO_2(Y_2O_3)$ to tetragonal. Approximately 60 % of the HfO_2(4 mol. % Y_2O_3) was monoclinic after holding for 2 hours at 1600°C. The $HfO_2(Y_2O_3)$ with no alumina added had a strength of 329 MPa (std. dev. of 28 MPa). Monolithic outer (Al_2O_3-15 vol. % HfO_2), monolithic inner (Al_2O_3-15 vol. % HfO_2(4 mol. % Y_2O_3)) and three-layer composites had strengths of 457.7 MPa (std. dev. of 30.2 MPa), 436.7 MPa (std. dev. of 22.2 MPa) and 492.3 MPa (std. dev. of 31 MPa). The thermal expansion of the monolithic inner and monolithic outer materials were both approximately 8.4×10^{-6}/°C over the temperature range 25-1000°C. The slightly higher strength of three-layer composites is not to likely due to transformation-induced stresses since sintering occurred in the monoclinic stability range for the unstabilized HfO_2. Higher yttria content will be used to stabilize the tetragonal polytype in the inner layer composition. Rapid heating of dense bars to the tetragonal stability range will be used to determine if three-layer HfO_2 bars can be fabricated with high strength due to transformation-induced stress. Alternatively, $HfO_2 \cdot ZrO_2$ solid solutions will be made to lower the monoclinic --> tetragonal transformation temperature.

Status of milestones

Milestone 1 is partly completed. Room temperature strength above 1200 MPa have been achieved on aqueous cast three-layer bars, but not on large sample sizes. Development of parameters for non-aqueous casting has not been achieved.

Publications

J. J. Hansen, R. A. Cutler, D. K. Shetty and A. V. Virkar, "Indentation Fracture Response and Damage Resistance of Al_2O_3-ZrO_2 Composites Strengthened by Transformation-Induced Residual Stresses," J. Am. Ceram. Soc., 71[12] C-501-C-505 (1988).

References

1. A. V. Virkar, J. L. Huang, and R. A. Cutler, "Strengthening of Oxide Ceramics by Transformation Induced Stresses," J. Am. Ceram. Soc., 70 [3] 164-170 (1987).

2. R. A. Cutler, J. J. Hansen, A. V. Virkar, D. K. Shetty, and R. C. Winterton, "Strength Improvement in Transformation Toughened Ceramics using Compressive Residual Surface

Stresses," Advanced Structural Ceramics Vol. 78, ed. by P.F. Becher, M. V. Swain, and S. Somiya (Materials Research Society, Pittsburgh, PA, 155-163, 1987).

3. R. A. Cutler, J. D. Bright, A. V. Virkar, and D. K. Shetty, "Strength Improvement in Transformation-Toughened Alumina by Selective Phase Transformation," J. Am. Ceram. Soc., 70 [10] 714-18 (1987).

4. A. V. Virkar, J. F. Jue, J. J. Hansen and R. A. Cutler, "Measurement of Residual Stresses in Oxide-ZrO_2 Three-Layer Composites," J. Am. Ceram. Soc., 71[3] C-148-C-151 (1988).

5. J. J. Hansen, R. A. Cutler, D. K. Shetty and A. V. Virkar, "Indentation Fracture Response and Damage Resistance of Al_2O_3-ZrO_2 Composites Strengthened by Transformation-Induced Residual Stresses" J. Am. Ceram. Soc., 71[12] C-501-C-505 (1988).

6. R. A. Cutler, S. L. Bruner, D. W. Prouse, A. V. Virkar, and D. K. Shetty, "Processing and Characterization of Transformation Toughened Ceramics with Strength Retention to Elevated Temperatures," in Ceramic Technology for Advanced Heat Engines Project Semi-Annual Technical Progress Report (Apr.-Sept. 1988), Oak Ridge National Laboratory, Oak Ridge, TN.

7. K. Tsukuma and T. Takahata, "Mechanical Property and Microstructure of TZP and TZP/Al_2O_3 Composites," Advanced Structural Ceramics Vol. 78, ed. by P.F. Becher, M. V. Swain, and S. Somiya (Materials Research Society, Pittsburgh, PA, 123-135, 1987).

1.2.4 Silicate Matrix

Low Expansion Ceramics for Diesel Engine Applications

J. J. Brown, R. E. Swanson (VPI and SU), and F. A. Hummel (Consultant)

Objective/scope

The major objective of this research is to investigate selected oxide systems for the development of a low expansion, high thermal shock resistant ceramic. Specifically, it is the goal of this study to develop an isotropic, ultra-low expansion ceramic which can be used above 1200°C and which is relatively inexpensive.

Technical progress

This research program includes the synthesis, property characterization, and fabrication of candidate low thermal expansion ceramics from four systems based upon aluminum phosphate, silica, mullite, and zircon. In the first two systems, the goal is to stabilize low thermal expansion, high temperature, high crystal symmetry phases via solid solution formation. In mullite, deviation from stoichiometry and solid solution formation are utilized to reduce the thermal expansion. In zircon, the crystal anisotropy and thermal expansion are reduced via solid solution formation. Based upon earlier data of the investigators, compositional ranges are evaluated by fabricating experimental specimens and determining phase content plus microstructure, thermal expansion, solidus temperature, and density. Those compositions which exhibit acceptable sintering, phase composition, and expansion characteristics are studied in more detail, including flexure strength, creep, thermal conductivity, and crystal structure. Finally, those ceramic compositions exhibiting the best combination of properties are evaluated as to their fabrication behavior in the form of specimens having masses up to about 0.5 kg.

$AlPO_4$-β-$LiAlSiO_4$ System

Selected bulk sample properties for the compositions $Li_{0.46}AlP_{0.54}Si_{0.46}O_4$ (Sample A6), $Li_{0.5}AlP_{0.5}Si_{0.465}O_{3.93}$ (Sample A15),

and $Mg_{0.035}Li_{0.41}AlP_{0.52}Si_{0.48}O_4$ (Sample C6) have been determined and are summarized in Table 1. The retained modulus of rupture (MOR) values were previously measured and reported in our last semiannual progress report.

The density of each of the three compositions was lower than 84% theoretical. Specimens of all three compositions were sintered at 1190°C for property measurements. Because 1190°C is approaching the melting temperatures of the samples (about 1205°C for sample A15, 1210°C for sample C6, and 1246°C for sample A6), a sample preparation method such as heat pressing, should be utilized to increase density.

Work has continued to investigate the possibilities of ion substitution for Li^+. Sample composition, processing, and phases present are summarized in Table 2. For the starting composition $Li_{0.48}AlP_{0.52}Si_{0.48}O_4$, 12.5 mol% of Li^+ was replaced by Cu^{2+}, Fe^{2+}, and Zn^{2+} to form compositions $Cu_{0.03}Li_{0.42}AlP_{0.52}Si_{0.48}O_4$ (Y-115), $Fe_{0.03}Li_{0.42}AlP_{0.52}Si_{0.48}O_4$ (Y-116), and $Zn_{0.03}Li_{0.42}AlP_{0.52}Si_{0.48}O_4$ (Y-117), respectively. The selection of these ions was based on the consideration of the ionic radius ratio, valency, and coordination number because they were intentionally introduced to substitute for Li^+ as the stuffing ion in the structure. However, all three compositions were multiphase after heat treatments.

Sample Y-110 has an initial composition of $Li_{0.48}AlP_{0.52}Si_{0.48}O_{3.52}N_{0.32}$, where N^{3-} was purposely introduced to substitute for O^{2-} using Si_3N_4 as a raw material. The sample was fired at 800°C for 12 hours in air, then at 1180°C for 72 hours in a nitrogen atmosphere. The reacted sample had a phase composition of β-$LiAlSiO_4$ solid solution. The bar sintered from the sample powders had an average coefficient of thermal expansion (CTE) of -9.9 x 10^{-7}/°C between 30 and 1000°C. This CTE value was more negative than that of -6.6 x 10^{-7}/°C previously reported for the composition $Li_{0.48}AlP_{0.52}Si_{0.48}O_4$ without N^{3-} substitution for O^{2-}. More work will be done to investigate the effect of anion exchange on phase composition and thermal expansion of the solid solution.

Mullite System

Studies have been completed into modifying the thermal expansion behavior of the mullite crystal structure. Previous attempts to significantly reduce mullite's thermal expansion coefficient by forming various mullite solid solutions were unsuccessful. Consequently, the idea of systematically disrupting lattice vibrations by introducing additional vacancies was explored as a means of altering the expansion behavior of mullite.

Table 1. Density and Porosity Data for Selected Solid Solution Compositions.

Sample No.	Composition	Specimen Sintering Temp.(°C)	Bulk Density (g/cm^3)	Theoretical Density (%)	Open Porosity (%)
A6	$Li_{0.46}AlP_{0.54}Si_{0.46}O_4$	1190	2.001	80.7	18.66
A15	$Li_{0.5}AlP_{0.5}Si_{0.465}O_{3.93}$	1190	2.058	83.2	16.0
C6	$Mg_{0.035}Li_{0.41}AlP_{0.52}Si_{0.48}O_4$	1190	1.971	78.0	21.2

Table 2. Summary of Sample Composition Processing and Phases Present for Composites with Li^+ Ion Substitution.

Sample No.	Composition	Sample Processing Temp.(°C)/Time(h)	Phase	CTE $\alpha(x10^{-7}/°C)$
Y-115	$Cu_{0.03}Li_{0.42}AlP_{0.52}Si_{0.48}O_4$	1180/48,1200/60,1200/40	multiphase	N.A.*
Y-116	$Fe_{0.03}Li_{0.42}AlP_{0.52}Si_{0.48}O_4$	1180/48,1200/60,1200/40	multiphase	N.A.
Y-117	$Zn_{0.03}Li_{0.42}AlP_{0.52}Si_{0.48}O_4$	1180/48,1200/60,1200/40	multiphase	N.A.
Y-110	$Li_{0.48}AlP_{0.52}Si_{0.48}O_{3.52}N_{0.32}$	880/12,1180/72 (in N_2)	solid solution	-9.9

*N.A. = Not Available

Experimental - A sol-gel procedure utilizing tetraethyl orthosilicate (TEOS) and aluminum tri-sec butoxide was used for mullite synthesis in this study. The sol-gel procedure is outlined in the flow chart in Figure 1.

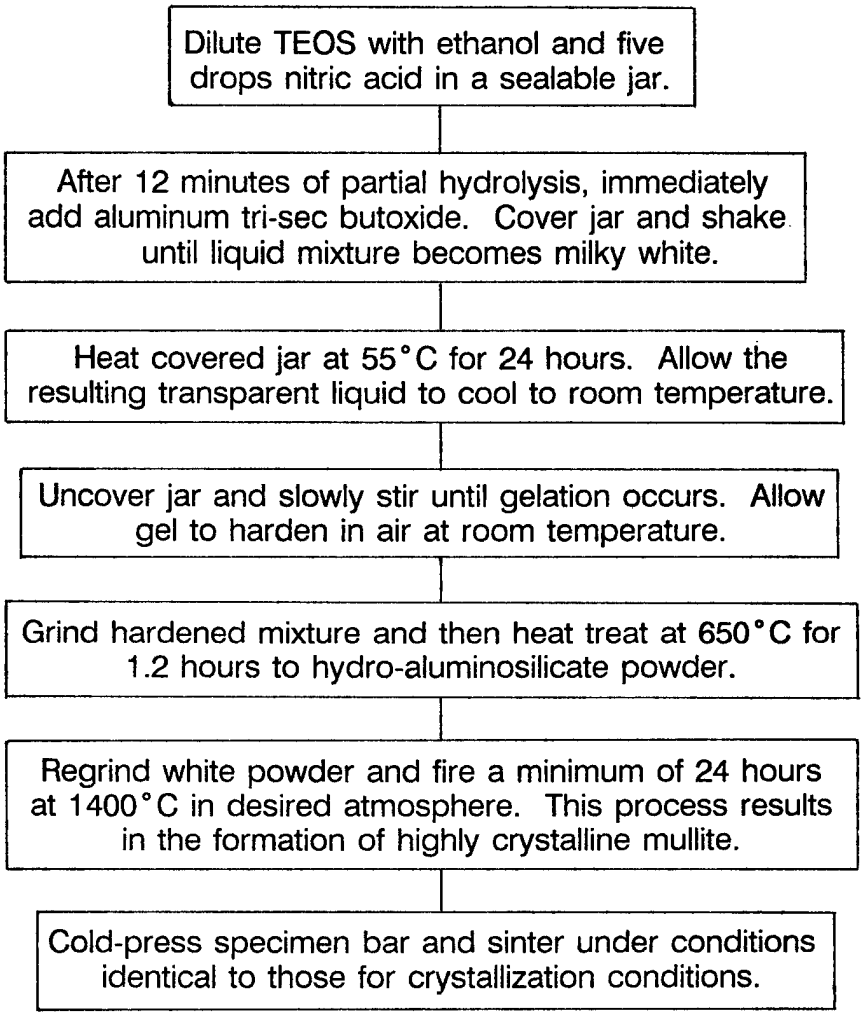

Figure 1. Sol-gel process for mullite synthesis.

The resulting mullite precursors were fired in oxygen-deficient atmospheres generated by CO and CO_2 mixtures at high temperatures. Crystallization conditions for this process in air require a firing temperature of 1400°C and a reaction time of about 24 hours. These crystallization conditions were used to synthesize a series of mullite samples in atmospheres with oxygen partial pressures of 10^{-10} and 10^{-9}. These atmospheres were also used to synthesize another series of samples fired at 1500°C for 36 hours. The selection of oxygen partial pressures was based primarily on the capability to maintain consistent CO/CO_2 mixtures at reaction temperatures of 1400 and 1500°C. Mullite processing environments are listed in Table 3.

Table 3. CTE[a] values of mullite samples processed in reducing atmospheres.

Sample	Processing[b] Temp(°C)/Time(h)	p_{O_2} (atm)	Mean CTE[c]	Standard Deviation	Min. CTE	Max. CTE
K1-0[d]	1400/24	.21	54.8	1.58	52.0	56.4
K1-0b[d]	1400/24	.21	55.8	1.54	52.3	56.9
K1-1[d]	1400/24	10^{-10}	56.4	1.12	53.2	56.9
K1-2[d]	1400/24	10^{-9}	57.5	0.36	56.7	57.8
K1-2b[d]	1400/24	10^{-9}	54.9	2.38	49.8	56.7
K1-4	1400/24	10^{-10}	57.4	0.48	56.6	58.5
KB-0	1500/36	.21	56.4	1.32	56.3	57.8
KB-1	1500/36	10^{-10}	55.6	2.23	52.0	58.5
KB-2	1500/36	10^{-9}	55.9	1.83	52.3	57.7
KB-2b	1500/36	10^{-9}	55.3	2.61	49.8	58.5

[a]CTE and Standard Deviation units are x 10^{-7} μm/°C.
[b]Sintering conditions are identical to sample processing conditions except for sample K1-4 which was sintered for 72 hours.
[c]Based on 10 observations.
[d]Samples previously reported.

The sample chamber was flushed with the appropriate CO/CO_2 gas mixture for approximately 35 minutes before firing and later allowed to cool to room temperature under the same reaction atmosphere. Successfully completed samples were then cold-pressed into bars and sintered under conditions identical to their respective crystallization conditions. These sintered bars were later used to test thermal expansion characteristics. In addition, samples from each sol-gel batch were synthesized in normal atmospheric conditions (1400°C/24h) for comparison to their possible oxygen-deficient counterparts.

Extensive sample characterization was conducted during sample development so that possible differences in precursor/sample formation could be identified. Differential thermal analysis (DTA) was conducted on samples taken from each independent sol-gel batch in the series of mullite samples fired at 1400°C for 24h. All DTA runs were conducted from 30°C to 1400°C at a heating rate of 10°C per minute. Following crystallization in oxygen-deficient atmospheres, DTA was conducted twice on each sample so that possible re-oxidation reactions after heating to 1400°C in air could be identified. In addition, sample differences in x-ray diffraction patterns collected from 15 to 70 degrees 2θ were also investigated.

Finally, repeated dilatometer measurements from 50°C to 1000°C with a heating rate of 10°C per minute were conducted on each samples. Expansion testing was conducted 10 times on each sample so that basic statistics could be used to test for any significant difference in thermal expansion values. A corresponding value for the linear CTE was computed for each run from which a sample mean CTE was computed.

Results and Discussion - Phase identification was obtained by means of X-ray diffraction (XRD) peak analysis. X-ray patterns for all samples fired at 1400°C/24h (Series K1) showed the formation of pure, highly crystalline mullite in all atmospheric conditions tested. X-ray patterns of all samples fired in reducing atmospheres showed a positive shift in all 2θ values when compared to their respective air-fired standards. Average 2θ value differences between the standard air samples and reduce fired samples ranged from -0.6 to -0.14 degrees 2θ. However, because the shifts in all reflections for a given sample are basically the same in magnitude and direction, this shift may be attributed to sample processing procedure rather than to the creation of additional vacancies in the structure. It is interesting to note that samples x-rayed after sintering show a decrease in 2θ values toward those found in their respective standard.

In response to these shifts, phase equilibrium following these processing conditions was re-examined. Sample K1-4 was sintered for 72 hours in its crystallization atmosphere of 10^{-10} atm. X-ray peak analysis indicated that 2θ values for K1-4, like other K1 samples fired in reducing atmospheres, shifted back toward its air fired standard (Sample K1-0). This similar behavior to samples fired for shorter periods reconfirmed probable equilibrium under the minimum firing conditions (1400°C/24h). The series of samples fired at 1500°C/36h (Series KB) also showed similar 2θ value shifts. These shifts are still not understood and would require future study. In addition, all samples showed no significant increase in X-ray peak diffuseness which also indicated no significant increase in defects, such as vacancies, in the mullite structure.

DTA examination of the K1 series precursor material following individual heat treatments (650°C/1.2h, air) revealed differences only in the extent of alcohol removal. These differences can possibly be attributed to small differences in the amount of material that underwent heat treatment. Following their crystallization in oxygen-deficient atmospheres, DTA runs were conducted twice on each K1 sample so that possible re-oxidation reactions after heating to 1400°C in air could be identified. Though there were fluctuations in the minima of the DTA curves ranging from 790°C to 976°C, no correlations could be found between DTA curve minima and crystallization atmosphere. DTA runs for corresponding K1 standard samples fired in air showed a similar fluctuation in DTA curve minima along with no correlation to the sample counterpart fired in a reduced atmosphere. DTA was not undertaken for the KB series of samples fired at 1500°C/36h in the reducing atmospheres.

Table 3 includes thermal expansion data for the mullite specimens synthesized in reducing atmospheres. A statistical analysis of the data indicated that the reducing atmospheres had no effect on the thermal expansion behavior of the mullite structure.

Summary - A simple, reproducible sol-gel method for producing highly crystalline mullite has been established.

Highly crystalline mullite samples have been synthesized in normal and reducing atmospheres of 10^{-10} and 10^{-9} atmospheres.

Attempts to introduce additional vacancies into the mullite structure have been unsuccessful.

Silica System

The chemically stabilized β-cristobalite was modified by various ionic substitutions in an attempt to reduce its thermal expansion. Efforts of the present studies were concentrated on the substitution of the divalent cation which occupies the interstitial site in the β-cristobalite structure. The substitution was based on the chemical formula $MO \cdot Al_2O_3 \cdot xSiO_2$, where M represents the divalent cation. Sol-gel processing was used for all the sample preparations since processing techniques to stabilize β-cristobalite by solid state reaction were unsuccessful, possibly due to the size effect of the starting oxides.

Experimental - The starting materials used for sol-gel processing include tetraethyl orthosilicate [$Si(OC_2H_5)_4$], aluminum tri-sec butoxide [$Al(OC_4H_9)_3$], aluminum nitrate [$Al(NO_3)_2 \cdot 9H_2O$)], barium acetate [$Ba(OH_3CO_2)_2$), strontium chloride [$SrCl_2 \cdot 6H_2O$], zinc nitrate [$Zn(NO_3)_2 \cdot 6H_2O$)], iron chloride [$FeCl_2 \cdot 4H_2O$], copper chloride [$CuCl_2 \cdot 2H_2O$)], nickel nitrate [$Ni(NO_3)_2 \cdot 6H_2O$], lead nitrate [$Pb(NO_3)_2$], and tin chloride [$SnCl_2 \cdot 2H_2O$]. Sample compositions corresponding to the chemical formula $MO \cdot Al_2O_3 \cdot xSiO_2$ were prepared. Both [$Al(OC_4H_9)_3$] and [$Al(NO_3)_2 \cdot 9H_2O$] were used as Al precursors, and M = Ba, Sr, Zn, Fe, Cu, Ni, Pb, and Sn.

The starting materials were weighed and mixed in ethanol followed by the addition of deionized water to the solution. The molar ratio of water to the framework cations (Al + Si) was kept at 2, 4, and 10 for each composition. Hydrolysis and condensation reactions were carried out in both acid and base-catalyzed conditions. A gel resulted after the solution was allowed stand at ambient temperature for 24 hours. The gel sample was dried at 60~70°C, and then gradually heated to 1000°C for 24 hours.

All samples were characterized by XRD and differential scanning calorimetry (DSC). DTA was used to monitor the gel to crystal conversion. Samples showing a pure β-cristobalite phase were pressed into bars and sintered for thermal expansion measurements using a dual push rod dilatometer.

Results and Discussion - Phase analyses of the compositions studied are summarized in Table 4. Although the sample preparation, heat treatment, and the precursors of the framework cations were identical to those used previously in this study, β-cristobalite was not obtained for most of the compositions. β-cristobalite with a trace amount of α-cristobalite was found to be present only in the samples doped with Sr and Cu. The final phases obtained did not appear to be influenced by the form of the Al precursor used.

Table 4. Summary of the Synthesis Results for $MO \cdot Al_2O_3 \cdot xSiO_2$ Compounds

Composition	Phase Present
$BaO \cdot Al_2O_3 \cdot 30SiO_2$	α-crist,* amorphous
$BaO \cdot Al_2O_3 \cdot 40SiO_2$	α-crist, amorphous
$SrO \cdot Al_2O_3 \cdot 30SiO_2$	β-crist, α-crist (trace)
$SrO \cdot Al_2O_3 \cdot 40SiO_2$	β-crist, α-crist (trace)
$ZnO \cdot Al_2O_3 \cdot 30SiO_2$	$ZnAl_2O_4$, amorphous
$ZnO \cdot Al_2O_3 \cdot 40SiO_2$	amorphous, $ZnAl_2O_4$ (trace)
$NiO \cdot Al_2O_3 \cdot 30SiO_2$	amorphous, α-crist (trace)
$NiO \cdot Al_2O_3 \cdot 40SiO_2$	amorphous, α-crist (trace)
$SnO \cdot Al_2O_3 \cdot 30SiO_2$	SnO_2, amorphous
$SnO \cdot Al_2O_3 \cdot 40SiO_2$	SnO_2, amorphous
$PbO \cdot Al_2O_3 \cdot 30SiO_2$	α-crist, amorphous
$PbO \cdot Al_2O_3 \cdot 40SiO_2$	α-crist, amorphous
$CuO \cdot Al_2O_3 \cdot 30SiO_2$	β-crist, α-crist (trace)
$CuO \cdot Al_2O_3 \cdot 40SiO_2$	β-crist, α-crist (trace)
$FeO \cdot Al_2O_3 \cdot 30SiO_2$	amorphous, α-crist (trace)
$FeO \cdot Al_2O_3 \cdot 40SiO_2$	amorphous, α-crist (trace)

*Crist = cristobalite

It was suspected that phase separation may have occurred in the gel, resulting in the formation of solute-rich and solvent-rich regions. The presence of an amorphous phase and the crystallization of SnO_2 and $ZnAl_2O_4$ may be attributed to this effect. Therefore, processing of each composition was repeated by varying the solution pH from 4 to 8 and the $H_2O/(Al + Si)$ ratio from 2 to 10. However, the results obtained were unchanged from those shown in Table 4 except for the Cu-doped samples. When the $H_2O/(Al + Si)$ ratio was increased to 10 and the pH value was adjusted to 8 prior to the hydrolysis reactions, both the $CuO \cdot Al_2O_3 \cdot 30SiO_2$ and $CuO \cdot Al_2O_3 \cdot 40SiO_2$ compositions showed a pure β-cristobalite phase and α-cristobalite was not detected.

Based on the preliminary results, the $CuO \cdot Al_2O_3 \cdot xSiO_2$ series of compositions was further studied by extending x from 20 to 60 and following the preparation procedure described above. After drying at 70°C for 2 days, the gel behavior upon heating was characterized by DTA as shown in Figure 2. The weak endothermic peak is attributed to desorption of physically adsorbed water. The exothermic peak corresponds to the combustion of carbon.

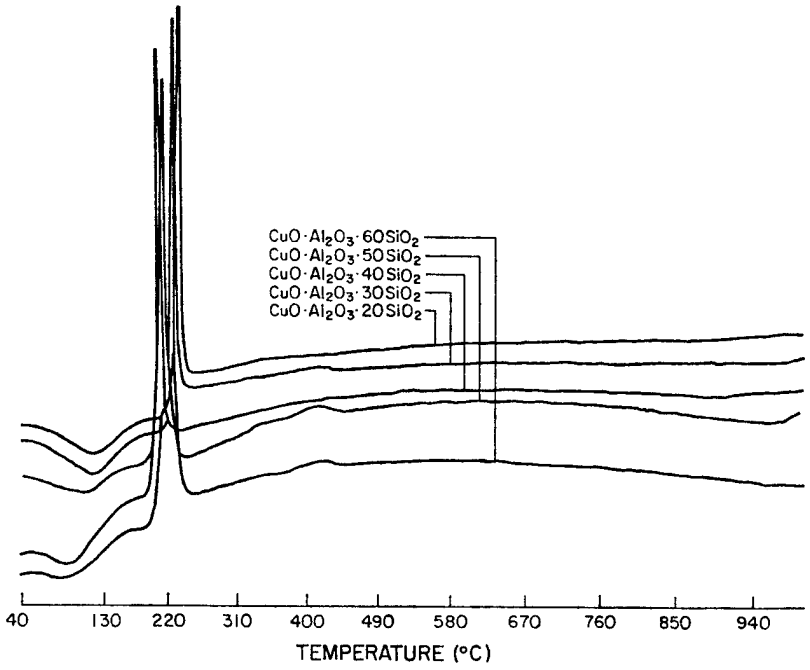

Figure 2. DTA curves of dried gel heated at $10^{o}C$/min from the $CuO \cdot Al_2O_3 \cdot xSiO_2$ composition.

XRD results of the reacted samples are shown in both Figure 3 and Table 5. Pure β-cristobalite phase with good crystallinity was observed for the $CuO \cdot Al_2O_3 \cdot xSiO_2$ series of compositions except for $CuO \cdot Al_2O_3 \cdot 20SiO_2$. A trace amount of a second phase was precipitated from the $CuO \cdot Al_2O_3 \cdot 20SiO_2$ composition as a result of the high ($CuO + Al_2O_3$) concentration.

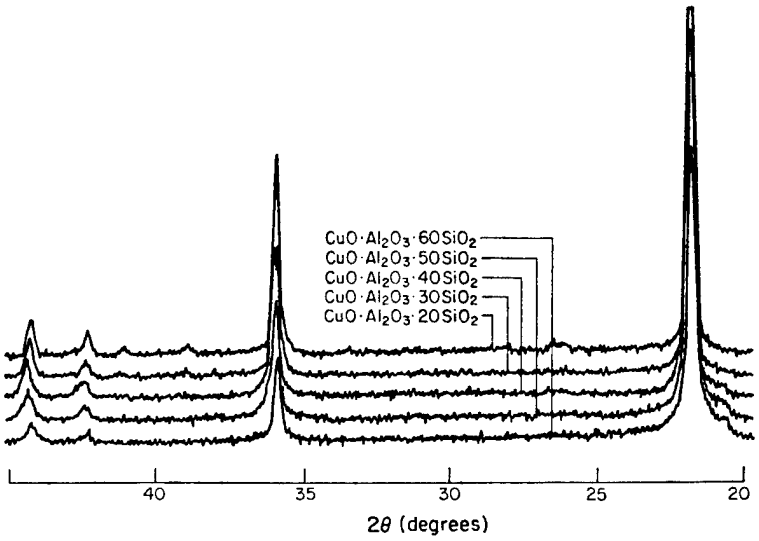

Figure 3. XRD patterns of $CuO \cdot Al_2O_3 \cdot xSiO_2$ compositions fired at 1000°C.

Table 5. Phase Analyses and CTE of the $CuO \cdot Al_2O_3 \cdot xSiO_2$ Compositions

Composition	Phase Present	CTE 30-1000°C $\alpha(x10^{-7}/°C)$
$CaO \cdot Al_2O_3 \cdot 20SiO_2$	β-crist, unknown (trace)	81
$CuO \cdot Al_2O_3 \cdot 30SiO_2$	β-crist	75
$CuO \cdot Al_2O_3 \cdot 40SiO_2$	β-crist	79
$CuO \cdot Al_2O_3 \cdot 50SiO_2$	β-crist	77
$CuO \cdot Al_2O_3 \cdot 60SiO_2$	β-crist	78

The presence of α-cristobalite was determined by means of DSC since trace amounts of α-cristobalite are detectable only by DSC. Figure 4 shows the DSC results for the series of Cu-stabilized cristobalite samples. Since the presence of α-cristobalite was not detected, thermal expansion measurements were made, and the results are included in Table 5.

Although the phase purity of Cu-stabilized β-crystobalite has been significantly improved when compared to the Ca-stabilized β-cristobalite, the CTE value of the Cu-stabilized β-cristobalite remains high regardless of the Cu concentration. This may suggest that the thermal expansion of β-cristobalite is not controlled by the interstitial cation, or that the size of the interstitial cation is not large enough to maintain the extended structure. Therefore, work on the effects of substitution of framework cations and the introduction of larger interstitial cations into β-cristobalite should be considered in future research.

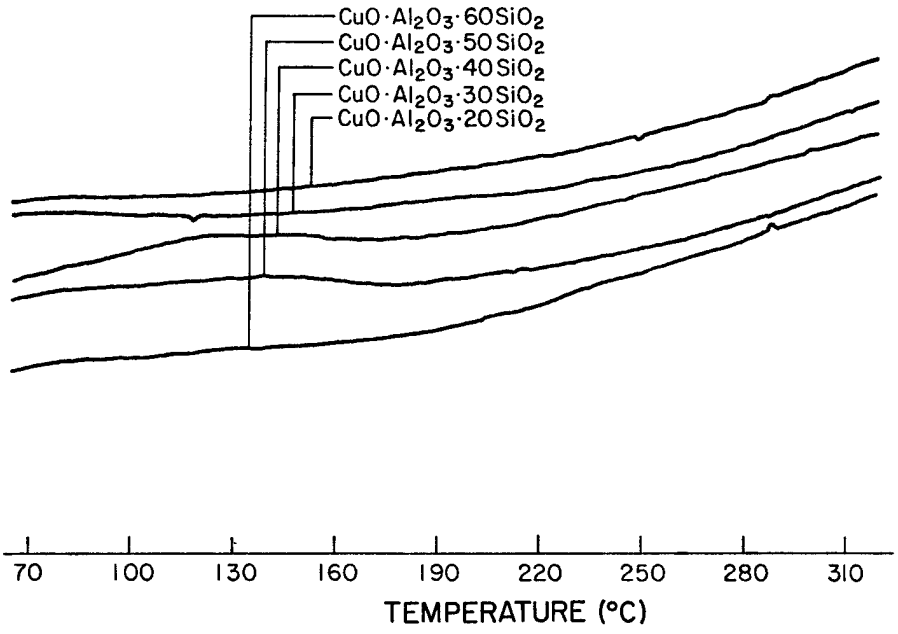

Figure 4. DSC curves of the Cu-stabilized β-cristobalite at 20°C/min scanning rate.

Zircon (NZP) Systems

As previously reported, two compositions have been identified that have nearly zero linear thermal expansion up to 1200°C and also possess low expansion anisotropy: $Rb_{0.5}Cs_{0.5}Zr_2(PO_4)_2$ and $Ca_{0.5}Mg_{0.5}Zr_4(PO_4)_6$. During this reporting period, work has focused on further characterization of these two compositions. The heat treatments of the compositions have not been optimized.

Bulk Density and Porosity - The percent theoretical density (TD) for both compounds exceeded 94% as shown in Table 6, and is in close agreement with values reported (92-99%) in the literature.[1,2] Open porosities were measured as 4.5% and 3.4% for $Ca_{0.5}Mg_{0.5}Zr_4(PO_4)_6$ and $Rb_{0.5}Cs_{0.5}Zr_2(PO_4)_3$, respectively. Sample shrinkage was larger in $Rb_{0.5}Cs_{0.5}Zr_2(PO_4)_3$ (12.5%) than in $Ca_{0.5}Mg_{0.5}Zr_4(PO_4)_6$ (10.6%). Meanwhile, more water was absorbed in $Ca_{0.5}Mg_{0.5}Zr_4(PO_4)_6$ (1.41%) than in $Rb_{0.5}Cs_{0.5}Zr_2(PO_4)_3$ (1.03%).

Table 6. Shrinkage, density, and porosity of bulk samples of $Ca_{0.5}Mg_{0.5}Zr_4(PO_4)_6$ and $Rb_{0.5}Cs_{0.5}Zr_2(PO_4)_3$.

Compound	Shrinkage (%)	Bulk Density (g/cm^3)	%TD	Open Porosity (%)	Water Absorption (%)
$Ca_{0.5}Mg_{0.5}Zr_4(PO_4)_6$	10.6	3.101	94.1	4.5	1.41
$Rb_{0.5}Cs_{0.5}Zr_2(PO_4)_3$	12.5	3.202	95.9	3.4	1.03

Thermal Shock Resistance - Thermal shock resistance of the sintered bars was measured using the water quench method which involves the maximum quench temperature difference (ΔT_m) without observable cracking and the number of repeated quenchings from 1200°C. As shown in Table 7, the maximum quench temperature difference was 1475°C for the compound $Ca_{0.5}Mg_{0.5}Zr_4(PO_4)_6$; however, the compound $Rb_{0.5}Cs_{0.5}Zr_2(PO_4)_3$ resisted fracture up to 1625°C. The sample $Ca_{0.5}Mg_{0.5}Zr_4(PO_4)_6$ cracked after 6 repeated quenches, while the specimen $Rb_{0.5}Cs_{0.5}Zr_2(PO_4)_3$ withstood 20 thermal cycles.

Modulus of Rupture, Fractography, and Microstructure - MOR data were obtained from 3-point and 4-point bending tests, and their average values are summarized in Table 8. Average MOR values of $Rb_{0.5}Cs_{0.5}Zr_2(PO_4)_3$ (49.14 and 52.71 MPa from 4-point and 3-point, respectively) were over twice those of $Ca_{0.5}Mg_{0.5}Zr_4(PO_4)_6$ (21.48 and 23.13 MPa from 4-point and 3-point bending tests, respectively).

Table 7. Thermal shock resistance of $Ca_{0.5}Mg_{0.5}Zr_4(PO_4)_6$ and $Rb_{0.5}Cs_{0.5}Zr_2(PO_4)_3$.

Compound	ΔT_c (°C)	Allowable Repeated Quenches with ΔT = 1200°C
$Ca_{0.5}Mg_{0.5}Zr_4(PO_4)_6$	1475	5 times
$Rb_{0.5}Cs_{0.5}Zr_2(PO_4)_3$	>1625*	>20 times**

* No cracking observed up to maximum temperature difference of 1625 C used in the experiments.

** No cracking observed after 20 repeated quenches.

Table 8. MOR data for $Ca_{0.5}Mg_{0.5}Zr_4(PO_4)_6$ and $Rb_{0.5}Cs_{0.5}Zr_2(PO_4)_3$.

$Ca_{0.5}Mg_{0.5}Zr_4(PO_4)_6$			$Rb_{0.5}Cs_{0.5}Zr_2(PO_4)_3$		
Sample	**3-point (MPa)**	**4-point (MPa)**	**Sample**	**3-point (MPa)**	**4-point (MPa)**
1	26.44	18.70	1	50.52	46.67
2	20.12	23.46	2	52.25	46.59
3	20.46	20.67	3	54.57	53.71
4	24.03	21.26	4	50.06	47.57
5	24.59	23.33	5	56.16	51.18
Average	23.13	21.48	**Average**	52.71	49.14

Fractography of the two specimens was investigated by scanning electron microscopy (SEM). The fractography of $Rb_{0.5}Cs_{0.5}Zr_2(PO_4)_3$ at low magnification shows a relatively rough fracture surface. The overall fracture surfaces for $Ca_{0.5}Mg_{0.5}Zr_4(PO_4)_6$ are relatively smooth compared with that of $Rb_{0.5}Cs_{0.5}Zr_2(PO_4)_3$. At higher magnification prominent fracture features are evident which show that $Rb_{0.5}Cs_{0.5}Zr_2(PO_4)_3$ had a transgranular fracture path and hackle-type ridges, whereas $Ca_{0.5}Mg_{0.5}Zr_4(PO_4)_6$ is characterized by more intergranular fracture paths and rib-marks.[3] SEM examination of the microstructure of the compounds revealed that the grains in the $Rb_{0.5}Cs_{0.5}Zr_2(PO_4)_3$ sample are finer and more spherical than those in the $Ca_{0.5}Mg_{0.5}Zr_4(PO_4)_6$ specimen.

Long Term Thermal Stability - Phase stability of the compounds was examined using DTA. Both specimens exhibited phase stability up to 1500°C. Long-term thermal stability was then investigated by holding the samples at 1400°C for 96h. No changes were detected in $Ca_{0.5}Mg_{0.5}Zr_4(PO_4)_6$, but XRD phase identification results revealed the presence of ZrO_2, Rb_2O, and Cs_2O in compound $Rb_{0.5}Cs_{0.5}Zr_2(PO_4)_3$ following thermal exposure. This instability is likely due to the decomposition of P_2O_5.

Reproducibility of low expansion samples of $Ca_{0.5}Mg_{0.5}Zr_4(PO_4)_6$ - Table 9 summarizes the results of statistical analyses of thermal expansion data for multiple samples of $Ca_{0.5}Mg_{0.5}Zr_4(PO_4)_6$. The mean α value from 10 lots was calculated as $-5 \times 10^{-7}/°C$, while the average value from 10 replicate tests was $-4.5 \times 10^{-7}/°C$.

Table 9. Statistical analysis of thermal expansion data for $Ca_{0.5}Mg_{0.5}Zr_4(PO_4)_6$ samples.

Statistical Value	Lot-to-lot Variability	Replicate Test Variability
Average Value ($\bar{x}$)	$-5.0 \times 10^{-7}/^{o}C$	$-4.5 \times 10^{-7}/^{o}C$
Standard Deviation (s)	$0.72 \times 10^{-7}/^{o}C$	$1.78 \times 10^{-7}/^{o}C$
Standard Error ($s/\sqrt{n}$)	$0.228 \times 10^{-7}/^{o}C$	$0.74 \times 10^{-7}/^{o}C$
Coefficient of Variation ($s/\bar{x}$)	-0.144	-0.557

Even though average values from two different analyses showed similar α values, differing by 10%, the differences in standard deviation and in coefficient of variation were 60% and 80%, respectively. Standard deviation for the lot-to-lot variability ($0.72 \times 10^{-7}/°C$) was much smaller than that for the replicate test variability ($1.78 \times 10^{-7}/°C$). In addition, the coefficient of variation for the lot-to-lot variability (-0.144) was closer to zero than that for the replicate test variability (-0.557). A t-value and an F-value[4] calculated from the observed values for the lot-to-lot variability and the replicate test variability were -3.69 and 0.027, respectively.

Summary of Present Results - All of the compounds considered in this study were synthesized by solid-state reaction. P_2O_5 was used directly to make NZP compounds, with acetone serving as a mineralizer as well as an aid to homogenize mixtures. Heat treatments were conducted at 1100°C for 24h and at 1300°C for 4h, followed by furnace cooling to room temperature. Linear thermal expansion was measured up to 1000°C, while axial thermal expansion was measured up to 1400°C. Experimental results for unoptimized samples are shown in Table 10.

Table 10. Summary of properties of $Ca_{0.5}Mg_{0.5}Zr_4(PO_4)_6$ and $Rb_{0.5}Ca_{0.5}Zr_2(PO_4)_3$.

Material Property	$Ca_{0.5}Mg_{0.5}Zr_4(PO_4)_6$	$Rb_{0.5}Cs_{0.5}Zr_2(PO_4)_3$
Density (g/cm^3)	3.101	3.203
% Shrinkage	10.6	12.5
% Theoretical density	94.1	95.9
% Open porosity	4.5	3.4
% Water absorption	1.41	1.03
Thermal shock resistance:		
Max. temp. difference (°C)	1475	>1625
Allowable repeated quenches with $\Delta T = 1200°C$	5 times	>20 times
Modulus of rupture (MPa):		
3-point bending	23.13	52.71
4-point bending	21.48	49.14
Fractography	Transgranular; relatively rough; hackle-type mark.	Intergranular; relatively smooth; rib mark.
Long-term thermal stability after 96 h at 1400°C	Stable structure.	Decomposed to raw materials.
Microstructure	Coarse, non-spherical grains.	Fine, spherical grains.

Discussion

In view of the fact that the program to survey the NZP class of compositions has been underway for nearly three years and is nearing completion, it is felt appropriate to discuss the overall results at this time.

Most of the conventional low thermal expansion materials have some deficiencies which limit their use and application.[5] Lithium-alumino-silicate (LAS) has a limited range of use, owing to its low melting temperature.[6,7] In the case of aluminum titanate, it exhibits structural instability (decomposition into rutile and corundum) below 1300°C.[8] Vitreous silica goes through devitrification when held at higher temperatures, resulting in cristobalite formation.[9] Recent work has identified $NaZr_2(PO_4)_3$ (NZP) and its crystal structural analogs as a family of materials with a potential for low thermal expansion.[10,11]

The purpose of this study was to synthesize new, low thermal expansion materials based on the NZP-type structure. The study has screened a large number of NZP compositions and recently focused on two compounds, $Ca_{0.5}Mg_{0.5}Zr_4(PO_4)_6$ and $Rb_{0.5}Cs_{0.5}Zr_2(PO_4)_3$, with the linear α values of $-5\times10^{-7}/°C$ and $-0.3\times10^{-7}/°C$, respectively.

Ternary compounds - Among twenty-five different ternary compounds synthesized with Na^+ substitutions by cations with +1 to +5 electron valences, only one compound showed a monoclinic structure at room temperature. Except for $LiZr_2(PO_4)_3$, all other systems were isostructural with $NaZr_2(PO_4)_3$, which has an $R\bar{3}C$ (hexagonal) structure.[12] The compounds showing an NZP structure at room temperature but structural instability at elevated temperatures included systems substituted by transition elements with electron valences of +2 (Mn, Ni, Cu, and Zn), + 3 (Y, La, Al, and Cr), +4 (Ti, Zr, Hf, Si, and Ce), and +5 (V, Nb, and Ta) electron valences, as well as by Mg (from alkaline-earth group) with a very small radius of 0.74Å. The structural instability was confirmed by high temperature XRD analyses and linear thermal expansion behavior.

All systems with structural instabilities exhibited a diffraction intensity change during high temperature XRD analysis, which can be associated with the texturing[13] or order-disorder transition.[14] One example showing a phase instability at a high temperature, the $MnZr_4(PO_4)_6$ system, is shown in Figures 5 and 6 and given in Tables 11 and 12, in comparison with the $RbZr_2(PO_4)_3$ compound which is considered to be stable.

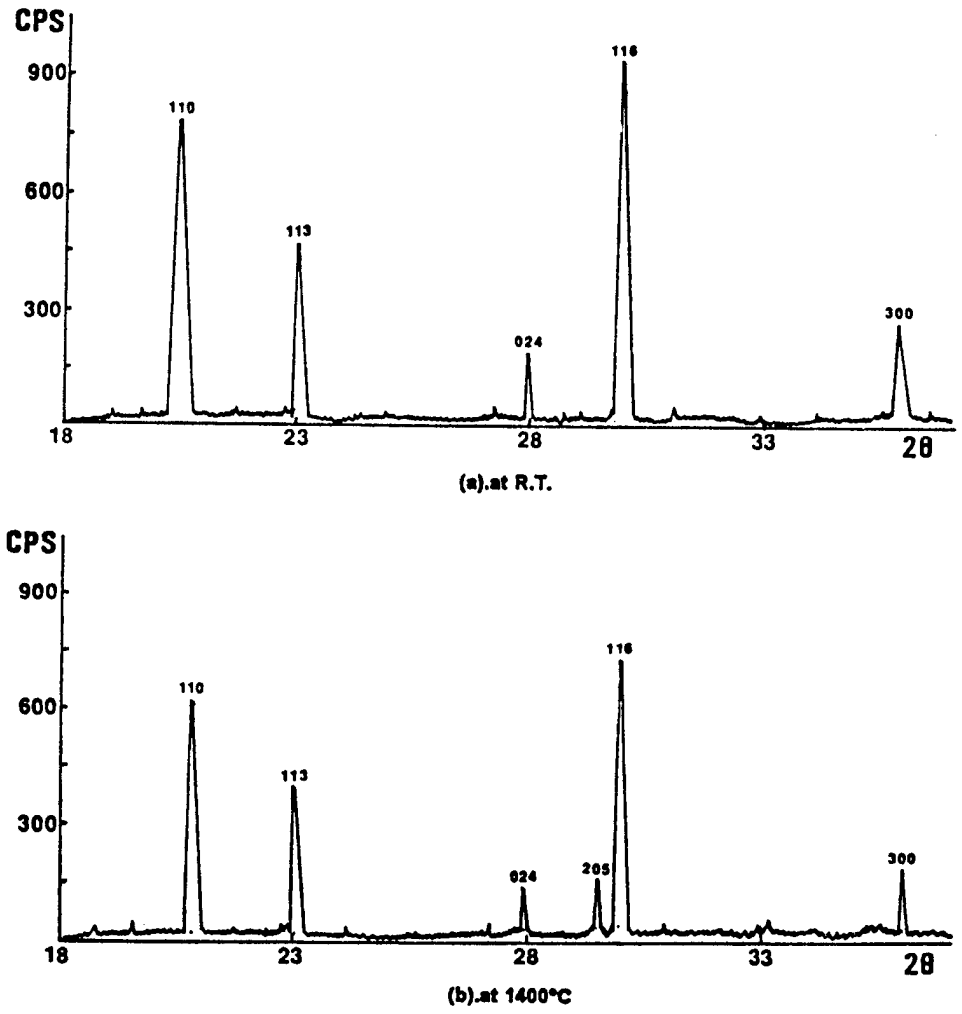

Figure 5. Diffraction patterns of $RbZr_2(PO_4)_3$ at room temperature (R.T.) and 1400^{o}C.

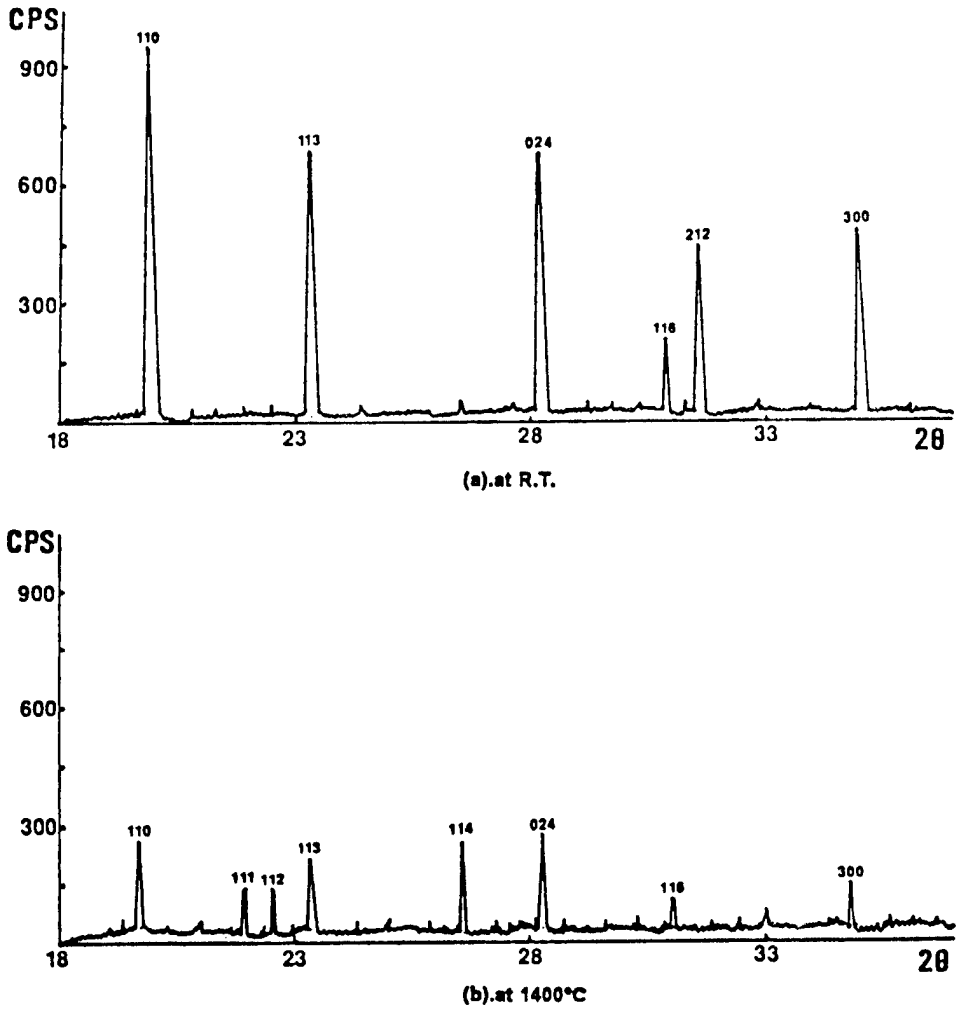

Figure 6. Diffraction patterns of $MnZr_4(PO_4)_6$ at room temperature (R.T.) and 1400^{o}C.

Table 11. Comparison of diffraction intensities of $RbZr_2(PO_4)_3$ for the selected planes at R.T. and 1400°C.

Temperature (°C)	Diffraction Intensity[CPM(counts per minute)]					
	(110)	(113)	(024)	(205)	(116)	(300)
R.T.	42527	24517	9586	-	53538	15979
1400	39391	25100	7685	9091	45922	12988

Table 12. Comparison of diffraction intensities of $MnZr_4(PO_4)_6$ for the selected planes at R.T. and 1400°C.

Temperature (°C)	Diffraction Intensity(CPM)								
	(110)	(111)	(112)	(113)	(114)	(024)	(116)	(212)	(300)
R.T.	52541	-	-	35021	-	29723	11544	25117	23116
1400	9665	7836	8302	9747	10487	15551	6004	-	7476

Figures 5 and 6 show the diffraction peaks of $RbZr_2(PO_4)_3$ and $MnZr_4(PO_4)_6$ at room temperature and 1400°C, respectively. Diffraction patterns of $RbZr_2(PO_4)_3$ at room temperature exhibited the five major peaks of (110), (113), (024), (116), and (300); however, at 1400°C, an additional diffraction peak (205) was observed along with the diffraction peaks observed at room temperature. Although the diffraction peaks observed at room temperature were reduced in intensity at 1400°C, their relative intensities were approximately equal. Detailed comparisons of the diffraction intensities for the five major peaks are summarized in Table 11.

Five major peaks and (212) with strong intensity were observed for $MnZr_4(PO_4)_6$ at room temperature. At 1400°C, the diffraction intensities of the peaks were lowered significantly, and relative intensity ratios changed. Furthermore, many other peaks appeared, including (111), (112), (114), while the (212) peak disappeared. Detailed diffraction intensities are compared in Table 12.

The $R\bar{3}C$ structure, reviewed in Appendix 1, shows that there exist six general positions: 6(a) and (b), 12(c), 18(d) and (e), and 36(f). It is known that $NaZr_2(PO_4)_3$ occupies 12(c), 18(e), 6(b), and 36(f) in the unit cell,[15] leaving the two other general positions as vacancies. Other studies[16-19] show extra Na cations occupying the site of M_{II} (shown in Figure 7), which corresponds to the position of 18(e).[20]

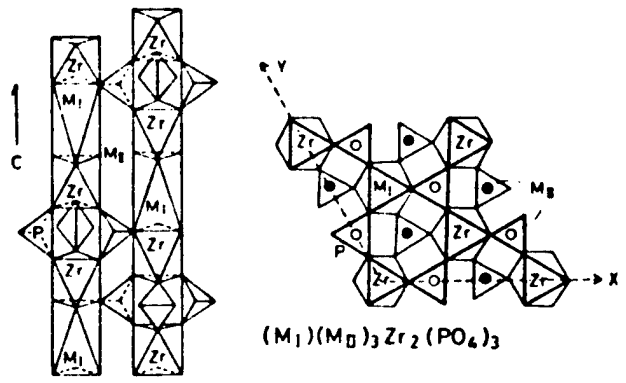

Figure 7. Schematic of alkali sites in $NaZr_2(PO_4)_3$-type structures (taken from ref. 11).

Elements substituted by +2, +3, or +4 create vacancies of one-half, one-third, or one-quarter of the Na ion positions, respectively. Also, for the systems with +5 cation valence, elements with +5 valence substitute for Zr^{+4} randomly and create vacancies in place of Na ions. The complex and open structure of NZP might make it possible to locate elements with +2 or more valence in the M_{II} or other positions instead of the Na position 6(b). This explanation may clarify the change in diffraction intensity owing to the atomic movement observed in some of the systems substituted with transition elements with +2 valence, elements with +3, +4, +5 valence, and Mg.

Ionic radii for the elements selected in this study to replace Na are summarized in Table 13; the values are based on a coordination number of 6.

Table 13. Ionic radii of elements selected to modify the NZP-type structure (summarized from ref. 37).

Elements with +1 valence	Ionic Radii (Å)	Elements with +2 valence	Ionic Radii (Å)	Elements with +3 valence	Ionic Radii (Å)	Elements with +4 valence	Ionic Radii (Å)	Elements with +5 valence	Ionic Radii (Å)
Li	0.68	Mg	0.74	Y	0.97	Ti	0.64	V	0.4
Na	0.98	Ca	1.04	La	1.04	Zr	0.82	Nb	0.66
K	1.33	Sr	1.20	Al	0.57	Hf	0.82	Ta	0.66
Rb	1.49	Ba	1.20	Cr	0.64	Si	0.39		
Cs	1.65	Mn	0.91			Ce	0.88		
		Ni	0.74						
		Cu	0.80						
		Zn	0.83						

Finally, it can be said that the range of possible ionic substitutions for Na in ternary NZP-type compounds includes selected elements of valences +1 to +5. However, with the exception of Ca (1.04Å) only seven elements having ionic radii greater than 0.98Å formed the stable structure without changing its skeletal framework and the atomic positions.

Quarternary and quinternary compounds - Based on results of the present study of the basic ternary systems, seven stable ternary compounds (modified by Na,K,Rb,Cs,Ca,Sr,Ba) were selected for substitutional solid solution studies using alkali and alkaline earth elements in quarternary systems. Several combinations of Ca-Mg-Na were selected for quinternary compound formation. From the experimental results of the solid solubility for the quarternary and quinternary systems to modify the NZP-type structure, the following results are summarized and tabulated in Table 14.

Table 14. Systems showing solid solubility among quarternary and quinternary compounds considered.

System	Ionic Size Difference of elements substituted	System	Ionic Size Difference of elements substituted
$Rb_{0.5}K_{0.5}Zr_2(PO_4)_3$	10.7%	$Ba_{0.25}K_{0.5}Zr_2(PO_4)_3$	3.6%
$Rb_{0.25}Cs_{0.75}Zr_2(PO_4)_3$	9.7%	$Sr_{0.25}Na_{0.5}Zr_2(PO_4)_3$	18.3%
$Rb_{0.5}Cs_{0.5}Zr_2(PO_4)_3$	9.7%	$Mg_{0.25}Ca_{0.25}Zr_2(PO_4)_3$	28.8%
$Rb_{0.75}Cs_{0.25}Zr_2(PO_4)_3$	9.7%	$Mg_{0.125}Ca_{0.375}Zr_2(PO_4)_3$	28.8%
$Na_{0.25}K_{0.75}Zr_2(PO_4)_3$	26.3%	$Mg_{0.25}Sr_{0.25}Zr_2(PO_4)_3$	38.3%
$Na_{0.5}K_{0.5}Zr_2(PO_4)_3$	26.3%	$Mg_{0.25}Ba_{0.25}Zr_2(PO_4)_3$	46.4%
$Na_{0.75}K_{0.25}Zr_2(PO_4)_3$	26.3%	$Ca_{0.25}Sr_{0.25}Zr_2(PO_4)_3$	13.3%
$Ca_{0.25}Na_{0.5}Zr_2(PO_4)_3$	5.8%	$Ca_{0.25}Ba_{0.25}Zr_2(PO_4)_3$	24.6%
$Ca_{0.125}Na_{0.75}Zr_2(PO_4)_3$	5.8%	$Ba_{0.25}Sr_{0.25}Zr_2(PO_4)_3$	13.0%
$Ca_{0.375}Na_{0.25}Zr_2(PO_4)_3$	5.8%	(1/16Ca1/16Mg3/4Na)· $Zr_2(PO_4)_3$	28.8%
$Ba_{0.25}Na_{0.5}Zr_2(PO_4)_3$	29.0%		

The systems with substitutions of combined alkali-alkali elements Rb-Cs and Na-K showed complete solubility, exhibiting ionic size differences of 9.7% and 26.3%, respectively. In systems with substitutions of combined Rb-K, only one combination of 1/2Rb-1/2K exhibited solubility, even though the ionic size difference (10.7%) was smaller than that of Na-K (26.3%).

Among the systems substituted with one-half mole of an alkali element and one-quarter mole of an alkaline earth element, the combinations of large alkaline earth elements and small alkali elements showed complete solubility. Other mole combinations of 1/8Ca-3/4Na and 3/8Ca-1/4Na also supported the solubility trend observed in this finding.

Combinations of alkaline earth and other alkaline earth elements with one-quarter mole for each component showed solid solubility irrespective of ionic size difference, the largest difference being 46.4% (Mg-Ba). Meanwhile, the 3/8Ca-1/8Mg combination showed solubility, but 1/8Ca-3/8Mg was not completely soluble. This might be explained from the instability of the ternary compound $MgZr_4(PO_4)_6$, because the combination of a higher concentration of Mg compared with the concentration of Ca showed a separation into two phases.

That result also can be extended to the quinternary system of CaO-MgO-Na_2O-ZrO_2-P_2O_5. Two phases were obtained for the system with a higher mole percent of Mg(1/8Mg,3/16Mg), whereas the system with the smallest amount of Mg(1/16Mg) showed complete solubility.

Systems showing a single phase had extra diffraction peaks which might be coming from the ordering behavior. A relationship has already been developed between the static concentration waves generating the atomic distribution in an ordered phase and the X-ray diffraction pattern, showing more diffraction peaks due to superlattice reflections.[21] Therefore, it can be said that the trend approaching a solid solution in the NZP-type quarternary and quinternary systems is related to the ionic size difference as well as to the tendency to make a more ordered structure.

Effect of substitution on lattice parameters - Lattice parameter measurements have been made for the selected systems using XRD with the maximum accuracy of 0.0005nm at room temperature. Lattice parameters for the systems considered and ionic size of the elements selected to substitute for the Na cation in the NZP-type structure are presented in Table 15.

Table 15. Lattice parameters and ionic radii of the systems considered.

System	Lattice Parameters(Å at R.T.)		Ionic Radius of
	a-axis	c-axis	Elements Substituted(Å)
$RbZr_2(PO_4)_3$	8.65	24.43	1.49
$CsZr_2(PO_4)_3$	8.58	24.96	1.65
$MgZr_4(PO_4)_6$	8.90	21.84	0.74
$CaZr_4(PO_4)_6$	8.78	22.69	1.04
$BaZr_4(PO_4)_6$	8.59	23.89	1.38
$MnZr_4(PO_4)_6$	8.88	21.81	0.91
$NiZr_4(PO_4)_6$	8.42	23.15	0.74
$YZr_6(PO_4)_9$	8.29	24.75	0.97
$TiZr_8(PO_4)_{12}$	8.25	23.92	0.66
$CeZr_8(PO_4)_{12}$	8.31	24.75	0.88
$NbZr(PO_4)_3$	8.25	23.92	0.66
$TaZr(PO_4)_3$	8.39	23.85	0.66
$Rb_{0.5}Cs_{0.5}Zr_2(PO_4)_3$	8.62	24.69	1.49(Rb) & 1.65(Cs)
$Ca_{0.5}Mg_{0.5}Zr_4(PO_4)_6$	8.79	22.65	0.74(Mg) & 1.04(Ca)
(3/8Ca1/8Mg)· $Zr_2(PO_4)_3$	8.79	22.64	0.74(Mg) & 1.04(Ca)

Even though Na^+ is not included in its structure along the a-axis,[11,22] it is well documented that the change in the lattice parameters occurring upon replacement of cations for Na occurs in the a-axis as well as in the c-axis, experimentally.[22-26] In addition, the general trend observed in alkali element-modified systems is that the structure expands in the c-direction but contracts in the a-direction with the substitution of large cations.[26]

In alkali (Rb,Cs) and alkaline earth (Mg,Ca,Ba)-modified systems, the larger the cation substituted, the larger the c-axis but the smaller the a-axis. For the systems substituted with transition elements (Mn, Ni), the trend is opposite that of alkali and alkaline earth-modified systems, i.e., the larger the cation, the smaller the c-axis but the larger the a-axis. In systems substituted with elements with +4 electron valence (Ti,Ce), the large cation substitution appeared to contribute to increases of both the a- and c-axes. The systems substituted with Nb and Ta (same ionic size and +5 electron valence) showed slight differences in the lattice parameters of the a- and c-axes.

Ternary compounds $RbZr_2(PO_4)_3$ and $CsZr_2(PO_4)_3$ had lattice parameters of 8.65Å and 8.58Å for the a-axis, and 24.43Å and 24.96Å for the c-axis, respectively. Meanwhile, the lattice parameters of $Rb_{0.5}Cs_{0.5}Zr_2(PO_4)_3$ were calculated as 8.62Å and 24.69Å for the a- and c-axes, respectively. Lattice parameters for the Ca-Mg modified quarternary compounds likewise fell within the values of their respective ternary compounds.

Figure 8 shows a plot of the c-axis lattice parameters versus the a-axis lattice parameters for the ternary systems considered. The dotted zone represents the systems having the phase and structure stabilities previously discussed. Additionally, the lattice parameters for $NaZr_2(PO_4)_3$, $KZr_2(PO_4)_3$, and $SrZr_4(PO_4)_6$, known to be stable phases and cited in other work[22,24,27] are presented in Figure 8 and summarized in Table 16 with other data. The lattice parameters of systems showing phase stability in the NZP-type ternary compounds range from 8.58Å to 8.80Å for the a-axis, and from 22.69Å to 24.96Å for the c-axis.

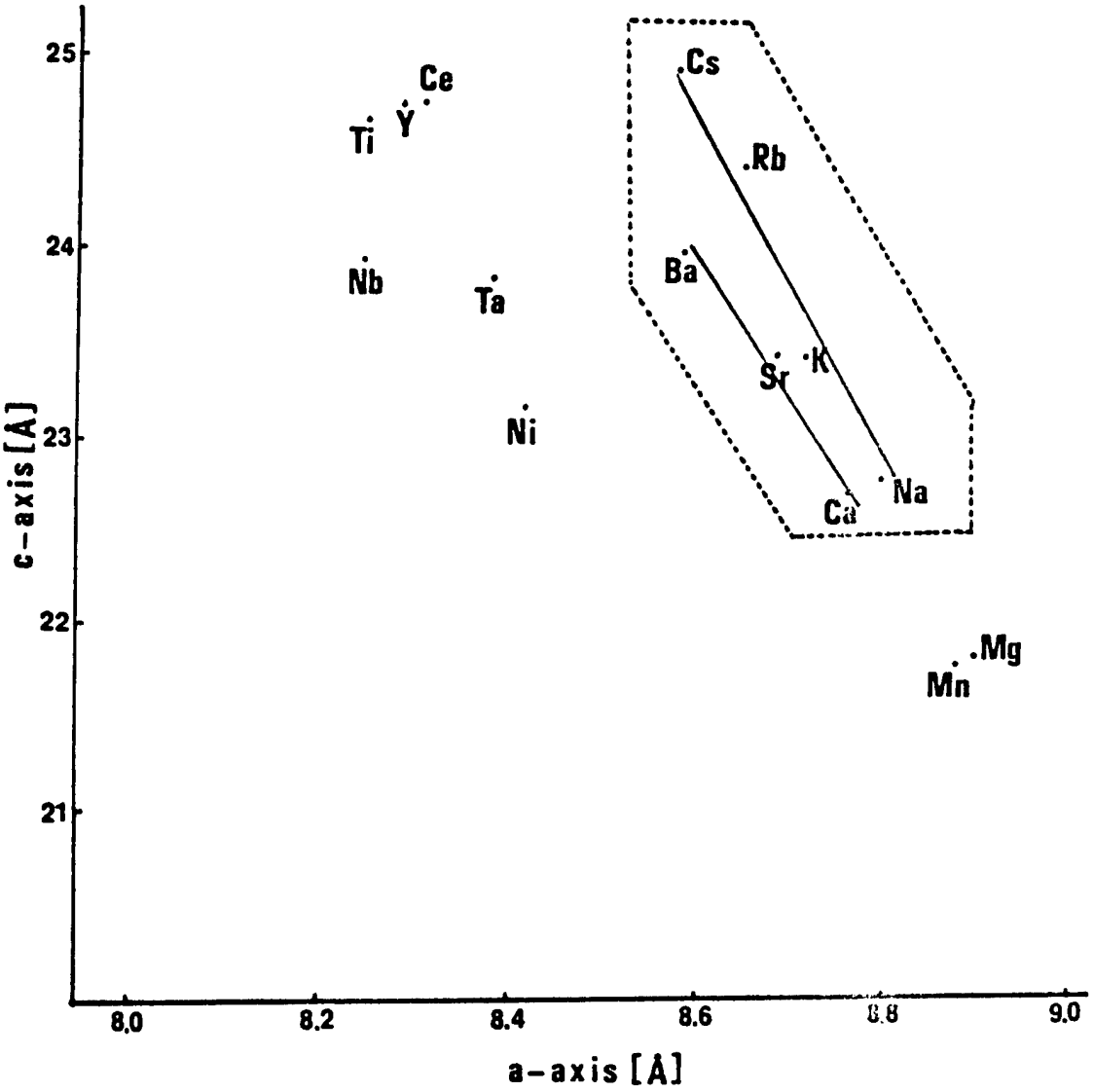

Figure 8. Plot of lattice parameters c versus a for $MZr_2(PO_4)_3$: where M = Na, K, Rb, Cs, 0.5 Mg, 0.5 Ca, 0.5 Sr, and 0.5 Ba [$KZr_2(PO_4)_3$ taken from ref. 24; $NaZr_2(PO_4)_3$ taken from ref. 22; and $SrZr_4(PO_4)_6$ taken from ref 27.]

Table 16. Lattice parameters for the systems showing phase stability in the NZP-type ternary compounds.

System	Lattice Parameters(Å at R.T.)		Ionic Radius of
	a-axis	c-axis	Elements substituted(Å)
*$NaZr_2(PO_4)_3$	8.80	22.76	0.98
**$KZr_2(PO_4)_3$	8.71	23.89	1.33
$RbZr_2(PO_4)_3$	8.65	24.43	1.49
$CsZr_2(PO_4)_3$	8.58	24.96	1.65
$CaZr_4(PO_4)_6$	8.78	22.69	1.04
+$SrZr_4(PO_4)_6$	8.69	23.39	1.20
$BaZr_4(PO_4)_6$	8.59	23.89	1.38

*From ref. 22
**From ref. 24
+From ref. 27

The results of this study correlate well with other reported data in showing a decrease of the a-axis and an increase of the c-axis with large cation substitutions. Also the lattice parameter of the c-axis including octahedra, consisting of substitution elements and oxygen, was found to be dependent on the ionic size of substituted elements irrespective of the electron valences of +1 and +2. Vacancies formed by the substitution of elements with +2 electron valence did not greatly affect the lattice parameter of the c-axis. This means that Ca,Sr, and Ba atoms easily replaced half of the positions of the Na cation in the NZP structure without changing its skeletal framework, thereby maintaining equilibrium.

Thermal expansion behavior

Linear thermal expansion behavior of NZP-type compounds - Excluding the NZP-type modified systems showing sudden changes in thermal expansion, the linear aggregate thermal expansion behavior investigated in this study can be classified into three categories: negative, positive, and transition (from negative to positive). The substitutional elements are categorized accordingly in Table 17.

Most of the substitutional elements tended to promote positive thermal expansion. However, elements such as Li, Na, K, and Ca tended to contract their sintered bodies, and combinations of elements including Na,K, or Ca also resulted in negative linear expansion. Two exceptions were combinations of 1/4Ca-1/4Ba and 1/4Ca-1/4Sr which promoted positive behavior, probably due to the effects of Ba and Sr. Other exceptions were systems with combined Ca-Mg (1/4Ca-1/4Mg and 3/8Ca-1/8Mg) which exhibited a transition from negative to positive at around 600°C.

Substitutions of Rb, Cs, or combinations of Rb and Cs which led to low linear α values also resulted in a transition from negative to positive at around 500°C. Moreover, the transition elements of Ni and Zn, showing low linear aggregate α values of $10\times10^{-7}/°C$ and $5\times10^{-7}/°C$, respectively, exhibited the transition at about 500°C.

The expansion of a three-dimensional framework can be considered the sum of a bond-length expansion and a tilting effect.[28] The apparent thermal expansions of bonds between the individual atoms and oxygen resulted from both the stretching of the bond length,[11] which is related to the strength of the chemical bond, and the changing of the bond angle with rising temperature. The apparent thermal expansion coefficients for several metal-oxygen bonds were empirically determined by Hazen et al.[29] Tilting of polyhedra is restricted

Table 17. Effect of substitution elements on thermal expansion.

Linear CTE Behavior	Substitution Elements
Positive	1/2Mg, 1/2Ba, 1/2Sr, 1/2Cu, 1/2Mn, 1/3Cr, 1/3Y, 1/3Al, 1/4Zr, 1/4Si, 1/4Hf, 1/4Ce, 1/4Ti, Ta, Nb, V, (1/4Ca-1/4Ba), (1/4Ca-1/4Sr), (1/4Ba-1/4Sr), (1/4Mg-1/4Ba), (1/4Mg-1/4Sr)
Negative	Li, Na, K, 1/2Ca, (1/2K-1/2Rb), (1/2K-1/4Ba), (1/2Na-1/4Ba), (1/2Na-1/4Ca), (1/8Ca-3/4Na), (3/8Ca-1/4Na), (1/8Na-1/16Ca-1/16Mg)
Transition	Rb, Cs, (1/4Rb-3/4Cs), (1/2Rb-1/2Cs), (3/4Rb-1/4Cs), 1/2Ni, 1/2Zn, (1/4Ca-1/4Mg), (3/8Ca-1/8Mg)

to the direction of channels.[30] The more restricted the tilt is in the direction of the channel, the lower the thermal expansion.

Correlation between linear α and axial α - The axial α data and linear α values up to 1000°C are summarized in Table 18, and the ratios of axial α values along a- and c-axes are also included. Except for the $NbZr(PO_4)_3$ and $TaZr(PO_4)_3$ systems, the c-axis expanded with increasing temperature while the a-axis contracted. As reviewed earlier,[11,31,32] the positive thermal expansion of the c-axis strains the PO_4 tetrahedra bridge linking the $O_3ZrO_3MO_3ZrO_3$ groups (where M represents the substituted cation) in the direction of the c-axis, so that the O-P-O bond angles spread in the direction of the c-axis. Consequently, the PO_4 tetrahedra contracted in the direction normal to this spreading, and the α_a actually became negative, which affected the expansion of the c-axis.

Systems substituted by the Rb and Cs having very low anisotropy showed good agreement between calculated average α from axial α values and linear measured α, considering the experimental error and the accuracy of the equation ($\alpha_l = 2/3\alpha_a + 1/3\alpha_c$) for the hexagonal system.[23]

Systems classified as having phase instability, i.e., $MgZr_4(PO_4)_6$, $YZr_6(PO_4)_9$, $TiZr_8(PO_4)_{12}$, and $CeZr_8(PO_4)_{12}$, exhibited large differences (up to $29x10^{-7}/°C$) between the calculated and measured linear α. Evidently, the inconsistency of these data is a result of the atomic movement due to phase instability and the effect of ZnO added to aid sintering. The powders examined by high temperature XRD did not include the zinc oxide sintering aid.

However, in systems of $MnZr_4(PO_4)_6$ and $NiZr_4(PO_4)_6$, also confirmed as having an unstable phase, a relatively good correlation was obtained for the relationship between the calculated linear α and the measured linear α. Axial thermal expansion measurements revealed phase instabilities in these systems above 1000°C.

System $BaZr_4(PO_4)_6$, showing the largest anisotropy [$\Delta\alpha(\alpha_c - \alpha_a) = 346x10^{-7}/°C$] and the largest anisotropy ratio (4.16), exhibited a large decrease in measured linear thermal expansion compared with that calculated. This may be attributed to the lowering of the thermal expansion due to the microcracking, which can result from the large thermal expansion anisotropy verified in the literature both theoretically[33-35] and experimentally.[36-39]

The linear thermal expansion of the $CaZr_4(PO_4)_6$ system was measured as $-18x10^{-7}/°C$, reflecting a large decrease compared to the calculated linear thermal expansion. The only differences between the two different polycrystalline bodies of the measured axial α and the linear α are the addition

Table 18. Axial and linear CTE values for selected systems with low thermal expansion.

System	Axial CTE ($\times 10^{-7}/°C$) α_a	α_c	Calculated α_l ($\times 10^{-7}/°C$)	Measured α_l ($\times 10^{-7}/°C$)	$\lvert\alpha_c/\alpha_a\rvert$
$RbZr_2(PO_4)_3$	-12	30	2	2	2.50
$CsZr_2(PO_4)_3$	-9	23	2	5	2.56
$MgZr_4(PO_4)_6$	-22	58	5	16	2.64
$CaZr_4(PO_4)_6$	-38	79	1	-18	2.08
$BaZr_4(PO_4)_6$	-67	279	45	15	4.16
$MnZr_4(PO_4)_6$	-51	112	3	7	2.20
$NiZr_4(PO_4)_6$	-70	172	10	10	2.46
$YZr_6(PO_4)_9$	-27	62	3	14	2.30
$TiZr_8(PO_4)_{12}$	-30	34	-9	20	1.13
$CeZr_8(PO_4)_{12}$	-35	57	-4	11	1.63
$NbZr(PO_4)_3$	24/-25	-61/79	-4/10	4	2.54/3.16
$TaZr(PO_4)_3$	38/-35	-35/78	13/1	11	0.92/2.23
$Rb_{0.5}Cs_{0.5}Zr_2(PO_4)_3$	-11	21	-0.3	-0.3	1.91
$Ca_{0.5}Mg_{0.5}Zr_4(PO_4)_6$	-39/-14	66/47	-4/6	-5	1.69/3.36
$(3/8Ca1/8Mg)Zr_2(PO_4)_3$	-47/-18	81/67	-4/10	-10	1.72/3.72

of ZnO and the sintering time applied. To explain this particular behavior, a close examination of crystallinity was done and will be presented in the subsequent section.

The systems substituted by +5 electron valence, i.e. $NbZr(PO_4)_3$ and $TaZr(PO_4)_3$, showed fairly good agreement between the calculated and measured linear α up to 1000°C, even though their axial thermal expansion behavior exhibited a transition characteristic at 600°C. Their axial thermal expansion behavior might be explained by an order-disorder transition.

Effect of crystallinity on thermal expansion - Table 19 lists the measured linear α values for the sintered bars with ZnO and without ZnO, as well as the calculated linear thermal expansion values. The zinc oxide used to promote the sinterability, which is based on an ionic exchange mechanism[2] due to the similar ionic radii of Zn^{+2}(0.83Å) and Zr^{+4}(0.82Å),[40] significantly affected the thermal expansion of $CaZr_4(PO_4)_6$. The linear α for the sintered bar without ZnO was much closer to the calculated value. In addition, the difference between the linear α without ZnO ($-4x10^{-7}/°C$) and the calculated linear α ($1x10^{-7}/°C$) is considered within the allowable range of experimental error.

Table 19. Measured and calculated linear CTE values for the $CaZr_4(PO_4)_6$ system

Linear CTE	With ZnO	-18
($x10^{-7}/°C$)	Without ZnO	-4
Calculated Linear CTE (from Table 18)		1

The intensity of the peak/background for the sintered powders with/without ZnO are compared in Table 20, and X-ray diffraction patterns are shown in Figure 9. Five major peaks with over 1000 counts per seconds (CPS) and one minor peak were selected to compare the diffracted intensity ratio of the peak/background: (104), (110), (113), (024), (116) for the major peaks, and (015) for the minor peak. The relative ratios of intensity for the powder with ZnO to that for the powder without ZnO for the major peaks ranged from 0.858

Table 20. Intensity ratios of peak/background for the sintered $CaZr_4(PO_4)_6$ with/without ZnO.

Condition	Peak/ Background					
	(104)	(110)	(015)	(113)	(024)	(116)
With ZnO	2.419	2.703	1.534	3.036	2.749	3.173
Without ZnO	2.120	2.320	1.234	2.657	2.407	2.757

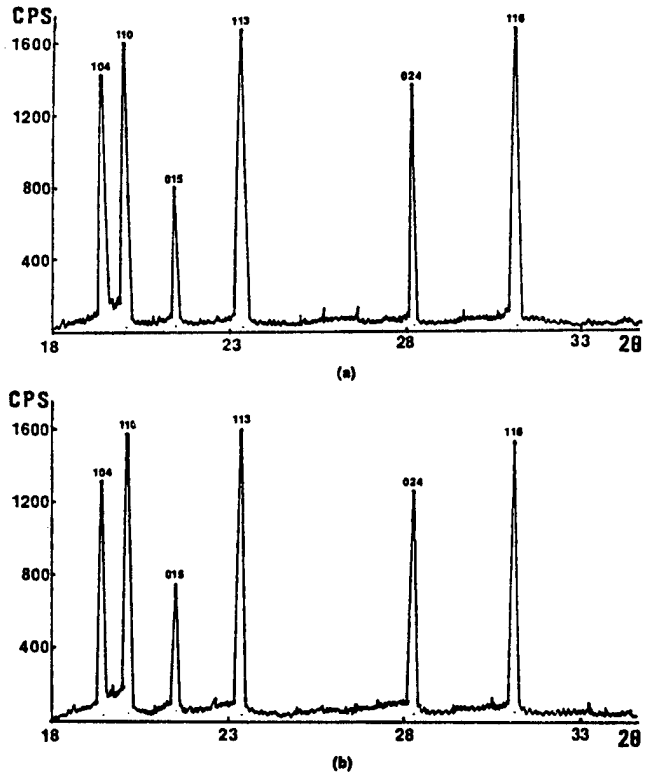

Figure 9. XRD patterns for the sintered $CaZr_4(PO_4)_6$ without ZnO (a), with ZnO (b).

[for the (110) plane] to 0.876 [for the (104) and (024) planes], with the average relative ratio being 0.871, representing a decrease in crystallinity with the addition of ZnO in $CaZr_4(PO_4)_6$.

In powders without ZnO with better crystallinity, the minor peaks were found to be clearer than powders with ZnO with poorer crystallinity. The diffraction intensity of (015) for the powders with ZnO was decreased more than that of the expected value from the tendency observed in the major peaks; i.e., a 19.6% decrease compared with the reduction of 12.9% in the major peaks. Even for (202) and (205), which exist in samples without ZnO, diffracted peaks are not seen clearly in the powdered samples with ZnO.

From the above discussion, the crystallinity may be one of the factors affecting thermal expansion behavior, especially when considering complex systems like NZP structures. The effect of crystallinity on thermal expansion may be extended to explain the difference between linear thermal expansion results from this study and those reported by others.

Some of the materials processed by different methods in other studies[10,11,23,41,42] showed large disparity in linear α values compared to materials prepared in this study; however, most of the materials showed good agreement, as previously described. $KZr_2(PO_4)_3$ is representatively included in the category which does not show a good correlation with the data determined in this study. Its thermal expansion was reported as $4x10^{-7}/°C$ by Oota et al.,[11,30] whereas in the present study a linear α value of $-22x10^{-7}/°C$ was determined. The difference in linear α values may be related to crystallinity, which is affected by processing techniques. Therefore, for an application requiring a temperature close to 1400°C, it is recommended that $Ca_{0.5}Mg_{0.5}Zr_4(PO_4)_6$ be used.

Appendix 1
Crystal Structure of NZP Compounds

From the Weissenberg data,[12] the space group of $NaZr_2(PO_4)_3$ was identified as $R\bar{3}C$. In the space group R3C (hexagonal axes), the following point positions exist:[43]

(0,0,0;1/3,2/3,2/3;2/3,1/3,1/3) +

6(a) (0,0,1/4;0,0,3/4)
6(b) (0,0,0;0,0,1/2)
12(c) ±(0,0,z;0,0,1/2 + z)
18(d) (1/2,0,0;0,1/2,0;1/2,1/2,0;1/2,0,1/2;1/2,1/2,1/2)
18(e) ±(x,0,1/4;0,x,1/4;x,x,1/4)
36(f) ±(x,y,z;y,x-y,z;y-x,x,z;y,x,1/2+z;x,x-y,1/2+z;y-x,y,1/2+z)

From the calculation of Patterson projection, section and electron density distributions,[15] the positions of the twelve zirconium, the eighteen phosphorus, and the six sodium atoms were found to be located in 12(c), 18(e), and 6(b) in the unit cell. Seventy-two oxygen atoms were confirmed to be positioned in 2x36(f) points. The structural data and atomic parameters for $NaZr_2(PO^4)_3$ are listed in Table 21.

The crystal structure of $NaZr_2(PO_4)_3$ has been described in terms of PO_4 tetrahedra and ZrO_6 octahedra which are linked at the corners forming a three-dimensional network, illustrated in Figure 10(a). Each oxygen atom simultaneously belongs to a PO_4 group and to a ZrO_6 group. The sodium atoms are in the octahedra formed by the triangular faces of two ZrO_6 octahedra, as illustrated in Figure 10(b). The $O_3ZrO_3NaO_3ZrO_3$ groups formed may be considered as major structural units of the atomic arrangement. Such groups are mutually linked in the c-direction by PO_4 tetrahedra in such a way that empty trigonal prisms of oxygen atoms are formed. The endless columns resulting from this linking are also connected normal to the c-direction by the PO_4 tetrahedra.[22]

The group $Zr_2(PO_4)_3^-$ is considered to be a major structural unit in the atomic arrangement. Two crystallographically different sites for oxygen atoms, which are designated as O(1) and O(2), exist in the skeletal framework in the $NaZr_2(PO_4)_3$ structure. Each PO_4 tetrahedron is composed of two O(1) and two O(2) sites, and Na cations are positioned in Na(1) sites surrounded octahedrally by only O(2) atoms. In $NaZr_2(PO_4)_3$, there is a Na(2) site in

addition to a Na(1) site in the interstitial space which can accommodate extra Na^+.[18]

Table 21. Structural and atomic data of $NaZr_2(PO_4)_3$ compiled from ref. 17 and 22.

a)

Space Group: $R\bar{3}C$

Unit Cell Dimensions: a= 8.8043 ± 2Å

c= 22.7585 ± 9Å

V= 1527.7 Å^3

Cell Constant: 6Na in 6(b): (0, 0, 0; 0, 0, 1/2)

12Zr in 12(c): ±(0, 0, z; 0, 0, 1/2+z)

18P in 18(e): ±(x, 0, 1/4; 0, x, 1/4; $\bar{x}$, $\bar{x}$, 1/4)

$36O_1$ and $36O_2$ in 2X36(f): ±(x, y, z; $\bar{y}$, x-y, z; y-x, $\bar{x}$, z; $\bar{y}$, $\bar{x}$, 1/2+z; x, x-y, 1/2+z; y-x, y, 1/2+z)

b)

Atom	x	y	z
Na	0	0	0
Zr	0	0	0.14568 (0.14568±1)
P	0.2916 (0.2909±6)	0	1/4
O(1)	0.1841 (0.1860±15)	-0.0165 (-0.0144±15)	0.1956 (0.1949±5)
O(2)	0.1911 (0.1913±15)	0.1675 (0.1683±15)	0.0876 (0.0866±5)

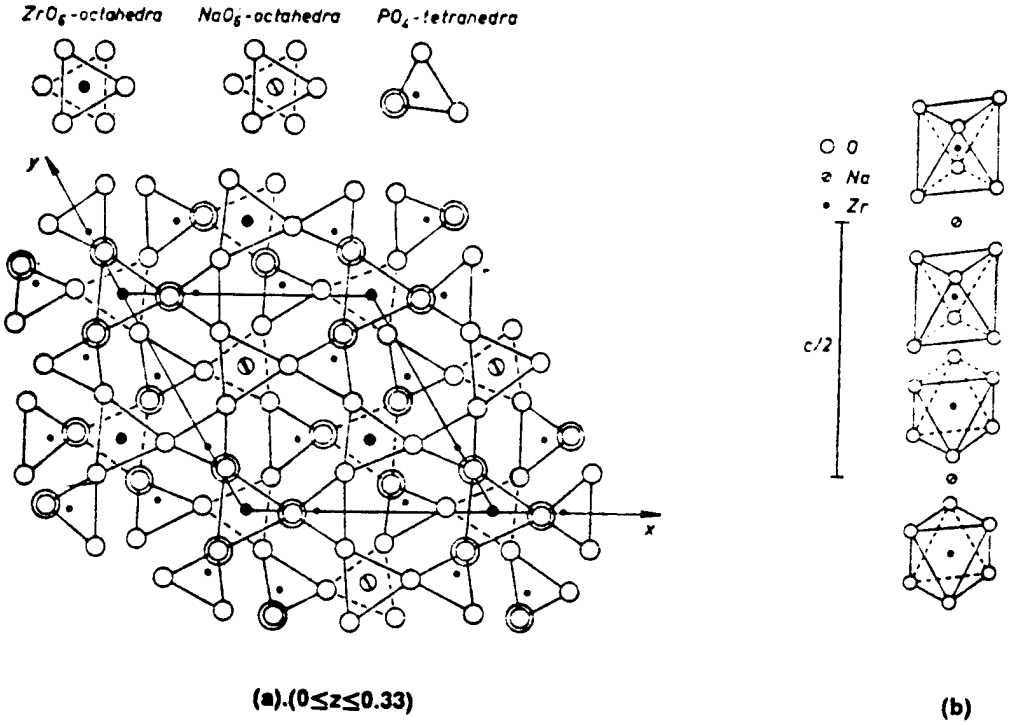

Figure 10. Schematic drawing showing the structure of $NaZr_2(PO_4)_3$ (taken from ref. 22).

References

1. J.B. Goodenough, H.Y-P. Hong, and J.A. Kafalas, "Fast Na^+-ion Transport in Skeleton Structures," *Mat. Res. Bull.*, 11, 203-220 (1976).

2. D.K. Agrawal, and V.S. Stubican, "Synthesis and Sintering of $Ca_{0.5}Zr_2P_3O_{12}$-Low Thermal Expansion Material," *Mat. Res. Bull.* 20, 99-106 (1985).

3. V.D. Frechette, "Markings on Crack Surfaces of Brittle Materials: A Suggested Unified Nomenclature," *Fractography of Ceramic and Metal Failures, ASTM STP 827*, J.J. Mecholsky, Jr., and S.R. Powell, Jr., Eds., ASTM, 104-109 (1984).

4. H. Sahai and J. Berriostchinson, *A Dictionary of Statistical, Scientific, and Technical Terms*, Weadworth Pub. Co., 1981.

5. S.Y. Limaye, W.C. Morgan, and T.B. Jackson, "New Low Thermal Expansion Structural Ceramics," First Quarterly Report (Dec. 1, 1987 - Feb. 29, 1988), DOE Report No. DOE/ER/80502-1.

6. J.S. Moya, A.G. Verduch and M. Hortal, "Thermal Expansion of β-Eucryptite Solid Solutions," *Trans. & Journ. of British Ceram. Soc.*, 73 [6], 177-178 (1974).

7. H. Schulz, "Thermal Expansion of Beta Eucryptite," *J. Am. Ceram. Soc.*, 57 [7], 313-318 (1974).

8. E. Kato, K. Daimon, and J. Takahashi, "Decomposition Temperature of β-Al_2TiO_5," *J. Am. Cer. Soc.*, 63 [5-6], 355-356 (1980).

9. W.H. Dumbaugh, Jr., and J.W. Malmendier, "Refractory Glasses," *High Temperature Oxides, Part IV,* Edited by A.M. Alper, Academic Press, New York and London, 1-14 (1971).

10. J. Alamo and R. Roy, "Ultralow Expansion Ceramics in the System Na_2O-ZrO_2-P_2O_5-SiO_2," *J. Am. Ceram. Soc.*, 67 [5], 78-80 (1984).

11. T. Oota and I. Yamai, "Thermal Expansion Behavior of $NaZr_2(PO_4)_3$-type Compounds," *J. Am. Ceram. Soc.*, 69 [1], 1-6 (1986).

12. G.H. Stout and L.H. Jensen, *X-ray Structure Determination*, The Macmillan Co., New York, 1968.

13. B.D. Cullity, *Elements of X-Ray Diffraction*, Addison-Wesley Pub. Co., Inc., 1978.

14. W.D. Kingery, H.K. Bowen, and D.R. Uhlmann, *Introduction to Ceramics*, John Wiley & Sons, 1976.

15. M.J. Buerger, *Crystal Structure Analysis*, Wiley, New York, 1960.

16. D. Tranquil, J.J. Capponi, and J.C. Joubert, "Crystal Structure and Ionic Conductivity in $Na_4Zr_2Si_3O_{12}$," *J. Solid State Chem.*, 39, 219-29 (1981).

17. H.Y-P Hong, "Crystal Structures and Crystal Chemistry in the $Na_{1+x}Zr_2Si_xP_{3-x}O_{12}$," *Mat. Res. Bull.*, 11, 173-182 (1976).

18. M. Nagai, S. Fujitsu, T. Kanazawa, and H. Yanagida, "The Dependence of Structure and Conductivity in Three-dimensional Phosphate Ionic Conductors on Composition," *J. Mat. Sci.*, 16, 1633-1642 (1981).

19. J.P. Boilot, J.P. Salanie, G. Desplanches, and D.L. Potier, "Phase Transformation in $Na_{1+x}Si_xZr_2P_{3-x}O_{12}$ Compounds," *Mat. Res. Bull.*, 14, 1469-1477 (1979).

20. C. Delmas, R. Olazcuaga, G. Le Flem, P. Hagenmuller, F. Cherkaoui, and R. Brochu, "Crystal Chemistry of the $Na_{1+x}Zr_{2-x}L_x(PO_4)_3$ (L=Cr, In, Yb) Solid Solutions," *Mat. Res. Bull.*, 16, 285-290 (1981).

21. A.G. Khachaturyan, "Ordering in Substitutional and Interstitial Solid Solutions," *Prog. Mat. Sci.*, 22, 1-150 (1978).

22. L. Hagman and P. Kierkegaard, "The Crystal Structure of $NaMe_2^{IV}(PO_4)_3$;Me^{IV}=Ge,Ti,Zr," *Acta Chem. Scan.*, 22 [6], 1822-1832 (1968).

23. G.E. Lenain, H.A. McKinstry, S.Y. Limaye, and A. Woodward, "Low Thermal Expansion of Alkali-Zirconium Phosphates," *Mat. Res. Bull.*, 19 [11], 1451-1456 (1984).

24. M. Sljukic, B. Matkovic, and B. Prodic, "The Crystal Structure of $KZr_2(PO_4)_3$," *Z. Kristallographie*, 130, 148-161 (1969).

25. N.G. Chernorukov, I.A. Korshunov, and T.V. Prokof'eva, "Crystallographic Characteristics of Double Phosphates and Arsenates of Zirconium, $M^{II}Zr_4(PO_4)_6$, $M^{I}Zr_2(AsO_4)_3$, and $M^{II}Zr_4(AsO_4)_6$," *Sov. Phys.-Crystallogr. (Engl. Transl.)*, 23 [4], 475 (1978).

26. J. Alamo and R. Roy, "Crystal Chemistry of the $NaZR_2(PO_4)_3$, NZP or CTP, Structure Family," *J. Mat. Sci.*, 21, 444-450 (1986).

27. JCPDS X-ray Diffraction File No. 33-1360.

28. H.D. Megaw, "Crystal Structures and Thermal Expansion," *Mat. Res.Bull.*, 6 [10], 1007-1018 (1971).

29. R.M. Hazen, C.T. Prewitt, "Effects of Temperature and Pressure on Interatomic Distances in Oxygen-Based Minerals," *Am. Min.*, 62, 309-315 (1977).

30. C.E. Holcombe, Jr., "Observations on Very Low Expansion Oxides," *J. Less-Com. Met.*, 60, 135-136 (1978).

31. R.M. Hazen, L.W. Finger, D.K. Agrawal, and H.A. McKinstry, "High-Temperature Crystal Chemistry of Sodium Zirconium Phosphate (NZP)," *J. Mat. Res.*, 2 [3], 329-337 (1987).

32. G.E. Lenain, H.A. McKinstry, J. Alamo, and D.K. Agrawal, "Structural Model for Thermal Expansion in $MZr_2P_3O_{12}$(M=Li, Na, K, Rb, Cs)," *J. Mat. Sci.*, 6, 17-22 (1987).

33. J. Neter, W. Wasserman, and G.A. Whitmore, *Applied Statistics*, Allyn and Bacon, 1982.

34. M. Ortiz, "A Continuum Theory of Crack Shielding in Ceramics," Trans. ASME, 54, 54-58 (1987).

35. Y. Fu and A.G. Evans, "Some Effects of Microcracks on the Mechanical Properties of Brittle Solids-I.Stress, Strain Relations," *Acta Metall.*, 33 [8], 1515-1523 (1985).

36. J.A. Kuszyk and R.C. Bradt, "Influence of Grain Size on Effects of Thermal Expansion Anisotropy in $MgTi_2O_5$," *J. Am. Ceram. Soc.*, 56 [8], 420-423 (1973).

37. J.J. Cleveland and R.C. Bradt, "Grain Size/Microcracking Relations for Pseudobrookite Oxides," *ibid.*, 61 [11-12], 478-481 (1978).

38. E.A. Bush and F.A. Hummel, "High-Temperature Mechanical Properties of Ceramic Materials: I. Magnesium Dititanate," *J. Am. Cer. Soc.*, 41 [6], 189-195 (1958).

39. R.W. Rice and R.C. Pohanka, "Grain-Size Dependence of Spontaneous Cracking in Ceramics," *J. Am. Ceram. Soc.*, 62 [11-12], 559-563 (1973).

40. F.D. Bloss, *Crystallography and Crystal Chemistry*, Holt Reinhart and Winston, Inc., 1971.

41. R. Roy, D.K. Agrawal, J. Alamo, and R.A. Roy, "A New Structural Family of Near-Zero Expansion Ceramics," *Mat. Res. Bull.*, 19 [4], 471-477 (1984).

42. T. Oota and I. Yamai, "Low Thermal Expansion $KZr_2(PO_4)_3$ Ceramic," *Yogyo Kyokai Shi*, 95 [5], 71-77 (1987).

43. The International Union of Crystallography, *International Tables for X-Ray Crystallography*, The Kynoch Press, England, 1969.

Status of milestones

Status of milestones is presented in Table 22 and Figure 11 which reflect a 6-month no-cost time extension.

Publications

None this period.

Table 22. Key to major milestones

VPI 1.1	Process selection for phosphate- and silicate-based systems (Oct. 31, 1986)
VPI 1.2	Process selection for mullite- and zircon-based systems (Oct. 31, 1986)
VPI 2.1	Complete literature review (Oct. 31, 1986)
VPI 3.1	Complete upgrade of characterization facility (Dec. 31, 1986)
VPI 4.1	Complete initial screening of phosphate-based systems (Dec. 31, 1987)
VPI 4.2	Complete initial screening of silicate-based systems (Dec. 31, 1987)
VPI 4.3	Complete initial screening of zircon-based systems (Dec. 31, 1987)
VPI 4.4	Complete initial screening of mullite-based systems (Dec. 31, 1987)
VPI 5.1	Complete second-stage property and characterization evaluation of phosphate-based systems (Sept. 30, 1988)
VPI 5.2	Complete second-stage property and characterization evaluation of silicate-based systems (Oct. 31, 1988)
VPI 5.3	Complete second-stage property and characterization evaluation of mullite-based systems (Nov. 30, 1988)
VPI 5.4	Complete second-stage property and characterization evaluation of zircon-based systems (Dec. 31, 1988)
VPI 6.0	Complete scale-up specimen fabrication of most promising low-expansion ceramics (Feb. 28, 1989)

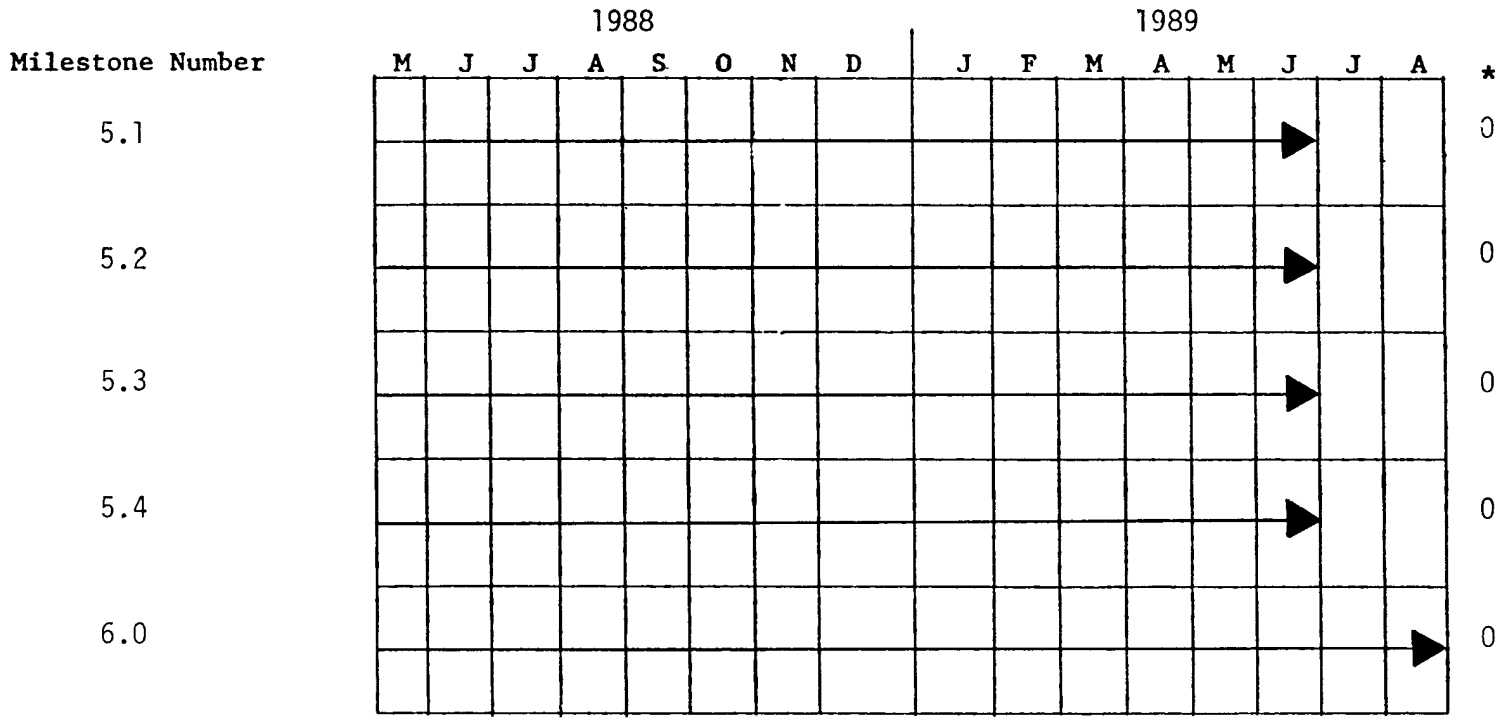

*On, Ahead of, or Behind Schedule.

Figure 11. Milestone status.

1.3 THERMAL AND WEAR COATINGS

1.3.1 ZrO_2 Base Coatings

Fabrication and Testing of Corrosion-Resistant Coatings
B. W. Sheldon and D. P. Stinton (Oak Ridge National Laboratory)

Objective/scope

Sodium corrosion of silicon carbide and silicon nitride components in gas turbine engines is a potentially serious problem. The outer surfaces of SiC and Si_3N_4 parts oxidize at high temperatures to form an SiO_2 layer which inhibits further oxidation. Sodium which is present in high-temperature combustion atmospheres reacts with the SiO_2 to form a low melting glass that is no longer protective. α-Al_2O_3 coatings can be used to provide oxidation resistance; however, sodium also attacks these coatings, and the α-alumina is converted to the sodium containing ß-alumina phase ($Na_2O \cdot 11\ Al_2O_3$). Unfortunately, the α to ß reaction spalls the coating from the substrate because of the associated volume expansion. The objective of this program is to develop a coating that will protect the underlying SiC or Si_3N_4 from sodium corrosion and provide simultaneous oxidation protection. A chemical vapor deposition (CVD) process will be developed for the application of ß-alumina coatings. The effect of the combustion environment upon coating characteristics such as microstructure, strength, adherence, and other properties will then be evaluated.

Technical progress

The GTE Corporation is developing a multiple-layer coating to reduce or eliminate contact stress damage to the ceramic components in gas turbine engines under a subcontract with ORNL. This coating consists of a graded transition layer ($AlN/Al_xO_yN_z$) that gradually increases the thermal expansion of the coating from that of the substrate to that of the zirconia-toughened alumina contact stress coating. Ultimately, we plan to address the problem of thermal expansion mismatch between alumina and either silicon carbide or silicon nitride by making use of this existing technology, and depositing our coatings onto this inter-coating. Currently we are studying the chemistry and conditions for deposition by using commercially available TiC/TiN toolbits with a thermal expansion coefficient close to that of alumina.

The successful development of a CVD process to form ß-alumina requires the proper selection of reactants. Halogenated species ($AlCl_3$, etc.) that are typically used in CVD systems are impractical because sodium salts (NaCl, etc.) are likely to form instead of the desired oxide. Trimethyl aluminum (TMA) is used for the low-temperature deposition of Al_2O_3 coatings for microelectronic applications. This previous work with TMA provides useful information on using it to deposit protective coatings. TMA is pyrophoric in air; therefore, our CVD apparatus was modified during this period to permit safe handling and evaporation of this reactant.

ß-alumina can conceivably be formed by the simultaneous oxidation of TMA and sodium vapor; the latter can be obtained by evaporation from a sodium melt. An initial sodium evaporation experiment was performed with sodium metal to examine oxide deposition in the absence of TMA. This experiment was plagued by the redeposition of sodium metal, which poses serious safety and disposal problems. Further experiments with this system will not be continued until several alternative chemistries are examined.

NaOH evaporation was investigated as a safer sodium source, and it was successfully evaporated in preliminary CVD experiments. Unfortunately, thermodynamic data on TMA and ß-alumina are not available in the SOLGASMIX data base which was used to determine the stable phases under various processing conditions. If the simpler case of Na_2O deposition is considered, calculations show that NaOH redeposition is favored over Na_2O formation in an oxidizing atmosphere. The addition of a small amount of hydrogen to the gas flowing past the NaOH melt leads to a gas phase where Na vapor, rather than NaOH, is the dominant sodium-containing vapor species. This enhanced evaporation may permit a reduced deposition temperature; however, the formation of water vapor during TMA oxidation still leads to the thermodynamic stability of NaOH rather than Na_2O.

To obtain conditions which permit the deposition of ß-alumina coatings, the NaOH must be hot enough to permit sufficient vaporization (probably over 873 K). Alumina deposition from TMA at these temperatures can be complicated by homogeneous nucleation (i.e., powder formation). Recently reported results[1] do show that alumina can be deposited from TMA at temperatures up to at least 893 K (620°C). Powder production was simultaneously observed; however, thermal diffusion was believed to remove the powder from the substrate surface in this cold-walled system, such that a good coating was still obtained. Our initial experiments were performed with a hot-wall system (i.e., without a significant amount of thermal diffusion) in the absence of sodium. To decrease the level of supersaturation in the vapor phase, and thus reduce the likelihood of powder formation, the reactant concentrations were lower than those used by Gustin and Gordon; however, powder formation without any significant amount of coating was observed in our system at atmospheric pressure (0.10 MPa) and 843 K (570°C). This powder formation was eliminated by operating at reduced pressure (0.0093 MPa), and a uniform coating was obtained. We believe that this coating is alumina; however, the sample has not yet been characterized. To further reduce the problems associated with powder formation, the current CVD system will be modified to permit deposition in a cold-wall configuration.

Our initial experiments indicate that determining operating conditions for high-quality ß-alumina coatings will be a difficult process. Therefore, the first set of experiments in the modified system will continue our current efforts using only TMA and oxygen to obtain information about the process conditions which produce good alumina coatings at relatively high temperatures (approximately 800-1000 K). NaOH will then be reintroduced to the process to study the production of ß-alumina coatings.

Another possible route to ß-alumina formation is to change the aluminum source. The formation of Na_2O is thermodynamically favored over NaOH formation in a reducing atmosphere. Unfortunately, alumina deposition from TMA requires an oxidizing atmosphere. Aluminum isopropoxide [$Al(OC_3H_7)_3$] is a reasonable alternative because it has been used for CVD of alumina by pyrolysis in a reducing atmosphere. However, the TMA is preferable because it can be adequately vaporized at room temperature. The isopropoxide requires vaporization at an elevated temperature, similar to Na or NaOH, and the high temperature vaporization of these two species independently requires a more elaborate CVD system. The aluminum isopropoxide/NaOH system will be examined if work with the TMA/NaOH system is unsuccessful.

Because the production of ß-alumina by CVD is a complex reaction system, we will attempt to verify the anticipated results of improved corrosion resistance without waiting for the production of good coatings. Monolithic α-alumina and ß-alumina samples will be hot pressed and corrosion tested accordingly. These tests should further justify continued efforts to produce ß-alumina coatings.

Status of milestones

The February 1989 milestone of identifying a sodium reactant has been satisfied with the choice of NaOH. Final proof that NaOH is adequate is linked to the July 1989 milestone of producing a high-quality ß-alumina coating. If there are problems with producing a high-quality coating from these reactants, several possible alternatives have been identified and are readily available.

Reference

1. K. M. Gustin and R. G. Gordon, *J. Electron Mater.* **17**, 509 (1988).

Development of Adherent Ceramic Coatings to Reduce Contact Stress Damage of Ceramics
H. E. Rebenne, C. D'Angelo, and J. H. Selverian (GTE Laboratories)

Objective/Scope

The objective of this program is to develop oxidation-resistant, high toughness, adherent coatings for silicon based ceramics. These coatings will be deposited on reaction bonded Si_3N_4 (RBSN), sintered SiC (SSC), and HIP'ed Si_3N_4 (HSN) and used in an advanced gas turbine engine. A chemical vapor deposition (CVD) process will be used to deposit the coatings. These coatings will be designed to provide the best mix of mechanical, thermal and chemical properties.

Technical Highlights

Flexure Strength Tests

Measurement of the modulus of rupture (MOR) of coated and uncoated samples was completed. These tests were done at room temperature, 1000°C, and 1200°C on as-coated bars and bars oxidized for 500 hours in static air at a high temperature (1000° or 1200°C) after coating. Dimensions of the bars were 2 in x 1/4 in x 1/8 in, and a standard four-point test was used. The schedule of tests is described in Table 1. The average MOR values and one standard deviation are listed in Table II.

Table I. Number of bars of each substrate strength tested at each combination of conditions. Tests were conducted with a standard four-point apparatus. Dimensions of tests bars were 2 in. x 1/4 in. x 1/8 in.

Sample Preparation	Temperature of Strength Test			
	25°C	1000°C	1200°C	1375°C
Uncoated				
Unoxidized	20	5	5	5
Oxidized at 1000°C	5			
Oxidized at 1200°C	5			
Coated				
Unoxidized	10	5	5	
Oxidized at 1000°C	5			
Oxidized at 1200°C	5			

After MOR testing, the unoxidized bars were examined optically and in the SEM to determine the failure origin. For the uncoated bars, the majority (47 out of a total of 57 examined) failed at a defect in the bulk of the bar (>1 mm from a corner). This trend was independent of substrate and test temperature, with the exception of RBSN tested at 1375°C. A summary of failure origin is given in Table III. The defect at which failure originated was typically a large pore or a large grain. Examples of these two types of failure sites are given in Figs. 1 and 2.

Table II. Room-temperature and high-temperature strength of coated and uncoated materials as determined by a four-point bend test. Dimensions of test bars were 2 in. x 1/4 in. x 1/8 in.

Substrate	MOR (MPa)			
	25°C	1000°C	1200°C	1375°C
HSN				
Uncoated	822±117	608±22	411±37	121±8
Coated	419±105	557±31	393±53	*
Uncoated, ox. at 1000°C	679±187	*	*	*
Uncoated, ox. at 1200°C	689±158	*	*	*
Coated, ox. at 1000°C	310±85	*	*	*
Coated, ox. at 1200°C	520±41	*	*	*
RBSN				
Uncoated	273±37	272±13	233±40	254±16
Coated	134±33	245±35	224±42	*
Uncoated, ox. at 1000°C	253±22	*	*	*
Uncoated, ox. at 1200°C	300±15	*	*	*
Coated, ox. at 1000°C	176±50	*	*	*
Coated, ox. at 1200°C	197±40	*	*	*
SSC				
Uncoated	401±55	352±20	398±68	416±68
Coated	287±116	258±118	320±77	*
Uncoated, ox. at 1000°C	324±72	*	*	*
Uncoated, ox. at 1200°C	416±64	*	*	*
Coated, ox. at 1000°C	173±62	*	*	*
Coated, ox. at 1200°C	328±65	*	*	*

* No tests planned at these conditions.

After coating the bars, the failure originated at a corner for the majority of bars examined. Of 53 coated bars examined, 30 failed at a corner (see Table III). The tendency to fail at a corner appeared to be more pronounced in bars tested at high temperatures based on the limited number of samples examined. When the failure area was viewed at high magnification in the SEM, flaws such as large pores or grains were usually not detected. Also, the coating was usually intact and still attached to the substrate. This is illustrated in Fig. 3. The lack of a flaw suggested that there might be high residual stress in the substrate near the interface which was superimposed on the applied stress from the MOR test.

Additional MOR testing was done to investigate the large drop in room-temperature strength which occurred as a result of applying the coating. Two aspects of the coating process and one aspect of the substrate preparation process were considered. First, the substrates are heated to the CVD process temperature in argon and maintained at this temperature for the duration of the coating cycle, which is typically 4 hours. To determine whether this "heat treatment" has any effect on MOR, 5 samples of each substrate material were heated in argon at 1000°C for 4 hours

and then flexure strength tested at room temperature. A comparison between the treated (Table IV) and untreated (Table II) samples shows no apparent decline in strength. Small increases in average MOR were actually measured for each substrate material.

Table III. Summary of evaluation of bars after flexure strength testing to determine failure source.

Sample Description	No. of Bars Examined	No. of Bars Failed at Location		
		Corner	Near Corner*	Center
Uncoated				
25°C MOR				
RBSN	17	1	4	12
SSC	0	-	-	-
HSN	20	4	2	14
1000°C MOR				
RBSN	5	1	0	4
SSC	0	-	-	-
HSN	5	1	2	2
1200°C MOR				
RBSN	0	-	-	-
SSC	0	-	-	-
HSN	5	0	1	4
1375°C MOR				
RBSN	5	3	2	0
SSC	0	-	-	-
HSN	0	-	-	-
Coated				
25°C MOR				
RBSN	10	4	3	3
SSC	10	2	5	3
HSN	8	7	1	0
1000°C MOR				
RBSN	0	-	-	-
SSC	5	3	1	1
HSN	5	5	0	0
1200°C MOR				
RBSN	5	3	2	0
SSC	5	5	0	0
HSN	5	1	1	3

* Failure originated >1 mm from a corner, but not near the center of the bar.

Table IV. Room-temperature flexure strength of uncoated MOR bars receiving various treatments. Dimensions of test bars were 2 in. x 1/4 in. x 1/8 in.

Substrate	Treatment*	No. of Bars Tested	MOR (MPa)
RBSN	1	5	314±26.2
SSC	1	5	412±43.0
HSN	1	5	867±89.6
RBSN	2	10	291±27.1
SSC	2	10	400±81.7
HSN	2	10	826±69.4
RBSN	3	10	271±53.2
SSC	3	10	387±63.4
HSN	3	10	753±83.9

* Treatment 1: Heated in flowing argon at 1000°C for 4 hours.
Treatment 2: Heated in flowing argon at 1200°C for 1 hour.
Treatment 3: Heated in flowing argon at 1200°C for 1 hour, then etched in a mixture of H_2 and Cl_2 at 1000°C for 20 minutes.

Another substrate treatment which may affect measured flexure strength is the grinding of the bars prior to coating (bars were ground to a 320-grit finish). This may induce compressive stresses which are then relieved during the coating process. As a result, the MOR measured on the uncoated bars could be artificially high, and the actual drop in strength after coating could be smaller than that measured. To test this effect, 10 samples of each substrate material were annealed for 1 hour at 1200°C in argon and then flexure strength tested at room temperature. The results are reported in Table IV. Relative to unannealed samples (see Table II), the average MOR remained the same or increased slightly. Hence, if there was a grinding-imposed stress, the annealing used did not relieve it.

Finally, the substrates are exposed to a chemical etch-type treatment during coating. The surface of the substrate is not completely covered with coating nuclei during the early stages of coating growth and hence is exposed to the reactive gas mixture. At the coating temperature, etching is thermodynamically possible. In addition, the AlN CVD process uses a reducing atmosphere, and this could alter the oxide layer which is usually present on the surface of Si_3N_4- and SiC-based ceramics. To test these effects on flexure strength, 10 samples of each substrate were annealed as above and then "etched" for 20 minutes in a mixture of H_2 and Cl_2 at 1000°C. After this treatment, average MOR declined slightly for each substrate material relative to the unetched samples (see Table IV). In particular, the MOR dropped 6.8% for RBSN, 3.4% for SSC, and 8.9% for HSN.

These studies, though only preliminary, suggest that the large drop in strength measured after coating is not related to a particular CVD process step and may be related to residual stresses developed in the coating layer, coating/substrate interface, or near-surface region of the substrate. Additional MOR tests will be conducted during Phase II to identify the cause(s) of the drop in strength.

Contact Stress Tests

The effectiveness of the coating in reducing contact stress damage of each of the substrate materials is being assessed by conducting point contact tests. The test involves contacting two coated specimens at a point. Since the MOR bars used throughout the program have flat faces, pins with a curved edge had to be specially fabricated for each substrate and coated. The schedule selected for contact stress testing was to evaluate a total of 20 bar + pin pairs of each substrate - 10 at room temperature, 5 at 1000°C, and 5 at 1200°C. The contact stress tests and analysis of results were subcontracted to Garrett Turbine Engine Company, Auxiliary Power Division. The required number of bars and pins were coated and sent to Garrett for testing. Results are not yet available.

Final Report

Phase I of this program was completed at the end of March. All milestones were met, and the Final Report was submitted. A Statement of Work for Phase II was prepared and submitted.

Status of Milestones

All of the milestones from Phase I of the contract were met. The milestones for Phase II have not yet been written.

Communications/Visits/Travel

10/24-27/88 - H. J. Kim and D. W. Oblas attended the 26th Automotive Technology Development Contractors' Coordination Meeting in Dearborn, MI. D. W. Oblas presented a paper entitled "Ceramic Coatings to Reduce Contact Stress Damage of Ceramics - Characterization."

11/11/88 - H. J. Kim and H. E. Rebenne visited Oak Ridge National Laboratory to present a review of Phase I and discuss plans for Phase II of the program.

01/15-18/89 - H. J. Kim attended the 13th Annual Conference on Composites and Advanced Ceramics in Cocoa Beach, FL.

Problems Encountered

None.

Publications

D. W. Oblas, C. D'Angelo, H. E. Rebenne, and V. K. Sarin, "Ceramic Coatings to Reduce Contact Stress Damage of Ceramics: Performance Testing," to be published in Proc. 26th Automotive Technology Development Contractors' Coordination Meeting.

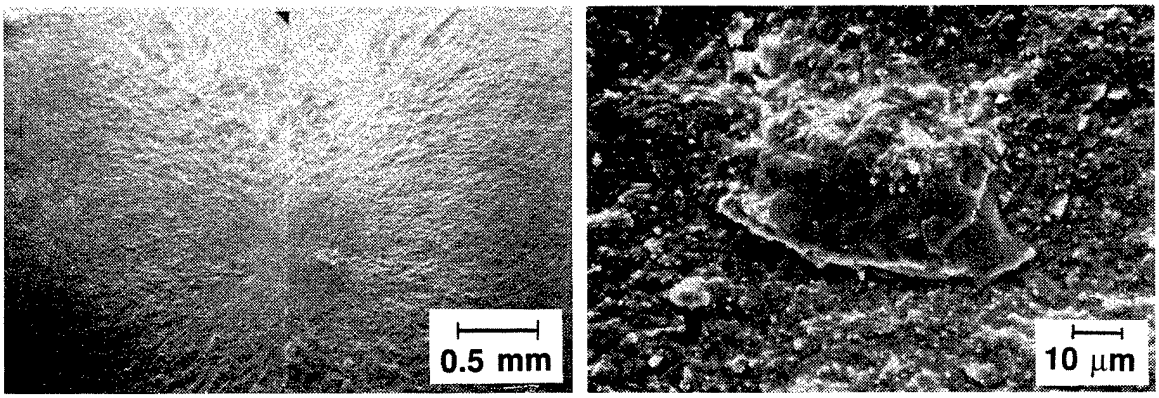

Figure 1. Fractured surfaces of an uncoated HSN bar showing failure originating at a large grain. This bar was flexure strength tested at 1200°C.

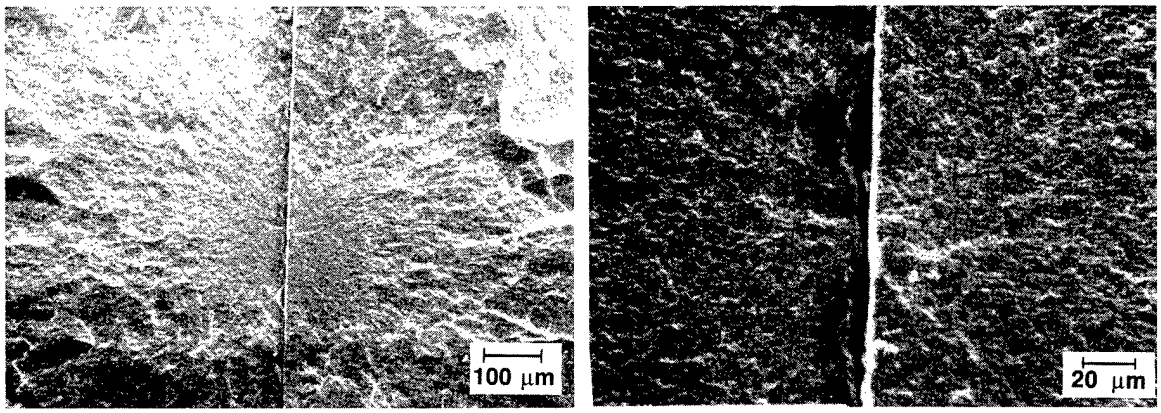

Figure 2. Fractured surfaces of an uncoated HSN bar showing failure originating at a large pore. This bar was flexure strength tested at room temperature.

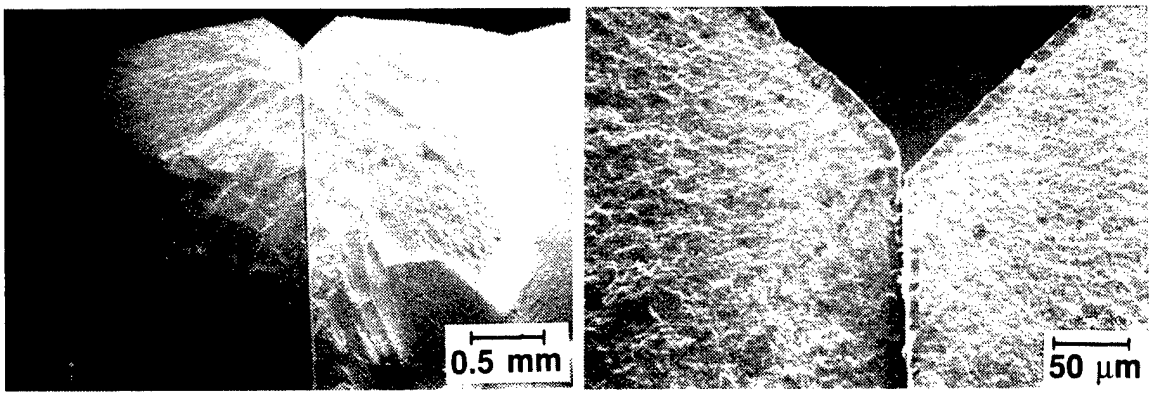

Figure 3. Fractured surfaces of a coated HSN bar showing failure originating at a corner. This bar was flexure strength tested at 1000°C.

Wear Resistant Coatings

C. D. Weiss (Caterpillar, Inc.)

Objective/scope

The goal of this technical program is to develop wear-resistant coatings for piston ring and cylinder liner components for low heat-loss diesel engines.

Wear resistant coatings will be applied to metallic substrates utilizing plasma spraying, vapor deposition (CVD/PVD),and enameling coating processes. First the adherence of each coating for each coating process to the metallic substrate will be optimized. Methods which can be utilized for improving the adherence of these coatings include development of unique substrate preparation methods before application of the coating, grading coating compositions to match thermal expansion, compositional changes, laser or electron beam fusing and/or optimizing coating thickness. Once the adherence of each coating system is optimized, each coating will be screened for friction and wear at 350 C under lubricated conditions. Coatings which show promise after this initial screening will be further optimized by adjustments to chemistry and hard particle content to meet the friction and wear requirements. Then the optimized coating systems will be fully characterized for oxidation resistance, adherence, uniformity, thermal shock resistance, friction and wear.

Selection of the most promising coatings and coating processes will be made after the characterization task. Criteria for selection will include not only performance (i.e. wear, adhesion, friction coefficient, thermal shock resistance and thermal stability) but manufacturability/cost factors, as well. Utilizing both criteria a coating system having acceptable cost/benefit relationships will be selected.

Technical progress

Modification of a tensile pull test was completed and the adherence of the plasma sprayed and chemical vapor deposited coatings determined. These results are listed in Table 1. All the chemical vapor deposited coatings had tensile pull adherence values above 4000 psi, in shear. (Note- the shear strength of the epoxy is 4000 psi.) In addition the following plasma spray coatings had tensile pull adherence values above 4000 psi when applied to either a cast on or tool steel substrate: prealloyed Ni, Cr, high Mo powder, high carbon iron- Mo composite, self-fluxing high Mo blend, high Co, Mo, Cr alloy, Hohman PS212. The self-fluxing Ni-Cr alloy spalled from the tool steel after application and disbonded from the surface of the cast iron at 2500 psi shear. Slightly poorer adherence values on both cast iron and tool steel (1810 psi and 1460 psi, respectively). were obtained with the chrome oxide-silica composite plasma sprayed coating.

Table 1
Results of Tensile Pull Adherence Testing-Plasma Coating

Coating:	Shear (PSI):	
	Cast Iron	Tool Steel
Self-Fluxing Ni-Cr Alloy	>4000	Spalled
Self-Fluxing High Mo Blend	>4000	>4000
Prealloyed Ni,Cr, High Mo Powder	>4000	>4000
High Co, Mo, Cr Alloy	>4000	>4000
Graded Zirconia Coating -		
Bond Coat/Top Coat	2940	1630
Bond Coat/50-50/Top Coat	2180	1910
Bond Coat/50-50/25-75/Top Coat	1890	1730
ZrO_2-TiO_2-Y_2O_3 Graded Coating -		
Bond Coat/Top Coat	>4000	1870
Bond Coat/50-50/Top Coat	1570	2950

Grading the zirconia coating with bond coat in an attempt to reduce the thermal stresses which develop within the coating when the coating is heated, adversely affects the coating adherence when these coatings are applied to cast iron. However, grading the coating with bond coat improves the adherence of the coating when the coating is applied to tool steel. Grading the ZrO2-TiO2-SiO2 coating with bond coat also adversely affected the coating adherence when the coating was applied to cast iron and improved the coating adherence when the coating was applied to tool steel.

The friction and wear screening of the plasma sprayed Falex disks processed at Caterpillar, Table 2, illustrated that both the high carbon iron-molybdenum and chrome oxide-silica composite powder coatings recorded low coefficient of friction values and low-to-medium disk and pin wear when these coatings were run against a ceramic pin. These coatings also recorded low coefficient of friction values when run against a 440C pin, but the 440C pin demonstrated medium-to-high pin wear. Low coefficient of friction values as well as low disk and pin wear were recorded by the self-fluxing Ni-Cr alloy plasma coating when run against the ceramic or 440C pins.

Table 2

Results of Falex Friction and Wear Testing - Plasma Coating

	440C Pin		Ceramic Pin	
Plasma Coating on Disk	Coeff of Friction	Comments	Coeff of Friction	Comments
High Carbon Iron Mo Comp.	0.02-0.11	low to medium disk & pin wear	0.01-0.13	low to medium disk & pin wear
Cr_2O_3-SiO_2 Comp Powder	0.04-0.16	low disk, high pin wear	0.09-0.13	low to medium disk & pin wear
Self-Fluxing Ni-Cr Alloy	0.10-0.20	low disk, medium pin wear	0.09-0.18	low to medium disk & pin wear
Prealloyed Ni, Cr, High Mo Powder	0.02-0.11	medium disk and pin wear	0.07-0.13	low pin and disk wear
High Co, Mo, Cr Alloy	0.18-0.33	medium disk and pin wear	0.18-0.22	medium disk and pin wear
Graded Zirconia	0.15-0.24	medium disk, low-to-medium pin wear	0.13-0.20	medium disk, low-to-medium pin wear
Hohman PS 212	0.09-0.26	medium disk and pin wear	0.04-0.15	medium disk, low pin wear
ZrO_2-TiO_2-Y_2O_3 Comp			0.13-0.37	medium disk, high pin wear

The self-fluxing high molybdenum blend recorded relatively high coefficient of friction values and medium-to-high pin wear when run against either the ceramic or 440C pins. In addition, the high Mo, Co, Cr alloy, graded zirconia coating and ZrO2-TiO2-SiO2 composite coatings all recorded high coefficient of friction values when run against either the ceramic or 440C pins. Finally, the PS212 coating performed significantly better when run against the ceramic pin than the 440C pin.

Table 3

Results of Falex Friction and Wear Testing-CVD Coatings

	440 Pin		Ceramic Pin	
CVD Coating on Disk	Coeff of Friction	Comments	Coeff of Friction	Comments
Chrome Carbide	0.024-0.31	medium disk, high pin wear	0.09-0.22	medium disk, low pin wear
TiN/TiC Layer Coating	0.24-0.24	medium disk, high pin wear	0.07-0.15	low disk and pin wear
Mid-Temp. Ti(C,N)	0.18-0.22	medium disk and pin wear	0.08-0.18	low disk and pin wear

Table 4

Results of Falex Friction and Wear Coating-Enamel Coatings

	440 Pin		Ceramic Pin	
Coating on Disk	Coeff of Friction	Comments	Coeff of Friction	Comments
Cr_2O_3 Plasma Sprayed Over Co-Based Enamel	0.09-0.31	low-to-medium disk, medium pin wear	0.07-0.22	low-to-medium disk, medium pin wear
CrC_3 Plasma Sprayed Over Co-Based Enamel Co-Based Enamel			0.07-0.18	medium disk, low-to-medium pin wear

Of the three chemical vapor deposited (CVD) coatings evaluated, the mid-temperature Ti(C,N) recorded both the lowest coefficient of friction and the least amount of pin and/or disk wear when run against either a ceramic or 440C pin. Both the chrome carbide and TiN/TiC layered CVD coatings recorded high coefficient of friction values and medium to high pin wear when run against the 440C pin (Table 3).

Table 4 illustrates that the chrome carbide and the chrome oxide coatings plasma sprayed over an enamel bond coat recorded reasonably low coefficient of friction values and low-to-meduim disk and pin wear when run against a ceramic pin. However, when the plasma sprayed chrome oxide over enamel coating was run against the 440C pin high coefficient of friction values and medium to high pin wear was recorded.

The Hohman A-6 double rub shoe machine was modified with a 3 hp motor to allow for testing of specimens with higher coefficients of friction values. With the modification, unlubricated friction values of up to 0.5 can be evaluated without stalling the motor. A calibration procedure is being developed to verify the consistency of the test data obtained from this equipment. This will be followed by a series of runs with plasma sprayed chrome carbide shoes running against a chrome oxide disk. This material pair will be used as a baseline for the coatings developed and evaluated in this program.

Status of milestones

MS1 Manufacture of 400 adherence test specimens- complete
MS2 Manufacture friction and wear test specimens- complete
MS3 Identify a minimum of 12 adherent coating systems- complete
MS4 Identify 12 coating systems for friction and wear optimization- complete

Publications

M.H. Haselkorn,"Wear Resistant Ceramic Coatings for Diesel Engine Components", was presented at CERAMTEC 89, February 1, 1989, Dearborn, Mi.

Development of Wear Resistant Ceramic Coatings for Diesel Engine Components

M. G. S. Naylor (Cummins Engine Company, Inc.)

Objective/scope

The objective of this program is to develop advanced wear resistant coatings for in-cylinder components for future, low heat rejection diesel engines. Coatings and substrates (for piston rings and cylinder liners) are to be developed to meet the following requirements:

1. Low wear (as measured in laboratory rig tests at ambient temperature and 350°C). Wear coefficients in the range $5x10^{-12}$ to $5x10^{-11}$ $mm^3/mm/N$ are targeted (at 350°C).

2. Low friction coefficients when tested under boundary lubricated conditions (target 0.1) and unlubricated conditions (target 0.2) at ambient temperature and 350°C.

3. Good thermal shock resistance.

4. High adherence and compatibility with substrate materials up to 650°C.

5. High uniformity and reproducibility.

Technical progress

Wear testing

Wear testing and microstructural characterization of air plasma sprayed (APS) chromium oxide, high velocity (HV) thermal sprayed 88% WC-12% Co and HV chromium carbide-tungsten carbide-nickel-chromium "ring" coatings have been completed. Tests were performed with grey iron and slurry-sprayed silica-chromia-alumina (SCA) "liner" materials. The test conditions and results are listed in Tables 1-4.

APS chromium oxide coatings - Wear data for APS Cr_2O_3 coatings tested against grey iron liners are shown in Fig. 1. Two Cr_2O_3 materials have been tested so far: an 800 μm thick Metco 136 Cr_2O_3-TiO_2-SiO_2 material and a 100 μm thick Union Carbide Cr_2O_3 with no additives. Measurement of liner wear coefficients is in progress.

In comparison with the baseline electroplated (EP) chromium/grey cast iron wear system, the Cr_2O_3 wear systems are shown in Fig. 1b, which suggests that the ceramic system offers most advantage at lower temperatures. In fact, the difference in activation energies between Cr and Cr_2O_3 is less than the statistical error in measuring these values.

Table 1. Wear rates and friction coefficients for Air Plasma Sprayed Chromium Oxide ring coatings (Metco powder). Cameron Plint tests: load = 225 N; frequency = 20 Hz; stroke = 5 mm; test duration = 360 min (lubricated), 60 min (unlubricated).

Ring Material	Liner Material	Lubricant	Temperature (°C)	Ring Wear ($mm^3/mm/N$)	Liner Wear ($mm^3/mm/N$)	Friction Coeff
Metco Cr_2O_3	Grey Iron	Fresh CE/SF 15W40	262	$4.59x10^{-12}$	$7.94x10^{-10}$	0.196
Metco Cr_2O_3	SCA	Fresh CE/SF 15W40	275	$2.35x10^{-10}$	$6.30x10^{-11}$	0.108
Metco Cr_2O_3	SCA	Fresh CE/SF 15W40	344	$7.70x10^{-11}$	$6.42x10^{-11}$	0.109
Metco Cr_2O_3	SCA	Fresh CE/SF 15W40	353	$4.49x10^{-11}$	$1.71x10^{-10}$	0.110
Metco Cr_2O_3	SCA	Engine-tested CE/SF 15W40	259	$1.03x10^{-10}$	$1.23x10^{-10}$	0.223
Metco Cr_2O_3	SCA	None	436	$2.60x10^{-9}$	$7.53x10^{-10}$	>0.75

For APS Cr_2O_3 sliding against SCA (Fig. 2), the wear coefficients displayed little if any temperature sensitivity. Compared to the baseline system, SCA liner wear coefficients were lower, but this was at the expense of higher ring (Cr_2O_3) wear. The low temperature sensitivity suggests a predominantly stress-activated (as opposed to thermally activated) wear process with this system. As a practical in-cylinder tribology system, this materials combination is probably not viable, due to the high ring wear coefficients, but the concept of a low activation energy wear system may be useful if this behavior is typical of other ceramic-on-ceramic wear systems.

Figure 3 illustrates a significant advantage of the Cr_2O_3/SCA system over the baseline materials when using an engine-tested lubricant for the wear tests. The baseline system showed a large (approximately one order of magnitude) increase in wear coefficients compared to tests run with fresh oil, while the Cr_2O_3/SCA combination showed essentially no change in wear. Thus, it is important to test candidate coating systems in used oil in order to gain a true picture of the performance benefits which would be obtained in engine tests.

Table 1. Wear rates and friction coefficients for Air Plasma Sprayed Chromium Oxide ring coatings (Metco powder). Cameron Plint tests: load = 225 N; frequency = 20 Hz; stroke = 5 mm; test duration = 360 min (lubricated), 60 min (unlubricated).

Ring Material	Liner Material	Lubricant	Temperature (°C)	Ring Wear ($mm^3/mm/N$)	Liner Wear ($mm^3/mm/N$)	Friction Coeff
Metco Cr_2O_3	Grey Iron	Fresh CE/SF 15W40	262	4.59×10^{-12}	7.94×10^{-10}	0.196
Metco Cr_2O_3	SCA	Fresh CE/SF 15W40	275	2.35×10^{-10}	6.30×10^{-11}	0.108
Metco Cr_2O_3	SCA	Fresh CE/SF 15W40	344	7.70×10^{-11}	6.42×10^{-11}	0.109
Metco Cr_2O_3	SCA	Fresh CE/SF 15W40	353	4.49×10^{-11}	1.71×10^{-10}	0.110
Metco Cr_2O_3	SCA	Engine-tested CE/SF 15W40	259	1.03×10^{-10}	1.23×10^{-10}	0.223
Metco Cr_2O_3	SCA	None	436	2.60×10^{-9}	7.53×10^{-10}	>0.75

For APS Cr_2O_3 sliding against SCA (Fig. 2), the wear coefficients displayed little if any temperature sensitivity. Compared to the baseline system, SCA liner wear coefficients were lower, but this was at the expense of higher ring (Cr_2O_3) wear. The low temperature sensitivity suggests a predominantly stress-activated (as opposed to thermally activated) wear process with this system. As a practical in-cylinder tribology system, this materials combination is probably not viable, due to the high ring wear coefficients, but the concept of a low activation energy wear system may be useful if this behavior is typical of other ceramic-on-ceramic wear systems.

Figure 3 illustrates a significant advantage of the Cr_2O_3/SCA system over the baseline materials when using an engine-tested lubricant for the wear tests. The baseline system showed a large (approximately one order of magnitude) increase in wear coefficients compared to tests run with fresh oil, while the Cr_2O_3/SCA combination showed essentially no change in wear. Thus, it is important to test candidate coating systems in used oil in order to gain a true picture of the performance benefits which would be obtained in engine tests.

Table 2. Wear rates and friction coefficients for Air Plasma Sprayed Chromium Oxide ring coatings (U-Car powder). Cameron Plint tests: load = 225 N; frequency = 20 Hz; stroke = 5 mm; test duration = 360 min (lubricated), 60 min (unlubricated).

Ring Material	Liner Material	Lubricant	Temperature (°C)	Ring Wear ($mm^3/mm/N$)	Liner Wear ($mm^3/mm/N$)	Friction Coeff
UCAR Cr_2O_3	Grey Iron	Fresh CE/SF 15W40	196	$2.48x10^{-12}$		0.318
UCAR Cr_2O_3	Grey Iron	Fresh CE/SF 15W40	200	$3.34x10^{-12}$		0.251
UCAR Cr_2O_3	Grey Iron	Fresh CE/SF 15W40	276	$1.66x10^{-11}$		0.174
UCAR Cr_2O_3	Grey Iron	Fresh CE/SF 15W40	287	$2.05x10^{-11}$		0.223
UCAR Cr_2O_3	Grey Iron	Fresh CE/SF 15W40	358	$2.25x10^{-11}$		0.132
UCAR Cr_2O_3	Grey Iron	Fresh CE/SF 15W40	361	$4.17x10^{-11}$		0.177
UCAR Cr_2O_3	Grey Iron	Super-Refined Mineral Oil	200	$6.20x10^{-12}$		0.227
UCAR Cr_2O_3	Grey Iron	Super-Refined Mineral Oil	348	$1.59x10^{-11}$		0.357
UCAR Cr_2O_3	SCA	Fresh CE/SF 15W40	197	$2.32x10^{-10}$		0.248
UCAR Cr_2O_3	SCA	Fresh CE/SF 15W40	332	$2.44x10^{-10}$		0.130
UCAR Cr_2O_3	Polished SCA	Fresh CE/SF 15W40	197	$7.87x10^{-11}$		0.227
UCAR Cr_2O_3	SCA	None	351	$2.77x10^{-9}$		0.884

Table 3. Wear rates and friction coefficients for high velocity thermal spray 88% WC-12% Co ring coating. Cameron Plint tests: load = 225 N; frequency = 20 Hz; stroke = 5 mm; test duration = 360 min.

Ring Material	Liner Material	Lubricant	Temperature (°C)	Ring Wear ($mm^3/mm/N$)	Liner Wear ($mm^3/mm/N$)	Friction Coeff
WC-Co	Grey Iron	Fresh CE/SF 15W40	151	6.04×10^{-13}	8.22×10^{-12}	0.210
WC-Co	Grey Iron	Fresh CE/SF 15W40	146	4.08×10^{-13}	1.15×10^{-11}	0.204
WC-Co	Grey Iron	Fresh CE/SF 15W40	257	3.17×10^{-12}	7.88×10^{-10}	0.171
WC-Co	Grey Iron	Fresh CE/SF 15W40	256	1.44×10^{-12}	9.53×10^{-10}	0.169
WC-Co	Grey Iron	Engine-tested CE/SF 15W40	149	1.84×10^{-12}	1.24×10^{-10}	0.196
WC-Co	High Phosphorus Grey Iron	Fresh CE/SF 15W40	151	4.62×10^{-13}	6.84×10^{-12}	0.208
WC-Co	High Phosphorus Grey Iron	Fresh CE/SF 15W40	257	2.06×10^{-12}	3.87×10^{-10}	0.172
WC-Co	SCA	Fresh CE/SF 15W40	148	9.12×10^{-12}	7.42×10^{-11}	0.216
WC-Co	SCA	Fresh CE/SF 15W40	255	2.95×10^{-11}	1.63×10^{-10}	0.180

Table 4. Wear rates and friction coefficients for high velocity thermal spray Cr_3C_2-WC-Ni-Cr ring coating. Cameron Plint tests: load = 225 N; frequency = 20 Hz; stroke = 5 mm; test duration = 360 min.

Ring Material	Liner Material	Lubricant	Temperature (°C)	Ring Wear ($mm^3/mm/N$)	Liner Wear ($mm^3/mm/N$)	Friction Coeff
Cr_3C_2-WC-Ni-Cr	Grey Iron	Fresh CE/SF 15W40	149	$4.78x10^{-12}$	$1.33x10^{-11}$	0.223
Cr_3C_2-WC-Ni-Cr	Grey Iron	Fresh CE/SF 15W40	148	$3.98x10^{-12}$	$1.47x10^{-11}$	0.228
Cr_3C_2-WC-Ni-Cr	Grey Iron	Fresh CE/SF 15W40	359	$2.03x10^{-10}$		0.129
Cr_3C_2-WC-Ni-Cr	Grey Iron	Engine-tested CE/SF 15W40	148	$3.76x10^{-11}$	$4.06x10^{-10}$	0.121
Cr_3C_2-WC-Ni-Cr	High Phosphorus Grey Iron	Fresh CE/SF 15W40	148	$2.49x10^{-12}$	$1.61x10^{-11}$	0.213
Cr_3C_2-WC-Ni-Cr	High Phosphorus Grey Iron	Fresh CE/SF 15W40	150	$2.72x10^{-12}$	$1.59x10^{-11}$	0.230
Cr_3C_2-WC-Ni-Cr	Ion-nitrided Type 1 Niresist	Fresh CE/SF 15W40	153	$1.41x10^{-11}$	$4.80x10^{-11}$	0.213
Cr_3C_2-WC-Ni-Cr	SCA	Fresh CE/SF 15W40	149	$6.16x10^{-12}$	$1.08x10^{-10}$	0.219

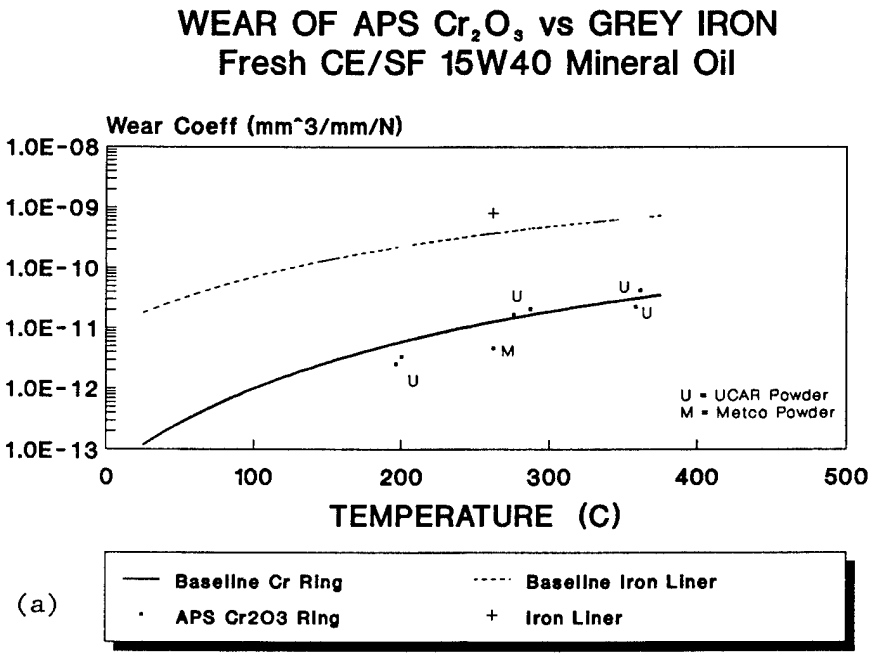

(a)

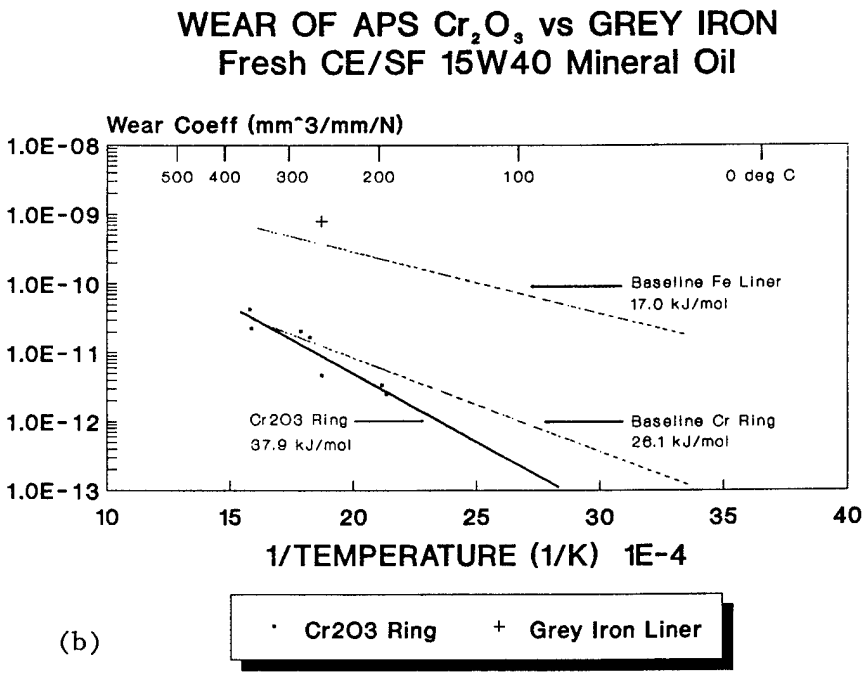

(b)

Fig. 1. Wear rate of lubricated APS Cr_2O_3 vs grey cast iron as a function of temperature (data points). The solid line represents the wear rate of electroplated chroimum sliding against grey cast iron, and the broken line represents wear rates of grey iron against electroplated chromium. Cameron Plint data. (a) Log (wear coefficient) vs temperature; (b) log (wear coefficient) vs the reciprocal of absolute temperature (activation energy plot).

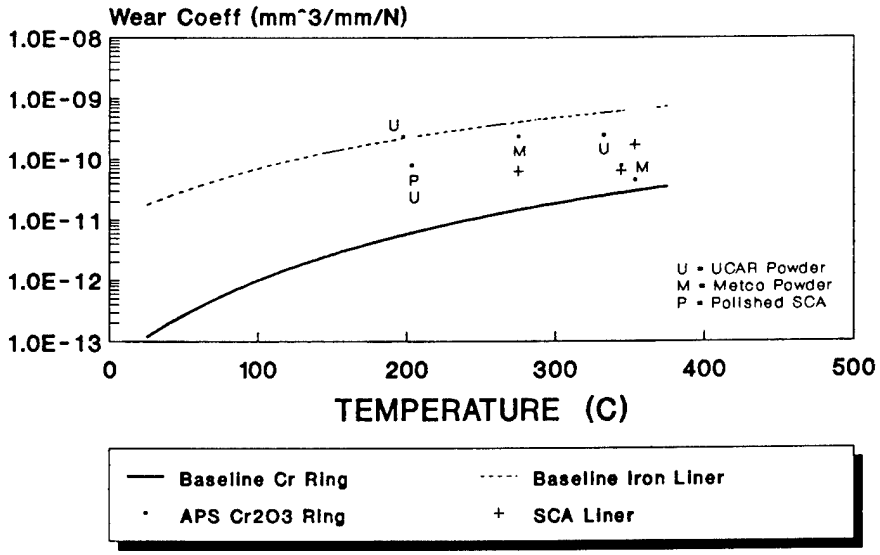

Fig. 2. Wear rate of lubricated APS Cr_2O_3 vs silica-chroma-alumina as a function of temperature (data points). The solid line represents the wear rate of electroplated chromium piston rings sliding against grey cast iron, and the broken line represents wear rates of grey iron against electroplated chromium. Cameron Plint data.

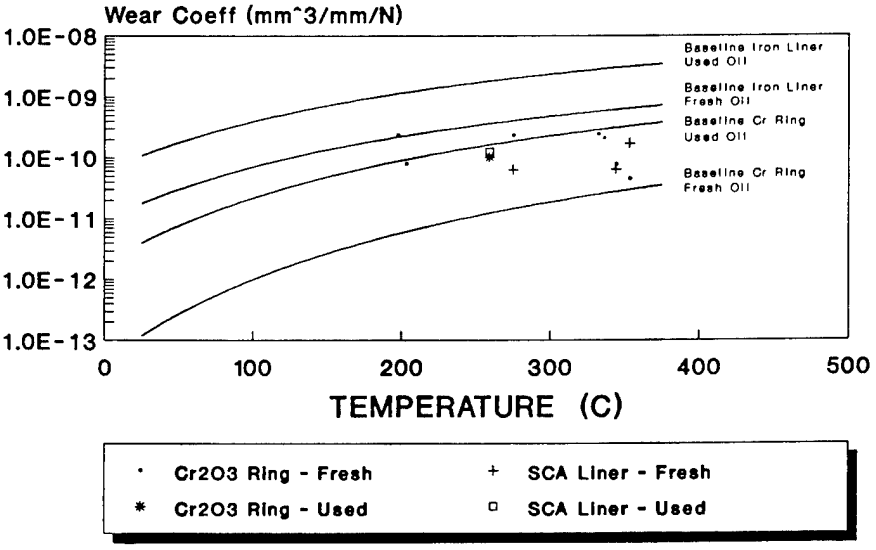

Fig. 3. Wear rate of lubricated APS Cr_2O_3 vs silica-chromia-alumina as a function of temperature (data points) in fresh and engine-tested lubricants. Cameron Plint data.

High velocity WC-Co coatings - Very low ring and liner wear coefficients were obtained for the HV WC-Co/grey iron wear couple (Table 3, Fig. 4). Two types of grey iron were used for this study, a standard low alloy pearlitic grey iron and a low alloy, high phosphorus pearlitic iron. Wear coefficients were approximately the same for both materials. At 150°C test temperature, liner wear rates were much lower than for the baseline system, while at 250°C, liner wear rates were comparable for the two systems. The activation energy plot (Fig. 4b) thus shows a much higher liner wear activation energy for the WC-Co/grey iron combination than for EP Cr/grey iron. Ring wear activation energies were similar for both systems. The large increase in liner wear with increasing temperature for the WC-Co/grey iron system is thought to have resulted from increased abrasive action due to cracking of the WC-Co coating at the higher test temperatures. This cracking is thought to be due to high thermal expansion mismatch with the HK40 stainless steel substrate and poor coating adherence. The coating thickness was relatively large (250 μm).

Wear performance for the WC-Co/grey iron system was degraded in engine-tested lubricant (Fig. 5), although wear rates were still lower than for the baseline system in *fresh* oil.

With a SCA wear counterface, behavior similar to the CR_2O_3/SCA system was obtained (Fig. 6), with liner wear rates being improved at the expense of higher ring wear (compared to WC-Co/grey iron). The wear rate of the SCA was higher than that of the HV WC-Co.

High velocity Cr_3C_2-WC-Ni-Cr coatings - Wear data for tests with the HV Cr_3C_2-WC-Ni-Cr ring coating are listed in Table 4. The Cr_3C_2-WC-Ni-Cr/grey iron wear couple showed lower liner wear coefficients than the baseline system, with comparable ring wear rates (Fig. 7). The wear performance was severely degraded in engine-tested lubricant (Fig. 8), offering little advantage over the baseline system. The Cr_3C_2-WC-Ni-Cr coating cracked at the higher test temperatures (250°C), as did the HV WC-Co coating. Coating thickness for the Cr_3C_2-WC-Ni-Cr material was also around 250 μm.

The Cr_3C_2-WC-Ni-Cr/SCA wear couple showed slightly higher ring wear and slightly lower liner wear than the baseline system (Fig. 9). The wear rate of the SCA was higher than that of the Cr_3C_2-WC-Ni-Cr coating, as for the WC-Co/SCA wear couple. It is interesting to note that the Cr_3C_2-WC-Ni-Cr/grey iron system had lower ring *and* liner wear rates than the Cr_3C_2-WC-Ni-Cr/SCA wear couple.

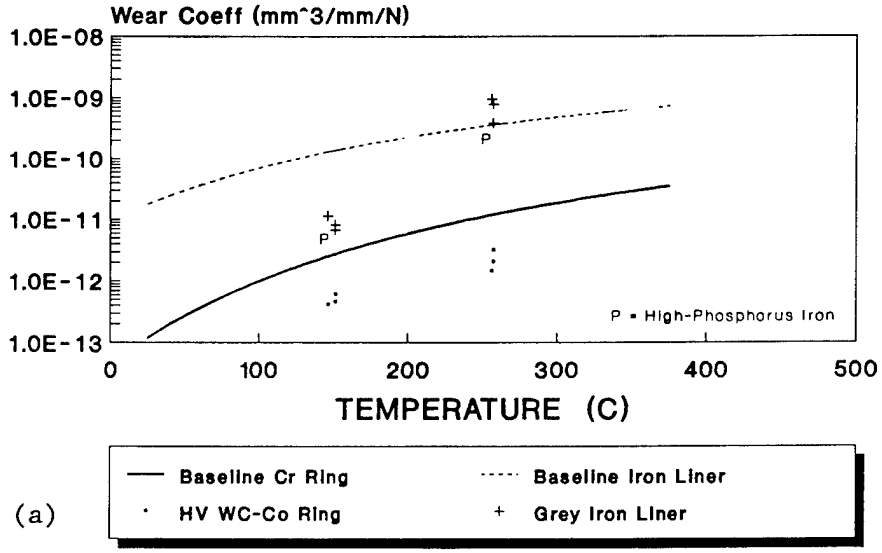

(a)

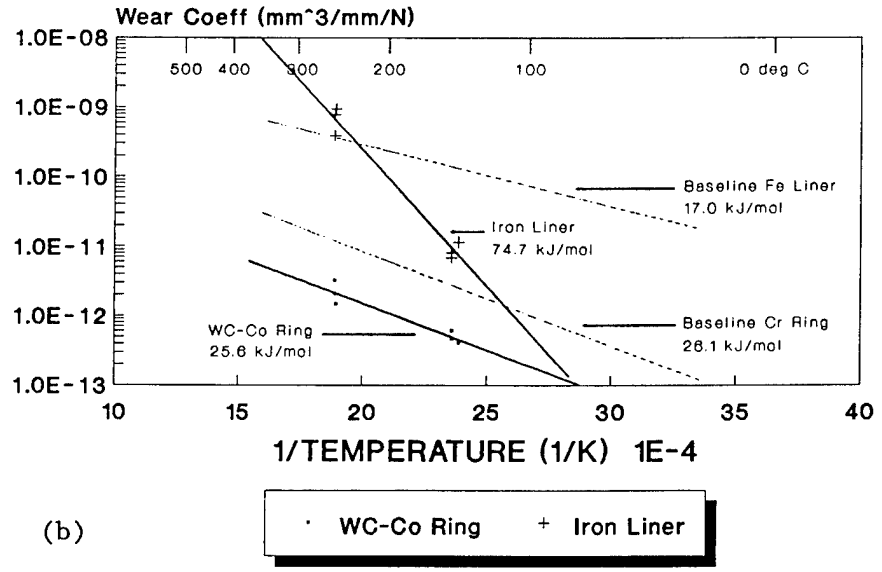

(b)

Fig. 4. Wear rates of lubricated HV WC-Co vs grey cast iron as a function of temperature (data points). The solid line represents the wear rate of electroplated chromium sliding against grey cast iron, and the broken line represents wear rates of grey iron against electroplated chromium. Cameron Plint data. (a) Wear (wear coefficient) vs temperature; (b) log (wear coefficient) vs the reciprocal of absolute temperature (activation energy plot).

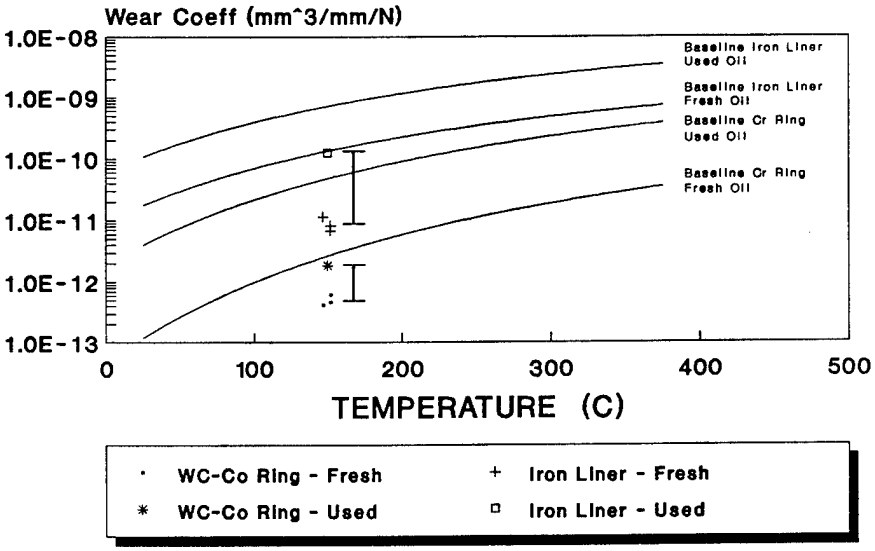

Fig. 5. Wear rate of lubricated HV WC-Co vs grey cast iron as a function of temperature (data points) in fresh and engine-tested lubricants. Cameron Plint data.

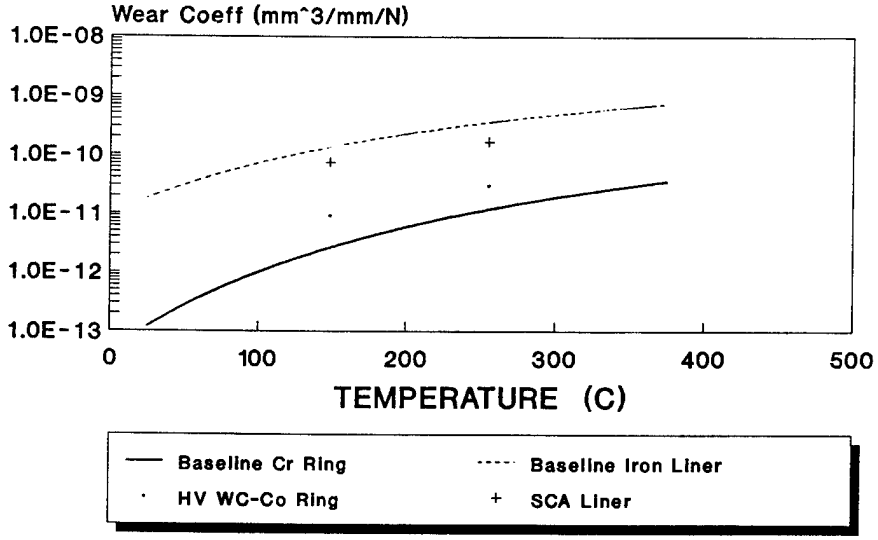

Fig. 6. Wear rate of lubricated HV WC-Co vs silica-chromia-alumina as a function of temperature (data points). The solid line represents the wear rate of electroplated chromium piston rings sliding against grey cast iron, and the broken line represents wear rates of grey iron against electroplated chromium. Cameron Plint data.

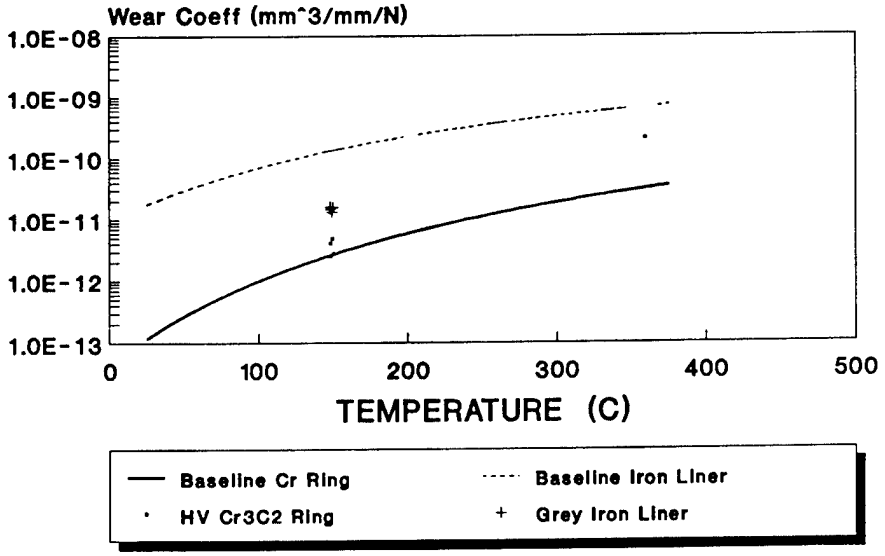

Fig. 7. Wear rates of lubricated HV Cr_3C_2-WC-Ni-Cr vs grey cast iron as a function of temperature (data points). The solid line represents the wear rate of electroplated chromium piston rings sliding against grey cast iron, and the broken line represents wear rates of grey iron against electroplated chromium. Cameron Plint data.

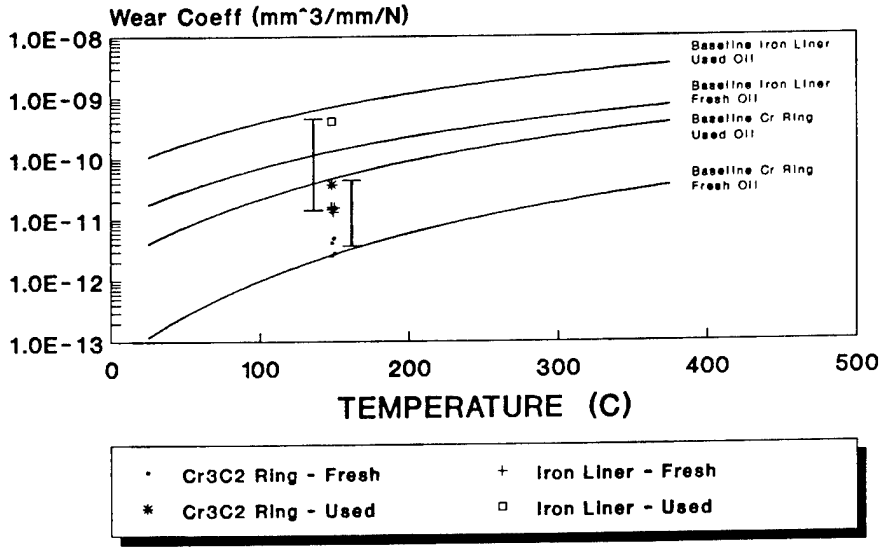

Fig. 8. Wear rate of lubricated HV Cr_3C_2-WC-Ni-Cr vs grey cast iron as a function of temperature (data points) in fresh and engine-tested lubricants. Cameron Plint data.

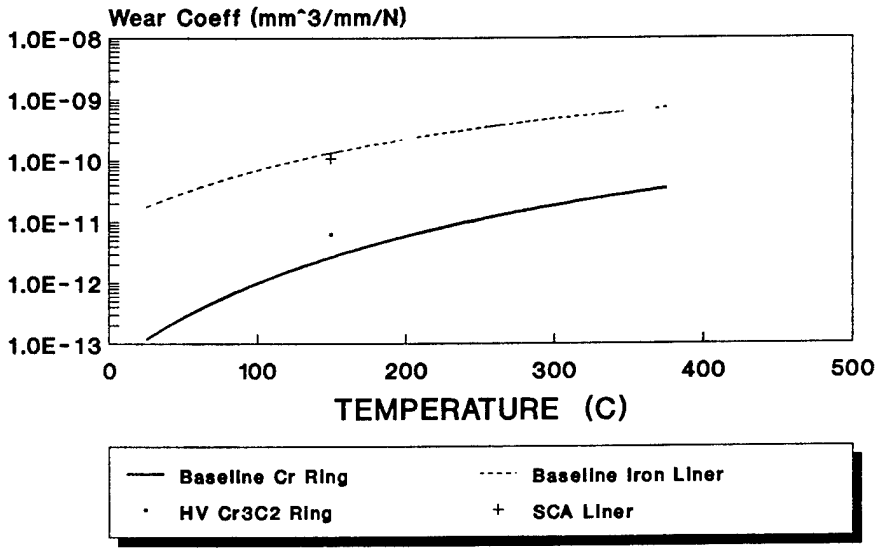

Fig. 9. Wear rates of lubricated HV Cr_3C_2-WC-Ni-Cr vs silica-chromia-alumina as a function of temperature (data points). The solid line represents the wear rate of electroplated chromium piston rings sliding against grey cast iron, and the broken line represents wear rates of grey iron against electroplated chromium. Cameron Plint data.

Microstructural characterization and adherence testing

APS chromium oxide - Figures 10 and 11 show the microstructures of the APS Cr_2O_3 coatings tested in this program. The initial tests were performed with a coating sprayed from Metco 136 powder, having a thickness of approximately 100 μm. The second coating to be tested was sprayed using a Union Carbide Cr_2O_3 powder with no additives. The spray parameters for this second coating are listed below (test 3).

A study of the effect of plasma spray process variables on coating adhesion and microstructure has been conducted for APS chromium oxide (Cr_2O_3). Two powders were used: a commercial Cr_2O_3-TiO_2-SiO_2 (Metco 136) and a pure Cr_2 material (U-Car). In all cases, a Metco 447 bond coat was used. The test parameters are listed in Table 5, key variables being powder composition, powder feed gas (argon or oxygen), powder feed rate and spray velocity (arc gas flow rate). Two guns were used: an Avco gun for lower velocities, and a Plasmadyne SG-100 gun with various nozzles for higher velocities (tests 9, 10, 13 and 14 produced Mach 1 spray velocities). In addition, test 15 used an inert argon shroud around the plasma spray.

The bond strengths of the coatings were measured by tensile pull tests (using fixtures bonded to the coating with epoxy cement). Bond strength data are presented in Table 6 and Fig. 12. Light microscopy was used to determine the relative porosity levels of the coatings (listed in Table 7).

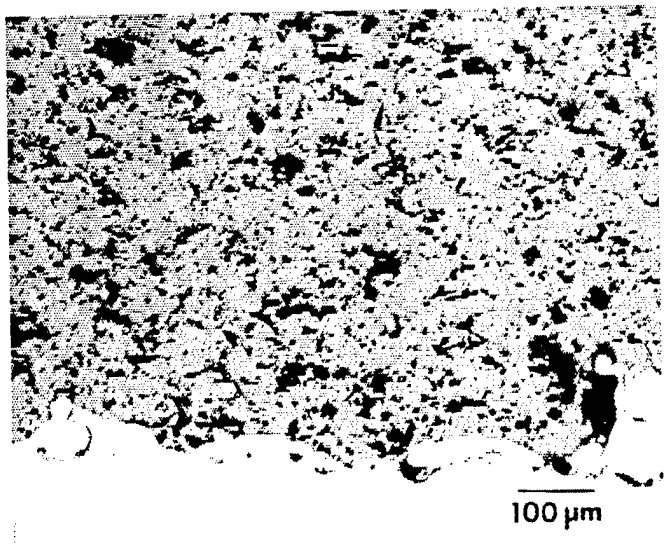

Fig. 10. Light micrograph of Metco Cr_2O_3 coating.

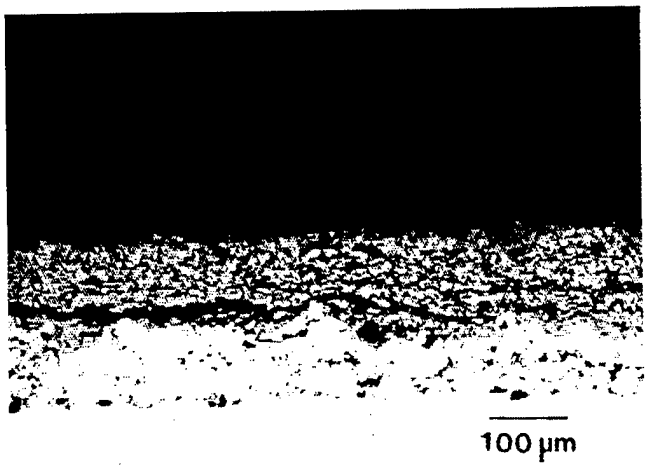

Fig. 11. Light micrograph of U-Car Cr_2O_3 coating.

Table 5. Chromium oxide spray conditions.

Test	Amps	Volts	Arc Gas	Mix Gas	Pwdr Gas	Hopper	Gun	Nozzle	Powder
1	600		40	12-He		40%	Avco	065	M-136
2	500		40	12-He		40%	Avco	065	M-136
3	500		60	3-Hyd	10	30%	Avco	315	M-136
4	500		60	3-Hyd	10	30%	Avco	315	U-Car
5	600		40	12-He	20-Oxy	1%	Avco	315	M-136
6	600		40	12-He	20-Oxy	1%	Avco	315	U-Car
7	900	35	50	60-He	12	1%	SG-100	165	M-136
8	900	35	50	60-He	12	1%	SG-100	165	U-Car
8-A	700	34	50	60-He	15	1%	SG-100	165	U-Car
8-B	700	34	50	60-He	15	1%	SG-100	165	M-136
9	700	52	270	45-AR,N	18	3 RPM	SG-100	360	M-136
10	700	52	270	45-AR,N	18	3 RPM	SG-100	360	U-Car
11	700	34	50	60-He	15	1%	SG-100	165	M-136
12	700	34	50	60-He	15	1%	SG-100	165	U-Car
13	1000	45	115	45-AR,N	10	1.4 RPM	SG-100	360	M-136
14	1000	45	115	45-AR,N	10	1.4 RPM	SG-100	360	U-Car
15	900	51	116	83-He	6	1.4 RPM	SG-100	165	M-136

Note: Test 15 used an inert argon shroud with nitrogen coolers

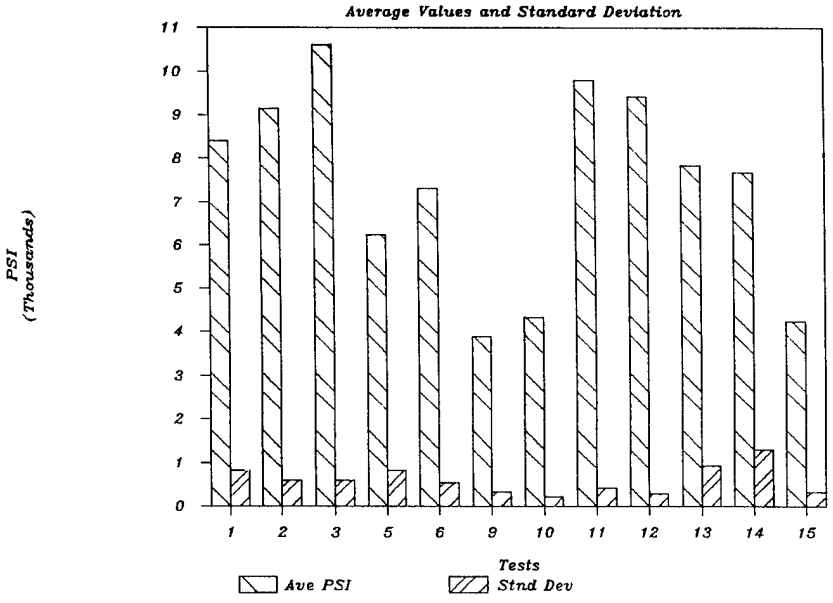

Fig. 12. Tensile bond strength data for APS chromium oxide coatings produced by various spray conditions (listed in Table 5).

Table 6. Tensile bond test results for chromium oxide coatings (see Table 5 for spray conditions).

Test	Force	PSI	Ave	Deviation	Powder	Mode
1	6600	8403	8403	832	Metco 136	Bnd/25%Cer
	5800	7385				Bond
	7400	9422				Ceramic
2	7800	9931	9146	602	Metco 136	Bnd/Epo
	7100	9040				Bnd/Epo
	6650	8467				Epoxy
3	8800	11205	10610	591	Metco 136	Epoxy
	8500	10823				Epoxy
	7700	9804				Epoxy
5	4000	5093	6239	825	Metco 136	Bnd/Cer Int
	5500	7003				Bnd/Cer Int
	5200	6621				Bnd/Cer Int
6	5250	6685	7321	548	U-Car	Bnd/Cer Int
	5700	7257				Bnd/Cer Int
	6300	8021				Int/Cer
9	2950	3756	3883	325	Metco 136	Bnd/Cer Int
	3400	4329				Bnd/Cer Int
	2800	3565				Int/Bnd
10	3650	4647	4329	227	U-Car	Bnd/Cer Int
	3300	4202				Bnd/Cer Int
	3250	4138				Int/Bnd
11	8000	10186	9846	480	Metco 136	Epoxy
	7200	9167				Epoxy
	8000	10186				Epoxy
	7900	10059	9815	610	Metco 136	Epoxy
	7050	8976				Epoxy
	8175	10409				Epoxy
12	7400	9422	9433	299	U-Car	Epoxy
	7700	9804				Epoxy
	7125	9072				Epoxy
13	5175	6589	7841	939	Metco 136	Ceramic
	6350	8085				Ceramic
	6950	8849				Ceramic
14	5650	7194	7692	1309	U-Car	Epoxy
	5025	6398				Epoxy
	7450	9486				Epoxy
15	3350	4265	4244	338	Metco 136	Bnd/Cer Int
	3000	3820				Bnd/Cer Int
	3650	4647				Bnd/Cer Int

Table 7. Relative levels of porosity/microcracking of chromium oxide coatings assessed by light microscopy. 1 = LOWEST; 5 = HIGHEST.

Test	1	2	3	4	5	6	7	8	8A	8B	9	10	11	12	13	14	15
Porosity	2	3	2	2	1		1		3	1	3	3	5	4	1		2

The following conclusions were drawn from the above study:

1. The pure Cr_2O_3 had slightly greater adherence than the Metco 136 (disregarding failures in the epoxy), but there was no significant effect on density.

2. The oxygen powder feed gas produced higher densities but lower bond strengths than with argon. The lower bond strength may have resulted from oxidation of the bond coat.

3. Reducing the powder feed rate resulted in slightly higher bond strength, but had no effect on density.

4. Higher velocity coatings generally had lower bond strengths. There was no consistent effect of velocity on density for these conditions.

5. The argon shroud with inert cooling produced a coating with fairly low bond strength and average density.

Wear test samples have been prepared using the conditions of test 3 (the optimum combination of bond strength and density), for both types of powder. The coatings were applied to an HK40 austenitic stainless steel substrate (4 in. diam). Results for the U-Car coating are described above.

High velocity WC-Co - Although the wear rates for the HV WC-Co material were extremely low, the coating was found to crack during the 250°C wear tests. Light micrographs of the pre-test coating showed almost continuous cracking at the substrate interface, indicating poor adherence (Fig. 13a). The microstructure was comprised of 5 μm WC particles in a Co matrix with low levels of porosity (<10%). The coating hardness was 1050 ($\pm$ 60) kgfmm^{-2} (Knoop, 100 gf). SEM examination revealed little solutionizing of the carbide particles (Fig. 13b).

High velocity Cr_3C_2-WC-Ni-Cr - The microstructure of the HV Cr_3C_2-WC-Ni-Cr was comprised of 10 μm particles of WC and mixed Cr/W carbides in a Cr-Ni matrix (Fig. 14). Porosity was approximately 10-15%. The coating hardness was 1000 ($\pm$ 45) kgfmm^{-2} (Knoop, 100 gf).

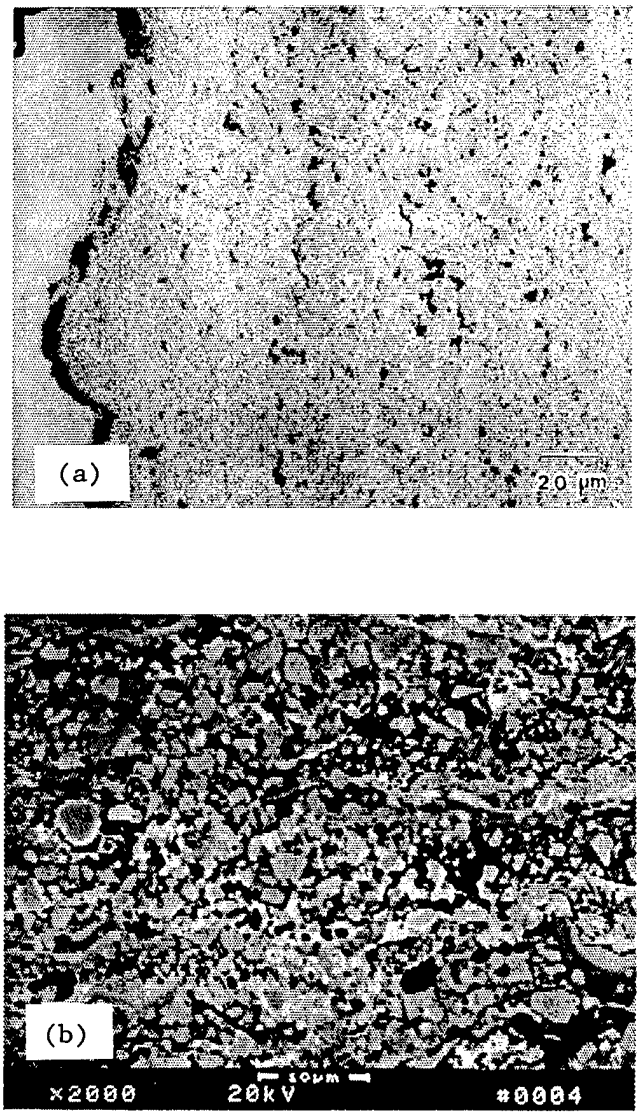

Fig. 13. Micrographs of high velocity thermal spray 88% WC-12% Co. (a) Light micrograph; (b) SEM micrograph (backscattered electron image).

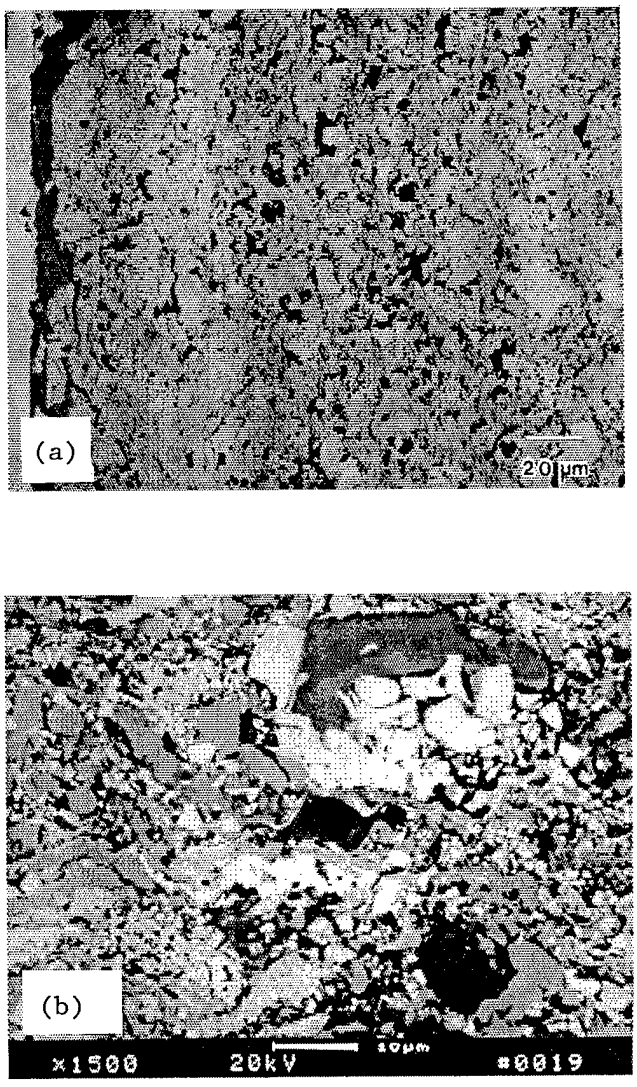

Fig. 14. Micrographs of high velocity thermal spray Cr_3C_2-WC-Ni-Cr. (a) Light micrograph; (b) SEM micrograph (backscattered electron image).

Analysis of worn surfaces - Analysis of the Cr_2O_3 wear surfaces was presented in the previous semiannual report. SEM micrographs of wear surfaces for the two HV coatings are shown in Figs. 15 and 16, for a grey cast iron counterface. In both cases, the carbide particles were polished smooth and protruded slightly from the softer metallic binder phase. The HV Cr_2O_3-WC-Ni-Cr surface revealed more porosity or inter-splat fracture, and also showed possible evidence of fracture within the ceramic phases (Fig. 16). It is difficult to determine the microstructural features responsible for the difference in wear behavior of the two HV materials investigated, but factors may include grain size, inter-splat adhesion, porosity and hardness/toughness of the ceramic phases.

Status of milestones

Task 1 - Experimental plan and coating deposition
Task 2 - Characterization
Task 3 - Selection of coating
Task 4 - Fabricate components
Task 5 - Reporting
Task 6 - Quality assurance

Tasks 1 (duration 18 months) and 2 (duration 16 months) are in progress and on schedule.

Publications

None

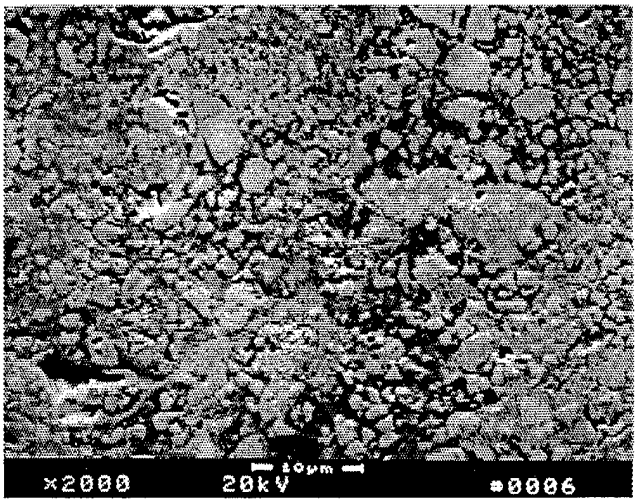

Fig. 15. Wear surface of HV WC-Co
Counterface: grey cast iron
Lubricant: CE/SF 15W40
Temperature: 150°C
Cameron Plint, 225 N, 20 Hz, 5 mm stroke, 360 min.

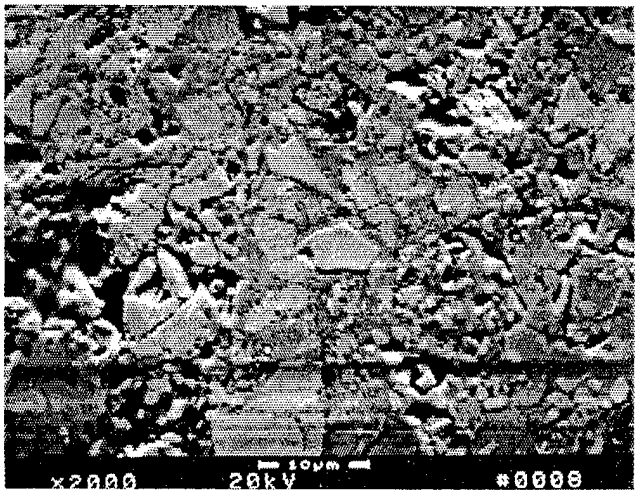

Fig. 16. Wear surface of HV Cr_3C_2-WC-Ni-Cr
Counterface: grey cast iron
Lubricant: CE/SF 15W40
Temperature: 150°C
Cameron Plint, 250 N, 20 Hz, 5 mm stroke, 360 min.

1.4 JOINING

1.4.1 Ceramic-Metal Joints

Joining of Ceramics for Heat Engine Applications
M. L. Santella (Oak Ridge National Laboratory)

Objective/scope

The objective of this task is to develop strong reliable joints containing ceramic components for applications in advanced heat engines. Presently, this work is focused on the joining of partially stabilized zirconia and silicon nitride by brazing. The technique of vapor coating ceramics to circumvent wetting problems that was developed for brazing zirconia at low temperatures will also be applied to brazing silicon nitride. The emphasis of this activity during FY 1989 will be on: (1) completing the initial assessment of zirconia joint strength, (2) high-temperature brazing of titanium-vapor-coated silicon nitride, (3) correlating braze joint microstructures with strength data to identify factors controlling joint strength, and (4) developing a method of calibrating the indentation fracture technique to determine the accuracy of residual stresses measurements in ceramic-to-metal joints.

Technical progress

Areas in which there was significant technical activity are outlined in the following sections.

Brazing of zirconia

Microstructure of Ti-vapor-coated ZrO_2 braze joints - The results of initial microstructure analysis and strength testing of ZrO_2 braze joints were discussed in previous reports. A more thorough micro-analysis is continuing, and some general observations obtained for Ti-vapor-coated ZrO_2 braze joints, as well as the results obtained from examination of ZrO_2-ZrO_2, ZrO_2-cast iron, and ZrO_2-Ti joint strength test specimens, are detailed in this report.

A detailed view of a braze joint microstructure, Fig. 1, shows that two layers were found at the Ti-vapor-coated ZrO_2 surface after brazing. Microchemical analysis by scanning electron microscopy (SEM) indicated that the dark layer directly in contact with the ZrO_2 was the remnant of the original Ti vapor coating. The second layer, which formed between the Ti vapor coating and the braze filler metal, had a composition of 22Ag-30Cu-25Sn-19Ti-4Zr, wt %. The microstructure shown in Fig. 1 indicates that the Ti vapor coating isolated the ZrO_2 from direct contact with the liquid filler metal, and that wetting resulted from reaction of the braze filler metal with the Ti coating to form a metallic or intermetallic reaction layer. The combined thickness of the two reaction layers was approximately the same as the thickness of the Ti vapor coating before brazing, nominally 0.6 μm. These reaction

layers were so thin that accurate chemical analysis was not possible because the volume of material activated by electron probe microanalysis is typically of the same width or larger that the width of the layers.

Visual examination of the braze joints showed that the ZrO_2 within about 1 mm of the brazed surfaces became black due to the depletion of oxygen. This discoloration indicates that some reaction between the ZrO_2 and the Ti vapor coating occurred during brazing. One possible reaction is the reduction of ZrO_2 by the solid Ti vapor coating to form TiO. However, standard free energy data indicate that the reduction of ZrO_2 by Ti is not favorable at the brazing temperature of 735°C:

$$ZrO_2(s) + 2\ Ti(s) = 2\ TiO(s) + Zr(s) \qquad \Delta G^\circ = +6.4\ \text{kcal/mol}.$$

In other words, ZrO_2 is be more stable because of its lower free energy of formation.

A second possible reaction between the ZrO_2 and the Ti vapor coating is diffusion of oxygen out of the ZrO_2 into the Ti. Oxygen is relatively mobile in ZrO_2 and interstitially soluble in α-Ti up to 34 at. %. The thermodynamic property that governs the oxidation-reduction behavior of Ti-O solutions is the partial molar free energy of the oxygen. When pure Ti is placed in contact with ZrO_2 at constant temperature, the Ti will extract oxygen until a concentration is reached where the partial molar free energy of oxygen in the solution equals the free energy of formation of ZrO_2. Figure 2 shows the partial molar free energy of oxygen in Ti-O interstitial solutions and the free energies of formation of some stoichiometric titanium oxides at 735°C. The solid horizontal line indicates the free energy of formation of ZrO_2 at the same temperature. As shown in this free energy diagram, oxygen will diffuse out of the ZrO_2 until the oxygen concentration in the Ti reaches about 45 at. %.

This analysis indicates that Ti and ZrO_2 will react at the brazing temperature, and suggests that a possible reaction product might be substoichiometric TiO. However, the reaction predicted relies on oxygen diffusion out of the ZrO_2 and in situ transformation of the Ti vapor coating rather than on the formation of a new phase at the ZrO_2-Ti vapor coating interface due to chemical reaction. This difference in reaction details is subtle but may be important because interface phases formed by chemical reaction are generally thought to promote better adhesion of vapor coatings compared to those formed by diffusion alone. Partial oxidation of the Ti vapor coating may also explain why it did not react completely with the braze filler metal.

The other features in Fig. 1 are the Ag-rich and Cu-rich braze filler metal phases which appear as light and dark regions, respectively, and the ZrO_2. The dark particles in the ZrO_2 are actually pores which were not eliminated during sintering of the oxide. The microstructure at the brazed ZrO_2 surface was the same for joints of ZrO_2-ZrO_2, ZrO_2-Fe, and ZrO_2-Ti.

Flexure testing of zirconia active substrate braze joints - The results of initial flexure testing of the Ti-vapor-coated ZrO_2-ZrO_2, ZrO_2-Fe, and ZrO_2-Ti braze joints have been discussed previously, and are summarized in Table 1 for reference. Optical examination of the broken test bars indicated that most of them fractured near one of the brazed surfaces regardless of materials and testing temperature. This not surprising because the greater strength and stiffness of the ZrO_2, cast iron, and Ti compared to those of the Ag-30Cu-10Sn braze filler metal would cause strain to be concentrated in the braze filler metal layer during flexure testing. This observation also suggested that adhesion of the Ti vapor coating to the ZrO_2, and bond zone microstructure were important factors for determining joint strength.

The fracture characteristics of selected test bars were examined in more detail by SEM. The overall fracture surface of one of the high strength (σ_f = 571 MPa) ZrO_2-ZrO_2 joints tested at room temperature is shown in Fig. 3(*a*). The fracture surface was relatively planar. Also, large fragments of the braze filler metal adhered to the surface after testing and indicate that failure occurred simultaneously along both of the brazed ZrO_2 surfaces. Examination at higher magnification, Fig. 3(*b*), showed that the appearance of much of the surface was similar to the fracture appearance of monolithic ZrO_2, and confirmed that a substantial amount of fracturing in this joint specimen occurred in the ZrO_2 just below the ZrO_2-Ti vapor coating interface. The fracture appearance of this specimen is compared in Fig. 4 to that of a lower strength (σ_f = 269 MPa) ZrO_2-ZrO_2 joint tested at room temperature. Some fracturing occurred in the ZrO_2 in the lower strength joint, but the relatively smooth areas shown in Fig. 4(*b*) indicate that failure in this joint was accompanied by a large amount of debonding between the ZrO_2 and the Ti vapor coating.

The general fracture pattern of the ZrO_2-ZrO_2 joints tested at 200°C was similar to that of the joints tested at 25°C. An example of the fracture appearance from a test done at 400°C is shown in Fig. 5. The fracture surfaces at this test temperature were typically smooth and contained only isolated fragments of metallic phases. Essentially no fracturing of the ZrO_2 was found for the 400°C tests, but failure was mainly associated with debonding at the ZrO_2-Ti vapor coating interface. For the tests done at 575°C fracture occurred exclusively through the metallic phases.

The fracture surface shown in Fig. 6(*a*) is typical of the higher strength (354-399 MPa) ZrO_2-Fe joints tested at 25°C. These test specimens were characterized by regions that were relatively flat and other areas where large fragments of the ZrO_2 was pulled out of the base material. This behavior indicates that the joints failed by a combination of debonding at the ZrO_2-Ti vapor coating interfaces and fracturing of the ZrO_2 near the brazed surfaces. A more detailed examination of the surface shown in Fig. 6(*a*) indicated that fracture initiated near the ZrO_2-Ti vapor coating interface and eventually led to the pullout of a large piece of the ZrO_2 adjacent to the brazed surface. Examination of the fracture surface near the tensile face of the specimen at higher magnification, Fig. 6(*b*), showed that areas of the Ti coating were still adhering to the zirconia after fracture.

The lower strength (25, 36, 102, and 149 MPa) ZrO_2-Fe joints tested at 25°C behaved in a completely different manner. In this case, the braze filler metal did not adhere to the Ti-vapor-coated ZrO_2; and while it bonded to the Cu plating, the Cu plating did not adhere to the Fe. When the joints were tested, the layer composed of the resolidified braze filler metal and the Cu plating simply fell away from the joint. Microchemical analysis in the SEM indicated that the filler metal fragments, remnants of the Cu plating, and the surface of the cast iron all contained high levels of phosphorus and potassium. These contaminants apparently were introduced by improper process control or cleaning procedures during the Cu-plating operation and were responsible for the very low ZrO_2-Fe joint strengths recorded at all four test temperatures.

The uncontaminated ZrO_2-Fe joints tested at 200°C and 400°C failed in much the same manner as those tested at 25°C, but also had indications of ductile failure in the metallic phases. The ZrO_2 half of a ZrO_2-Fe joint tested at 400°C, shown in Fig. 7(*a*), indicates that fracture may have initiated near the ZrO_2-Ti vapor coating interface, but that its path was mainly through the metallic bond zone layer. Failure occurred by ductile void coalesence in the metal layer as shown in Fig. 7(*b*). Microchemical analysis showed that the surface in Fig. 7(*b*) was entirely Cu, and confirmed that failure was associated primarily with the Cu plating on the cast iron. Joint strength at 575°C was also limited by the strength of the Cu plating.

The ZrO_2 surface of a ZrO_2-Ti joint tested at 25°C is shown in Fig. 8. The tension face of this bend bar is at the top of Fig. 8 and a large portion of surface is covered by the metallic bond zone layer. Further examination and microchemical analysis indicated that failure initiated near the interface between the Ti half of the joint and a Ti-Cu intermetallic layer formed by reaction of the Ag-30Cu-10Sn, wt %, filler metal with the Ti metal. Figure 8 also shows that the fracture path eventually diverted to the ZrO_2 just below the ZrO_2-Ti vapor coating interface. The strength of this joint was 470 MPa, and the fracture characteristics of several of the higher strength joints were identical to this one. In the lower strength ZrO_2-Ti joints tested at 25°C, failure initiation occurred near the ZrO_2-Ti vapor coating interface, and the fracture paths were along this interface and in the ZrO_2 near the interface.

The behavior of the ZrO_2-Ti joints tested at 200°C was similiar to that of the lower strength joints tested at 25°C, but with slightly more debonding at the ZrO_2-Ti vapor coating interface and some fracture through the Ti-Cu intermetallic phases near the bulk Ti surface. Failure in the ZrO_2-Ti joints tested at 400°C and 575°C was associated with intermetallic and metallic phases in the bond zones of the joints.

The SEM observations of joints tested at 25°C indicate that for all three joint types the highest joint strengths were associated with partial or complete fracturing of the ZrO_2 beneath the Ti-vapor-coated surfaces. The high strength ZrO_2-ZrO_2 joints failed almost entirely through the ZrO_2. Considerable fracture through the ZrO_2 was also observed for the higher strength ZrO_2-Fe and ZrO_2-Ti joints. Similarly, the trend for the lower strength joints was that fracture was characterized by a noticeable fraction of debonding at the ZrO_2-Ti vapor coating

interfaces as illustrated by Fig. 4. Overall, the good strength of the joints indicates that the adhesion of the Ti vapor coating was excellent and was a critical factor in determining joint strength. The 25°C data also indicate that the strength of all three types of joints decreased as debonding of the Ti vapor coating from the ZrO_2 surfaces became more prevalent. These observations imply that room-temperature joint strength can be increased by improving the strength and uniformity of bonding of the Ti vapor coating to the oxide surfaces.

Even in the ZrO_2-ZrO_2 joints that fractured entirely through the ZrO_2, the joint strength at 25°C was below that of the monolithic ZrO_2. This fact along with the observation that fractures in the ZrO_2 always occurred near the brazed surfaces indicates that near-surface microcracking in the ZrO_2 may have controlled joint strength in cases where adhesion of the Ti vapor coating was complete. All ZrO_2 coupons were ground to a relatively fine finish (180-220 grit diamond) and carefully cleaned before vapor coating with Ti and brazing, but no special attempt was made to remove surface damage that may have resulted from grinding operations. No microcracks were observed on unstrained metallographically prepared surfaces, but it is known that preexisting surface damage can reduce joint strength. In addition, the difference in thermal expansion coefficients between the ZrO_2 and the braze filler metal ($\Delta\alpha \approx 9$ μm/m/°C) will produce residual stresses near the brazed ZrO_2 surface which will contribute to the ZrO_2-ZrO_2 joints having lower strength than the monolithic ZrO_2.

The difference in thermal expansion coefficients between the ZrO_2 and the cast iron ($\Delta\alpha \approx 4$ μm/m/°C) undoubtedly was responsible for the lower room-temperature strength of the ZrO_2-Fe joints compared to the ZrO_2-ZrO_2 joints. The residual stresses produced in the ceramic-metal joint would be much larger than those produced by the metallic braze filler metal layer of a ceramic-ceramic joint. Furthermore, a tensile component of residual stress would exist normal to the brazed ZrO_2 surface and it would reduce the level of applied stress necessary to cause failure.

Titanium was also selected for making ZrO_2-metal joints because its thermal expansion coefficient is approximately the same as that of the ZrO_2 ($\alpha \approx 10$ μm/m/°C). The higher average and maximum room-temperature strengths of the ZrO_2-Ti joints compared to the ZrO_2-Fe joints are an indication that residual stresses were minimized in the ZrO_2-Ti joints. However, the room temperature strength of the ZrO_2-Ti appeared to be limited by the strength of a Ti-Cu intermetallic layer that formed on the Ti surface during brazing, rather than adhesion of the Ti vapor coating on the ZrO_2.

The strength of the ZrO_2-ZrO_2 joints decreased progressively at 200°C and 400°C. At 200°C, debonding at the ZrO_2-Ti vapor coating interface appeared to increase, and at 400°C it was the predominate failure mode. The SEM examination of fracture surfaces indicated that joint strength at the higher temperatures was roughly an inverse function of the debonded area on the ZrO_2 surfaces. Adhesion of coatings is promoted by strong atom-atom bonding within the interfacial region, low local stress levels, and the absence of time-dependent degradation phenomena, but the factors that may limit adhesion are many

and they are not all well understood. The observation that debonding at the ZrO_2-Ti vapor coating interface became more prevalent at temperatures above 25°C may be an indication that chemical bonding or chemical reaction between the ZrO_2 and the Ti coating were never achieved. This conclusion is consistent with the thermodynamic analysis presented earlier, and it suggests that adhesion of the Ti vapor coating to the ZrO_2 surfaces was due to a mechanical interlocking mechanism or weak chemical bonding at an abrupt type of interface. The reduced adhesion at higher test temperatures that is implied by lower joint strengths, and the increase in debonded area on the fracture surfaces could both be the result of a relaxation of bonding at the interface between the ZrO_2 and the Ti coating by either of these mechanisms, and could be compounded by stresses induced by differential thermal expansion.

Loss of strength due to relaxation of mechanical interlocking at the Ti-vapor-coated ZrO_2 surface could also explain the lower strength of the ZrO_2-Fe and ZrO_2-Ti joints tested at 200°C. Fracture in the ZrO_2-Fe joints tested at 200°C was complicated by a component of ductile failure through the Cu plating in many specimens which contributed to lower joint strengths. A mixed failure mode combined with some debonding at the ZrO_2-Ti vapor coating interface observed in the ZrO_2-Ti joints tested at 200°C undoubtedly contributed to the lower strength of these joints as well.

The strength of the ZrO_2-Fe joints tested at 400°C was dominated by failure through the Cu plating applied to the cast iron. The Cu plating was used to prevent reaction of the braze filler metal with graphite in the cast iron. However, carbon has limited solubility in Cu and no apparent solubility in Ag. Therefore, it is possible that Cu plating of the cast iron may be unnecessary for obtaining acceptable braze joints with the Ag-30Cu-10Sn, wt %, filler metal. Eliminating the Cu plating may also result in improved joint strengths and reduced data scatter at 400°C.

Fracture through intermetallic layers at the bulk Ti surface was the main failure mode of the ZrO_2-Ti joints tested at 400°C. Titanium and copper react vigorously to form several brittle intermetallic phases which appeared to limit the strength of the ZrO_2-Ti joints at all test temperatures. Reduction or elimination of these phases by brazing with a lower-Cu braze filler metal may be one way of improving the strength of these joints.

The strengths of all three types of joints converge to relatively low values for testing at 575°C, and in each case failure was associated with fracture through the metallic phases. This is not surprising; the solidus temperature of the braze filler metal is near 620°C, so 575°C represents a very high temperature for joint strength testing. The test data presented indicate that the practical limit for obtaining reasonably strong joints with Ag-30Cu-10Sn filler metal is in the range of 400°C to 575°C.

This study confirmed that vapor coating with Ti is an effective way of promoting the brazing of ZrO_2 with a Ag-30Cu-10Sn alloy (AWS BVAg-18). Analysis of braze joint test specimens indicated that adhesion of the Ti vapor coating to the brazed ZrO_2 surfaces was

generally very good. The data further suggested that obtaining good coating adherence is a prerequisite to obtaining high strength braze joints, and that improvements in adhesion would improve joint strength at all test temperatures.

Brazing of silicon nitride

The metallographically prepared specimens of Ti-vapor-coated Si_3N_4 braze joints were examined for the presence of cracks that may have been present before brazing or that may have resulted from brazing. No cracks were found for the joint made with the 72Ag-28Cu braze filler metal. Cracks which intersected the brazed Si_3N_4 surface were found in both of the other joints. For the 82Au-18Ni braze filler metal, cracks up to 95 μm in length that extended 40 μm below the brazed surface were observed. For the 50Au-25Ni-25Pd braze filler metal, cracks up to 50 μm long extending 15 μm below the joint surface were found. The Si_3N_4 surfaces of these joints were left in the as-fired condition prior to vapor coating with Ti. They were not examined for cracks prior to brazing so these data do not demonstrate whether the cracks were actually produced by brazing. The data do, however, indicate a possible correlation between cracking and the behavior of the Ti vapor coating because the coating remained intact after brazing only for the 72Ag-28Cu alloy.

In the previous report it was noted that flexure strength data for joints made with the 72Ag-28Cu filler metal had higher average strength (326 ± 38 MPa) and lower scatter (m = 7.7) than joints made with the 50Au-25Ni-25Pd filler metal (σ_f = 264 ± 102 MPa, m = 2.4). Also, all of the flexure bars broke through the Si_3N_4, and with only a few exceptions the crack paths were within about 50 μm of the Si_3N_4-metal interfaces. The joint surfaces of these specimens were diamond ground to a 30 μm finish before being coated with Ti. These specimens also were not examined for cracking before the braze joints were made, or before flexure testing. However, all of this data together suggests that preexisting surface flaws or flaws induced at the Si_3N_4 joint surfaces during brazing may have controlled joint strength. Experiments to examine this problem in more detail are progressing.

Status of milestones

141106 Complete microstructural analysis of initial zirconia-to-zirconia and zirconia-to-metal braze joint flexure test specimens.

Results of this work are complete and are detailed in a publication draft entitled "Brazing Titanium-Vapor-Coated Zirconia." This manuscript is currently being cleared for journal publication. Draft copies of the manuscript are available on request.

Publications

The paper entitled "Strength and Microstructure of Titanium-Vapor-Coated Silicon Nitride Braze Joints" was presented at the 3rd International Symposium on Ceramic Materials and Components for Engines, November 28, 1988, in Las Vegas, and was accepted for publication in the conference proceedings.

Unpublished work

A talk entitled "Ceramic Joining for High Performance Applications" was presented at the Sixteenth Annual WATTec Interdisciplinary Technical Conference and Exhibition, February 16, 1989, in Knoxville, TN.

Table 1. Fracture strength of Ti-vapor-coated ZrO_2 braze joint flexure test bars

Joint	Test Temperature (°C)	No. of specimens (MPa)	Range of strength (MPa)	Average strength
ZrO_2-ZrO_2	25	14	269–571	421 ± 95
	200	7	239–459	355 ± 74
	400	9	199–370	292 ± 55
	575	9	48–149	101 ± 32
ZrO_2-Cast Fe	25	9	25–399	241 ± 150
	200	4	58–363	246 ± 118
	400	6	53–364	203 ± 128
	575	7	16–101	51 ± 28
ZrO_2-Ti	25	9	307–470	370 ± 52
	200	8	106–353	266 ± 85
	400	9	137–212	178 ± 20
	575	7	49–128	102 ± 23

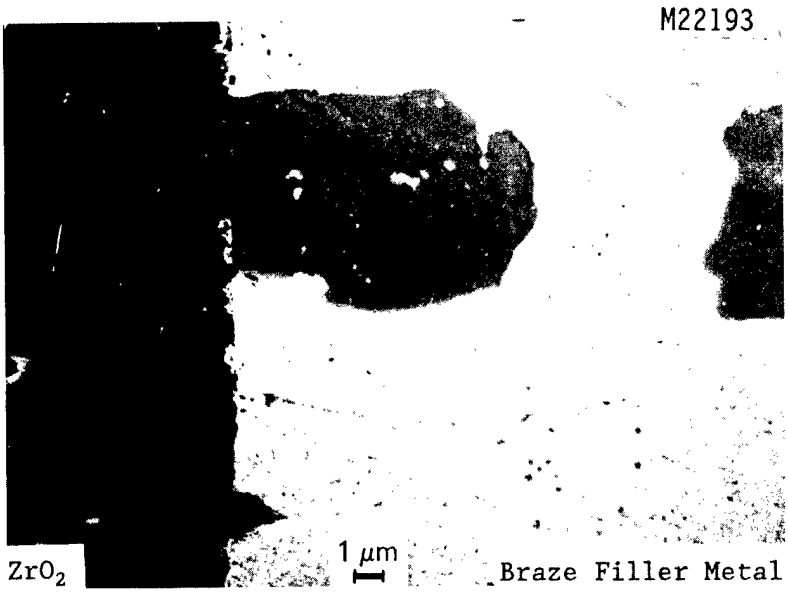

Fig. 1. Microstructure at Ti-vapor-coated ZrO_2 surface after brazing with a Ag-30Cu-10Sn, wt %, filler metal.

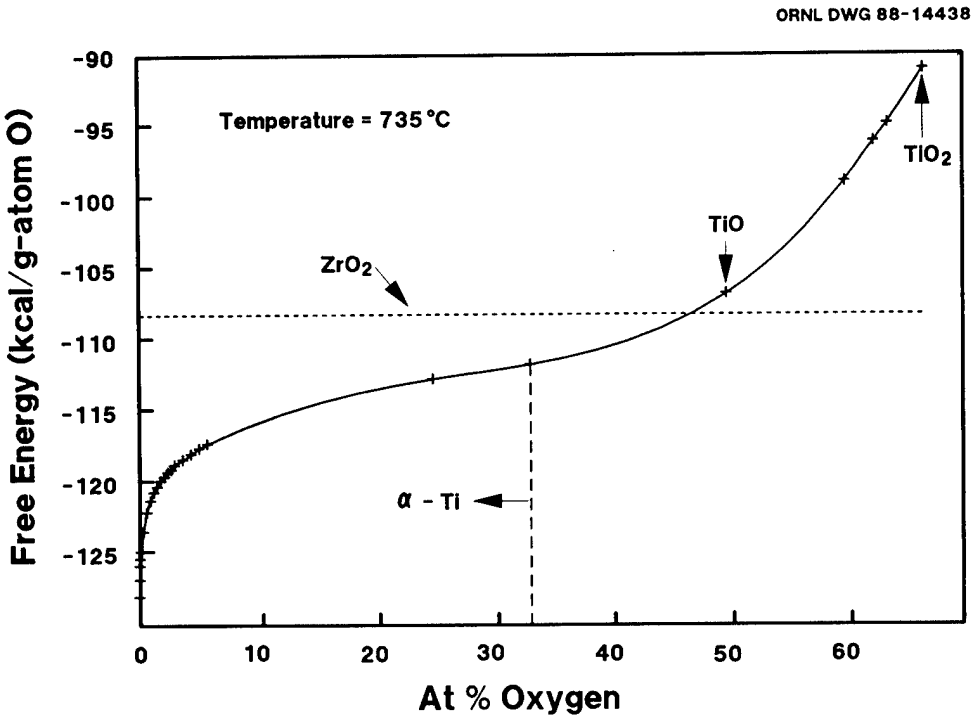

Fig. 2. Free energy of ZrO_2, titanium oxides, and Ti-O solutions.

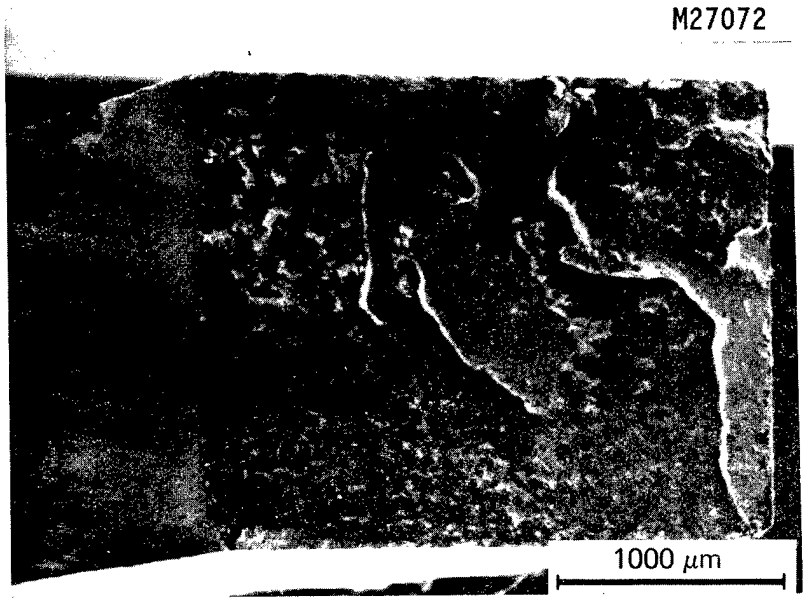

(a)

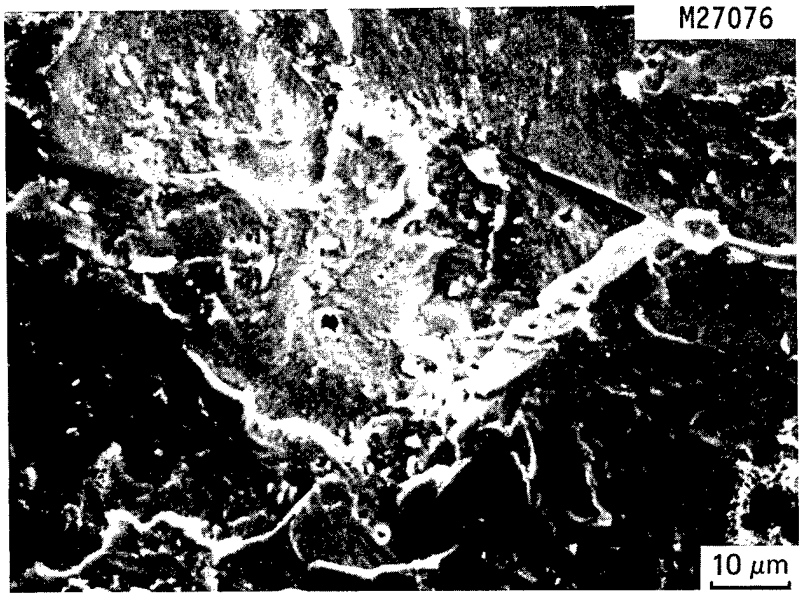

(b)

Fig. 3. SEM micrographs of high strength ZrO_2-ZrO_2 specimen tested at 25°C: (*a*) overall appearance, (*b*) ZrO_2 appearance beneath Ti-vapor-coated surface.

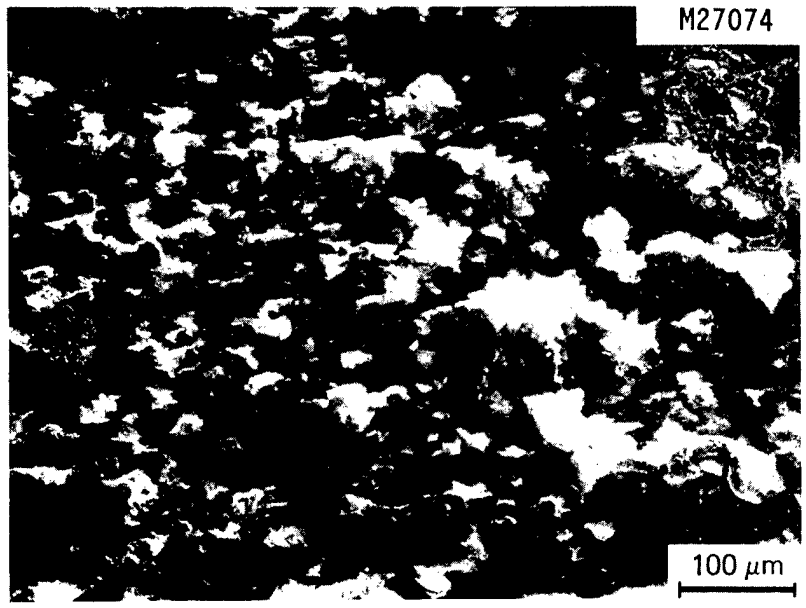

(a)

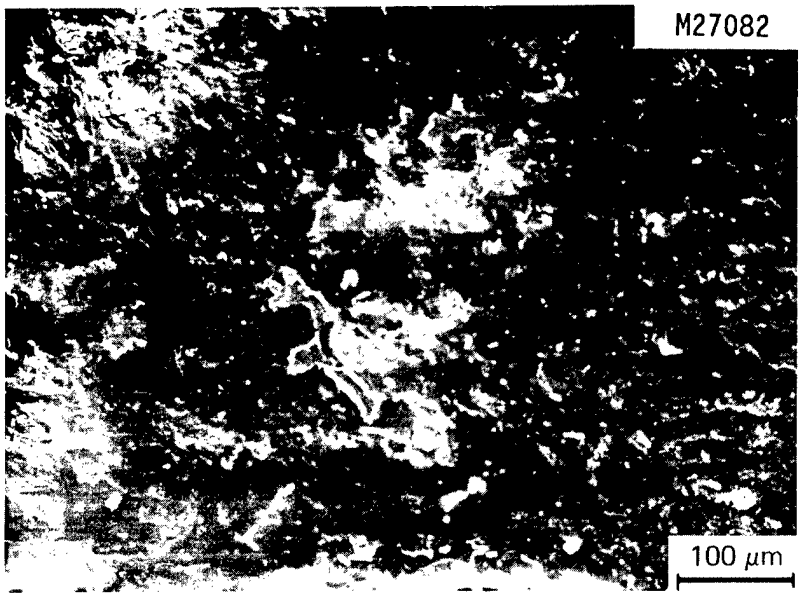

(b)

Fig. 4. SEM micrographs of ZrO_2-ZrO_2 specimens tested at 25°C: (*a*) σ_f = 571 MPa, and (*b*) σ_f = 269 MPa.

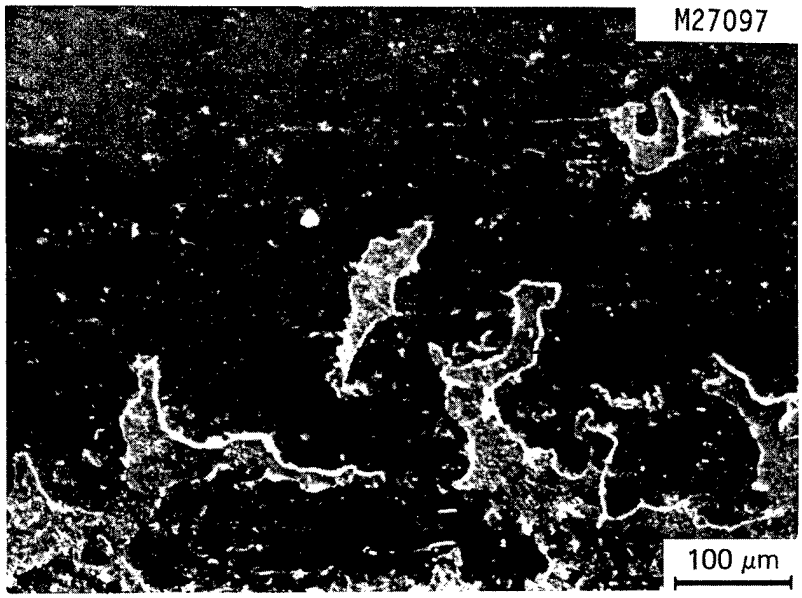

Fig. 5. Fracture surface of ZrO_2-ZrO_2 specimen tested at 400°C showed evidence of debonding at ZrO_2-Ti vapor coating interface.

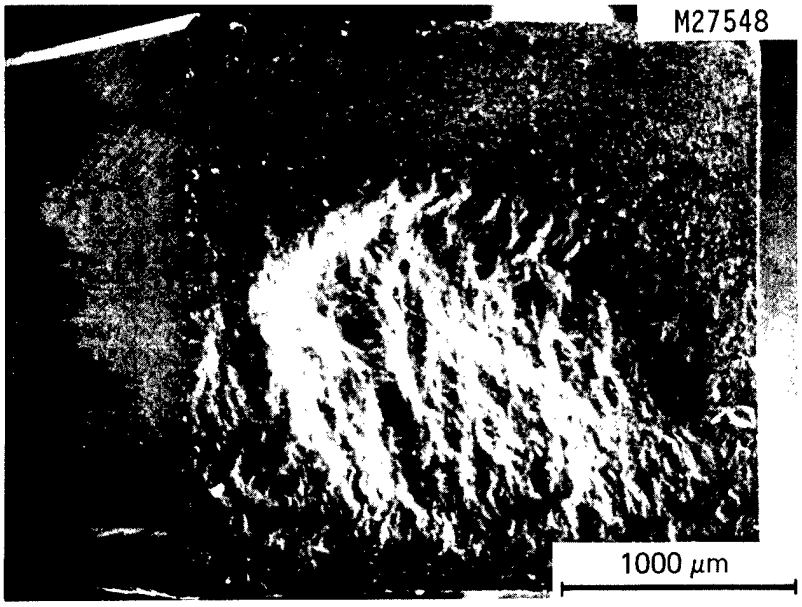

(a)

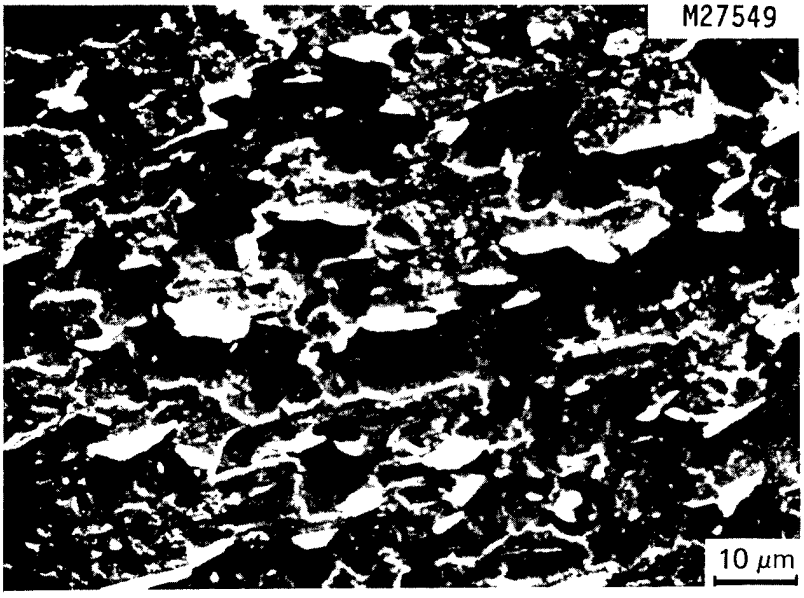

(b)

Fig. 6. SEM micrographs of high strength ZrO_2-Fe specimen tested at 25°C: (*a*) overall appearance, and (*b*) ZrO_2 surface near tensile face of bend test bar.

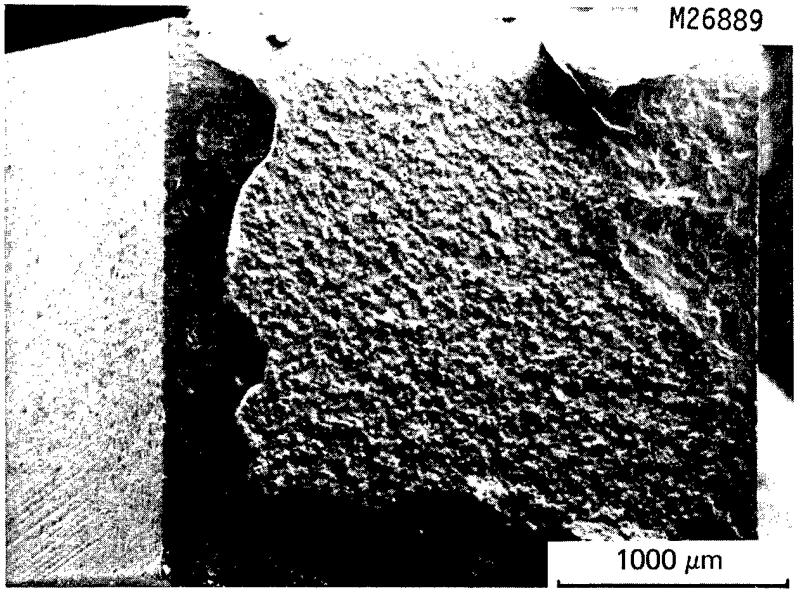

(a)

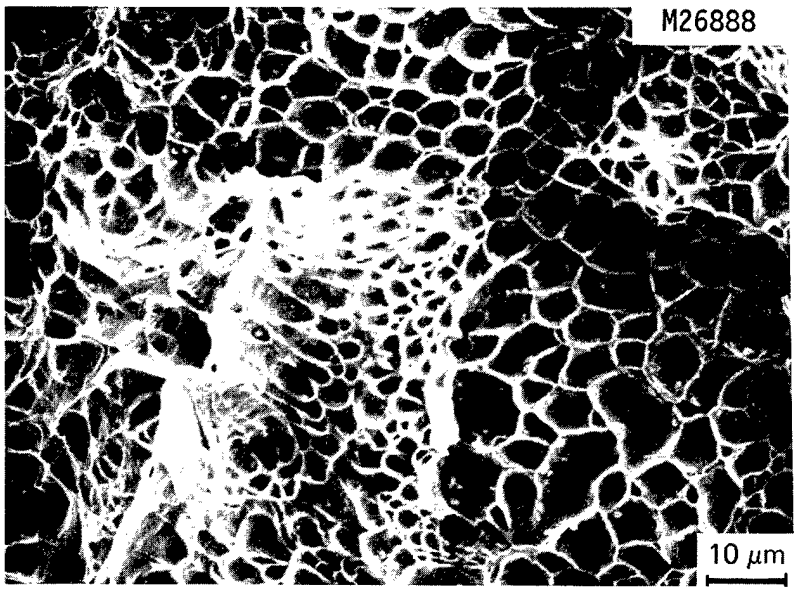

(b)

Fig. 7. SEM micrographs of ZrO_2 half of ZrO_2-Fe specimen tested at 400°C: (*a*) overall appearance, and (*b*) fracture appearance in Cu plating.

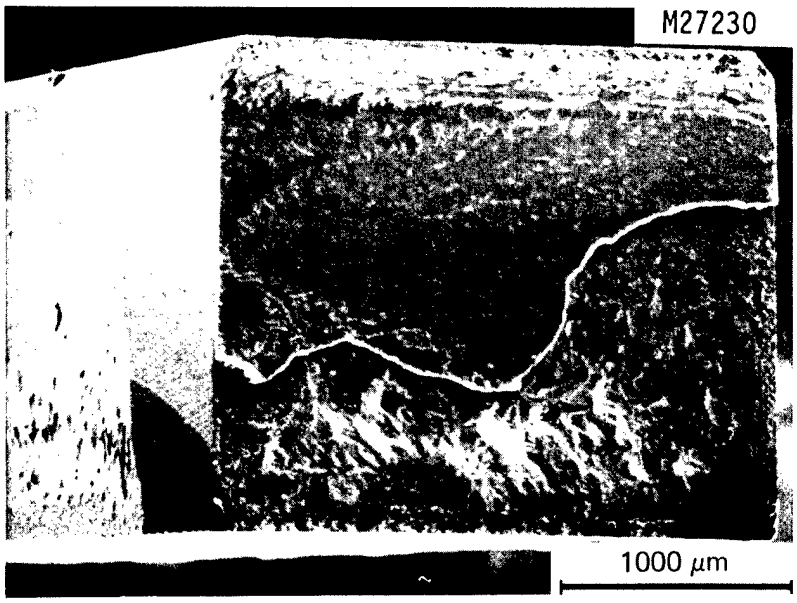

Fig. 8. Overall fracture appearance of ZrO_2 half of ZrO_2-Ti specimen tested at 25°C.

Analytical and Experimental Evaluation of Joining Silicon Nitride to Metal and Silicon Carbide to Metal for Advanced Heat Engine Applications - GTE Laboratories Incorporated

Objective/scope

The goal of this work is to demonstrate analytical tools for use in designing ceramic-to-metal joints including the strain response of joints as a function of the mechanical and physical properties of the ceramic and metal, the materials used in producing the joint, the geometry of the joint, externally imposed stresses both of a mechanical and thermal nature, temperature, and the effects of joints exposed for long times at high temperature in an oxidizing (heat engine) atmosphere. The maximum temperature of interest for application of silicon carbide to metal and silicon nitride to metal containing joints is 950°C. The initial joint fabrication work shall include "experimental" joints whose interfacial area is not less than two square centimeters. The work shall also include demonstration of the potential for scale-up of the joint size to interfacial areas of commercial significance, applicability of the analytical joint modeling tools and the ability to use these tools to design and predict the mechanical and thermal stability of the larger joints. These joints, referred to as "scale-up" joints, shall have an interfacial area of at least twenty square centimeters.

Technical progress

Finite Element Analysis (FEM) addressed the relative effectiveness of Mo vs Ni interlayers. Results showed that low yield stress Ni was more effective than low expansion coefficient Mo. Experimental results with coupon shear tests confirm this prediction.

The effects of temperature on the mechanical properties of the joint materials have been included in the finite element analysis (FEA) of the Task 2 joints. FEA has shown that the low yield stress Ni interlayer is better at reducing residual stress in the joint than is the low expansion coefficient Mo interlayer.

Good wetting was observed for the 950°C braze alloys, Palni, Palniro 1, Palniro 4, and Palniro 7, on Zr- and Ti-coated SNW1000.

An induction furnace was designed, installed, and calibrated for the elevated temperature mechanical testing.

The high temperature strength of brazed joints prepared with Palni and Palniro series alloys was measured. Hot shear testing at 500°C in an argon atmosphere indicated that the performance of the braze joint at 500°C is at least equivalent or better than the room temperature strength.

FEM analyses of proposed joint designs were conducted to determine the optimum interlayer thickness. In addition, the effect of peripheral groove radius and ta-

pering the end of the structural alloy were examined. The optimal interlayer thickness for Ni in the proposed configuration was found to be 1 mm. Grooves were determined to be beneficial but insensitive to radius. Tapering the structural alloy joint end was also beneficial.

An analytical framework for the evaluation of torsion tests has been proposed. In addition, the thermal and mechanical waveforms needed for cyclic testing have been generated.

Braze alloy design work resulted in qualification of Au-Ni-Ti and Au-Pd-Ni-Ti for 650°C. The Pd-Au system was previously reported as the choice for 950°C.

The nature of braze-ceramic interaction has been the subject of continued evaluation. TEM was used to document the reaction in the glassy phase.

Design/Criteria/Stress Analysis

Finite element analysis was performed on a Task II type specimen configuration utilizing an interlayer. The material properties are summarized in Table 1. Of particular interest is the use of Nioro braze properties of 62 ksi yield based on recent tests and a pure nickel interlayer with a yield stress of 8.5 ksi. Results of the FEM analysis yielded relative stress values of 2 compared with 9 and 10 in earlier cases without interlayers. Additional runs were made to determine the relative effect of Mo vs Ni as an interlayer. It was shown that Ni alone is significantly more effective than Mo alone. Slight improvements can be had by combining Ni and Mo if the NI is in contact with the ceramic. This arrangement is particularly effective, since the outer Mo layer reduces the contraction stresses on the ceramic because of its low coefficient of expansion. The Ni adjacent to the ceramic deforms to accommodate any remaining contraction. The constitutive equations used for this analysis were based on the room temperature stress-strain curves of each component in the joint.

Table 1: Materials Properties for FEM

	Ceramic	Structural Alloy Braze		Interlayers	
Properties	**PY6**	**Incoloy 909**	**Nioro**	**Mo**	**Ni**
Young's Modulus	43,000 ksi	23,000 ksi	8,150 ksi	46,000 ksi	29,500 ksi
Poisson's Ratio	0.23	0.24	0.36	0.3	0.31
Yield Stress	121 ksi	150 ski	62.0 ksi	80 ksi	8.5 ksi
Coeff. of Linear Thermal Expan.	3.4 E-6/C	9.0 E-6/C	17.5 E-6/C	6.4 E-6/C	13.4 E-6/C -18.3 E-6/C Rm. T-900°C

A new FEA of the joint was conducted with modified constitutive equations derived as a function of temperature; however, the mechanical properties of the braze were assumed to be temperature independent. Also, the number of elements was increased to highlight the stress distribution around critical crack initiation sites. The number of elements used was 166, 56, 140, and 192 for the ceramic, braze, interlayer, and structural alloy, respectively. While the predictions of the model were unchanged from those reported earlier, the accuracy of those predictions has been improved.

Temperature-dependent power law equations were used for the plastic deformation of the metal joint components. The following assumptions were made:

1. The strain hardening exponent, n, is independent of temperature

2. The strength coefficient, f(T), is a linear function of temperature

3. The young's modulus E(T), is a linear function of temperature

$$\sigma = E(T)\,\epsilon \qquad \text{in elastic range} \qquad \text{Eq. 1}$$

$$\sigma = f(T)\,\epsilon^{n} \qquad \text{in plastic range} \qquad \text{Eq. 2}$$

$$E(T) = E_o(1-\alpha\, T/T_m) \qquad \text{Eq. 3}$$

where σ, ϵ, E(T), n, and f(T), are true stress, true strain, Young's modulus, strain hardening exponent, a strength coefficient, respectively. α is a constant that equals 0.33 and 0.47 for the ceramic and braze, respectively. The ceramic was treated as a perfect elastic material, while the braze alloy was treated as an elastic-perfect plastic material.

The materials' properties as a function of temperature were used to calculate E(T), n, and f(T) for the components in the ceramic-metal joint system (Table 2). An improved FEA of the joint was performed using these modified constitutive equations, Equations 1-3. ABAQUS, version 4-5-138 was used for the FEA.

Table 2: The Temperature Dependence of the Elastic Modulus, E(T), Strain Hardening Exponent, n, and Strength Coefficient, f(T)

Material	E(T)	n	f(T)
Ni	-0.052T + 215.04	0.235	0.23T + 390.96
Mo	-0.060T + 329.37	0.099	-4.33T + 1136.51 ($20°C \leq T < 200°$)
			1.57T + 238.53 ($200°C \leq T < 300°$)
			-0.54T + 588.71 ($300°C \leq T < 800°$)
			-0.15T + 277.53 ($800°C \leq T < 1000°$)
Incoloy 909	-0.0054T + 158.69	0.0575	-0.35T + 1387.98
Ceramic	-0.049T + 279.52	1.00	N/A
Braze (Au-28% Ni)	-0.035T + 58.88	0.00	99.5 ksi

Mises equivalent stress determines the deformation of the metal components, while the maximum principal stress will determine cracking of the ceramic components. Therefore, contours of Mises equivalent stress in the metal and of the maximum principal stress in the ceramic were used to judge the joint's materials and design. For all of the analyses, 8 node biquadratic elements were used for the metal components. A fine mesh spacing was used for the interlayer to show the nonlinear plastic behavior of that layer.

The data shows that the Ni interlayer results in a lower principal stress in ceramic compared to the Mo interlayer. Therefore, Ni will reduce the chance of cracking in the ceramic. Mises equivalent stress in the Mo interlayer exceeds 2.00E8 Pa, whereas in the Ni interlayer this level of stress only occurs in the vicinity of the interface between the Ni and Incoloy 909.

Temperature Dependent Constitutive Equations for Joining Materials

Constitutive Equations for Ni and Incoloy 909 and PY6

The materials used in the ceramic-metal braze joint with a low α interlayer or a low yield stress σ_y, interlayer are:

Ceramic	PY6
Interlayer	Ni (low yield stress, σ_y)
Braze	Nioro
Structural Alloy	Incoloy 909

The constitutive equations for Ni, Incoloy 909 and PY6 were derived above. The constitutive equations for Ni and Incoloy 909 are given by equation 1 and a modified form of equation 2, given as equation 4.

$$\sigma = (AT + B)\epsilon^n \qquad \text{in the plastic range} \tag{4}$$

where for Ni $E(T) = -0.05197T + 215.0395$
$A = -0.2282$
$B = 390.9629$
$n = 0.235$

and where for Incoloy 909 $E(T) = -0.005415T + 158.6933$
$A = -0.34775$
$B = 1387.9768$
$n = 0.0575$

The constitutive equation for PY6 is:

$$\sigma = 279.518(1-0.33T/1900)\epsilon \tag{5}$$

Constitutive Equation for Nioro

A simple tension test on Nioro foil was carried out at room temperature. Experimental data are:

Elastic Modulus	5,568.00	ksi
Ultimate tensile strength	103.65	ksi
Yield strength	84.39	ksi
Elongation	0.048	

These data are close to the data in "Data Compilation for Ceramic-Metal Joining."[1] Because the testing machine was not extremely accurate, the data in "Data Compilation for Ceramic-Metal Joining" were used to derive the temperature dependent constitutive equation for Nioro.

Basic assumptions are:

1. Strain hardening coefficient n is independent of temperature.

2. f(T) is a linear function or piecewise linear function of temperature.

3. Young's modulus (E(T) is a linear function of temperature.

4. Ultimate tensile strength and yield strength are linear functions of temperature, and they are equal to zero at the melting temperature.

The equations for Nioro utilized the following coefficients:

where $E(T) = 58.875(1-0.47T/950)$ (GPa)
$A = -1.2558526$
$B = 1235.9366$
$n = 0.1289285$

The constitutive equations are shown in Figure 1.

Optimization of Ceramic-Metal Brazing Joint Geometry

Finite Element Analysis

Using the constitutive equations derived in the February Report for Ni, Incoloy 909 and PY6, the constitute equation derived in the previous section for Nioro, finite element analyses were carried out to optimize the geometry of the ceramic-metal brazing joint with Ni as the interlayer. The temperature change used was from the melting temperature of Nioro (950°C) to room temperature (20°C). This work was done at the University of Illinois by using ABAQUS Version 4-6-170 on a Covax computer.

The three basic geometries and finite element meshes of the ceramic-metal joint are shown in Figures 2 to 4.

Thickness of Ni Interlayer

For the basic geometry shown in Figure 2a, the thickness of the Ni interlayer was varied from 0.7 mm to 1.1 mm. Contours of the Mises equivalent stress (Figure 2b) and the largest principal stress of the ceramic-metal brazing joint after brazing were generated. The Mises equivalent stress and the largest principal stress for interlayer thicknesses equal to 0.7, 0.8, 0.9, 1.0 and 1.1 mm are shown in Figure 5. From the data on Ni in this figure, it can be noted that the joint with a Ni interlayer thickness of 1.0 mm seemed to be superior.

Effect of Groove

The geometry of the ceramic-metal brazing joint with a groove is shown in Figure 3a. The radius of the groove was varied from 0.3 mm to 1.0 mm. Contours of the Mises equivalent stress (Figure 3b) and the largest principal stress were generated. Comparing these data, it can be noted that the effect of the size of the groove is small. However, it is apparent that the von Mises equivalent and the largest principal stresses are reduced by introducing a groove.

Effect of Tapered End of the Structural Alloy

The geometry of a ceramic-metal brazing joint with a tapered end is shown in Figure 4a. The parameter a of the conic shape was varied from 0.2 mm to 1.0 mm. Contours of the Mises equivalent stress (Figure 4b) and the largest principal stress were calculated. Comparing these data, it can be noted that the effect of the size of the groove is small. However, comparing Mises equivalent stress and the largest principal stress for various configurations, it is obvious that these two stresses are reduced by tapering the end of the structural alloy.

Brazing Alloy Development

Alloys were considered for brazing Incoloy 909 to molybdenum because of the close thermal expansion match of the latter to silicon nitride. The gold alloys containing higher gold content than the lowest congruent melting composition will react with nickel or iron-based alloys resulting in an eroded braze joint. The resulting higher nickel-gold alloy will be much harder and will be a less forgiving joint between two dissimilar materials.

Four (4) gold alloy systems were studied:

Gold-Copper-Nickel-Titanium
Gold-Nickel-Titanium
Gold-Palladium-Nickel-Titanium
Gold-Nickel-Silicon-Titanium

The most promising alloy of the 4 gold alloy systems studied were gold-nickel-titanium system with nominal composition of:

Ni	3%
Ti	0.6%
Au	Balance
Liquidus	1020°C
Solidus	1000°C
Brazing Temperature	1020°C-1040°C

The alloy is very ductile, with a Knoop hardness of about 130.

An alloy with slightly higher melting temperature had a composition of:

Gold	91.5%
Nickel	2.0%
Palladium	5.0%
Titanium	1.5%

The liquidus/solidus of 1133°C/1077°C makes this alloy stronger at 650°C use temperature. This alloy with knoop hardness of 170 is less forgiving to plastic flow at elevated temperature than the gold-nickel-titanium alloy.

Gold-Based Alloy

Gold	87	-97%
Nickel	1	-12%
Titanium	.5	-1.5%
32 alloy compositions evaluated		
Liquidus	975 - 1030°C	
Solidus	961 - 1010°C	
Excellent system for Molybdenum.		

Gold-Nickel-Silicon Alloy

Gold	91	-98%
Nickel	1	-9%
Silicon	.1	-2%
Titanium	1	-2%
Liquidus	980 - 1070°C	
Solidus	940 - 1000°C	

47 alloy compositions studied.
Excellent wetting alloy.
Hard alloy.
Very ductile alloy.

Gold-Based Alloy

Gold	85	-94%
Nickel	2.5	-4.5%
Copper	2.5	-6.5%
Liquidus	950 - 1050°C	
Solidus	900 - 950°C	

22 alloy compositions investigated.
Wetting obtained, but melting temperature is too low. While the alloy is ductile, the "good alloys" were too hard.

Gold-Based Alloy

Gold	89	-94.5%
Palladium	5	-10%
Nickel	0	-3%
Titanium	0.5	-2%
Liquidus	1109 - 1232°C	
Solidus	1054 - 1185°C	

17 alloy compositions studied.
Excellent wetting alloy systems.
Excellent ductility and low hardness.

Only a few structural alloys are available that can be heated to 950°C in oxidizing atmosphere for long periods of time. Recommended precious metals such as palladium or platinum can be heated in air and are ductile and soft. These should be the principal materials for joining to silicon nitride.

$$\frac{950°C + 273°C}{1450°C + 273°C} = \frac{1223K}{1723K} = .71$$

950°C Brazing Alloy

Wetting tests of possible 950°C braze alloys were conducted on Ti-coated SNW1000. The detailed procedure was described in previous reports. Table 3 lists the compositions and test temperatures for each of the four brazes studied. The test temperatures were 110% of the alloy's liquidus in °K. All of the braze alloys wet the substrate very well. Figure 6 shows the wetting angle as a function of time for all four braze alloys.

Table 3: Braze Compositions and Test Temperatures Used in the Wetting Experiments for the 950°C Braze Alloy. All of the Braze Alloys are Manufactured by GTE Wesgo.

	Composition (wt. pct.)			Test
Braze	**Au**	**Ni**	**Pd**	**Temperature (°C)**
Palni	--	40	60	1389
Palniro 1	50	25	25	1260
Palniro 4	30	36	34	1272
Palniro 7	70	22	8	1168

During wetting tests between Palni braze and Zr-coated SNW1000, a large amount of outgassing occurred. Wetting tests were carried out in a mass spectrometer/vacuum system to determine the nature and source of this gas. Mass spectroscopy showed that a large amount of N_2 gas was given off as the Palni braze wet the Zr-coated SNW1000. The data suggest that the Pd in the Palni braze reacts with Si_3N_4 to form Pd_2Si or PdSi and N_2.

Table 4 shows the results of other wetting tests of various brazes on Zr-coated and uncoated SNW1000.

Table 4: Outgassing Results - Braze Material on SNW1000

Sample	Total Gas Pressure*	Major Gas Species
SNW1000 1300°C	193 microns	N_2, H_2
Palni/Zr Film 1300°C	800**	N_2
Palni w/o Zr 1300°C	75	N_2
(Au-Pd-Ni-Ti)/Zr Film 1180°C	131	H_2, N_2
(Au-Pd-Ni-Ti) w/o Zr 1180°C	158	H_2, N_2
Nioro w/o Zr 980°C	70	N_2

*Pressure normalized for values w/o the 3 liter volume.

**There is an initial pressure increase in the first 10 seconds for all of the samples, but this specimen showed, in addition, a burst of gas some time later.

Cylindrical Specimen NDE

When the Task II specimens will be brazed, it will be useful to have information concerning the extent of bonding in addition to mechanical test results. With that goal in mind, some preliminary experiments were performed brazing a 1/16-in. thick molybdenum ring to a 0.5-in. diameter SNW1000 (GTE Wesgo silicon nitride -2 w/o Al_2O_3-13 w/o Y_2O_3). The 0.2-in. length of the Mo ring yields a braze area of 2 cm^2 as called for in Task II. Two braze alloys were used: Cusil ABA GTE Wesgo 63 w/o Ag-35.25 w/o Cu-1.75 w/o Ti and an experimental alloy 91.75 w/o Au-5 w/o Pd-2 w/o Ni-1.25 w/o Ti. The brazed cylinders were evaluated using microfocus x-ray radiography. The samples were oriented at a slant with respect to the beam so that both the front and the back of the ring braze joint were exposed.

The results of this procedure are given in Figure 7. Large unbonded areas are seen with the Au-Pd-Ni-Ti sample in the radiograph given in Figure 7a. The exterior portion of the braze shown in Figure 7b at the right has a nonuniform fillet with significant bare patches between beads of braze. In contrast, the Cusil ABA sample shows no unbonded area in the radiograph and a continuous, uniform fillet in the optical photograph.

Transmission Electron Microscopy of Brazed Joints

Two pieces of Ti-coated Al_2O_3 were brazed with Nioro at 980°C for 10 minutes. The Al_2O_3 grain boundaries near the Ti-coated surface had a high density of precipitates (Figure 8). Figure 9 shows a triple point in the Al_2O_3 away from the Ti-coated surface. This triple point has a pocket of glass which is precipitate free. These two micrographs indicate that the titanium reacts with the glass phase at the grain boundaries to produce a precipitate. This reaction between the titanium and the grain boundary glass phase may produce tensile stresses which would lower the strength of the Al_2O_3.

Silicon Nitride-Metal Joint Development

Interlayers

The study of ceramic-metal pairs indicated that additional layers of materials are needed to accommodate the residual stress resulting from differential expansion. Interlayer materials were screened using rectangular coupon samples and shear tests in a fashion analogous to the work already reported. Figure 10 shows a brazed coupon sample containing an interlayer. Two general groups of interlayer candidates were identified. One set includes relatively low yield strength materials such as copper or nickel. The other consists of low coefficient of expansion materials such as Mo. Table 5 provides a summary of both nitride and silicon carbide shear tests data for samples containing interlayers. The results of shear strength measurements are the average of 3 and 6 tests. Results to date indicate that materials such as Mo and W are useful for their intermediate thermal expansion coefficients. it is believed that the low oxidation resistance of these materials can be addressed by utilizing designs which do not expose them to oxygen. Cu and Ni were also shown to be promising. Additional study is in progress in this area to finalize material selection and optimize thickness. This experimental data is consistent with the modeling predictions that Ni would outperform Mo.

Table 5:

Materials System	Thickness (in.)	Shear Strength (ksi)
SNW1000-Zr coating-Nioro-Nb-Incoloy	0.04	6.9
SNW1000-Zr coating-Nioro-W-Incoloy	0.04	17.4
SNW1000-Zr coating-Nioro-Ni-Incoloy	0.005-0.02	15.0
SNW1000-Zr coating-Nioro-Mo-Incoloy	0.01, 0.04	10.2
SNW1000-Zr coating-Nioro-Cu-Incoloy	0.02, 0.04	19.2
SiC-Ta coating-Nioro-Cu-Incoloy	0.01, 0.04	0.4
SiC-Zr coating-Nioro-Cu-Incoloy	0.04	2.6
SiC-Zr coating-Nioro-Mo-Incoloy	0.04	0.3

Mechanical Testing of Brazed Joints

Furnace Construction

An induction furnace was designed and installed on an MTS machine for torsion testing of brazed joints at 650 and 950°C. The temperature difference between the surface of the sample and the brazed joint was measured. This temperature difference is significant because, when testing the actual brazed joint, only the surface temperature of the sample can be measured. One thermocouple recorded the surface temperature of the sample, while another thermocouple was placed in the location of the brazed joint (Figure 11). Equation 6 describes the relationship between the surface temperature, T_s, and the joint temperature, T_j, both in degrees Celsius.

$$T_s = 60.66 + 0.97\ T_j \qquad \text{Eq. 6}$$

The plot of surface temperature versus joint temperature is shown in Figure 12. The sample temperature was held within 5°C of the desired temperature with little difficulty.

Shear Testing

The high temperature joint strength of Palni and Palniro series brazes was measured with coupon lap joint samples. The substrate materials chosen for 950°C were Zr- (or Ti-) coated SNW1000, Mo, W, Nb and Ni. The Mo, W, Nb or Ni will serve as interlayer in the final joint design.

Palni and Palniro 4 braze alloys on Nb and Mo substrates were used for the preliminary tests. The selection of these brazes was based on their relatively high solidus temperatures, 1238°C and 1135°C, respectively.

Hot shear testing was performed in an argon atmosphere. The test temperature, 500°C, was selected due to the temperature limit of fixture. The samples were equilibrated at 500°C for 30 min. before being tested at 0.01 inch/min. crosshead speed. Ti was substituted for Zr as a coating for the Nb-SNW1000 coupons. This substitution was made because a strong interaction between the Zr coating and braze alloys at 1200°C prevented the Nb-SNW1000 system from bonding.

Table 6 shows the results of hot shear tests. The braze alloys studied did not show significant weakening at 500°C. For SNW (Zr coated)-Mo system, Palniro 4 resulted in a high shear strength. However, Palni provided strength equivalent to the room temperature strength of the SNW-Nioro-Mo system. Fracture always occurred in the braze. This implies that the thermal stresses developed at the ceramic-metal interface were not high enough to cause cracking of the ceramic. Overall, results from this limited number of tests indicate that the performance of the brazed joints at 500°C is better than or equivalent to strength levels seen at 20°C. This is primarily due to the reduction of the thermal mismatch between the ceramic and metal substrates.

Table 6: Results of the Hot Shear Tests

System	Bond Area (cm^2)	Testing Temp(°C)	Shear Strength (ksi)	Comments
SNW1000 (Zr)-Palni-Nb	0.96	-	-	No bonding after brazing
SNW100 (Zr)-Palniro 4-Nb	0.96	-	-	" " "
SNW1000 (Ti)-Palni-Nb	0.96	525	12.3	-
SNW1000 (Ti)-Palniro 4-Nb	0.96	525	7.4	-
SNW1000 (Zr)-Palni-Mo	0.96	525	6.2	-
SNW1000 (Zr-Palni-Mo	0.96	525	4.8	-
SNW1000 (Zr)-Palniro 4-Mo	1.10	525	> 15.2	No failure at 15.2 ksi
SNW1000 (Zr)-Palniro 4-Mo	1.10	526	-	Failed during Preloading

Torsion Testing

In order to establish baseline information for the torsion tests of ceramic-metal braze joints, Incoloy 909 and Inconel 718 specimens without braze joints were tested at room temperature with the rotational strain rate of 0.00087 rad/inch/sec. The torsion tests were conducted with zero axial load. These curves were converted to (maximum) shear stress vs shear strain, using equations shown below for the elastic and plastic regions. This analysis was taken from Dieter[2].

$\tau = 2\ M_t/\pi r^3$ in the elastic region

$\tau = 1/2\ \pi r^3\ (\theta' dM_t/d\theta' + 3\ M_t)$ in the plastic region

$\gamma = r\theta' = \theta/L$, or $\theta' = \theta/L$

where M_t, r, θ, and L are the applied torque, the radius of the specimen gauge section, rotational angle and the gauge length, respectively. The maximum shear stress occurred at the surface of the specimens, which will eventually cause the fracture of the material.

Further, these shear stress vs shear strain curves were changed into effective stress vs effective strain in uniaxial tensile mode using stress and strain invariant functions.

$\tau = \sigma_1' = -\sigma_3'$, $\sigma_2' = 0$

$\gamma = 2\epsilon_1'$; $\epsilon_1' = -\epsilon_3'$, $\epsilon_2' = 0$

Therefore,

$$\sigma_{effective} = \sqrt{3}\ \sigma_1'$$

$$\epsilon_{effective} = 2/\sqrt{3}\ \epsilon_1'.$$

since $$\sigma_{effective} = 1/\sqrt{2}\ [(\sigma_1-\sigma_2)^2 + (\sigma_2-\sigma_3)^2 + (\sigma_3-\sigma_1)^2]^{1/2}$$

and $$\epsilon_{effective} = 2/\sqrt{3}\ [(\epsilon_1-\epsilon_2)^2 + (\epsilon_2-\epsilon_3)^2 + (\epsilon_3-\epsilon_1)^2]^{1/2}.$$

The resulting curves of τ vs γ and $\sigma_{effective}$ vs $\epsilon_{effective}$ are shown in Figures 13 and 14.

At high temperature, the residual stress in the ceramic component of the brazed structure can be reduced significantly. Therefore, it is highly possible to

have a failure at the brazed region due to the temperature limit of the braze alloys. Since von Mises equivalent stress, i.e. effective stress governs the deformation of the braze alloys and interlayer materials, this simple approach given below can be used to link the experimental results with the finite element analysis (FEA) which can predict the location and level of maximum von Mises equivalent stress. At room temperature, the maximum principal stress in the ceramic will control the failure of the joint structure. Also, the direction of maximum principal stress (σ_1) at the ceramic surface is parallel to axial line of the ceramics due to its cylindrical geometry. Based on this approximation, the equation as below is true for the ceramic and metal components:

$$\sigma_{fracture} = \sigma_{applied} + \sigma_{residual},$$

where $\sigma_{applied}$ and $\sigma_{fracture}$ can be measured from the ceramics with and without brazed joints, while $\sigma_{residual} = \sigma_1$, which is from the prediction of FEA.

Thermal Fatigue Evaluation

The thermal fatigue experimental cycle has been developed. The maximum temperatures were based on contractual requirements. Both of these temperatures were taken to be for engines running at maximum power under steady state conditions. The lower temperatures of each thermal cycle were selected to simulate the temperatures experienced at steady state, idle speed.

Geometry and mass of the rotor play a large part in determining the internal temperatures of the rotor/shaft system; therefore, one system was chosen as a model. Thermal maps of the ceramic turbine rotor and structural alloy shaft cross section of the chosen model were based on work done at General Motors on their gas turbine engine.[3]

A temperature of 650°C is the lower of the two braze joint service temperatures for both the Si_3N_4 and the SiC, and this corresponds well to work being done at this time. The location of the 650°C isotherm was marked on the thermal map for steady state, maximum conditions for both materials. This same area was then examined on the thermal maps for steady state, idle conditions. The idle temperatures were found to be 335°C and 465°C for the Si_3N_4 and SiC, respectively. The SiC required approximately 66 seconds to reach 650°C from 465°C and return again,[4] while the Si_3N_4 cycle was approximately twice as long. A graphical representation of the cycle can be seen in Figure 15.

The same method was used to develop the thermal cycle for the 950°C cycle. The idle temperature is raised as the entire operating temperature of the hot section is raised in the gas turbine engine.[5] This is the most efficient way of operating the engine because of increased response time when the temperature differences between maximum speed temperature and idle speed temperature are small. The cy-

cle time was therefore left the same as in the previous cycle. Figure 16 summarizes the cycle for a 950°C maximum temperature.

Mechanical Fatigue Evaluation

The ceramic joining program requires demonstration of the ability of the joint to withstand 1000 cycles of mechanical fatigue. The state of stress and loading cycle have been determined. As with the thermal fatigue evaluation, the mechanical cycle was developed with the idea of simulating the stresses developed in a gas turbine engine, and the model used was the engine currently being tested by General Motors.

The braze joint area of a rotor/shaft assembly experiences many stresses, one of them being torsional. The torque experienced at maximum and idle speeds is 185 in-lb and 35 in-lb, respectively. The cycle time was 1/3 seconds from low to high. A graph of the proposed cycle is seen in Figure 17.

Status of Milestones

Finite Element Analysis (FEA) of Mo and Ni interlayers was completed. The low yield stress Ni interlayer produced lower residual stress levels in the joint than did the Mo interlayer. Shear testing of coupon lap joints supported this conclusion.

Assembly of Task 2 specimen for the performance test has been postponed (7/1/89) due to vacuum pump repairs.

Communications/Visits/Travel

Meeting on 11/30/88 at GTE Laboratories with Professor K.-S. Kim, University of Illinois, to discuss Task 2 and Task 3 geometries. Meeting on 1/11/89 with H. Mizuhara of GTE Wesgo about high temperature braze design.

Frequent phone consultations occurred with H. Mizuhara of GTE Wesgo and Professor K.-S. Kim of the University of Illinois.

Problems Encountered

None.

Publications

E.M. Dunn, S. Kang, H. Mizuhara, K.-S. Kim, "Analytical and Experimental Evaluation of Joining Silicon Nitride to Metal and Silicon Carbide to Metal," Proceedings of the 26th Automotive Technology Development Contractors' Coordination Meeting, Dearborn, MI, Oct. 24-27, 1988, Society of Automotive Engineers, Inc., Warrendale, PA, submitted for publication.

References

1. S. Kang and E. Dunn, Data Compilation for Ceramic-Metal Joining, GTE Laboratories Incorporated, 1987.

2. G. Dieter, **Mechanical Metallurgy,** McGraw Hill, p. 379-387.

3. G. Costakis, Unpublished Notes, February 27, 1989, General Motors Corporation.

4. N. Rau, Private Communication, March 16, 1989, General Motors Corporation.

5. C. Mader, Private Communication, April 3, 1989, General Motors Corporation.

6. D. Turner, Private Communication, March 31, 1989, General Motors Corporation.

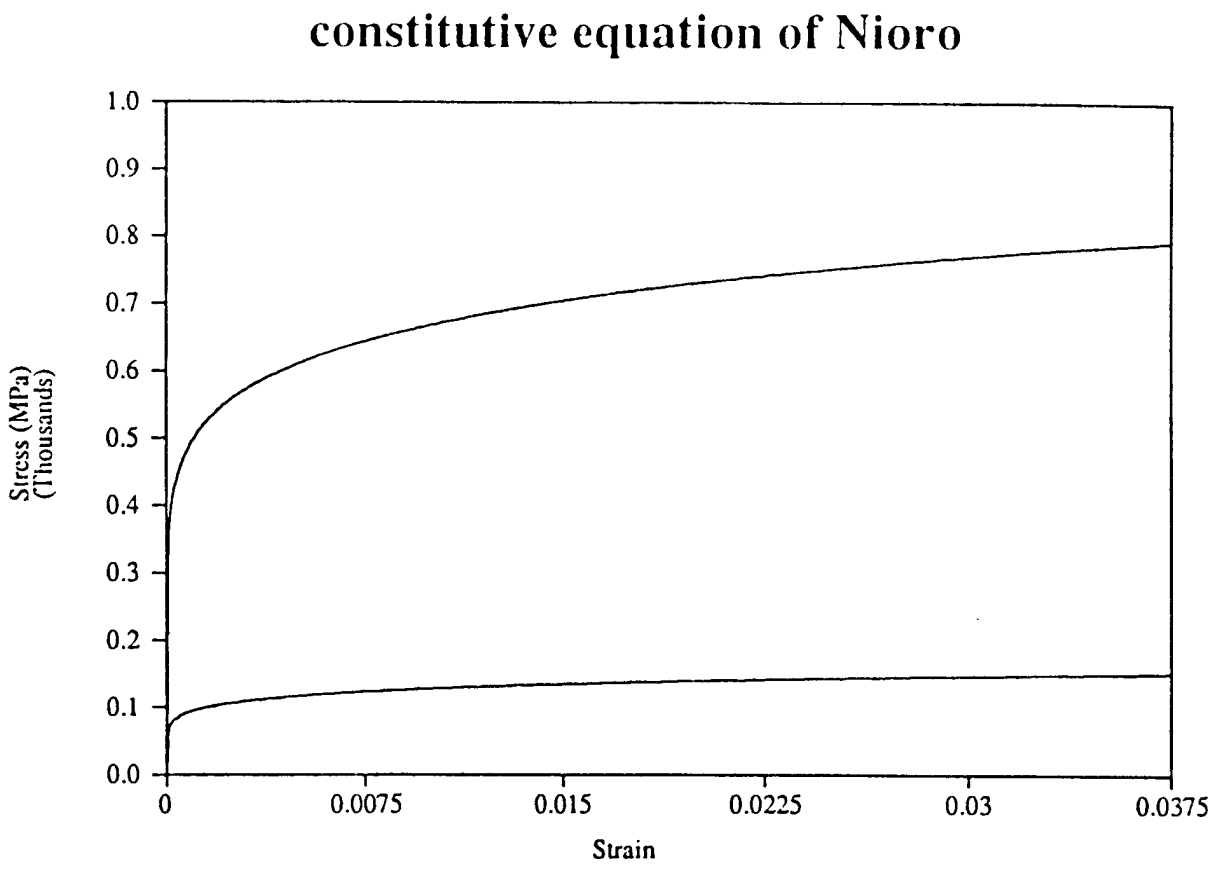

Figure 1. Stress strain curve of Nioro. Upper curve is for T=20°C and lower curve is for T=800°C.

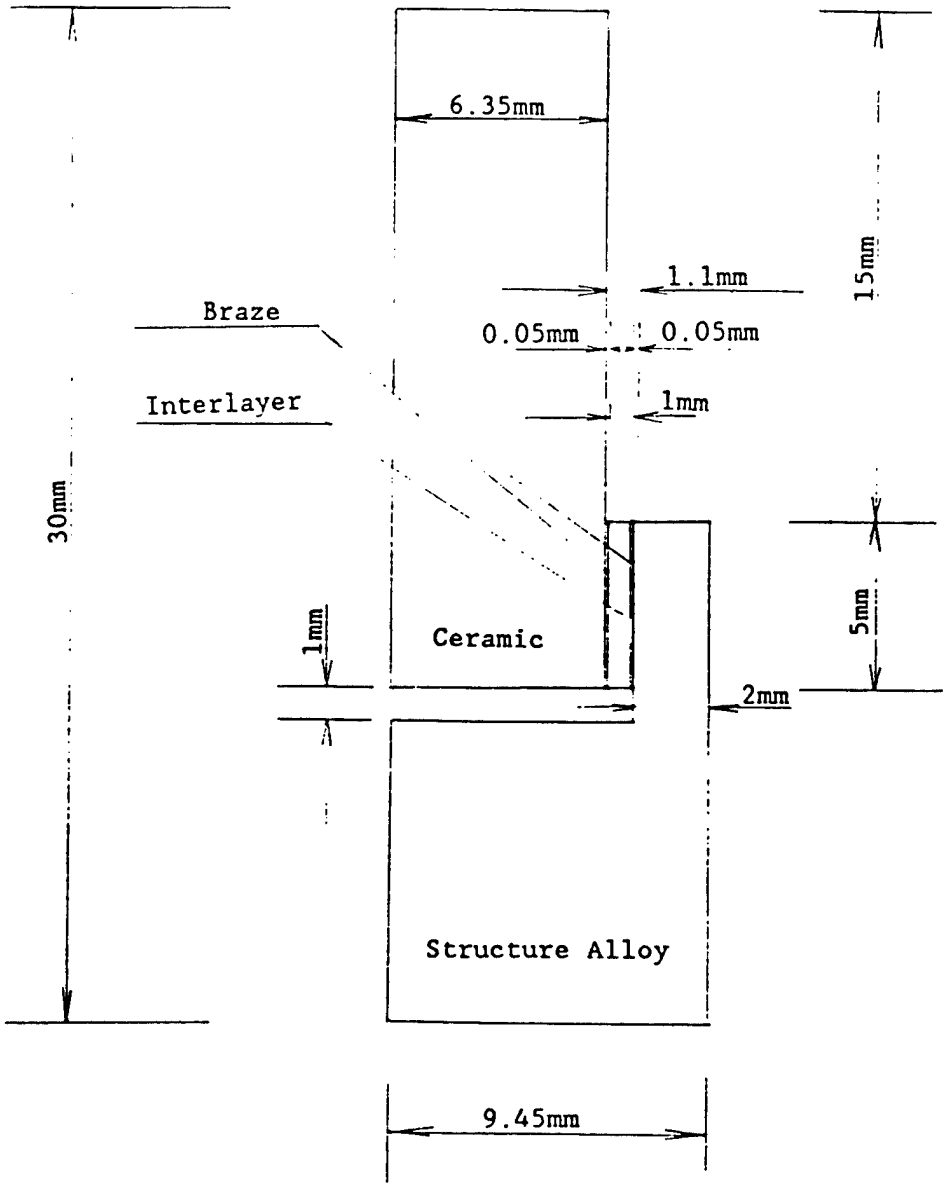

Figure 2a. Basic geometry 1. Thickness of the interlayer changes from 0.7 mm to 1.0 mm

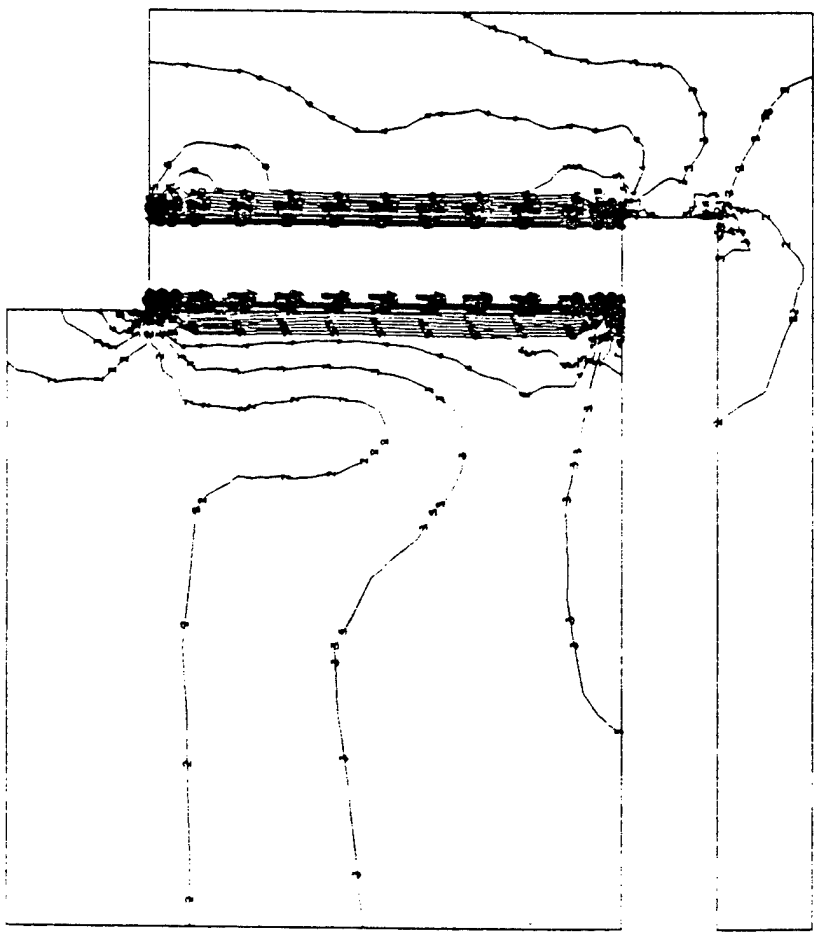

MISES

	VALUE
1	+3.10E+01
2	+3.10E+07
3	+6.20E+07
4	+9.31E+07
5	+1.24E+08
6	+1.55E+08
7	+1.86E+08
8	+2.17E+08
9	+2.48E+08
10	+2.79E+08
11	+3.10E+08
12	+3.41E+08
13	+3.72E+08
14	+4.03E+08
15	+4.34E+08
16	+4.65E+08
17	+4.96E+08
18	+5.27E+08
19	+5.58E+08
20	+5.89E+08
21	+6.20E+08
22	+6.51E+08
23	+6.82E+08
24	+7.13E+08
25	+7.44E+08
26	+7.75E+08
27	+8.06E+08
28	+8.37E+08
29	+8.68E+08
30	+9.00E+08

Figure 2b. Contours of Mises equivalent stress in ceramic-metal brazing joint of basic geometry 1. Thickness is equal to 1.0 mm.

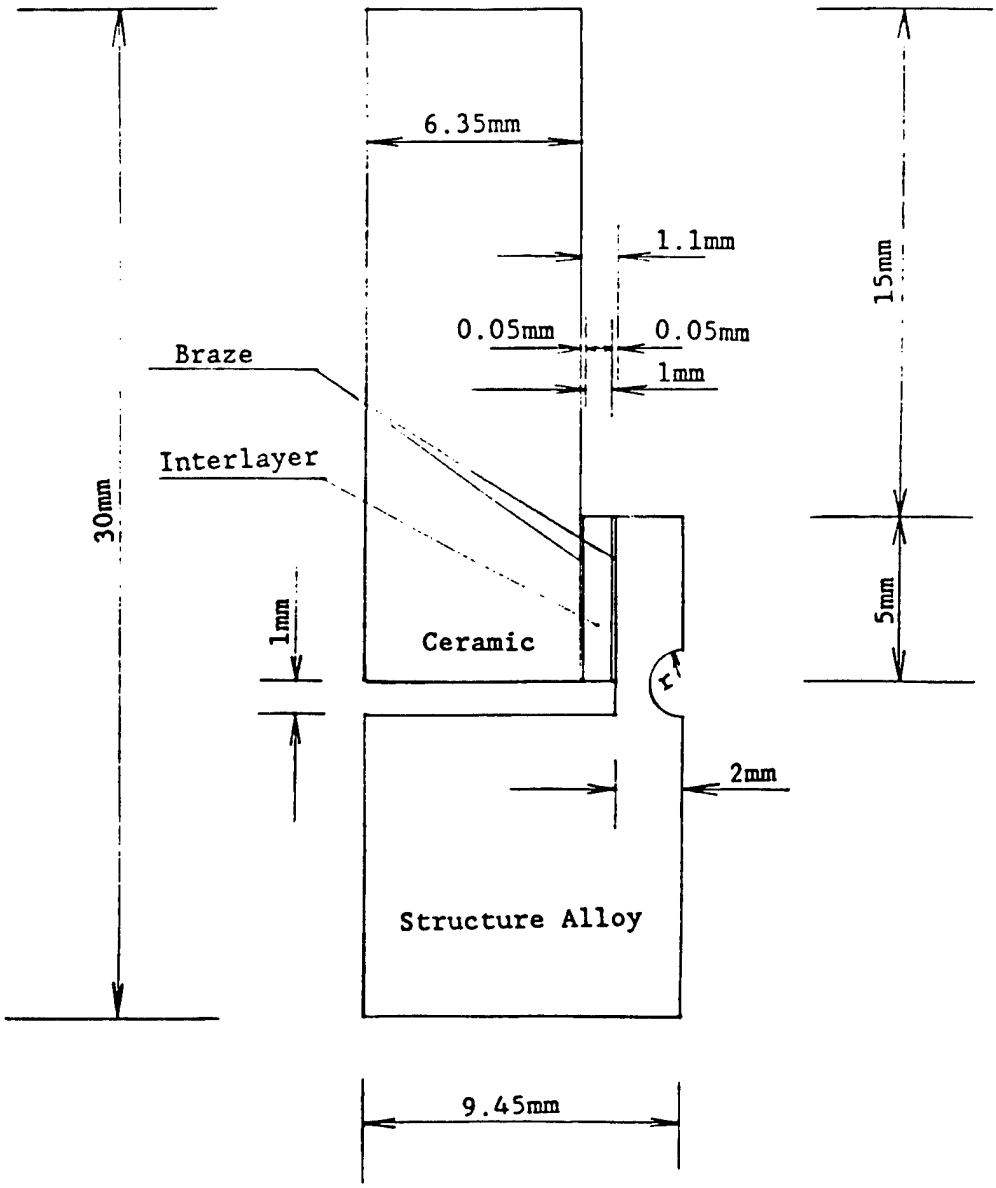

Figure 3a. Basic geometry 2. Radius of the groove changes from 0.3 mm to 1.0 mm

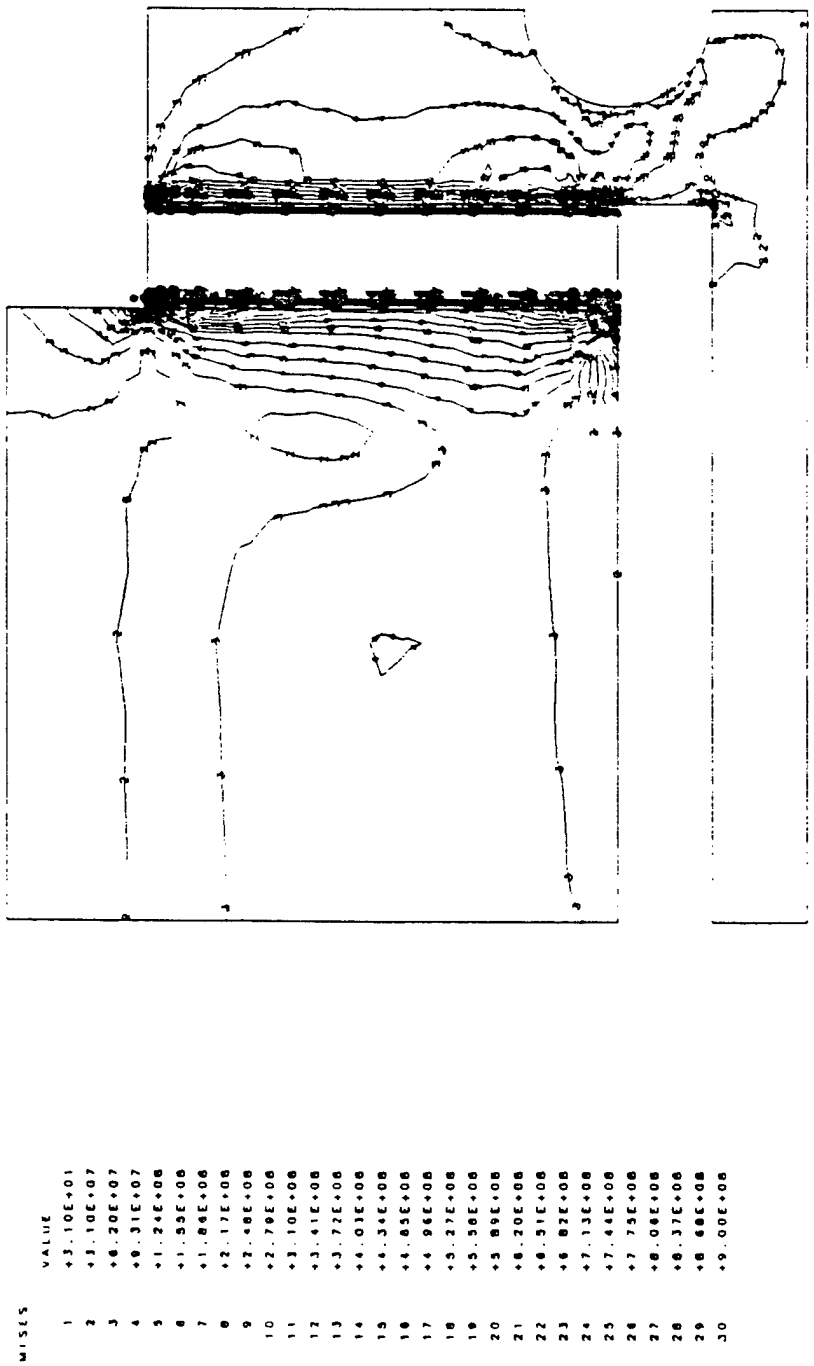

Figure 3b. Contours of Mises equivalent stress in ceramic-metal brazing joint of basic geometry 2. Radius of the groove is equal to 1.0 mm.

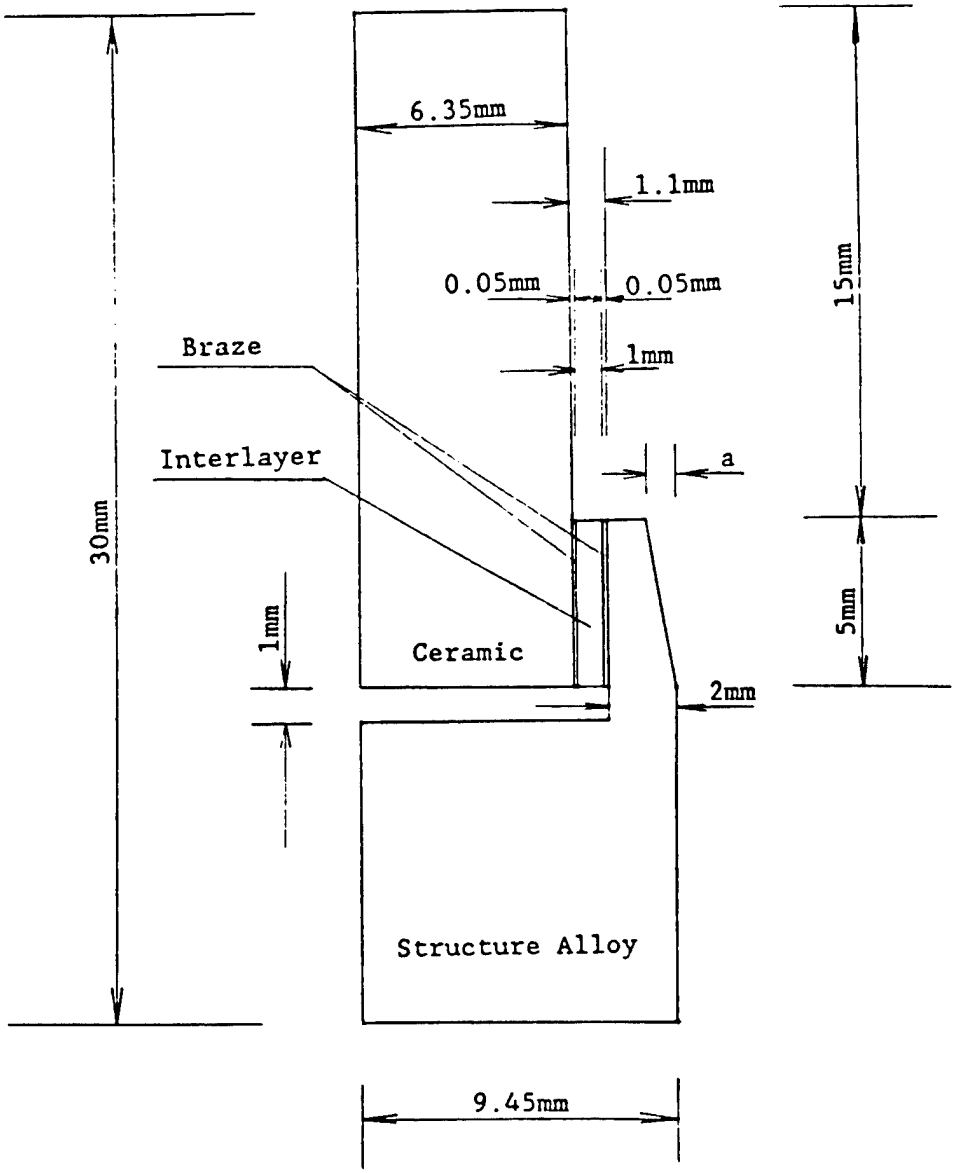

Figure 4a. Basic geometry 3. Parameter a of the conic shape changes from 0.2 to 1.0 mm

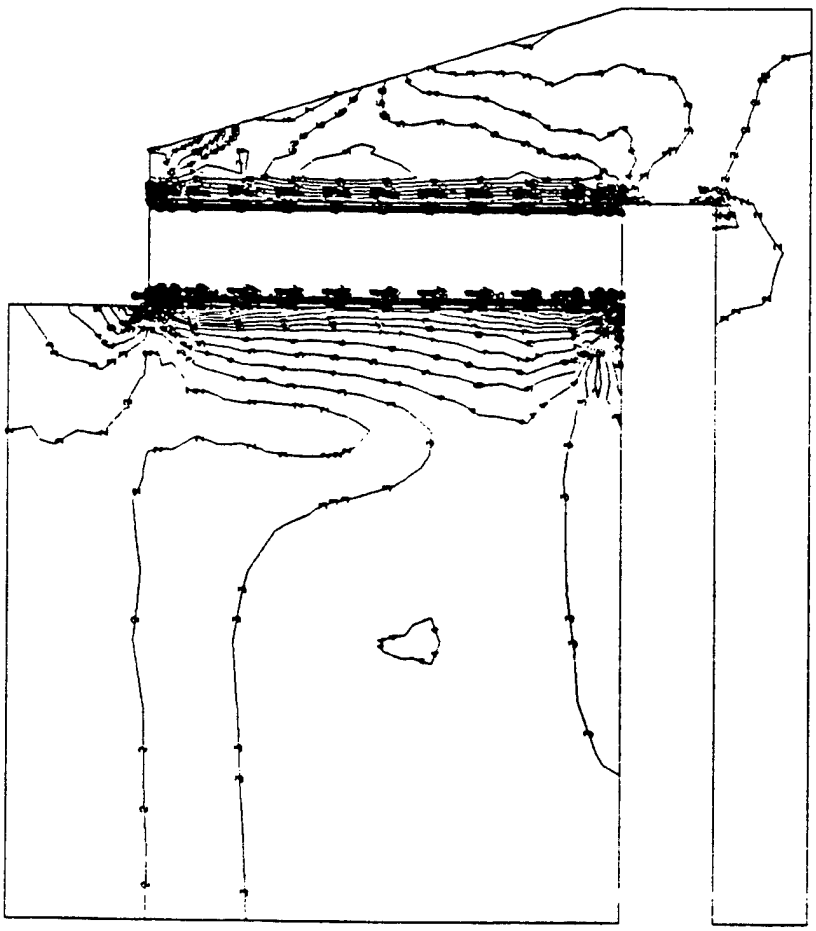

MISES	VALUE
1	+3.10E+01
2	+3.10E+07
3	+6.20E+07
4	+9.31E+07
5	+1.24E+08
6	+1.55E+08
7	+1.86E+08
8	+2.17E+08
9	+2.48E+08
10	+2.79E+08
11	+3.10E+08
12	+3.41E+08
13	+3.72E+08
14	+4.03E+08
15	+4.34E+08
16	+4.65E+08
17	+4.96E+08
18	+5.27E+08
19	+5.58E+08
20	+5.89E+08
21	+6.20E+08
22	+6.51E+08
23	+6.82E+08
24	+7.13E+08
25	+7.44E+08
26	+7.75E+08
27	+8.06E+08
28	+8.37E+08
29	+8.68E+08
30	+9.00E+08

Figure 4b. Contours of Mises equivalent stress in ceramic-metal brazing joint of basic geometry 3. Parameter a of conic shape is equal to 1.0 mm.

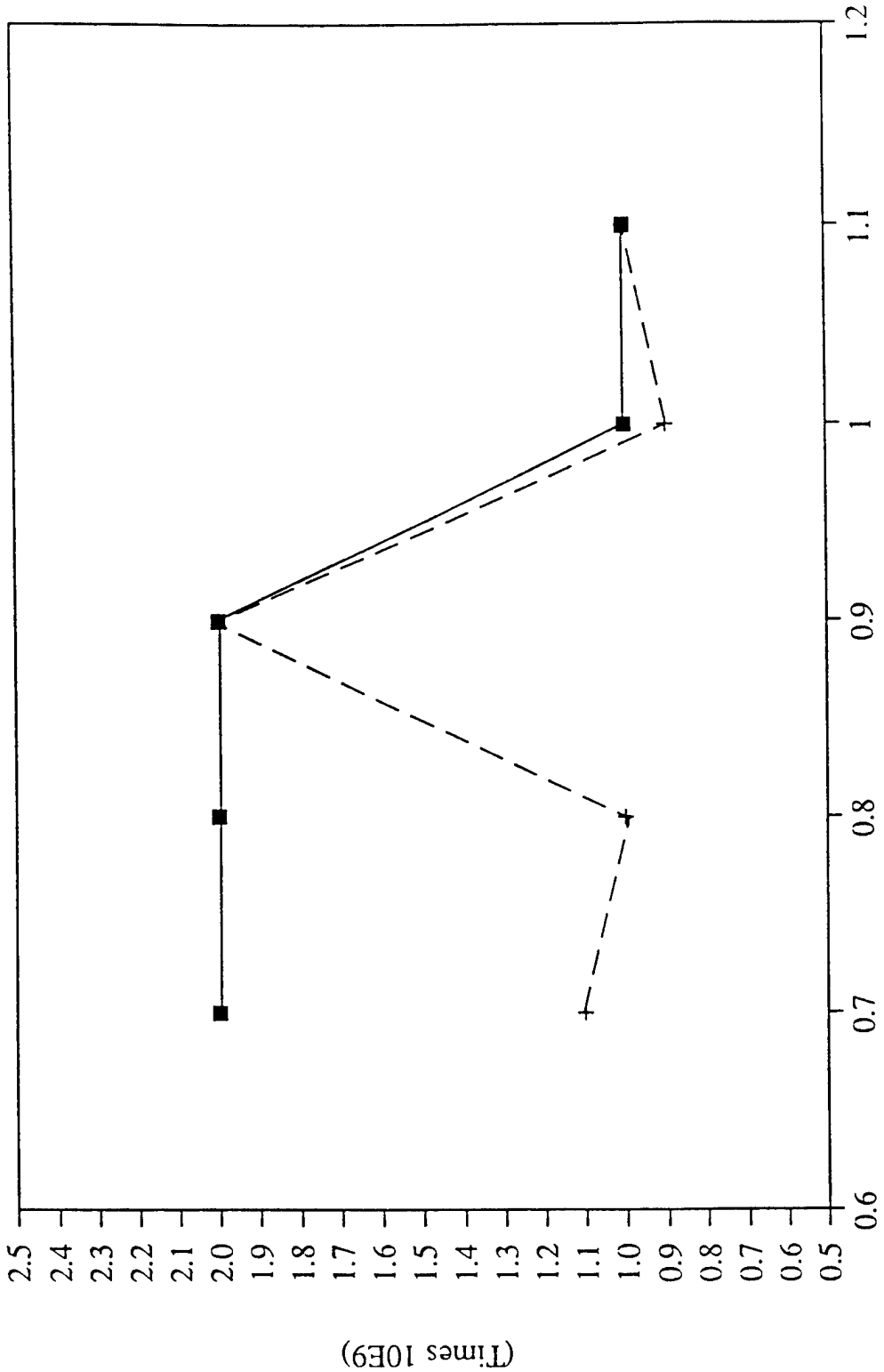

Figure 5. The largest principal stress and Mises equivalent stress of basic geometry 1. thickness is from 0.7 mm to 1.1 mm.

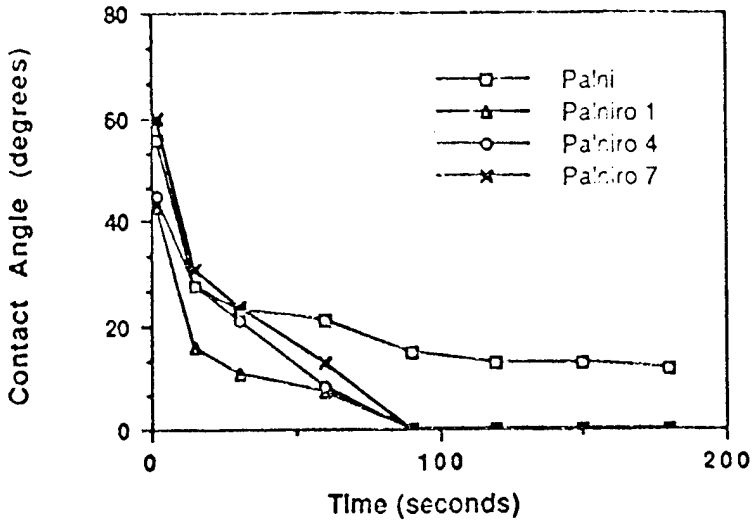

Figure 6: **Plot of contact angle versus time for Palni, Palniro 1, Palniro 4 and Palniro 7 on Ti-coated SNW1000**

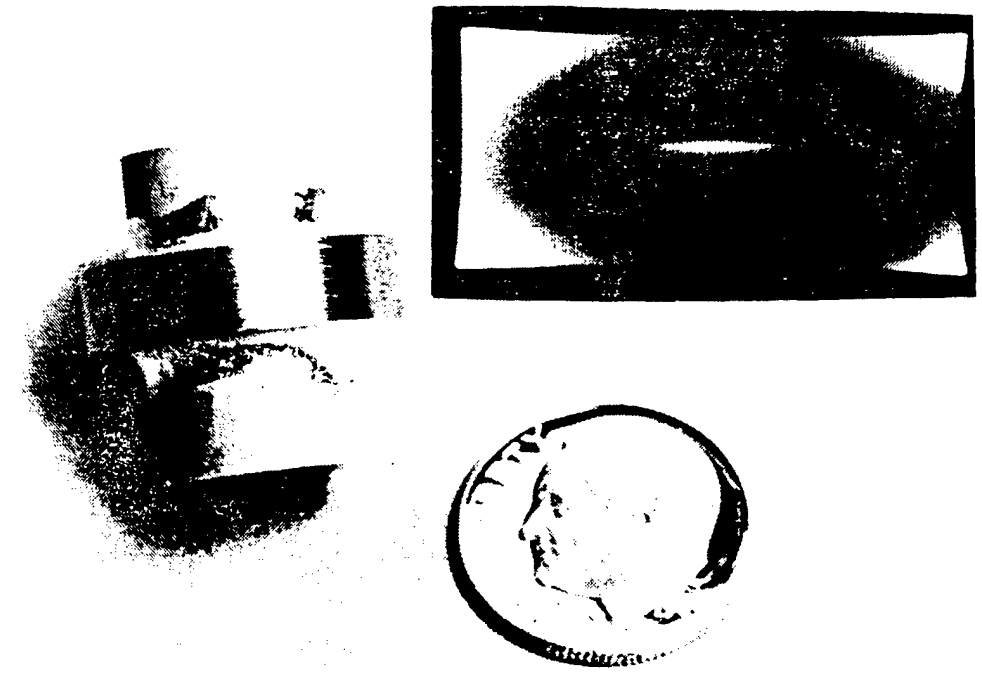

(a)

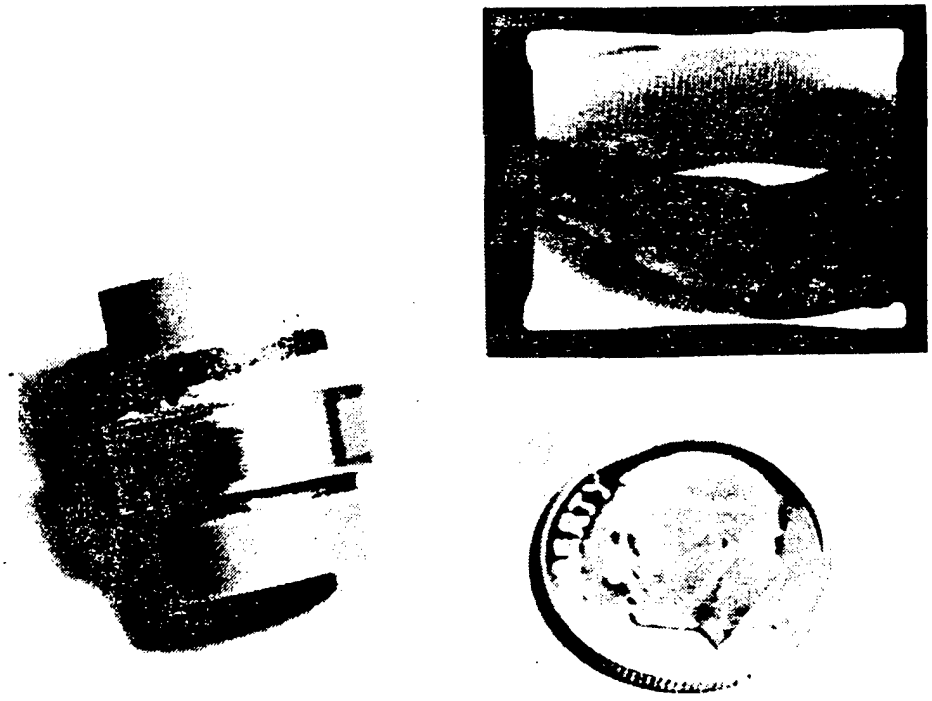

(b)

Figure 7. SNW 1000 silicon nitride cylinders brazed to molybdenum rings. Microfocus x-ray radiograph is at upper right of each figure. (a) Cusil ABA braze and (b) Au-Pd-Ni-Ti braze.

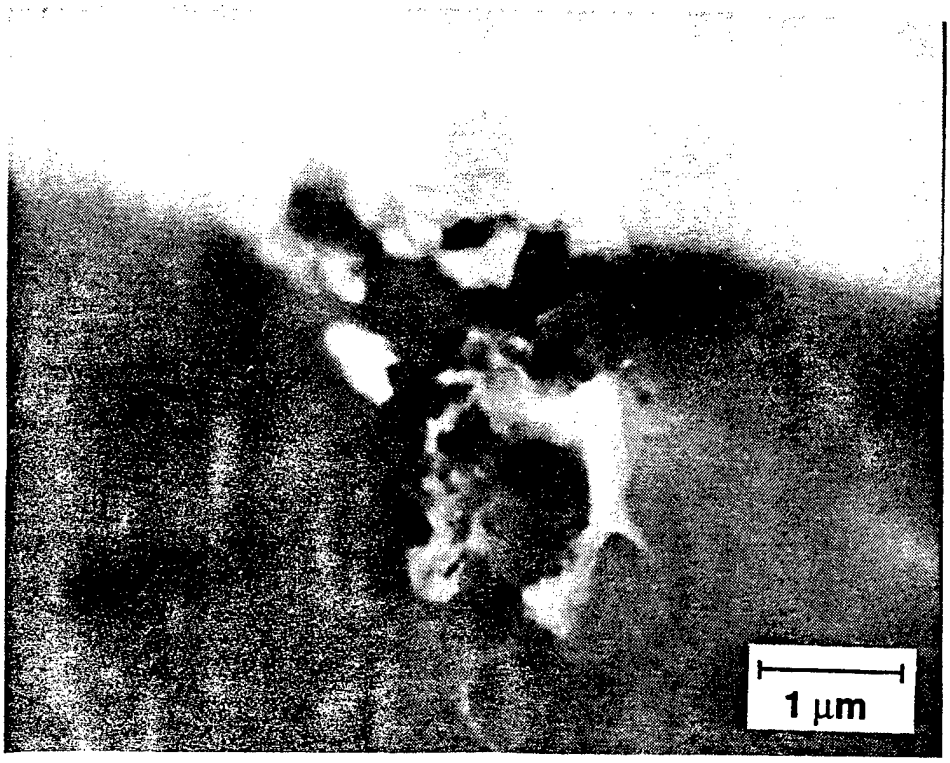

Figure 8. Grain boundary near the Ti_3Al layer showing many precipitates in the glassy phase.

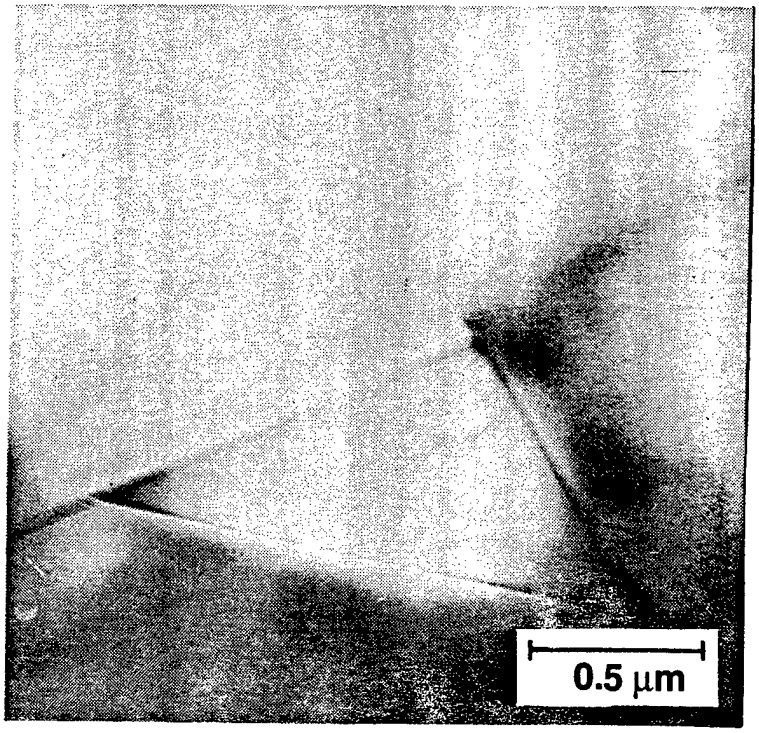

Figure 9. Glass phase at a triple-point in Al_2O_3.

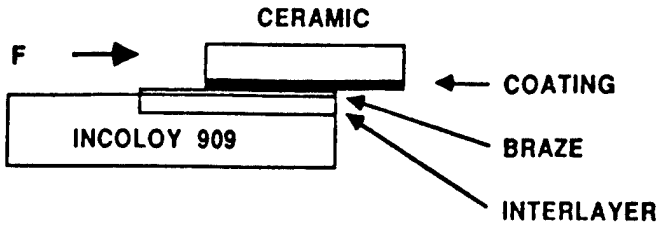

Figure 10. Schematic illustrating shear test samples of ceramic-metal joints containing an interlayer

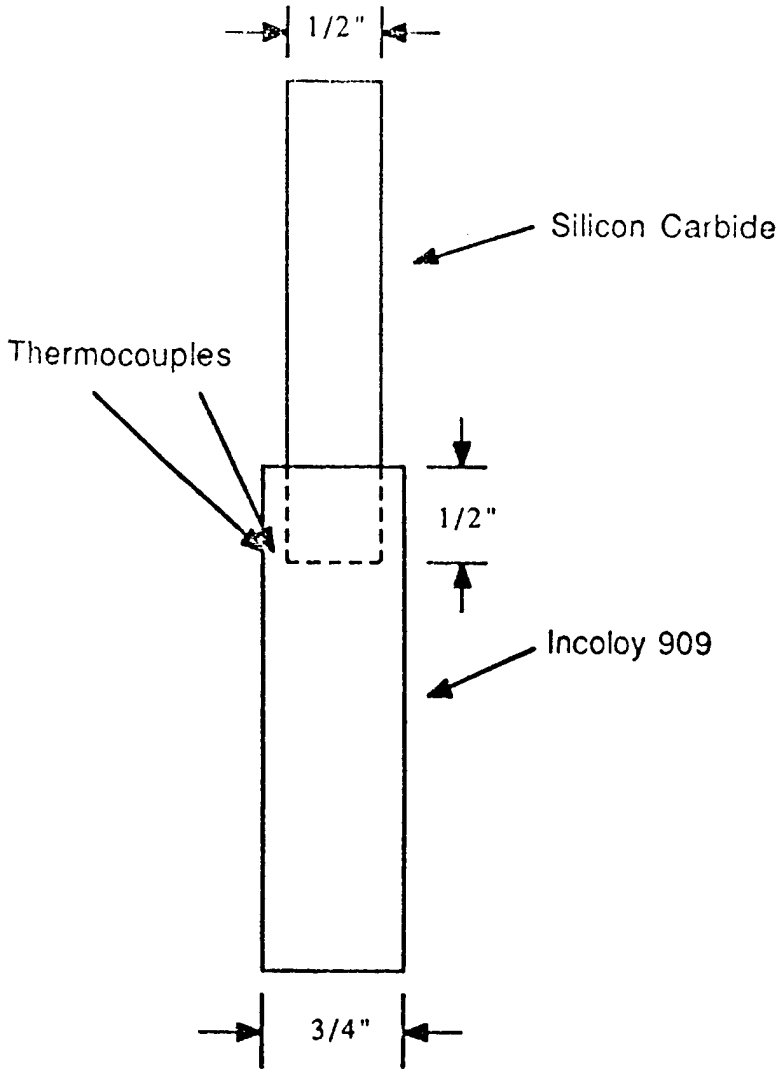

Figure 11. **Schematic of thermocouple placement**

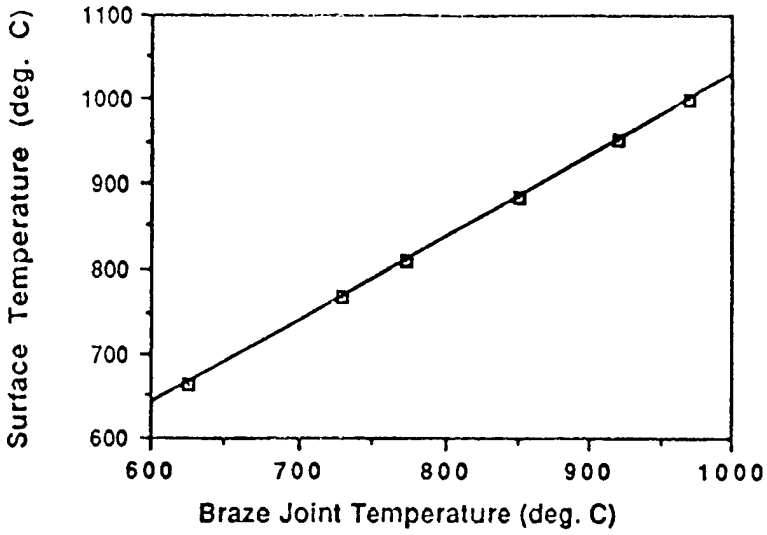

Figure 12. Plot of surface temperature versus joint temperature

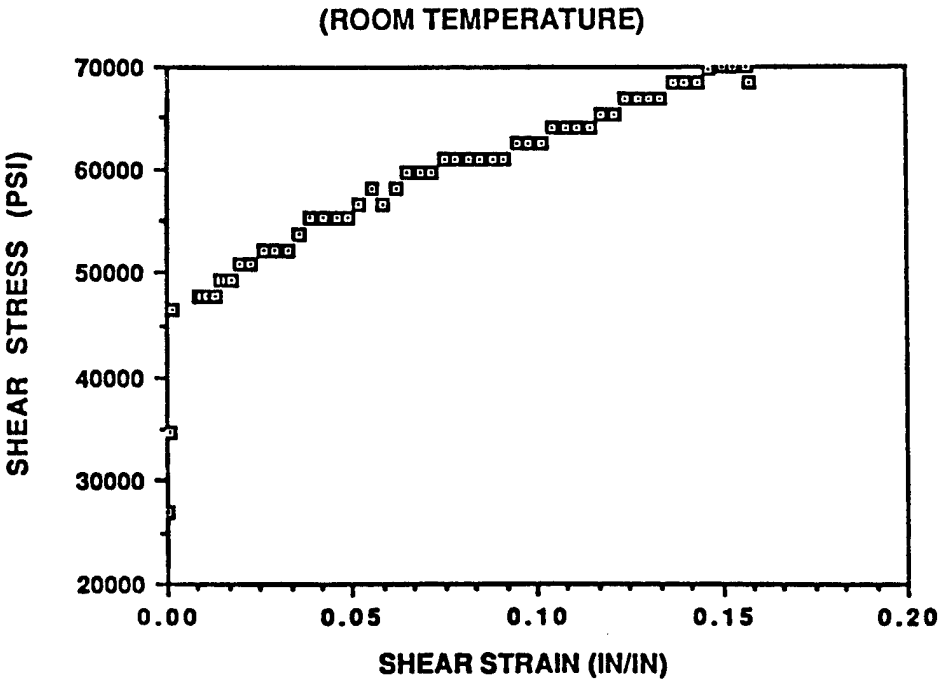

(a)

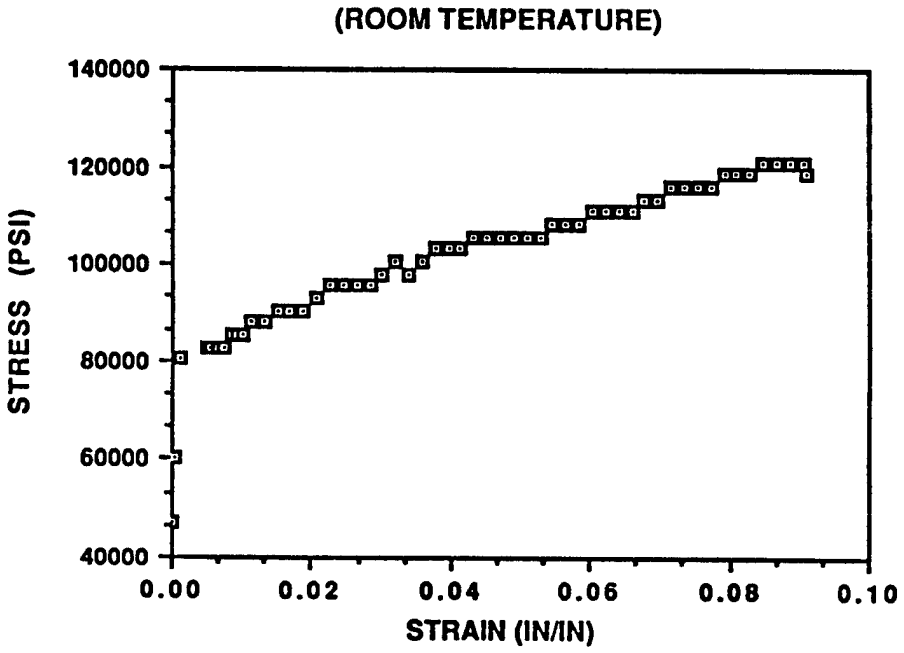

(b)

Figure 13. Incoloy 909 tested at R.T. (a) shear stress vs shear strain; (b) effective stress vs effective strain

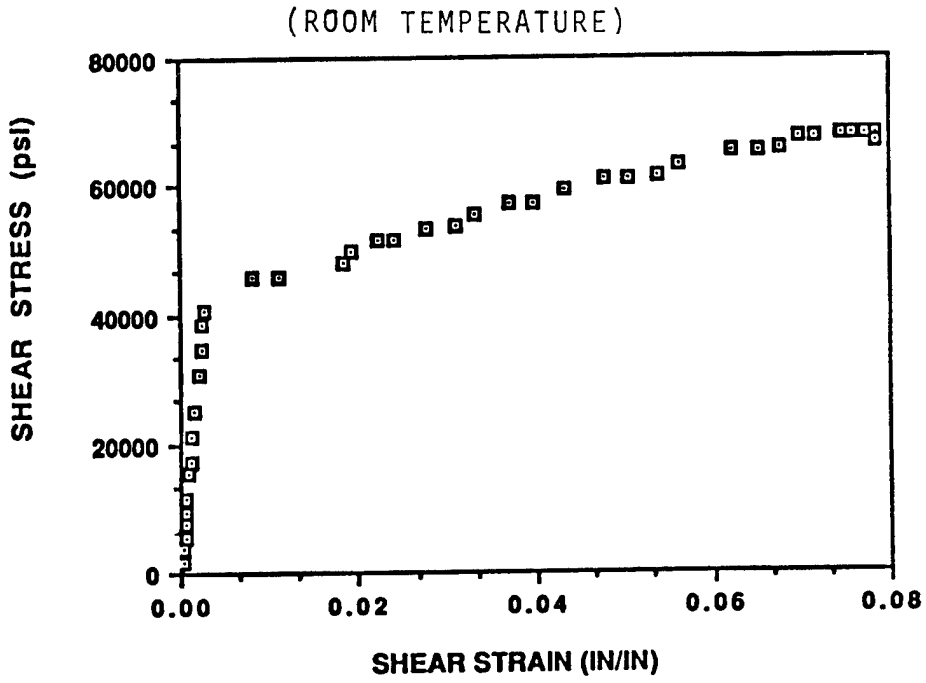

(a)

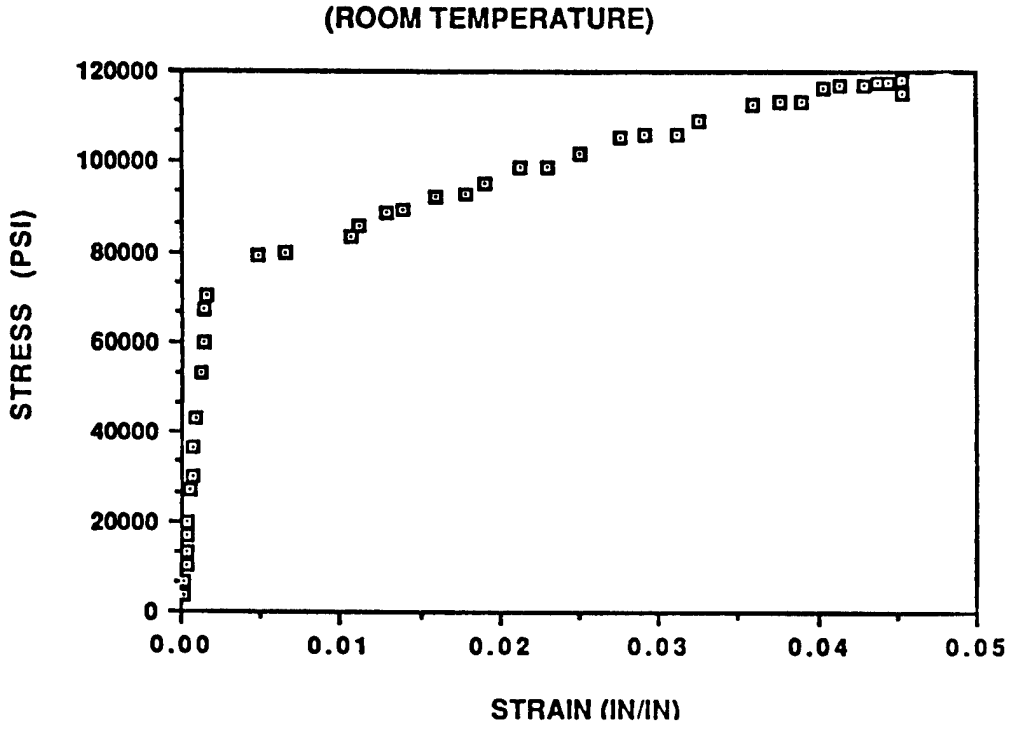

(b)

Figure 14. Inconel 718 tested at R.T. (a) shear stress vs shear strain; (b) effective stress vs effective strain

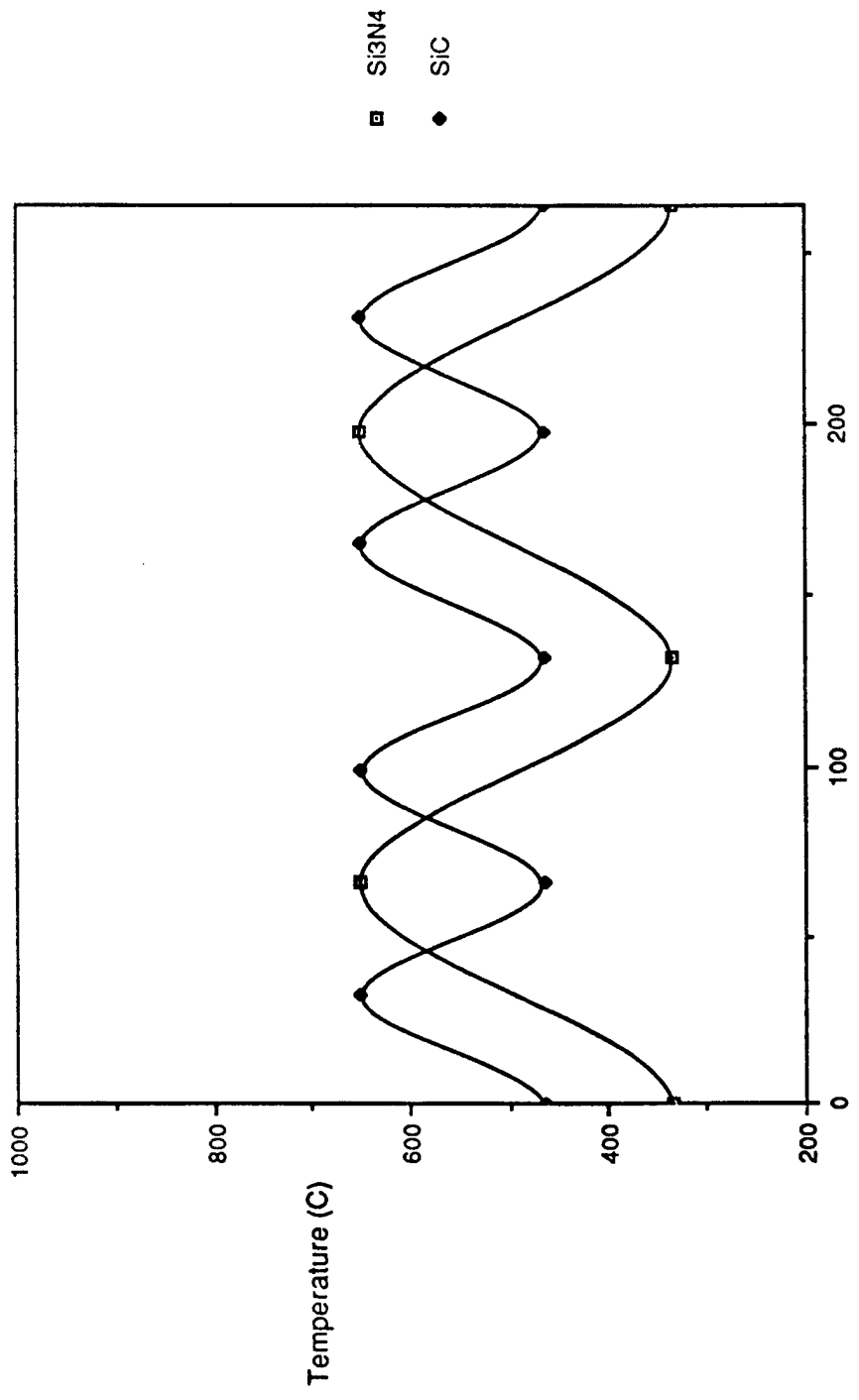

Figure 15. Proposed Time vs Temperature Plot for Thermal Cycle with Max. Temperature of 650C

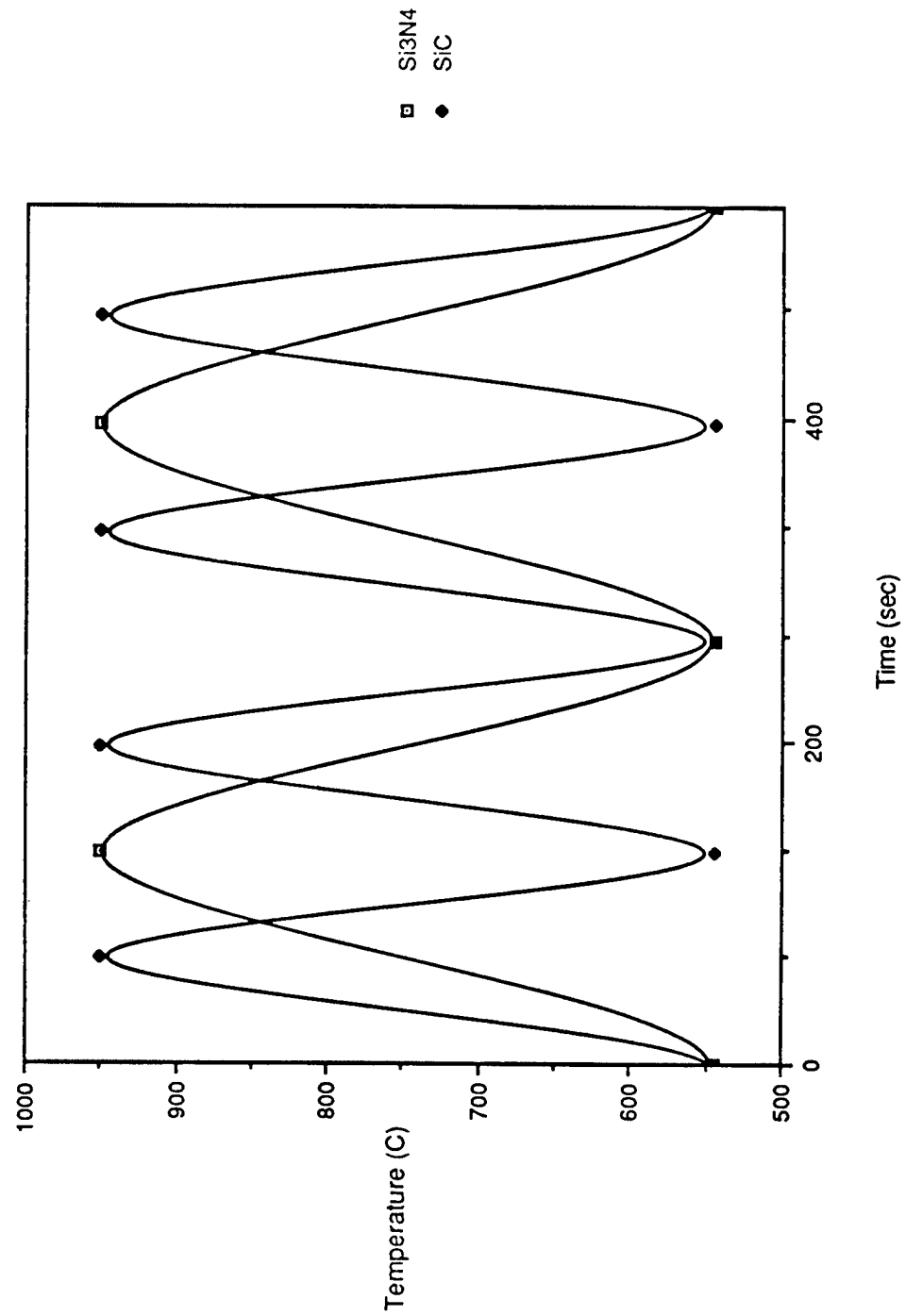

Figure 16. Proposed Time vs Temperature Plot for Thermal Cycle with Max. Temperature of 950C

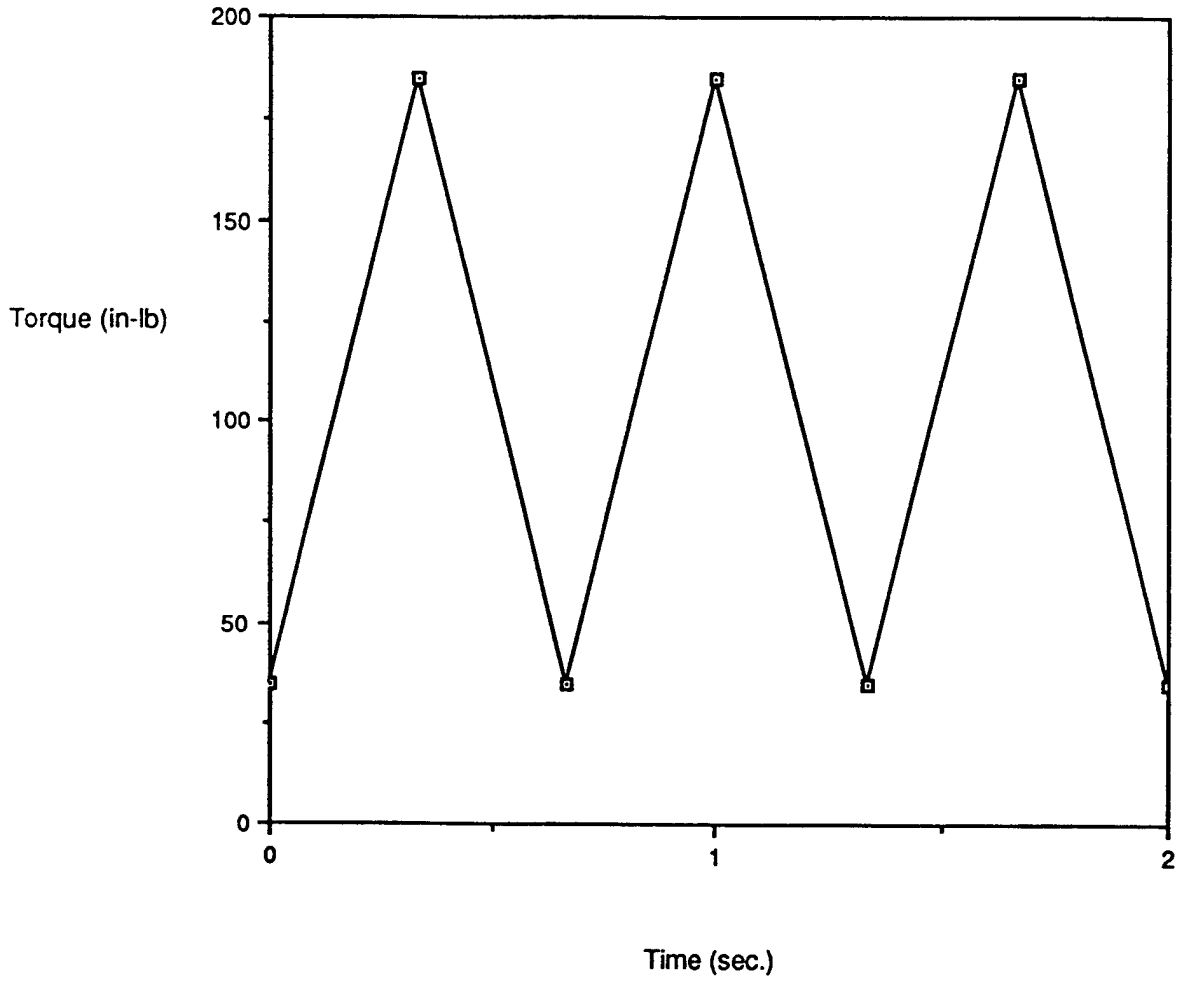

Cycle Time: 1/3 sec
Max. Torque: 185 in-lb
Min. Torque: 35 in-lb

Figure 17. Proposed Time vs Torque Plot for Engine Simulation Experiment

Analytical and Experimental Evaluation of Joining Ceramic Oxides to Ceramic Oxides and Ceramic Oxides to Metal for Advanced Heat Engine Applications

A. T. Hopper, J. Ahmad, and A. Rosenfield
(Battelle Columbus Division)

Objective/scope

The objective of this project is the development of procedures necessary for the design of reliable, high strength ceramic oxide-to-ceramic oxide and ceramic oxide-to-metal joints. The research program consists of analytical and experimental tasks employing Zirconia as the ceramic. The experimental work dealing with ceramic oxide-to-metal joints is being done by Dr. James Cawley and Mr. Eunsung Park of The Ohio State University and by Dr. Daniel Hauser of The Edison Welding Institute. The experimental work dealing with ceramic-oxide to ceramic-oxide joints is being done by B. S. Majumdar and S. L. Swartz.

The goal of the analytical work is a predictive model that can be used in engineering design of ceramic joints. This work consists of several subtasks involving residual stress modeling, deterministic stress and fracture mechanics modeling, engineering design modeling, probabilistic modeling, and model validation. Inputs to these models come from the experimental efforts.

The experimental work involves the fabrication and testing of small scale and scaled up joints to determine the mechanical behavior of these ceramic joints. Experiments include measurement of elastic constants and of stress-strain curves as a function of temperature, tensile strength, shear strength, Mode I and Mode II fracture toughness, creep deformation, time dependent strength, and strength degradation from hot oxidizing gases and from thermomechanical cycles.

Technical progress

1.0 Analytical Efforts

In the present reporting period, Finite Element Analyses of the Zirconia-Zirconia disk specimen geometry shown in Figure 1 were performed. This is one of the specimen types to be used in the fracture mechanics experiments. Analyses were performed for four different a/R ratios and four different crack angles (θ) with respect to the loading line. The purpose of these analyses was to provide accurate Mode I and

Mode II stress intensity factor solutions for toughness determination and to develop crack length (a) versus compliance solutions for inferring crack length during tests.

The results for $\theta = 0$ are summarized in Table 1. For this case, the Mode II stress intensity factor (K_{II}) is zero. The quantities given in Table 1 are defined below:

$$F_{I,II} = K_{I,II} \frac{RB}{P} \sqrt{\pi a}$$

where a, R, B and P are as shown in Figure 1. The symbols δM and δL denote nondimensionalized crack mouth and load-point displacements defined as:

$$\bar{\delta}_{M,L} = \frac{EB}{P} \delta_{M,L}$$

where E is the Young's Modulus of the material. The analyses were performed assuming the plane stress condition.

The results show that the load point displacement (δ_L) is relatively insensitive to crack length. Therefore, the crack mouth opening(δ_M) at the center of the crack may be a better parameter to use in crack length determination. Figure 2 shows the crack opening profile corresponding to each a/R ratio. In the Figure 2, $\bar{V}$ denotes the nondimensional crack opening displacement and r is the distance measured from the center of the disk.

TABLE 1. Finite element analysis results for $\theta = 0$

a/R	F_I	$\bar{\delta}_L$	$\bar{\delta}_M$
0.1	0.9731	5.3706	0.1289
0.2	1.0165	5.3822	0.2697
0.4	1.1925	5.6499	0.6434
0.667	1.6829	6.3924	1.6145

Table 2 contains results corresponding the various θ values considered in the analyses. Currently, work is underway to generate similar solutions for ceramic-cast iron specimens of both the disk and the bend bar types.

TABLE 2. Tabulation of finite element analysis of compression disk specimens.

θ deg.	F_I	F_{II}	$\bar{\delta}_L$	$\bar{\delta}_M$	F_I	F_{II}	$\bar{\delta}_L$	$\bar{\delta}_M$
	R/a = 2.5				R/a = 1.5			
0	1.1925	0.0	5.6499	0.6434	1.6830	0.0	6.3924	1.6145
5	1.1344	0.4857	5.6578	0.6195	1.4924	0.9919	6.3953	1.5128
10	0.9700	0.9403	5.6825	0.5498	1.0196	1.7822	6.9577	1.2400
15	0.7156	1.3320	5.7220	0.4384	0.4197	2.2663	6.4309	0.8397
	R/a = 10.0				R/a = 5.0			
0	0.9731	0.0	5.3711	0.1289	1.0165	0.0	5.3922	0.2697
5	0.9411	0.3456	5.3714	0.1716	0.9793	0.3758	5.3941	0.2611
10	0.8490	0.6895	5.3735	0.1279	0.8774	0.7205	5.3982	0.2358
15	0.7019	0.9713	5.3751	0.0940	0.7055	1.0502	5.4067	0.1945

2.0 Experimental Efforts

2.1 Ceramic-Ceramic Joints

At the start of this reporting period a large zirconia/zirconia bond had been fabricated by hot pressing using a calcia-titania-silica (CTS) interlayer that contained approximately 30 weight percent of zirconia powder. Neither the strength of the joints nor the reproducibility of the process were known.

2.1.1 CTS + Zirconia Interlayer. Four-point bend tests of the large bond at room-temperature resulted in an average strength of 65.6 MPa, which yields a joint efficiency of 11 %. based on an as-produced strength of 620 MPa for zirconia. However, the heating cycles necessary to join zirconia to itself can reduce the strength of the ceramic by as much as a factor of two, so that a joint efficiency greater than 50 % is unlikely to be achieved. The scatter in bond strength is represented by a Weibull modulus of 6.1, which is comparable to reported values for ceramic-metal joints.

Fracture surface examination showed that the crack propagated through the CTS interlayer, which appeared to be porous, possibly due to shrinkage during solidification. Uneven distribution of zirconia particles in the CTS interlayer material was also observed.

The second large-scale bond proved to be weaker than the first (58.3 vs 65.6 MPa), with comparable data scatter. Mechanical damage was suspected during bend-bar machining, as manifest by specimen breakage during cutting as well as the low strengths of sound specimens. Accordingly, two additional large bonds were made in order to evaluate improved machining procedures. Prior to machining they were subjected to non-destructive inspection using a C-Scan apparatus to determine whether pre-existing defects in the bonds can be identified. Figure 3 is an example showing both 'good' and 'bad' local regions.

An improved machining procedure, which used a non-aqueous solvent for the cutting lubricant, did not reduce the breakage of bend-test specimens during machining. At this point it was decided that the inherent strength of CTS is too low and this interlayer system was temporarily abandoned.

2.1.2 Glass-ceramic and Zirconia Interlayers. The glass-ceramic (Corning 9606) was evaluated as a replacement for CTS because it is used in aerospace applications (strength > 175 MPa at room temperature). This is a magnesia-alumino-silicate glass ceramic (which was mistakenly referred to as lithium-alumino-silicate in the last bimonthly report) and has a thermal expansion of approximately $5 \times 10^{-6}/^{o}C$. Small blocks of zirconia (19 by 13 mm in cross section and 13 mm thick) were joined with the glass-ceramic + zirconia (GCZ) interlayer at a temperature of 1350 C with a maximum pressure of 70 kPa. Bend-test specimens were easily

machined from these joined blocks. Recently completed bend tests on these specimens gave strengths that ranged between 95 MPa and 130 MPa. These strengths are larger than joints fabricated using the CTS interlayers. Also, no problems in machining were encountered. The effort during the next reporting period will be directed at improving the GCZ joint strengths by optimization of the interlayer preparation and the time-temperature-pressure cycle, translating this joining method to the large-scale (two-inch diameter) billets, and machining joined billets into specimens for the mechanical evaluation.

2.1.3 Other Interlayer Materials. Several other interlayer materials were investigated. These included CTS without zirconia, CaO-$Al2O_3$-SiO_2 (CAS), sol-gel derived Mg-PSZ powder, and sol-gel derived Al_2O_3/ZrO_2. None of these systems appeared to be promising for reasons given in the Bi-Monthly Reports issued during this reporting period.

2.2 Ceramic-Metal Brazes

The ceramic-metal joining work is being carried out in a vacuum hot press, modified to accept a thermocouple inserted into a hole drilled in the cast iron specimen for better control of specimen temperature during brazing.

2.2.1 Brazing of Sputter-Coated Zirconia to Vapor-Coated Cast Iron. Partially stabilized zirconia was brazed to nodular cast iron with braze alloy 604 filler metal at 735 C for 10 minutes. The zirconia was first sputter coated with 0.3μm titanium at NASA Lewis Research Center and the cast iron was ground to 220 grit and vapor coated with 40μm copper. The thickness of 0.3μm was chosen because the thickness of the titanium layer affects the strength of the joint and 0.3μm is believed to be close to an optimum thickness. The joint had very low strength such that the specimen could not be machined to fabricate test specimens. Reasons for poor joint quality were investigated.

2.2.2 Evaluation of Copper Coating Technique for Cast Iron. Early results indicated there might be a problem with the copper deposition layer. To investigate this, two similar-metal couples were brazed: (1) as-ground nodular cast iron (NCI) to as-ground NCI and (2) copper-coated NCI to copper-coated NCI. The copper coated NCI was produced using evaporation. The difference between the as-ground NCI joint and the copper-coated NCI joint was startling. The microstructure of the copper-coated joint was characterized by the existence of a population of large flaws which in some cases were along the interface between the filler metal and the NCI and in other cases appeared to completely break up the continuity of the filler metal. The microstructure of the as-ground NCI joint, on the other hand, appeared uniform and coherent. The disruption of the filler metal around exposed graphite nodules appeared very localized. Apparently some aspects of the as-deposited copper layer were very detrimental to the development of a bond.

We next attempted to improve the electroplating procedure through the use of a strike plate prior to electrodeposition in the sulfate bath. A strike plate was deposited using a dilute copper-cyanide and sodium-cyanide solution followed by a 3-minute plate form a copper sulfate bath. Because it was noted in the previous experiment that a very strong bond developed between the as-ground NCI samples, in these experiments the as-ground NCI to as ground NCI experiment was repeated and a joint was attempted between as-ground NCI and a sample of Ti-coated PSZ supplied by ORNL. All of the specimens were strongly bonded.

2.2.3 Brazing Titanium-Coated Zirconia to As-Ground Cast Iron. Because a particularly sound small-area braze was obtained between as-ground NCI and partially-stabilized zirconia (PSZ), which had been Ti coated, using the RF sputter coating process, large-area brazes were attempted between ground NCI and Ti-coated PSZ.

Visual examination of the specimen indicated that the filler metal had completely melted but also had wetted and flowed up the sides of the NCI. Nondestructive ultrasonic examination showed continuous voids in the brazed joint. The cause of the voids was not known but was thought to be due to the release of argon that was trapped in the Ti layer during the argon sputter coating.

Three bend-bars were machined from the joined billet The bars were tested in 4-point bending, and the strengths are given in Table 3:

TABLE 3. Strength of zirconia/nodular cast iron bonds.

Specimen No.	Strength, MPa
MCB-4	162
MCB-5	76
MCB-6	161

All the bend bars showed the presence of flaws (as large as 0.5 mm) before they were tested. Despite the presence of these flaws, the measured strengths of up to 160 MPa are very encouraging.

2.2.4 Brazing Titanium-Coated Zirconia to Copper-Plated Cast Iron at ORNL. It was then decided to investigate whether use of couples with an electrodeposited copper layer on the NCI and a NASA sputter-coated Ti layer on the PSZ could produce successful bonds using ORNL procedures. Bonds were made using several thicknesses of Ti and no voids were detected by ultrasonic examination.

The specimens that had been brazed at ORNL were then cut into several pieces for SEM, TEM and optical-metallographic examination of the bonds. For all thicknesses, a Ti layer was visible in the optical microscope. In addition, primary Ag and Cu solid solutions plus a third phase, which appeared to be Ti rich, were evident when thicker Ti layers were used.

To better characterize the microstructure a method of preparing TEM specimens was developed. A three-mm-diameter disk was cut using an abrasive slurry drill instead of an ultrasonic cutter. The disk was polished to a thickness of about 70 μm and dimpled to produce a small hole, about 0.4 mm diameter. The disk was then ion milled without a mask for 30 minutes using only the upper gun, and then for 45 minutes using both guns. This method was successful in that the interface between the zirconia and the filler metal was thin enough for TEM examination.

Milestones

The program is significantly behind schedule because of the difficulties we have experienced in manufacturing joints for testing and analysis. We will complete manufacture and testing of the ceramic-to-ceramic joints during the next reporting period but are faced with uncertainty concerning the ceramic-to-metal joints. We are currently working with ORNL to determine the source of our difficulty in making good ceramic-to-metal joints. The analysis is proceeding but is behind schedule because the joint manufacture tasks are behind schedule.

Publications

S. L. Swartz, B. S. Majumdar, A. Skidmore, and B. C. Mutsuddy, "Joining of Zirconia Ceramics with a CaO-TiO_2-SiC_2 Interlayer", Materials Letters, Volume 7, number 11, February 1989.

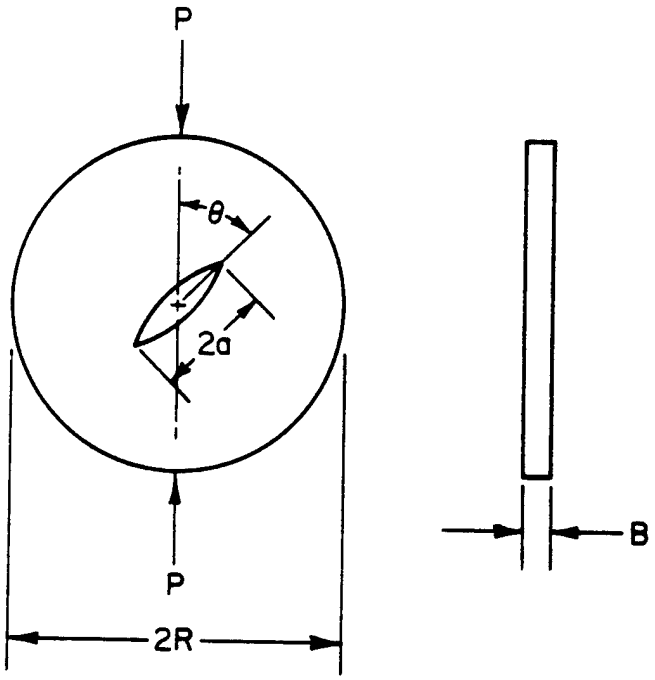

FIGURE 1. Compression disk specimen geometry.

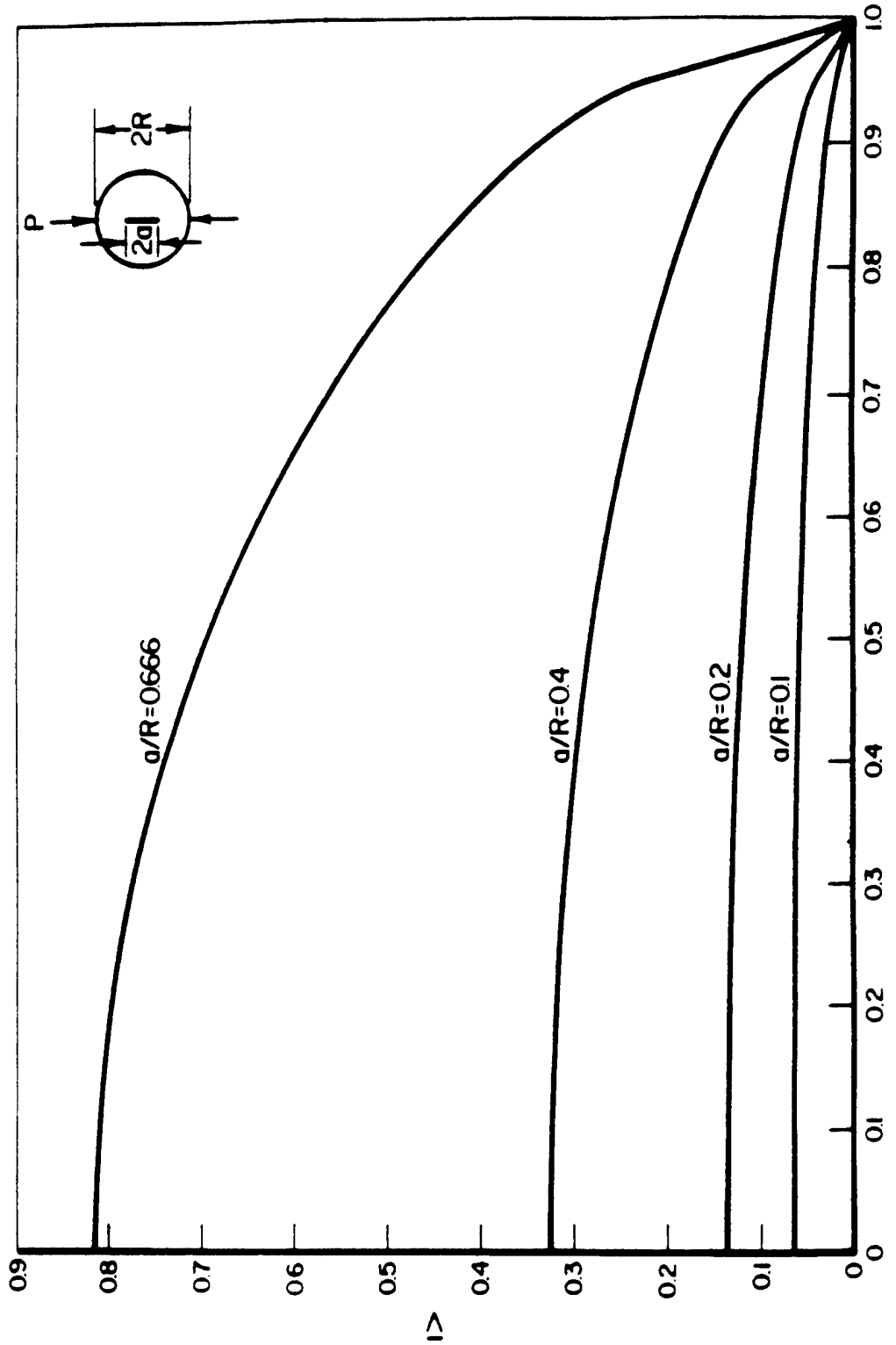

FIGURE 2. Crack opening profiles for compression disk specimen ($\theta = 0$).

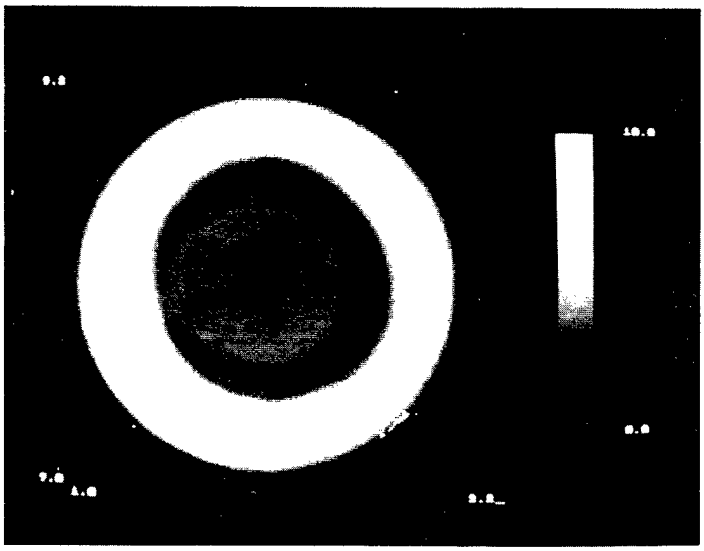

FIGURE 3. C-scan showing variation in ultrasonic wave intensity from the joint region. The outer edge of the annular white band corresponds to the periphery of the round billet. Dark region would correspond to the good joint, while a bright region would correspond to a poor joint.

Analytical and Experimental Evaluation of Joining Silicon Carbide to Silicon Carbide and Silicon Nitride to Silicon Nitride for Advanced Heat Engine Applications

G. A. Rossi, C. H. Bates, G. J. Sundberg, and F. J. Wu (Norton Company)

Objective/scope

The purpose of this program is to develop techniques for producing reliable ceramic-ceramic joints and analytical modeling to predict the performance of the joints under a variety of environmental and mechanical leading conditions including high temperature, oxidizing atmospheres. The ceramic materials under consideration are silicon nitride and silicon carbide. The joining approach for silicon nitride is based on the ASEA hot isostatic pressing process while the plan for silicon carbide is to co-sinter green forms together. These joining methods were selected to produce joints which exhibit the minimum possible deviation in properties from those of the parent ceramic materials. Analytical models will be experimentally verified by measurements on experimental size and scale-up joints produced as part of this work.

Background

Because of their strength, oxidation resistance, and other desirable high temperature properties, silicon nitride and silicon carbide are under extensive study for use in advanced gas turbine and internal combustion engines. In both engine types there are requirements for joining the ceramics to themselves, other ceramics, and various engineering alloys. Existing bonding methods lack the high temperature capabilities required for use in advanced heat engines. Further, analytical modeling techniques to predict joint reliability and performance have not been developed. These technical needs have prevented consideration of economically fabricating large, complex ceramic engine components from smaller, less complicated segments. The current program will address these issues for silicon nitride to silicon nitride and silicon carbide to silicon carbide joints.

Technical progress

Joining of Silicon Nitride to Silicon Nitride

At the writing of the last semi-annual report the joining of NCX5100 (4wt%Y_2O_3-Si_3N_4) with self-bonded and slip interlayers by glass encapsulated HIP co-densification was proven effective. The room temperature and 1300°C flexure strength data exhibited that consistent, reproducible strengths had been achieved with slip and bare join interlayers. The flexural fast fracture strengths of the joins with slip and self-bonded interlayers were similar and the time dependent material response of the joins at high temperature was required to enable selection of the superior join.

Creep and stress rupture evaluation of the joins performed at ORNL/HTML with MKFerber will be presented. Progress towards milestones will be discussed.

Procedure

The method by which joins were fabricated has been explained in prior reports [1,2].

All mechanical property evaluations were determined in flexure using Mil. Std. 1942 B geometry specimens, 3 mm x 4 mm x 55 mm, with the join plane in the center of the specimen oriented perpendicular to the long axis of the specimen. All flexure testing was performed in four point-quarter point loading on a 40 mm outer span. Flexural strength was measured at a 0:508 mm/min. cross-head speed. The number of flexural fast fracture specimens tested at 22°C and 1300°C were 12 and 8, respectively.

Stress rupture and creep testing were performed at a constant load equivalent to 200, 250 and 300 MPa stress. Tests were suspended after an arbitrarily determined survival time of 200 hrs. In addition to the real time measurement of strain during creep tests, the curvature of specimens after stress rupture testing was used to calculate the strain to failure (or if the sample survived, the maximum strain at 200 hrs). Fractography after strength testing was performed optically and by SEM.

Mechanical Property Evaluation

Join integrity of the self-bonded and slip interlayer joins was evaluated by flexural strength testing before stress rupture and creep testing. Two materials were tested, which are designated A and B. Material A was obtained from mixes 37 and 40, whereas material B was made from mix HM4.[3] Both materials have the same composition, i.e. 4wt%Y_2O_3-Si_3N_4, but B has a coarser grain size distribution than A.

The mean 22°C flexure strength of the A material unjoined control (1030.1 MPa) was greater than the self-bonded and slip interlayer joined samples (~881 MPa) due to two and one respective low strength (400 to 500 MPa) fractures initiating within the join (Table 1). The remainder of the joined samples failed within the parent material. Join fractures of the self-bonded material and slip interlayer materials originated at clearance between the joined surfaces that was incompletely eliminated during densification (Figure 1). Incomplete elimination of clearance may be due to inadequate shear at the join interface by the isostatically applied stress during densification, grinding scratches of greater depth than usual, or inadequate filling of the surface topography by the slip interlayer during sample preparation. The mean 22°C flexure strength of the B material with a self-bonded interlayer join was marginally less than the unjoined control with no fracture originating within the join. All of the fractures originating within the parent material were subsurface flaws from grinding damage. Absence of join failure was related to the low probability of failure of the small stressed join volume by the flexure test or a finer flaw population within the join relative to the parent material.

The mean 1300°C flexure strength of the A material unjoined control was greater than that of the self-bonded and slip interlayer joins (Table 2). The self-bonded joined material B exhibited the greatest flexural strength, 713.6 MPa. None of the 1300°C flexure tests exhibited fracture initiating at the join interlayer. Fracture originated at the tensile surface, but the cause was obscured by oxidation. The absence of join failure may be due to a low probability of failure at the small stressed join volume, a finer flaw population within the join relative to the parent material, or the blunting of flaws at the join by viscous flow of the grain boundary phase.

The 22°C and 1300°C flexural strengths of the self-bonded and the slip interlayer joins of material A were similar. Time dependent response of the material by stress rupture and creep testing at 1370°C was required for selection of the superior join interlayer.

The strain calculated from the measured curvature of flexure specimens after stress rupture at 250 MPa has been plotted in Figure 2. An arbitrary survival time of 200 hrs was selected. All data points at times shorter than 200 hrs indicate failure. The measured strain at failure was plotted as a function of the time to failure for the samples that failed under 200 hrs. The points at 200 hrs with the corresponding maximum strain were suspended tests.

The A material unjoined control exhibited a variable time to failure at 1370°C and 250 MPa. The stress of 250 MPa at 1370°C represents a transition in the behavior of the A material. At 200 MPa times to failure consistently exceeded 200 hrs and at 300 MPa the times to failure were all under 2 hrs. The joined A material accommodated more strain than the unjoined control, but all of the former failed before 200 hrs at 250 MPa. Fracture never originated at the join. The material A with self-bonded and slip interlayers exhibit similar creep rate. There was an apparent longer time to failure for the A materials with slip interlayer joins as compared to the self-bonded joins. This time to failure variability may be due to inherent material variability or a change of the parent material's creep behavior by the joining process. Causes for the apparent lifetime difference are being investigated.

Unjoined controls of the B material consistently survived to +200 hrs at 1370°C under stresses of 250 and 300 MPa. Self-bonded joined samples of the grade B material (with coarser microstructure) exhibited superior survival and creep resistance relative to the A material joins (Figure 2). The B joins survived a 200 hr exposure at 250 MPa and 1370°C with a maximum strain of 0.006. The mean flexure strengths of the self-bonded B material at 22°C and 1300°C were 786.8 MPa (std. dev. = 84.4 MPa) and 713.6 MPa (std. dev. = 36.5 MPa), respectively. Fracture never occurred at the join in the fast fracture tests of the B material. The joined B material with the slip interlayer has not been tested, but it may have improved stress rupture life compared to the self-bonded B material.

Creep of the silicon nitride joined samples was summarized by the representative deflection vs. time curves in Figure 3. Consistent with the stress rupture data, the A grade material with the self-bonded and slip interlayers failed before 200 hrs, and had similar creep rates, with the slip interlayer sample reaching longer times to failure. The B-unjoined control test was suspended before 200 hrs due to a heating element failure and did not fracture. The B-self bonded material had the lowest strain to failure of the joins and survived the exposure at 1370°C and 250 MPa.

The join geometry, interlayer, and material chosen for the remainder of the contract were the slip-bonded butt joins of material B.

Scaleup Evaluation

Evaluation of scaleup feasibility is ongoing with the following summary of results to date (Table III). The scaleup phase requires a join cross-section of 20.0 cm^2. It is possible to manufacture a dense, rectangular joined structure with 21.8 cm^2 cross-section of insufficient length for the tensile specimens for scaleup. A cylindrical monolith of greater cross-section than required was not densified. Densification of cylindrical joins of 20 cm^2 cross-section will be attempted soon.

Manufacture of Characterization Joins

Large mills of the B material have been used to manufacture 35 kg of NCX-5100 powder for the remainder of the contract. Joins and unjoined controls for the characterization phase of the contract have been manufactured. Joined rectangular billets of 2.8 cm x 3.6 cm x 8.4 cm final dimensions will be used for the manufacture of flexure and tensile (dog bone) specimens. HIPed to date were 32 rectangular billets, all of theoretical density. The dense rectangular billets will be sufficient to satisfy the flexure and tensile (dog bone) specimen requirements of the characterization phase (Task I) and approximately half of the verification phase (Task II).

Joined cylindrical samples of 2.03 cm diam. x 16.5 cm final dimensions to be used for DOE tensile specimens have been most difficult to fabricate. Successful joining of shorter, 10.2 cm, specimens used to confirm viability of the method did not present the green handling problems encountered by the longer and more unstable 16.5 cm samples. There has been much loss in green handling requiring numerous reworks. In addition. 10 kg of cylindrical stock was lost by thermal shock in a furnace control malfunction. Consequently, the outstanding sample balance for the characterization phase of 6 cylindrical joins will be filled in May, 1989.

Summary

The glass encapsulated HIPing of silicon nitride to silicon nitride joins was successfully used to obtain high strength creep resistant joins for use above 1300°C. Dense joins were fabricated with behavior similar to the parent material. Joined 4 wt% Y_2O_3-Si_3N_4 bodies of the B material exhibited mean 22°C and 1300°C flexural strengths of 786.8 MPa and 713.6 MPa, respectively, with no fracture initiating within the join. The joined B material survived 200 hrs at 1370°C under a constant stress of 250 MPa with a maximum strain of 0.006.

The slip interlayer joins of the B material will be used for the remainder of the contract. The joined and unjoined control stock for the flexural and tensile (dog bone) specimens required by the characterization phase have been manufactured. Most of the cylindrical joins for the DOE tensile specimens required by the characterization phase have been manufactured with six joins outstanding. Approximately half of the stock for the verification phase has been manufactured. The remainder of the characterization and verification joins will be made shortly. Scaleup feasibility will be performed in parallel.

Joining of Silicon Carbide to Silicon Carbide

In the previous semi-annual report, two joining methods for SiC/SiC were described, i.e. the slip/CIP method for green parts and the friction fitting of polished surfaces for dense parts. The latter method, however, did not work for parts with surface area larger than 1.5 cm^2, the probable reason being the lack of necessary flatness. An attempt to join two dense cubes of about 2.5 cm side with this method, by first coating the two friction fitted samples with a CVD SiC coating and then glass encapsulation ASEA HIPing failed. The cubes after the HIP run were found separated. Due to this failure and to the lack of polishing equipment capable of creating flat mirror like surfaces, this method was abandoned in favor of the slip/CIP method.

The slip/CIP method, which had worked satisfactorily for joining 3 x 3 x 6 cm green parallelepipeds on the 3 x 3 face as mentioned in the previous report, presented, however, problems when billets with larger dimensions were used. Due to the unavailability of large steel dies, green, cold isopressed blocks were made by pressing the beta SiC powder in rubber molds. These blocks were then cut and carefully machined to the dimension of 5.8 x 5.0 x 3.3 cm. The slip was applied to the 5.8 x 3.3 cm face of one block and the second block was pressed by hand against the first one, after which both were cold isostatically pressed at 207 MPa, carefully dried and then fired to 2100°C in Ar using the firing schedule that had given satisfactory results with the 3 x 6 x 6 cm blocks mentioned above. Unfortunately no joint was formed and other problems were noticed, i.e. lack of densification, density gradients, cracking mostly in proximity of the joint area, distortion after firing. For example, the typical fired density was about 90% of TD, lower than that measured on thinner billets (95-97% of TD) previously made with the same powder and same firing schedule in the same furnace. In addition, upon slicing the fired blocks, considerable density variations were found between the outer slices (92-93% of TD) and the inner slices (87-88%

of TD). The outer slices appeared shiny, whereas the inner slices had a central dull region clearly containing open porosity. It is likely that the density difference between the inner and outer regions in the fired body is the result of similar density variation in the green CIPed part. The density (wax method) of two green slices were found to be 1.92 g/cm3 and1.96 g/cm3 for the inner and outer regions, respectively. The density gradients in the green billets are believed to have caused the distortion noticed in the fired parts, which in general showed convex surfaces. Another possible cause for lack of densification in the core of the billet is the degassing which can take place at higher temperature after an impervious skin has already formed. The gases, mostly SiO and CO, would then create a counterpressure which opposes the sintering pressure. The cracking observed especially near the joint region may be due to localized stresses arising from different densification rates between interlayer and material, which in turn may be caused by green density differences.

After the unsuccessful attempts to joining CIPed 5.8 x 5.0 x 3.3 cm billets, billets with different dimensions were made by die pressing at 3 MPa in a steel die (12.5 x 7.6 x 2.9 cm after die pressing). The slip was applied to one face (7.6 x 2.9 cm) and the second billet was joined to the first with the usual procedure. These long (25 cm) samples were then CIPed, dried, and fired with the same firing schedule. The result was that no bond was formed, but the individual billets were uncracked and free from distortion, even though of relatively low density (90% of TD) and with density variations as noticed previously.

Given the repeated failures in bonding large billets, two attempts were made to join green billets (2.5 x 6.9 x 8.0 cm) with the glass encapsulation ASEA technology on the 2.5 x 6.0 cm face. With this method a preliminary degassing at high temperature is necessary to prevent pressure build up by the SiO and CO or other gases released during the HIPing run. Degassing was done at 1600°C in the first attempt under high vacuum, but the two billets came apart and appeared coated by a carbon layer, indicating possible thermal decomposition of SiC to Si and C. In a second attempt, the degassing was performed at 1500°C with a moderate vacuum, but also in this case the two billets were found separated. It was, therefore, decided to abandon this route.

The possibility of can encapsulation HIPing was also explored, but the idea was abandoned after contacts with two Massachusetts companies, IMT and NRC, for technical reasons (no suitable metal cans were available for HIPing at 1800 - 1900°C) and for excessive cost.

After the disappointing results obtained with large billets, it was decided to order a new split mold steel

die for pressing blocks of 3.8 x 2.9 x 2.1 cm, which were joined with the slip/CIP method on the 2.9 x 2.1 cm face. The fired sample had typical dimensions of 6.3 x 2.4 x 1.8 cm and could be used for machining 3 x 4 x 50 mm MOR bars (MIL 1942 B). Another die was ordered for pressing longer and wider blocks, i.e. 5.7 x 3.8 x 8 cm, to be joined together to make the "dog bone" (NBS type) tensile specimens for the characterization task. This die has not been received yet.

To date, 15 joined samples made with the 3.8 x 2.9 x 2.1 blocks have been made which should provide about 150 MOR bars for characterization. An improved beta-SiC powder has been used, which has consistently given a fired density of 97%, with small density variations (97.5% of TD outside, 96% inside). The slip was made with the same powder used to press the blocks. Eighteen bars have been already tested in 4 pt (20 and 40mm spans), 10 at room temperature and 8 at 1530°C. Eight control bars (no joint) machined out of billets made and fired in the same conditions were also tested at room temperature. The results are shown below.

	25°C (Joined)	25°C (Control)	1530°C (Joined)
Avg. MOR	309 MPa	382 MPa	313 MPa
Std. Dev.	98 MPa	43 MPa	72 MPa

Fractographic analysis results are not available yet, but optical microscopy suggests that some of the joined bars broke at the joint. These results are very encouraging and indicate that the goal of 138 MPa tensile strength can be met. The strength values reported above are better than those previously measured on 2 x 3 x 30 mm test bars, i.e. 186 MPa for joined bars and 241 MPa for controls. The main reasons for such improvement are believed to be better powder and optimized slip/CIP method.

Creep Modeling

The preliminary modeling procedure is completed. The user creep subroutine is completed and simple verification models were used to check the response of the subroutine against results from the literature and analytical solutions. The subroutine basically uses the theta projection constants to interpolate and extrapolate the creep strains from limited data to finite element models. The theta parameters can be calculated from uniaxial experimental data by means of a commercially available program called "Creep Curve Parameter Estimation" by R.W. Evans and B. Wilshire at University College, Swansea, UK [4]. All

additional subroutines and miscellaneous programs have been compiled and run with no major problems. The next step in the creep modeling milestone is to create simple models for which a known solution is available and verify their results against the output of the entire model. These verification runs will be done in the near future.

Oxidation Characterization Plan

The preliminary characterization experiments to describe the thickness of the oxidation layer as a function of the oxidation exposure time have been completed. Oxidized samples were submitted to x-ray diffraction to measure the oxidation layer thickness. The decrease in intensity of an x-ray beam as it passes through material is given by

$$I = I_0 \exp (\mu/\rho)\ \rho_{eff} \times x)$$

where I is the reflected intensity
I_0 is the incident intensity
(μ/ρ) is the mass absorption coefficient
ρ_{eff} is the effective density of the material
x is the pathlength of the beam

Both the reflected and incident intensities are measured values.

In addition, some samples were examined through SEM to verify x-ray measurements. Norton's SiC (NCX-4500) was oxidized at 1400°C and 1530°C for up to 200 hours, giving oxidation layer thicknesses up to 15 microns as shown in Figure 4. Similarly, Norton's Si_3N_4 (NCX-5100) was oxidized at 1200°C and 1300°C and results showed a greater resistance to oxidation (3 microns) compared to SiC. Both materials show the same level of scatter which can be associated to the measuring technique. Nevertheless, these curves provide the oxidation thickness range at these temperatures and will be used to determine the specific details of the oxidation characterization experimental plan.

Cyclic Fatigue Modeling

Cyclic fatigue experiments will be conducted at room temperature. If tests show no significant cyclic effect then further cyclic modeling will not be pursued. Cyclic fatigue is caused by the accumulation of damage equivalent to stepwise integration of static loads and damage due to the repetitive action of the loads (cyclic effect). If

samples show the same fatigue life independent of frequency, then there is no action of cyclic effect. A.G. Evans from UCLA Santa Barbara [5] has reported in the literature a method for quantifying cyclic fatigue damage from static data by assuming no cyclic effect. This mathematical formulation can be used to check the validity of our experimental predictions. Furthermore, a model to predict the probability of survival of a ceramic joint exposed to a static fatigue is being developed and depending on experimental results it may be implemented into finite element analysis. It is expected that if no cyclic effect is shown then the cyclic fatigue of ceramic joints can be predicted from A.G. Evans [2] cyclic-static model, our static-fast fracture model, and fast fracture statistical data.

Status of milestones

Due to the problems encountered in joining SiC and to the expected difficulties related to the fabrication of the joined small cylindrical tensile specimen for both characterization and verification tasks, the following milestone may not be met.

1.	Complete characterization testing	8/31/89
	If this milestone is not met, the following ones, which depend on it, may have to be adjusted.	
2.	Complete model development	9/30/89
3.	Complete testing and model validation on 2 cm2 joints	10/31/89
4.	Complete testing and model validation on 20 cm2 joints	1/31/90
5.	Complete final report	4/30/90

The status and resolution of the milestones will be discussed during our visit to ORNL the first week of May, 1989, with the ORNL contract monitor, Dr. M. Santella.

Publications

GJSundberg, MKFerber; "The Joining of Silicon Nitride for Heat Engine Applications", Proceeding of the 13th Annual Conference on Composites and Advanced Ceramics, Cocoa Beach, Florida, January, 1989, to be published in 1989.

References

1. ORNL Joining Contract Semi-Annual Report, April 12, 1988.

2. ORNL Joining Contract Semi-Annual Report, September 26, 1988.

3. ORNL Joining Contract Bi-Monthly Report, November to December, 1989.

4. R.W. Evans and B. Wilshire, "Creep of Metals and Alloys", The Institute of Metals, Book #304, UK, 1985, pp. 197-208.

5. A.G. Evans, "Fatigue in Ceramics", Int. Journ. of Fract., Vol. 16, No. 6, Dec. 1980, pp. 485-498.

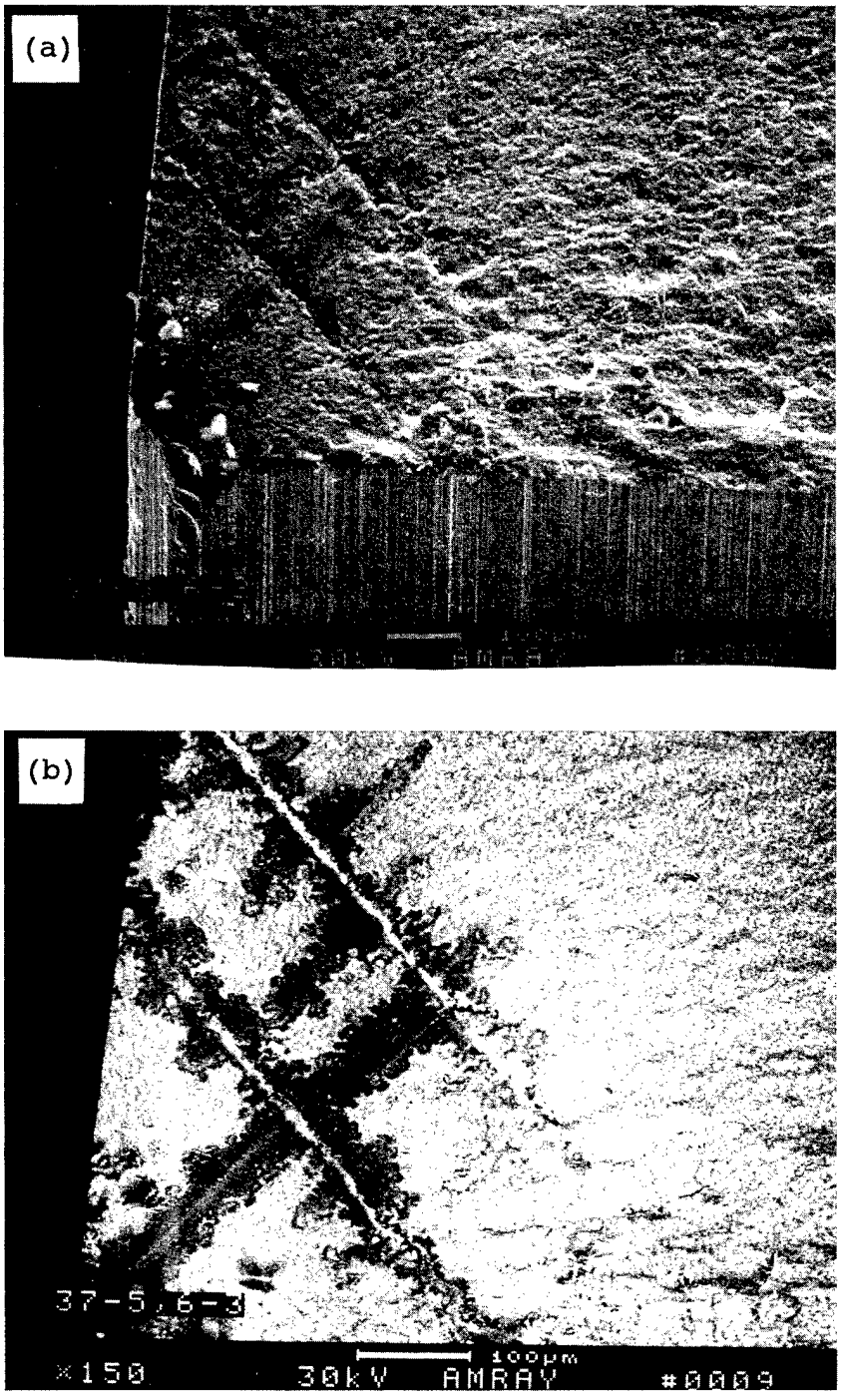

Fig. 1. Scanning electron micrographs of fracture surface of slip interlayer butt join. Material A. (a) Secondary electron image; (b) backscatter electron image.

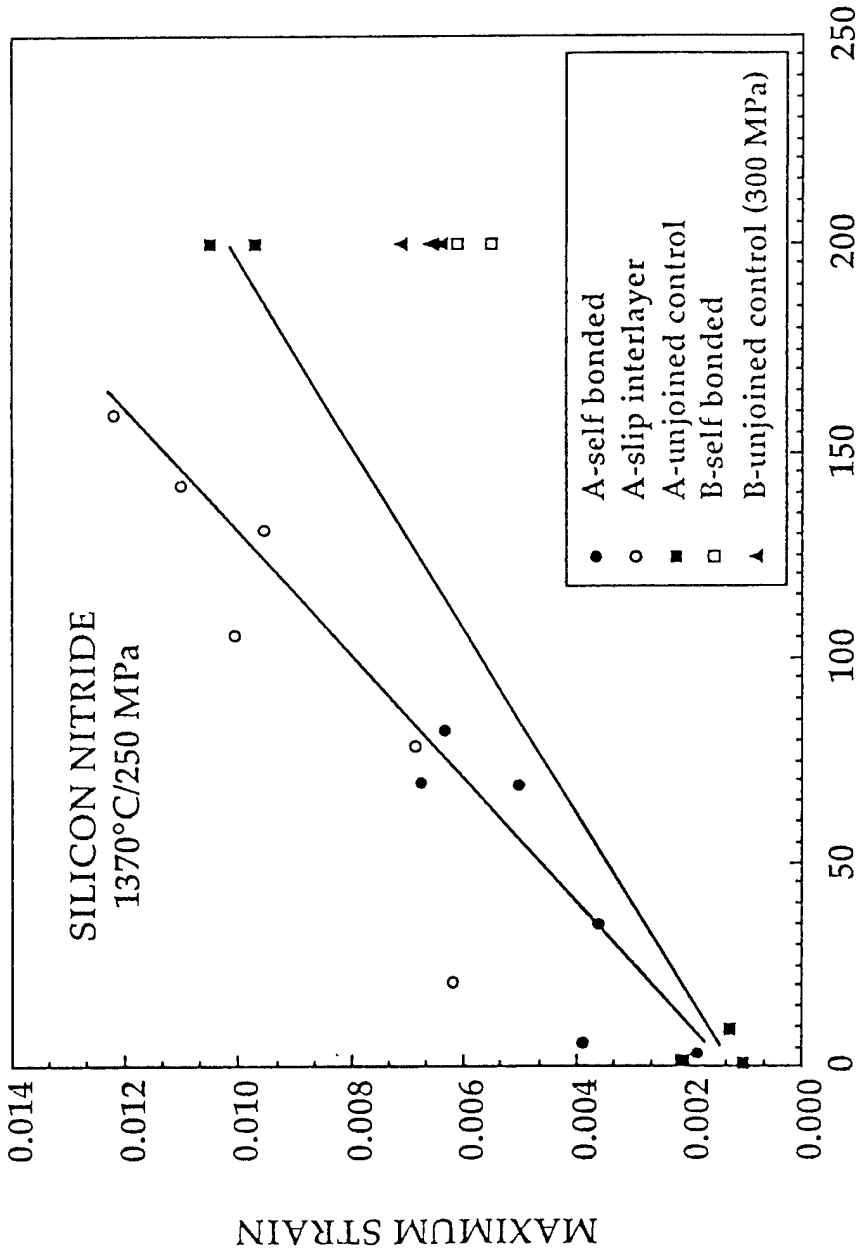

Fig. 2. Maximum strain as a function of time of post stress rupture specimens.

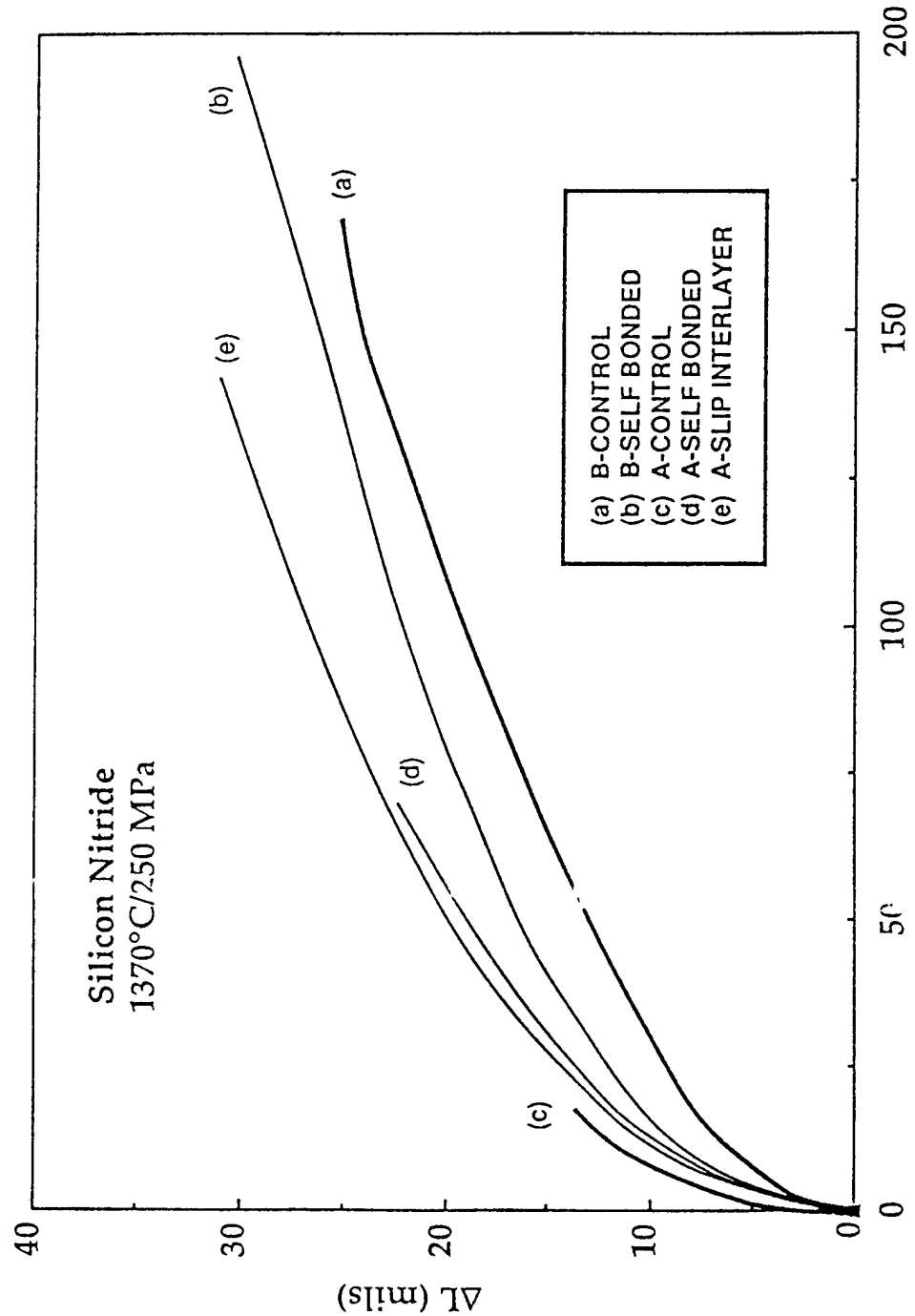

Fig. 3. Deflection as a function of time at 1370° and 250 MPa.

Table I

22°C Flexure Strength
(MPa)

	Mean	Std. Dev.	Failure at Join
A-self bonded	881.4	223.4	2
A-slip interlayer	881.8	202.2	1
A-unjoined control	1030.1	70.3	-
B-self bonded	786.8	84.4	0
B-unjoined control	841.0	68.2	-

Table II

1300°C Flexure Strength
(MPa)

	Mean	Std. Dev.	Failure at Join
A-self bonded	610.9	33.8	0
A-slip interlayer	649.5	35.2	0
A-unjoined control	704.8	24.1	-
B-self bonded	713.6	36.5	0

Table III

HIP Densification Summary
for Scale-Up Using HM-4 Powder

Sample Type	Target Dimensions (mm)	Cross-Section (cm^2)	Density (gm/cm^3)	Comments
Unjoined Monolith	23.5 x 92.7 x 121.9	21.79	3.239	100% Dense
Joined Slip/Butt	28.2 x 50.8 x 95.3	14.51	3.237	100% Dense
Joined Slip/Butt	28.2 x 50.8 x 184.1	14.51	2.939	98.8% Dense
Unjoined Monolith	63.5 diam. x 142.2	31.67	2.587	79.9% Dense

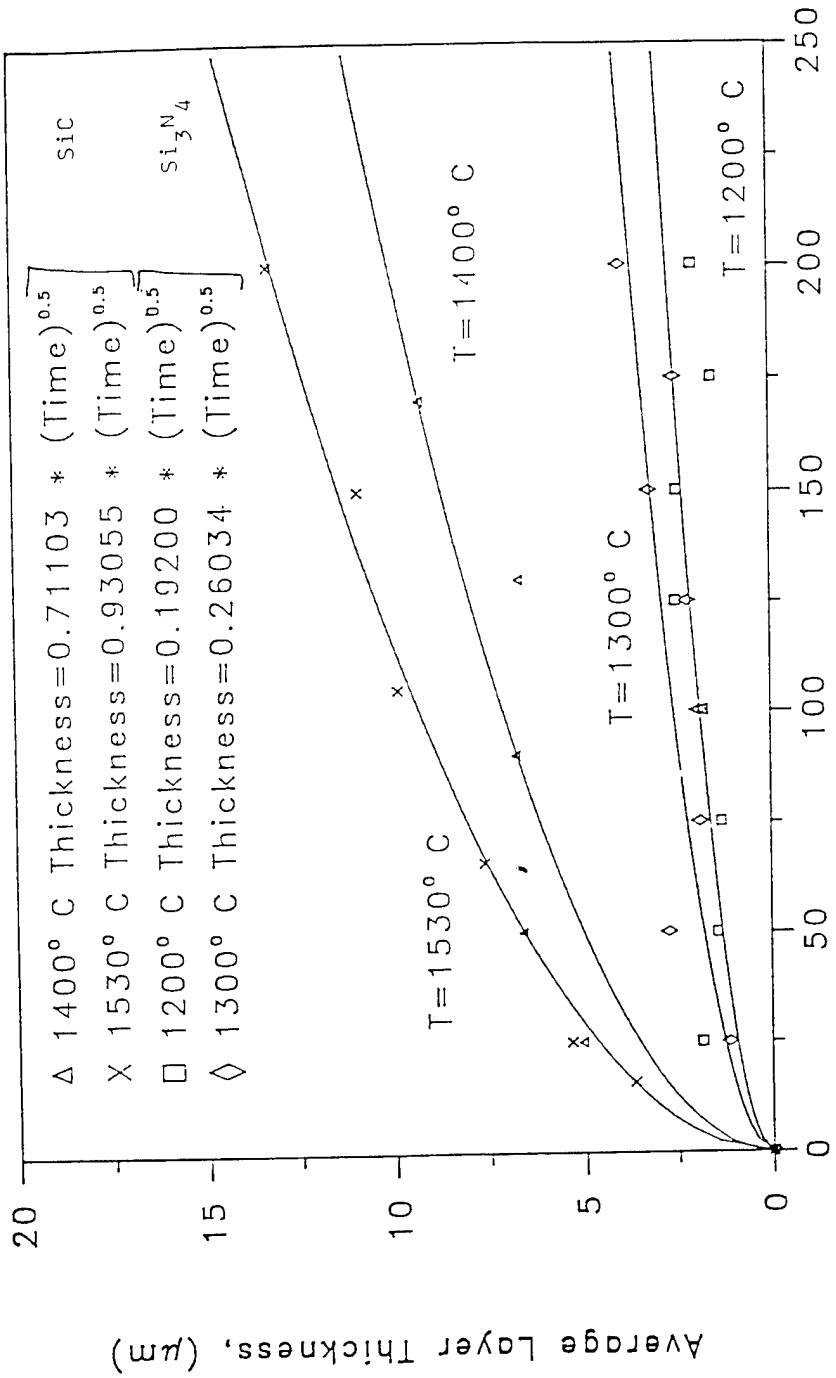

Fig. 4. Oxidation behavior of Norton's NCX-4500 and NCX-5100.

2.0 MATERIALS DESIGN METHODOLOGY

INTRODUCTION

This portion of the project is identified as project element 2 within the work breakdown structure (WBS). It contains three subelements: (1) Three-Dimensional Modeling, (2) Contact Interfaces, and (3) New Concepts. The subelements include macromodeling and micromodeling of ceramic microstructures, properties of static and dynamic interfaces between ceramics and between ceramics and alloys, and advanced statistical and design approaches for describing mechanical behavior and for employing ceramics in structural design.

The major objectives of research in Materials Design Methodology elements include determining analytical techniques for predicting structural ceramic mechanical behavior from mechanical properties and microstructure, tribological behavior at high temperatures, and improved methods for describing the fracture statistics of structural ceramics. Success in meeting these objectives will provide U.S. companies with methods for optimizing mechanical properties through microstructural control, for predicting and controlling interfacial bonding and minimizing interfacial friction, and for developing a properly descriptive statistical data base for their structural ceramics.

2.1 MODELING

2.1.1 Modeling

Microstructural Modeling of Cracks
J. A. M. Boulet (University of Tennessee)

Objective/scope

The goal of the study is to develop mathematical procedures by which existing design methodology for brittle fracture could accurately account for the influence of protrusion interference on fracture of cracks with realistic geometry under arbitrary stress states. To predict likelihood of fracture in the presence of protrusion interference, a simulation will be developed. The simulation will be based on a three-dimensional model of cracks with realistic geometry under arbitrary stresses.

Technical progress

We have previously reported plane strain and plane stress solutions for the problem of a Griffith crack subjected to arbitrary biaxial stress at infinity with interference of two wedge-shaped protrusions (one on each crack face) at an arbitrary position on the crack. The stress fields associated with these solutions have been used to calculate the stress intensity factors (SIF's) at both crack tips. Using the well-known biaxial form of Griffith's fracture criterion, we found that the presence of a single interference site at the middle of the crack has little influence on the predicted fracture stress.

Our model has been extended to include multiple interference sites (wedge-shaped protrusion pairs). We have found that the influence of interference on the fracture stress increases monotonically with the number of interference sites. The fact that the influence increases monotonically with the number of sites is not surprising. The greater the number of sites, the more shear is carried by the protrusions and the less by the crack tips. Because of this result, one would expect the influence of interference to be substantial when it occurs at many sites. Given that the influence of interference increases with the number of interaction sites, it is logical to consider extending our results to include a large number of sites. But, we have shown that the present model would not give accurate results in this case.

Because the influence of protrusion interference is expected to be significant, it is appropriate to generalize our method to accomodate a three-dimensional model. Such a model could include, for instance, a penny-shaped crack in triaxial stress with interference sites at various places on the crack. Development of a three-dimensional model has begun.

It is unreasonable to expect to know precise protrusion geometries and interference locations for a real crack. However, it is reasonable to expect to know key parameters of statistical distributions of protrusion geometries and interference locations for a real crack.

Given these, a protrusion interference model like that being developed could be incorporated in a simulation (based, for instance, on Monte Carlo methods) to predict the influence of interference on the likelihood of fracture.

Given the ability to simulate interference in real cracks, we can develop a procedure for incorporating the results of simulation into current design practices can be explored.

Status of milestones

The milestone schedule is as follows:

2111003	07-01-89	Choose method for solving three-dimensional protrusion interference elasticity problem.
2111004	07-15-89	Represent crack faces as mathematical surfaces embedded in Euclidean space.
2111005	08-15-89	Model protrusion interference kinematics.
2111006	10-01-89	Solve three-dimensional protrusion interference elasticity problem.
2111007	02-01-90	Develop computer-based implementation of mathematical model.
2111008	04-01-90	Define experiments for verification of mathematical model.
2111009	07-01-90	Conduct and evaluate experiments to verify mathematical model.
2111010	08-15-90	Define numerical simulation based on previously verified mathematical model.
2111011	01-01-91	Implement previously defined simulation on computer.
2111012	04-01-91	Define design procedure based on computer-based simulation.
2111013	07-01-91	Identify methods for gathering data required for design procedure.
2111014	12-31-91	Obtain experimental verification of design procedure.

2.2 CONTACT INTERFACES

2.2.1 Static Interfaces

The Elastic Properties and Adherence of Thin Films and Coatings on Ceramic Substrates
D. L. Joslin (University of Tennessee)

Objective/scope

The objective of this research is the examination of the effects of ion bombardment on the structure of thin ceramic films on ceramic substrates. The material combinations will include oxide films that have (a) no solid solubility, (b) limited solid solubility, and (c) complete solid solubility with the substrate material (also an oxide). An important part of the task is the development of techniques for determination of elastic and plastic properties of thin films or coatings on ceramic substrates and for the determination of the strength of the bond between the film and substrate. This development was started during the previous contract period and is continuing. These techniques will be used to determine the hardness, elastic modulus, and adherence of each material combination. The main testing techniques will be the ultra-low load micro-indentation tester (Nanoindenter) and thermal cycling tests.

Technical progress

In connection with the development of techniques for characterizing the mechanical properties of the films/coatings and the interface adhesion, measurements have been made on diamondlike carbon (DLC) films deposited on sapphire, AlON, glass, and silicon substrates, and on SiC surfaces that were both amorphous and crystalline. This set of samples provides a wide range of structures and properties for evaluating the testing techniques.

Hardness data taken on the adherent DLC films show that the substrate affects the measured hardness, and that the measured hardness value approaches that of the substrate alone at increasing indentation depths. In contrast, hardness data from the nonadherent DLC films show no substrate effects--the measured hardness is virtually the same at each of the depths sampled. This is because the film/substrate interface is perpendicular to the direction of indentation, and is therefore subjected to substantial shear stresses during the indentation process. A weak interface cannot support shear stresses, so the shear stresses produced during indentation are not effectively transferred across the interface. Because of this, the substrate cannot plastically deform to the same extent that it would have if the film were adherent, and the substrate's effect on the measured hardness would not be as great. Similar results were obtained for both substrates that were harder and softer than the DLC films.

The data did not give substrate-independent values for either the adherent or the nonadherent DLC films. The measured modulus values depend more on the exerted normal stresses than on the shear stresses. Although the film/substrate interface for a nonadherent film is weak in shear, it can support compressive normal stresses. Thus the substrate affects the modulus measurements for both the adherent and the nonadherent films. The modulus of these films is between 36 and 100 GPa.

These results indicate that the nanoindenter is capable of qualitatively distinguishing between adherent and nonadherent films.

In preparation for the ion beam mixing experiments, the computer codes TRIM and PROFILE were used to design the ion beam conditions for the first series of experiments. In these experiments an ion beam of oxygen and an inert ion beam will be used to irradiate 1000 ° Cr films sputter deposited on single crystal Al_2O_3 (c-axis normal to the surface). The energy required to deposit the oxygen at the Cr/Al_2O_3 interface was found to be 80 keV.

In preparation for the Cr_2O_3/Al_2O_3 mixing experiments, sputtering parameters are now being determined for rf sputter deposition of the Cr_2O_3 films.

Status of milestones

None

Publications

None

2.2.2 Dynamic Interfaces

Studies of Dynamic Contact of Ceramics and Alloys for Advanced Heat Engines

K. F. Dufrane and P.A. Gaydos (Battelle Columbus Division)

Objective/scope

The objective of the program is to develop an understanding of the friction and wear processes of ceramic interfaces based on experimental data. The supporting experiments are to be conducted at temperatures to 650 C under reciprocating sliding conditions reproducing the loads, speeds, and environment of the ring/cylinder interface of advanced engines. The test specimens are to be carefully characterized before and after testing to provide detailed input to the model. The results are intended to provide the basis for identifying solutions to the tribology problems limiting the development of these engines.

Technical progress

Apparatus

The apparatus developed for this program uses specimens of a simple flat-on-flat geometry, which facilitates specimen procurement, finishing, and testing. The apparatus reproduces the important operating conditions of the piston/ring interface of advanced engines. The specimen configuration and loading is shown in Figure 1. The contact surface of the ring specimen is 3.2 x 19 mm. A crown with a 32 mm radius is ground on the ring specimen to insure uniform contact. The ring specimen holders are pivoted at their centers to provide self-alignment. A chamber surrounding the specimens is used to control the atmosphere and contains heating elements to control the temperature. The exhaust from a 4500 watt diesel engine is heated to the specimen temperature and passed through the chamber to provide an atmosphere similar to that of actual diesel engine service. A summary of the testing conditions is presented in Table 1.

Materials

Ring and Cylinder Materials

The compositions of the various materials used in the study are presented in Table 2. A variety of monolithic and coating materials were selected to represent various chemical compositions and materials with previously demonstrated successful sliding performance.

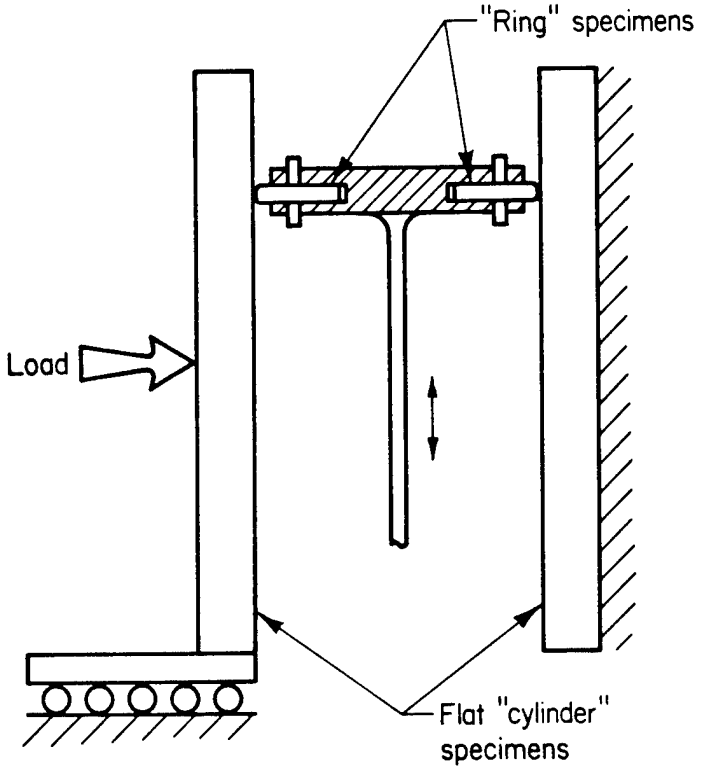

Figure 1. Test specimen configuration and loading

TABLE 1. SUMMARY OF TESTING CONDITIONS

Sliding Contact:	Dual flat-on-flat
"Cylinder" Specimens:	12.7 x 32 x 127 mm
"Ring" Specimens:	3.2 x 19 x 19 mm
"Ring" crown radius:	32 mm
Motion:	Reciprocating, 108 mm stroke
Reciprocating Speed:	500 to 1500 rpm
Average Specimen Speed:	1.8 to 5.4 m/s
Load:	to 950 N
Ring Loading:	to 50 N/mm
Atmosphere:	Diesel exhaust or other gases
Measurements:	Friction and wear (after test)

TABLE 2. MATERIALS FOR EVALUATION

Monolithic Ceramics	Coatings
YPSZ	Tribaloy 400
MPSZ	METCO 130 (13 TiO_2, 87 Al_2O_3)
ATTZ	METCO 501 (30 Mo, 12 Cr, bal Ni)
α SiC	Plasmalloy 312M ($MoSi_2$)
SiC/Al_2O_3	Cr_2O_3 (5 Cr, bal Cr_2O_3)
Sialon	Jet-Kote WC (12 Co, bal WC)
K162B (TiC - Ni/Mo)	Cr (Electroplated)
Si_3N_4	PS212 (Cr_3C_2 + BaF_2/CaF_2 + Ag)
	VR73 (WC/TaC/TiC/Co)
	VA 20 (WC/TaC/TiC/Ni)
	CA 815 (Cr_3C_2/Ni)
	Mo
	Duplex (WC and Mo)
	Ion Implanted (N in Cr_2O_3)

TABLE 3. COMPARISON OF APPROXIMATE RING WEAR COEFFICIENTS

Ring Material	Cylinder Material	Lubricant	Temperature, C	Ring Loading, N/mm	Friction Coefficient	Hardness Used in Calculation, kg/mm^2	Average Ring Wear Coefficient	
							Dimensionless	$mm^3/N-m$
Cr	Cast Iron	SAE 30	100	17.5	--	975	5×10^{-9} (a)	2×10^{-10}
Cr	Cast Iron	SDL-1	100	12.3	0.03 - 0.04	975	8×10^{-8}	3×10^{-9}
WC	SiC/Al_2O_3	SDL-1	260	14.5	0.04 - 0.09	2080	3×10^{-7}	5×10^{-9}
SiC/Al_2O_3 (b)	Cr_2O_3	SDL-1	260	12.3	0.03 - 0.08	2000	5×10^{-7}	8×10^{-9}
ESA	Cr_2O_3	SDL-1	260	12.3	0.03 - 0.06	2200	6×10^{-7}	9×10^{-9}
WC	Cr_2O_3	SDL-1	260	13.9	0.03 - 0.08	2080	6×10^{-7}	1×10^{-8}
Cr_2O_3 (c)	Cr_2O_3 (c)	SDL-1	260	12.3	0.04 - 0.08	2000	1×10^{-6}	2×10^{-8}
Cr_2O_3	Cr_2O_3	SDL-1	260	13.4	0.05 - 0.08	2000	1×10^{-6}	2×10^{-8}
VR73	Cr_2O_3	SDL-1	260	12.3	0.05 - 0.09	2200	1×10^{-6}	2×10^{-8}
Cr_2O_3	SiC/Al_2O_3	SDL-1	260	15.7	0.04 - 0.08	2000	1×10^{-6}	2×10^{-8}
Si_3N_4	Si_3N_4 (d)	SDL-1	260	15.7	0.04 - 0.08	2000	1×10^{-6}	2×10^{-8}
Si_3N_4	Si_3N_4	SDL-1	260	12.3	0.05 - 0.06	2000	3×10^{-6}	5×10^{-8}
αSiC	αSiC	SAE10	20	17.0	0.04 - 0.08	2700	3×10^{-6}	4×10^{-8}
Cr_2O_3	Cr_2O_3	LB625	260	12.3	0.02 - 0.16	2000	5×10^{-6}	9×10^{-8}
Duplex	Cr_2O_3	SDL-1	260	12.3	0.04	2000	1×10^{-4}	2×10^{-6}
Cr	Cast Iron	SDL-1	260	15.7	0.07 - 0.1	975	1×10^{-5}	4×10^{-7}
Cr_3C_2	Cr_2O_3	SDL-1	260	14.0	0.13	2650	2×10^{-5}	3×10^{-7}
Cr	Si_3N_4	SDL-1	260	12.3	0.14	975	1×10^{-4}	4×10^{-6}

(a) Typical actual diesel truck engine experience
(b) CC7000
(c) Nitrogen-ion implanted
(d) Surface modified by Ceraprep process

Liquid Lubricants

The primary lubricant used in the experiments has been SDL-1, a polyolester synthetic oil. This oil is subject to rapid oxidation at temperatures above approximately 250 C and produces tenacious decomposition products. With this limitation, alternate lubricants were considered to permit higher temperature operation.

The benefits of specially formulated high temperature lubricants are their resistance to high temperatures and their ability to burn off cleanly when they do decompose. In addition to the two polyalkylene glycol fluids evaluated previously, a supply of experimental high temperature lubricant was also obtained from Dow Chemical. This fluid is reported to be stable at temperatures to 400 C. Lubrizol has also agreed to supply at least one and possibly two high temperature liquid lubricants for evaluation.

Solid Lubricants

Three types of high temperature solid lubricants have been procured. Two grades of carbon graphites suitable for temperatures up to 620 C will be used as sliders that may provide a dry lubricant film. A second type of solid lubricant is a MoS_2-impregnated alloy having a temperature capability of 400 C. Ring specimens will be formed from this material and will be evaluated for friction and wear characteristics. A $Ga/In/WSe_2$ self-lubricating compact was also fabricated for evaluation. This compact remains thermally stable up to 800 C[1] and exhibits good friction and film transfer characteristics from room temperature to 540 C. Depending on the final strength of this composite, it may be used as a ring specimen or as a slider that supplies lubrication to the ring/cylinder interface.

Work began on modifying Battelle's engine rig to accept spring-loaded solid lubricant samples. These solid lubricants will be used as wipers to supply the stationary specimens with a film of dry lubricant. The experiments are expected to determine whether such films can control the wear on the ring specimens and whether the wipers will have a useful life at the needed transfer rates.

Wear Experiments

Lubricant Evaluation

In the first phase of the study the need for lubrication at the ring/cylinder interface was established by the high friction coefficients and wear rates measured during dry sliding of monolithic ceramics and ceramic coatings. With lubrication, the wear rates of ceramic coatings such as Cr_2O_3 and WC tested at 260 C were found to approach those measured in heavy duty truck engines with conventional ring/cylinder materials. With the need for lubrication, the maximum operating temperature with ceramics was found to be limited by the availability of suitable lubricants. A summary of the wear and friction data obtained under a variety of conditions is shown in Table 3.

Material Evaluation

During the past six months the last of the material analysis was completed. Ion-implanted chromia, silicon carbide whisker-reinforced alumina, and the last of the electro spark alloying (ESA) coatings were evaluated. The results are presented below as well as in Table 3.

Nitrogen ion-implanted chromia was run self-mated at 260 C in SDL-1 (polyolester). Ion implantation is a surface treatment that is reported to greatly increase the wear resistance of materials. Tests were conducted to see if the ion-implanted chromia ring/cylinder pair has substantially better wear performance than non treated chromia pairs operated under the same conditions. The results of the test runs are shown below. The ion implantation showed no effect on wear of self-mated chromia specimens.

Ring Material	Cylinder Material	Ion Implanted	Wear Coefficient Dimensionless	Wear Coefficient mm^3/Nm	Friction Coefficient
Cr_2O_3	Cr_2O_3	No	$1x10^{-6}$	$2x10^{-8}$	0.05-0.08
Cr_2O_3	Cr_2O_3	Yes	$1x10^{-6}$	$2x10^{-8}$	0.04-0.08

Ring specimens of silicon carbide whisker-reinforced alumina run against chromia stationary specimens in SDL-1 gave impressive friction and wear results. The wear coefficient calculated after a four hour test at 260C was 4.9×10^{-7} (dimensionless) or 8.3×10^{-9} mm^3/Nm, and the friction coefficient averaged 0.038. This ring material gave the lowest wear of all the monolithic ceramics tested during this program and equalled the performance of tungsten carbide-coated rings.

The last two of the ESA coatings were also evaluated during this reporting period. The ring coatings were a WC+TiC+TaC+Co coating designated VR73 and a duplex coating composed of a tungsten bond coat with a top layer of molybdenum. The coatings were run against chromia stationary specimens with SDL-1 at 260 C. The results of these tests are shown below along with other 260 C experiments lubricated with SDL-1 for comparison.

Ring Material	Cylinder Material	Wear Coefficient Dimensionless	Wear Coefficient mm^3/Nm	Friction Coefficient
WC	SiC/Al_2O_3	$3x10^{-7}$	$5x10^{-9}$	0.04-0.09
ESA	Cr_2O_3	$6x10^{-7}$	$9x10^{-9}$	0.03-0.06
VR73	Cr_2O_3	$1x10^{-6}$	$2x10^{-8}$	0.05-0.09
Cr	YPSZ	$1x10^{-4}$	$4x10^{-6}$	0.2-0.3
Duplex	Cr_2O_3	$1x10^{-4}$	$2x10^{-6}$	0.05

Environmental Testing

Environmental testing was conducted to determine which constituents of the diesel exhaust have the greatest effect on the friction and wear of ceramics in ring/cylinder application. Ring and cylinder materials were both plasma sprayed Cr_2O_3; the lubricant used was SDL-1 (polyolester); and environments of breathing air, nitrogen, and steam were used at a temperature of 260 C. The table below shows the results obtained from this testing.

	Wear Coefficients		Friction Coefficients	
Environment	Dimensionless	mm3/Nm	Range	Average
Air	2.2×10^{-6}	3.7×10^{-8}	0.02-0.09	0.04
Nitrogen	1.7×10^{-6}	2.8×10^{-8}	0.03-0.10	0.06
Steam	5.2×10^{-6}	8.8×10^{-8}	0.06-0.19	0.12

The ring wear rate in the inert nitrogen atmosphere was slightly lower than measured in the air environment. Perhaps the oxygen in the air environment accelerated the degradation of the lubricant. The steam environment resulted in wear rates and friction coefficients over twice as high as those of the nitrogen or air environments. While the running specimens were at 260 C, portions of the environmental chamber were cool enough to condense the steam. The resulting water probably diluted the lubricant and/or washed it out of the wear zone and thereby reduced its lubricative benefits. Compared with the effect of temperature alone on lubricant degradation and increased wear rates, it appears that the composition of the operating atmosphere has relatively little effect on observed ring wear rates.

Status of milestones

The study is progressing in accordance with the overall milestone schedule.

Publications

"Dynamic Contact of Ceramics in Ring-Cylinder Applications" by K.F. Dufrane and P.A. Gaydos submitted for publication in the CCM proceedings.

Gaydos, P.A., and Dufrane, K.F., "Lubrication of Ceramics in Ring/Cylinder Applications", SAE Paper 890999, 1989.

References

1. Gardos, M.N., "An Analysis of the Ga/In/WSe_2 Lubricant Compact", ASLE Transactions, Vol. 28, p. 231.

2.3 NEW CONCEPTS

Investigation of Advanced Statistical Concepts of Fracture in Brittle Materials

C. A. Johnson and W. T. Tucker (General Electric Company)

Objective/scope

The design and application of reliable load-bearing structural components from ceramic materials requires a detailed understanding of the statistical nature of fracture in brittle materials. The overall objective of this program is to advance the current understanding of fracture statistics, especially in the following four areas:

- Optimum testing plans and data analysis techniques.
- Consequences of time-dependent crack growth on the evolution of initial flaw distributions.
- Confidence and tolerance bounds on predictions that use the Weibull distribution function.
- Strength distributions in multiaxial stress fields.

The studies are being carried out largely by analytical and computer simulation techniques. Actual fracture data are then used as appropriate to confirm and demonstrate the resulting data analysis techniques.

Technical progress

Work during this reporting period concentrated on the development of bootstrap techniques and associated computer code for estimation of confidence and tolerance bounds on Weibull parameters and strength estimates for "Class IV" problems. Class IV problems are those where the fracture data include specimens from multiple specimen sizes and loading geometries, while the component of interest may be of yet a different size and loading configuration.

As the term "bootstrap" implies, these methods "pull themselves up by their own bootstraps." That is, they gather information about variability in estimates by evaluating only the data available in the particular data set of interest. A good review of bootstrap techniques and their basis can be found in Reference 1. The techniques are readily applied to a variety of distributions, but to our knowledge, have not yet been applied to the Weibull distribution with size scaling.

Bootstrapping techniques characterize a combination of the intrinsic uncertainty of estimation due to sampling error in the data set (error due to testing only a limited sample of the material of interest) and any additional uncertainty due to inefficiencies of the

estimator. Bootstrap methods are ultimately dependent on an estimator to digest the experimental measurements of fracture strength and estimate parameters on the distribution and/or strengths of components with other sizes and loading geometries. As reported in earlier semi-annual reports, a series of estimators based on linear regression and maximum likelihood have been developed that allow analysis of Class IV data. These estimators have been used in the current effort.

Two types of bootstrap have been developed: parametric and non-parametric. Both types involve simulation and analysis of many "artificial" data sets that are derived either directly or indirectly from the experimental data. In non-parametric bootstrapping, no assumption of the form of the strength distribution is made prior to generation of the simulated data sets. The simulated data is created by randomly choosing strengths from the original data "with replacements." That is, after a strength is chosen from the list of experimental strengths, it will still be available to be chosen again within that same data set. Therefore, each simulated data set is virtually guaranteed to have some repeat observations. (The simulated data sets generally have the same number of observations within each specimen geometry as the original experimental data set.)

In parametric bootstrapping, an estimator is used to estimate the distribution parameters that best describe the experimental data. Simulated strength data is then generated by randomly choosing simulated specimens from the infinite population of specimens also involves the use of a random number generator. For each specimen to be simulated, a random number is chosen within the interval from zero to one. The Weibull distribution function is solved for the fracture strength and the random number is substituted as the probability of failure for that specimen. All other parameters such as Weibull modulus, sigma zero and specimen size/geometry are either known or assumed, therefore, the strength of that simulated specimen is fully defined.

In both parametric and non-parametric bootstrapping, each of the simulated data sets is analyzed using a suitable estimator. (In parametric bootstrapping, it is most rational to use the same estimator that was used to analyze the experimental data.) The variability in estimates from the numerous simulated data sets reflects the intrinsic variability of the estimator in analyzing data similar to the original experimental data set. The results can then be used with the experimental data set to state confidence bounds on estimates of distribution parameters and tolerance bounds on estimates of strengths.

The bootstrapping technique is computationally intensive, but it offers the intriguing potential of estimating confidence and tolerance on a variety of very complex problems, even beyond Class IV (such as those involving multiple flaw populations, multiaxial stresses, strength degradation due to slow crack growth, etc.). If an estimator can be designed to estimate all the adjustable parameters of a given model, then the bootstrapping technique should be capable of estimating confidence bounds on all the parameters and tolerance bounds on

estimated strengths. (It should be pointed out that the better the quality of the estimator, the smaller the width of the bounds.) In addition, bootstrap techniques offer opportunities to correct for "bias" (the tendency of an estimator to give consistently high or consistently low estimates relative to the true value), and to estimate the "goodness-of-fit" of the data relative to the assumed model which in this case is the size-scaled, two-parameter Weibull distribution function.

A computer code was written to allow non-parametric and parametric bootstrapping of strengths using the Class IV estimators described in earlier reports. The code includes one maximum likelihood and two linear regression estimators with options of size-scaling the data according to volume, surface area or edge length. The strength data can be in the form of tensile and/or bend specimens with rectangular and/or circular cross-sections. (Other loading geometries will be available in the future.) The results are displayed both in table form and graphically. The output includes confidence bounds on the Weibull modulus (at various levels of confidence) and tolerance bounds (also at various levels of confidence) on strength estimates at user chosen values for component size and strength quantile.

The code was used to analyze several sub-groups as well as the entire data set of 137 specimens of sintered SiC described in earlier bimonthly and semi-annual reports. The data set consisted of three different specimen sizes (Mil Std 1942 MR specimens A, B and C) tested in two different testing geometries (three- and four-point bending) for a total of six different combinations of specimen size and testing configuration. Each group contained approximately 18 specimens with the exception of the four-point B group which contained 48 specimens.

Bootstrap analysis of 48 four-point bend specimens of specimen size B resulted in confidence bounds on estimates of the Weibull modulus that were compared with previous Monte Carlo studies of such confidence bounds in Class I problems. The comparison showed excellent agreement.

The 54 three-point bend specimens (18 each of sizes A, B and C) were analyzed using parametric and non-parametric analyses and the resulting tolerance bounds were compared with those from the Class III analysis of the same data using likelihood ratio and conditional integration techniques (reported in earlier bimonthly reports). In this case, the parametric bootstrap and likelihood results were approximately 20 percent narrower than the other analyses. This in an example of a potential weakness of the non-parametric bootstrap analysis. If the experimental data set has uncharacteristically good agreement (or poor agreement) with the overall Weibull model, then the non-parametric analysis will automatically reproduce that unusual characteristic in the simulated data sets. In turn, the estimated tolerance intervals from the non-parametric analysis will be narrower (or wider for the case of poor agreement) than that estimated using the parametric bootstrap.

A graphical comparison of parametric vs non-parametric analysis of the entire SiC data set is included in Fig. 1. In both cases, maximum likelihood was used in analyzing the original 137 strengths and all subsequent bootstrap-simulated data sets. The maximum likelihood estimates of Weibull modulus and sigma zero are recorded on the upper right of each figure. These estimates are identical on the two figures since the original data sets and the maximum likelihood analyses are identical in both cases. Also printed on the line with the Weibull modulus is the bootstrap estimate of the 95 percent confidence interval on the modulus (shown in parentheses). The intervals for the two methods are not identical (they should not be expected to be so) but are in excellent agreement. Similar intervals were available for sigma zero but were not displayed.

The individual specimen strengths are included on both figures using six different open symbols to identify the six different specimen sizes and configurations. The two straight lines on each figure illustrate the 0.5 (median) and 0.05 quantile behaviors as estimated by maximum likelihood as a function of specimen size. Failure was observed primarily from surface-related defects, therefore the size axis is stressed area. Since the estimation of quantiles does not involve bootstrapping, the straight lines are identically positioned in the two figures. The two curved lines (approximately hyperbolic in shape) bounding the 0.05 quantile illustrate the 95 percent tolerance bounds on that quantile as estimated by one of the bootstrap approaches. Thus the 0.05 quantile line can be used to estimate the strength at which five percent of a given sized component should fail; while the tolerance bounds then describe the uncertainty in that estimate.

The resulting tolerance bounds for the two methods of bootstrap are remarkably similar as can be seen by the nearly identical points of intersection with the axes of the two figures. Results to date show, however, that the non-parametric bootstrap is more prone to bias (especially with smaller data sets) and, as mentioned earlier, has a greater sensitivity to data sets that contain some "apparent outliers."

Confirmation of both parametric and non-parametric bootstrapping was done using simulation techniques. The simulation was carried out by choosing a Weibull modulus and sigma zero for a hypothetical material that conforms with the Weibull strength distribution. "Experimental" data sets were simulated and then input for the full bootstrap analysis. This process was repeated 1000 times. For each bootstrap, the actual Weibull modulus and the actual strength at several specified specimen sizes were compared with the confidence and tolerance intervals output by the bootstrap. This is a very computationally intensive operation but was repeated for parametric and non-parametric analysis of both the maximum likelihood and linear regression (regressing size on strength) estimators. The data set for each case consisted of six groups of ten specimens, three-point and four-point bending of specimens sizes A, B and C (patterned after the SiC experiments). The results included information about all possible intervals, but the following comments will concentrate on the 95 percent interval. In all cases studied,

between 92 and 95 percent of the simulations included the real Weibull modulus and fracture strength within the 95 percent limits estimated by the bootstrap methods. It is concluded, therefore, that the parametric and non-parametric bootstrap techniques are both valid and useful methods for estimating confidence and tolerance bounds on Class IV problems of strength analysis.

Status of milestones

The milestone on development of parametric and non-parametric bootstrap methods for estimation of confidence and tolerance bounds has been completed.

Publications

1. W. T. Tucker and C. A. Johnson, "Confidence Bounds on Strength Estimates," Proceedings of 26th Automotive Technology Development Contractors' Coordination Meeting, October, 1988.

References

1. B. Efron, "Bootstrap Methods: Another Look at the Jackknife," *The Annals of Statistics*, **7**, No. 1, 1-26, 1979.

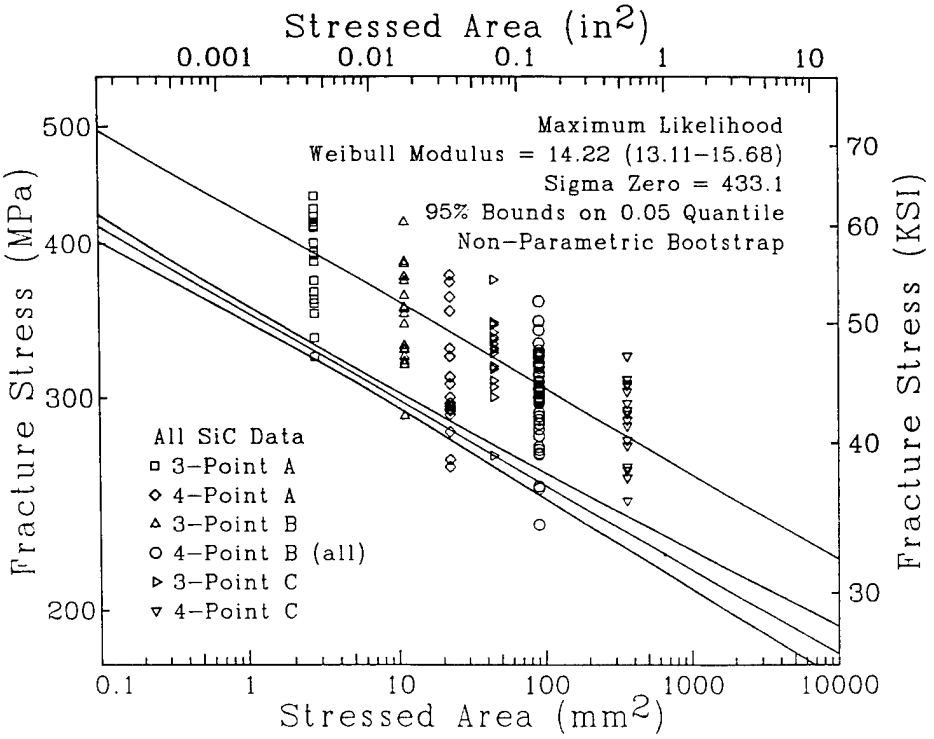
Stressed Area (in2)
0.001
0.01
0.1
1
10
Maximum Likelihood
Weibull Modulus = 14.22 (13.11-15.68)
Sigma Zero = 433.1
95% Bounds on 0.05 Quantile
Non-Parametric Bootstrap
All SiC Data
3-Point A
4-Point A
3-Point B
4-Point B (all)
3-Point C
4-Point C
Fracture Stress (MPa)
Fracture Stress (KSI)
500
400
300
200
70
60
50
40
30
0.1
1
10
100
1000
10000
Stressed Area (mm2)

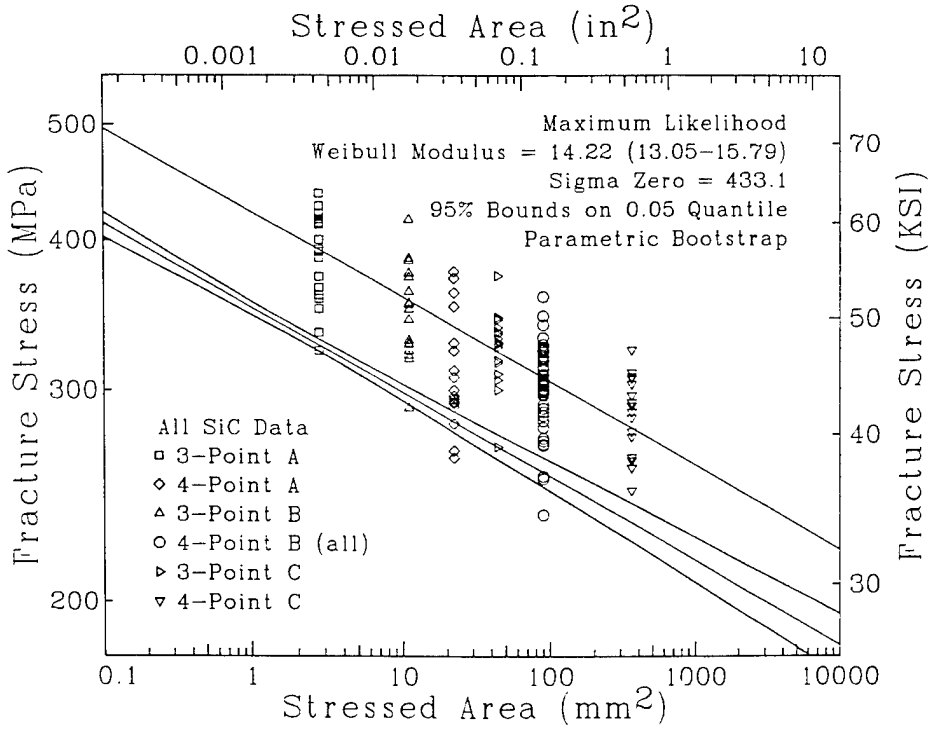
Stressed Area (in2)
0.001
0.01
0.1
1
10
Maximum Likelihood
Weibull Modulus = 14.22 (13.05-15.79)
Sigma Zero = 433.1
95% Bounds on 0.05 Quantile
Parametric Bootstrap
All SiC Data
3-Point A
4-Point A
3-Point B
4-Point B (all)
3-Point C
4-Point C
Fracture Stress (MPa)
Fracture Stress (KSI)
500
400
300
200
70
60
50
40
30
0.1
1
10
100
1000
10000
Stressed Area (mm2)

Figure 1

3.0 DATA BASE AND LIFE PREDICTION

INTRODUCTION

This portion of the project is identified as project element 3 within the work breakdown structure (WBS). It contains five subelements, including (1) Structural Qualification, (2) Time-Dependent Behavior, (3) Environmental Effects, (4) Fracture Mechanics, and (5) Nondestructive Evaluation (NDE) Development. Research conducted during this period includes activities in subelements (1), (2), and (3). Work in the Structural Qualification subelement includes proof testing, correlations with NDE results and microstructure, and application to components. Work in the Time-Dependent Behavior subelement includes studies of fatigue and creep in structural ceramics at high temperatures. Research in the Environmental Effects subelement includes study of the long-term effects of oxidation, corrosion, and erosion on the mechanical properties and microstructures of structural ceramics.

The research content of the Data Base and Life Prediction project element includes (1) experimental life testing and microstructural analysis of Si_3N_4 and SiC ceramics, (2) time-temperature strength dependence of Si_3N_4 ceramics, and (3) static fatigue behavior of PSZ ceramics.

Major objectives of research in the Data Base and Life Prediction project element are understanding and application of predictive models for structural ceramic mechanical reliability, measurement techniques for long-term mechanical property behavior ins structural ceramics, and physical understanding of time-dependent mechanical failure. Success in meeting these objectives will provide U.S. companies with the tools needed for accurately predicting the mechanical reliability of ceramic heat engine components, including the effects of applied stress, time, temperature, and atmosphere on the critical ceramic properties.

3.1 STRUCTURAL QUALIFICATION

Microstructural Analysis of Structural Ceramics

B. J. Hockey, Jr. and S. M. Wiederhorn
(The National Institute of Standards and Technology)

Objective/scope

The objective of this part of the program is to identify the mechanisms of failure in structural ceramics subjected to mechanical loads in various test temperatures and environments. Of particular interest is the damage that accumulates in structural ceramics as a consequence of high temperature exposure to environments and stresses normally present in heat engines.

Design criteria for the use of ceramics at low temperature differ from those at high temperature. At low temperature ceramics are elastic and brittle; failure is controlled by a distribution of flaws arising from processing or machining operations, and the largest flaw determines the strength or lifetime of a component. By contrast, at high temperature where ceramics are viscoelastic, failure occurs as a consequence of accumulated, or distributed damage in the form of small cavities that are generated by the creep process. This damage effectively reduces the cross-section of the component and increases the stress that must be supported. Such increase in stress is in a sense autocatalytic, since it increases the rate of damage and eventually leads to failure as a consequence of loss in cross section. When this happens, the individual flaw loses its importance as a determinant of component lifetime. Lifetime now depends on the total amount of damage that has occurred as a consequence of the creep process. The total damage is now the important factor controlling lifetime.

Recent studies of high temperature failure of the non-oxide ceramics intended for use for heat engines indicates that for long term usage, damage accumulation will be the primary cause of specimen failure. Mechanical defects, even if present in these materials, are healed or removed by high temperature exposure so that they have little influence on long term lifetime at elevated temperature. In this situation, lifetime can be determined by characterizing the nature of the damage and rate of damage accumulation in the material at elevated temperatures. In ceramic materials such as silicon nitride and the sialons, such characterization requires the use of high resolution techniques of analysis because of the fine grain size of these materials: hence the need for transmission electron microscopy as an adjunct to the mechanical testing of ceramics for high temperature applications is apparent.

In this project, the creep and creep-rupture behavior of several ceramic materials will be correlated with microstructural damage that occurs as a function of creep strain and rupture time. Materials to be studied include: sialons; hot-pressed silicon nitride; and sintered silicon carbide. This project will be coordinated with WBS 3.4.1.3, Tensile Creep Testing, with the ultimate goal of developing a test methodology for assuring the

reliability of structural ceramics for high temperature applications.

Technical progress

Over the past six months microstructural characterization efforts were primarily directed to the study of a SiC Whisker reinforced reaction sintered silicon nitride obtained form GTE. The creep behavior of this material as well as its monolithic counterpart is currently being investigated under WBS 3.4.1.3. As a consequence, the ultimate goal of this phase of the study will be to provide a detailed description of the effect of microstructure on creep deformation and damage accumulation processes for this composite material and its monolithic counterpart.

To date, preliminary results have been obtained on the whisker reinforced material in the as-received condition and after tensile creep deformation. Specifically the latter condition has so far included three samples that failed in tension at 1200°C under different applied stresses. For the most part the scale of the microstructure necessitated the use of analytical transmission electron microscopy; however, a comprehensive view of whisker distribution, cavitation damage distribution, and creep crack development was best obtained by optical examinations of polished sections. With this in mind, Figure 1 - although illustrating cavitation and creep crack development - provides a representative view of the macrostructure of this composite material. Chiefly, SiC whiskers (light gray), ranging in length from microns to roughly 20 microns, are seen to be randomly distributed within a matrix of (unresolved) silicon nitride grains (darker gray regions). Here it should be noted that while the plane of Fig. 1 contains the hot-pressing direction and whisker alignment is not apparent, a systematic evaluation of texture development has not been made.

As already noted, TEM examination provided a more detailed view of the as-received microstructure, and to this end the salient aspects are summarized with reference to Figures 2-4. Most of the SiC whiskers had a slightly tapered, needle morphology. From edge-on views (Fig. 2) and end-on views (Fig. 3), SiC whiskers lengths ranged from microns to about 20 microns and their diameters ranged from about 0.2 to a maximum of 1.0 microns. On the basis of limited electron diffraction data, the whiskers appear to be predominantly of the 6H hexagonal structure with the [0001] direction paralled to the whisker axis. The whiskers are typically highly faulted along the basal planes (Fig. 2) and also invariably exhibited a characterstic "core and rim" structure, with the core being defined by defect clusters and impurity (typically Fe-and Ca-rich) precipitates (Fig 2 and 3). Although not readily apparent in Fig. 3, end-on views generally showed dislocations extending radially from the core boundary to the grain surface. In contrast, the silicon nitride grains were generally equi-axed and defect

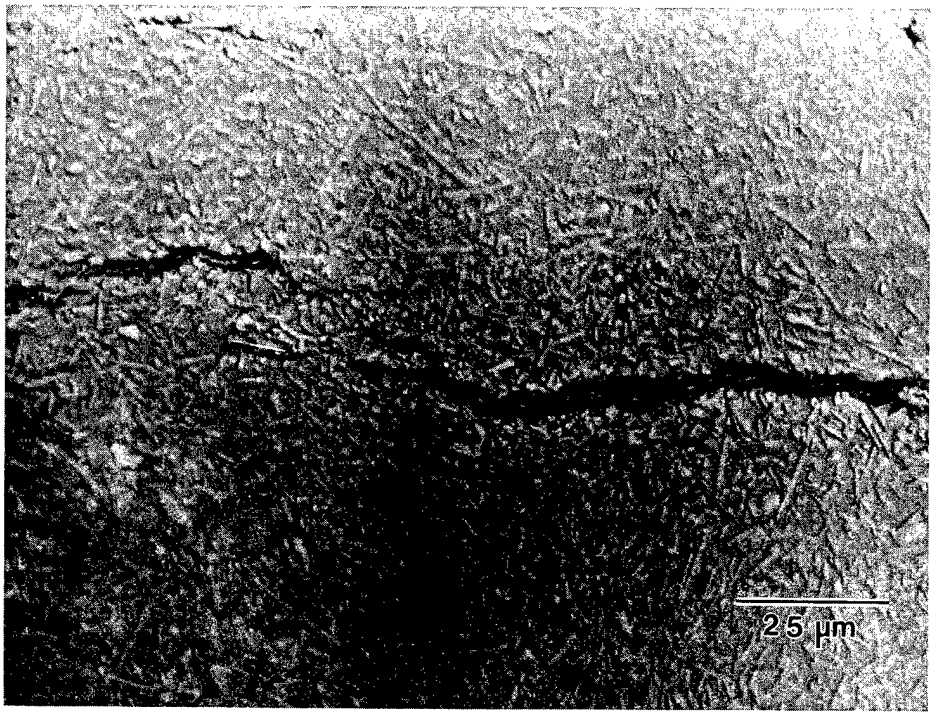

Fig. 1. Optical micrograph of SiC/Si_3N_4 composite crept to failure in tensile creep at 1200°C. Illustrates cavitation induced creep crack development by link-up of tensile oriented crack segments. Note random distribution of individual SiC whiskers (light grey) within matrix of unresolved Si_3N_4 grains (darker grey areas).

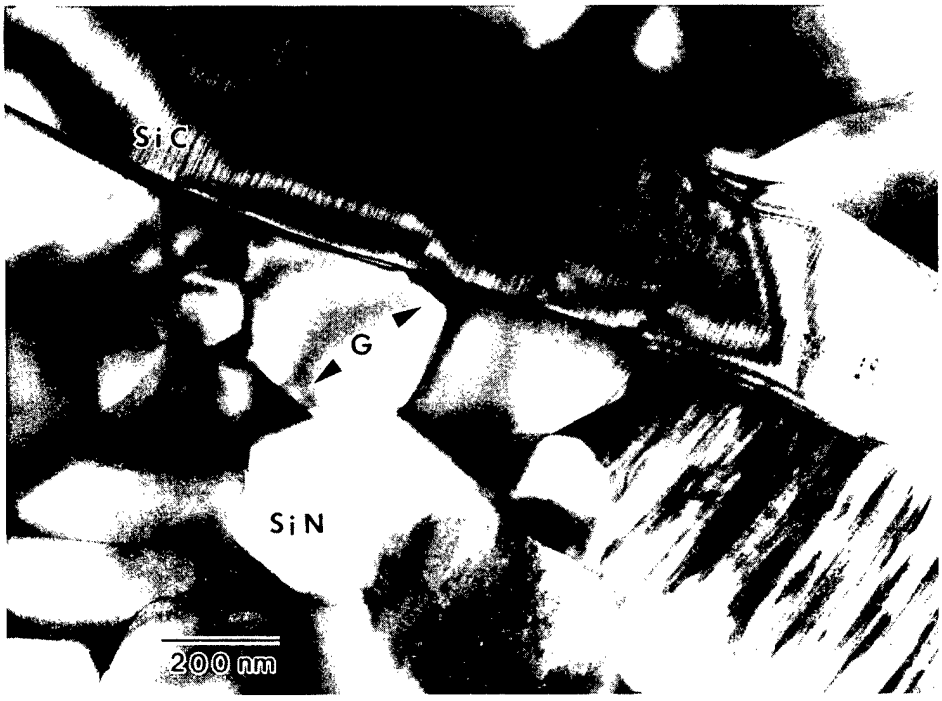

Fig. 2. TEM micrograph of as-received microstructure showing sections of SiC whiskers (labeled) dispersed within Si_3N_4 grains. Note presence of glass at triple grain junctions (e.g. at G). Edge-on view of SiC whisker illustrates characteristic basal faulting and distribution of defects and impurity precipitates within axial "core" region.

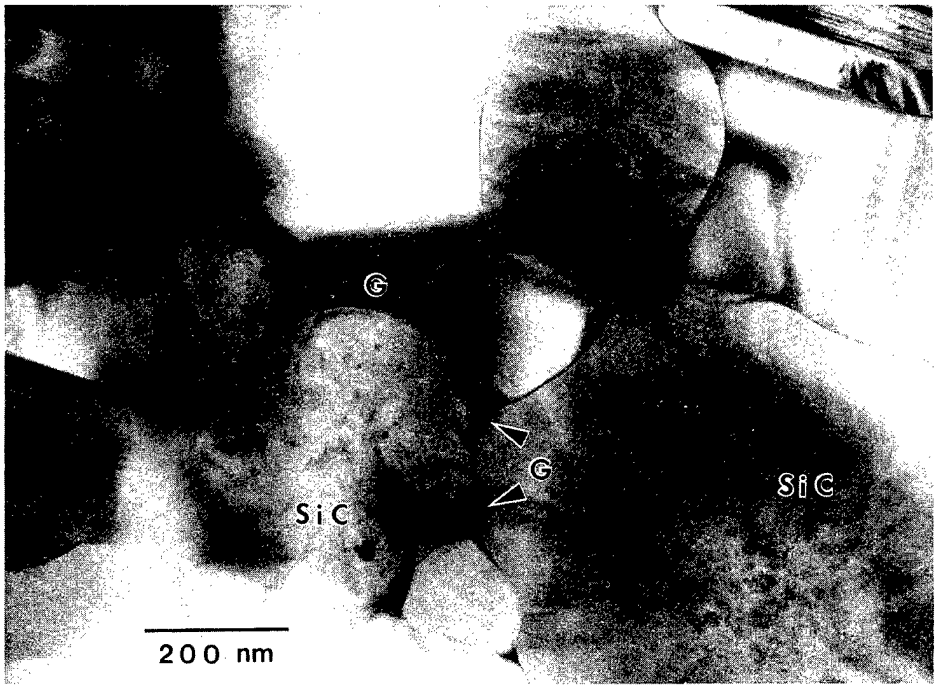

Fig. 3. TEM micrograph of as-received microstructure showing cluster of nearly parallel SiC whiskers viewed end-on (axial cross-sections). Axial "core" region of whiskers contains high density of Fe-and Ca-rich impurity precipitates. Note relatively high concentration of intergranular glass surrounding SiC whiskers.

free. While most of the silicon nitride grains were sub-micron is size, a number of abnormally large grains of 10 to 20 micron dimensions were found distributed within the material. Again limited electron diffraction data indicated the β-Si_3N_4 hexagonal structure.

In addition to the two crystal phases, the composite also contained a glassy phase in the as-received condition. This glass, qualitatively determined to be a yttria silicate glass with alumina and calcia as minor constituents (Fig. 4), is primarily concentrated at triple junctions and along the SiC whiskers. It is, however, also found as a thin (1 to 10 nm) interfacial layer separating adjacent grains, and thus appears to wet the surfaces of both crystalline phases.

Observations on the three samples crept to failure in tension at 1200°C began with optical examination of polished sections parallel to the stress axis. In general these observations revealed irregular distributions of isolated cavities and creep crack segments in various stages of development (Fig. 1). Although the test conditions covered a narrow range of applied stress (75 - 100 MPa), a definite difference in creep crack development and distribution was noted. With increasing stress - and hence decreasing strain rate and increasing lifetime - there is an increased density of short, relatively wide creep crack segments which are uniformly distributed within the gauge section. Conversely, with increasing stress - and hence increased strain rate and decreased lifetime - cavitation damage is more concentrated, resulting ultimately in a few relatively long, narrow cracks.

As might be expected, TEM examination of these tensile crept samples confirmed that creep deformation is controlled by the continuous glassy matrix and that the development of dilatational strains readily results in intergranular cavitation. No evidence of deformation induced defects(e.g. dislocations or twins) was found within either the Si_3N_4 grains or SiC whiskers. In general, cavitation was found to occur at two sites within the microstructure: one being at distributed triple grain junctions, as seen in Fig. 5; the other being along the interfaces of SiC whiskers (usually oriented normal to the applied stress), as seen in Fig. 6. In the latter case, the cavities tend to be extended along the entire whisker interface, effectively forming micron sized "cracks" which are considered to act as creep crack nuclei. Somewhat complicating the issue of intergranular cavitation, however, is the observation that the original intergranular glass showed a strong tendency to devitrify during the creep tests at 1200°C, Fig. 7. In this regard, crystallization appears to occur primarily within triple grain junctions and within relatively wide two grain interfaces, but not along the relatively narrow (10 nm or less) interfaces separating adjacent Si_3N_4 grains. While the crystalline phase has not yet been definitively identified, compositional analysis shows it to be nearly pure yttria silicate,

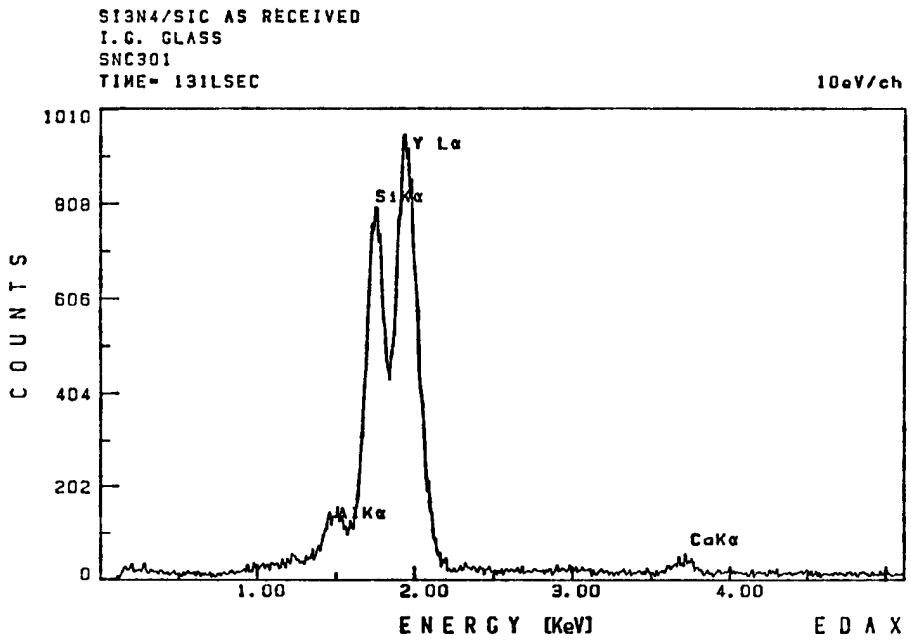

Fig. 4. EDS spectrum from intergranular glass in as-received sample showing glass contains yttria and silica as major constituents and alumina and calcia as minor constituents.

Fig. 5. TEM micrograph from sample after tensile creep at 1200°C showing cavities produced at triple grain junctions as a result of deformation.

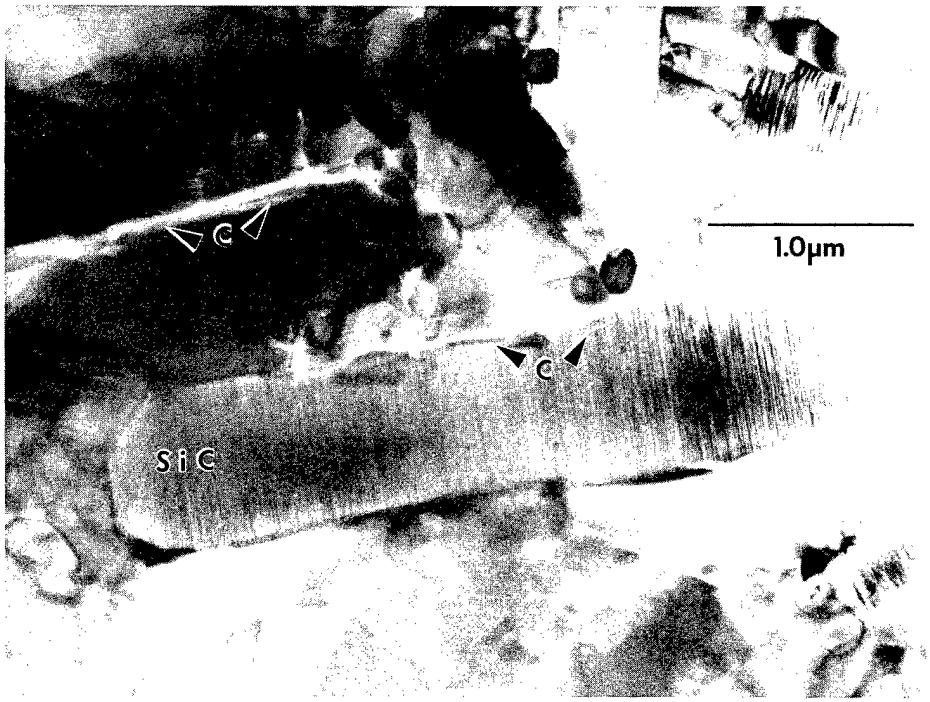

Fig. 6. TEM micrograph of sample after tensile creep at 1200°C showing full facet cavitation along interfaces of whiskers oriented normal to applied stress. Rapid cavity growth along whisker interfaces effectively results in micron size "cracks".

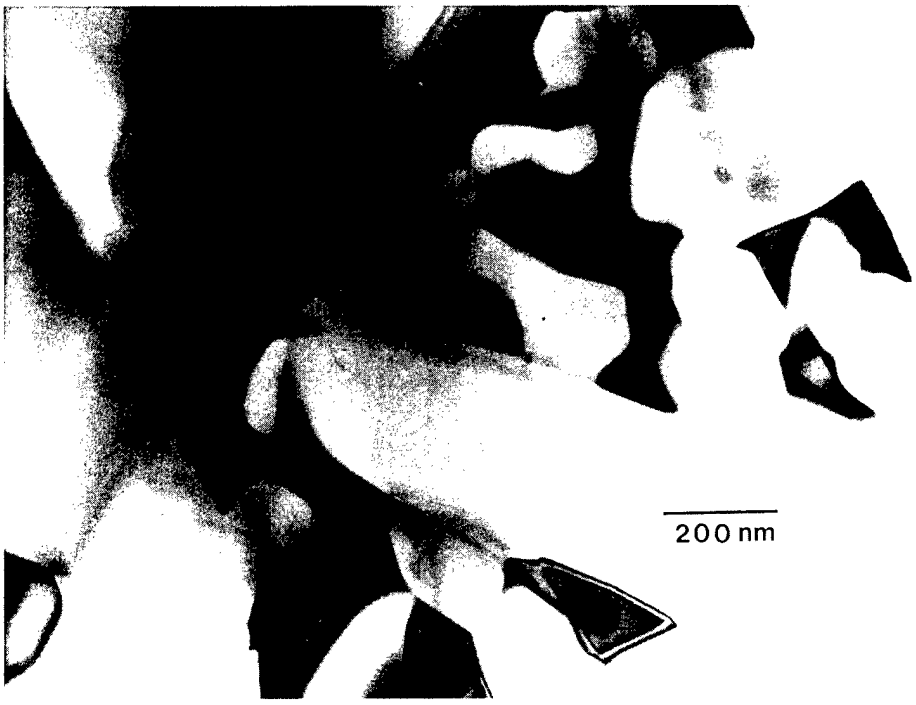

Fig. 7. TEM micrograph illustrating occurrence of intergranular glass devitrification (crystallization) produced during creep test at 1200°C. Note, single reflection gives rise to strong contrast within seemingly isolated regions distributed over relatively large area.

i.e. depleted of the minor concentrations of alumina and calcia originally present within the glass.

The nature of this crystalline phase as well as the nature and location of residual glass in crept samples is currently being investigated. More generally, microstructural analysis studies will be extended to include whisker reinforced samples tested under a wider range of conditions (stress and temperature). Also, similar studies will be conducted on the monolithic counterpart (i.e. reaction sintered silicon nitride without SiC whiskers) to better determine the effect of whisker reinforcement on high temperature behavior.

Status of milestones

All milestones are currently on schedule. Microstructural analysis by ATEM is being applied to a SiC whisker reinforced Si_3N_4 material after tensile creep, and a similar analysis will be applied to its monolithic counterpart after completion of creep tests (milestone 311101). The results will be described in a talk to be presented at the Ceramic Science and Technology Congress, Anaheim CA, Oct. 1989. Also, a paper on this work will be written and subsequently published in the proceedings of the 14th Annual Conference on Composites and Advanced Ceramics, Jan. 1990, (Milestone 311102).

Publications

A paper entitled "Effect of Microstructure on the Creep of Siliconized Silicon Carbide" is currently being submitted for publication.

Physical Properties of Structural Ceramics

R. K. Williams and R. S. Graves (Oak Ridge National Laboratory)

Objective/scope

The structural ceramics which will be used in the combustion chambers of advanced heat engines must also thermally isolate the metallic parts of the engine from the high temperature combustion gases. The ceramics being considered for this application are complex materials which are toughened by the presence of a second phase. The purpose of this task is to develop an improved understanding of the factors which determine the thermal conductivities of these structural materials at high temperatures. This study is required because the thermal conductivities of the ceramics of interest are generally not known at high temperatures, and the theory has not yet been sufficiently developed to yield reliable predictions. The influences of second-phase type, content, shape, and of parallel energy transport by photons are of particular importance. At present our understanding of these variables is at best only qualitative.

Technical progress

Low thermal conductivity ceramics are required for insulated diesel engines, and transformation toughened Al_2O_3-Cr_2O_3-ZrO_2 materials have been proposed[1] for this application. To assist in resolving some difficulties with the thermal conductivity data reported[1] for these materials, some new experimental data have been obtained and compared to the results of a theoretical calculation.

The sample was machined from material produced at the University of Michigan.[2] The nominal composition was Al_2O_3–20 mol % Cr_2O_3 + 20 vol % ZrO_2, but microprobe analysis showed the Cr_2O_3 and ZrO_2 contents were 7 mol % and 16 vol %. The thermal conductivity data were obtained in a steady-state comparative longitudinal heat flow apparatus which has been described elsewhere.[3] The absolute uncertainty of the results is 2 to 3%.

Theoretical values were obtained by using Callaway's formula[4] to determine the thermal conductivity of the corundum matrix and Bruggeman's formula[5] to define the effect of the ZrO_2 phase. The strength of the phonon-point defect scattering produced by Cr^{+3} substitution was estimated by using the results of an experimental study[6] which showed that most of the effect is due to mass difference. The thermal conductivity of the ZrO_2 phase was assumed to be independent of temperature and equal to 2 $Wm^{-1}\ K^{-1}$.

The experimental and calculated thermal conductivity values are compared in Fig. 1. The measured values are about 15% lower than calculated and this discrepancy is somewhat larger than expected. The possibility that ZrO_2 may have some solubility in the corundum matrix is being investigated, since it could explain the observation. Calculations for the nominal composition, 20 mol % Cr_2O_3–20 vol % ZrO_2, show that the thermal conductivity should equal about 4.5 $Wm^{-1}\ K^{-1}$ at 1000 K. This value is about twice as large as the thermal conductivity of partially stabilized zirconia (PSZ).[7]

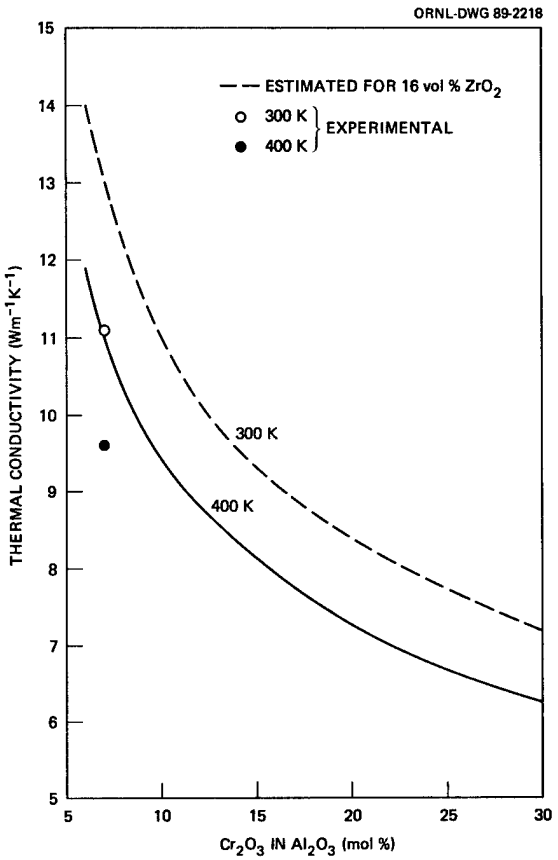

Fig. 1. Comparison of experimental and calculated thermal conductivity values.

The low expansion ceramics being developed at Virginia Polytechnic Institute[8] are also potentially useful in insulated diesel engines because thermal stresses generated across the insulation would be minimized. To assess the insulation characteristics of these materials, three samples were supplied by VPI to ORNL. Some properties of the materials are shown in Table 1.

Table 1

Composition	Density (Mg/m^3)	Crushing strength (MPa)	Microstructure
$Rb_{0.5}Cs_{0.5}Zr_2(PO_4)_3$	2.29		Single phase
$Mg_{0.5}Ca_{0.5}Zr_4(PO_4)_6$	2.12	91	Single phase
$Mg_{0.4}Li_{0.4}Al\ P_{0.52}Si_{0.48}O_4$	3.14	168	Two phase, second phase - 10 vol %

The crushing strength of the Rb/Cs compound was not high enough for thermal conductivity measurements in the comparative heat flow apparatus but data were obtained on samples of the other two compositions.

The results are shown in Fig. 2. Both materials are good insulators; the thermal conductivity of the Mg/Li composition is comparable to stabilized zirconia, the values for the Mg/Ca compound are in the range found for amorphous materials. Additional experiments will be required to identify the strong scattering mechanism which produces these unusually low thermal conductivities. Radiation transport, which degrades the properties of an insulating ceramic at high temperature, should also be investigated because examination under the microscope shows that these materials are translucent.

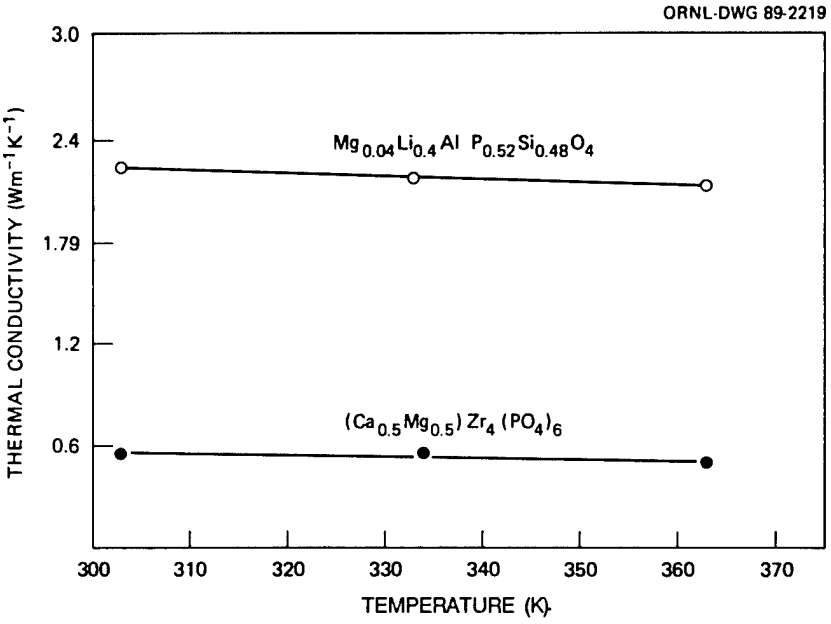

Fig. 2. Thermal conductivity measurements of Mg/Li and Mg/Ca compounds.

References

1. T. Y. Tien, T. K. Brog and A. K. Li, *Proceedings of the 23rd Automotive Technology Department Contractors Coordination Meeting, P-165*, Society of Automotive Engineers, Inc., Warrendale, PA (1985), p. 215.

2. T. Y. Tien, University of Michigan, private communication, September 1988.

3. R. K. Williams, R. K. Nanstad, R. S. Graves, and R. G. Berggren, *J. Nucl. Mater.* **115**, 211 (1983).

4. J. Callaway, *Phys. Rev.* **113**, 1046 (1959).

5. J. M. Wimmer, H. C. Graham, and N. M. Tallan, *Electrical Conductivity in Ceramics and Glasses, Part B*, ed. N. M. Tallan, Marcel Dekker, Inc., New York, NY (1974), p. 628.

6. R. K. Williams, R. S. Graves, M. A. Janney, T. N. Tiegs, and D. W. Yarbrough, *J. Appl. Phys.* **61**, 4894 (1987).

7. R. K. Williams, J. B. Bates, R. S. Graves, D. L. McElroy, and F. J. Weaver, *Int. J. Thermophysics* **9**, 587 (1988).

8. J. J. Brown, R. E. Swanson, and F. A. Hummel, *Ceramic Technology for Advanced Heat Engines Project Semiannual Progress Report for April through September 1988*, ORNL/TM-11116 (March 1989), p. 125.

Project Data Base
B. L. P. Keyes (Oak Ridge National Laboratory)

Objective/scope

The objective of this task is to develop a comprehensive computer data base containing the experimental data on properties of ceramic materials generated in the overall program effort. This computer system is intended to provide a convenient and efficient mechanism for the compilation and dissemination of the large amounts of data involved. The database will be made available in electronic form to all project participants. In addition, periodic hard copy summaries of the data, including graphical representation and tabulation of raw data, will be issued to provide convenient information sources for project participants.

Technical progress

Two data base summary reports were completed through draft form during this semiannual reporting period. (See titles under Publications below.) The first summary contains data base information on zirconias and zirconia-toughened aluminas and includes material characterization information for the materials covered in the previous summary report.[1] The zirconia report has been reviewed, revised, and submitted for publication. The second summary, composed of data base information on silicon carbides and silicon nitrides, including whisker-reinforced silicon nitrides, has been reviewed and is now being revised. Both reports should be available sometime during the next semiannual reporting period.

Table 1 shows the present distribution of information in the system. The data base now has 30 files covering material characterization information, testing information, and test results. A recently added bibliography file contains complete references for the source documents of the data contained in the system. A file containing the glossary information used in the silicon-based ceramic data base summary report[2] has also been incorporated into the system and will become the basis for a help file.

Recent problems encountered with dBASE III+'s memo-type text fields have been resolved. Much of the data being stored are text describing processing methods, microstructures, testing methods, and general information of interest. The memo-type fields were chosen at file creation time because they could handle large quantities of text. However, retrieving and copying these fields was taking more time and effort than seemed reasonable, and keyword searches were not permitted. In late March, the memo fields were broken down into 80 character strings and stored separately, with sequence numbers and category titles, in a text file where access is simple, copying is quick, and searching for keywords is possible. The fields are still linked to the rest of the system by material name, batch code, and a reference code for traceability. This alteration should provide the user with more flexibility and easier access to the text.

Future plans call for the basic system software to be upgraded to dBASE IV as soon as that package becomes available. The user interface for the data base will be created within the dBASE IV structure because of the more powerful programming features of that package. Upgrading the system will probably set the completion date of the interface back a few months to give the programmer time to learn the new features and to change the existing work on the interface over to the new version.

Work for the next semiannual period will concentrate on locating and inputting alumina-based ceramic test results and material information for the next data base summary which is due for completion September 30, 1989. Work will continue on upgrading the system and development of the user interface as time and resources permit.

Status of milestones

All milestones are presently on schedule.

Publications

B. L. P. Booker, *Ceramic Technology for Advanced Heat Engines Project Data Base: September 1988 Summary Report*, ORNL/M-755, Oak Ridge National Laboratory, Oak Ridge, Tennessee.

B. L. P. Keyes, *Ceramic Technology for Advanced Heat Engines Project Data Base: March 1989 Summary Report*, work in review, Oak Ridge National Laboratory, Oak Ridge, Tennessee.

References

1. M. K. Booker, *Ceramic Technology for Advanced Heat Engines Project Data Base: A Summary Report*, ORNL/M-462, Oak Ridge National Laboratory, Oak Ridge, Tennessee, April 1988.

Table 1. CTAHE Data Base Summary as of March 31, 1989

Material Class	Tensile	MOR 4-Pt	MOR 3-Pt	Fatigue Tests: Cyclic	Fatigue Tests: Interrupted	Fatigue Tests: Dynamic	Fracture Toughness	Thermal Expansion	Weld Shear	Wear Resist.	Elastic Modulus*	Shear Modulus*
Alumina-based	27	132	1	15			18	1			26	
Alumina + whiskers	11	161	9				44	5			11	
Silicon nitrides	16	174	10	5		16	48	34		2	2	1
Silicon nitrides + whiskers	50	34		15			31	14			16	16
Silicon carbides		65				13	5	17		2		
Zirconia-based	28	1276		43	215		54		57		92	
Other		7					2	1				
Totals	132	1849	20	78	215	29	202	72	57	4	147	17

Material Class	Material Charact.	Hardness*	X-Ray Diff.	Density*	Chemical Analyses	Thermal Shock	Thermal Conduct.	Thermal Diffusivity	Poisson's Ratio	Specific Heat	Oxid. Rate
Alumina-based	9				14	2	3				
Alumina + whiskers	27			7		6	13				
Silicon nitrides	29	2	49	15	6		9	10	2	9	1
Silicon nitrides + whiskers	44	4		2			9	16	17	9	3
Silicon carbides	6		17	5	39						
Zirconia-based	37		72	158	43						
Other	12				4						
Totals	164	6	138	187	106	8	34	26	19	18	4

3532 total records

* Characteristic values for properties at various material and environmental conditions

3.2 TIME-DEPENDENT BEHAVIOR

Characterization of Transformation of Toughened Ceramics
J. J. Swab (U.S. Army Materials Technology Laboratory)

Objective/scope

Because of their unusual combination of properties, transformation toughened zirconia, specifically yttria tetragonal zirconia polycrystal materials (Y-TZP), are considered candidate materials for components of advanced diesel engines. However, Y-TZPs are susceptible to a loss of strength and toughness after long times at elevated temperatures. Accordingly, two tasks were initiated to define the extent and magnitude of these potential losses.

The first task exposed a variety of Y-TZPs to 1000°C for 100 and 500 hours to determine if room temperature strength and toughness changed after exposure. The second task was to determine the performance of these Y-TZPs under a combination of elevated temperature and stress. This was to be completed using stepped-temperature stress-rupture and stress-rupture tests.

Technical progress

During a visit to ORNL in early November an agreement was reached to phase out characterization of monolithic zirconia materials and begin characterization of other types of toughened ceramics, (i.e., particulate, whisker and fiber toughened). This transition has begun but delays have been encountered in obtaining the materials. Billets of one ZTA from Kyocera-Feldmuhle have been received and are being machined into flexure specimens.

Recognizing that zirconia-based materials will have restricted use in advanced engines due to temperature limitations the test matrix has been adjusted to include the following:

Room temperature MOR and Klc;
Room temperature MOR and Klc after 500 hours at 700-800°C
Stepped-Temperature Stress-Rupture from 600 to 1000°C.

Some TZP and PSZ materials currently on hand will also be included for comparison. Performance under these moderate temperature conditions will determine if further testing at elevated temperatures is necessary for the new toughened ceramics.

As a result of this change in program objective the furnaces used testing must be modified. These structural modifications are necessary due to the projected high loads that the toughened ceramics will be able to handle at moderate temperatures. The modifications have been completed and testing of the most promising TZP materials has been started. However, the results are preliminary and further work is needed before meaningful information can be obtained.

A small billet of TOSOH Super Z material was obtained and machined into flexure specimens. This is a sintered/HIP'ed tetragonal zirconia containing 4.2 w/o yttria and 20 w/o alumina. The density and MOE were measured as 5.5 g/cc and 259 GPa. These agreed very well with the values reported by the company and did not change after 500 hrs at 1000°C. However, the as-received strength was well below the company reported value of 2400 MPa, see Fig. 1. Also the material showed a strength drop from 1812 MPa to 1336 MPa after 500 hrs at 1000°C. NOTE: Only two specimens were used to determine the strength at each condition.

Also during this period, I subjected a sintered and sintered/HIP'ed Y-TZP (YZ-110) supplied by Norton, Co. to stepped-temperature stress-rupture tests. Figures 2 and 3 summarize the results. The sintered version (Fig. 2) performed on par with the other sintered Y-TZPs which were tested previously. (See the June-July 1988 Bimonthly Report.)

The sintered/HIP'ed version performed slightly better than the Hitachi hot-pressed material. (See June-July 1988 Bimonthly Report for comparison.) However, when compared to the other HIP'ed materials it performed better, in that it did not show the anomalous time-dependent failure that has been seen in other HIP'ed Y-TZPs (1). It did undergo a color change, except that it changed from charcoal grey to burnt orange whereas the other HIP'ed materials changed to off white. The color change is due to the oxidation while the final color is a function of the type and amount of impurities.

The technical report entitled "Properties of Yttria-Tetragonal Zirconia Polycrystal (Y-TZP) Materials After Long Term Exposure to Elevated Temperatures" has been completed and is currently being distributed.

References

1. Swab, J.J., Katz, R.N. and Starita, C.J., "Effects of Oxygen Non-Stoichiometry on the High-Temperature Performance of an Yttria-Tetragonal Zirconia Polycrystal Material," *Adv. Ceram. Mat.*, 3 [3] 283-84 (1988).

Status of milestones

Publication of the in-house technical report, although delayed, is now complete.

Machining of the new toughened ceramics has slipped because of difficulties that arose in the procurement of the material.

Publications

Swab, J.J., "Properties of Yttria-Tetragonal Zirconia Polycrystal (Y-TZP) Materials After Long Term Exposure to Elevated Temperatures," MTL TR89-21, March 1989.

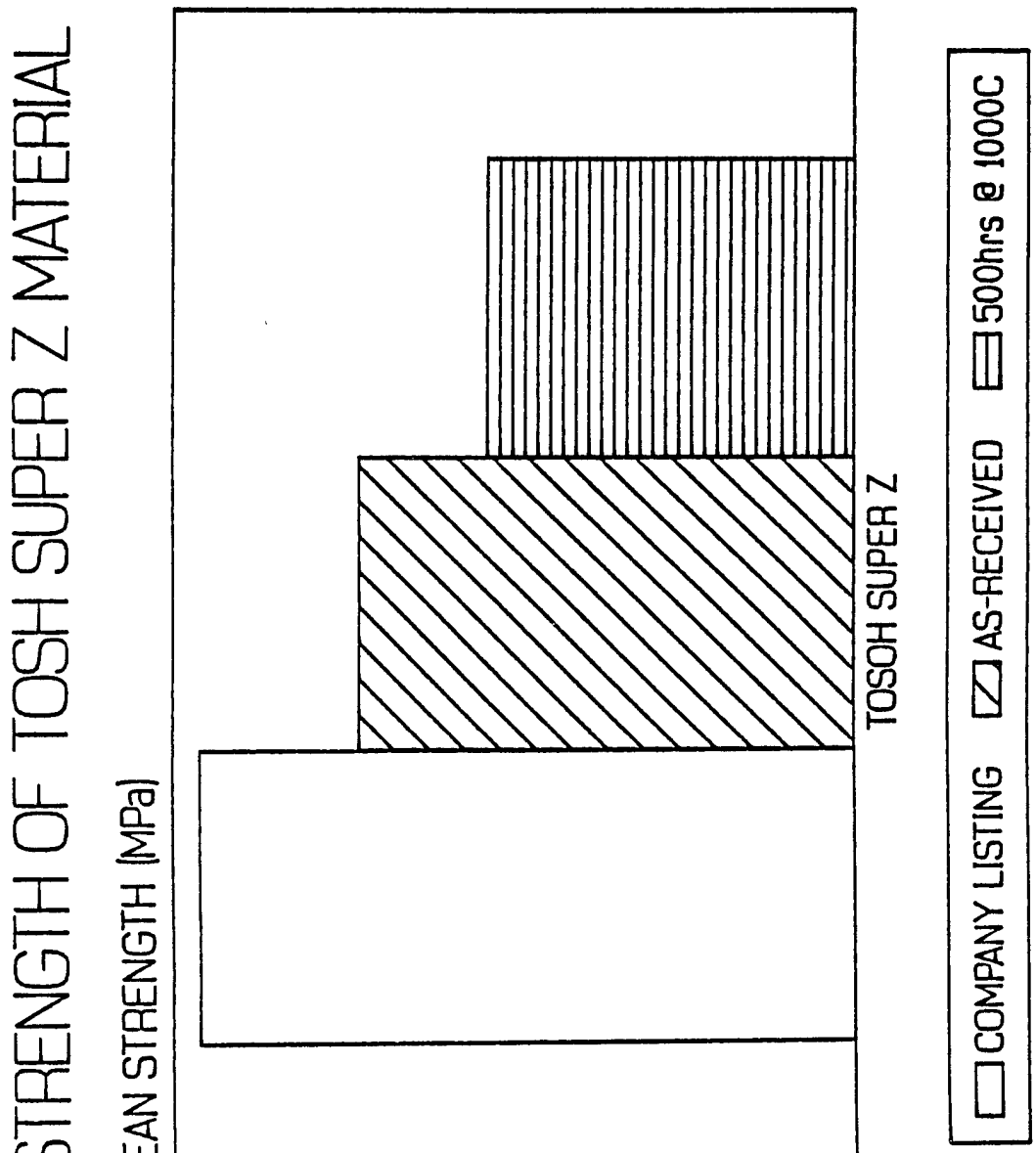
STRENGTH OF TOSH SUPER Z MATERIAL
MEAN STRENGTH (MPa)
2500
2000
1500
1000
500
0
TOSOH SUPER Z
COMPANY LISTING
AS-RECEIVED
500hrs @ 1000C

Fig. 1

STEPPED-TEMPERATURE STRESS-RUPTURE

YZ110-S AS RECEIVED

STRENGTH AT 25 °C = 909 MPa

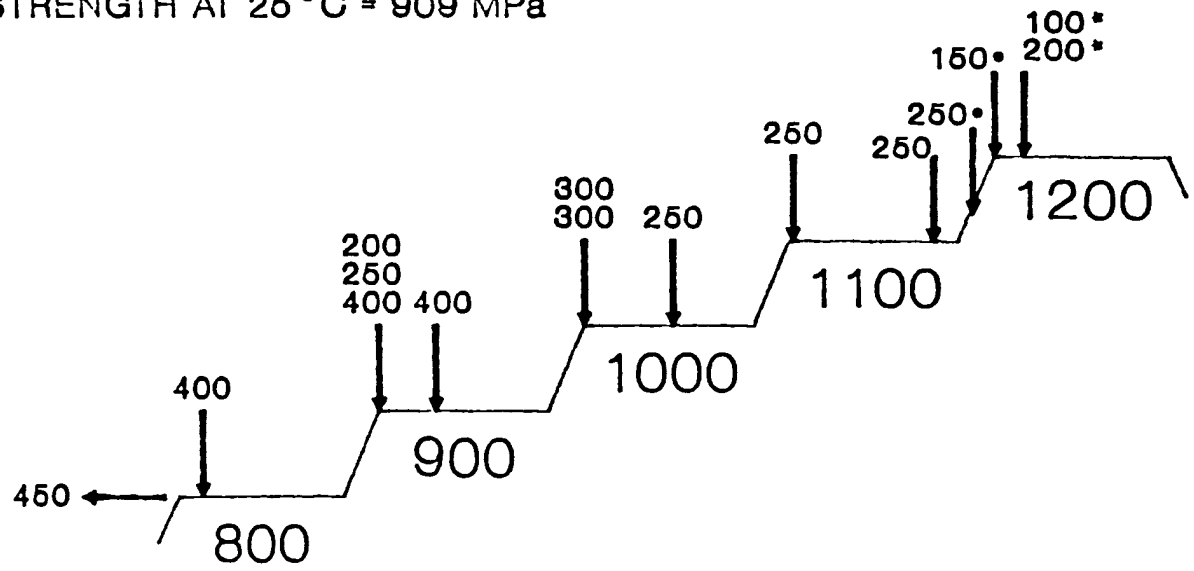

- • CREEP FRACTURE
- * TEST TERMINATED DUE TO CREEP
- + CREEP PRESENT

STRESS IN MPa

TEMPERATURE IN °C

Fig. 2

STEPPED-TEMPERATURE STRESS-RUPTURE

YZ110-H AS RECEIVED

STRENGTH AT 25 °C = 1466 MPa

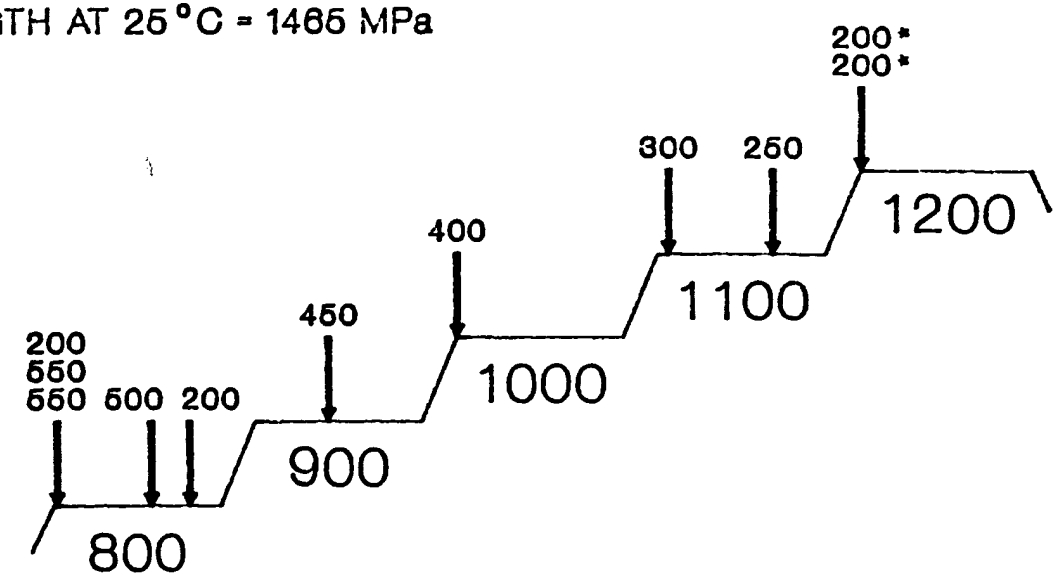

- CREEP FRACTURE
* TEST TERMINATED DUE TO CREEP
+ CREEP PRESENT

STRESS IN MPa

TEMPERATURE IN °C

Fig. 3

Fracture Behavior of Toughened Ceramics

P. F. Becher, P. Angelini, and W. H. Warwick (Oak Ridge National Laboratory)

Objective/scope

Because of their excellent toughness, ceramics such as zirconia-toughened alumina and whisker- and fiber-reinforced ceramics are candidates for use in engine components. The enhanced toughness of the zirconia-toughened materials is due to a stress-induced transformation of the tetragonal ZrO_2 phase. Whisker- and fiber-reinforced ceramics utilize crack bridging and deflection processes to obtain increased toughness. However, these materials can still be susceptible to slow crack growth and thus strength degradation. Also, there is evidence that at temperatures above 700°C, time-dependent aging effects can reduce the concentration of the phase involved in the transformation toughened materials leading to significant losses in toughness and strength. Again, it is essential that mechanisms responsible for both the slow crack growth and aging behavior be well understood. Similarly the toughening behavior in whisker-reinforced ceramics and their high-temperature performance must be evaluated in order to develop materials for the particular applications of interest.

In response to these needs, studies have been initiated to examine toughening and delayed failure properties of transformation toughened and whisker-reinforced materials. Particular emphasis has been placed on understanding the effect of microstructure upon processes responsible for variations in toughness and high-temperature strength. In addition, fundamental insight into the creep and slow crack growth behavior associated with these materials is being obtained.

Technical highlights

Previous studies have shown that whisker-reinforced ceramics exhibit high-fracture toughness and strength[1-6] (and maintain these to quite high temperatures[6-9]), excellent resistance to both thermal shock,[9] room temperature slow crack growth,[8,10] and fatigue at temperatures of up to 1100°C.[7] As a result, these materials appear to have excellent potential for high-temperature applications. The elevated-temperature fatigue studies[7] did reveal that creep processes can be initiated during very long-term exposures to stress at 1100°C and above in whisker-reinforced aluminas. However, this is noted only at applied stresses of 450 MPa which are nearly 75% of the fast fracture strength at 1100°C, and even then the amount of creep deformation is extremely small ($\epsilon << 0.1\%$) even after 14 weeks.

Studies of the creep behavior of toughened ceramics which are reinforced with whiskers seek to understand how microstructure and composition can be used to extend the performance of such materials at elevated temperatures. Toughening by whisker reinforcement provides one of the only means to design toughened strong ceramics at elevated temperatures. The upper service temperature limit of such composites

will be defined by creep and fatigue behavior and not toughness. Therefore, one must determine how to design for both toughness and creep resistance.

With the recent completion of the modifications of the one existing four-point flexure creep rig, studies of the creep behavior of whisker-reinforced ceramics in air have been reinitiated. An additional creep frame has been fabricated and funding for the high-temperature extensiometer has been requested. The initial studies investigated the relationships between creep rates and temperature and applies stress. This work will be extended to include the effects of whisker content and matrix microstructure on creep behavior. As seen in the preliminary data in Table 1, the creep resistance does improve, e.g., the creep rates decrease with increase in whisker content.

A significant portion of the studies of the creep in four-point flexure in air of SiC whisker (20 vol %) reinforced alumina composites versus unreinforced alumina ceramics have been completed. The preliminary results of the creep rate generated during the initial portion of the secondary creep regime as a function of applied stress and temperature are shown in Fig. 1. The results show that the creep resistance of alumina ceramics at 1200 and 1300°C is significantly improved (1) by obtaining small increase in grain size of the alumina during processing and (2) by the addition of SiC whiskers.

Status of milestones

Completion of milestone 321307 (submit paper on the creep behavior of alumina-20 vol % SiC whisker composites) will be delayed until July 1989 due to required shutdown of the existing creep rig for repairs to the extensiometer and to need to add a staff member to conduct microstructural analysis. A postgraduate position has been filled to conduct creep experiments as well as the microstructural analysis studies previously conducted by Dr. P. Angelini, who moved into program management.

Publications

P. F. Becher, P. Angelini, W. H. Warwick, and T. N. Tiegs, "Elevated Temperature Static Fatigue/Creep Rupture of Alumina Reinforced with 20 Vol% SiC Whiskers," submitted for publication to the *Journal of the American Ceramic Society*.

References

1. P. F. Becher and G. C. Wei, "Toughening Behavior in SiC-Whisker Reinforced Alumina," *J. Am. Ceram. Soc.* 67(12), C-267-69 (1984).

2. G. C. Wei and P. F. Becher, "Development of SiC-Whisker Reinforced Ceramics," *Am. Ceram. Soc. Bull.* 64(2), 298-303 (1985).

3. P. F. Becher and T. N. Tiegs, "Toughening Behavior Involving Multiple Mechanisms: Whisker Reinforcement and Zirconia Toughening," *J. Am. Ceram. Soc.* 70(9), 651-54 (1987).

4. P. F. Becher, C. H. Hsueh, P. Angelini, and T. N. Tiegs, "Toughening Behavior in Whisker-Reinforced Matrix Composites," *J. Am. Ceram. Soc.* 71(12), 1050-61 (1968).

5. T. N. Tiegs, P. F. Becher, and P. Angelini, "Microstructures and Properties of SiC Whisker-Reinforced Mullite Composites," to be published in *Proc. Int'l. Conf. on Mullite Ceramics*, Tokyo, Japan, Nov. 9-10, 1987.

6. P. F. Becher and T. N. Tiegs, "Advances in Structural Ceramics: Whisker-Reinforced Ceramics," pp. 941-44 in *Engineered Materials Handbook, Vol. 1-Composites*, C. A. Dostal (senior editor), ASM International, Metals Park, OH (1987).

7. P. F Becher and T. N. Tiegs, "Temperature Dependence of Strengthening by Whisker Reinforcement: SiC Whisker Reinforced Alumina in Air," *Adv. Ceram. Mater.* 3(2) 148-54 (1988).

8. P. F. Becher, T. N. Tiegs, and P. Angelini, "Whisker-Toughened Ceramic Composites," in *Fiber Reinforced Ceramics*, K. S. Mazdiyasni (editor), Noyes Publications, Park Ridge, NJ, in press.

9. T. N. Tiegs and P. F. Becher, "Thermal Shock Behavior of an Alumina-SiC Whisker Composite," *J. Am. Ceram. Soc.* 70(5), C-109-111 (1987).

10. P. F. Becher, T. N. Tiegs, J. C. Ogle, and W. H. Warwick, "Toughening of Ceramics by Whisker Reinforcement," pp. 61-73 in *Fracture Mechanics of Ceramics*, R. C. Brandt, A. G. Evans, D.P.H. Hasselman, and F. F. Lange (eds.), Plenum Publ. Corp., NY (1986).

Table 1. Creep of SiC whisker-reinforced alumina composites in air in four-point flexure at 1300°C. In each composite the matrix grain size is ~2 μm.

Whisker content (vol %)	Applied stress (MPa)	Creep rate 1/s
10	175	4.5×10^{-8}
20	175	2.8×10^{-8}
60	175	4.0×10^{-9}
10	100	6.3×10^{-9}
20	100	7.0×10^{-9}
60	100	2.0×10^{-9}

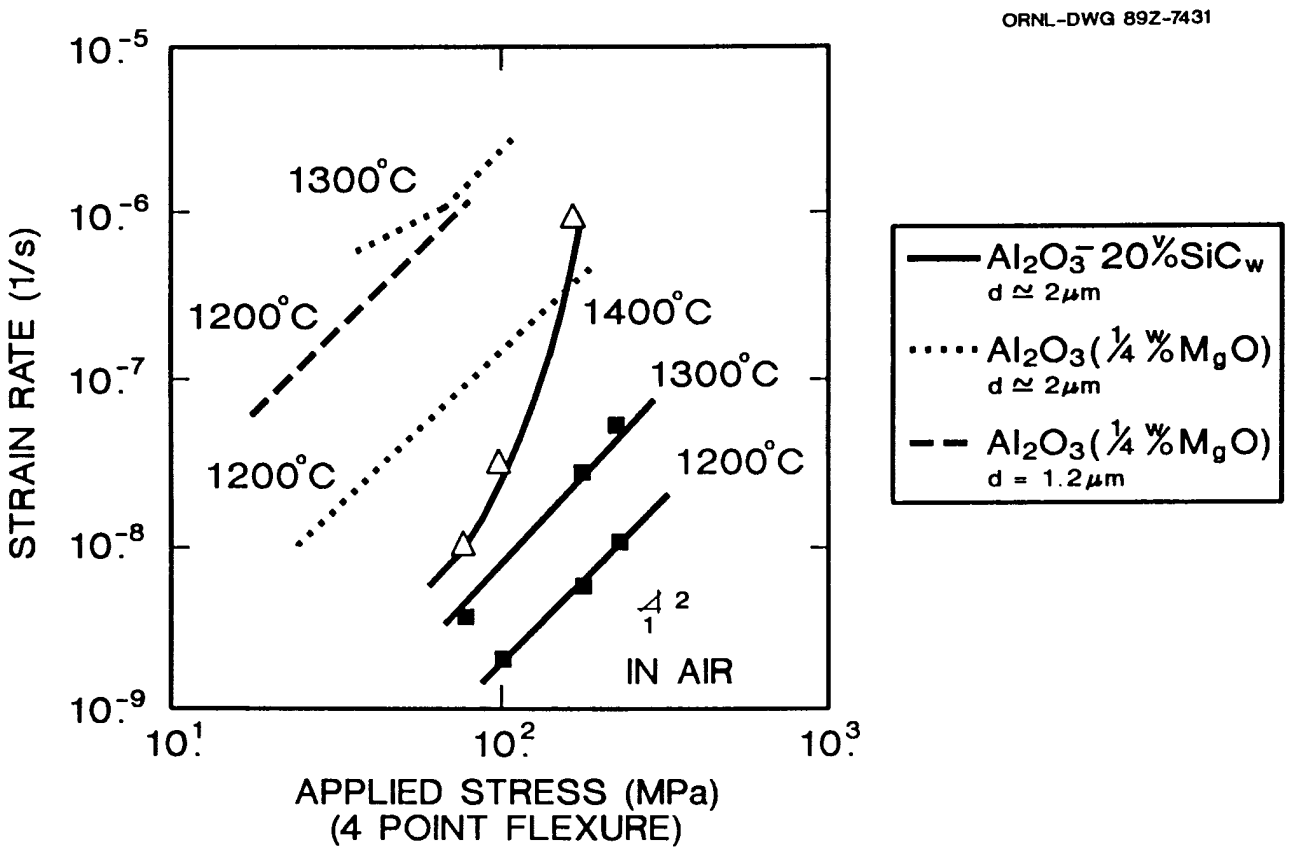

Fig. 1. Creep resistance of fine-grained alumina improved by increasing grain size and by addition of SiC whiskers. The secondary stage creep rates at 1200 and 1300°C in four-point flexure in air can be substantially decreased by the addition of SiC whiskers. Further decreases in creep rate should be possible by small increases in the matrix grain size as reflected by the decrease in creep rate of alumina with increase in grain size.

Cyclic Fatigue of Toughened Ceramics

K. C. Liu and C. R. Brinkman (Oak Ridge National Laboratory)

Objective/scope

The objective of this task activity is to develop, design, fabricate, and demonstrate the capability to perform tension-tension dynamic fatigue testing on a uniaxially loaded ceramic specimen at elevated temperatures.

Three areas of research have been identified as the main thrust of this task: (1) design, fabrication, and demonstration of a load train column which truly aligns with the line of specimen loading; (2) development of a simple specimen grip that can effectively link the load train and test specimen without complicating the specimen geometry and hence, minimize the cost of the test specimen; and (3) design and analysis of a specimen for tensile cyclic fatigue testing.

Technical progress

A batch of 45 uniform-gage tensile specimens, as shown in Fig. 1, was received in October 1988. The specimens were made from silicon nitride developed recently by Norton/TRW for high strength applications at high temperature, designated as NT-154 silicon nitride. Thirty-five specimens were made by cold-isostatic pressure forming and the remaining ones by slip casting. Tensile properties of cold-isostatic pressured specimens are currently being investigated.

Testing was performed in monotonic tension and in tension-tension cyclic fatigue loading at elevated temperatures. To avoid repetition, experimental details are referred to an earlier report.[1] In order to examine the effects of stressing rate on the tensile strength of this material, two diversely different stressing rates of 7.5 and 2100 MPa/min were used in tensile tests at each temperature above 1200°C. A much higher stressing rate of 21,000 MPa/min was used in cyclic fatigue tests so that each test could be completed in a reasonable time period.

Uniaxial tensile testing

A limited number of uniaxial tensile tests was performed at room and elevated temperatures. Test results were summarized in Table 1 and the data were plotted in Fig. 2. To facilitate comparisons, modulus of rupture (MOR) data obtained by Norton/TRW,[2] Garrett,[2] and the University of Dayton Research Institute (UDRI)[3] for NT-154 were also included in Fig. 2. On the same temperature basis, the tensile strength was generally lower than the MOR strength, as expected. However, the magnitude of the difference in strength between the tensile and MOR data remains uncertain due to the data scatter in the MOR data obtained by three different laboratories.

Comparisons showed that the ORNL tensile fast fracture data, indicated by closed symbols in Fig. 2, fell below the Garrett MOR data by about 20% or less in the temperature range below 1300°C. The largest

difference in strength between the MOR and tensile data at 1370°C might be biased by the single low tensile strength data point. The ORNL tensile strength and the MOR strengths obtained by Norton/TRW and UDRI at room temperature were about the same, but lower than that of Garrett by about 15%. Similarly, the difference between the ORNL tensile and UDRI MOR data was smaller compared to that between the ORNL tensile and Garrett MOR data in the temperature range below 1200°C. However, the difference between the ORNL tensile and MOR data widened as temperature increased to 1370°C. This erratic behavior might be attributed to variations from lot to lot. Observations further indicated that there was a strong influence of stressing rate on both the tensile and MOR strengths of NT-154 at high temperatures above 1100°C. The differences in tensile strength due to the decrease in stressing rate were about 20, 45, and 35% at 1200, 1300, and 1370°C, respectively, based on the limited test data. This behavior in MOR strength due to the decrease in stressing rate was also reflected in UDRI's MOR data. Figure 2 also showed that the tensile strength of NT-154 Si_3N_4 was superior in comparison to that of SNW-1000 Si_3N_4 previously tested at ORNL.[4]

Figure 3 illustrates the influence of stressing rate on the stress-strain behavior of this material at elevated temperatures. Under the high stressing rate at 2100 MPa/min, this material behaved virtually like an elastic solid. A hint of slight plastic deformation in specimen CP-8 at 1370°C was noticed shortly before rupture occurred. As the loading rate decreased to 7.5 MPa/min, the plastic deformation was more perceptible in the high stress range of specimen CP-13 (curve b) and CP-14 (curve c) as indicated in Fig. 3. However, as the temperature increased to 1370°C, the indication of plastic deformation was very pronounced when the load exceeded the 60% mark of the tensile strength. An analysis of the stress-strain curve showed that specimen CP-12 (curve f of Fig. 3) ruptured at 202.5 MPa with a plastic strain of 0.155% out of a total strain deformation of 0.252%.

Cyclic fatigue testing

Subsequent to the brief exploratory tensile testing described earlier, tensile cyclic fatigue tests were initiated on NT-154 silicon nitride at elevated temperatures. A total of seven cyclic fatigue tests were completed to date. As in the previous tests, two modes of cyclic loading were used: (a) a constant amplitude cyclic loading in tension-tension with an R-ratio of about 0.1 at a stressing rate of 21,000 MPa/min, and (b) cyclic loading from low to high stress levels in multiple steps generally known as "coaxing". Test parameters and results were tabulated in Table 2 and the test data were plotted in Fig. 4. The closed symbols indicate that failure occurred at the test condition indicated; whereas, the open symbols attached with an arrowhead indicate the end point of each intermediate cyclic loading, and that specimen failure did not occur at the indicated test condition. Intermediate loading steps were interconnected by short broken lines, which in all cases ended at the closed symbols indicating specimen failure.

The fatigue behavior of the material depicted in Fig. 4 is somewhat speculative due to the limitation in the number of test data obtained to date. The fatigue curves were determined visually based on the trend portrayed by the data points in the temperature group. Therefore, the fatigue curves must be regarded only as approximations at this time and will be subject to revisions as more test data become available.

A low fatigue performance, i.e., fewer than expected cycles to failure, in specimen CP-15 was caused by surface damage as pits resulting from the interaction between the specimen surface and the alumina probing rods of the mechanical strain extensometer. To avoid the same premature failure due to the probe damage on the specimen surface at high temperatures, the mechanical strain extensometer was used in the subsequent tests only for a short period to plot the initial fifty cycles of the stress-strain curves. The mechanical strain extensometer was then disengaged from the test specimen. For this reason, a noncontacting optical strain extensometer is desirable in long-term high-temperature testing.

General observations indicate that the fatigue behavior assumed in Fig. 4 can be approximated by a two-term power law relationship such as,

$$\sigma = AN_f^{-\alpha} + BN_f^{-\beta} , \qquad (1)$$

where σ is the fatigue strength, N_f the lifetime (the number of cycles to failure), and A, B, α, and ß, are material constants. The first term on the righthand side of Eq. (1) describes the low-cycles fatigue behavior, and the second term describes the high-cycle fatigue.

Specimen CP-21 was cycled from a low to high stress level in four intermittent steps, resulting in a considerable increase in fatigue strength generally known as coaxing. However, the coaxing effect was less discernable in the case of specimen CP-16 tested at 1200°C.

Publications

K. C. Liu, "Ceramic Specimen Heating by Induction Power," in *Proceedings of the Conference on Mechanical Testing of Engineering Ceramics at High Temperatures*, April 11-12, 1988, London, England; and in *Int. J. High Technol. Ceram.*, **4**, 203-210 (1988).

K. C. Liu, H. Pih, and D. W. Voorhes, "Uniaxial Tensile Strain Measurement for Ceramic Testing at Elevated Temperatures: Requirements, Problems, and Solutions," *Int. J. High Technol. Ceram.*, **4**, 161-79 (1988).

H. Pih and K. C. Liu, "Laser Diffraction Methods for High Temperature Strain Measurements," in *Proceedings of the 1989 Spring Conference of the Society for Experimental Mechanics*, Boston, MA, May 28-June 1, 1989 (accepted for publication).

K. C. Liu and C. R. Brinkman, "Exploratory High-Temperature Tensile and Cyclic Fatigue Characterization of Commercial MgO-PSZ," in the *Proceedings of the 3rd International Symposium on Ceramic Materials and Components for Engines*, Las Vegas, Nevada, November 27-30, 1988 (in press).

References

1. K. C. Liu and C. R. Brinkman, "Cyclic Fatigue of Toughened Ceramics," *Ceramic Technology for Advanced Heat Engines Project Semiannual Progress Report through September 1987*, ORNL/TM-10701, Oak Ridge National Laboratory, pp. 232-46, March 1988.

2. K. C. Liu, Oak Ridge National Laboratory, personal communications to B. J. McEntire, Norton/TRW Ceramics, Boston, Mass., October 1988.

3. N. L. Hecht, "Environmental Effects in Toughened Ceramics," in *Ceramic Technology for Advanced Heat Engines Project Semiannual Progress Report for April through September 1988*, ORNL/TM-11116, Oak Ridge National Laboratory, pp. 331-98, March 1989.

4. K. C. Liu and C. R. Brinkman, "Dynamic Tensile Cyclic Fatigue of Si_3N_4," pp. 189-97 in *Proceedings of the Twenty-Fifth Automotive Technology Development Contractors' Coordination Meeting*, P 209, Society of Automotive Engineers, Warrendale, PA, 1985.

Table 1. Results of tensile tests of Norton/TRW NT-154 silicon nitride at room and elevated temperatures

Specimen	Temperature (°C)	Modulus of elasticity [GPa (10^6 psi)]	Stress rate (MPa/min)	Tensile strength [MPa (ksi)]	Total strain at failure (%)	Plastic strain (%)
CP-18	25		2100	933 (135.3)		0
CP-5	1100	298.3 (43.3)	2100	642 (93.1)	0.214	0
CP-10	1200	292.9 (42.5)	2100	623 (90.4)	0.212	0
CP-14	1200	274.6 (39.8)	7.5	503 (72.9)	0.199	0.016
CP-6	1300	281.2 (40.8)	2100	529 (76.7)	0.186	0
CP-13	1300	234.4 (34.0)	7.5	288 (41.8)	0.152	0.029
CP-8	1370	261.6 (37.9)	2100	320 (46.5)	0.13	0.007
CP-12	1370	209.4 (30.4)	7.5	203 (29.4)	0.252	0.155

Table 2. Summary of cyclic fatigue tests of Norton/TRW NT-154 silicon nitride tested at elevated temperatures

Specimen	Temperature (°C)	Cyclic stress to failure [MPa (ksi)]	Intermediate cyclic stress [MPa (ksi)]	Number of cycles at intermediate cyclic loading	Number of cycles to failure
CP-16	1200		414.3 (60.1)	80,000	(80,000)[a]
		452.3 (65.6)		28,691	108,691
CP-15	1300		277.0 (40.2)	346,000	(346,000)
			292.2 (42.4)	119,300	(465,300)
		307.3 (44.6)		1,467	466,767
		Tests completed in February-March			
CP-19	1200	474.6 (68.9)			270
CP-20	1200	448.7 (65.1)			8,605
CP-21	1300		338.1 (49.0)	1,024,490	(1,024,490)
			357.5 (51.8)	233,240	(1,257,730)
			372.4 (54.0)	191,000	(1,448,730)
		387.5 (56.2)		44,383	(1,493,113)
CP-22	1300	387.5 (56.2)			278
CP-23	1300	361.2 (52.4)			762
CP-24	1370		207.0 (30.0)		150,000[b]

[a]Number of cycles accumulated at the end of intermediate loading.

[b]Test in progress.

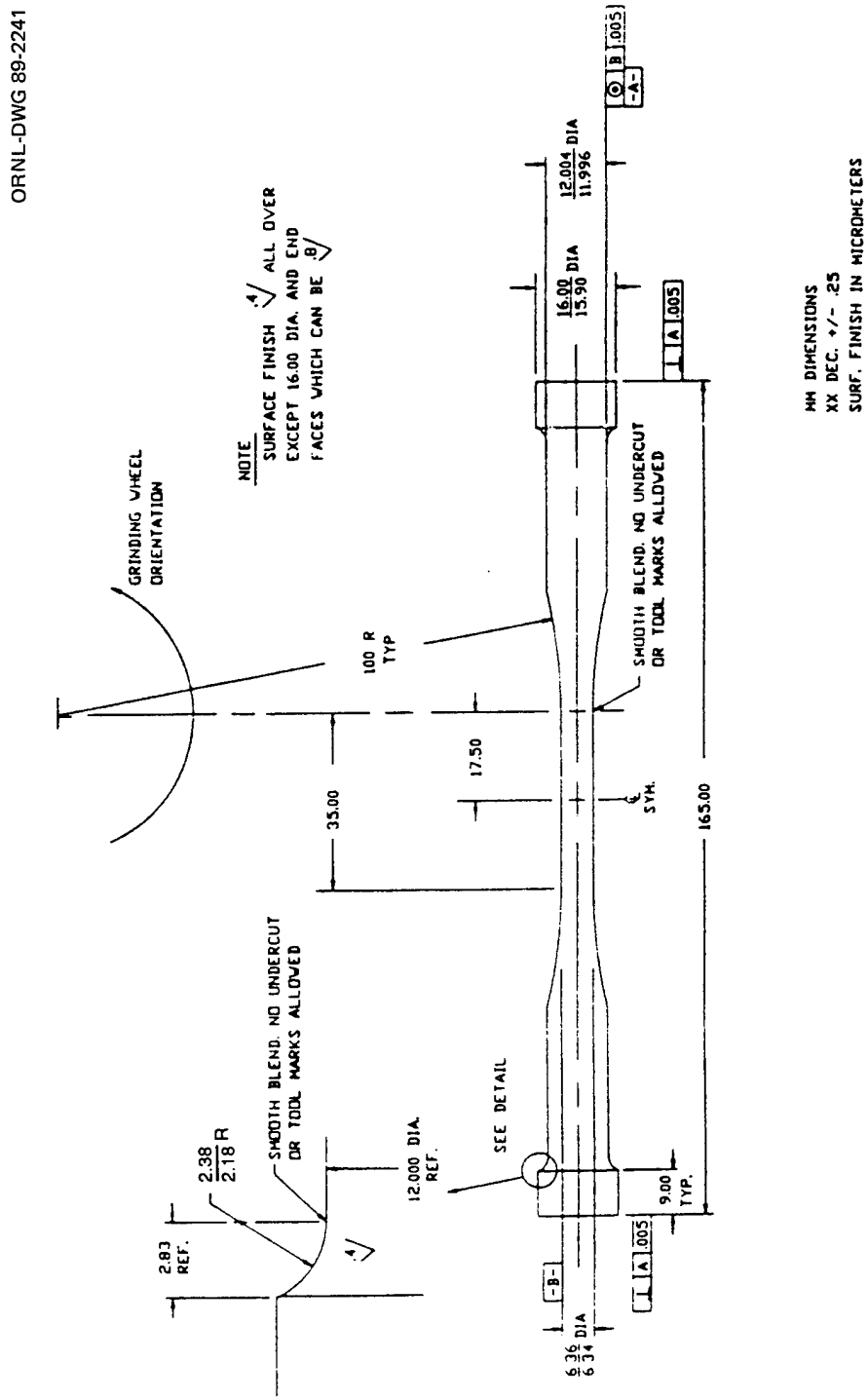

Fig. 1. Buttonhead cylindrical specimen.

ORNL-DWG 88-13054R

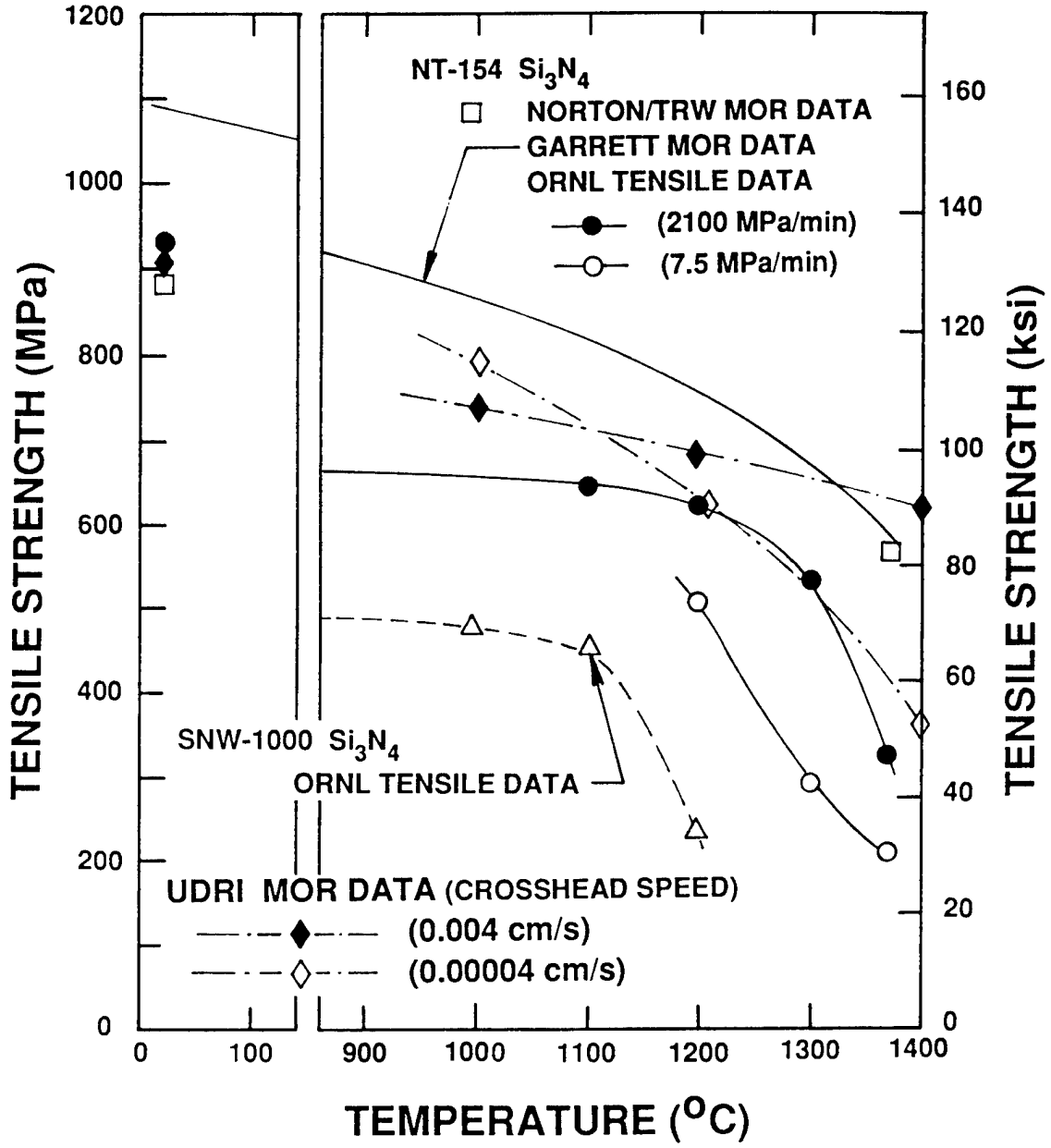

Fig. 2. Comparisons of ORNL tensile data and MOR data obtained by Norton/TRW, Garrett, and University of Dayton Research Institute for NT-154 Si_3N_4.

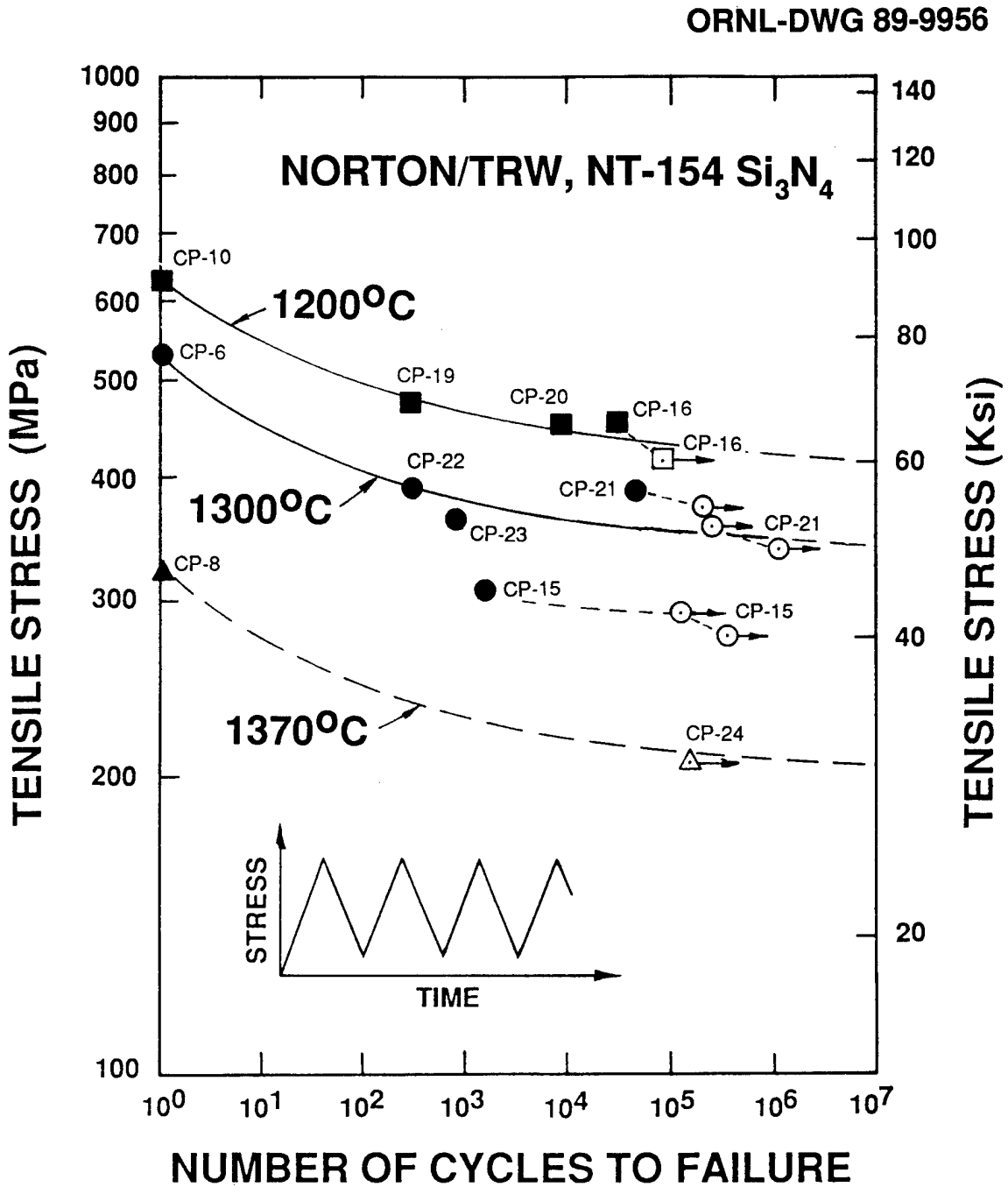

Fig. 3. Uniaxial stress-strain behavior of NT-154 silicon nitride tested at elevated temperatures.

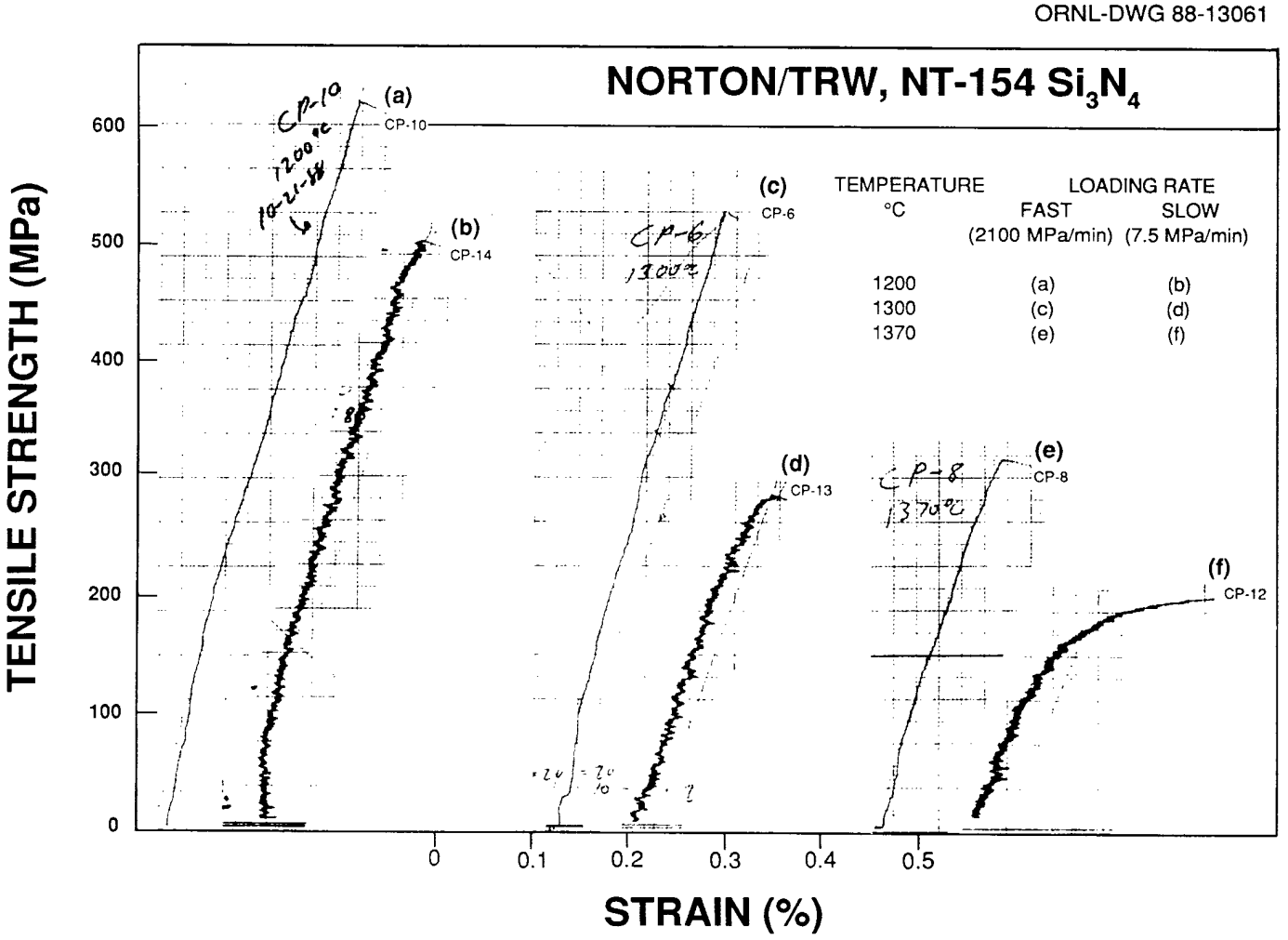

Fig. 4. Uniaxial tensile and cyclic fatigue of NT-154 Si_3N_4 tested at elevated temperatures.

Rotor Data Base Generation

M. K. Ferber and M. Jenkins (Oak Ridge National Laboratory)

Objective/scope

The goal of the proposed research program is to systematically study the tensile strength of a silicon nitride ceramic as a function of temperature and time in an air environment. Initial tests will be aimed at measuring the statistical parameters characterizing the strength distribution of three sample types (two tensile specimens and one flexure specimen). The resulting data will be used to examine the applicability of current statistical models as well as sample geometries for determining the strength distribution.

In the second phase of testing, stress rupture data will be generated by measuring fatigue life at a constant stress. The time-dependent deformation will also be monitored during testing so that the extent of high-temperature creep may be ascertained. Tested samples will be thoroughly characterized using established ceramographic, scanning electron microscopy (SEM), and transmission electron microscopy (TEM) techniques. A major goal of this effort will be to better understand the microstructural aspects of high-temperature failure including:

(1) extent of slow crack growth;
(2) evolution of cavitation-induced damage and fracture;
(3) transition between brittle crack extension and cavitation-induced growth; and
(4) crack blunting.

The resulting stress rupture data will be used to examine the applicability of a generalized fatigue-life (slow crack growth) model. If necessary, model refinements will be implemented to account for both crack blunting and creep damage effects. Insights obtained from the characterization studies will be crucial for this modification process. Once a satisfactory model is developed, separate stress-rupture (confirmatory) experiments will be performed to examine the model's predictive capability. Consequently, the data generated in this program will not only provide a critically needed base for component utilization in automotive gas turbines, but also facilitate the development of a design methodology for high-temperature structural ceramics.

Technical progress

During this reporting period, the strength of a commercial silicon nitride ceramic was determined at 25, 1100, and 1300°C. The test samples were in the form of flexure specimens having dimensions of $3 \times 4 \times 50$ mm. All testing was conducted using two specially designed flexure test systems each capable of holding up to three flexure samples. This equipment has been described elsewhere.[1] The loading rate for all tests was 44.5 N/s (10 lb/s). Approximately 50 samples were fractured at each temperature.

The resulting data were used to estimate the Weibull parameters m and σ_o in the expression

$$\ln \ln (1 - P_f) - 1 = m \ln \sigma_{max}/\sigma_o \ , \qquad (1)$$

where P_f is the failure probability and σ_{max} is the maximum stress in the flexure samples. These calculations involved the application of both linear regression and maximum likelihood techniques.

As shown in Fig. 1, the average strength dropped from 734 ± 108 MPa at 25°C to 516 ± 91 MPa at 1100°C. The strength did not change appreciably as the temperature was increased to 1300°C. Although the general temperature sensitivity of the fracture strength was similar to that measured at the University of Dayton Research Institute (UDRI),[2] the values associated with a given temperature were significantly different (Fig. 1). For example, the UDRI strengths determined using ATTAP size samples (3.175 × 6.3 × 50.8 mm) fell below the ORNL values. The difference could not be accounted for entirely by differences in specimen size alone. Furthermore, subsequent measure- ments at UDRI using 3 × 4 × 50 mm flexure samples yielded values significantly higher than those measured in the present study.

There are two possible explanations for these strength variations. First, the test samples used in the respective studies may have been machined differently. Surface roughness measurements are currently underway. The second possible reason for the variations in the data sets concerned observed differences in the phase composition of the silicon nitride samples. X-ray diffraction studies performed at UDRI indicated that the major phase in their material (for both specimen sizes) was ß Si_3N_4. The associated data are given in Fig. 2 (sample type 2). The asterisks indicate peaks which correspond to the ß Si_3N_4 phase. Although some secondary compounds were detected, their concentration was very low (<5%). However, the specimens used in the ORNL tests exhibited a significant number of secondary phases not associated with the ß Si_3N_4 (sample type 1 in Fig. 2). The secondary phases were identified as α Si_3N_4, yttrium silicon oxynitride, and yttrium silicate. Furthermore, the relative amount of these phases varied considerably from sample to sample. Finally, in the case of the room-temperature strength samples, there was no clear correlation between the nature of secondary phase present and the measured strength value.

The Weibull curves generated from the strength data are shown in Fig. 3. The Weibull modulus, m, measured at 1300°C was substantially higher than the values determined at either 25 or 1100°C. The increase in m at 1300°C, which is consistent with data generated at UDRI, may be due to oxidation-induced changes in the flaw population. Finally, the Weibull modulus associated with a given temperature was significantly lower than the value measured at UDRI. This difference may again reflect differences in the starting phase composition.

Studies aimed at examining the operational status of the tensile test equipment were continued this reporting period. These studies were primarily concerned with examining the long-term stability of the capacitance extensometers used to measure specimen deflection. Data

generated previously revealed a fairly substantial time-dependent variability in the extensometer output. In order to examine possible sources of these variations, a second creep test was initiated for a buttonhead sample of a 94% aluminum oxide. This test was conducted at 800°C using an applied stress of approximately 84 MPa. In addition to monitoring the extensometer and load cell outputs, the temperatures associated with the water-cooled grips, the capacitance head, and the signal conditioner electronics were also measured. All information was collected by a personal computer.

As shown in Fig. 4, the specimen deflection increased with time indicating the possibility of creep deformation. However, the curve deviated from linearity after about 20 h. This variation could be approximately correlated to a slight deviation in the time-dependence of the grip temperature (Fig. 4). Subsequent tests have confirmed that changes in the grip temperature can influence the extensometer readings. The extensometer data [Fig. 5(a)] also revealed the existence of short-term fluctuations occurring over periods of about 2 h. These fluctuations appeared to coincide with small variations in the applied load [Fig. 5(b)].

An intensive study aimed at improving the stability of the extensometer identified four major items required to resolve the problem:

(a) Control of the room HVAC system to minimize room temperature changes which would directly affect the electronics of the test machine, the extensometer, the furnace and furnace controllers, and the data acquisition system.

(b) Enclosure of the extensometer hardware and electronics in individual polymer boxes to buffer any ambient temperature changes and the effects of air currents.

(c) Control of the flow and the temperature of the grip cooling water to prevent direct changes of the heat flow in the specimen and to minimize localized changes in the ambient temperature.

(d) Adjustment of the furnace control parameters and stoppage of insulation "leaks" to minimize temperature fluctuations and convective currents within the furnace.

A number of "fixes" were subsequently implemented and completed to address each of these major items. A series of tensile tests were then conducted using a commercially available 94% aluminum oxide to verify the efficacy of the implemented "fixes." Figure 6 shows the stress-strain curves for 10 fast fracture tests conducted at room temperature, 800°C, and 1000°C. The average ultimate strength, ultimate strain, and elastic modulus results are shown in the figure. The curves show the superb ability of the present tensile testing set-up to provide repeatable and useful engineering data.

Results are shown in Fig. 7 for a series of constant load tension tests conducted at 1000°C in air at the indicated initial stress values. The curves are polynomial least square fits of the extensometer data and illustrate the ability of the testing system to characterize long-term strain deformation behavior.

The plot of strain versus time is contained in Fig. 8 where the data was collected for nearly 200 h at 1000°C in air for a specimen initially stressed in tension at 21 MPa. This curve of data points not only indicates the ability of the system to resolve changes in the material deformation but also verifies the elimination of the difficulties associated with ambient temperature changes noted earlier. The steady state strain rate is about 8×10^{-10}/s, which is an excellent demonstration of the capability of the system to measure very low strain rates.

The determination of the stress exponent for the material at 1000°C is shown in Fig. 9. The exponent of 5.5 is indicative of the high porosity of the material as well as the thermally activated mechanisms related to the presence of the glassy second phase.

Status of milestones

The statistical measurements involving the silicon nitride flexure samples were completed this reporting period (Milestone 321601).

References

1. M. K. Ferber, "Rotor Data Base Generation," pp. 302-306 in *Ceramic Technology for Advanced Heat Engines Semiannual Progress Report for October 1987 through March 1988*, ORNL/TM-10838, December 1988.

2. N. L. Hecht, "Environmental Effects in Toughened Ceramics," pp. 254-381 in *Ceramic Technology for Advanced Heat Engines Semiannual Progress Report for April 1987 Through September 1987*, ORNL/TM-10705, March 1988.

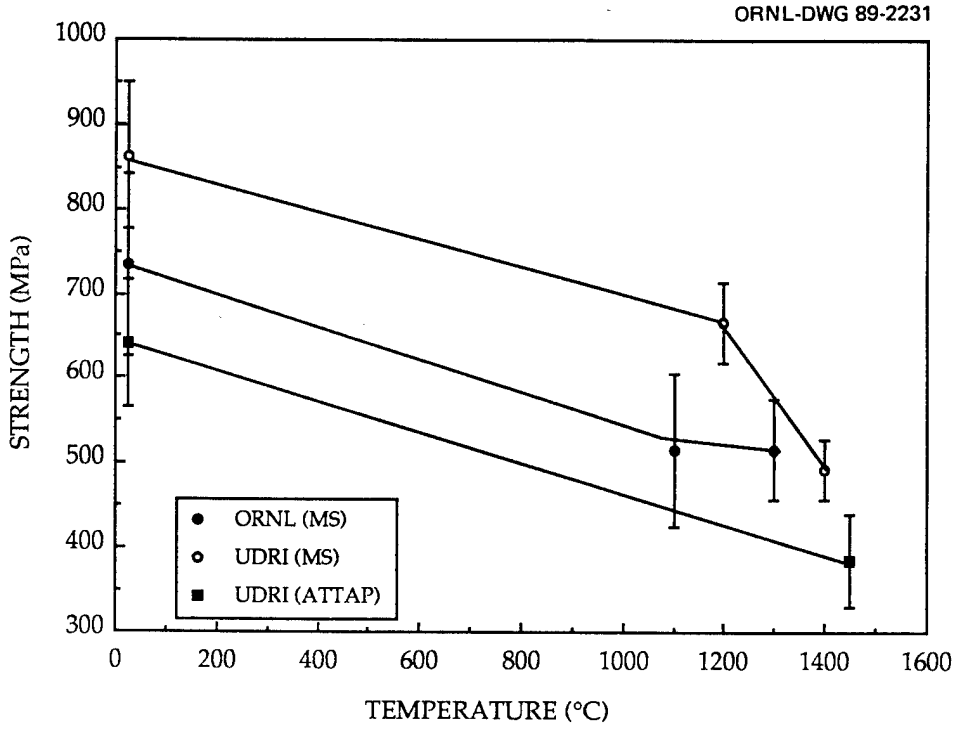

Fig. 1. Strength values obtained for commercial silicon nitride ceramic exhibited considerable variability.

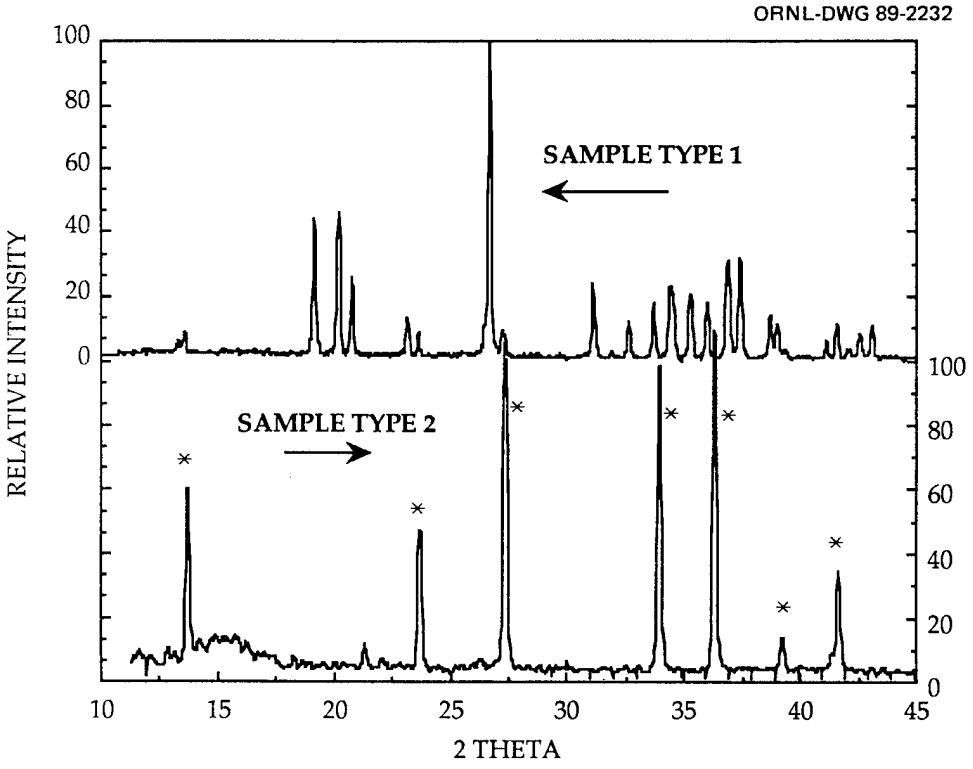

Fig. 2. Additional phases were present in the silicon nitride samples tested the present study.

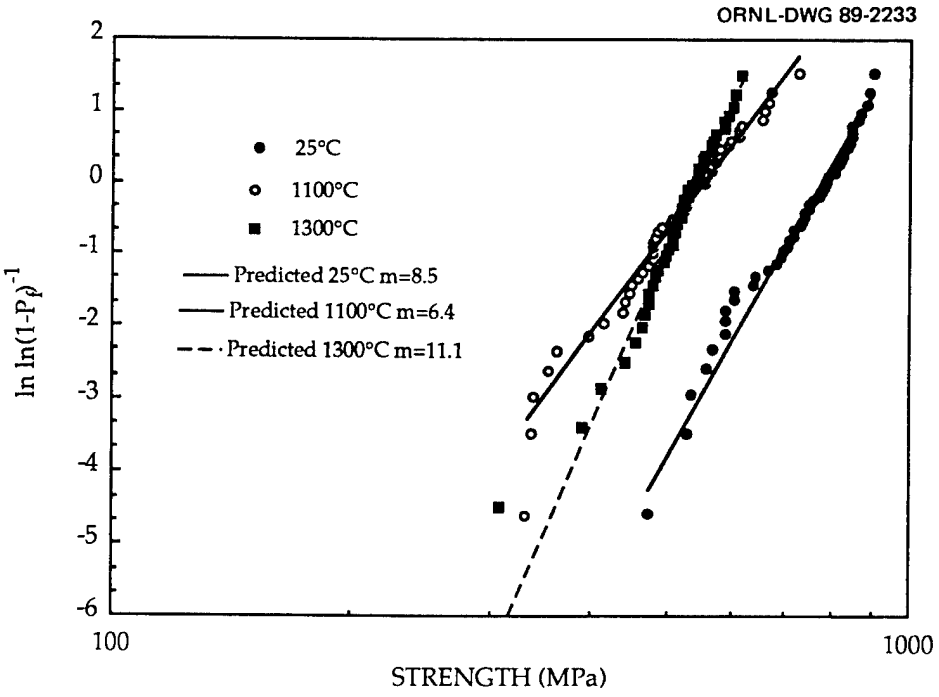

Fig. 3. Strength distribution for silicon nitride samples was influenced significantly by temperature.

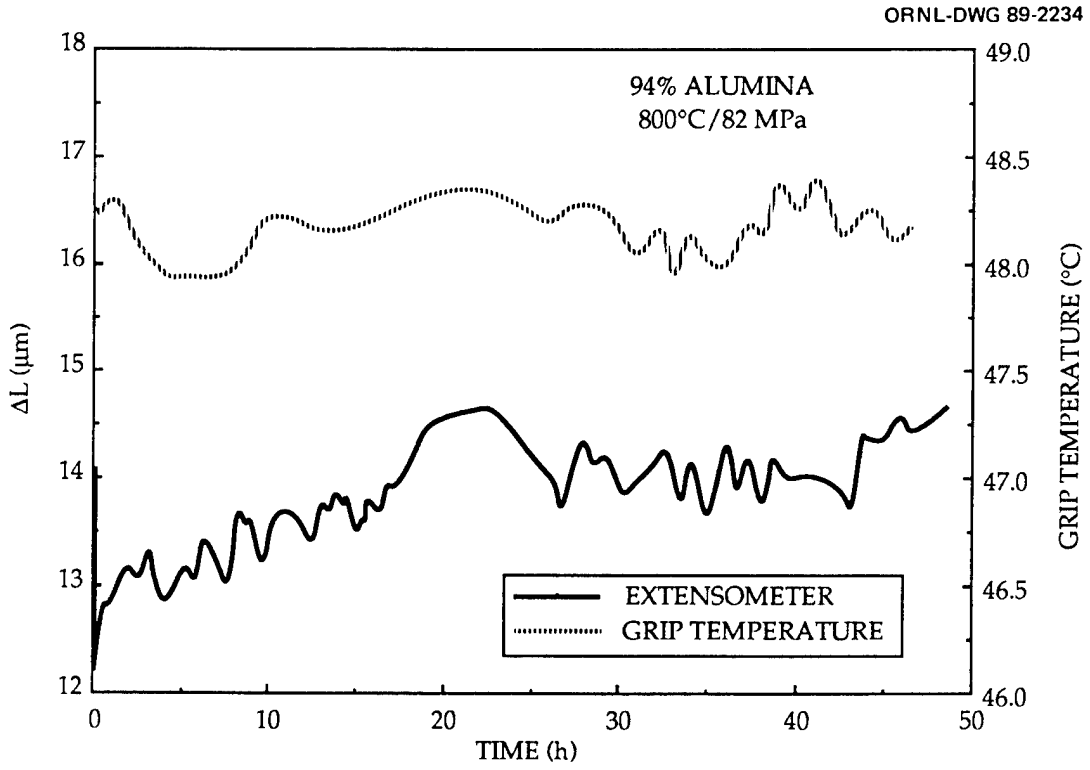

Fig. 4. Deflection data obtained for alumina sample exposed at 800°C and stressed at 84 MPa exhibited deviations from linearity after about 20 h. The grip temperature also exhibited a slight variation after 20 to 25 h of specimen exposure.

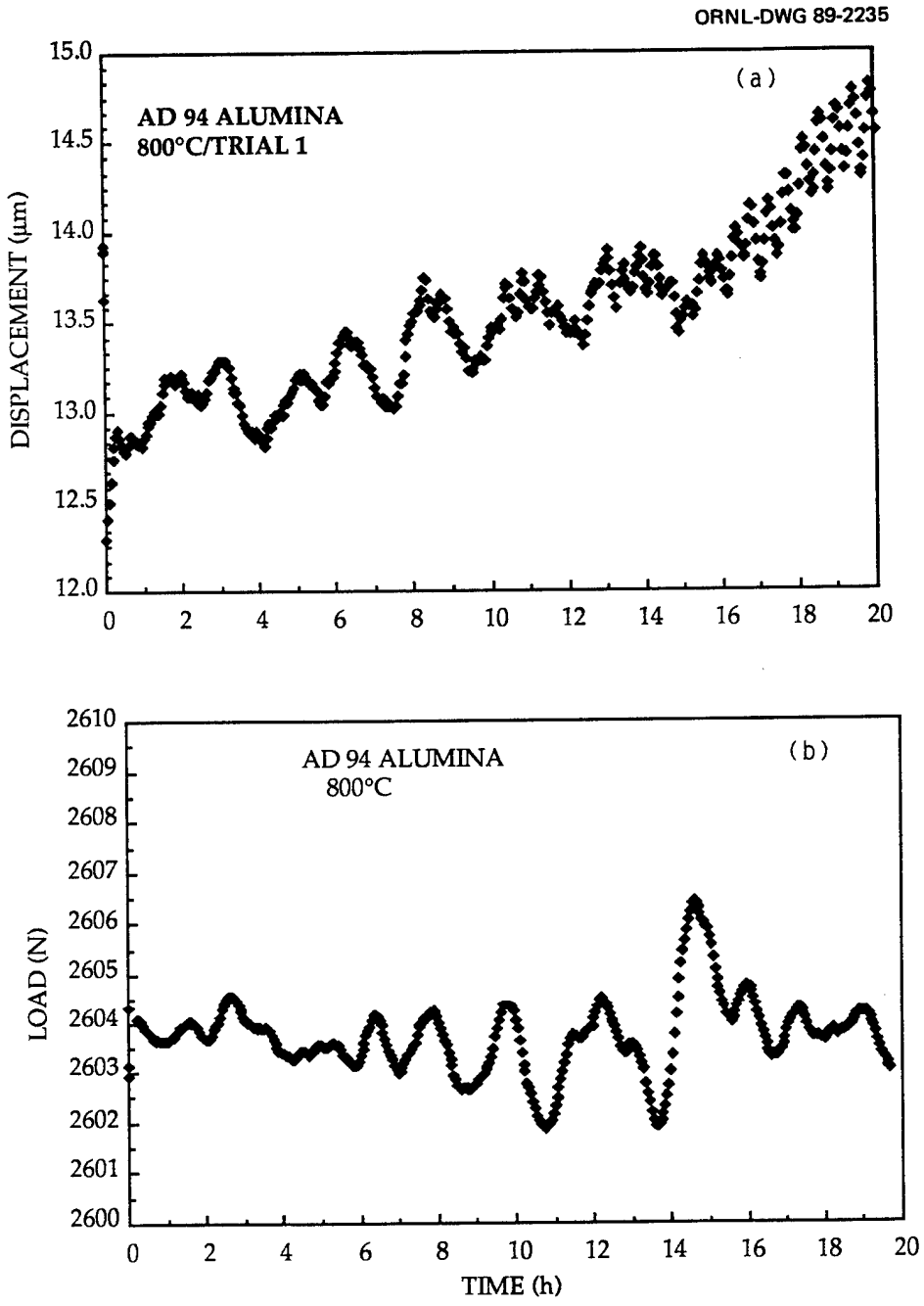

Fig. 5. Small time-dependent variations in the displacement (*a*) could be correlated with similar variations in the load (*b*).

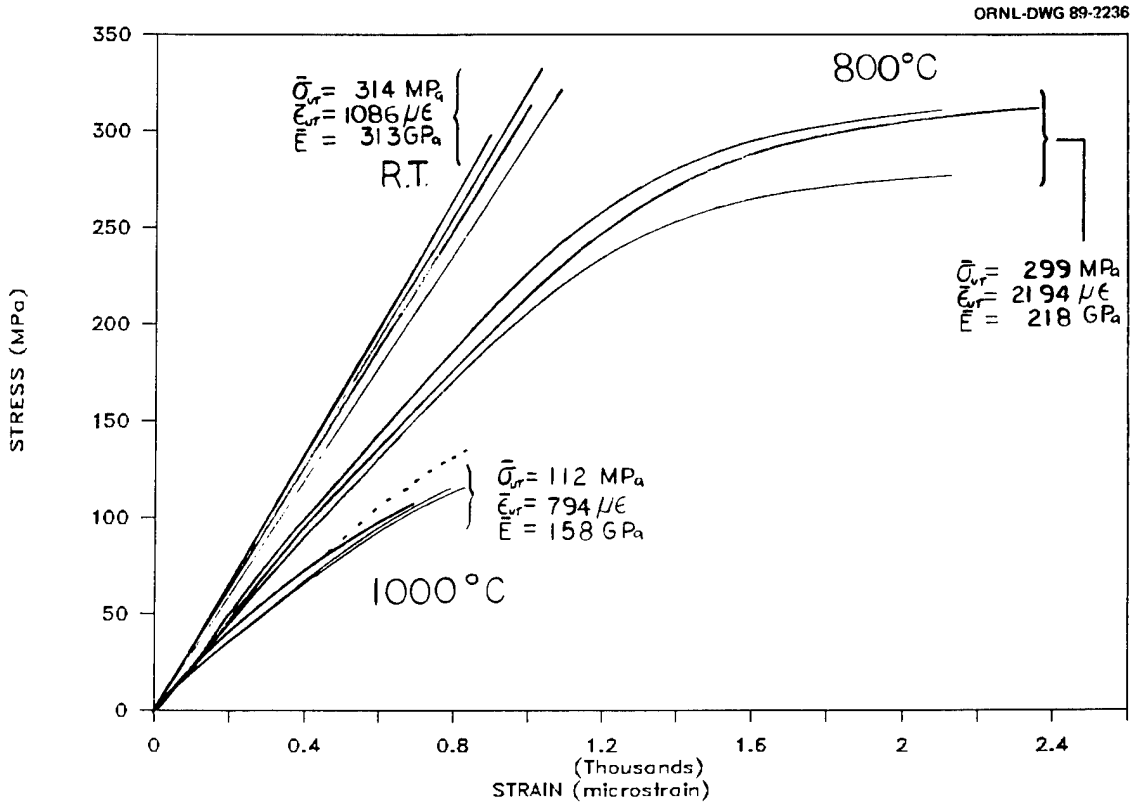

Fig. 6. Stress-strain curves for a 94% alumina at various temperatures.

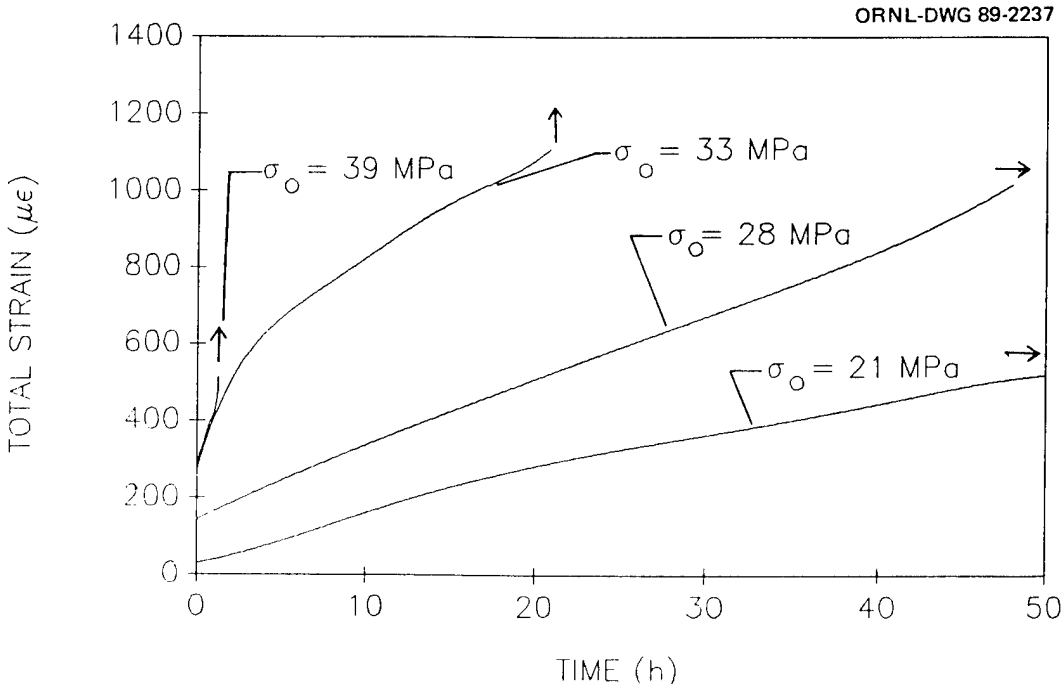

Fig. 7. Strain versus time curves for a 94% alumina at 1000°C.

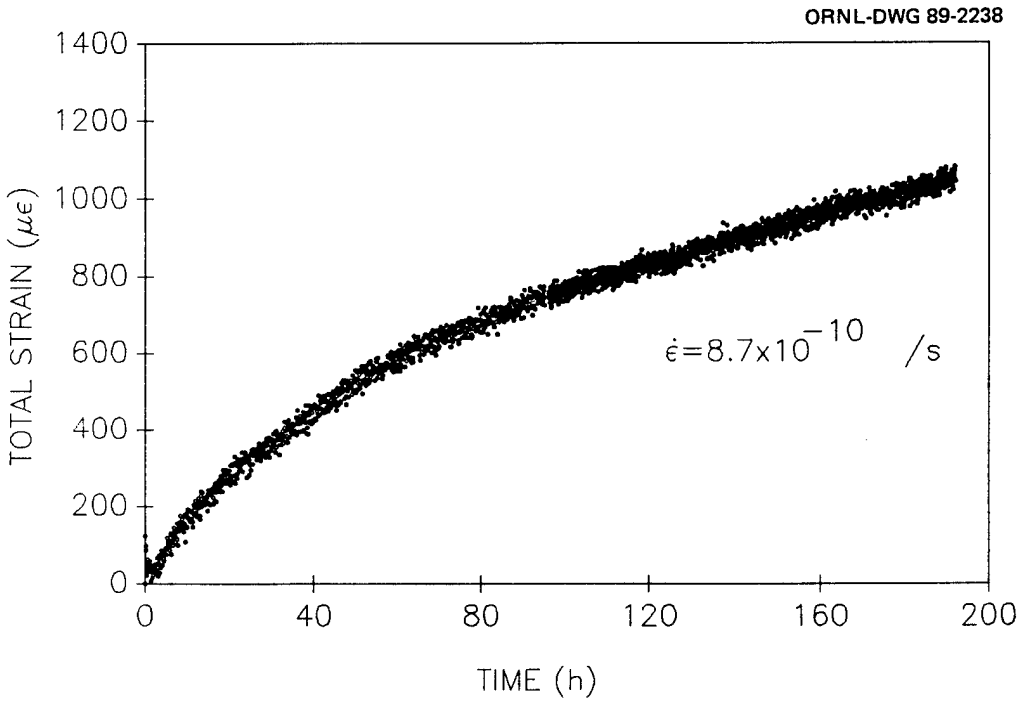

Fig. 8. Strain versus time curve for a 94% alumina at 1000°C with an initial tensile stress of 21 MPa.

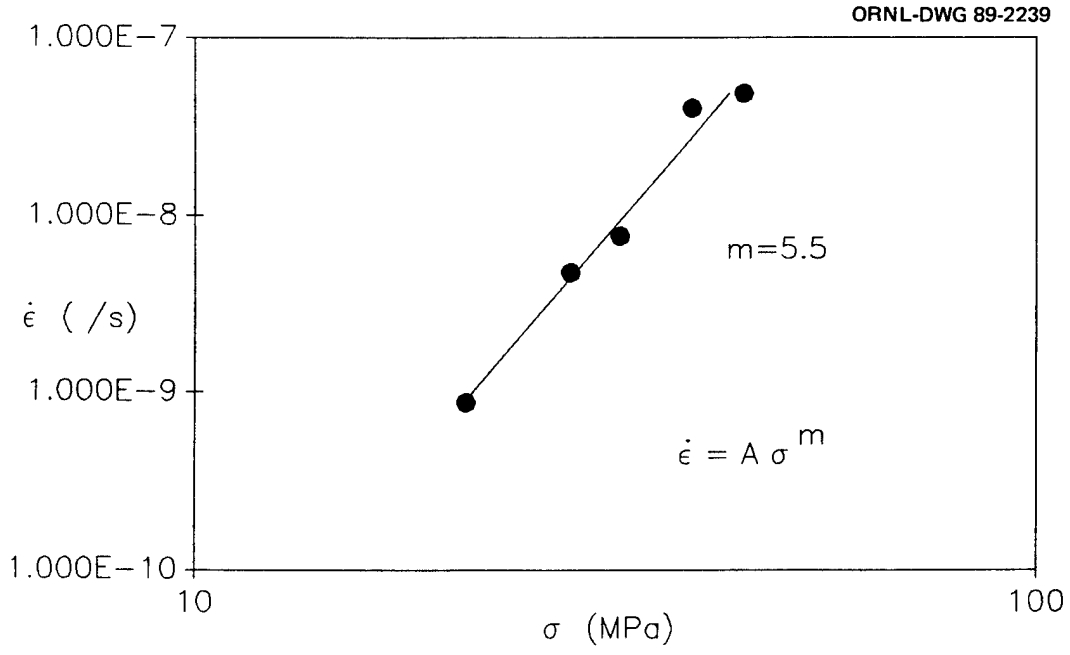

Fig. 9. Log-log plot of strain rate versus stress to determine the stress exponent for a 94% alumina at 1000°C.

Toughened Ceramics Life Prediction
J. A. Salem (NASA Lewis Research Center)

Objective/scope

The purpose of this research is to understand the room temperature and high temperature [≥1370°C (2500°F)] behavior of toughened ceramics, in particular SiC-whisker toughened Si_3N_4, as the basis for developing a life prediction methodology. A major objective is to understand the relationship between microstructure and the mechanical behavior within the bounds of a limited number of materials. A second major objective is to determine the behavior as a function of time and temperature. Specifically, the room temperature and elevated temperature strength and reliability, the fracture toughness, slow crack growth and the creep behavior will be determined for the as-manufactured material. The same properties will also be evaluated after long-time exposure to various high temperature isothermal and cyclic environments. These results will provide input for parallel materials development and design methodology development programs. Design codes developed in parallel with this effort will be verified.

Technical progress

Several hundred specimens of Garrett Si_3N_4 and SiC_w/Si_3N_4 were received and inspected with visual, radiographic, and acoustic methods. The inspection revealed unacceptable levels of machining damage on the specimen bevels and structural variations in the material. Because of the machining damage, the specimens were remachined. The most interesting structural aspects of the materials were revealed by radiography, illustrated in Fig. 1. The monolithic material exhibited a coarse cellular structure that was also visible to the naked eye. The composite material occasionally exhibited the same macro-cellular structure and banding or chemical layering similar to the billet geometry (a cylinder). Such radiographic observations have been related to density variations, however, no metallography or testing was performed to confirm the possibilities. Ultrasonic velocity measurements, which are sensitive to density variations, were similar for regions of radiographic dissimilarity, indicating chemical, rather than density variations. Very little anisotropy in composite or monolithic materials could be detected by velocity measurements (Table I). Velocity measurements on samples machined from different billets also showed little difference (Table II). The variation of velocity across the diameter of billets was also determined for the center 2cm of the billets and found similar (Table III). The HIPed RBSN Norton materials previously tested also exhibited density or chemical variations, while the HIPed SiC_w/RBSN did not (February-March 1988). The variations were noted to affect MOR strength. These structural and chemical variations are being considered in future material requirements, mechanical testing and analytical modeling.

The Ceramics Mechanical Testing Laboratory renovation is complete and two Instron 8500-series servo-hydraulic test machines, one with a 1500°C furnace, are scheduled to arrive in August 1989. One Instron

8500-series electro-mechanical machine, also with a 1500°C furnace has also been ordered. Specifications for dead weight, tensile creep systems have been determined.

Test results from these Garret Si_3N_4 and SiC_w/Si_3N_4 specimens and batches yet to be procured will provide data for verification of life prediction models being developed. Thus far, an analytical model has been developed for fast fracture prediction of transversely isotropic whisker reinforced ceramics.[1] A second reliability model for prediction of the time-dependent response of ceramic materials has now been developed.[2] The model integrates continuum damage mechanics principals and Weibull analysis, with emphasis on creep rupture phenomena. Results comparing the continuum and the microstructural equations highlights a strong resemblance between the two approaches.

References

1. S. F. Duffy and S. M. Arnold, "Noninteractive Macroscopic Reliability Model for Whisker-Reinforced Ceramic Composites," submitted to J. Comp. Matls.

2. S. F. Duffy and J. P. Gyekenyesi, "Time Dependent Reliability Model Incorporating Continuum Damage Mechanics for High-Temperature Ceramics."

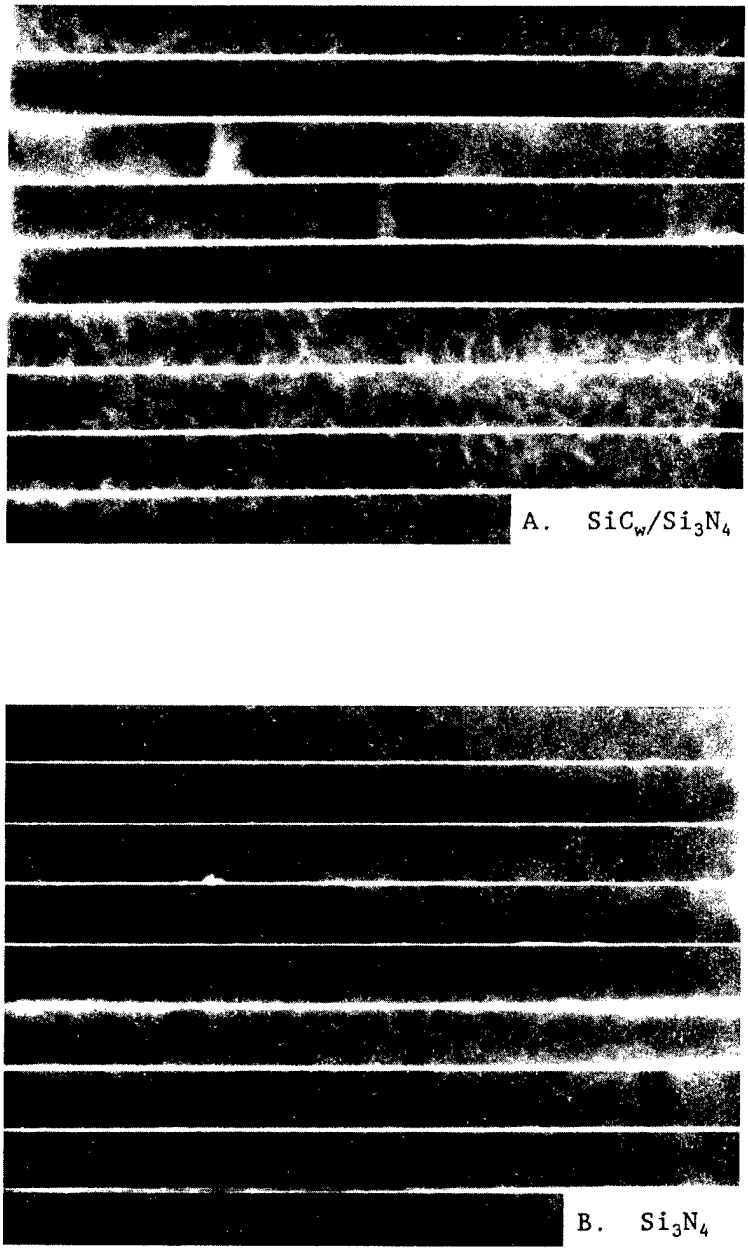

Fig. 1. X-ray radiographs of MOR bars machined from a cylindrical billet. Dark zones imply higher density or constituents with greater x-ray absorption.

Table I. Ultrasonic shearwave velocities in the transverse and longitudinal directions in MOR bars machined from cylindrical billets. Long axis of MOR bars were perpendicular to the billet radius.

Billet/ Specimen #	Velocity cm/us (Longitudinal)	Velocity (Transverse)	
C-2/03	0.628	0.626	(composite)
C-3/03	0.624	0.624	"
C-11/05	0.631	0.632	"
C-12/04	0.627	0.628	"
M-1/01	0.601	0.601	(monolithic)

Table II. Ultrasonic velocities in monolithic and composite billets.

Billet (composite)	Velocity (cm/us)	Billet (monolithic)	Velocity (cm/us)
C-12	1.082	M-1	1.081
C-11	1.092	M-2	1.082
C-8	1.083	M-3	1.088
C-3	1.075	M-C	1.082
C-2	1.082		

Table III. Variation of ultrasonic velocity across the diameter of monolithic and composite billets.

Distance from center (cm)	Velocity (cm/us)	
	Monolithic	Composite
-1.0	1.084	1.082
-0.5	1.083	1.083
0.0	1.081	1.082
+0.5	1.077	1.082
+1.0	1.077	1.082

Life Prediction Methodology

D. L. Vaccari and P. K. Khandelwal (Allison Gas Turbine Division of General Motors Corporation)

Objective/scope

The objective of this project is to develop and demonstrate the necessary nondestructive examination (NDE) technology, materials data base, and design methodology for predicting useful life of structural ceramic components of advanced heat engines. The analytical methodology will be demonstrated through confirmatory testing of ceramic components subject to thermal-mechanical loading conditions similar to those anticipated to occur in actual vehicular service. The project addresses fast fracture, slow crack growth, creep, and oxidation failure modes.

Technical progress

This is a new start for FY 1989.

Background - There are benefits to be derived from using structural ceramics as heat engine components due to the inherent advantages associated with ceramic's unique properties. However, before these benefits can be realized, the long-term reliability of structural ceramics must be both improved and quantified.

The design requirements for structural ceramic components in an automotive gas turbine engine include a turbine inlet temperature up to 2500°F and a 3500 hour service life encompassing both cyclic and steady-state operation that simulates the combined Federal Driving Cycle. The resulting stress state in the ceramic components will not only be multiaxial, but will be thermomechanically driven. As the ceramic gas turbine technology advances (supported by both government and industry funding), a primary challenge is to develop and validate the methodology required to adequately predict the time dependent failure modes of structural ceramics.

A ceramic component inevitably possesses "flaws." These flaws may be the result of the ceramic processing, machining, foreign object damage, etc. They may not cause fast fracture during initial application of full load. However, the flaws (or cracks) may grow in time due to load and temperature. This phenomenon is known as slow crack growth, or static fatigue, and can ultimately lead to component failure at submaximum load levels. Proven analytical methodologies are needed for the accurate crack growth prediction of these flaws. In addition, nondestructive evaluation (NDE) techniques and procedures are needed to identify those flaws that are inconsistent with acceptable component reliability.

Another failure mode of concern is creep. If the component changes shape (i.e. creeps) as a result of extended exposure to load and temperature, the component may no longer function properly. For example, turbine blades that creep so that they rub the outer flowpath wall may result in total breakage to the blades. Consequently, a methodology must be in place for the accurate assessment of this phenomenon.

Yet another concern is the potential oxidation of ceramic components. Although, for a given temperature, structural ceramics are relatively inert with respect to their metal counterparts, the operating temperature of structural ceramics in proposed automotive gas turbine engines is well in excess of a metal's capability in order to maximize the benefits that ceramics offer. Again, extended exposure to this hostile environment may lead to chemical reaction of the component's surface and subsequent strength degradation. An analytical technique of accurately quantifying this effect is required.

In summary, the future of structural ceramics used in gas turbine engines is partially dependent upon the development of reliable analytic algorithms for the life prediction of potential failure modes. The old fashioned, empirical method of "build 'em and bust 'em" is much too costly and time consuming to develop final component design configurations. The analytic schemes, when coupled with NDE techniques, should be able to provide superior designs early in a component's design/development cycle. Additionally, it is desirable that the material properties required to drive these analytic procedures be derived from simple, cost-effective, uniaxial specimen tests.

Approach - The objective of this program is to demonstrate that the usable life of a ceramic component operating in an automotive gas turbine can be adequately predicted. There are five primary tasks involved in accomplishing this:

Task 1. Materials selection
Task 2. Design methodology and data base development
Task 3. Development and application of nondestructive examination techniques
Task 4. Analytical tools
Task 5. Confirmatory component tests

There are two requirements for the first task, materials selection. The material must be available from a domestic supplier and the material must be suitable for an ATTAP component. Additionally, the material selected for the program must be tested in both the thermally aged condition as well as the nonaged condition to determine the influence of time and stress at temperature on subsequent behavior. Allison's ATTAP effort is currently investigating the use of a number of different material systems, including monolithic silicon carbide and silicon nitride as well as various fiber reinforced composites. The material Allison will use for this program is GTE's hot isostatic pressed (HIP) PY6 silicon nitride. This material is produced in the United States and is one of Allison's ATTAP rotor material candidates.

The second task deals with design methodology and the development of a data base. A significant portion of the program's effort will be expended in this task. The effort will concentrate on the following four failure modes:

- o fast fracture
- o slow crack growth

o creep
o oxidation

Both uniaxial and biaxial stress states will be explored. The objective is to generate the data base and the material constants required to drive the proposed analytic models that will be used to predict the material behavior. The test matrix includes both flexural and tensile testing, with enough specimens to get a statistically meaningful sample. Biaxial testing will be conducted to help discern between various proposed failure models and to help confirm proposed failure models. The testing will span the range from room temperature to 1400°C.

The third task of significant effort in this program will be in nondestructive examination (NDE). Various NDE techniques will be used. In the area of flaw detection, both ultrasonic imaging and microfocus radiography will be used on all of the test specimens. Computed tomography will also be used on selected specimens. In addition to flaw detection, ultrasonic techniques will be used to help characterize the material's general microstructure. Ultrasonic velocity measurements will be taken on all test specimens. Ultrasonic attentuation measurements will be made on selected specimens.

Task 4 addresses analytical tools. All of the computer codes to be used in the program fall into one of three categories. The first category is public domain software, which is software that is available for no license fee. The second category is software that is available on the open market but requires a fee. The final category represents the codes being developed specifically for this program, and those codes will become public domain codes at the end of the program. Examples of the codes intended for use include PATRAN, MSC/NASTRAN, and CARES. PATRAN is a finite element preprocessor used for model generation. MSC/NASTRAN is a finite element analyzer that will be used to calculate stresses in test specimens. CARES is a NASA developed code used as a post-processor to NASTRAN to calculate fast fracture failure. The newly developed codes will also run as post-processors to NASTRAN. The major point is that all of the analytical tools used in this program will be available to the public at the end of the program.

The fifth task of the program addresses the confirmatory tests. The analytical models proposed and developed during the program will be substantiated by testing. The confirmatory test specimens will simulate an engine rotor by capturing the significant features of a typical axial turbine rotor. The blades will be eliminated since they would provide an unnecessary complication and expense. Test conditions will simulate an engine environment with tests taking the form of both spin tests and quasistatic tests.

Progress - Efforts have concentrated on establishing a subcontract with GTE for providing the test specimens required in the program. Due to the length of time between initial proposal submittal and ultimate program award, new cost values had to be determined. Based on the projection of cost increases, the number of test specimens that are required is being reviewed. Other cost cutting measures are also being explored.

A review of the confirmatory test specimen geometry has also been performed. The originally proposed geometry differed somewhat from that of the gasifier turbine wheel in Allison's Advanced Turbine Technology Applications Project (ATTAP). The new test specimen geometry will more closely represent the general size of the actual turbine rotor. Additionally, the new geometry will be easier and less expensive to fabricate.

Discussions have been held regarding the geometry to be used for the tensile test specimens. It is desired to use the largest specimen possible from the blanks that GTE will be producing. Southern Research Institute and GTE have been consulted regarding potential specimen geometries. GTE has supplied several sample blanks for exploratory machining and testing.

NASA-Lewis has been contacted regarding the latest version of CARES, a computer code for predicting the fast fracture failure of ceramics. NASA has supplied Allison with the latest version of the code plus the appropriate documentation.

Per the program requirement, Allison has supplied MMES with a plan for testing thermally-aged and nonaged material. The plan includes thermal exposure in static oxidizing air as well as in an inert environment. After thermal exposure, MOR bars will be tested at room temperature. Subsequently, fractographic and analytic techniques such as SEM and X-ray diffraction will be used to examine the surface layers and fracture surface topography to relate the strength degradation failure mechanism, if any, to critical microstructural features. The results of these tests will be compared to the room temperature MOR values obtained from nonaged material. This will permit the assessment of the effect of thermally-aging (time and temperature) on material behavior. The plan also includes flexural specimen testing in air at three temperatures, and three stressing rates to measure the crack growth exponent (n). This data will provide guidance for the monotonic creep/stress rupture testing to be performed later in the program. MMES has concurred with the plan.

Status of Milestones

The program is currently on schedule. Since most of the project's milestones will be tied to the availability of test specimens produced by GTE, updated milestones will be prepared after GTE's subcontract is finalized.

Publications

Vaccari, D. L., and Khandelwal, P. K., "Life Prediction Methodology For Ceramic Components", to be published in proceedings of 26th ATD-CCM, Dearborn, Michigan, October 24-27, 1988.

3.3 ENVIRONMENTAL EFFECTS

Environmental Effects in Toughened Ceramics
Norman L. Hecht (University of Dayton)

Objective/scope

Since 1985 the University of Dayton has been involved in a three-phase project to investigate the effects of environment on the mechanical behavior of commercially available ceramics being considered for heat engine applications. In the first phase of this project, the effects of environment on the mechanical behavior of transformation-toughened ZrO_2 ceramics were investigated. In the second phase, two Si_3N_4 (GTE-PY6 and Norton/TRW-XL144) and one SiC (Hexoloy-α-SiC) were evaluated. In the third phase, presently in progress, the tensile, flexural, and fatigue strength of nine SiC and Si_3N_4 ceramics (see Table 1) are being evaluated at temperatures from 1000°-1400°C. Microstructure, chemistry, physical properties, and mechanical behavior from 25°-1400°C are also being investigated.

During the past six months (October 1988-March 1989) evaluations of two SiC and three Si_3N_4 ceramics were initiated, and the evaluation of Hexoloy SA and ST, EC-152, NT-154, PY6, and CVD-SiC was completed. In addition, the development of optical interferometry techniques to monitor strain, Raman spectroscopy to analyze SiC, and the compilation of a SiC and Si_3N_4 property data base from the literature continued.

Experimental procedures

Flexural strength measurements are made using two Instron Universal Testing Machines (Model 1123) following MIL-STD-1942(MR). Elevated

Table 1. Candidate SiC and Si_3N_4 Ceramics Selected for Evaluation

Carborundum Hexoloy α-SiC	Cold formed (injection molded or isostatic pressing) and pressureless sintered α-SiC with additions of B and Al (200 Tensile and 200 Flexure Specimens)
Carborundum Hexoloy ST	Cold formed and pressureless sintered α-SiC and TiB_2 (60 Flexure Specimens)
GTE - PY6	Injection molded and hipped β Si_3N_4 with additions of Y_2O_3 (200 Tensile and 200 Flexure Specimens)
Norton/TRW - NT154	Sintered and HIP'ed Si_3N_4 (100 Flexure and 100 Tensile Specimens)
CVD - SiC	SiC prepared by chemical vapor deposition techniques (60 Flexure Specimens)
Howmet - SN-4	Cold formed (die pressing/isostatic pressing) sintered and HIP'ed Si_3N_4 with 10% oxide sintering aids (Al_2O_3, Y_2O_3) (60 Flexure Specimens)
Ceradyne - Ceralloy 147-3	Cold formed (isopressing/slip casting/injection molding) sintered Si_3N_4 with additions of Y_2O_3 and Al_2O_3 (60 Flexure Specimens)
Kyocera - SN252	Cold formed (isopressed/slip cast/etc.) and sintered Si_3N_4 with additions of Yb_2O_3, Y_2O_3, and Al_2O_3 (note the sintering process is controlled to promote the growth of a β Si_3N_4 whisker phase in the Si_3N_4 matrix) (60 Flexure Specimens)
NGK Spark Plug - EC-152	Gas pressure sintered Si_3N_4 with additions of Al_2O_3 and Y_2O_3 (60 Flexure Specimens)

temperature measurements (1000°-1400°C) are conducted in two ATS #3320 high-temperature furnaces. Flexural strengths are measured on test specimens 3 x 4 x 50 mm with the tensile surface ground and polished to a 16-microinch finish [MIL-STD-1942(MR) specimen size B]. The long edges of the tensile surface are rounded and polished to minimize edge failures. Flexural strength is measured using four-point bend test fixtures, and the test specimens are loaded at machine crosshead speeds of 0.004, 0.0004, and 0.00004 cm/sec. For the room temperature measurements the bend fixtures are made of steel, and for the measurements at 1000°, 1200°, and 1400°C the bend fixtures are made of SiC. The four-point bend fixtures have an outer span of 4 cm and an inner span of 2 cm.

The dynamic fatigue analysis of each material is determined from the fast, medium, and slow loading rate strength data. The dynamic fatigue can be characterized by a ln-ln plot of fracture strength (σ_f) versus loading rate ($\dot{\sigma}$) which is expressed by the relationship:

$$\sigma_f = A'\dot{\sigma}^{(\frac{1}{n+1})} \qquad (1)$$

(where A′ is a constant). The constant, n, is a measure of the stress corrosion susceptibility of the material. Large values of n are synonymous with lower stress corrosion or fatigue.

The tensile strength measurements are made using an Instron Electro-Mechanical Test System (Model 1361) equipped with Super-Grip Instron Universal Coupling and Water-Cooled Holders for High-Temperature Tensile Testing. For high-temperature measurements, an Instron High-Temperature Short Furnace is used.

Fracture origins are determined by optical microscopy and SEM (JEOL/SM-80 with EG&G Ortec System 5000 Microanalysis System). The strength values are evaluated to determine Weibull parameters. Maximum likelihood estimates of the shape parameter, m (modulus), and the scale parameter, So (the 63rd percentile for the distribution of breaking strength), are determined in this analysis.

The elastic modulus of the candidate materials is measured by a Grindo-Sonic (Model MR35T) Transient Impulse/Elastic Modulus Apparatus.

The hardness of the candidate materials is measured by a Vicker's microindent hardness tester.

The microstructure and chemistry of the candidate materials are also studied. Polished sections from representative specimens are viewed by optical microscope (Nikon Epiphot), and freshly fractured sections are viewed by scanning electron microscope (JEOL JSM-840). X-ray fluorescence (EDXA) spectra are obtained using an EG&G Ortec System 5000 attachment to the JSM-840. Test specimens are examined by x-ray diffraction with a Norelco/Philips Electronic Instruments XRD System using CuKα radiation (40 KV, 25 μA) for analysis from 20° 2θ to 58° 2θ. In addition further chemical analysis of selected specimens is obtained using high-resolution scanning Auger spectroscopy (JEOL JAMP-30).

Thermal expansion is measured from 25°-1400°C using a Theta Industries Dilatronic II (Model 6024). Fracture toughness is measured by both the controlled flaw method and the microindent method.

Technical progress

Flexural strength and physical property measurements

The results of the physical property measurements obtained for Hexoloy SA, SN-4, NT-154, and PY6 are summarized in Table 2. The flexural strength data obtained for Howmet SN4, Kyocera SN-252, Hexoloy SA and ST, GTE-PY6, Norton/TRW NT-154, CVD SiC, and NTK EC-154 are summarized in Table 3. A series of bar graphs comparing flexural strength with loading rate and temperature for all the candidate materials evaluated are presented in Figures 1 and 2.

The flexural strength data obtained for each of the materials were also characterized by Weibull analysis. The results of these analyses are summarized in Table 4. The flexural strength data were used for preparing computer-generated graphs of ln σ_f versus ln $\dot{\sigma}$ and for determining n. The results of these calculations are summarized in Table 5, and the ln-ln plots generated are compiled in Appendix 1.

Photographs of typical fracture surfaces obtained by optical microscope and SEM were prepared. Photomicrographs of typical fracture surfaces for NT-154 are presented in Figures 3 through 6.

Table 2. Property Measurements Obtained

Property Measurement	Materials: Hexoloy SA	GTE PY6	Norton/TRW XL-154	Howmet SN-4
Density (g/cc)	3.17	3.27	3.23	3.23
Young's Modulus (GPa)	427	301	310	294
Hardness (kg/mm^2)	2727	1458	--	1605
Fracture Toughness CF/MI* ($MPa \cdot \sqrt{m}$)	2.6/3.4	6.1	--	3.7/6.8
Coefficient of Thermal Expansion ($10^{-6}/°C$)	5	3.3	--	--

*CF - Controlled Flaw
MI - Microindent

Table 3. Results of Flexural Strength Measurements

Material	Temperature °C	Machine Crosshead Speed cm/sec	Flexural Strength MPa	Standard Deviation MPa	Fracture Origin
SN-4	25	0.004	977	129	Surface flaws
	1000	0.004	744	91	Surface flaws
	1000	0.00004	514	47	Surface flaws possible SCG
	1200	0.004	402	40	Surface flaws
	1200	0.00004	312	15	Surface flaws possible SCG
	1400	0.004	190	--	Severe oxidation and blistering
SN-252	1000	0.004	526	31	At surface and edges due to the presence of large whiskers
	1000	0.00004	466	26	
	1200	0.004	478	43	At surface and edges due to the presence of large whiskers
	1200	0.00004	485	35	
	1400	0.004	459	29	At surface and edges due to large whiskers

Table 3. Results of Flexural Strength Measurements (Continued)

Material	Temperature °C	Machine Crosshead Speed cm/sec	Flexural Strength MPa	Standard Deviation MPa	Fracture Origin
	1400	0.00004	498	29	Specimens undergo severe plastic deformation prior to fracture
Hexoloy SA	25	0.00004	395	19	Surface and edge flaws (pits)
	1000	0.004	416	30	
	1000	0.0004	416	49	
	1000	0.00004	412	37	Surface and edge
	1200	0.004	435	53	flaws
	1200	0.0004	400	60	(pits/
	1200	0.00004	441	6	voids and possible
	1400	0.004	436	48	inclusions)
	1400	0.0004	415	40	
	1400	0.00004	390	36	
EC-152	1000	0.004	843	104	Surface
	1000	0.00004	768	70	flaws
	1200	0.004	826	35	Edge and
	1200	0.00004	610		surface flaws
	1400	0.004	389	59	Surface flaws
	1400	0.00004	269	--	Plastic deformation prior to fracture
NT-154	25	0.004	907	79	Surface/
	25	0.00004	749	51	subsurface and edge flaws

Table 3. Results of Flexural Strength Measurements (Continued)

Material	Temperature °C	Machine Crosshead Speed cm/sec	Flexural Strength MPa	Standard Deviation MPa	Fracture Origin
	1000	0.004	741	87	Surface and
	1000	0.00004	790	35	edge flaws
	1200	0.004	686	49	Surface/sub-
	1200	0.00004	622	39	surface and edge flaws
	1400	0.004	610	30	Plastic
	1400	0.00004	364	69	deformation prior to fracture
PY6	25	0.004	863	86	Surface flaws
	1000	0.004	736	43	Surface and
		0.0004	698	79	edge flaws
		0.00004	690	19	some inclu-sions
	1200	0.004	666	46	Surface flaws
		0.0004	619	32	some inclusions
		0.00004	574	44	
	1400	0.004	493	36	Surface flaws
		0.0004	351	40	some inclusions
		0.00004	308	27	SCG/specimen bending
Hexoloy ST	25	0.004	405	30	Surface flaws (pits)
	1000	0.004	375	56	Surface and
		0.00004	378	68	subsurface flaws (pits)
	1200	0.004	384	48	Surface and
		0.00004	395	49	subsurface flaws (pits)
	1400	0.004	352	35	Surface and
		0.00004	372	45	subsurface flaws (pits)

Table 3. Results of Flexural Strength Measurements (Concluded)

Material	Temperature °C	Machine Crosshead Speed cm/sec	Flexural Strength MPa	Standard Deviation MPa	Fracture Origin
CVD SiC	25	0.004	454	71	Surface, subsurface edge and side failures (pits and cracks)
	1000	0.004	658	164	Surface and edge flaws
		0.00004	537	171	Surface, subsurface, edge and side failures
	1200	0.004	495	41	Surface, subsurface and edge flaws
		0.00004	517	155	
	1400	0.004	511	90	Surface and subsurface flaws
		0.00004	582	77	

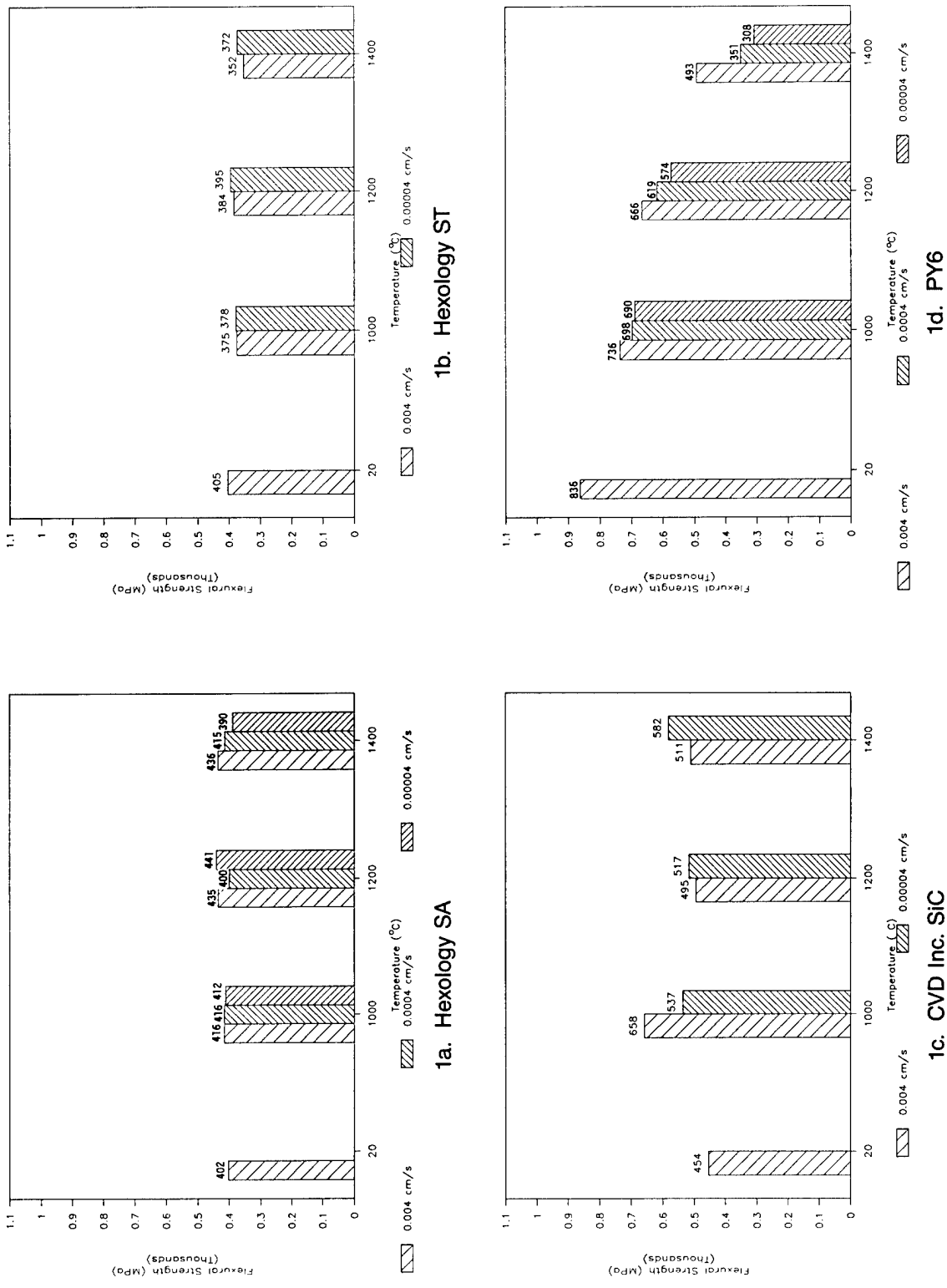

Figure 1. Flexural strength.

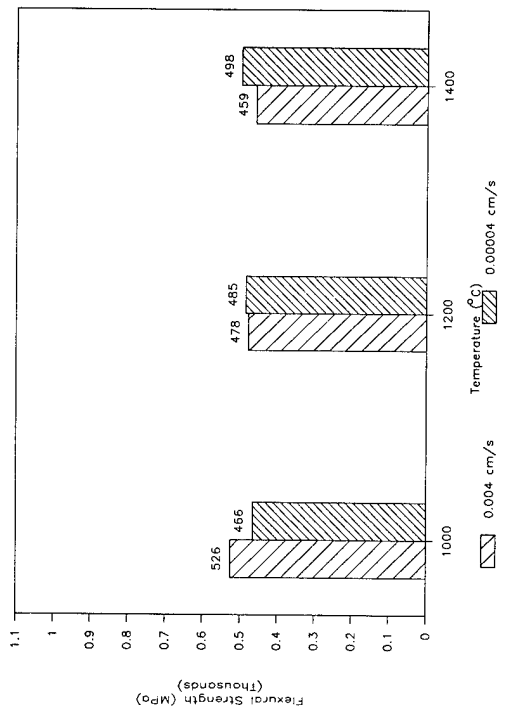

2b. SN-252

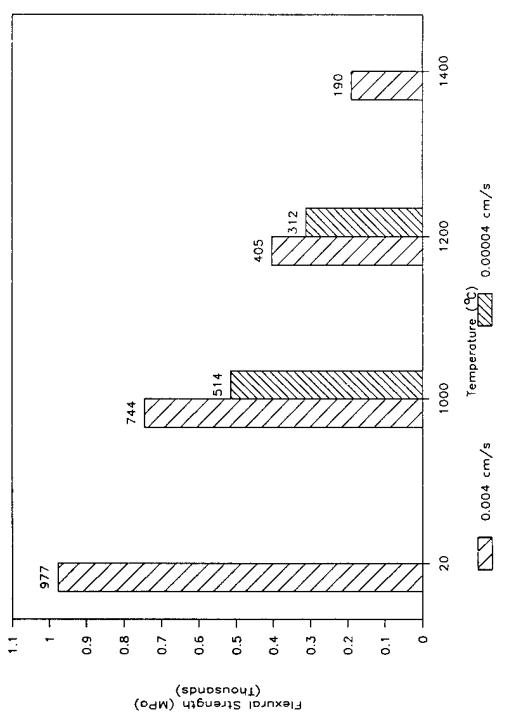

2d. SN-4

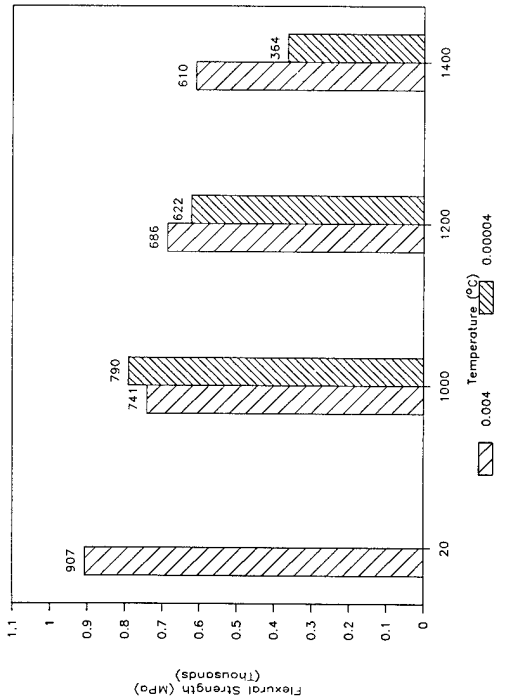

2a. NT-154

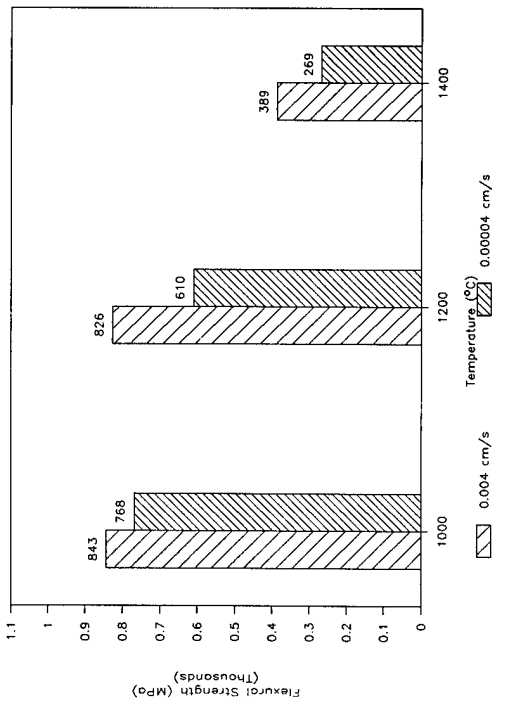

2c. EC-152

Figure 2. Flexural strength.

Table 4. Weibull Statistics for SiC and Si_3N_4 Specimens

Material Designation	Temperature °C	Loading Rate MPa/sec	Weibull Modulus m	Weibull[+] Scale-data So-MPa	Weibull[*] Scale-area So-MPa
Hexoloy SA	21	190	8.83	424	147
	1000	1.71	12.5	428	202
		17.1	11.03	436	186
		171	18.13	429	255
	1200	1.43	9.8	465	179
		14.3	8.67	424	144
		143	8.79	457	158
	1400	1.33	15.23	405	218
		13.3	12.18	432	200
		133	10.87	457	193
SN-252	1000	1.33	20.53	478	303
		133	19.19	540	331
	1200	1.19	19.94	499	311
		119	12.56	497	236
	1400	1.14	20.78	511	325
		114	18.68	472	285
NT-154	21	143	15.27	940	508
	1400	1.14	6.87	391	100
		114	23.11	624	415
SN-4	20	143	11.45	1025	452
EC-152	1000	133	9.86	887	343
	1200	119	24.7	842	576
GTE PY6	21	143	12.25	900	418
	1000	1.33	47.1	699	572
		13.3	10.2	732	291
		133	18.7	756	457
	1200	1.19	17.83	591	349
		11.9	22.2	634	414
		119	22.47	684	450

Table 4. Weibull Statistics for SiC and Si_3N_4 Specimens (concluded)

Material Designation	Temperature °C	Loading Rate MPa/sec	Weibull Modulus m	Weibull[+] Scale-data So-MPa	Weibull[*] Scale-area So-MPa
	1400	1.14	15.71	320	176
		11.4	12.14	367	169
		114	15.61	509	279
Hexoloy ST	1000	1.71	8.31	401	130
		171	7.68	399	118
	1200	1.43	9.47	416	155
		143	10.83	403	170
CVD Inc. SiC	21	190	10.83	10.83	10.83
	1000	1.71	4.04	593	59
		171	4.84	719	105
	1200	1.43	4.5	568	72
		143	14.59	513	269
	1400	1.33	12.54	611	289
		133	6.97	547	143

[+]So-Scale-data - The 63rd percentile for the distribution of strength for the specimens tested.

[*]So-Scale-area - Assumes a failure resulting from a surface flaw and adjusts the scale-data to account for specimen surface area.

Table 5. Slow Crack Growth Parameter (n) Values

Material	Temperature (°C)	n Values
Sohio Hexoloy α-SiC	1000	Slope not significantly greater than zero
	1200	Slope not significantly greater than zero
	1400	41
Kyocera SN-252	1000	37
	1200	Slope not significantly greater than zero
	1400	Slope significantly less than zero (n = -58)
Howmet SN-4	1000	12
	1200	17
Norton NT-154	1000	Slope not significantly greater than zero
	1200	46
	1400	7.6
NGK-SP EC-152	1000	50
	1200	14
GTE PY6	1000	73
	1200	30
	1400	8.8
Sohio Hexoloy ST	1000	Slope not significantly greater than zero
	1200	Slope not significantly greater than zero
	1400	Slope not significantly greater than zero

Table 5. Slow Crack Growth Parameter (n) Values (concluded)

Material	Temperature (°C)	n Values
CVD Inc. SiC	1000	Slope not significantly greater than zero
	1200	Slope not significantly greater than zero
	1400	Slope not significantly greater than zero

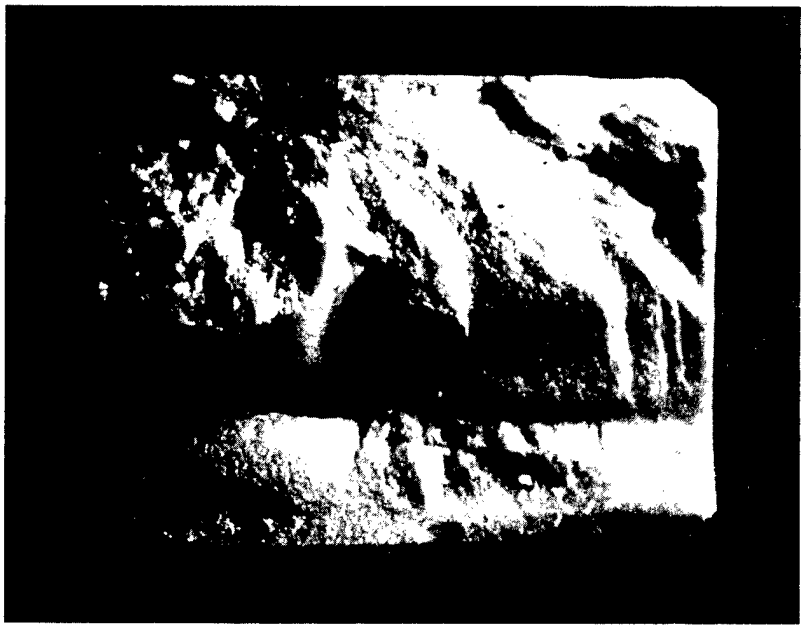

Figure 3. Typical fracture surface of NT-154 tested at 1000°C, 20X.

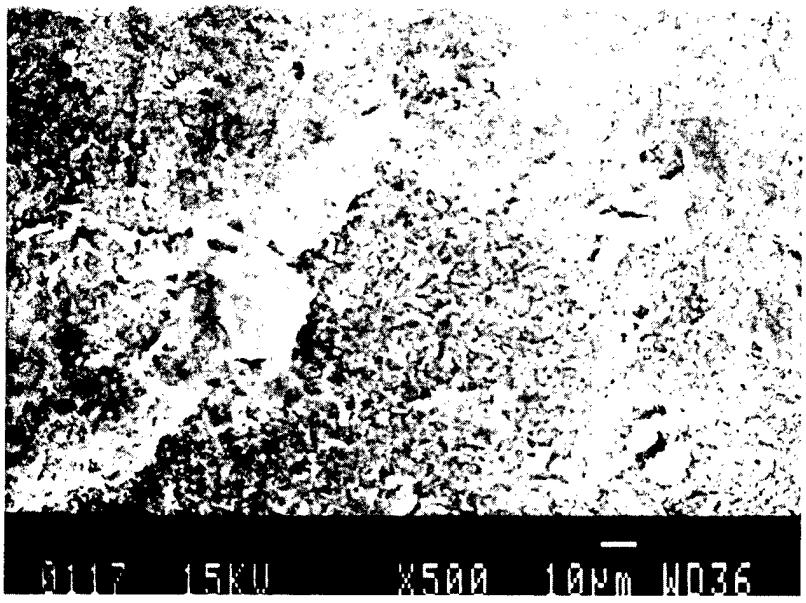

Figure 4. Typical fracture surface of NT-154 tested at 1000°C, 500X.

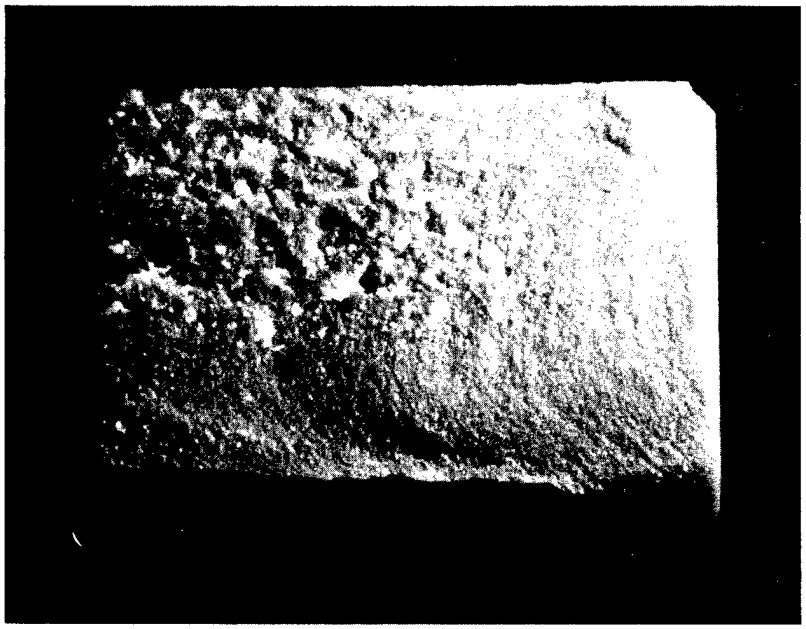

Figure 5. Typical fracture surface of NT-154 tested at 1400°C, 20X.

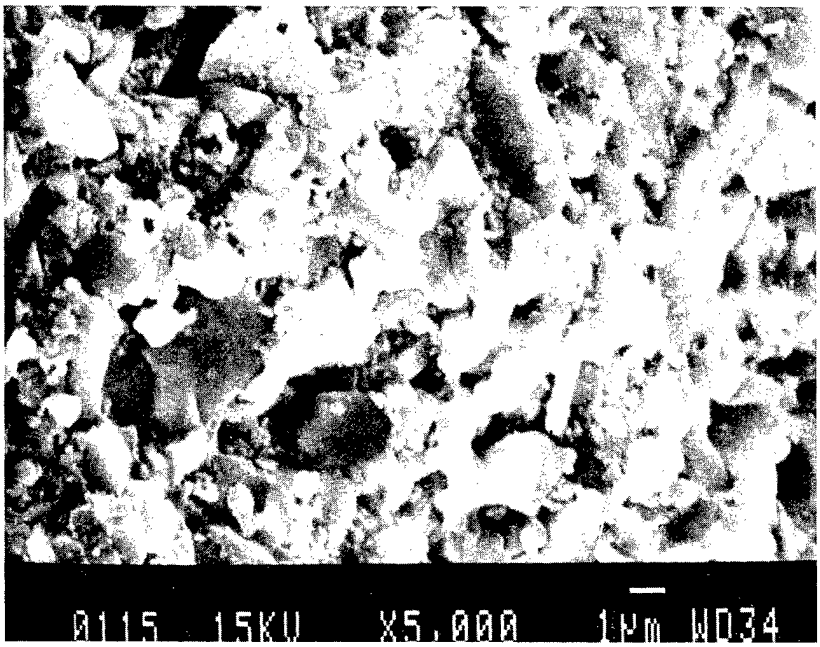

Figure 6. Typical fracture surface of NT-154 tested at 1400°C, 5000X.

Photomicrographs of typical fracture surfaces for EC-152 are shown in Figures 7 through 9, and for PY6 are shown in Figures 10 through 17.

Representative specimens of each material, as-received and after flexural testing, were examined by EDXA. The results of these semiquantitative analyses are summarized in Table 6.

Tensile strength measurements

As previously reported, a project to measure the tensile strength of Carborundum Hexoloy SA, GTE PY6, and Norton/TRW NT-154 from 20°-1400°C was initiated in October 1988. Tensile strength measurements were conducted on Hexoloy SA at 20°, 1000°, and 1400°C. The Instron Super-Grip System requires the use of buttonhead test specimens (see Figure 18). Several NT-154 tensile specimens were also tested at 20°C. A summary of the tensile test results is presented in Tables 7 and 8.

As shown in Table 7, 34 Hexoloy SA tensile specimens were tested at room temperature; 9 of the specimens (25%) failed at the buttonhead; 25 specimens failed in the gage section. Of the 25 specimens that failed in the gage section 23 were observed to have fracture initiation sites at surface flaws. It was further observed that a number of surface flaws were due to the remnants of radial grind marks which were not completely removed in the final longitudinal grinding operation. Radial grind marks were also observed in the area of the buttonhead radius for a number of the specimens. From an evaluation of the remaining Hexoloy-SA specimens it was found that the radius of curvature for several of the specimens was not in compliance with specifications, and the majority of specimens measured were observed to have a radius of curvature at or near the upper tolerance limit.

The heat treating of tensile specimens and different loading procedures were investigated as a means of reducing the number of buttonhead failures. Three specimens were slowly loaded to half the fracture load and held for 15 minutes to allow the copper collets to deform prior to rapid loading to fracture. Three additional specimens were heat treated to 1800°F for 50 hours prior to testing using similar loading procedures. Both the heat treating and the slow loading tended to reduce buttonhead failures.

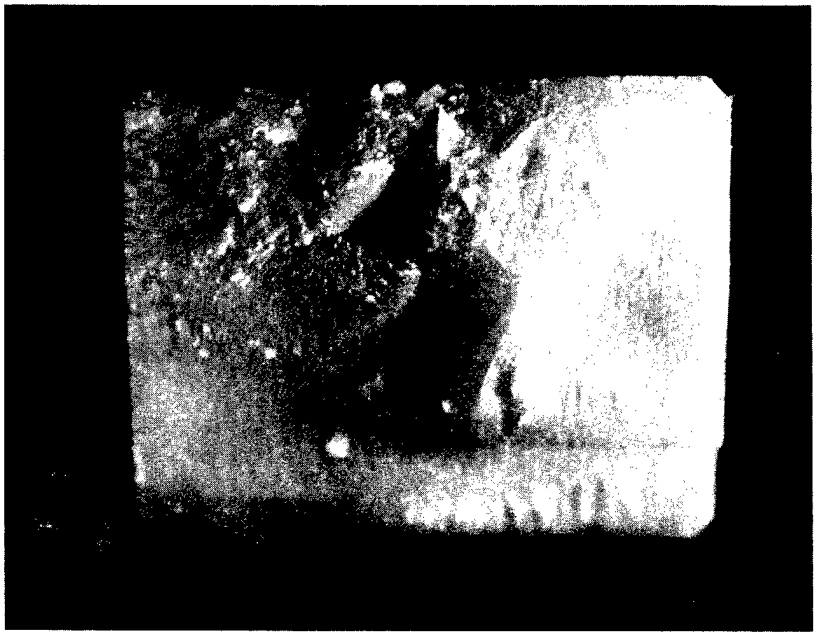

Figure 7. Typical fracture surface of EC-152 tested at 1000°C, 20X.

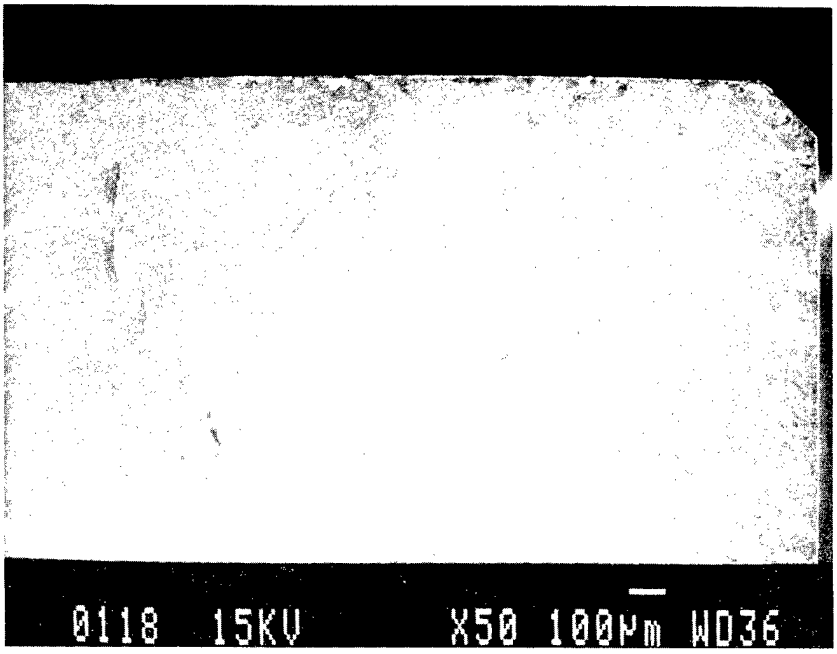

Figure 8. Typical fracture surface of EC-152 tested at 1000°C, 50X.

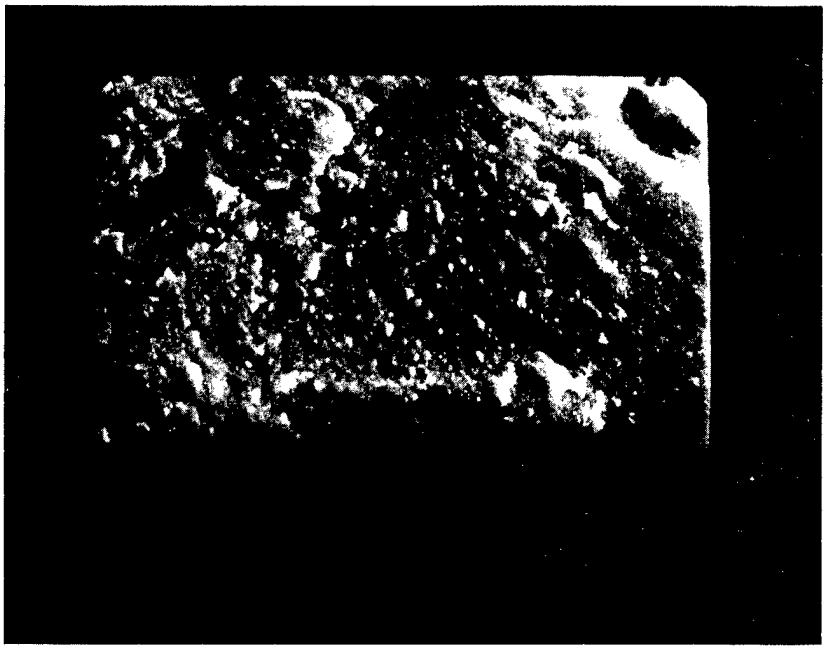

Figure 9. Typical fracture surface of EC-152 tested at 1000°C, 500X.

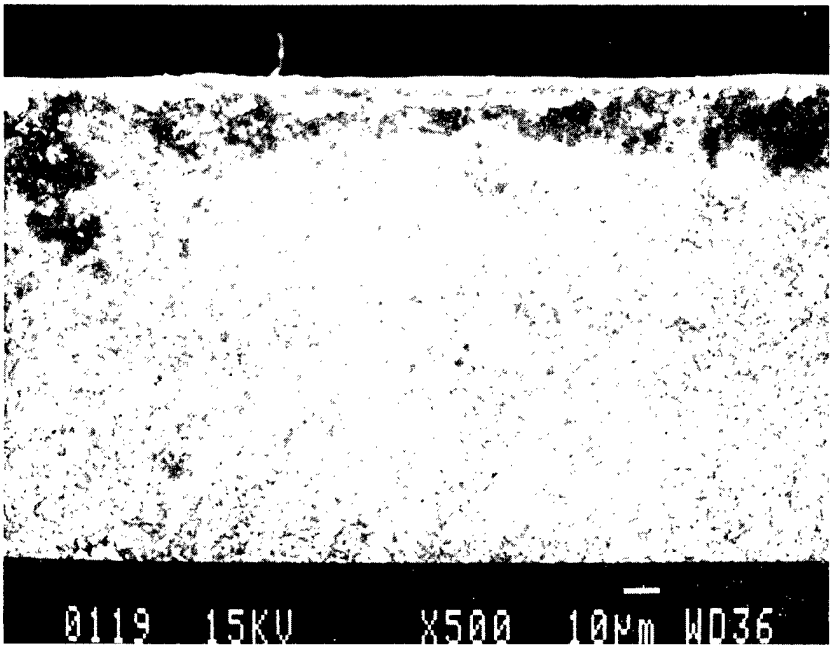

Figure 10. Typical fracture surface of PY6 tested at 1000°C, 20X.

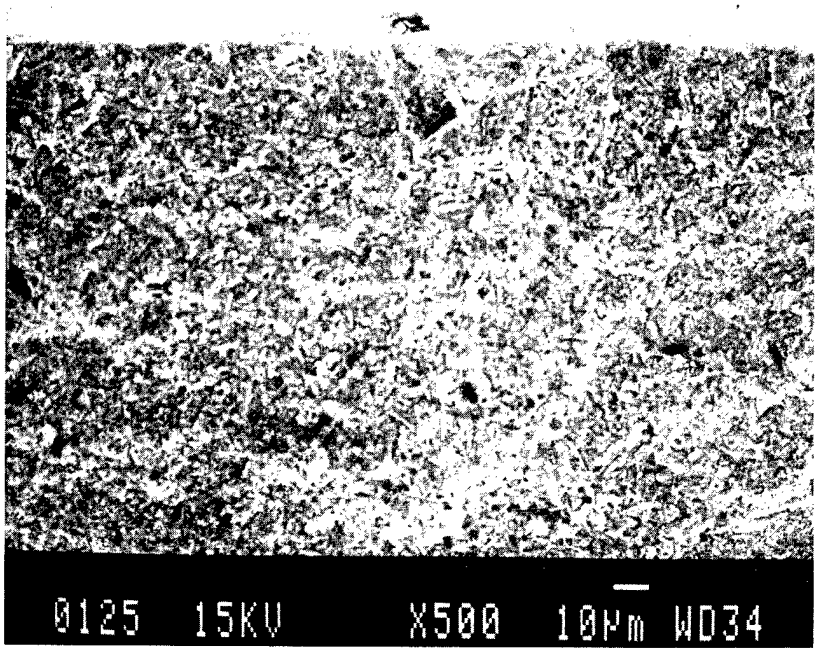

Figure 11. Typical fracture surface of PY6 tested at 1000°C, 500X.

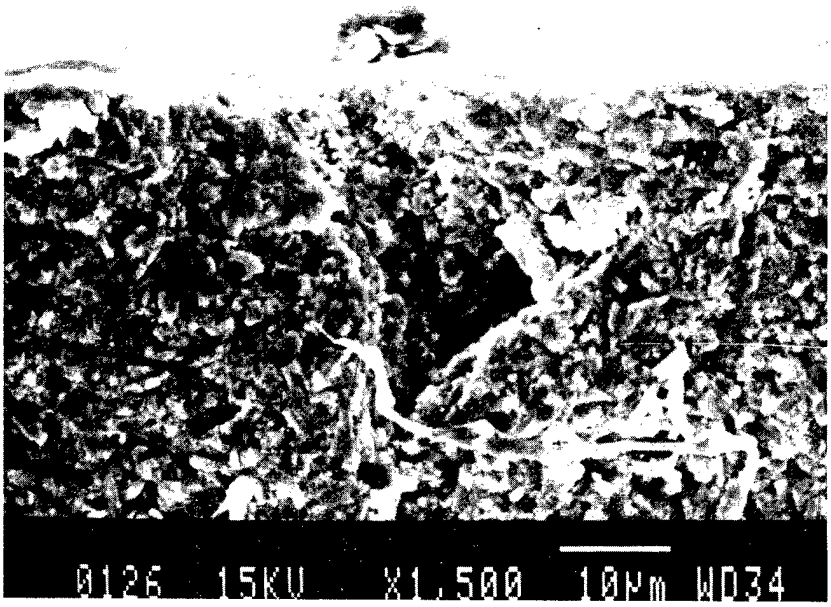

Figure 12. Typical fracture surface of PY6 tested at 1000°C, 1500X.

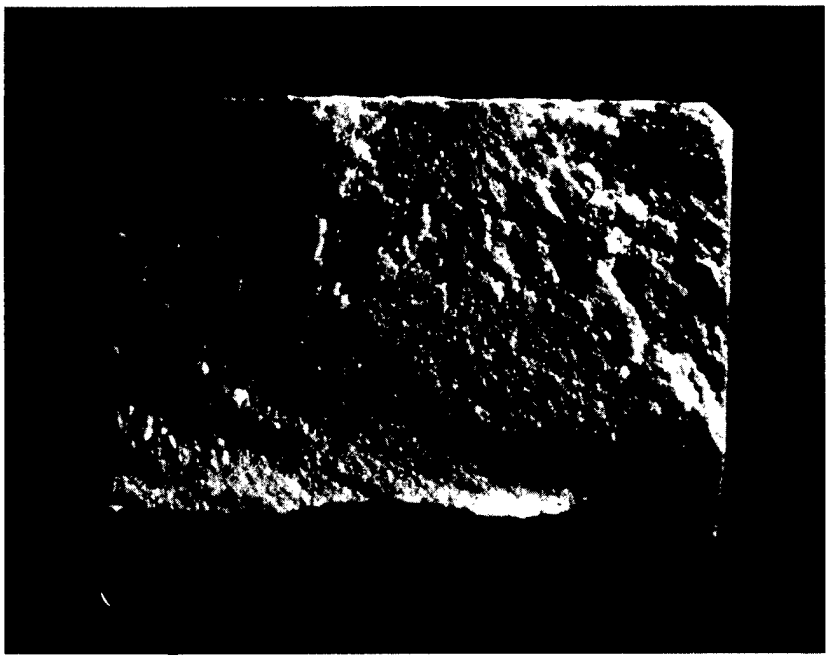

Figure 13. Typical fracture surface of PY6 tested at 1200°C, 20X.

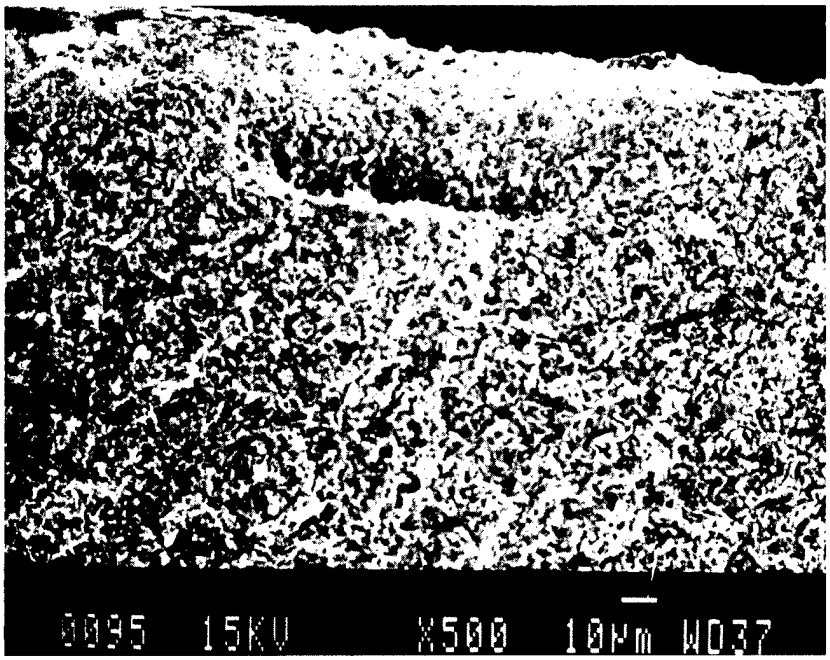

Figure 14. Typical fracture surface of PY6 tested at 1200°C, 500X.

Figure 15. Typical fracture surface of PY6 tested at 1400°C, 20X.

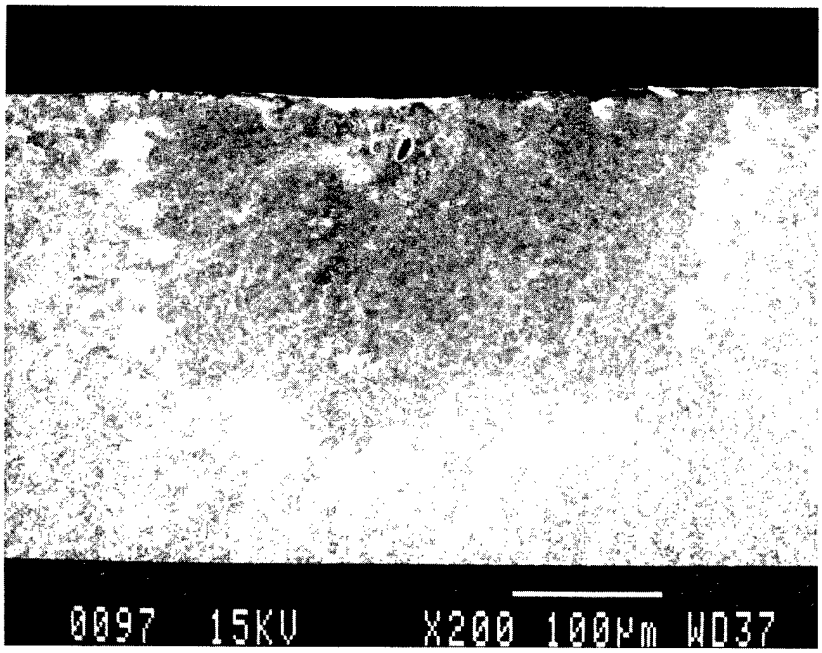

Figure 16. Typical fracture surface of PY6 tested at 1400°C, 200X.

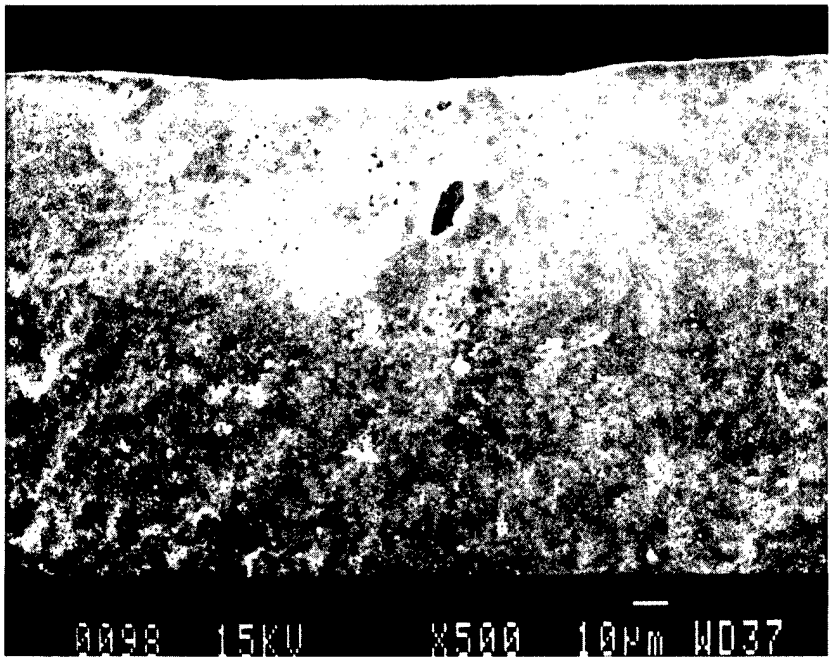

Figure 17. Typical fracture surface of PY6 tested at 1400°C, 500X.

Table 6. Semiquantitative Chemical Analysis of Candidate Materials

Material	Condition	Si_3N_4	Al_2O_3	Y_2O_3	Yb_2O_3	SiC	TiB_2
Kyocera SN-252	As-Received	93.06	0.40	0.30	6.24	--	--
	Tested at 1000°C	77.64	Trace	--	22.36	--	--
	Tested at 1200°C	73.74	Trace	--	26.26	--	--
	Tested at 1400°C	69.14	Trace	--	30.84	--	--
Howmet SN-4	As-Received	90.65	5.26	4.10	--	--	--
	Tested at 1000°C	89.65	5.07	5.28	--	--	--
	Tested at 1200°C	67.48	8.45	24.07	--	--	--
	Tested at 1400°C	89.71	5.16	5.13	--	--	--
NTK-EC	As-Received	90.65	4.40	4.94	--	--	--
	Tested at 1000°C	78.09	3.11	18.80	--	--	--
GTE-PY6	As-Received	76.23	--	23.77	--	--	--
	Tested at 1000°C	75.35	--	24.65	--	--	--
	Inclusion at Specimen Tested at 1000°C	89.22	1.22	9.56	--	--	--
	Tested at 1200°C	77.68	--	22.32	--	--	--
	Tested at 1400°C	78.65	--	21.35	--	--	--
Norton/TRW NT-154	Tested at 1000°C	84.34	--	15.66	--	--	--
	Tested at 1200°C	85.33	--	14.67	--	--	--
	Tested at 1400°C	82.93	--	17.07	--	--	--
Hexoloy SA	As-Received	--	--	--	--	100	--
Hexoloy ST	As-Received	--	--	--	--	79.3	20.7

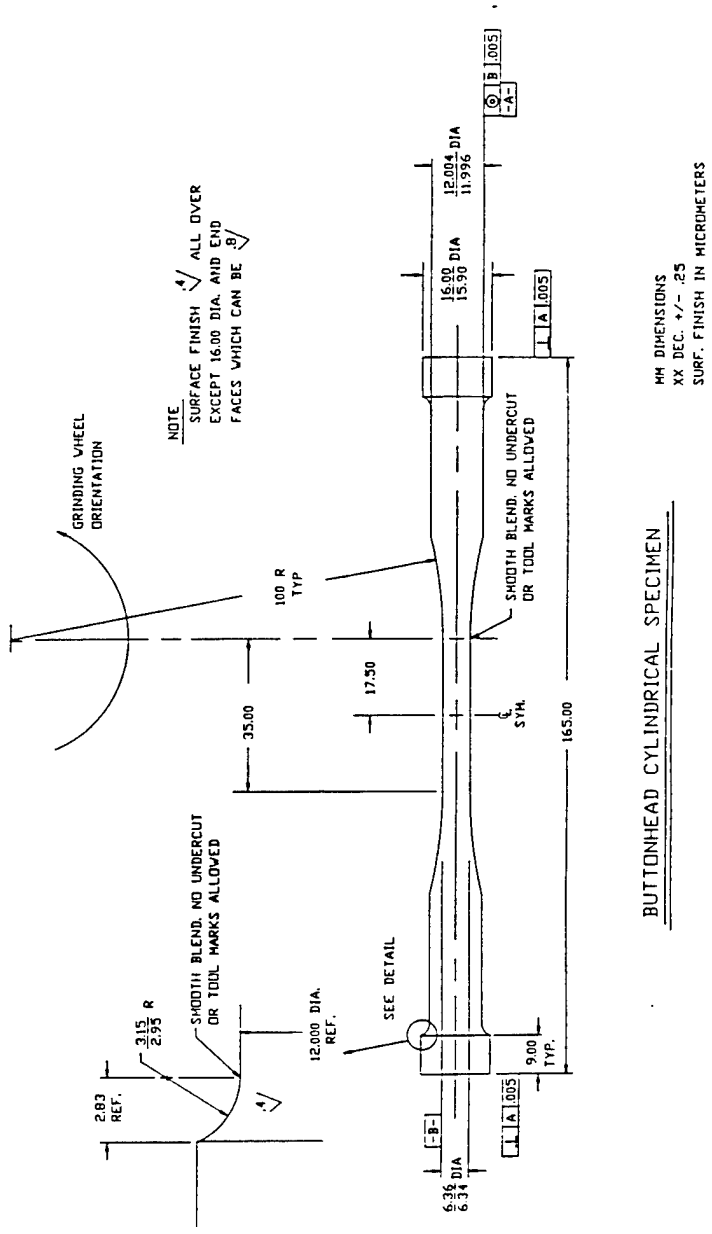

Figure 18. Buttonhead cylindrical specimen.

Table 7. Tensile Strength Measured for Hexoloy SA

1. @ 25°C-31.6 ksi (234 MPa)	(based on 27 specimens which failed in the gage section and 9 specimens which failed at the buttonhead)
2. @ 25°C-31.06 ksi (214 MPa)	(based on 3 specimens tested by procedures which allow the copper collets to deform and reduce contact stresses at the buttonhead)
3. @ 25°C-44.9 ksi (310 MPa)	(based on 3 specimens that were annealed at 1800°F for 50 hrs. prior to testing)
4. @ 1000°C-36.2 ksi (250 MPa)	(based on 15 specimens which failed in the gage section and 4 specimens which failed at the buttonhead)
5. @ 1400°C-36.2 ksi (250 MPa)	(based on 18 specimens which failed in the gage section and 3 specimens which failed at the buttonhead).

Table 8. Results of Tensile Testing Norton/TRW NT-154

Number	Load @ Failure (lbs.)	Failure	Condition	Collets	Comments
1	4220	B.H.*	As-Received	Cu	
2	4260	B.H.	As-Received	Cu	
3	3200	B.H.	As-Received	Cu	
13	3610	B.H.	As-Received	Cu	
14	3660	B.H.	As-Received	Cu	
11	4490	B.H.	As-Received	Cu	Tested at Oakridge
12	3950	B.H.	As-Received	Cu	Tested at Oakridge Silver, Compliant Layer
25	5720 (806 MPa)	gage	Remachined	New Cu	Deformed collets
26	4800	B.H.	Remachined	Old Cu	
27	4150	B.H.	Remachined	Steel	
28	5590 (786 MPa)	gage	Remachined	Old Cu	
29	5510 (772 MPa)	gage	Remachined & H.T.+	New Cu	Deformed collets Surface failure
30	6320	B.H.	Remachined & H.T.	Steel	Deformed collets
31	5970 (837 MPa) (Av - 801 MPa)X	gage	Remachined & H.T.	Ground Cu	Bulk Failure & inclusion

* B.H. - buttonhead

+ H.T. - heat treated (1800°F for 50 hrs)

X Average tensile strength for four specimens which broke in the gage section (this value is 80% of the room temperature flexural strength).

During this reporting period, 25 NT-154 tensile specimens were received from Norton/TRW. As shown in Table 8, five specimens were tested as received and all five failed in the buttonhead. Two additional NT-154 specimens were tested at ORNL and these also failed in the buttonhead. The remaining NT-154 specimens were carefully re-examined and it was found that the gage sections were well machined and no radial grind marks were observed. However, some radial grind marks and subsurface damage in the buttonhead radius were observed. Norton/TRW requested return of the remaining specimens for remachining and specimen heat treating. Four remachined specimens and three specimens that were remachined and heat treated were returned for tensile testing at room temperature. Heat treating was at 1000°C for 50 hours. Two of the remachined specimens broke in the gage section and two of the specimens broke in the buttonhead. Two of the heat-treated specimens broke in the gage section and one of the heat-treated specimens broke in the buttonhead. Both remachining and heat treating increased the load necessary for specimen failure and the probability for failure in the gage section. The increased loads required for failure also resulted in severe collet deformation.

As observed for the Hexoloy SA, it was found that when the copper collets were allowed to deform and reduce the disregistry between collet and specimen, the specimens broke in the gage section. It was further observed that all the specimens which failed in the gage section had a film of copper smeared around the shaft just below the button. However, this copper film was not observed when the specimen failed in the buttonhead. All that is observed in the case of the buttonhead failures is a very thin dark compression line just below the buttonhead. It appears that the use of slow loading procedures allows the copper collets to plastically flow and reduce the contact stresses due to radial mismatch. Dimensional mismatch between the collet radius and the radius at the buttonhead are of particular concern since machining both components for a perfect match is extremely difficult, particularly if large numbers of samples are to be tested.

A preliminary analysis of the dimensional mismatch problem was initiated. The configuration assumed for this analysis is shown graphically in Figure 19. For the case of stress concentration of a fillet on a round shaft, the existing tensile specimen geometry calls for a 3 mm root radius between the 12 mm diameter shank and the 16 mm diameter buttonhead. The major-to-minor diameter ratio is 1-1/3 and the root radius-to-shank diameter ratio is 0.25. Using engineering design curves, it was found that a round shaft with shoulder fillet in tension would have a theoretical stress concentration factor of 1.4 on the nominal applied stress of the shank. For an applied force of 5000 lbs., the nominal stress on the shank would be 28.5 ksi. Since a 3 mm root radius fillet is used to join the buttonhead, the actual stress at the fillet is 39.9 ksi (1.4 x 28.5 ksi). If the fracture toughness is 5 MPa $mm^{1/2}$ for Si_3N_4 and the assumed flaw geometry factor is one, then the critical flaw size would be 102 μm.

For the case of contact stresses, the contact surfaces are assumed cylindrical. The half width b of the contact area is given as:

$$b = \{\{2F_n/pl\}\{\{1-v_1^2\}/E_1\} + \{(1-v_2^2)/E_2\}/\{(1/d_1) + (1/d_2)\}\}^{0.5} \quad (2)$$

The contact stress S and shear stress T is given as:

$$S = 2F_n/plb \text{ and } T = F_t/bl \quad (3)$$

where:

S, T = stress, ksi
$F_{n,t}$ = force normal and tangential to surface, lb_f
p = pi
l = contact length, in.
v_1, v_2 = Poisson's ratio (Si_3N_4:0.27, steel:0.305)
E_1, E_2 = modulus, psi (Si_3N_4:45 x 10^6, steel:28 x 10^6)
d_1, d_2 = diameter of cylinders, in. ($d_{1,2}$=6 mm)

Assume that the line of contact occurs at the midpoint of the fillet; therefore, l = pd = 3.14 x 14/25.4 = 1.732 in. The remote applied force is 45 to $F_{n,t}$. Assume the fillet radius of the tensile specimen is enlarging due to wear of the cutting tool. The calculations are based on 1%, 2%, and 5% of ideal fillet radius of the buttonhead tensile specimen.

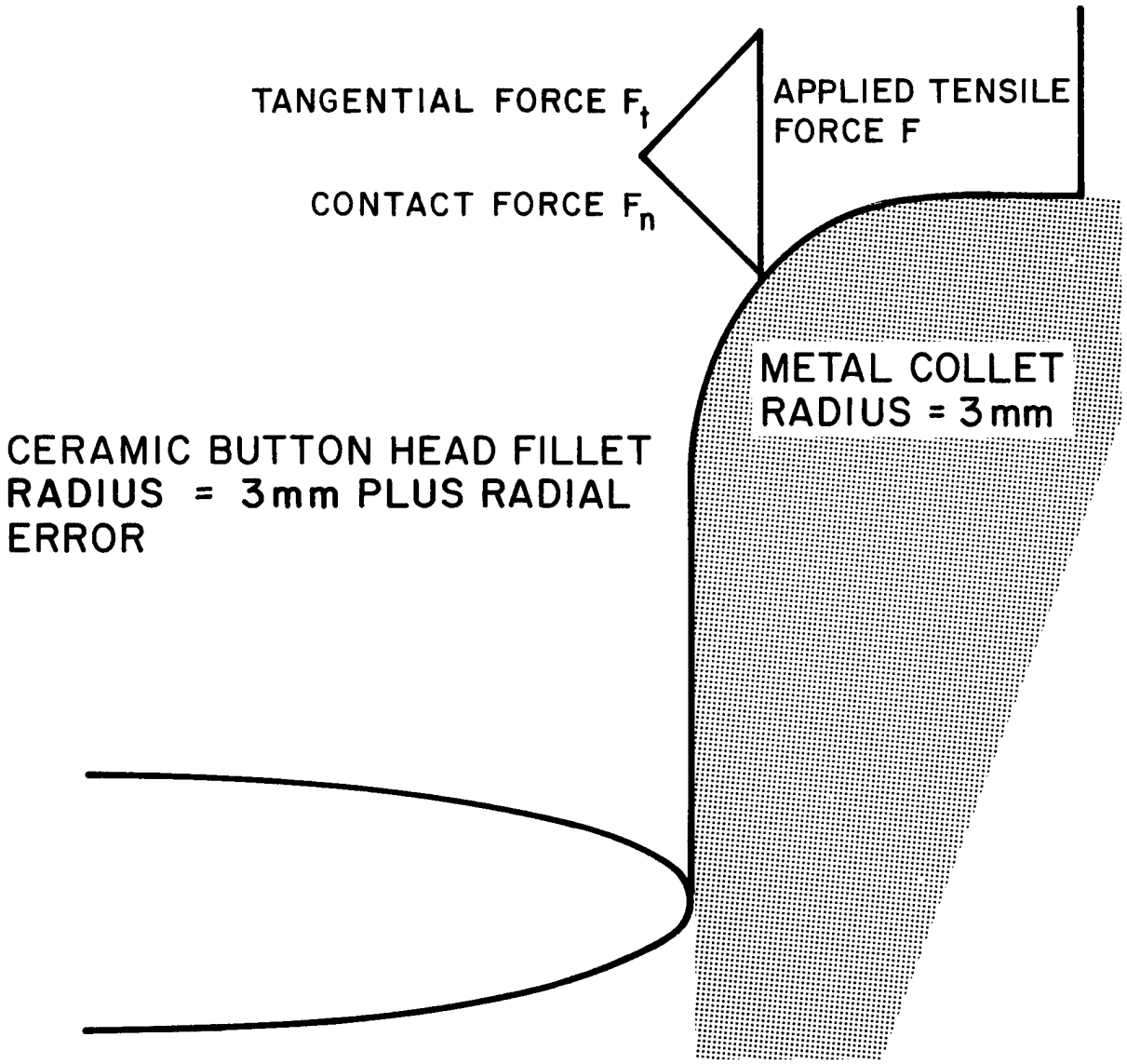

Figure 19. Buttonhead configuration for tensile specimen.

Case 1:

Assume the tensile specimen force is 2000 lbs. Therefore, $F_{n,t}$ = 1414 lbs.

% error of d_1	b, in	S, ksi	T, ksi
1	0.026	-20.3	31.4
2	0.018	-40.4	62.8
5	0.012	-44.5	68.0

Case 2:

Assume the tensile specimen force is 4000 lbs. Therefore, $F_{n,t}$ = 2828 lbs.

% error of d_1	b, in	S, ksi	T, ksi
1	0.036	-28.7	45.4
2	0.026	-40.4	62.8
5	0.017	-62.9	96.1

In each of the cases, the shear stress on the surface can easily interact with surface defects from grinding. The contact stresses are all compressive and decrease as a function of depth, but there is an associated tensile stress near the contact area that has not been accounted for which superimposes with the shear stress. The magnitude of these tensile stresses was not obtained due to time limitations.

Optical interferometry

As reported, development of optical interferometry to monitor tensile testing is in progress. Application of a speckle interferometric technique for nondestructive surface displacement and strain measurement was performed on a variety of specimens. Although a strained specimen may be effectively analyzed using a full-field analysis technique for the measurement of speckle correlation bands, a point-by-point technique of the measurement of the interference fringes formed by the speckles has been principally used in this study. This method offers several

advantages over the full-field technique including increased measurement sensitivity, the ability to measure bulk motion, and the ability to determine the displacement directionality.

Initially, speckle interferometry was used to evaluate tensile strain on specially prepared aluminum specimens. The point-by-point interference fringe analysis of an aluminum cylindrical specimen (ground flat on one side) yielded results indicating a variational displacement along the length of the specimen. This is expected to occur when the strain takes place within the observed region of the sample. The measured specimen displacement was 3.5 ± 0.7 μm (see Figure 20), which compares quite favorably with the theoretical displacement calculation of 4.2 μm, made using the assumption that the strain would only occur within the gauge section. After the aluminum specimens were studied, the procedures were applied to SiC tensile specimens. Figure 21 shows interference fringes generated by the speckle fields resulting from a nominal 10 μm in plane displacement of a SiC cylinder. Using the speckle interferometric point-by-point analysis, a bulk motion of 10.7 ± 0.5 μm was measured for this sample. Figures 22a and 22b refer to fringes resulting from a tensile strain and relaxation, respectively, of a SiC ceramic cylindrical specimen. The direction of the fringes yields information describing the actual direction of inplane specimen displacement. In addition, the nonsymmetry of the fringes is indicative of energy losses due to hysteresis effects in the elastic region of the ceramic material. Results of the analyzed strained specimen data showed a bulk motion of 75 μm. This displacement was much larger than the theoretically calculated displacement for this material made with the assumption that all strain motion would take place within the gage section of the specimen. However, if the strain were to occur over the entire length of the specimen, the theoretically calculated displacement would be 80 μm. With this information, it was possible to conclude that the specimen, when strained to its fracture point, would yield an invalid test, i.e., the sample would break at its buttonhead, and this conclusion was substantiated. It is apparent by this preliminary comparison that the speckle interferometric technique may be used to predict the occasion of an invalid tensile test.

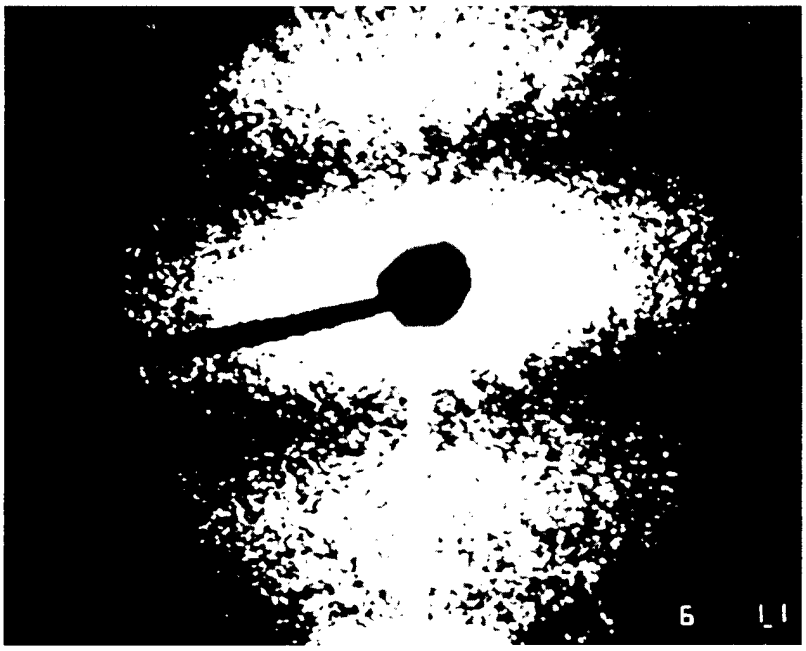

Figure 20. Interference fringes generated by the tensile strain of an aluminum test specimen.

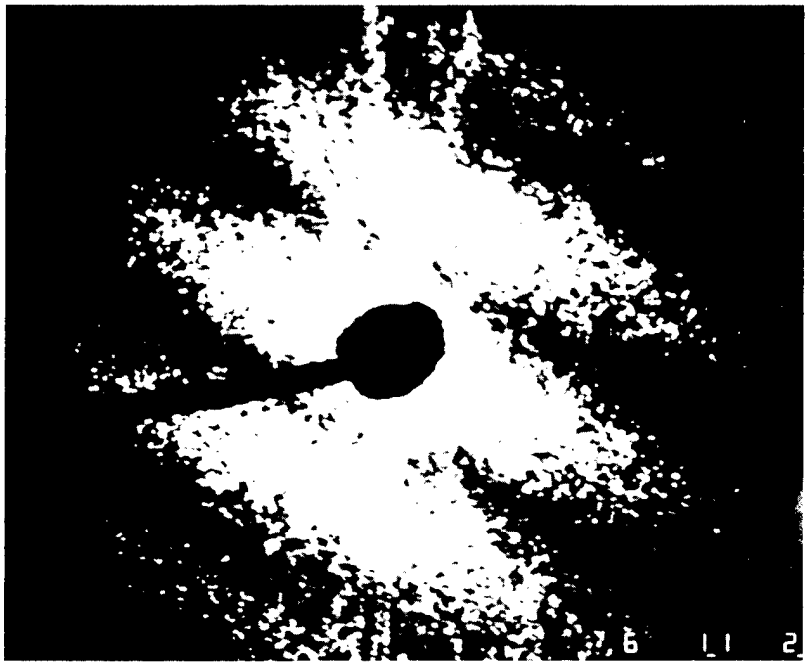

Figure 21. Interference fringes generated by in-plaine displacement of a Hexoloy SA cylinder by 10 μm.

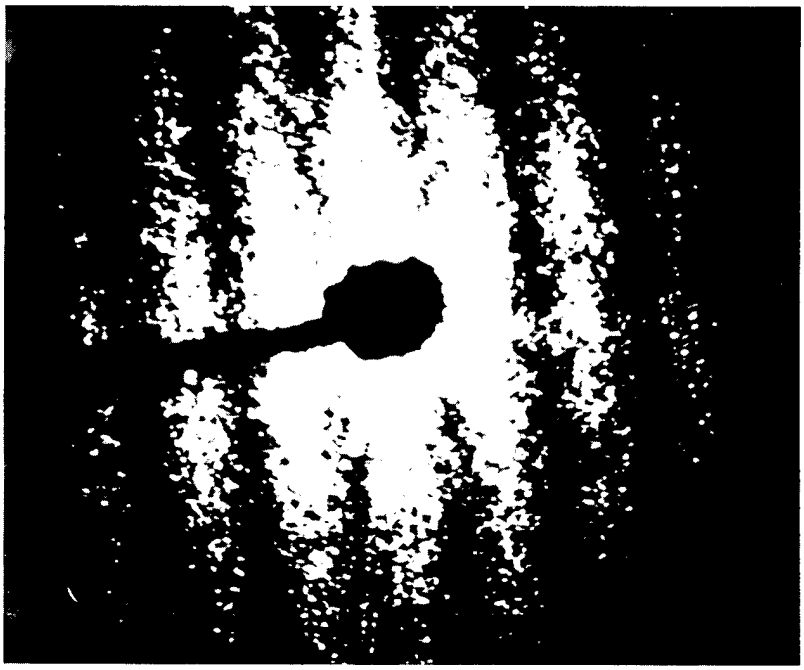

(a)

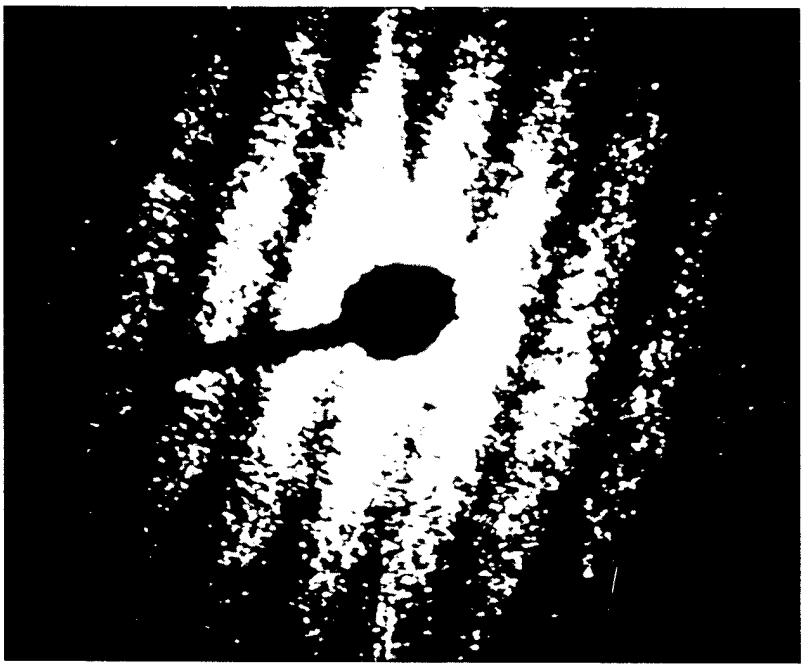

(b)

Figure 22. Interference fringes generated by the tensile strain (a) and relaxation (b) of a SiC specimen (specimen fractured at the buttonhead).

The application of speckle interferometry to inplane displacement measurement has also been extended to ceramic specimens maintained at elevated temperatures. The optical interferometer configuration has been modified, as shown in Figure 23, to overcome interference and system heating due to furnace radiation. An Argon laser line filter centered at 514.5 nm was used to block background light from the furnace. A hot mirror was placed in the optical train to reduce the heat load on the camera.

Rigid body displacement measurements of SiC specimens at elevated temperatures were also made. The SiC was heated to a predetermined temperature and allowed to reach thermal equilibrium. A known rigid body translation was applied to the specimen. The resulting speckle interferograms from this motion were analyzed with the point-by-point analysis method. Figures 24a and 24b show the interference fringes resulting from a 10 μm displacement at 1200°C and 1400°C, respectively. Although the image quality of the reproductions is poor, it was possible to experimentally determine the rigid body translations from the raw data.

The measured displacements were 10.1 $\pm$ .5 μm, 10.3 $\pm$ .5 μm and 11 $\pm$ 1 μm for 10 μm translations performed at 1000°C, 1200°C, and 1400°C, respectively. Background radiation emission from the specimen and furnace did degrade the signal-to-noise ratio of the collected data even with the line filter in place. As the temperature is increased, the noise contributed by background radiation increases. Reducing the amount of time the film is exposed to the extraneous light enhances the signal-to-noise ratio. However, the noise in the data collected at 1400°C still affects the measurement precision attained. Methods to further enhance the signal-to-noise ratio were investigated. By increasing the integration area used during data analysis the SNR was substantially improved.

The reliability of the strain measurements was further demonstrated by comparison of the interferometer measurements with mechanical strain gage measurements. A tensile stress was applied to an aluminum specimen, and the induced strain was measured with a WK-06-062AP-350 strain gage and with the speckle interferometer. Comparison of the measured strains showed an average random deviation of 2.5% for 4 measurements.

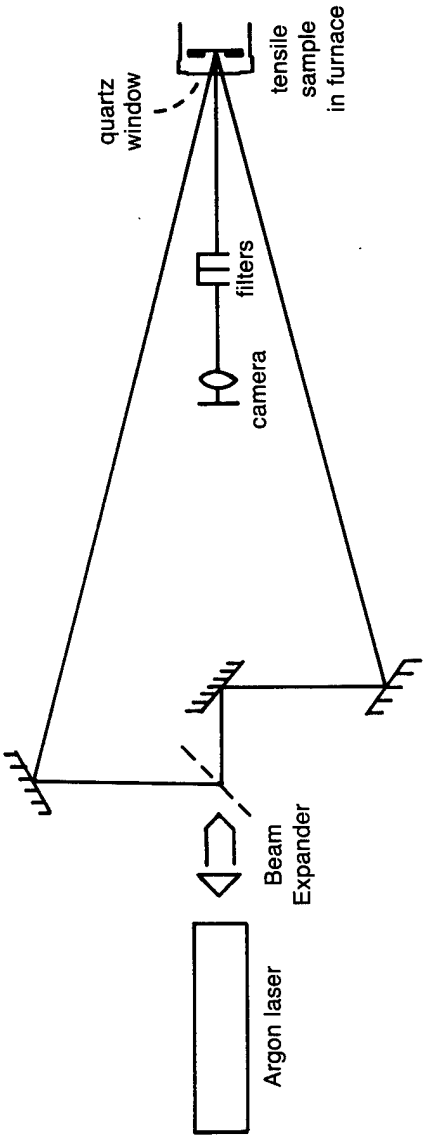

Figure 23. Speckle Interferometer Optical Configuration. The filters shown have been added to the configuration for use under elevated temperature conditions. The quartz window encloses the front of the furnance.

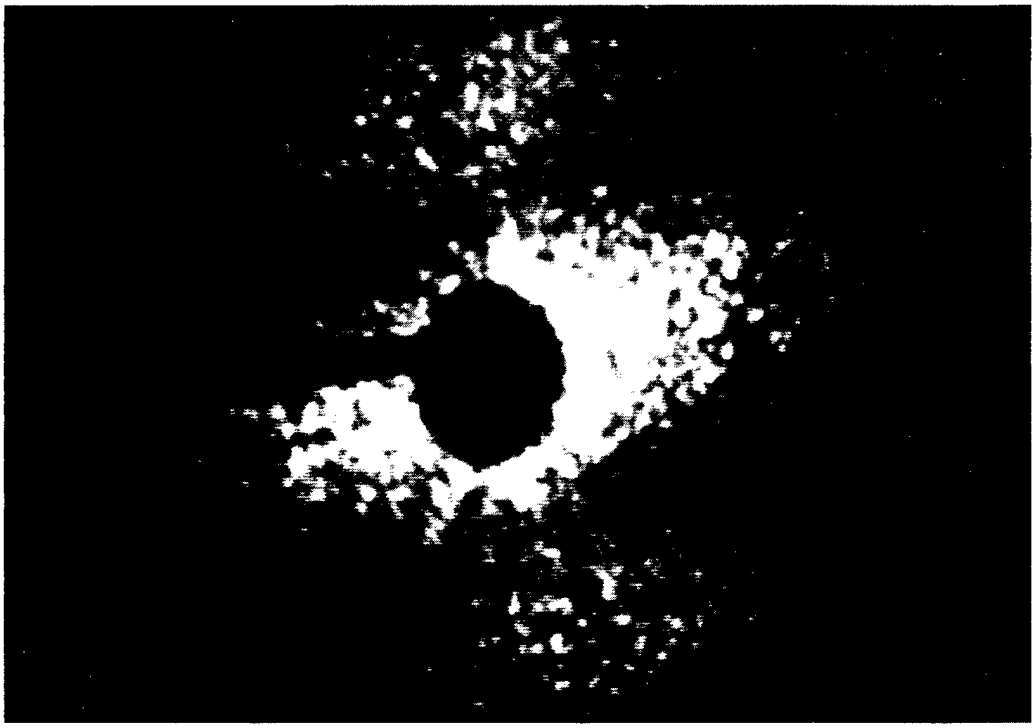

(a)

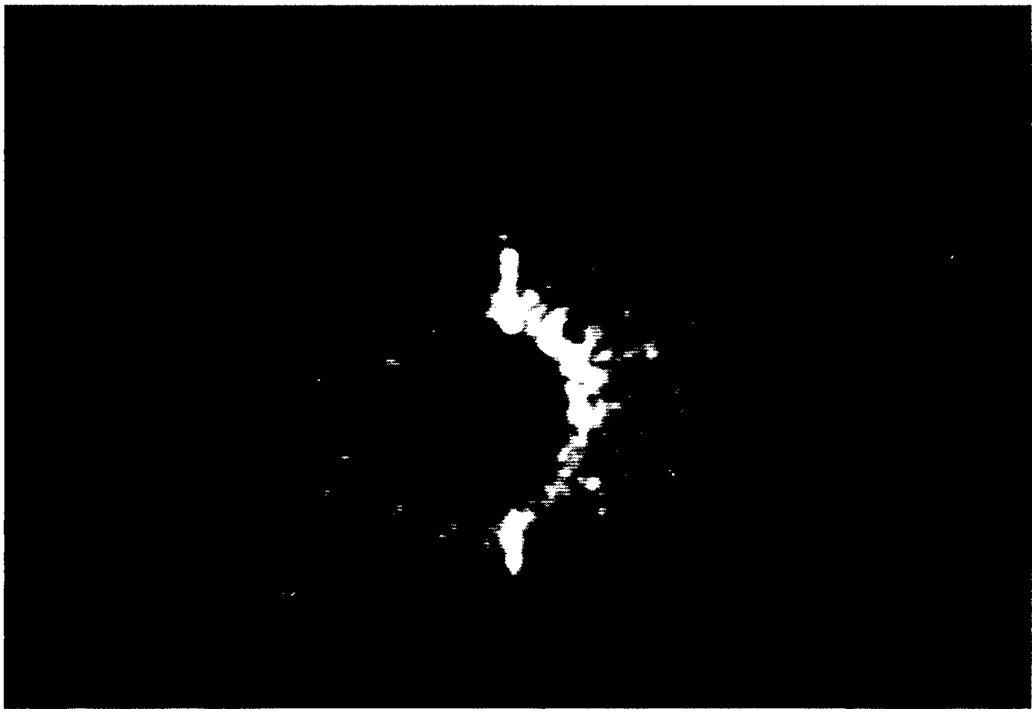

(b)

Figure 24. Speckle interferograms for SiC specimen displaced 10 μm at 1200°C (a) and 1400°C (b).

The speckle interferometer was also used to monitor SiC specimens tested at temperatures of 1000°C using a slow load rate of 0.001 in/min. During these tests a succession of speckle data was collected and analyzed to provide measurements of strain-to-failure. A typical plot of the measured strain as a function of load rate is shown in Figure 25, the initial oscillatory behavior is presumed to be strain induced in the specimen by other effects in the tensile tester (such as mechanical settling, reseating of the collets, etc.). Once these effects are minimized, the strain in the specimen approximates its expected linear behavior. The load required to reach such a condition has been found to be consistent from specimen to specimen.

Database Development

Activities to develop a more comprehensive database for SiC and Si_3N_4 ceramics from the literature was continued. Forty-eight literature sources have been reviewed and the data collected have been entered into our Dbase III program. Some of the property data stored in our program is summarized in Table 9, and the flexural strength data collected from 14 reference sources are summarized in Table 10. As part of our data collection activities we compared the flexural strength values reported by five different organizations for the major candidate SiC and Si_3N_4 ceramics.[1-5] The results of these comparisons are graphically displayed in Appendix 2.

As shown in Appendix 2 and Tables 9 and 10, there is considerable variation in the strength values measured for the different candidate SiC and Si_3N_4 ceramics. In addition there was considerable variation in the strength values reported by different organizations for the same materials. These observations suggest the need for better quality control by the materials' manufacturers.

---

1. IITRI (data published by D. Larsen)
2. ORNL (data supplied by M. Ferber)
3. UDRI (data generated in ORNL-sponsored project).
4. Garrett (data presented at ATTAP, August 1988).
5. Allison (data presented at ATTAP, August 1988).

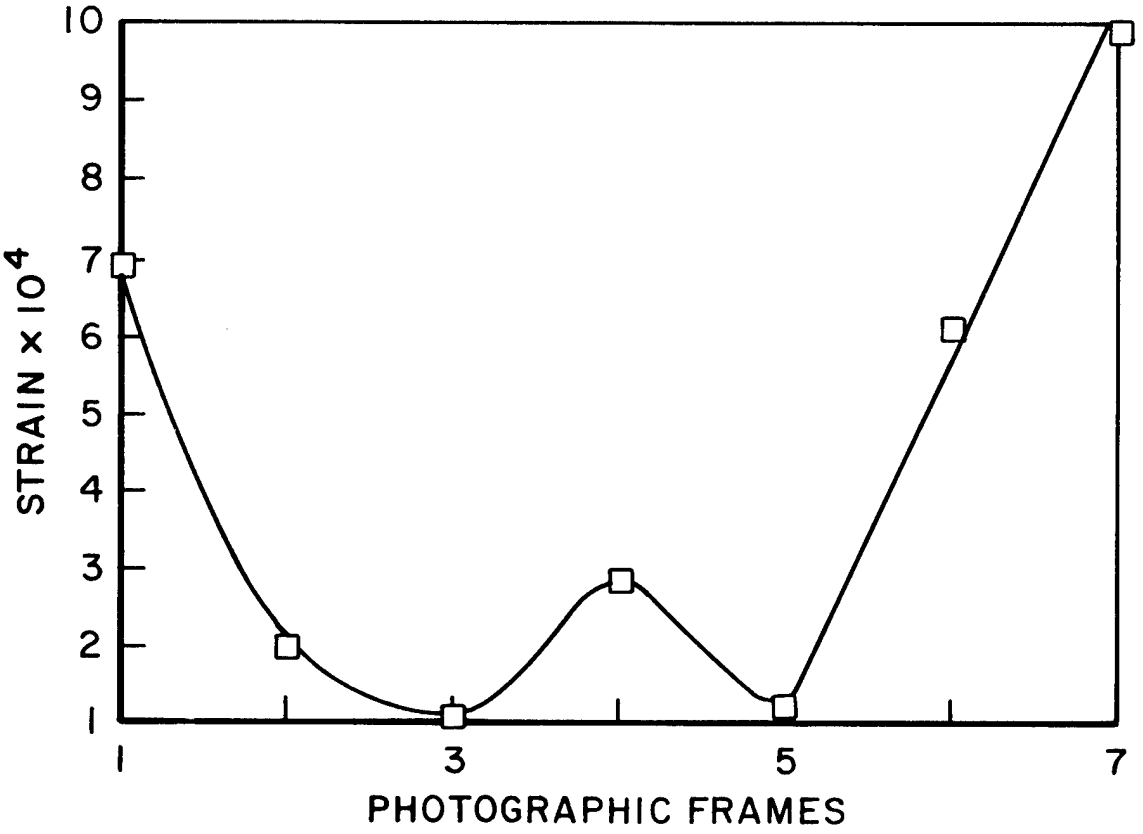

Figure 25. Strain measured for Hexoloy-SA specimen #63 tested in tension at 1000°C to failure at 866.4 kg (1910 lbs.) (tensile strength - 269 MPa).

Table 9. Summary of Property Data Collected

Material Designation	Manufacturing Process	Composition Material Type	Measured Density (g/cm^3)	Hardness (Kg/mm^2)	Coefficient of Expansion ($10^{-6}/°C$)	W/mk Thermal Conductivity	Avg. Flexural Strength/Test Temp. (MPa)	Weibull Modulus
AY6	SIN	$Si_3N_4+AP_2O_3+Y_2O_3$	3.24				696.4	9
AY6	slip cast, SN	$Si_3N_4+AP_2O_3+Y_2O_3$	3.23				834.3	20
AY6	injection molded, SN	$Si_3N_4+AP_2O_3+Y_2O_3$	3.25				896.4	14
AY6	hot pressed	$Si_3N_4+AP_2O_3+Y_2O_3$	3.22				930.8	13
AY6	injection molded, HIP	$Si_3N_4+AP_2O_3+Y_2O_3$	3.20				986	20
PY6	isopressed, SN	$Si_3N_4+Y_2O_3$	3.25				551.6	11
PY6	slip cast, SN	$Si_3N_4+Y_2O_3$	3.25				689.5	21
PY6	hot pressed	$Si_3N_4+Y_2O_3$	3.22				834.3	18
PY6	HIP	$Si_3N_4+Y_2O_3$	3.21				633.6/25°C 540.6/800°C 586.8/1000°C 431.6/1200°C 451.6/1400°C	7.3
PY6	SN	$Si_3N_4+Y_2O_3$					873	13
SN-α-SiC	SN	SiC	3.15				425	
NC-400-L	HP	SiC	2.70				148	
NC-400-H	HP	SiC	2.75				105	
β-HP-SiC	HP	SiC	3.17				265	
NC-201-HP	HP	SiC	3.32				728	
NC-203-HP	HP	SiC	3.35				760	
KT-SiC	HP	SiC	3.10				147	
NC-430	HP	SiC	3.09				117	
NC-433	HP	SiC	3.05				105	
NC-132 HPSN	HP	Si_3N_4					787/25°C	6.5

Table 9. Summary of Property Data Collected (Continued)

Material Designation	Manufacturing Process	Composition Material Type	Measured Density (g/cm^3)	Hardness (Kg/mm^2)	Coefficient of Expansion ($10^{-6}/°C$)	W/mk Thermal Conductivity	Avg. Flexural Strength/Test Temp. (MPa)	Weibull Modulus
NC-132	HP	Si_3N_4					725/1038°C	12.6
HPSN							725/1038°C	16.5
							679/1038°C	14.5
							666/1038°C	9.9
							665/1204°C	13.0
							688/1204°C	25.8
							609/1204°C	12.2
							545/1204°C	16.0
							484/1204°C	8.0
							411/1371°C	14.3
							363/1371°C	7.0
							313/1371°C	11.2
							401/20°C	
							772.82/20°C	
							750/300°C	
							720/600°C	
							686/900°C	
							640/1100°C	
							624.67/1200°C	
							505/1300°C	
							412/1350°C	
							335.5/1400°C	
							152.18/1204°C	
							85.14/1300°C	
							281.43/1000°C	

Table 9. Summary of Property Data Collected (Continued)

Material Designation	Manufacturing Process	Composition Material Type	Measured Density (g/cm^3)	Hardness (Kg/mm^2)	Coefficient of Expansion ($10^{-6}/°C$)	W/mk Thermal Conductivity	Avg. Flexural Strength/Test Temp. (MPa)	Weibull Modulus
FHPSN	HP	Si_3N_4 MgO					660/25°C	10
							697/704°C	6.4
							591/871°C	4.8
							599/871°C	6.7
							579/871°C	5.3
							548/1038°C	9.2
							596/1038°C	15.9
							531/1038°C	12.4
							481/1204°C	5.5
							439/1204°C	4.9
							368/1204°C	9.0
							324/1371°C	6.9
							254/1371°C	7.9
							213/1371°C	12.0
							415/20°C	
							409/400°C	
							375/600°C	
							364.67/800°C	
							358/900°C	
							390/1000°C	
							370/1050°C	
							337/1100°C	
							375/1150°C	
							340/1200°C	
							268/1250°C	
							248/1300°C	

Table 9. Summary of Property Data Collected (Continued)

Material Designation	Manufacturing Process	Composition Material Type	Measured Density (g/cm^3)	Hardness (Kg/mm^2)	Coefficient of Expansion ($10^{-6}/°C$)	W/mk Thermal Conductivity	Avg. Flexural Strength/Test Temp. (MPa)	Weibull Modulus
							584/20°C	
RBSN NC-350	RB	Si_3N_4	3.23				176.61/20°C	
NC-132	HP	Si_3N_4 +Y_2O_3	3.37				825	
NC-136	HP	Si_3N_4 +Y_2O_3	3.37				237	
NC-350	RB	Si_3N_4	2.53				921	
RBSN	RB	Si_3N_4	2.58				294	
RBSN	RB	Si_3N_4	2.77				206	
NC-203	HP	SiC	3.36				288	
α-SiC(1977)	SN	SiC	3.11				683	
α-SiC(1978)	SN	SiC	3.13				375	
NC-132	HP	Si_3N_4	3.18	2000		30	363	
α-SiC	SN	SiC					719.6-836.92°C	
							198/20°C	
							312/1200°C	
							265/1300°C	
NC-132	SN	Si_3N_4					695.7/20°C	
							688.5/500°C	
							684.4/800°C	
							476.6/1000°C	
							536/1200°C	
							519.33/1300°C	
							472.3/1400°C	
	HP	Si_3N_4			2.75×10^{-6}	200	1000.87	
							948.74/200°C	
							966.57/400°C	
							947.37/600°C	

Table 9. Summary of Property Data Collected (Concluded)

Material Designation	Manufacturing Process	Composition Material Type	Measured Density (g/cm^3)	Hardness (Kg/mm^2)	Coefficient of Expansion ($10^{-6}/°C$)	W/mk Thermal Conductivity	Avg. Flexural Strength/Test Temp. (MPa)	Weibull Modulus
NC-132	HP	Si_3N_4	3.14				840.35/800°C	
							870.53/1000°C	
							690.12/1200°C	
SNW-1000	SN	$Si_3N_4+AP_2O_3+Y_2O_3$	3.0				308.01/1375°C	16.5
							468/20°C	8.2
							420/20°C	
							364/800°C	
							272/1000°C	
							293/1100°C	
							276/1200°C	

Table 10. Summary of Flexural Strength Data for Reference Sources 1-14

Source No.	Material Designation	Type	Test No.	No. of Specimens	Temp. (°C)	Flexural Strength (MPa)
1	AY6	Si3N4	1	8	25	930
1	AY6	Si3N4	1	10	25	986
1	PY6	Si3N4	1	10	25	834
1	AY6	Si3N4	1	10	25	696
1	AY6	Si3N4	1	10	25	834
1	AY6	si3N4	1	10	25	896
1	PY6	Si3N4	1	9	25	551
1	PY6	Si3N4	1	6	25	689
2	PY6	Si3N4	1	36	25	633
2	PY6	Si3N4	2	2	800	540
2	PY6	Si3N4	3	2	1000	586
2	PY6	Si3N4	4	6	1200	431
2	PY6	Si3N4	5	8	1400	451
3	PY6	Si3N4	1	10	25	873
4	NC-400-L	SiC	1	0	25	148
4	NC-400-H	SiC	1	0	25	105
4	BETA-HP-SiC	SiC	1	0	25	265
4	NC-201-HP	SiC	1	0	25	728
4	NC-203-HP	SiC	1	0	25	760
4	KT-SiC	SiC	1	0	25	147
4	NC-430	SiC	1	0	25	117
4	NC-433	SiC	1	0	25	105
4	SN-ALPHA-SiC	SiC	1	0		425
5	NC-132-HPSN	Si3N4	1	30	25	787
5	NC-132-HPSN	Si3N4	2	15	704	730
5	NC-132-HPSN	Si3N4	3	5	704	731
5	NC-132-HPSN	Si3N4	4	30	871	728
5	NC-132-HPSN	Si3N4	5	30	871	759
5	NC-132-HPSN	Si3N4	6	30	871	727
5	NC-132-HPSN	Si3N4	7	5	871	818
5	NC-132-HPSN	Si3N4	8	15	1038	725
5	NC-132-HPSN	Si3N4	9	30	1038	725
5	NC-132-HPSN	Si3N4	10	30	1038	679
5	NC-132-HPSN	Si3N4	11	5	1038	666
5	NC-132-HPSN	Si3N4	12	30	1204	665
5	NC-132-HPSN	Si3N4	13	30	1204	688
5	NC-132-HPSN	Si3N4	14	30	1204	609
5	NC-132-HPSN	Si3N4	15	30	1204	545
5	NC-132-HPSN	Si3N4	16	5	1204	484
5	NC-132-HPSN	Si3N4	17	30	1371	411
5	NC-132-HPSN	Si3N4	18	30	1371	363
5	NC-132-HPSN	Si3N4	19	15	1371	313
5	NC-132-HPSN	Si3N4	20	30	20	401
5	NC-132-HPSN	Si3N4	21	11	20	772

Table 10. Summary of Flexural Strength Data for Reference Sources 1-14 (Continued)

Source No.	Material Designation	Type	Test No.	No. of Specimen	Temp. (°C)	Flexural Strenght (MPa)
5	NC-132-HPSN	Si3N4	22	3	300	750
5	NC-132-HPSN	Si3N4	23	3	600	720
5	NC-132-HPSN	Si3N4	24	3	900	686
5	NC-132-HPSN	Si3N4	25	3	1100	640
5	NC-132-HPSN	Si3N4	26	3	1200	625
5	NC-132-HPSN	Si3N4	27	3	1300	505
5	NC-132-HPSN	Si3N4	28	3	1350	412
5	NC-132-HPSN	Si3N4	29	2	1400	335
5	FHPSN	Si3N4	1	30	25	668
5	FHPSN	Si3N4	2	30	704	697
5	FHPSN	Si3N4	3	30	871	591
5	FHPSN	Si3N4	4	15	871	599
5	FHPSN	Si3N4	5	30	871	579
5	FHPSN	Si3N4	6	30	1038	548
5	FHPSN	Si3N4	7	10	1038	596
5	FHPSN	Si3N4	8	30	1038	531
5	FHPSN	Si3N4	9	35	1204	481
5	FHPSN	Si3N4	10	35	1204	439
5	FHPSN	Si3N4	11	35	1204	368
5	FHPSN	Si3N4	12	5	1371	324
5	FHPSN	Si3N4	13	29	1371	254
5	FHPSN	Si3N4	14	5	1371	213
5	FHPSN	Si3N4	15	0	20	415
5	FHPSN	Si3N4	16	3	400	409
5	FHPSN	Si3N4	17	2	600	375
5	FHPSN	Si3N4	18	3	800	364
5	FHPSN	Si3N4	19	2	900	358
5	FHPSN	Si3N4	20	4	1000	390
5	FHPSN	Si3N4	21	1	1050	370
5	FHPSN	Si3N4	22	2	1100	337
5	FHPSN	Si3N4	23	2	1150	375
5	FHPSN	Si3N4	24	3	1200	340
5	FHPSN	Si3N4	25	1	1250	268
5	FHPSN	Si3N4	26	1	1300	248
5	FHPSN	Si3N4	27	2	20	584
5	RBSN-NC 350	Si3N4	1	31	20	176
6	NC-132	Si3N4	1	24	25	825
6	NC-136	Si3N4	1	14	25	237
6	NCX-34	Si3N4	1	10	25	921
6	NC-350	Si3N4	1	16	25	294
6	RBSN	Si3N4	1	25	25	206
6	RBSN	Si3N4	1	16	25	288
6	NC-203	SiC	1	10	25	683
6	ALPHA-SiC(1977)	SiC	1	20	25	375

Table 10. Summary of Flexural Strength Data for Reference Sources 1-14 (Concluded)

Source No.	Material Designation	Type	Test No.	No. of Specimen	Temp. (°C)	Flexural Strength (MPa)
6	ALPHA-SiC(1978)	SiC	1	36	25	363
9	NC-132	Si3N4	1	30	25	720-837
10	ALPHA-SiC	SiC	1	6	20	198
10	ALPHA-SiC	SiC	2	4	1200	312
10	ALPHA-SiC	SiC	3	2	1300	265
11	NC-132	Si3N4	1	15	20	695
11	NC-132	Si3N4	2	2	500	688
11	NC-132	Si3N4	3	3	800	684
11	NC-132	Si3N4	4	5	1000	476
11	NC-132	Si3N4	5	3	1200	536
11	NC-132	Si3N4	6	3	1300	519
11	NC-132	Si3N4	7	3	1400	472
12		Si3N4	1	40	25	1000
12		Si3N4	2	3	200	948
12		Si3N4	3	4	400	966
12		Si3N4	4	4	600	947
12		Si3N4	5	4	800	840
12		Si3N4	6	4	1000	870
12		Si3N4	7	4	1200	690
12		Si3N4	8	4	1375	308
14	SNW-1000	Si3N4	1	12	20	468
14	SNW-1000	Si3N4	2	50	20	420
14	SNW-1000	Si3N4	3	7	800	364
14	SNW-1000	Si3N4	4	7	1000	272
14	SNW-1000	Si3N4	5	4	1100	293
14	SNW-1000	Si3N4	6	2	1200	276

Raman spectroscopy

The laser Raman microprobe facility has been used to obtain general structural information about selected SiC ceramic specimens. The system's ability to detect crystalline characteristics on a microscopic scale permits the determination of phase and the probable orientations of individual grains within the ceramic specimen. The specimens in this analysis include those from SOHIO (Hexoloy SA), CVD (SiC), and Raytheon (SiC). The SOHIO material has a hexagonal crystal structure, while the remaining materials are both chemical-vapor-deposited (CVD) SiC of cubic structure.

The system has been designed to allow selective probing of the lattice vibrational modes by providing polarization control of the incident and scattered radiation. The specimen is clamped to a translating/rotating stage which allows accurate positioning of the specimen for microscopic analysis. Using efficient signal collection and data normalization, spatial resolutions smaller than the apparent grain sizes in the SOHIO specimen can be reproducibly achieved. The cubic materials should have two first order Raman modes (lines), the transverse optical (TO) and the longitudinal optical (LO) modes, while the hexagonal material has about 15 modes.

The CVD specimen exhibited an apparent splitting of the normally doubly degenerate TO mode shown in Figure 26. The splitting as well as the relative strength of these split TO modes varies across the surface of the CVD material. The origin of this splitting is currently under investigation. It is thought to be due to a residual stress or some other influence in the specimen, perhaps due to layering, resulting from the CVD process. The variation of the splitting suggests either a nonuniformity of the orientation of the influence within the specimen, or a variation in the influence across the surface. The Raytheon specimen also displayed similar TO splitting, but to a lesser degree, as shown in Figure 27.

Figures 28 and 29 illustrate the results of studies of the SOHIO specimen at a fracture edge. The microprobe was stepped away from the edge at increments of 4 to 5 μm. The intensities of Raman lines from axial crystals depend on the polarization and directions of the incident

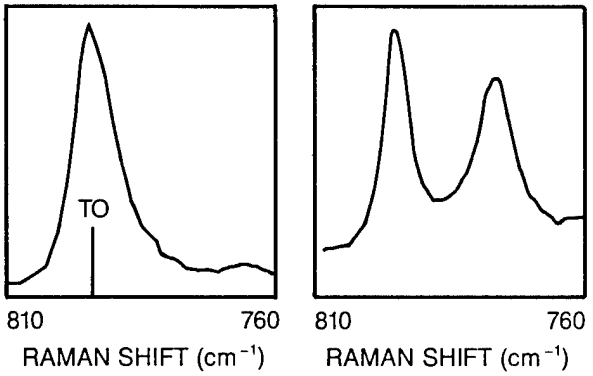

Figure 26: Two spectra from the cubic CVD SiC specimen. The spectrum of the expected TO mode is shown on the left. The right hand spectrum shows evidence of TO splitting.

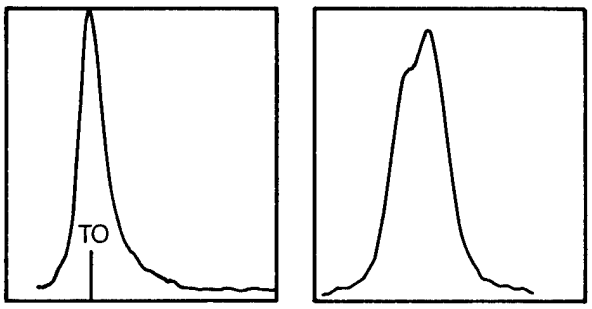

Figure 27. Mode splitting in the cubic Raytheon (cvd) SiC specimen. Note that the TO splitting is much smaller than shown in Figure 1.

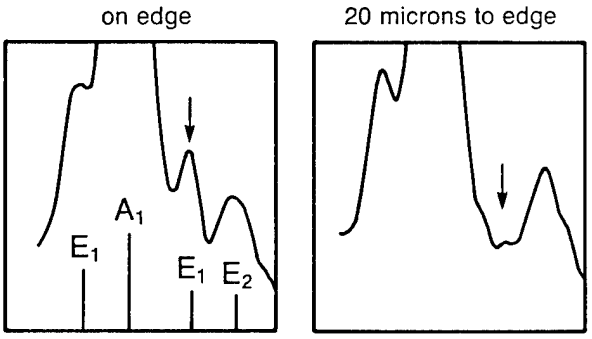

Figure 28: Fracture edge studies from the hexagonal SOHIO SiC specimen. A spectrum from the edge of the specimen (L) shows the presence of a sharp E_1 mode at 777 cm^{-1} which is not seen in the spectrum 20 m from edge (R).

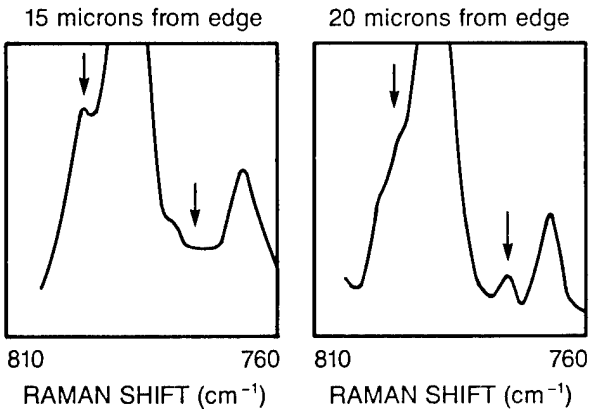

Figure 29: Same as Figure 3 except at a different location on the edge. The E_1 mode at 795 cm^{-1} appears (R) in a neighboring region.

and scattered light. Thus, the spectra show apparent variations in the crystalline orientations of neighboring grains. Quantitative interpretation of these kinds of observations requires both detailed theoretical modeling and extensive two-dimensional mapping of the Raman spectra from many specimens. The modeling is being pursued while the mapping effort will be limited to one-dimensional studies of selected specimens. Nevertheless, it is evident that the Raman microprobe provides a sensitive tool for studying these materials.

Analysis of specimen orientation in flexural strength measurements

During this reporting period we have also been conducting an analysis to theoretically evaluate the effects of the change in orientation of 4-point bend test bars in their fixtures from the conventional, wide-dimensional horizontal, to the alternative wide-dimension vertical. Of particular interest to this analysis was the possibility that the use of the alternative vertical test orientation might appreciably increase the ratio of volume-flaw-initiated failures to surface-flaw-initiated failures.

The analysis assumes that SiC and Si_3N_4 materials are subject to two principal failure modes: failures originating at surface flaws and failures originating at volume flaws. A Weibull model that takes into account the two failure modes is being employed to conduct parametric evaluations employing selected sets of Weibull volume and surface strength parameters. The Weibull parameters being used are representative of low-, medium-, and high-strength SiC and Si_3N_4 materials characterized in our project.

Although volume-flaw-initiated failures are seldom seen in conventional four-point flexural tests, such failures represent about 10% of tensile test failures. The relative distributions of volume and surface flaw failures in tensile tests are being used in conjunction with the Weibull parameters measured in 4-point flexural tests. The Weibull parameters determined in 4-point flexural tests are considered representative of the surface failure mode. It should be noted, however, that surface failure mode Weibull characteristics of flexural and tensile specimens are likely to differ. This is so because different specimen and

surface finishing techniques are employed in the preparation of tensile and flexural specimens. Weibull properties are functions of the surface flaw populations that result from specimen preparation.

From the available information it is not possible to identify individual values of both the Weibull modulus and the Weibull scale factor for the volume failure mode. (The analysis employs a two-parameter Weibull model.) However, there is a basis for the determination of combinations of modulus and scale factor values that are consistent with measured values and assumptions. Thus, the approach employed in the analysis is to evaluate the effects of various combinations of modulus and scale factor through a methodical variation of the parameters. This parametric evaluation is being conducted for the three classes of materials: high, medium, and low strength.

Based on the assumptions outlined above, the Weibull cumulative and distribution probabilities of failure for both surface and volume failure modes are being calculated for 4-point bend specimens oriented both horizontally and vertically in the flexural test apparatus. The relative fraction of volume failures depends on the value assumed for the volume failure mode Weibull modulus. High values of the volume mode Weibull modulus (associated with relatively tight flaw size distributions) are predicted to produce much higher percentages of volume failures in vertically oriented specimens than would low values of the modulus. For example, mid-strength, vertically oriented, 4-point bend specimens with a volume strength modulus of m = 49 would have about 18% volume failures while a mid-strength material with a volume modulus of m = 5 would experience less than 1% volume failure.

Conclusions

1. The SiC and SiC/TiB_2 ceramics had measured flexural strengths that remained relatively constant from 20°-1400°C irrespective of the loading rate (see Figure 1). These SiC ceramics also did not appear to be subject to slow crack growth at elevated temperatures.

2. The Si_3N_4 ceramics tended to have higher room temperature flexural strengths than those measured for the SiC ceramics; however, at the higher temperatures the flexural strength decreases markedly (see

Figure 2). In addition, the Si_3N_4 ceramics are susceptible to slow crack growth and plastic deformation at temperatures in excess of 1200°C (see Figure 30).

3. The tensile strength measured for the Hexoloy SA material was about 60% of the flexural strengths measured at 20°C, 1000°C, and 1400°C. Heat treating the Hexoloy-SA improved room temperature tensile strength about 40%. Allowing the copper collets to deform (flow) prior to rapid loading appeared to reduce the number of buttonhead failures during tensile testing. Preliminary tensile strength measurements of the NT-154 resulted in strength values that were about 80% of the measured flexural strength. Heat treating increased breaking loads by about 50%. Allowing the copper collet to deform prior to fast fracture also appeared to reduce buttonhead failures in the NT-154 material. However, more work is required in developing the tensile testing protocol to be used.

4. An effective technique for measuring strain during tensile testing has been developed. This technique uses speckle interferometry to measure displacements as small as 3-5 μm ($\pm$ 1/2 μm). This technique has proven effective at temperatures from 20°-1400°C.

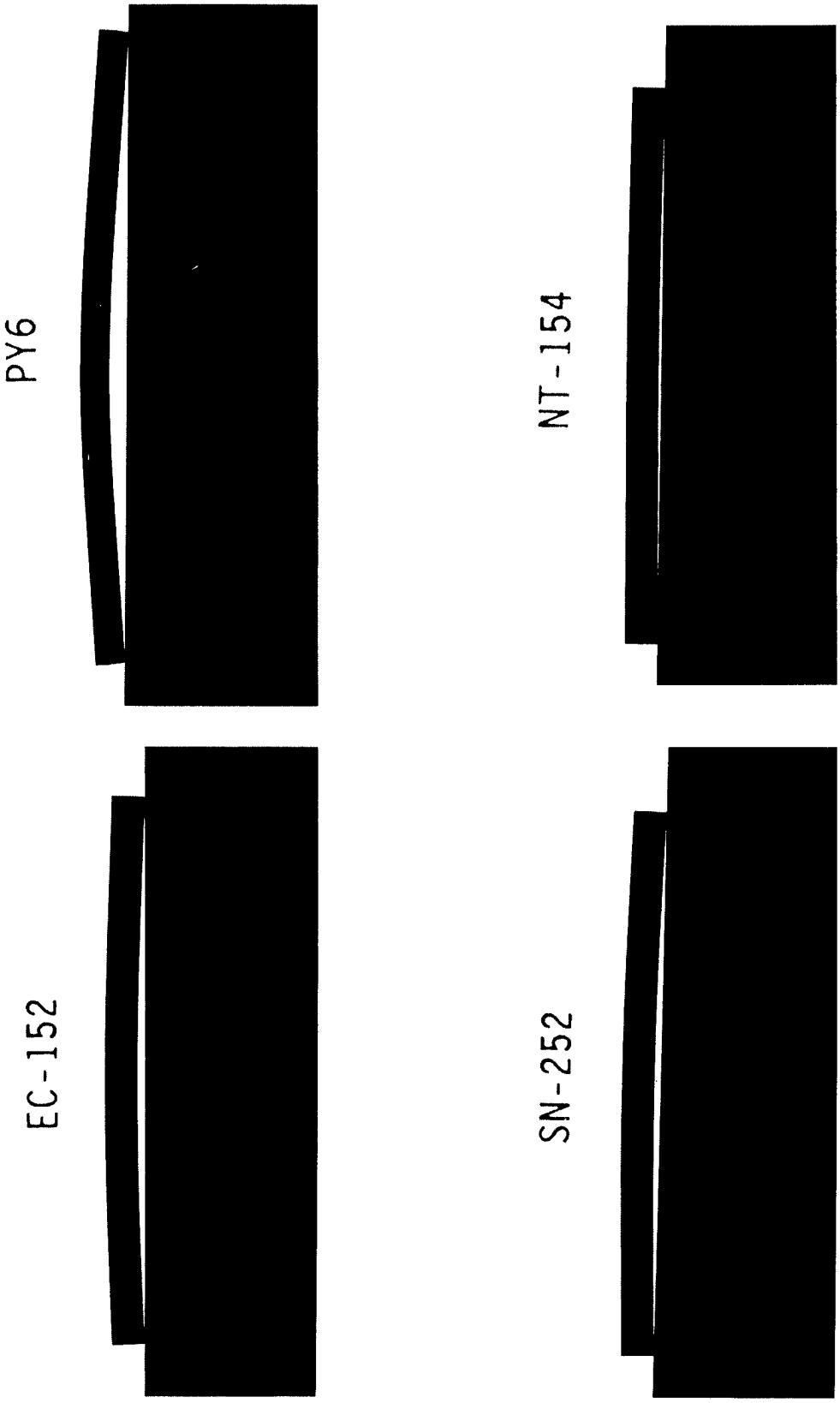

Figure 30. Shadowgrams of plastically deformed Si_3N_4 specimens slow loaded at 1400°C.

APPENDIX 1

Computer generated graphs of $\ln\sigma_f$ versus $\ln\dot{\sigma}$ for the eight candidate materials evaluated.

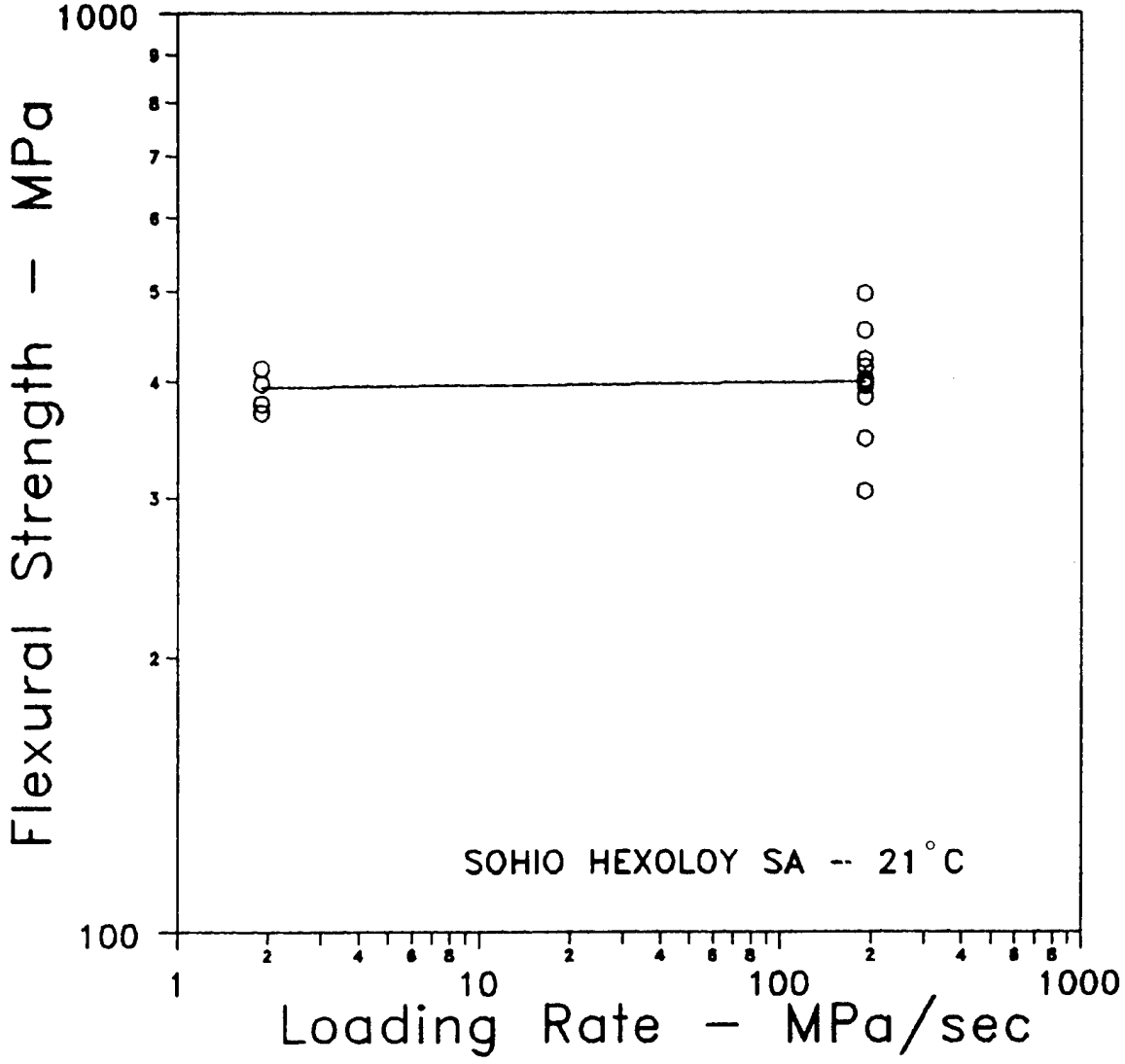
1000
9
8
7
6
5
4
3
2
100
Flexural Strength - MPa
SOHIO HEXOLOY SA -- 21°C
1
10
100
1000
Loading Rate - MPa/sec

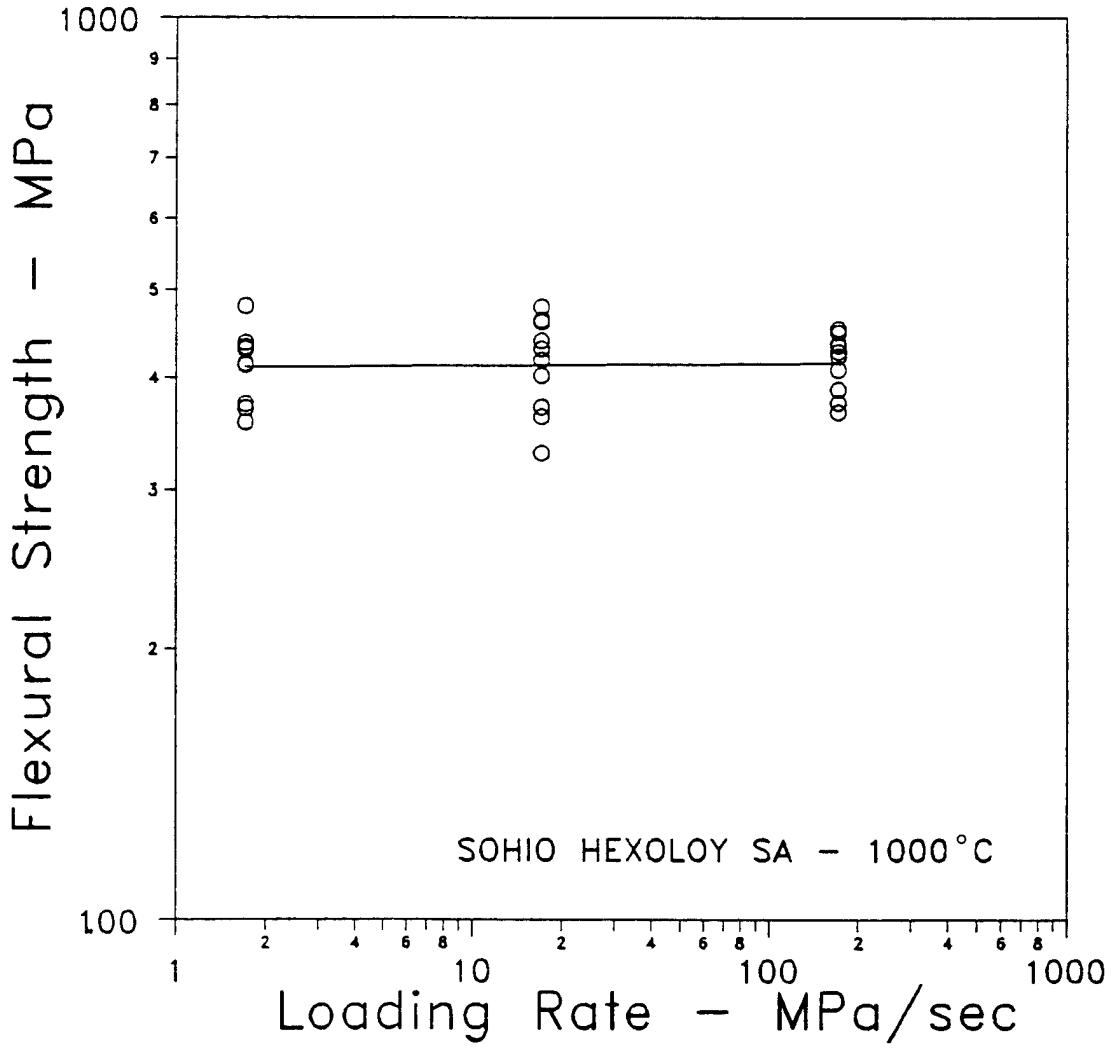
1000
9
8
7
6
5
4
3
2
100
Flexural Strength - MPa
SOHIO HEXOLOY SA - 1000°C
1
2
4
6
8
10
2
4
6
8
100
2
4
6
8
1000
Loading Rate - MPa/sec

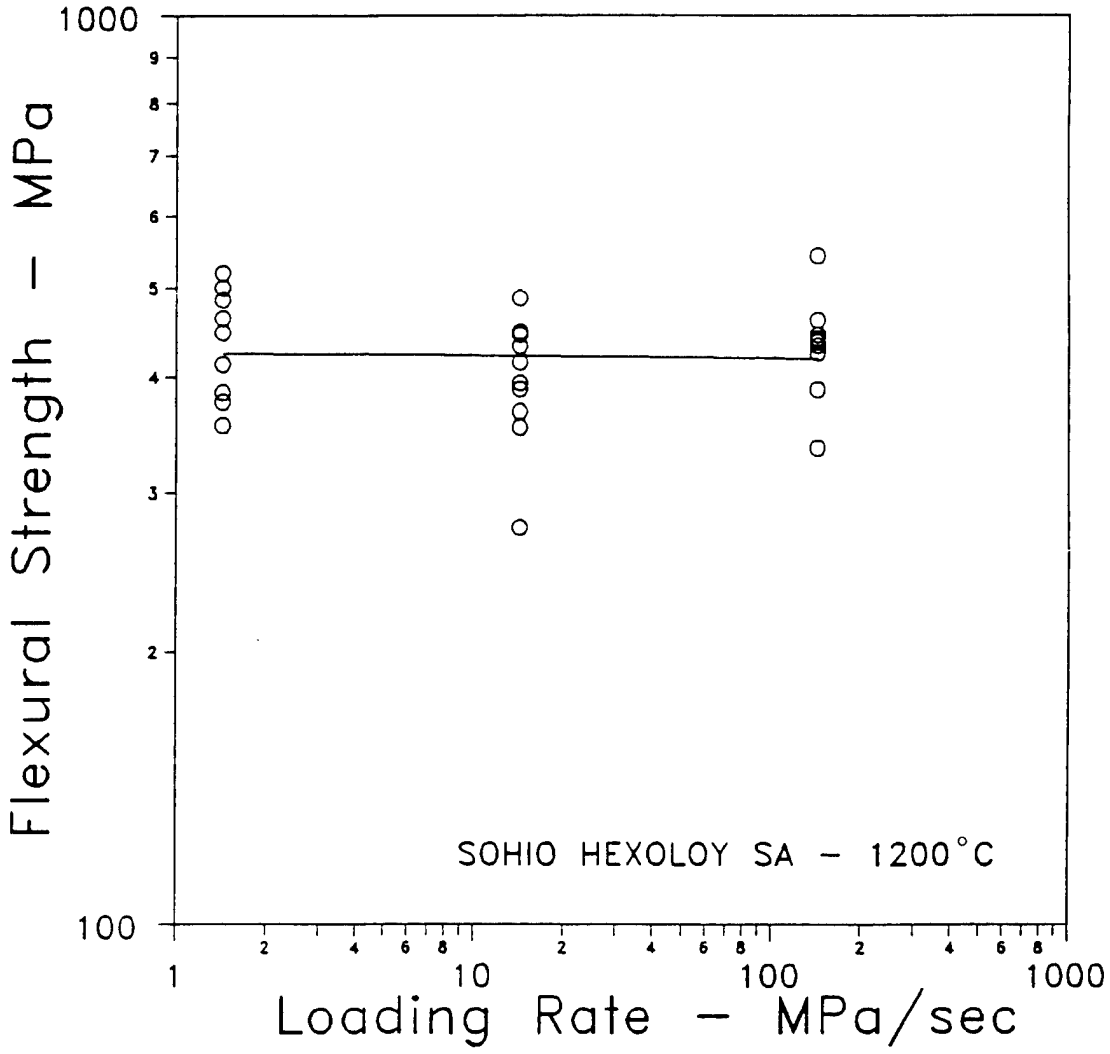
1000
9
8
7
6
5
4
3
2
100
Flexural Strength - MPa
SOHIO HEXOLOY SA - 1200°C
1
2
4
6
8
10
2
4
6
8
100
2
4
6
8
1000
Loading Rate - MPa/sec

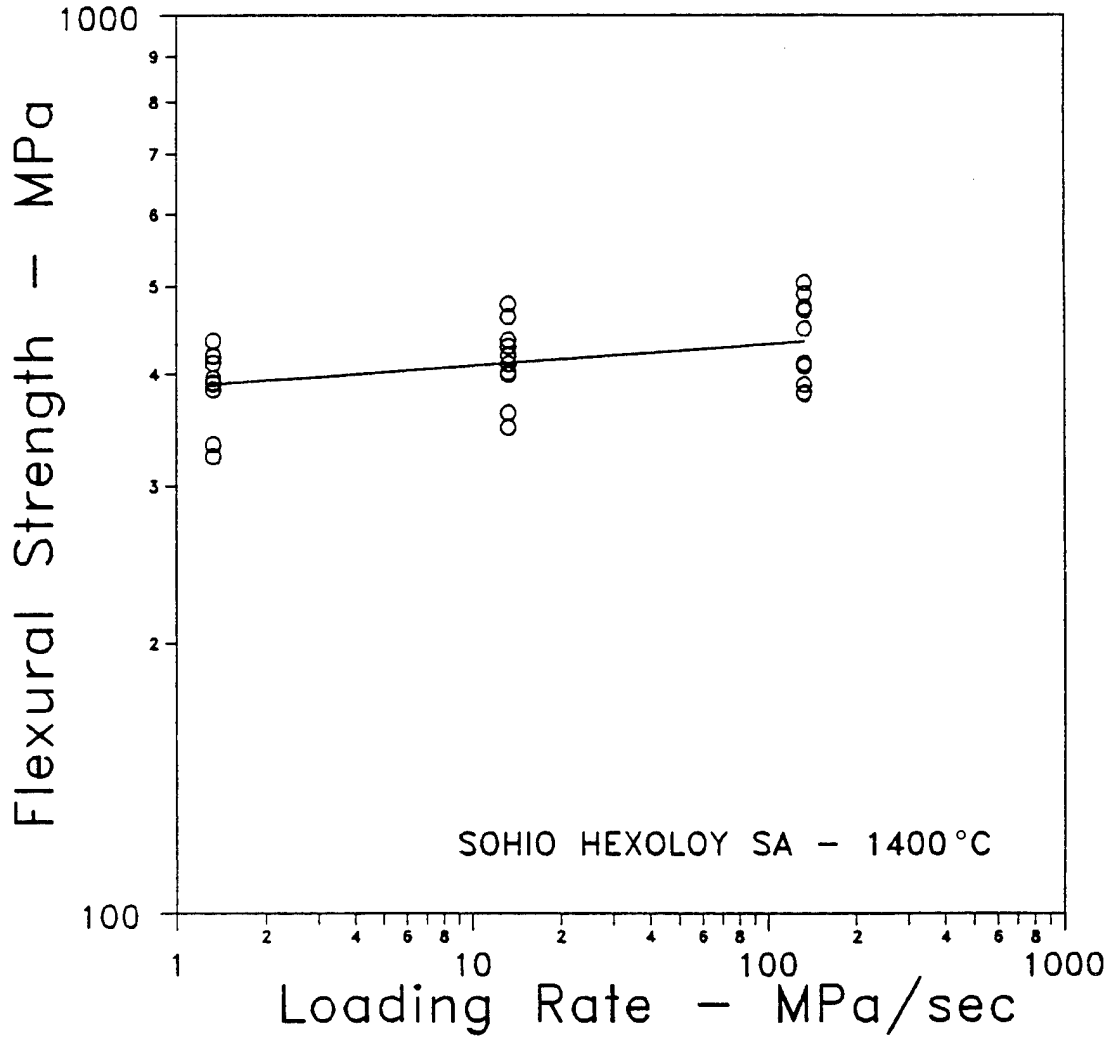
1000
9
8
7
6
5
4
3
2
100
Flexural Strength – MPa
SOHIO HEXOLOY SA – 1400°C
1
2
4
6
8
10
2
4
6
8
100
2
4
6
8
1000
Loading Rate – MPa/sec

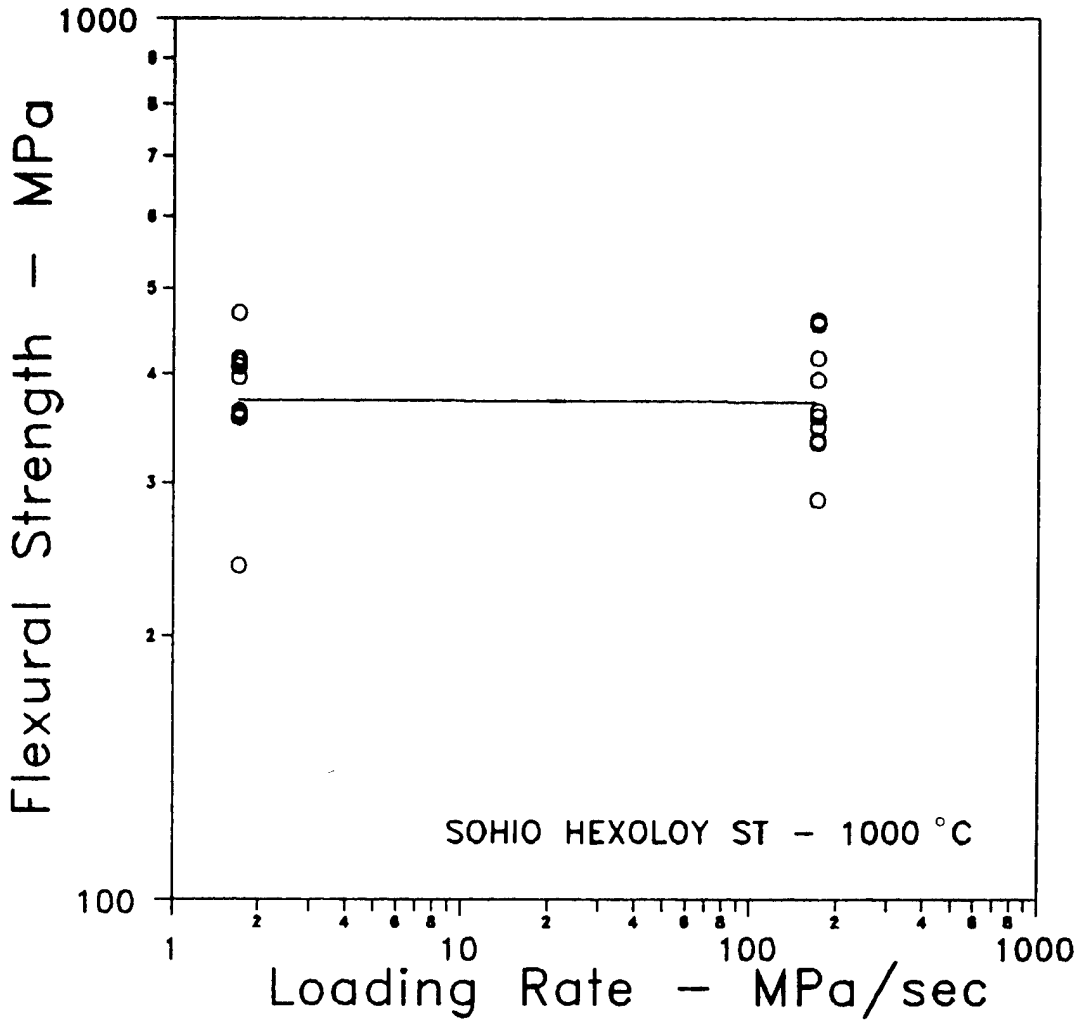
1000
100
Flexural Strength – MPa
SOHIO HEXOLOY ST – 1000 °C
1
10
100
1000
Loading Rate – MPa/sec

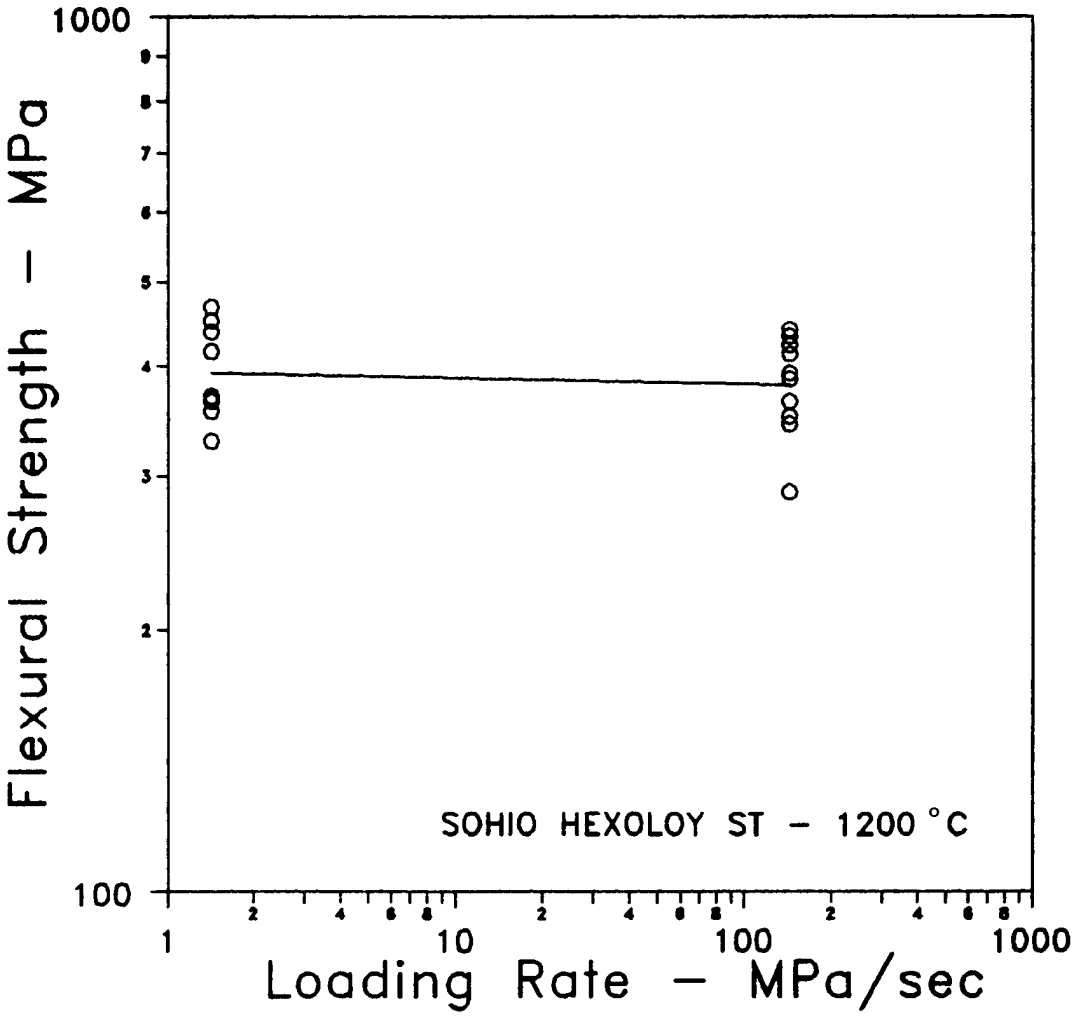
1000
9
8
7
6
5
4
3
2
100
Flexural Strength – MPa
SOHIO HEXOLOY ST – 1200 °C
1
2
4
6
8
10
2
4
6
8
100
2
4
6
8
1000
Loading Rate – MPa/sec

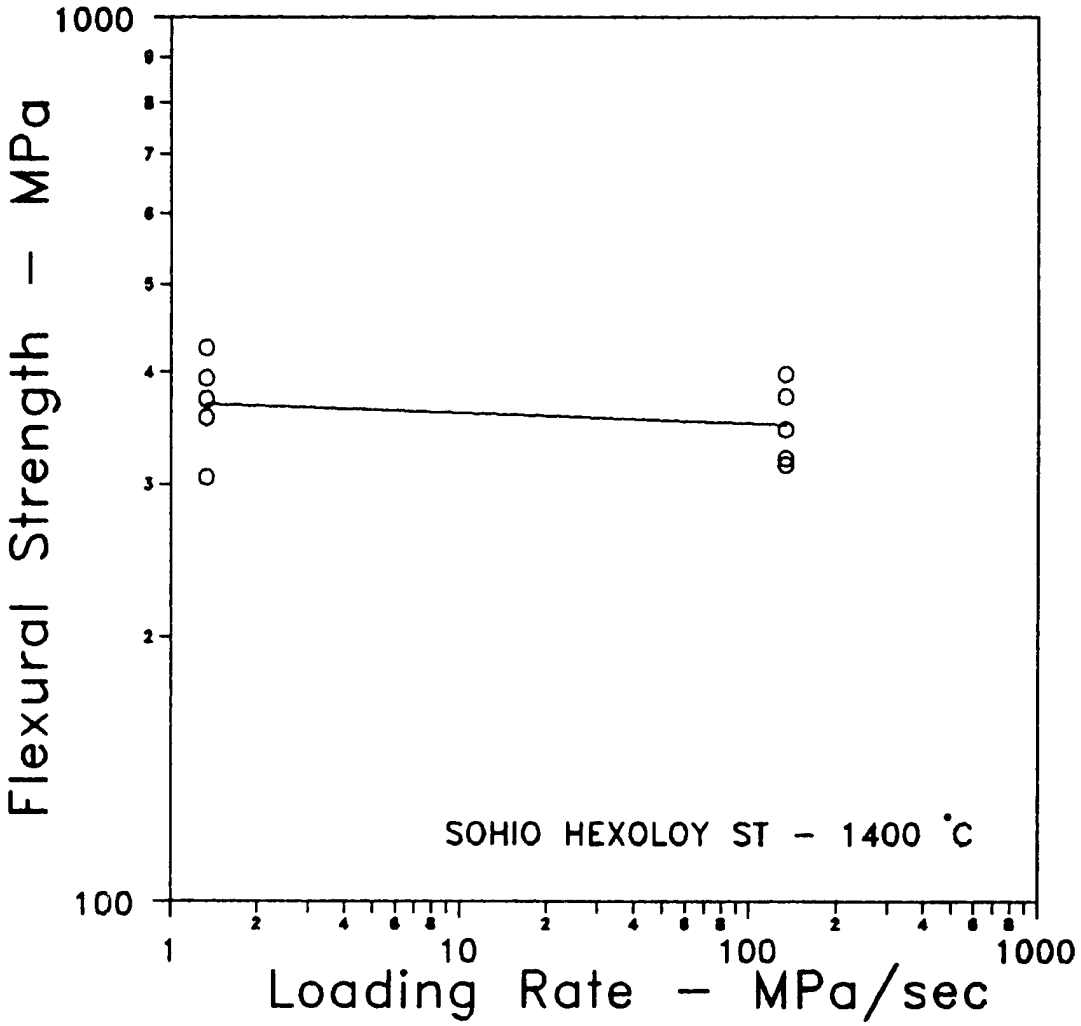
1000
100
Flexural Strength – MPa
SOHIO HEXOLOY ST – 1400 °C
1
10
100
1000
Loading Rate – MPa/sec

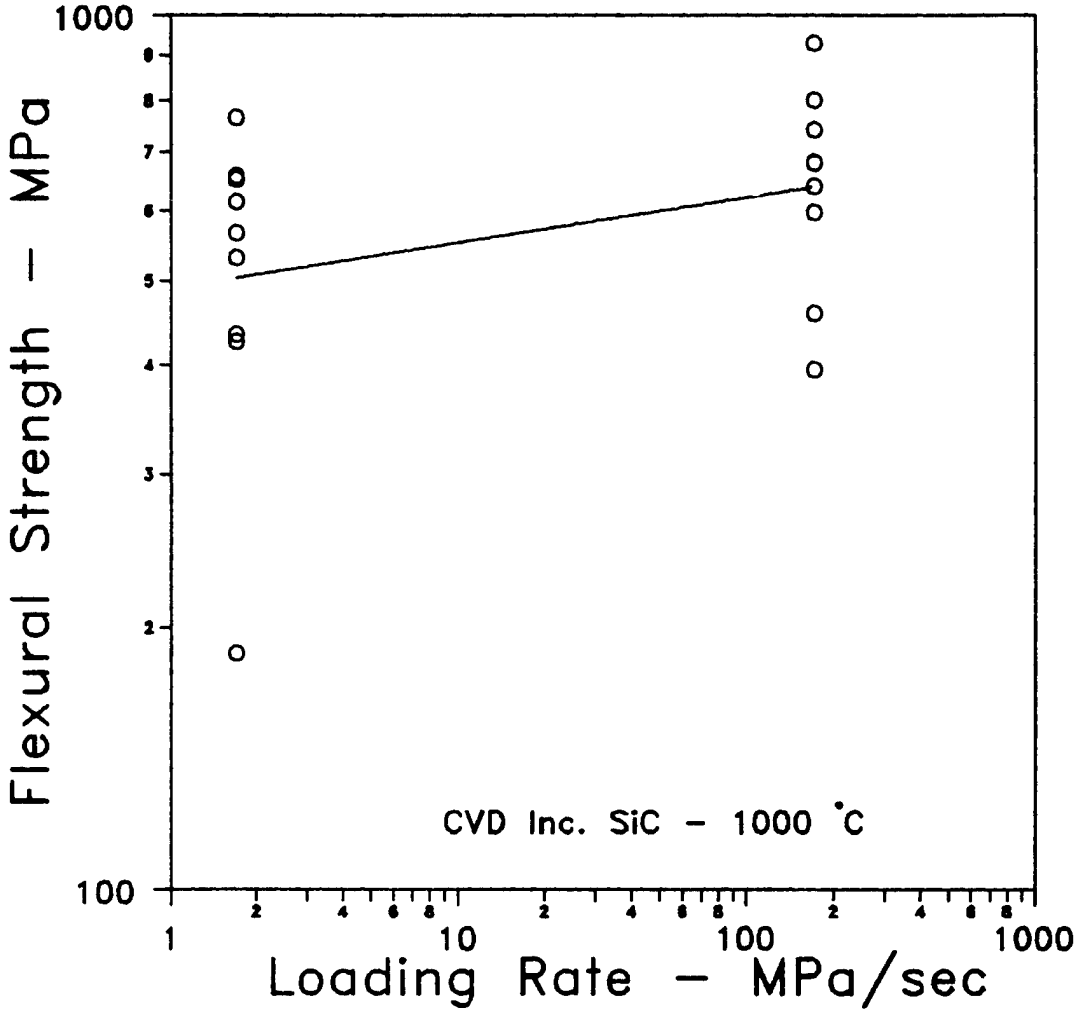
1000
100
Flexural Strength – MPa
CVD Inc. SiC – 1000 °C
1
10
100
1000
Loading Rate – MPa/sec

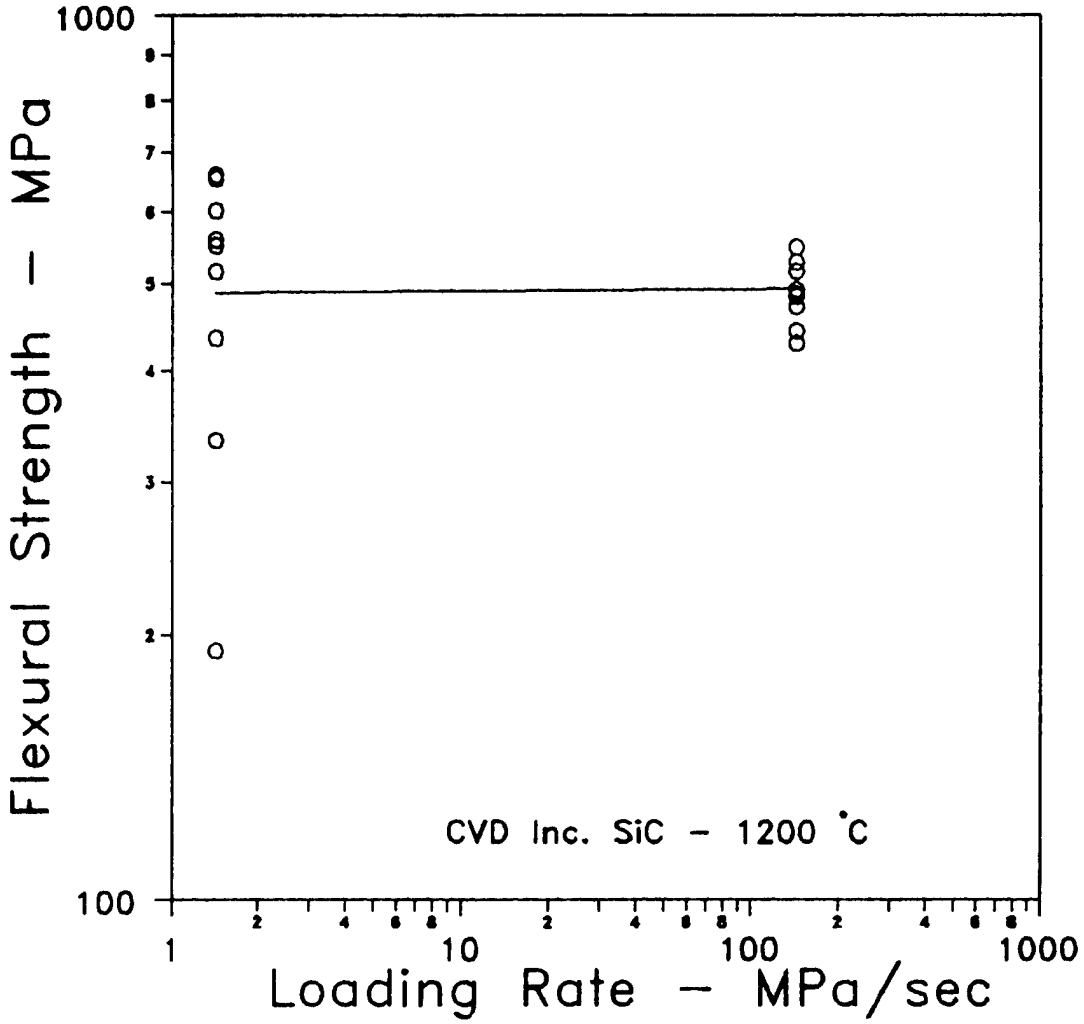
1000
100
Flexural Strength - MPa
CVD Inc. SiC - 1200 °C
1
10
100
1000
Loading Rate - MPa/sec

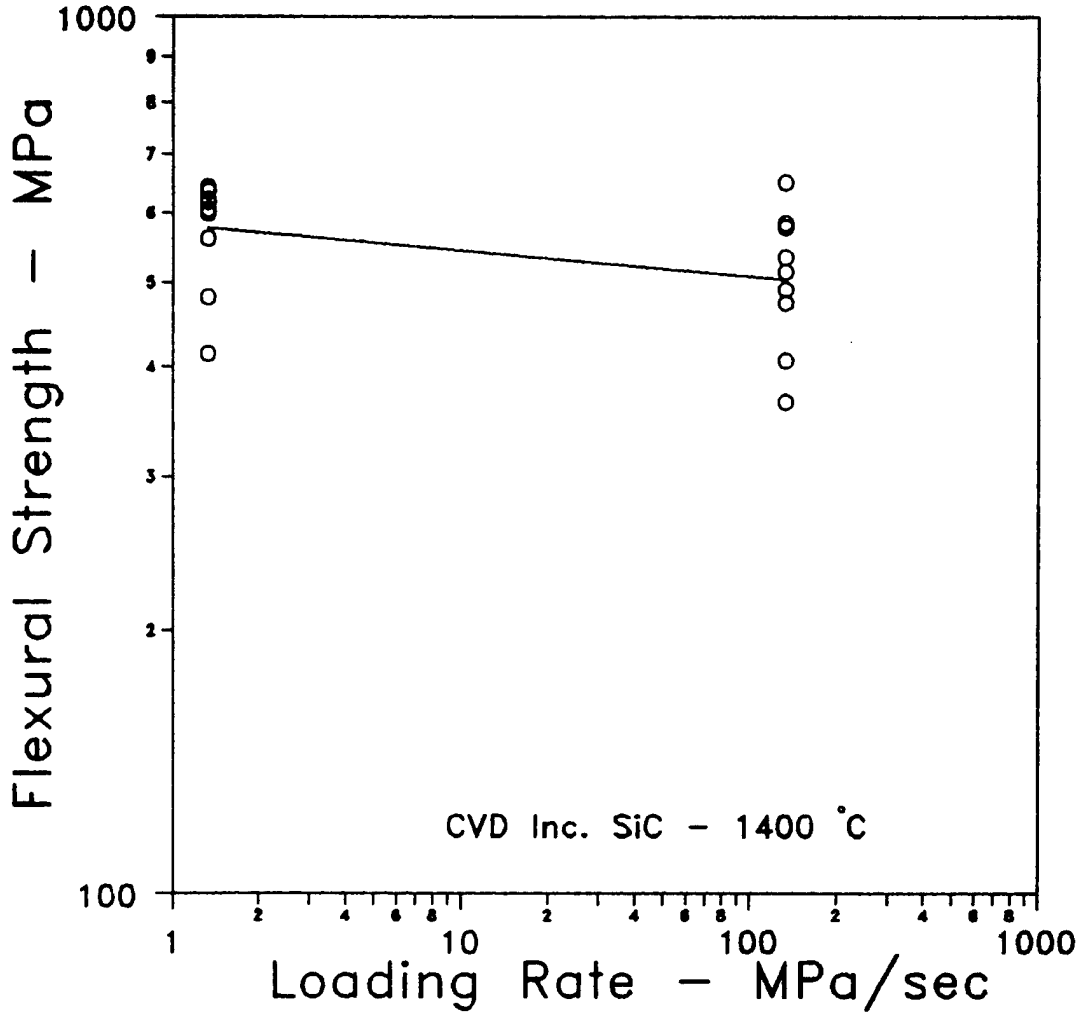
1000
9
8
7
6
5
4
3
2
100
Flexural Strength – MPa
CVD Inc. SiC – 1400 °C
1
2
4
6
8
10
2
4
6
8
100
2
4
6
8
1000
Loading Rate – MPa/sec

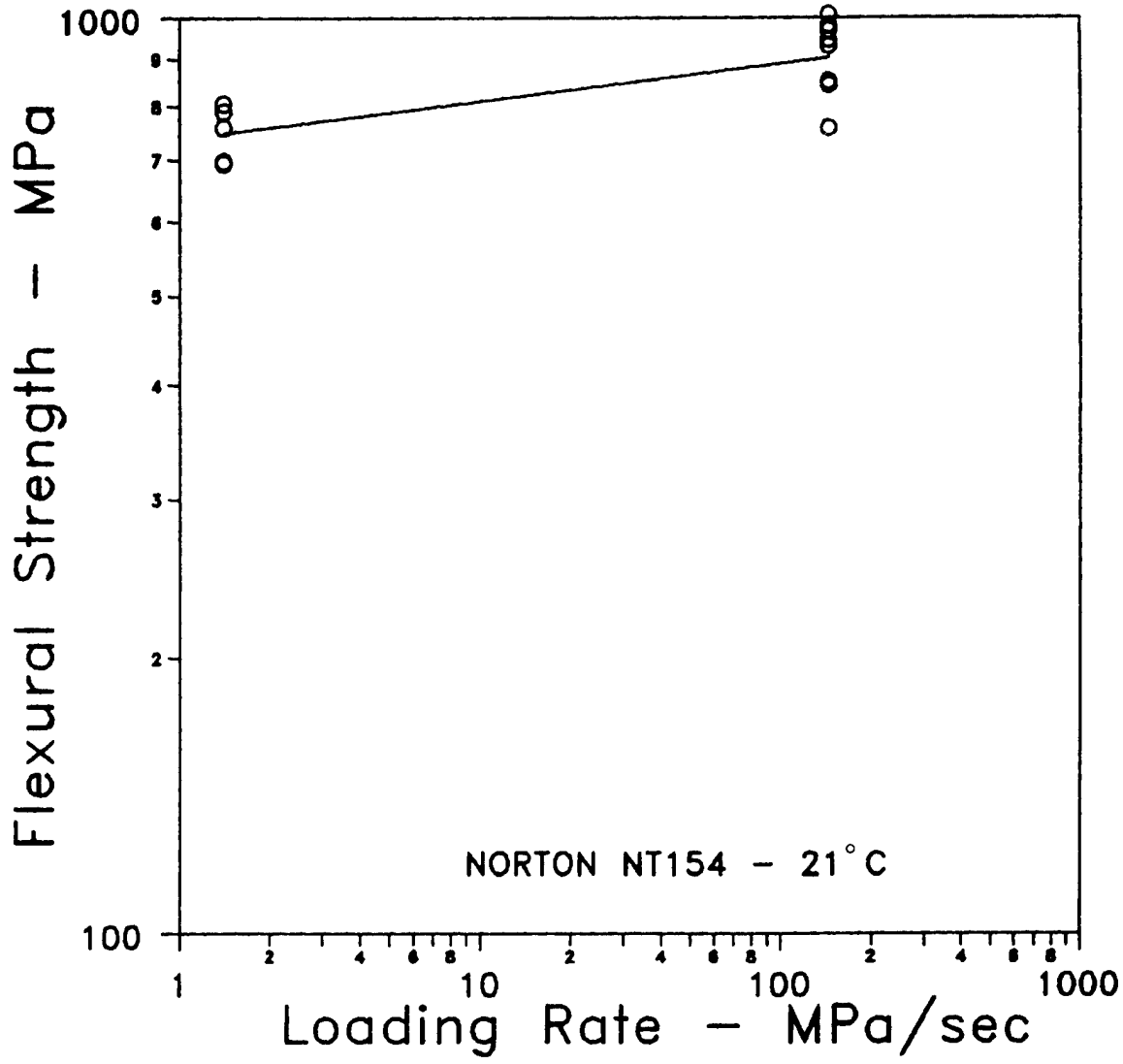
1000
9
8
7
6
5
4
3
2
100
Flexural Strength – MPa
NORTON NT154 – 21°C
1
2
4
6
8
10
2
4
6
8
100
2
4
6
8
1000
Loading Rate – MPa/sec

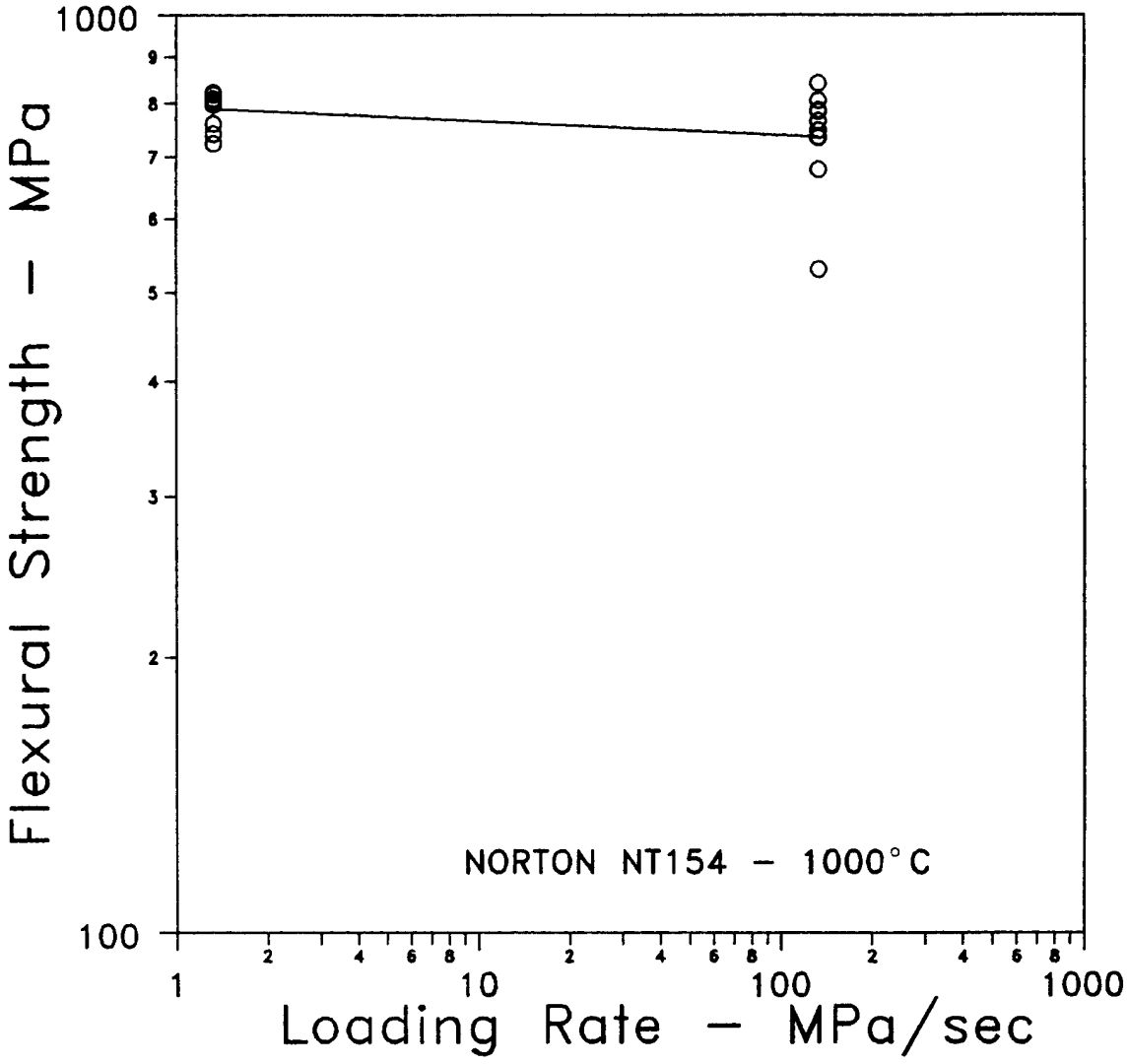
1000
9
8
7
6
5
4
3
2
100
Flexural Strength - MPa
NORTON NT154 - 1000°C
1
2
4
6
8
10
2
4
6
8
100
2
4
6
8
1000
Loading Rate - MPa/sec

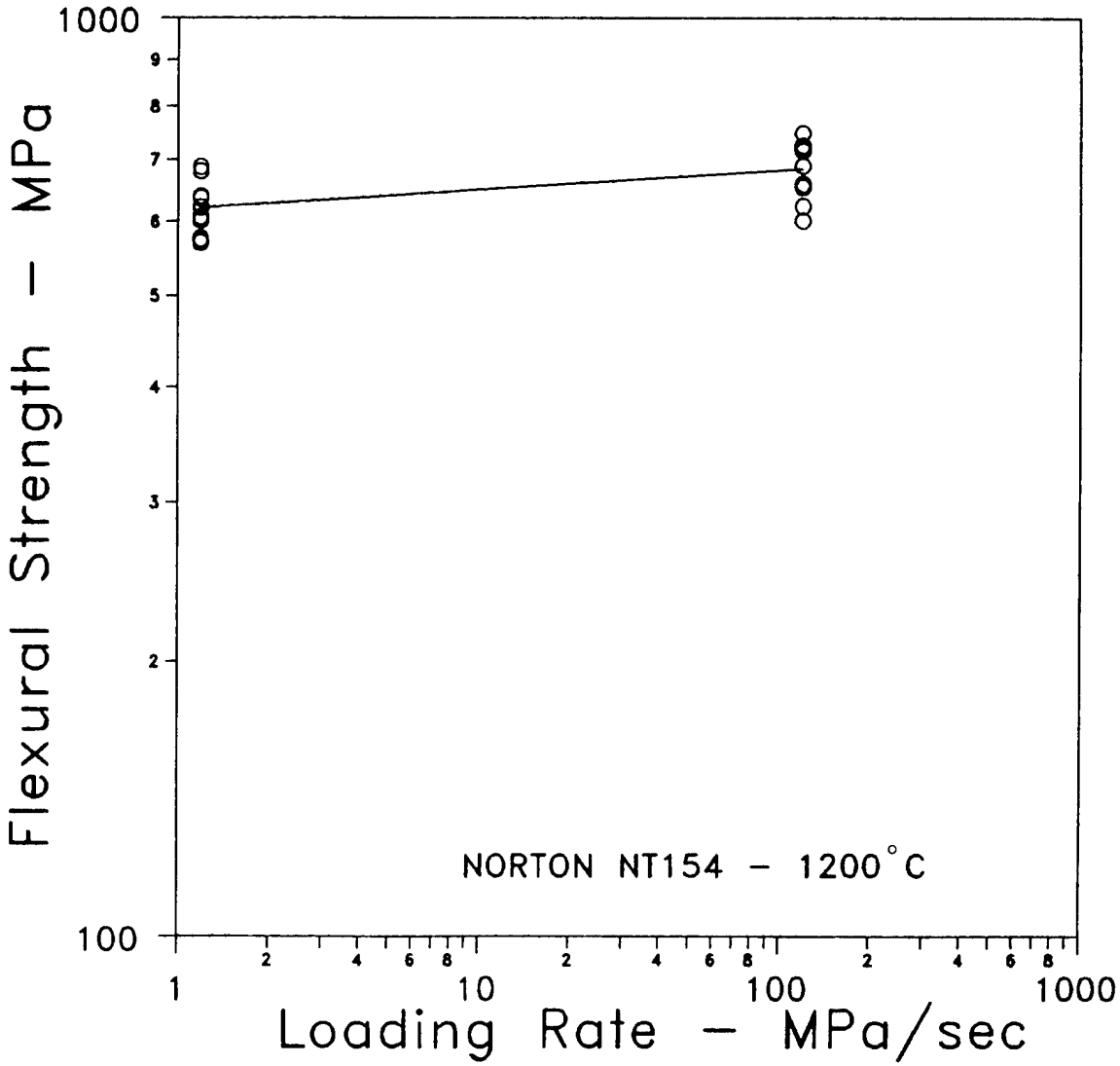
1000
9
8
7
6
5
4
3
2
100
Flexural Strength - MPa
NORTON NT154 - 1200°C
1
2
4
6
8
10
2
4
6
8
100
2
4
6
8
1000
Loading Rate - MPa/sec

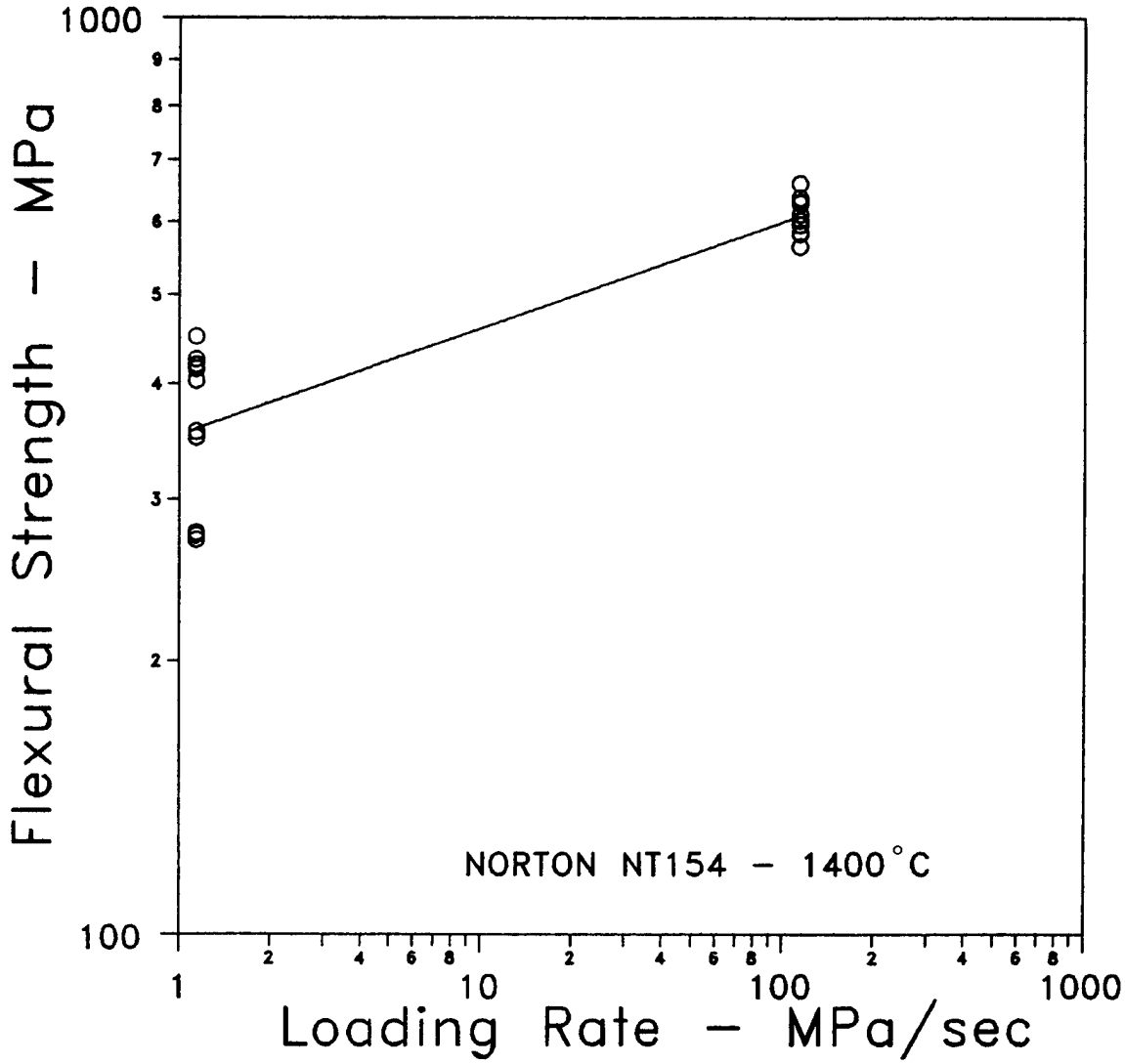
1000
9
8
7
6
5
4
3
2
100
Flexural Strength - MPa
NORTON NT154 - 1400°C
1
2
4
6
8
10
2
4
6
8
100
2
4
6
8
1000
Loading Rate - MPa/sec

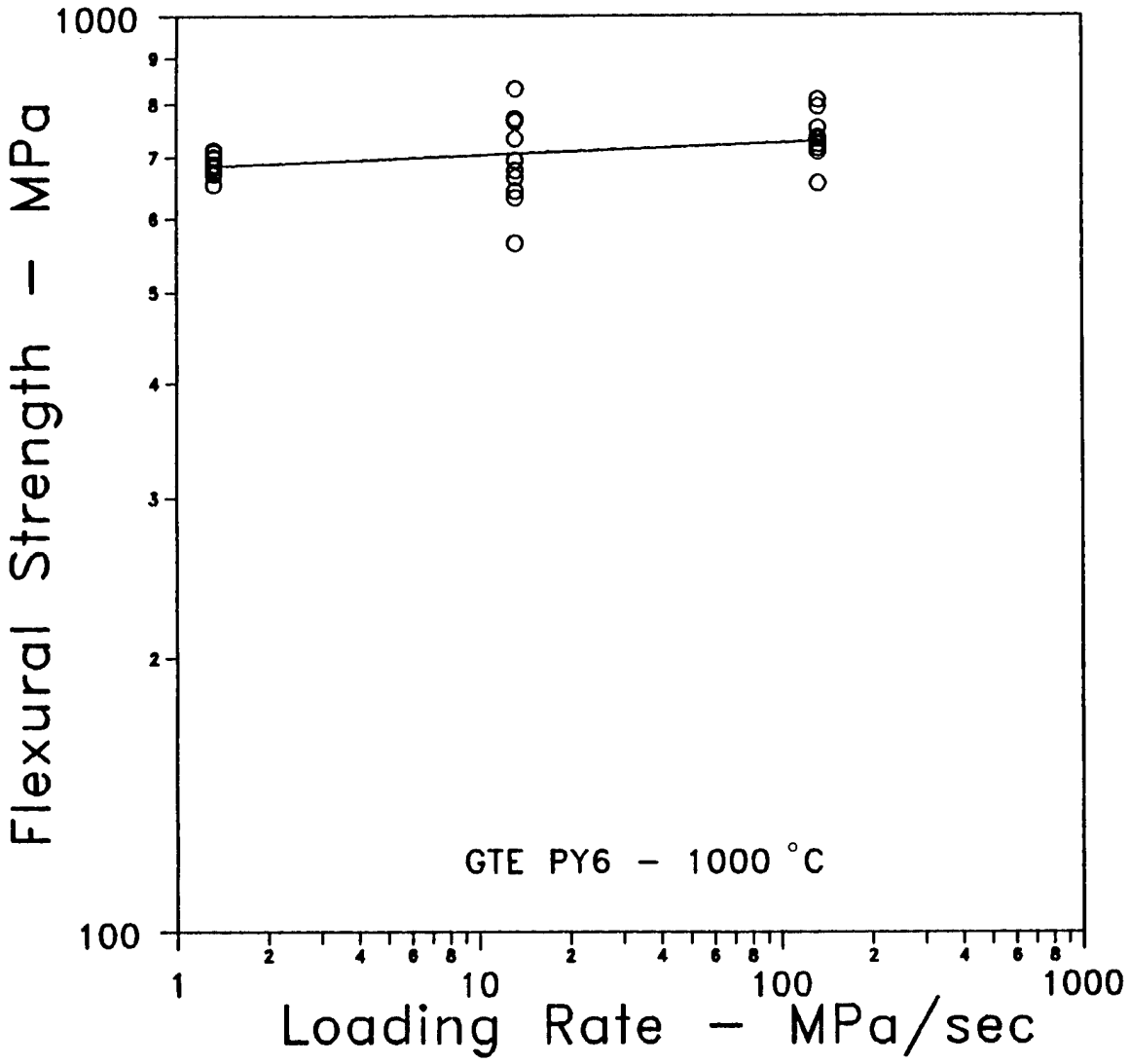
1000
9
8
7
6
5
4
3
2
100
Flexural Strength - MPa
GTE PY6 - 1000 °C
1
2
4
6
8
10
2
4
6
8
100
2
4
6
8
1000
Loading Rate - MPa/sec

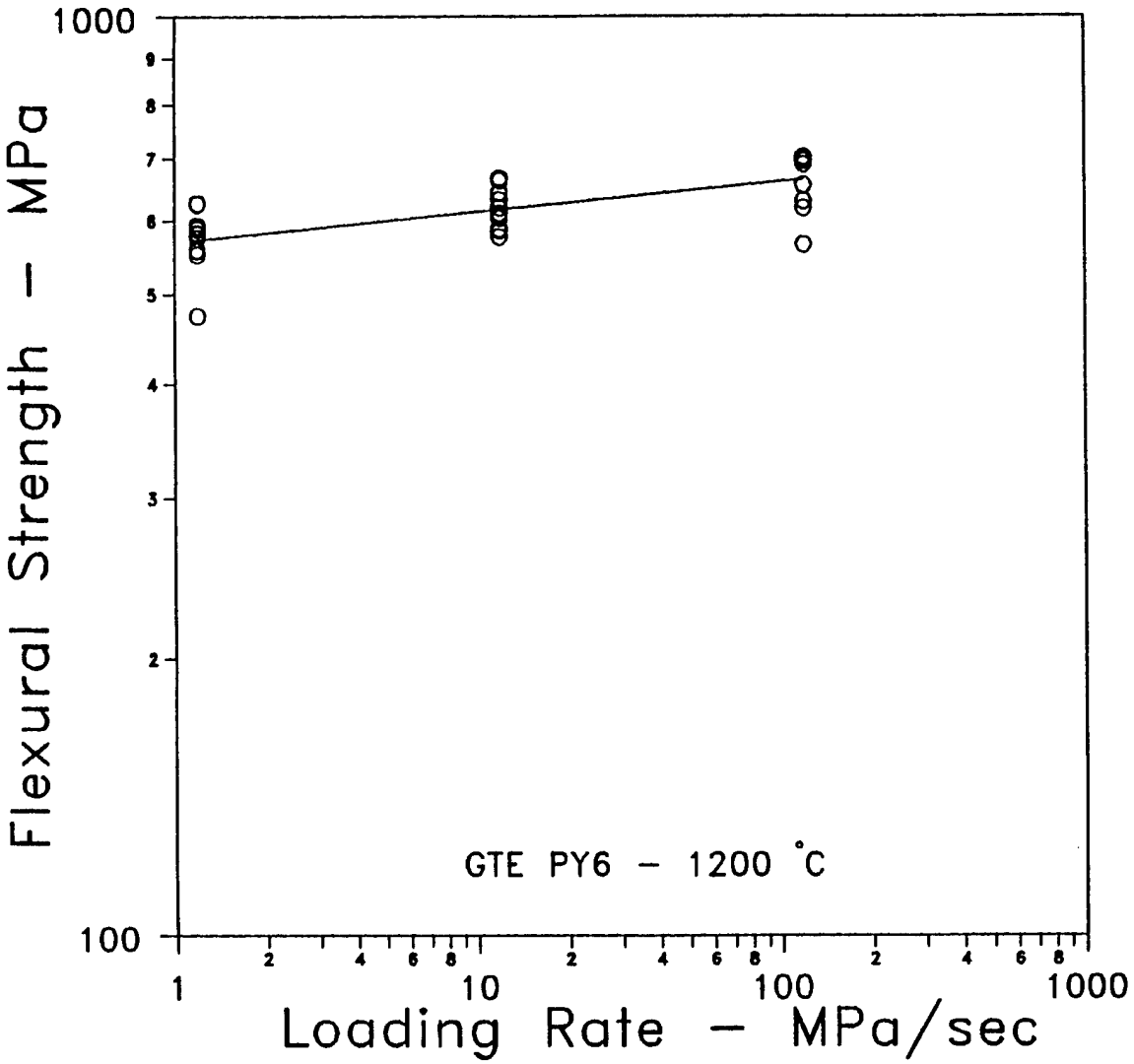
1000
9
8
7
6
5
4
3
2
100
Flexural Strength – MPa
GTE PY6 – 1200 °C
1
2
4
6
8
10
2
4
6
8
100
2
4
6
8
1000
Loading Rate – MPa/sec

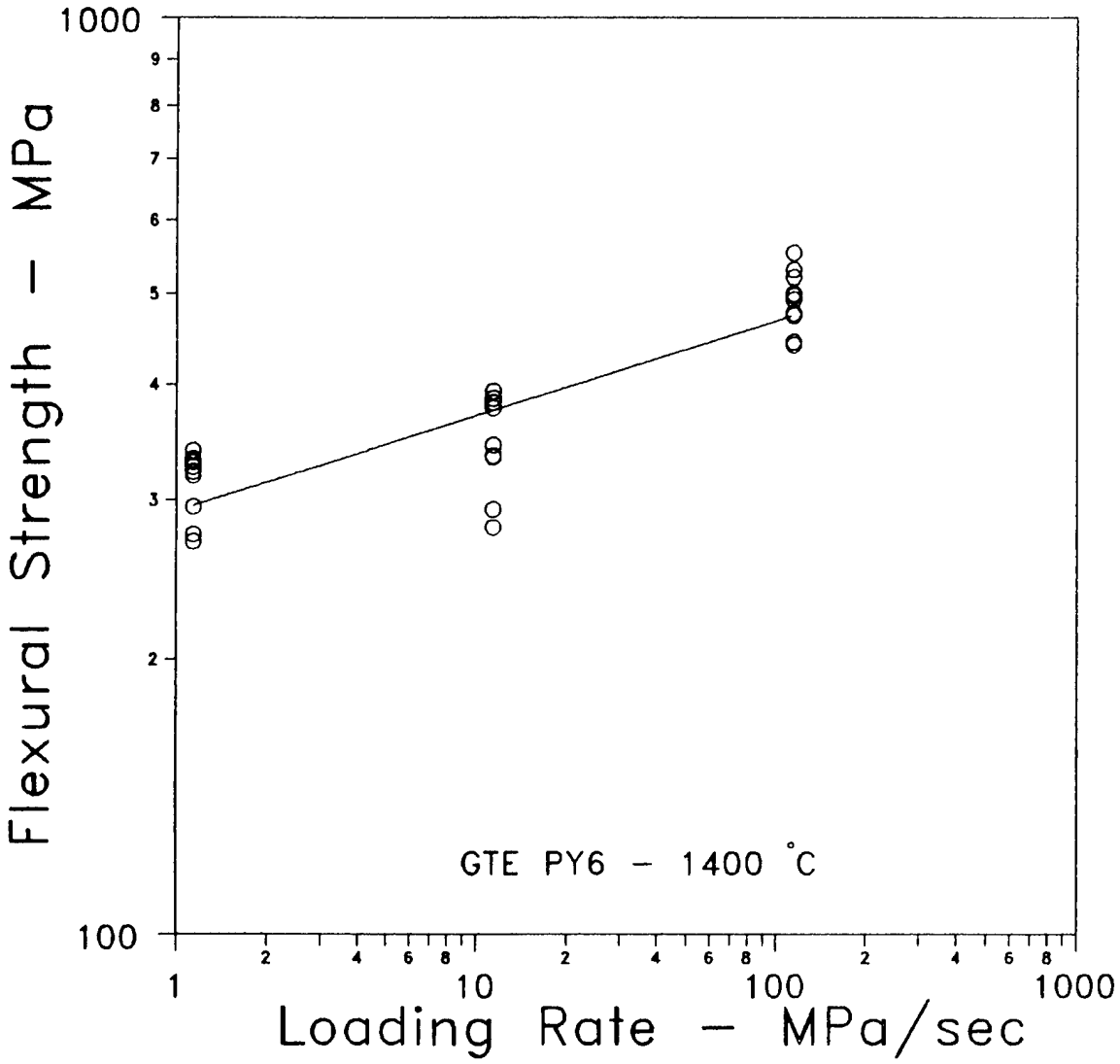
1000
9
8
7
6
5
4
3
2
100
Flexural Strength – MPa
GTE PY6 – 1400 °C
1
2
4
6
8
10
2
4
6
8
100
2
4
6
8
1000
Loading Rate – MPa/sec

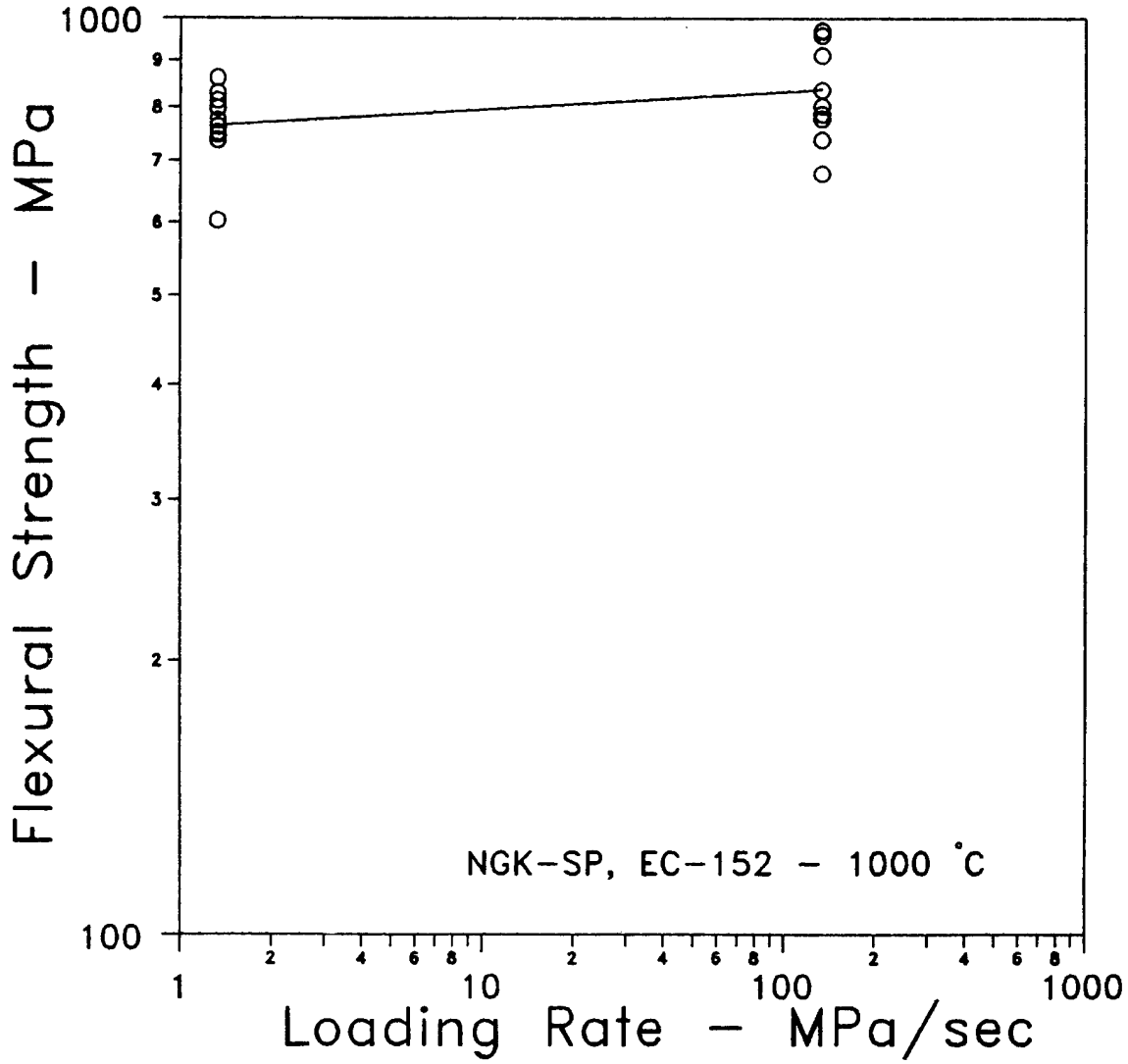
1000
9
8
7
6
5
4
3
2
100
Flexural Strength – MPa
NGK–SP, EC–152 – 1000 °C
1
2
4
6
8
10
2
4
6
8
100
2
4
6
8
1000
Loading Rate – MPa/sec

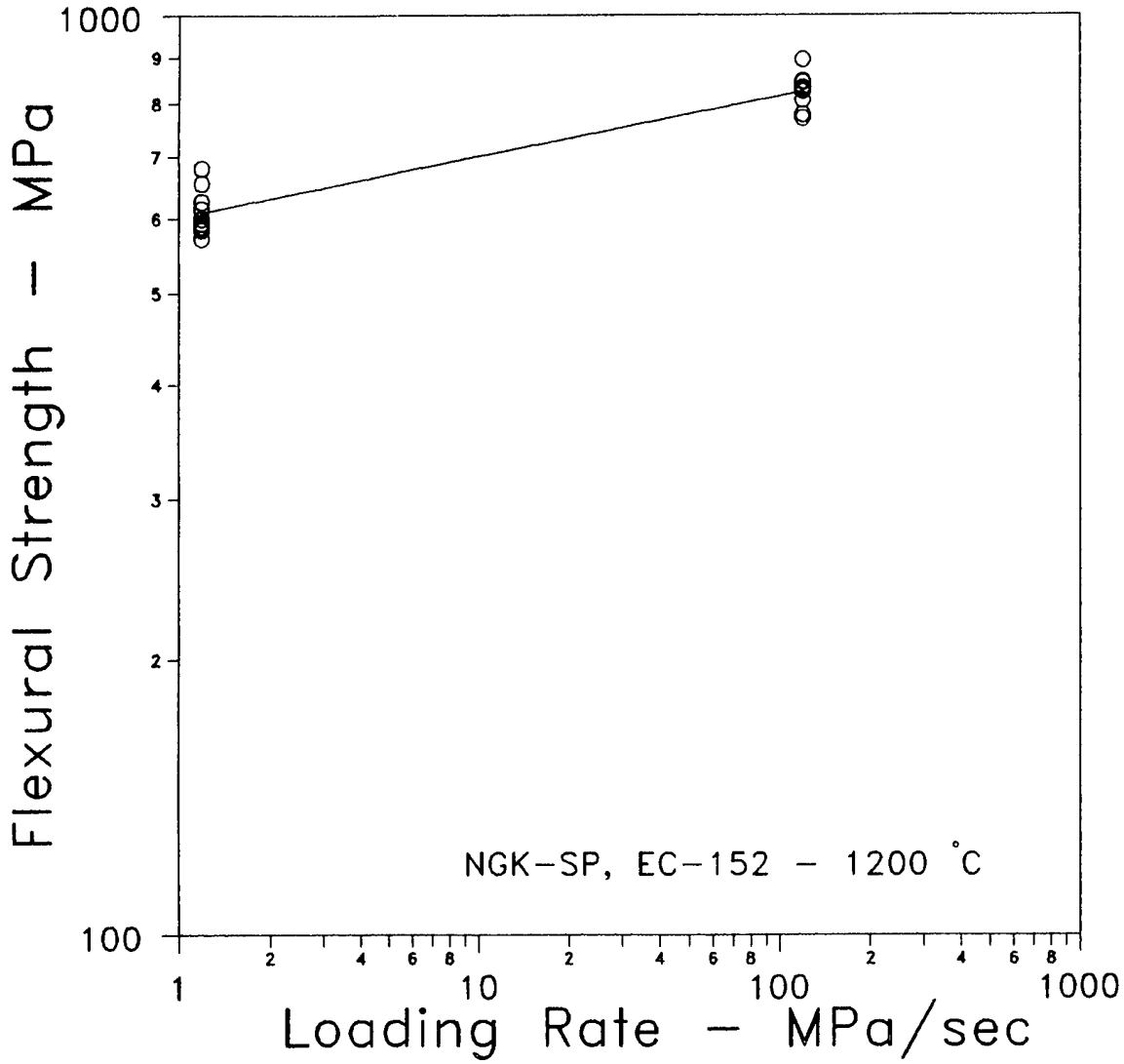
1000
9
8
7
6
5
4
3
2
100
Flexural Strength - MPa
NGK-SP, EC-152 - 1200 °C
1
2
4
6
8
10
100
1000
Loading Rate - MPa/sec

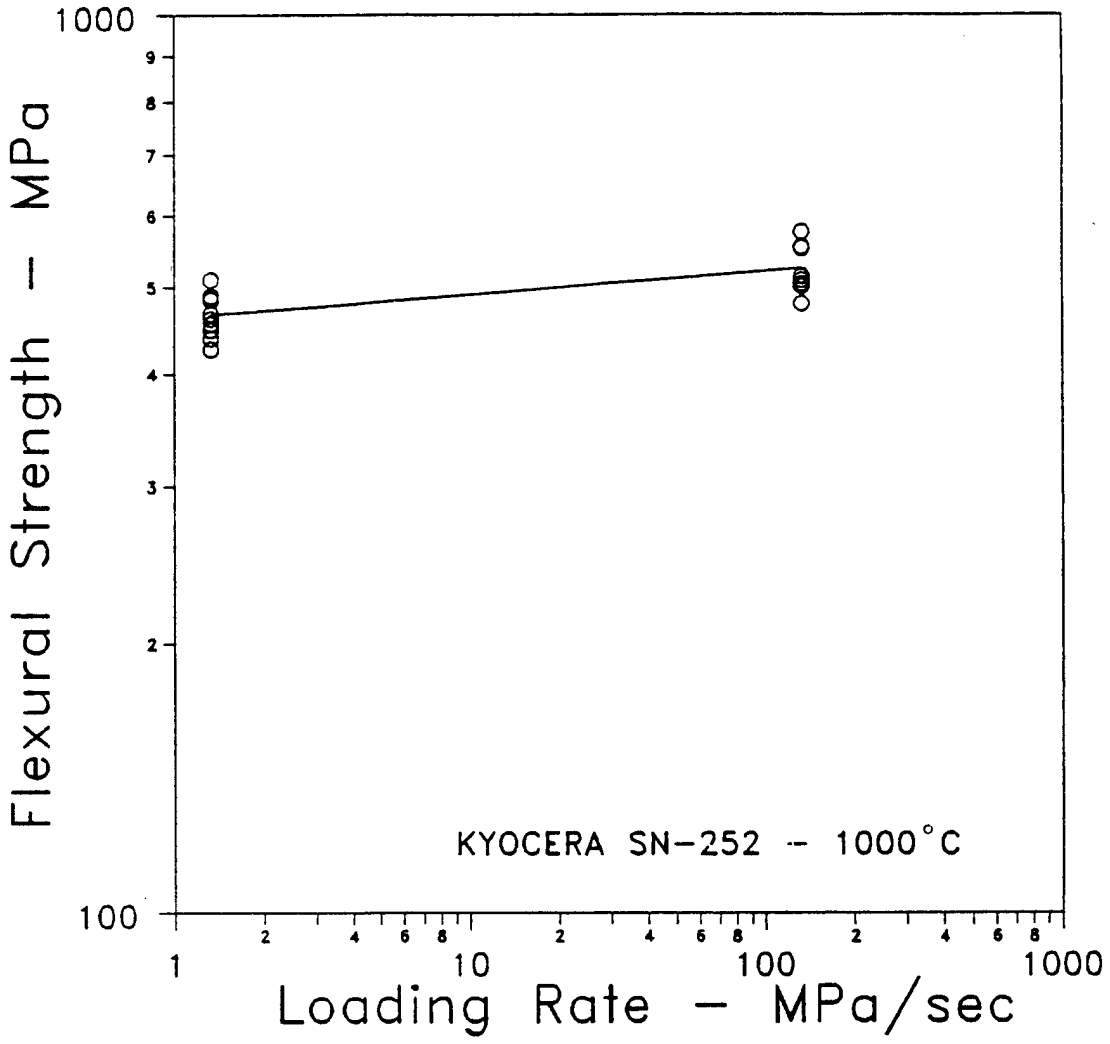
1000
9
8
7
6
5
4
3
2
100
Flexural Strength - MPa
KYOCERA SN-252 -- 1000°C
1
2
4
6
8
10
2
4
6
8
100
2
4
6
8
1000
Loading Rate - MPa/sec

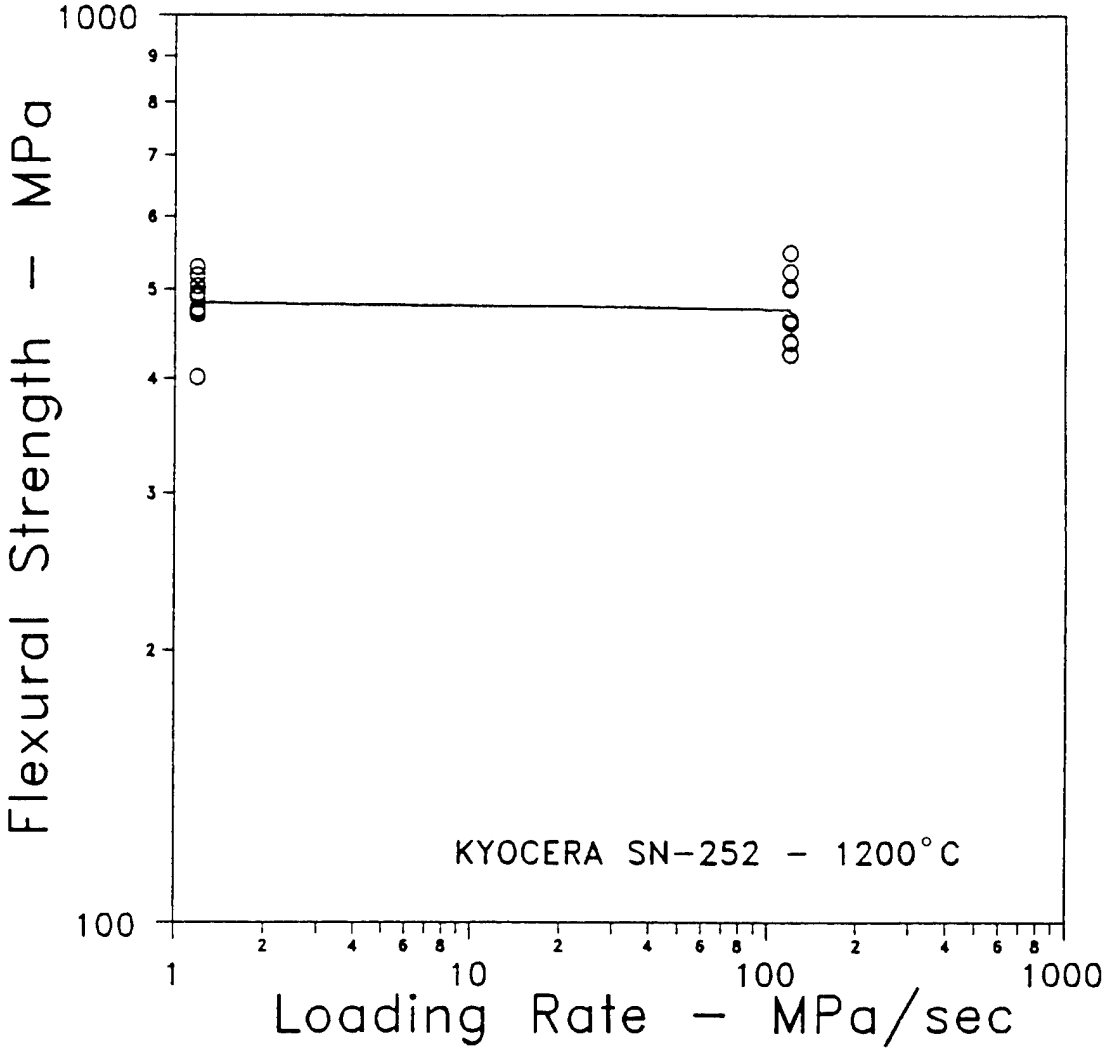
1000
9
8
7
6
5
4
3
2
100
Flexural Strength - MPa
KYOCERA SN-252 - 1200°C
1
2
4
6
8
10
2
4
6
8
100
2
4
6
8
1000
Loading Rate - MPa/sec

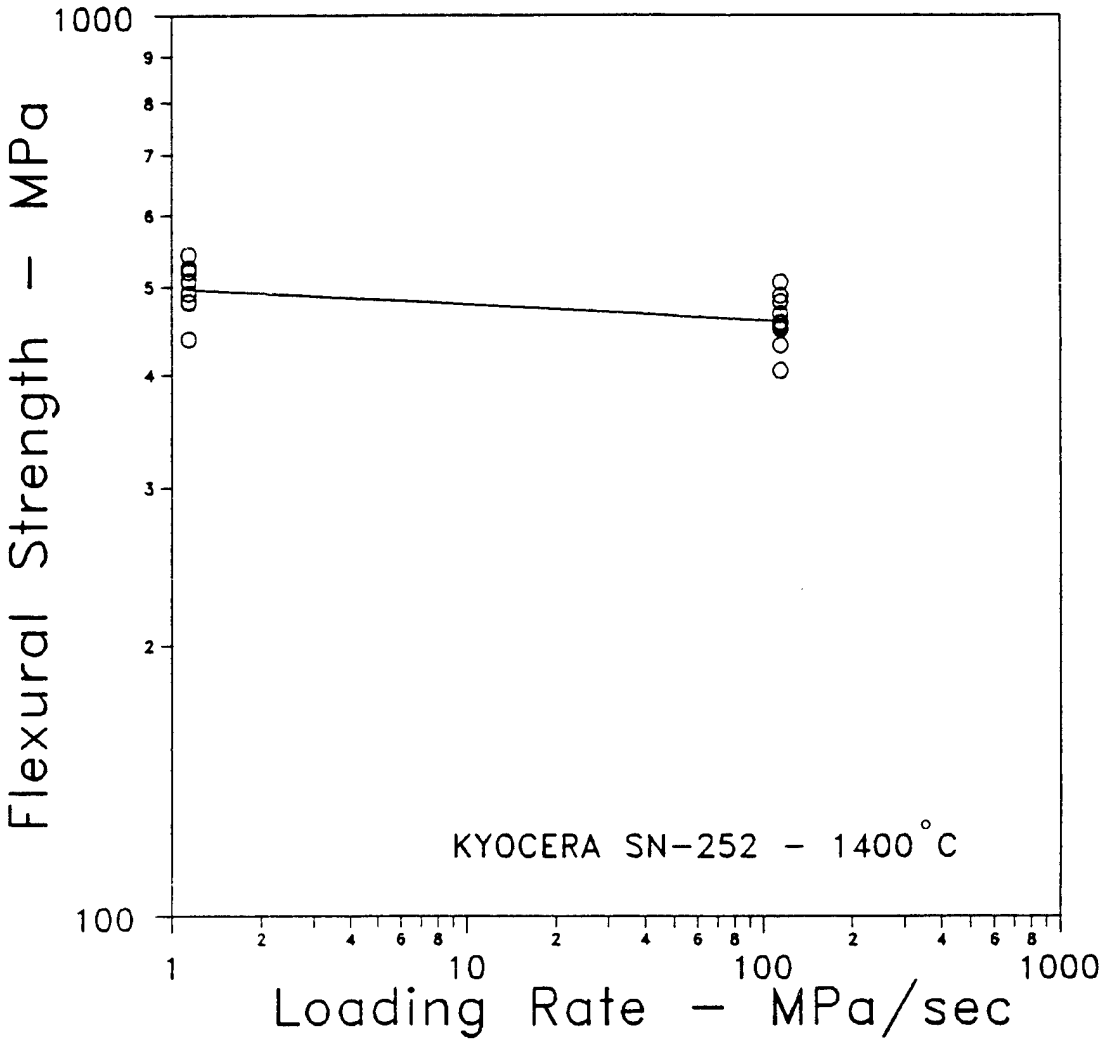
1000
9
8
7
6
5
4
3
2
100
Flexural Strength - MPa
KYOCERA SN-252 - 1400°C
1
2
4
6
8
10
100
1000
Loading Rate - MPa/sec

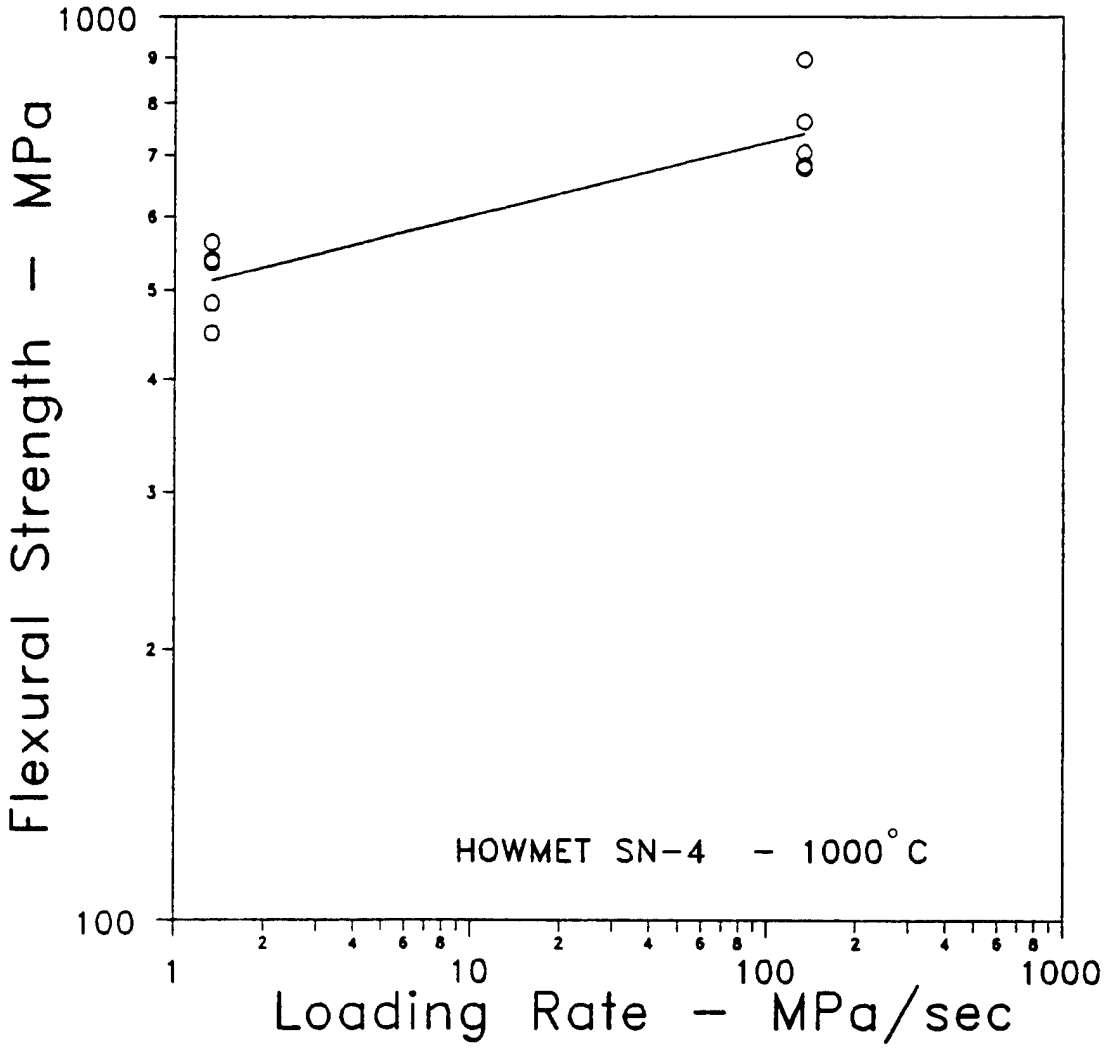
1000
9
8
7
6
5
4
3
2
100
Flexural Strength - MPa
HOWMET SN-4 - 1000°C
1
2
4
6
8
10
2
4
6
8
100
2
4
6
8
1000
Loading Rate - MPa/sec

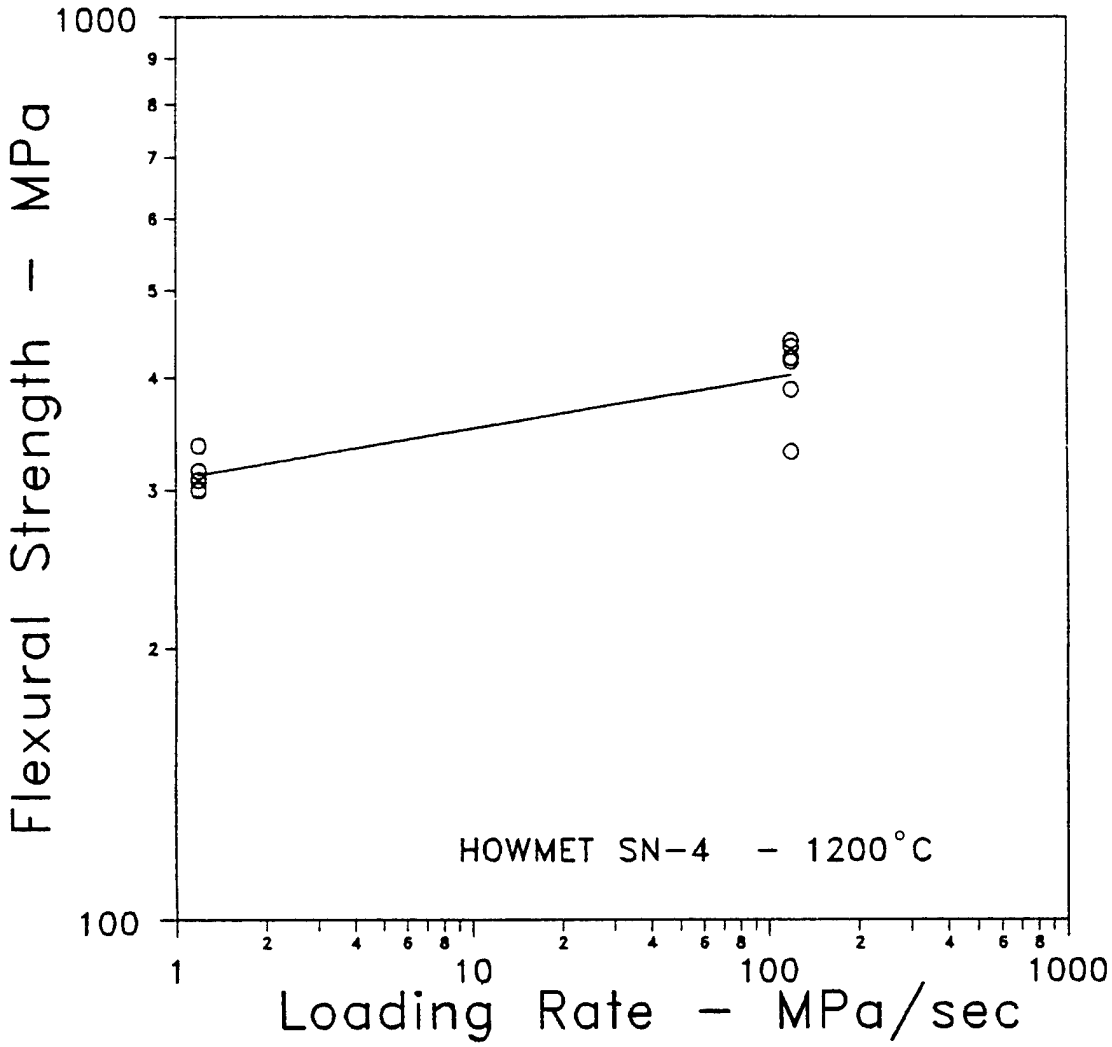
1000
9
8
7
6
5
4
3
2
100
Flexural Strength - MPa
HOWMET SN-4 - 1200°C
1
2
4
6
8
10
2
4
6
8
100
2
4
6
8
1000
Loading Rate - MPa/sec

APPENDIX 2

Flexural strength versus temperature reported by five different organizations for major candidate SiC/Si_3N_4 ceramics.

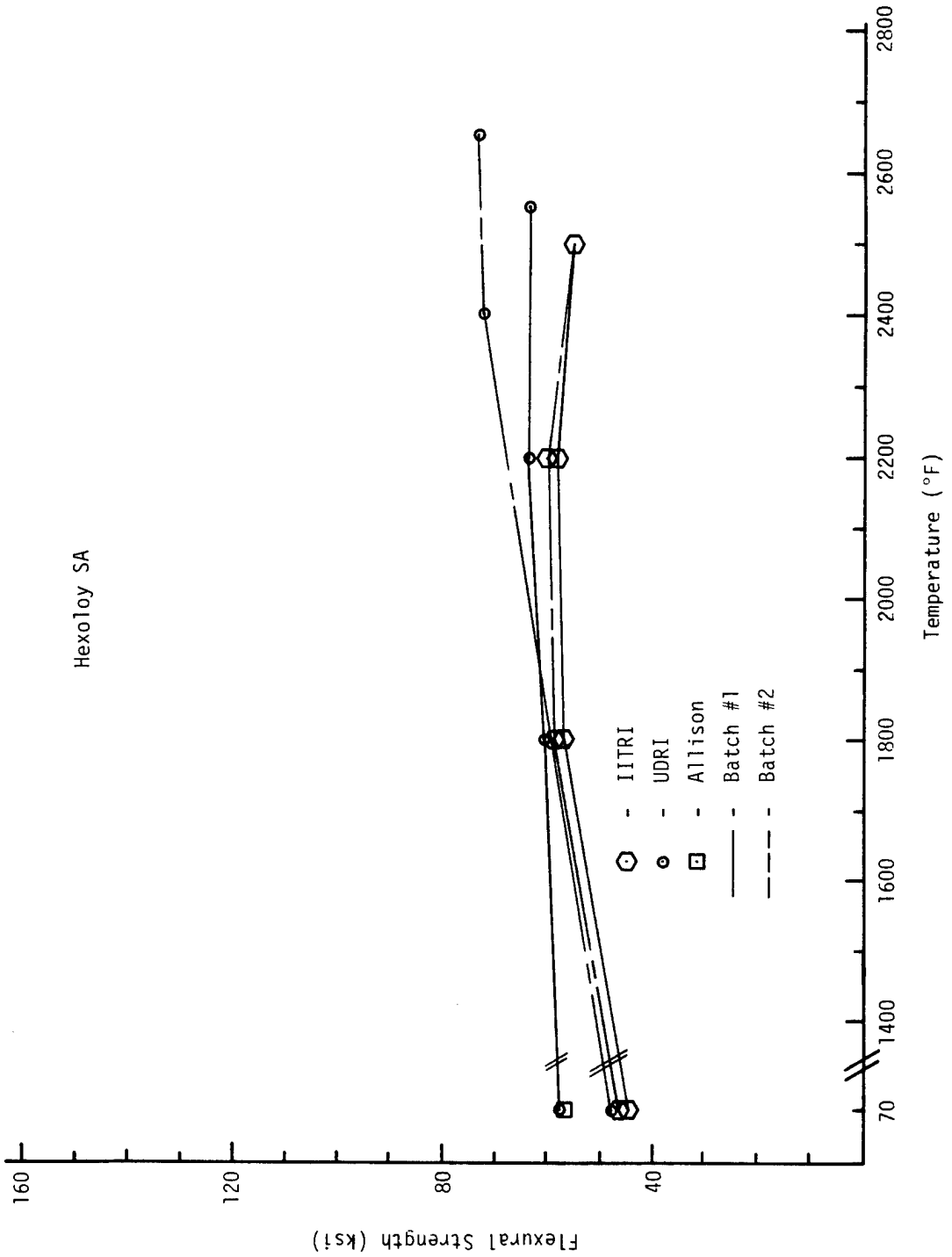
Hexoloy SA
Flexural Strength (ksi)
160
120
80
40
70
1400
1600
1800
2000
2200
2400
2600
2800
Temperature (°F)
- IITRI
- UDRI
- Allison
- Batch #1
- Batch #2

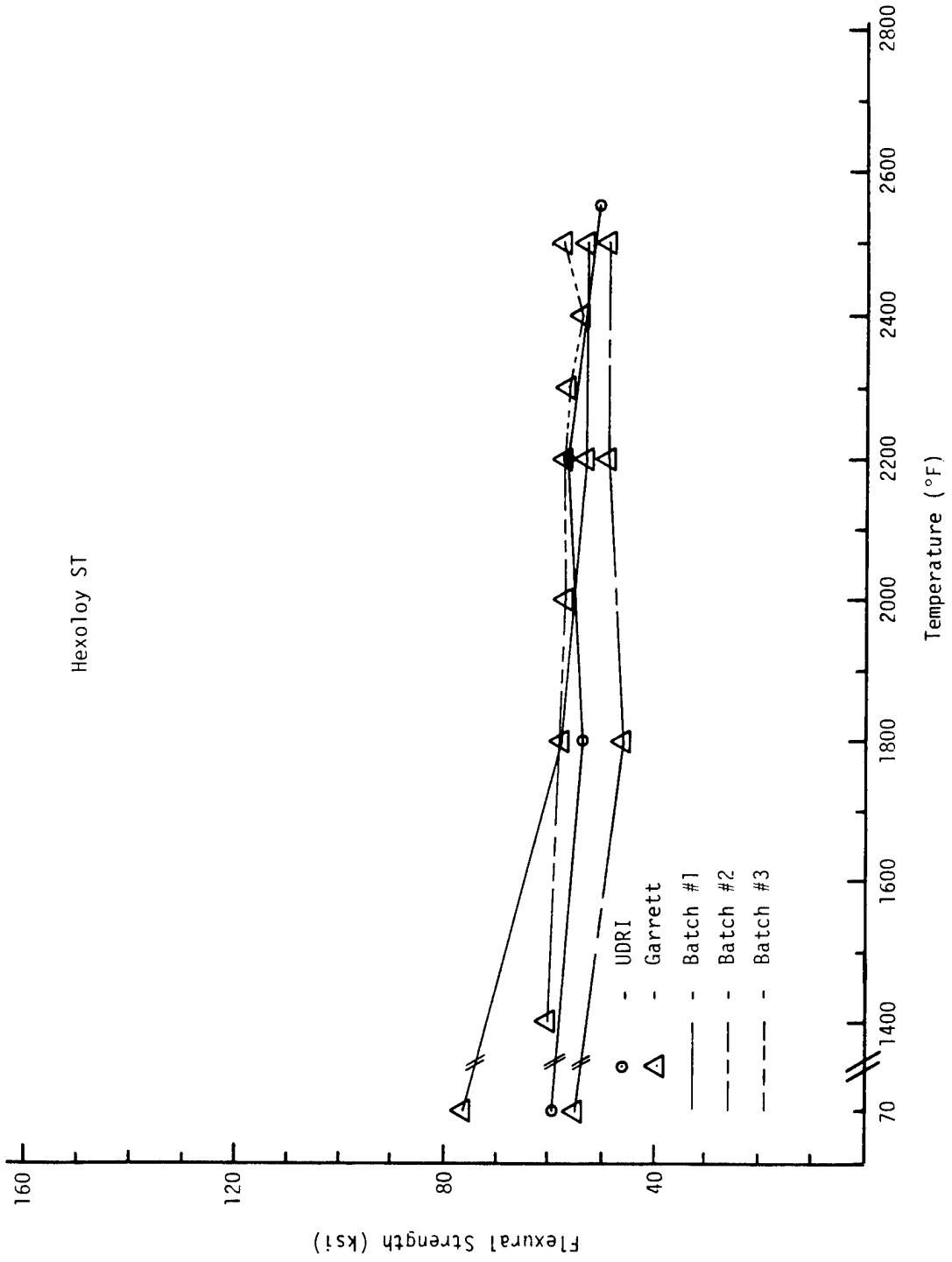
Hexoloy ST
Flexural Strength (ksi)
160
120
80
40
70
1400
1600
1800
2000
2200
2400
2600
2800
Temperature (°F)
- UDRI
- Garrett
- Batch #1
- Batch #2
- Batch #3

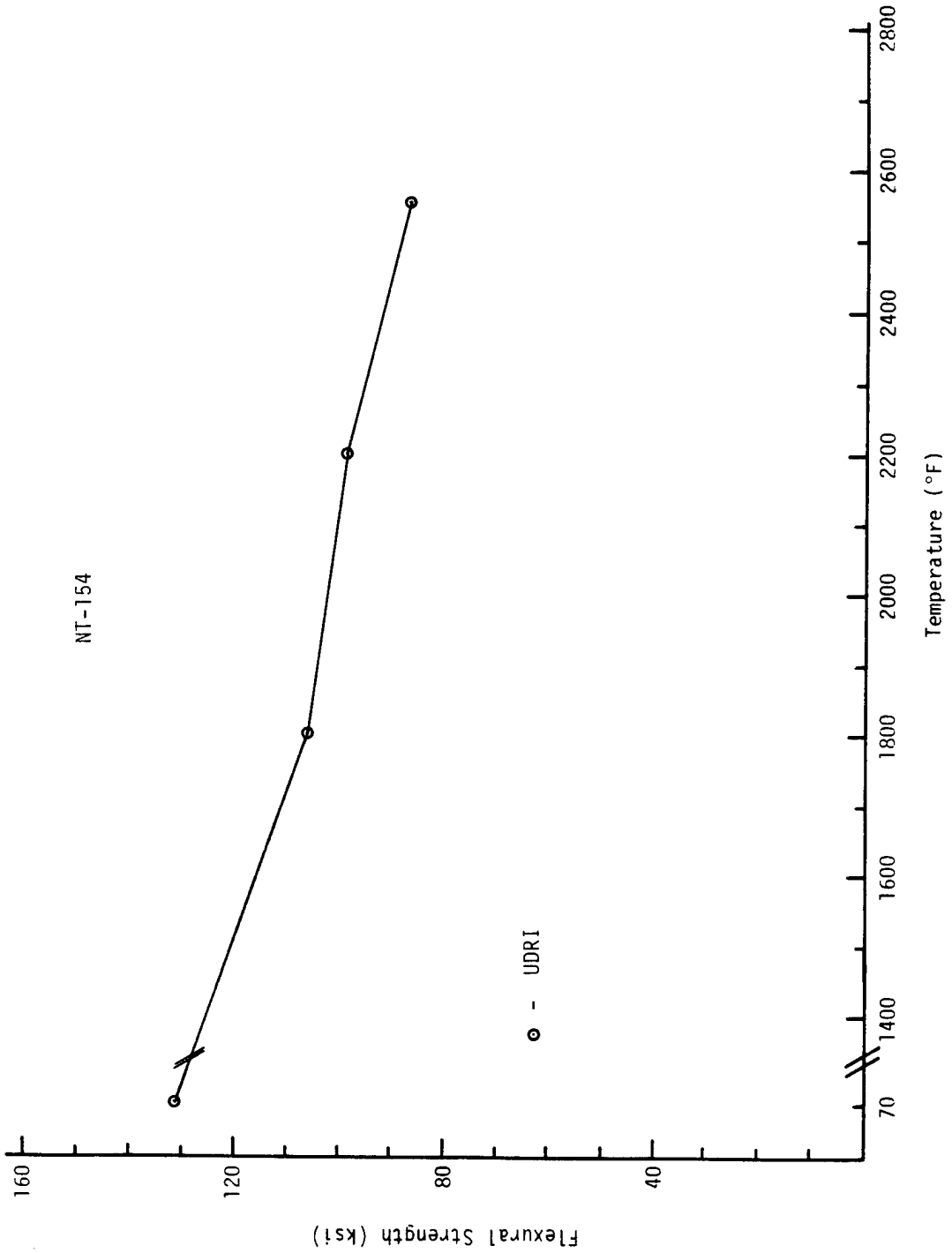
NT-154
⊙ - UDRI
Flexural Strength (ksi)
160
120
80
40
70
1400
1600
1800
2000
2200
2400
2600
2800
Temperature (°F)

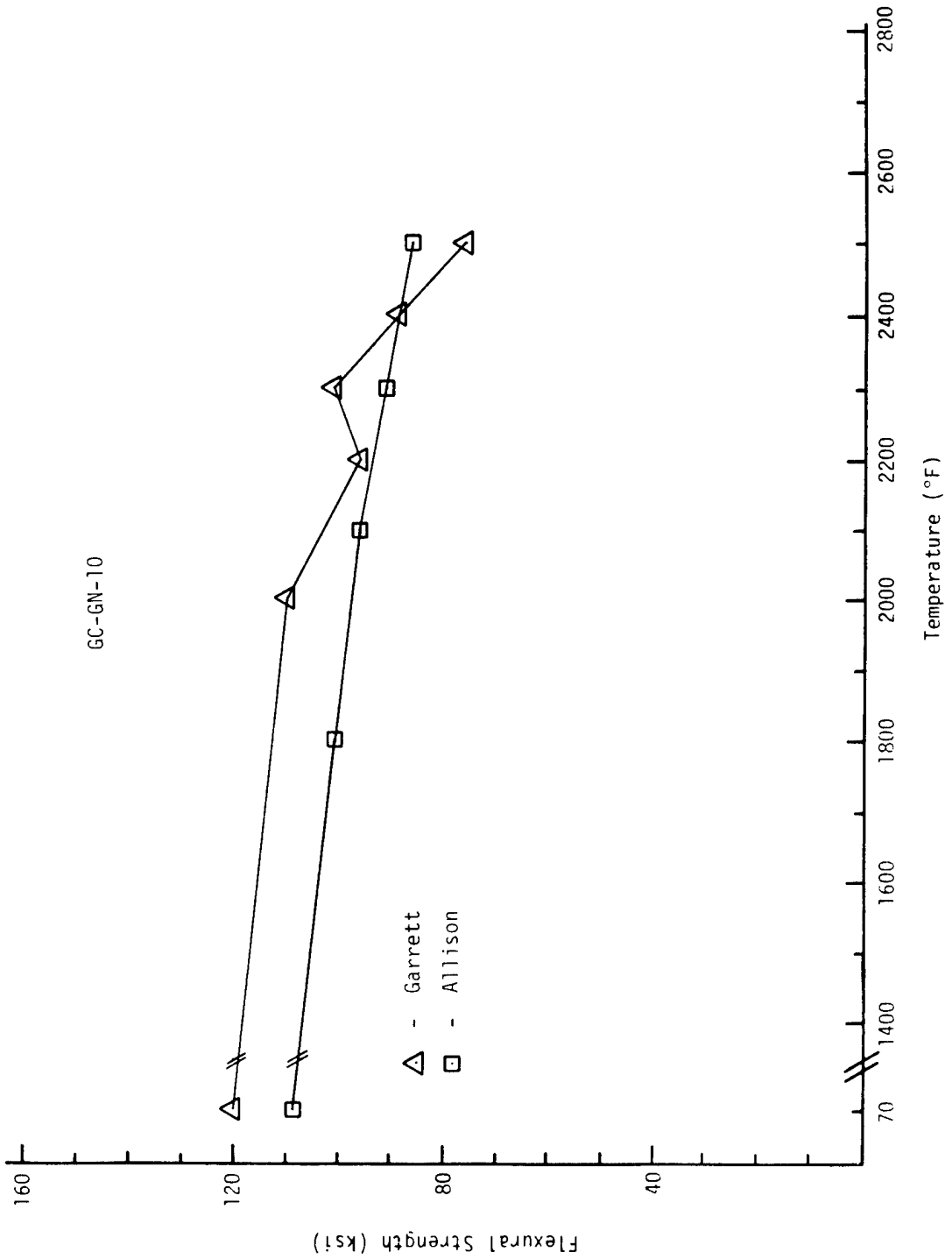
GC-GN-10
Flexural Strength (ksi)
160
120
80
40
70
1400
1600
1800
2000
2200
2400
2600
2800
Temperature (°F)
Δ - Garrett
□ - Allison

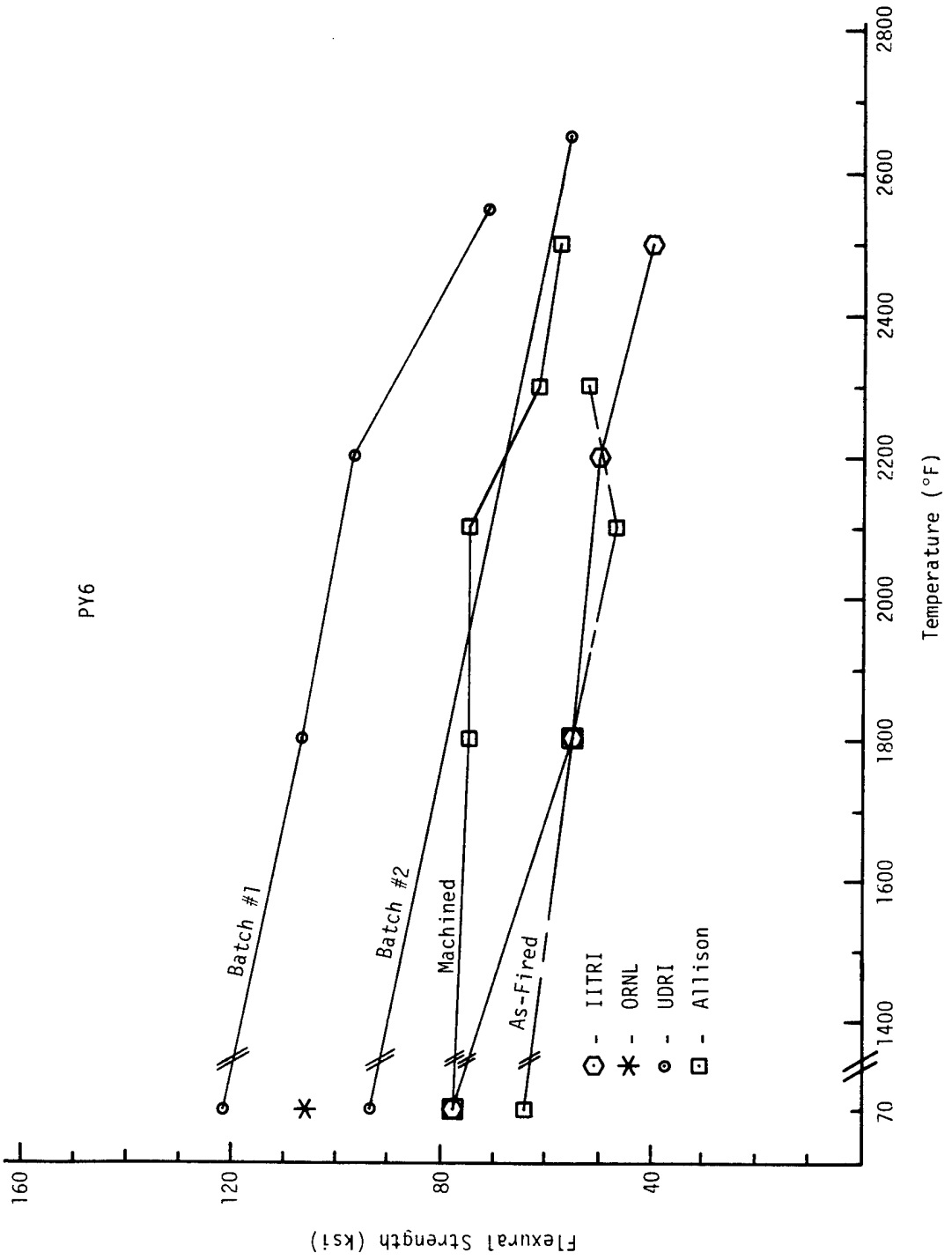
PY6
Batch #1
Batch #2
Machined
As-Fired
IITRI
ORNL
UDRI
Allison
Flexural Strength (ksi)
160
120
80
40
70
1400
1600
1800
2000
2200
2400
2600
2800
Temperature (°F)

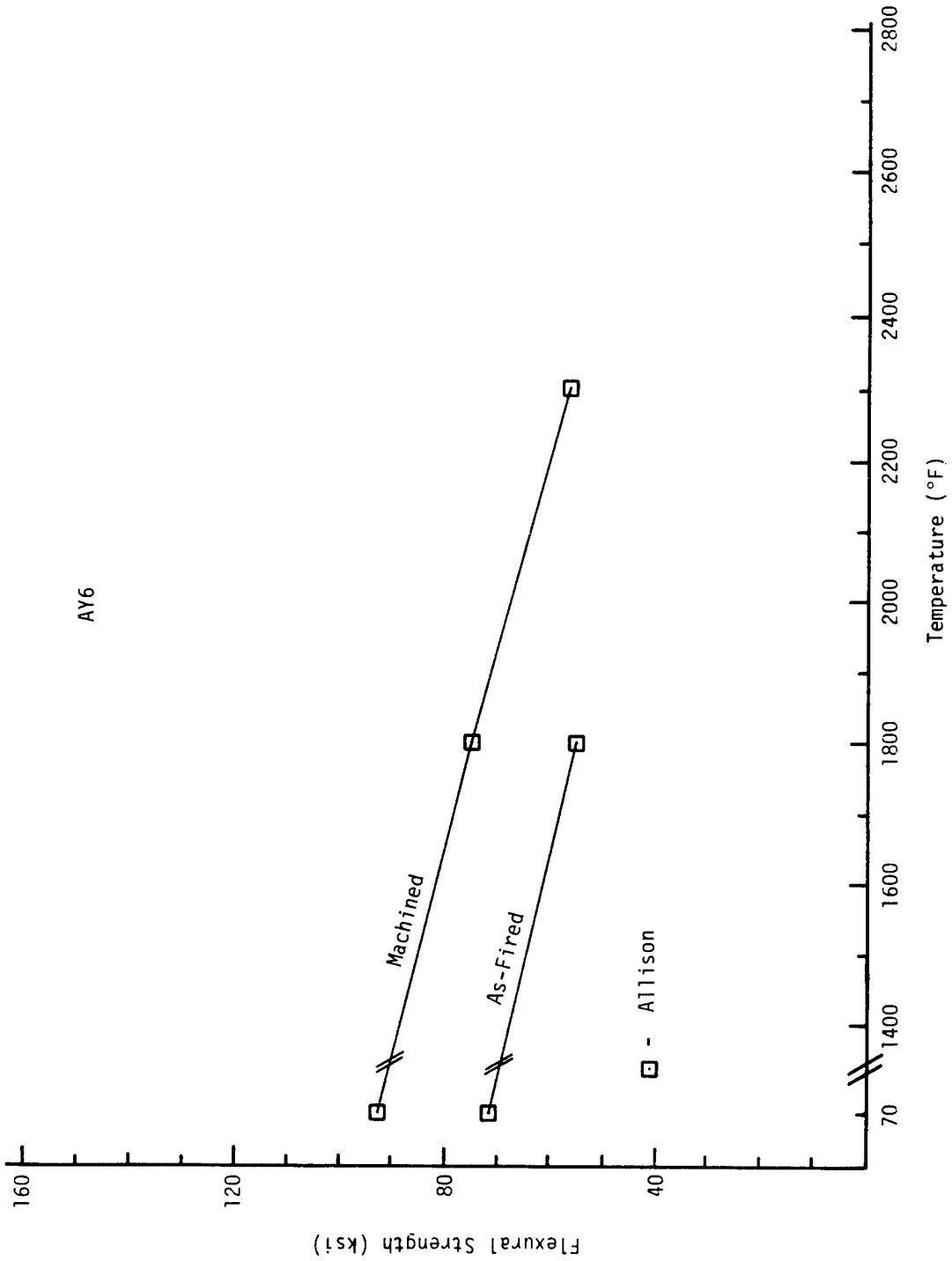
AY6
Machined
As-Fired
- Allison
Flexural Strength (ksi)
160
120
80
40
70
1400
1600
1800
2000
2200
2400
2600
2800
Temperature (°F)

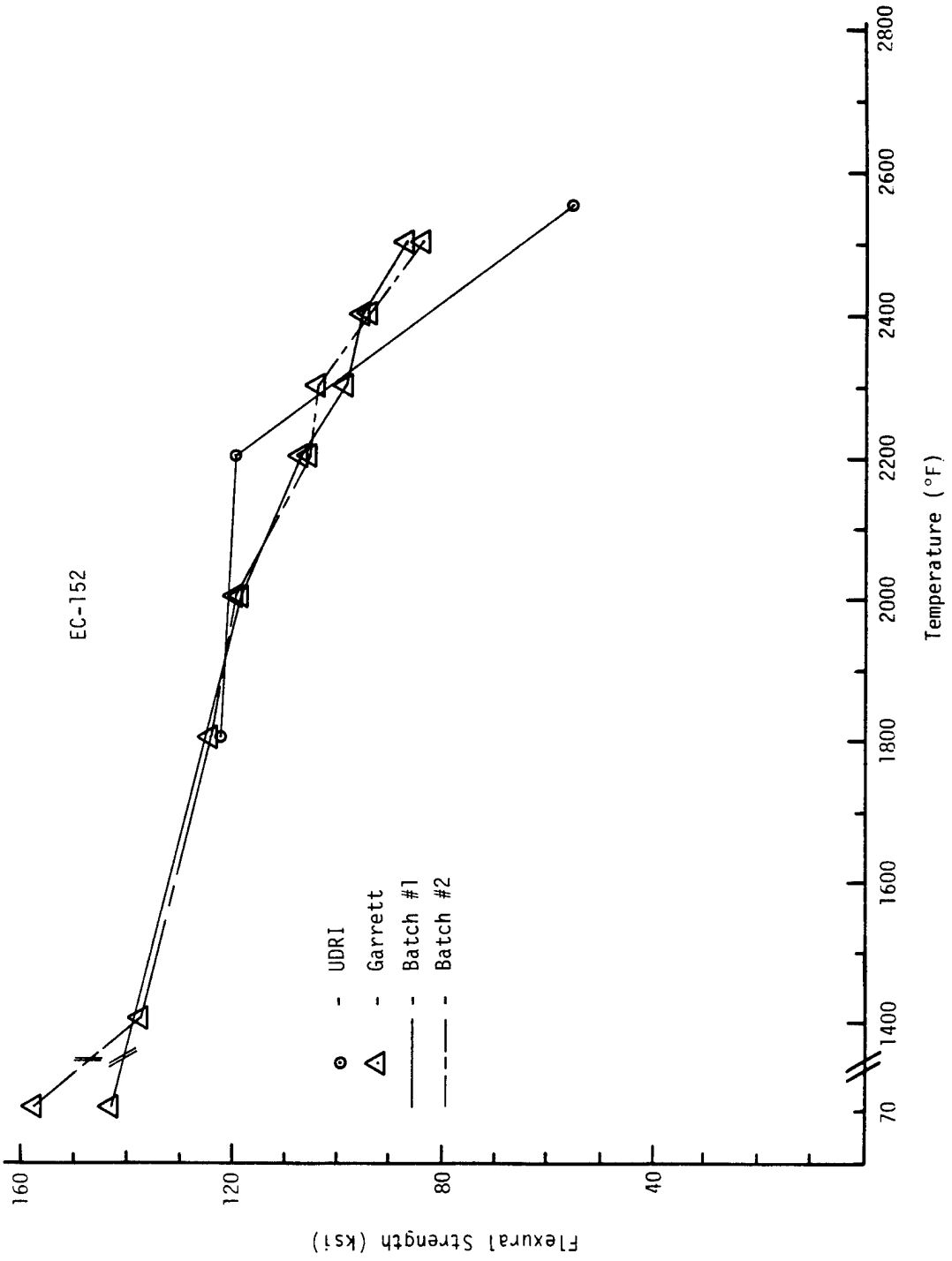
EC-152
Flexural Strength (ksi)
160
120
80
40
70
1400
1600
1800
2000
2200
2400
2600
2800
Temperature (°F)
⊙ - UDRI
△ - Garrett
——— - Batch #1
— — — - Batch #2

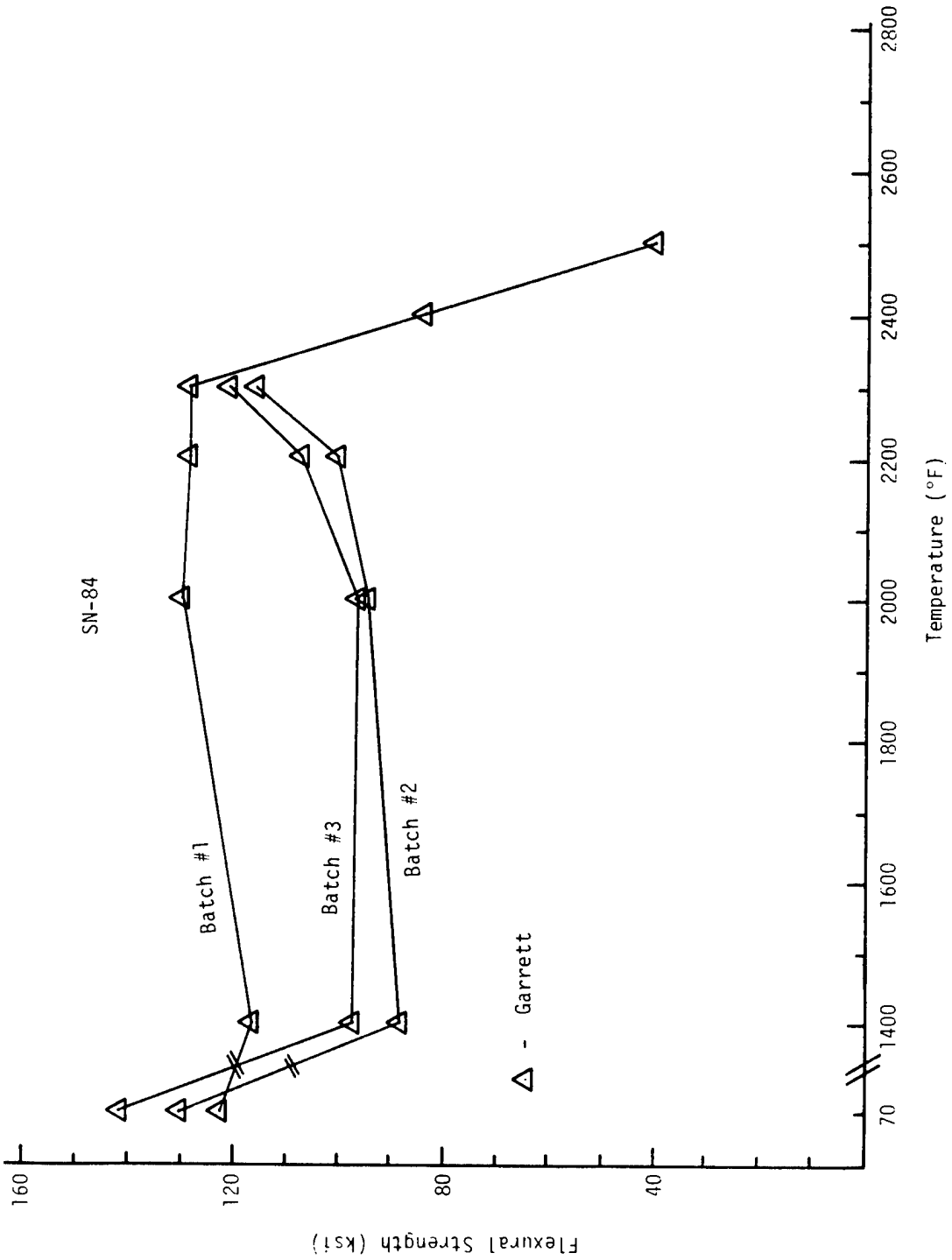
SN-84
Batch #1
Batch #3
Batch #2
Δ - Garrett
Flexural Strength (ksi)
160
120
80
40
70
1400
1600
1800
2000
2200
2400
2600
2800
Temperature (°F)

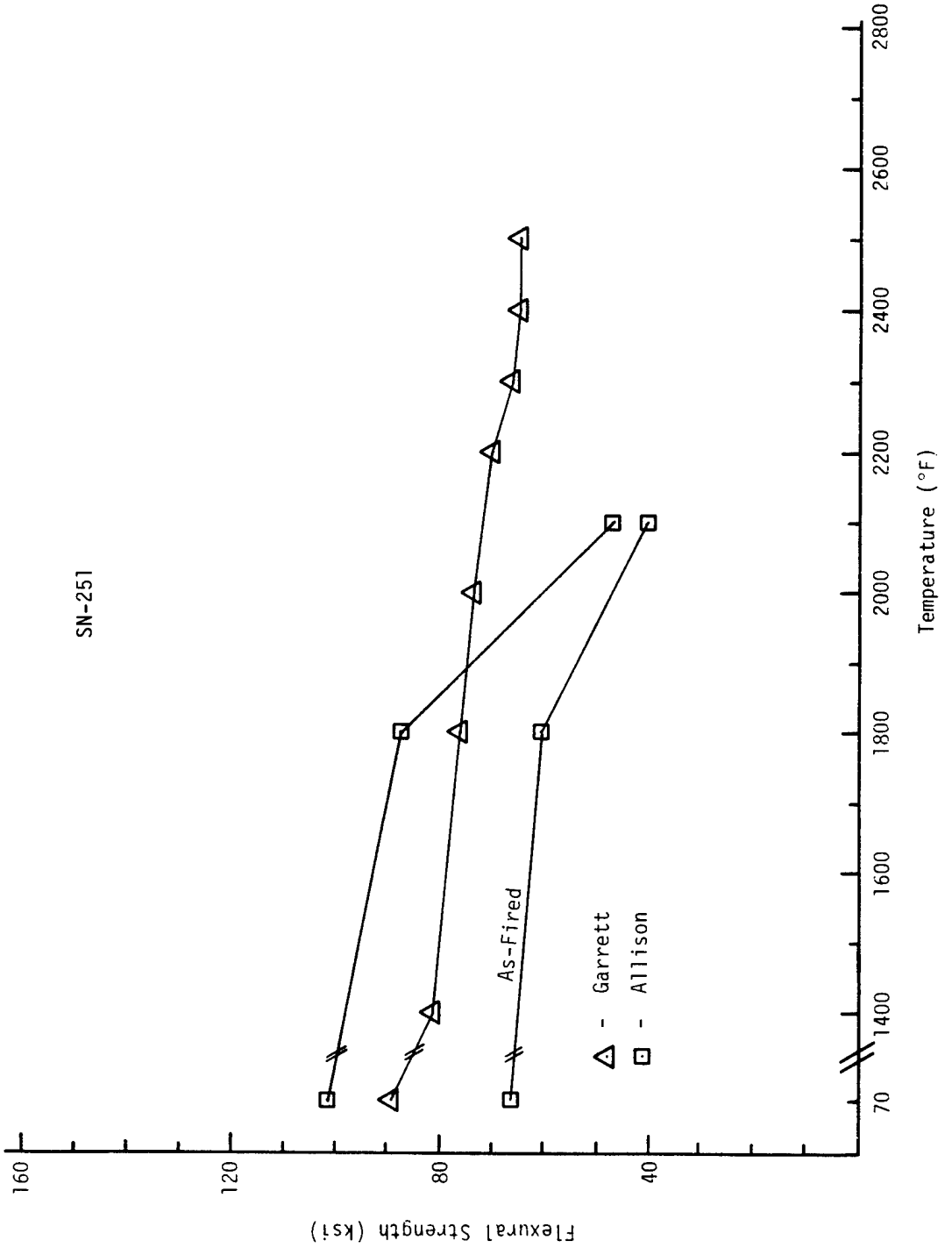
SN-251
As-Fired
Δ - Garrett
□ - Allison
Flexural Strength (ksi)
160
120
80
40
70
1400
1600
1800
2000
2200
2400
2600
2800
Temperature (°F)

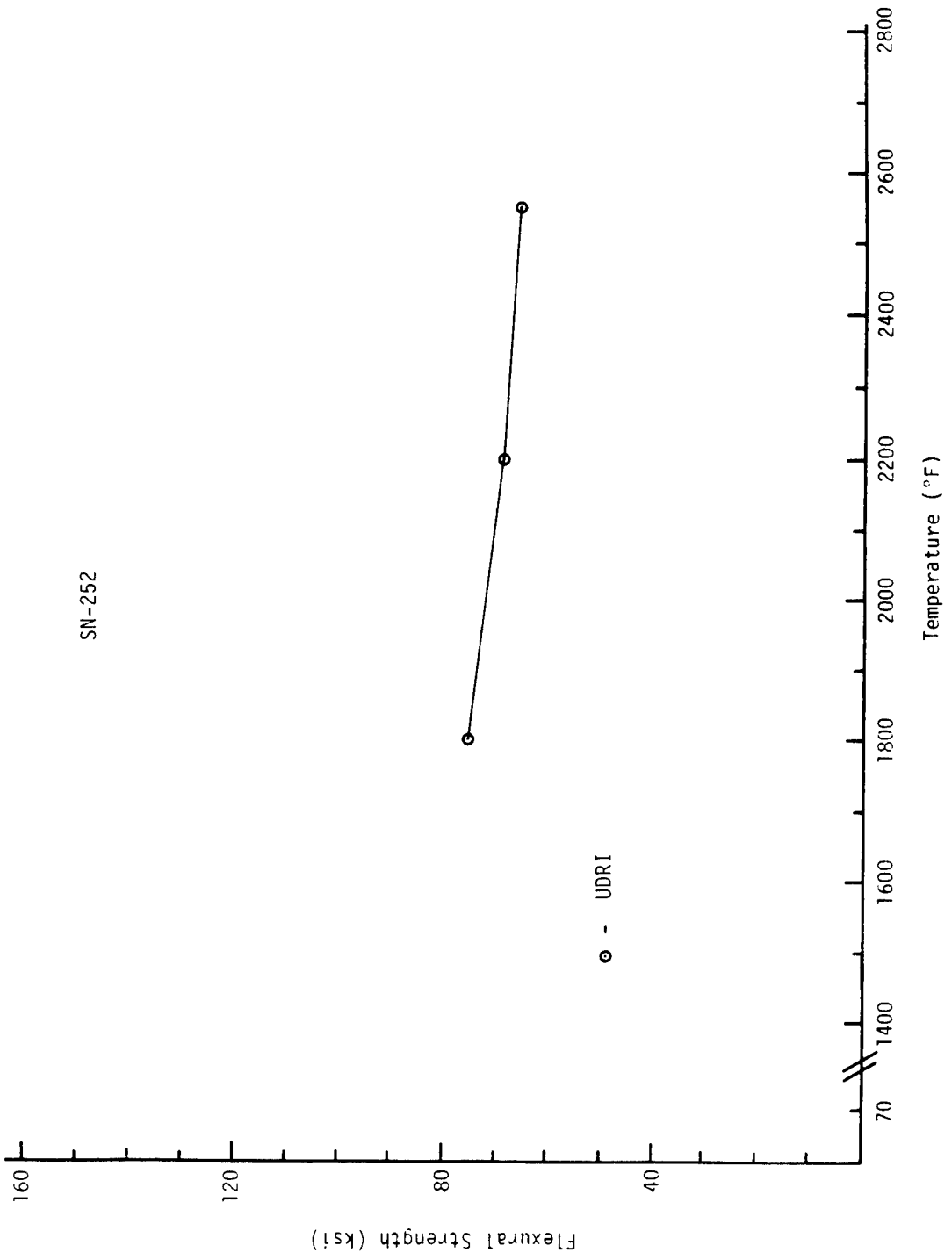
SN-252
⊙ - UDRI
Flexural Strength (ksi)
160
120
80
40
70
1400
1600
1800
2000
2200
2400
2600
2800
Temperature (°F)

Low Heat Rejection Diesel Coupon Test

C. R. Brinkman, G. M. Begun, R. L. Graves, W. K. Kahl, and K. C. Liu
(Oak Ridge National Laboratory)

Objective/scope

The objective of this task is to expose various structural ceramics to conditions found in a small diesel engine. Commercially available ceramics, as well as new candidate monolithic and whisker-toughened ceramics, will be fabricated into small modulus of rupture (MOR) bars, nondestructively examined, and exposed to a variety of operating conditions within a small diesel engine. Subsequent to exposure, the bars will be nondestructively and destructively examined and the results compared to an unexposed data base.

Technical progress

PSZ-TS

Four bars of this material were exposed to the combustion conditions of diesel engine No. 2, i.e., two-cylinder indirect-injection and air cooled, for 100 h. The engine burned a 50/50% blend of Philip's D-2 diesel fuel (reference) and an aromatic. The aromatic blend was a 53.5% (wt) Philip's Light Cycle Oil (LCO), and 46.5% (wt) Exxon Heavy Aromatic Naptha (HAN). Subsequent to exposure, the bars were subjected to Raman spectroscopy scans to determine any localized increases in apparent monoclinic content as was previously reported[1] for an engine which burned reference D-2 diesel fuel. Figure 1 is a plot of apparent* monoclinic content as a function of distance from the clamped or fixed end as held within the engine. North and South are designations assigned to each bar in order to define positioning within the engine. Figure 1 does show a localized increase in monoclinic content 12 to 15 mm from the clamped end of each bar.

Subsequent to Raman spectroscopy examination, the 50-mm bars were subjected to four-point bend rupture tests at room temperature. Results of these rupture tests were as follows:

Specimen number	Position in engine	Rupture strength (MPa)
PSZ-TS-70	North	544.66
PSZ-TS-145	South	532.74
PSZ-TS-142	South	499.05
PSZ-TS-143	North	427.68

The above comparisons with limited data indicates that position in the holder and thus orientation within the engine is not important.

*Percent monoclinic content assuming sample to be 100% monoclinic plus tetragonal.

Results from those four MOR tests are compared with the MOR control specimens (as fabricated) and 14 MOR results from bars exposed to the control diesel fuel environment in Table 1. The results are limited, but show that the synfuel environment was less deleterious to the strength, i.e., 15% decrease, than the control diesel fuel, i.e., 32%, in comparison to the as-fabricated material. Figure 2 is a Weibull plot comparing probability of failure of the fracture strengths of four bars exposed in the synfuel environment to the as-fabricated material.

PSZ-MS

A total of four bars of this material (MS-111, MS-112, MS-113, and MS-114) were exposed for 100 h in a diesel engine combustion environment. A synfuel mixture, as described above, again served as the fuel. Specific rupture values were as follows:

Specimen number	Position in engine	Rupture strength (MPa)
PSZ-MS-113	South	634.90
PSZ-MS-111	South	632.28
PSZ-MS-112	North	621.72
PSZ-MS-114	North	617.87

Results from four subsequent MOR tests conducted on the bars with similar tests conducted on bars exposed to the reference diesel fuel environment, and unexposed bars are shown in Table 1. Note that in this case, the reduction in strength (8-9%) is about the same regardless of the fuel in comparison to unexposed bar fracture strengths. Figure 3 is a Weibull plot comparing MOR results of the four bars previously exposed in the synfuel combustion environment with the unexposed or control material.

Figure 4 is a photograph showing the fracture locations of both the TS and MS grade materials that was given engine exposure. The MS grade materials shows random fracture locations whereas the TS grade fractures occurred near the upper loading points. Specimens TS-70 and TS-143 fractured about 15 mm from the cold or clamped end of the bar, coinciding with the location of maximum monoclinic content as shown in Fig. 1.

Silicon Nitride (WESGO SNW-1000)

A total of 12 bars has now been exposed for 100 h in the reference diesel fuel combustion environment. These bars have all been subject to four-point bend rupture at room temperature, and results are compared in Table 2 with unexposed or control fracture data. The comparison given in Table 1 shows a slight (7%) increase in mean fracture strength in comparison to the unexposed material. Figure 5 is a Weibull plot comparison of the exposed and unexposed rupture strengths. Results from fractographic analysis will be given in a subsequent report.

It should be mentioned that this particular lot of material was considerably weaker than the lots employed in the International Energy Agency investigation.

In that study, the following statistical information was obtained.

Mean strength: 652.3 MPa
Standard deviation: 73.8 MPa
Number of data results: 877
Weibull modulus:
Maximum likelihood: 10.47
Linear regression: 10.73

The manufacturer was contacted regarding the decreased strength of this lot (#174-MA-1607). He reported that this lot had been reheated to the sintering temperature. Ultrasonic inspection of the lot being used in this study (72 specimens) has indicated that all bars contained numerous indications. Some of which suggested voids larger than the 50 μm voids typical of sintered material. Surface wave results also detected numerous near-surface voids.

References

1. C. R. Brinkman et al., *Influence of Diesel Engine Combustion on the Rupture Strength of Partially Stabilized Zirconia*, ORNL-6513, Oak Ridge National Laboratory, Oak Ridge, TN, December 1988.

Table 1. Rupture strength of SNW-1000

Specimen number	Position in engine	Rupture strength (MPa)
SNW-1000-1	North	533.9
2	South	515.4
3	North	508.5
4	South	566.3
5	North	517.1
6	South	527.8
7	North	535.4
8	South	577.7
9	North	561.1
10	South	542.0
11	South	557.3
12	North	576.6

Table 2. Results of four-point bend tests[a] conducted on MOR bars of several different materials

Number of observations	Material condition	Weibull modulus		y-intercept		Average strength (MPa)	Standard deviation (MPa)	Reduction in average[b] strength (%)
		Linear regression	Maximum likelihood	Linear regression	Maximum likelihood			
				PSZ-TS				
53	As fabricated	31.7	48.6	-202.7	-310.2	587.3	20.3	0
4	Engine-exposed for 100 h[c]	10.4	15.3	-65.3	-95.5	501.0	52.6	15
14	Engine-exposed for 100 h[e]	3.5	4.2	-21.6	-25.4	401.8	120.5	32
				PSZ-MS				
40	As fabricated	29.2	29.7	-191.1	-194.5	682.9	28.6	0
4	Engine-exposed for 100 h[c]	85.4	100.0	-550.8	-644.4	626.7	8.2	8
20	Engine-exposed for 100 h[e]	19.8	22.0	-124.7	-141.9	625.0	38.7	9
				GTE Wesgo SNW-1000[d]				
40	As fabricated	10.8	11.2	-67.8	-70.5	506.5	56.3	0
12	Engine-exposed for 100 h[e]	26.4	26.2	-166.8	-165.3	543.3	24.1	7[f]

[a]Tests were conducted with a crosshead speed of $8.47 * 10^{-3}$ mm/s or a strain rate of $1.1 * 10^{-4}$ s^{-1}.

[b]Reduction in strength in comparison to as-fabricated material.

[c]Fuel was a 50/50% blend of Phillip's D-2 Diesel Fuel (reference fuel) and an aromatic blend.

[d]Material from lot number 174-MA-1607 and re-heat-treated to sintering temperature.

[e]Fuel was control diesel (reference fuel).

[f]Increase.

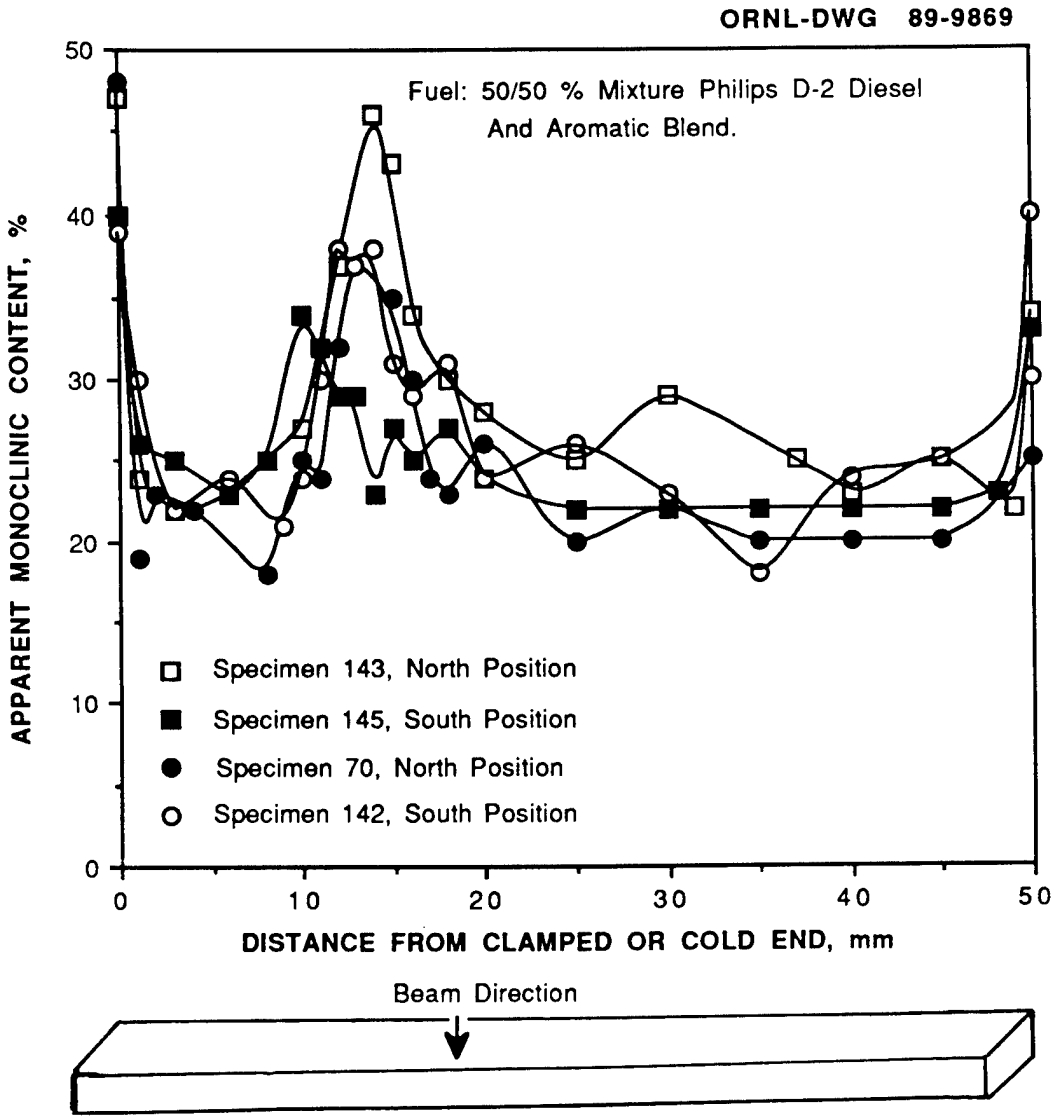

Fig. 1. Raman spectroscopy scans of PSZ-TS grade bars exposed for 100 h in diesel engine No. 2.

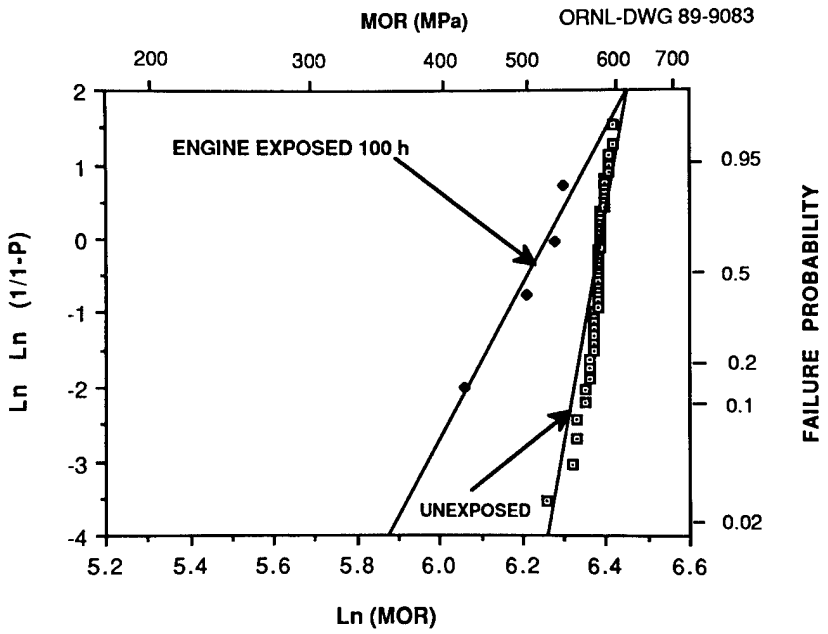

Fig. 2. Weibull plot comparing fracture strengths of four specimens (TS-70, TS-142, TS-143, and TS-145) of Nilcra PSZ-TS grade previously exposed for 100 h in diesel engine burning a synfuel mixture with fracture strengths of unexposed or control material. All tests were performed at room temperature.

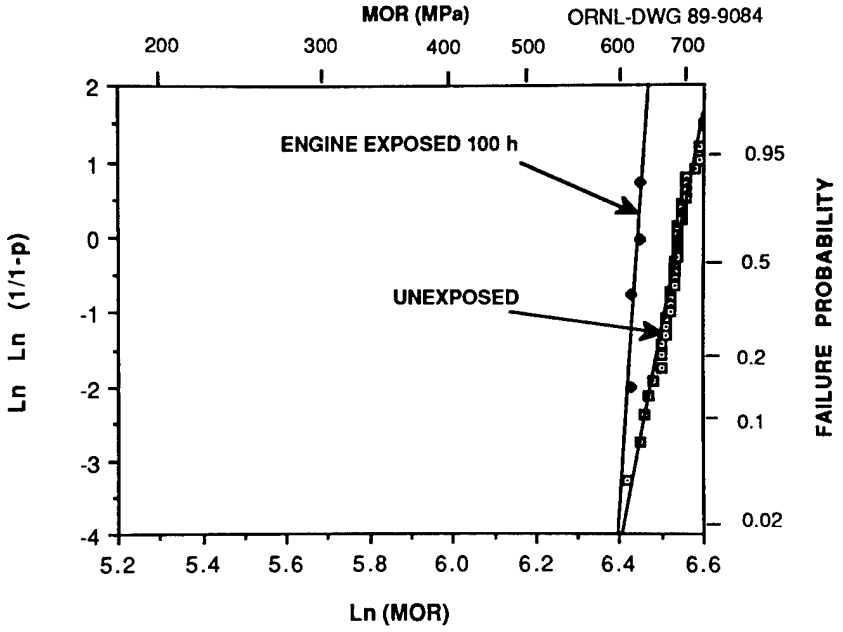

Fig. 3. Weibull plot comparing fracture strengths of four specimens (MS-111, MS-112, MS-113, and MS-114) of Nilcra PSZ-MS grade, previously exposed for 100 h in a diesel engine burning a synfuel mixture with fracture strengths of unexposed or control material. All tests were performed at room temperature.

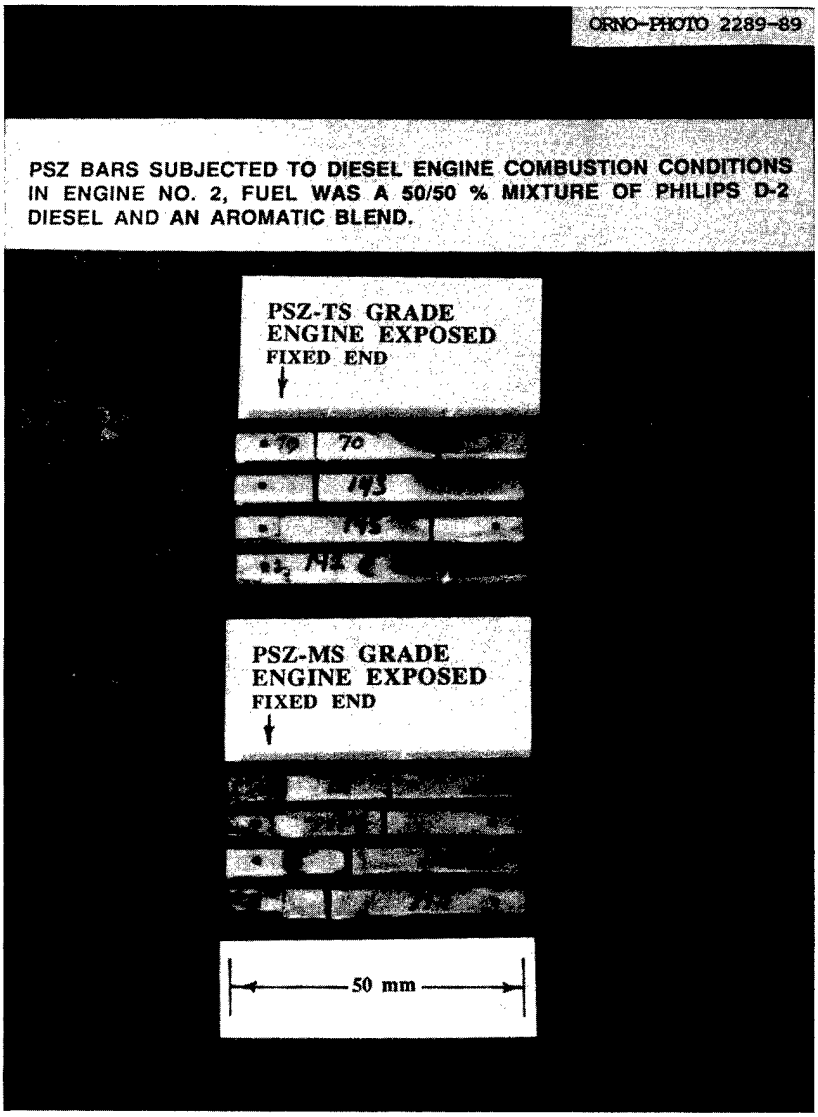

Fig. 4. Photograph of bars showing locations of rupture in four-point bending following engine exposure.

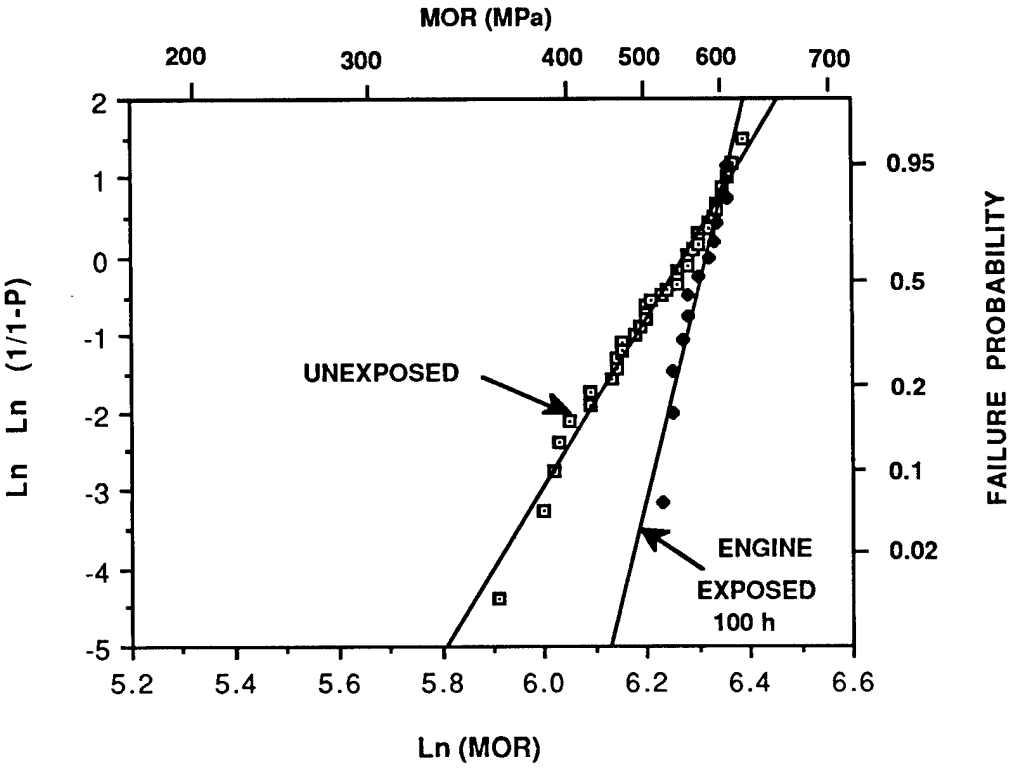

Fig. 5. Weibull plot comparing fracture strengths of twelve silicon nitride (WESGO SNW-1000) bars exposed for 100 h in a reference diesel fuel combustion environment with similar results from unexposed material.

3.4 FRACTURE MECHANICS

Testing and Evaluation of Advanced Ceramics at High Temperature in Uniaxial Tension

J. Sankar, A. D. Kelkar, and V. S. Avva (North Carolina A&T State University)

Objective/scope

The purpose of this effort is to test and evaluate advanced ceramic materials at temperatures up to 1500°C in uniaxial tension. Testing may include fast fracture strength, stepped static fatigue strength, along with analysis of fracture surfaces by scanning electron microscopy. This effort is comprised of the following tasks:

Task 1: Specifications for testing machine and controls plus procurement
Task 2: Identification of test material(s) plus procurement of specimens
Task 3: Identification of test specimen configuration
Task 4: Specifications for testing grips and extensometer plus procurement
Task 5: Specifications for testing furnace (procurement) and controls
Task 6: Development of test plan
Task 7: High temperature tensile testing
Task 8: Reporting (periodic)
Task 9: Final report

It is anticipated that this program will help in understanding the behavior of ceramic materials at very high temperatures in uniaxial tension.

Technical progress

During the reporting period, efforts were undertaken to study the creep rupture characteristics of sintered silicon nitride in the temperature range of 1000 to 1200°C in uniaxial tension. Efforts also are underway to create an inhouse testing program for this test, to be run on the Micro-PDP/11 computer attached to the MTS 880 testing machine. These tests are expected to give an idea of the strength characteristics of sintered silicon nitride in the elevated temperature ranges.

Status of milestones

Tasks 1-7 are complete.

Standard Tensile Test Development

S. M. Wiederhorn, T.-J. Chuang, Weijun Liu and D. E. Roberts
(The National Institute of Standards and Technology)

Objective/scope

This project is concerned with the development of test equipment and test procedures for measuring the tensile strength and creep resistance of ceramic materials to tensile stresses at elevated temperatures. Inexpensive techniques of measuring the creep and strength of ceramics at elevated temperatures are being developed and will be used to characterize the mechanical behavior of structural ceramics. The test methods will use self aligning fixtures, and simple grinding techniques for specimen preparation. Creep data obtained with tensile test techniques will be compared with data obtained using flexure and compressive creep techniques. The ultimate goal of the project is to assist in the development of a reliable data base and a methodology that can be used for structural design of heat engines for vehicular applications.

Technical progress

During the past six months, the creep and creep rupture behavior of hot-pressed silicon nitride, reinforced with SiC whiskers was studied as a function of applied stress and temperature. This work is being conducted in collaboration with Dr. J. G. Baldoni of the GTE Laboratories in Waltham, MA. The objective of this work is to evaluate the effect of silicon carbide whisker re-enforcement on the creep behavior and the lifetime of these composite materials.

Experimental Technique - The silicon nitride matrix was similar to the AY6 grade sold by GTE. The composite contained approximately 30 volume percent silicon carbide whiskers which were used for reinforcement. Dog-bone specimens, figure 1, developed as part of our tensile creep program were used in this study. The hot pressing direction of the billets used to make the test bars was perpendicular to the tensile axis. To assure failure of the test specimens within the gauge section of the tensile specimens, the gauge section was defined by surface grinding the central portion of the specimen with a 38 mm diameter grinding wheel so as to reduce the total thickness of the gauge section to ≈2mm. This reduction of gauge section represents a minor modification of the specimen geometry discussed in previous reports, figure 1. The width and length of the gauge sections were approximately 2.5mm and 10mm respectively.

Creep tests were conducted using the tensile equipment developed in an earlier phase of the project. The gauge length of the test specimen was monitored by placing small α-SiC flags on the central portion of the test specimen. The position of the flags were monitored as a function of time with a laser extensometer,

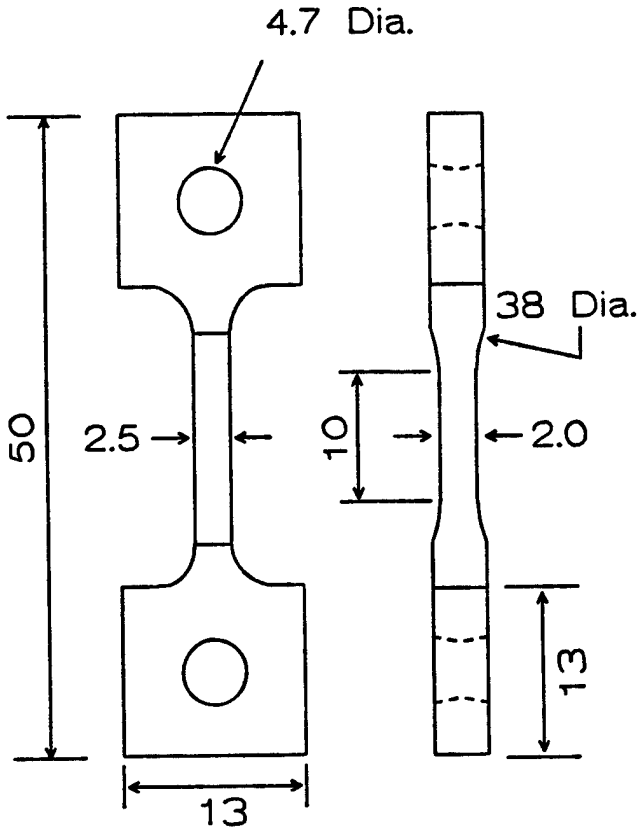

1. The major and minor faces of the flat dogbone-shaped tensile specimen. All dimensions are in millimeters. This figure is not drawn to scale.

which was capable of an accuracy of better than ±1μm in the measurement of distance between the two flags. This level of accuracy resulted in an accuracy of ±2μm in the displacement measurements during the evaluation of creep curves for each specimen. Details of the experimental apparatus will be published shortly (D. F. Carroll, S. M. Wiederhorn and D. E. Roberts, "A Technique for Tensile Creep Testing of Ceramics," J. Am. Ceram. Soc.).

In these studies, the test temperature ranged from 1100°C to 1250°. Tests were conducted in air, with a short ≈24 hour anneal to assure thermal equilibrium within the test furnace prior to application of the stress. After application of the stress, most specimens were permitted to creep to failure so that both the creep and creep rupture behavior as a function of applied stress and temperature could be determined. Preliminary studies were conducted on specimens exposed to temperature and applied stress for periods up to ≈400 hours. As transient effects were observed for periods exceeding ≈500 hours, some tests were also conducted on specimens that were pre-annealed in air for periods of ≈500 hours.

After testing, specimens were examined by optical and transmission electron microscopy to clarify the modes of deformation and fracture of this material. The results of this microstructural analysis is presented in a companion to this report [3.1, Microstructural Analysis of Structural Ceramics (NIST)]] and will not be discussed in detail here.

Results and Discussion - Although there was variability in the appearance of the creep data, a typical creep curve for this material is shown in figure 2a. As can be seen, a transient period of approximately 1/3 the total lifetime is followed by a linear curve indicating a long stable period of steady state creep. Of the 16 specimens tested to failure, only two gave any indication of tertiary creep, figure 2b, which was manifested by a small increase in the slope of the creep curve prior to failure. For the remaining specimens failure occurred without enhancement of the creep rate. For four of the specimens an inverse primary creep stage was observed, figure 2c. As such behavior could be a consequence of a small amount of bending due to misalignment of the loading pins in the holes prior to stress application, these inverse primary creep curves are probably an artifact of the experiment. For the same reason, curves with greatly enhanced primary creep stages may also be a consequence of specimen bending. Nevertheless, all of the curves exhibited an extended steady state creep behavior so that measurement of the steady state creep rate on the specimens studied was unequivocal.

For creep times >500 hours, the steady state creep rate was observed to be irreversible. This effect is illustrated in figure 3, which shows the creep curve for a specimen stressed at 1200°C for three different applied stresses. Application of 30 MPa to the specimen for >500 hours suggests a steady state creep rate of $\approx 1.3 \times 10^{-9}$ 1/s. After increasing the stress to 50 MPa, the specimen

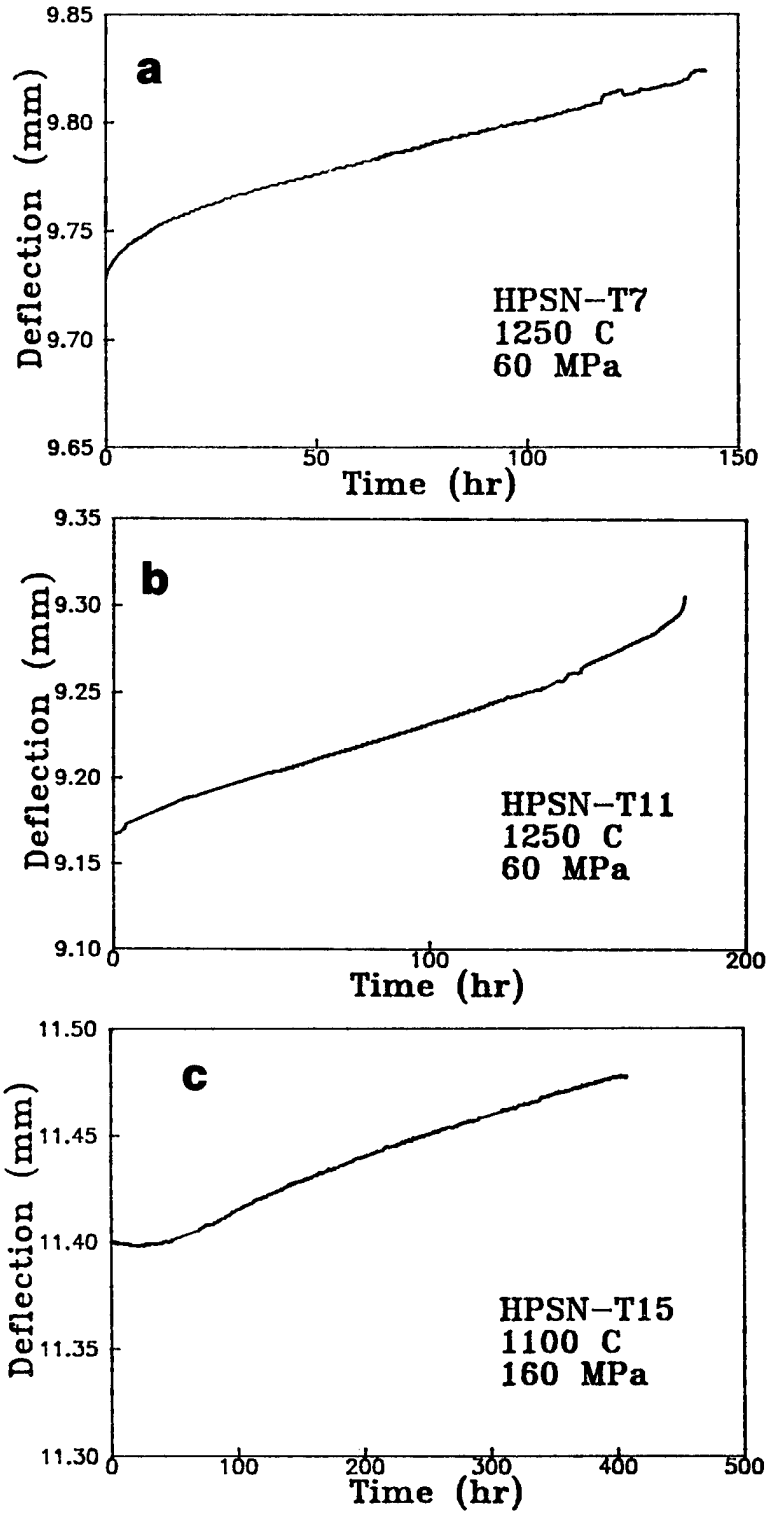

2. Typical creep curves for whisker reinforced silicon nitride: (a) curve shape representing most of the data; (b) curve showing some tertiary behavior; (c) curve showing an inverse primary stage (believed to be an artifact of the experiment). Note that all curves show relatively distinct secondary creep.

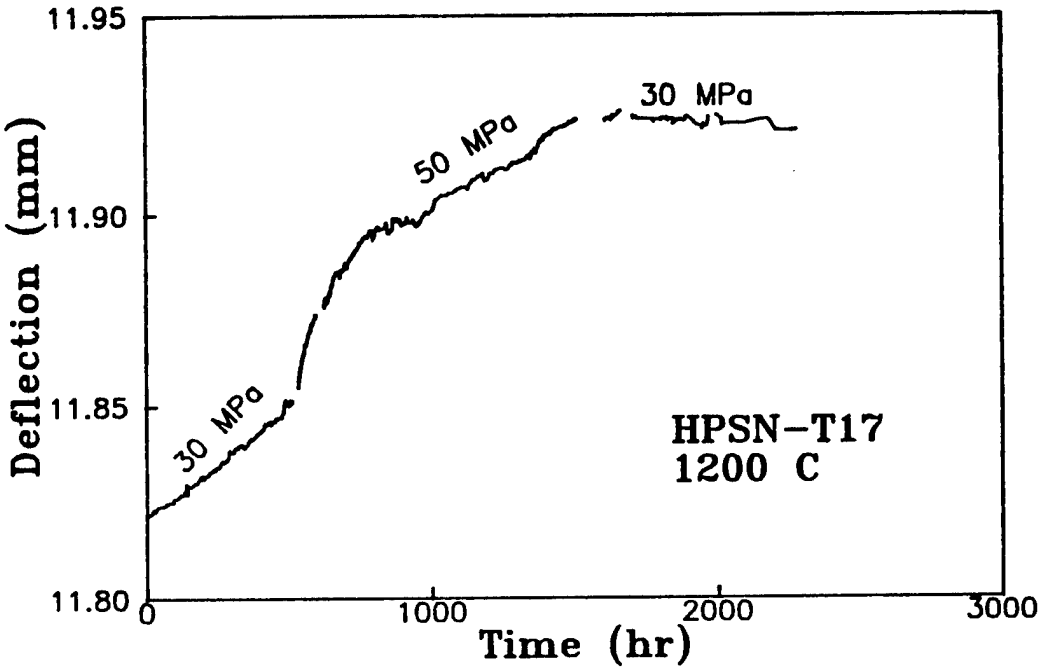

3. Effect of applied stress on the creep behavior. As the creep rate at 50 MPa is lower than that measured initially at 30 MPa, the effect of increasing the applied stress appears to be irreversible. This observation is confirmed by the fact that the creep of the material appears to arrest after decreasing the applied stress from 50 MPa to 30 MPa.

underwent a long transient creep period followed by a second steady state creep rate with a creep rate of $\approx 1.02 \times 10^{-9}$ 1/s, so that the steady state creep rate decreased despite the increase in stress, a behavior that is possible only if some sort of phase modification (probably devitrification of the bonding phase) as a consequence of the increase in stress. To confirm the permanent change in the creep behavior of the material, the stress was reduced to 30 MPa and the specimen subjected to creep deformation for ≈190 hours with no detectable creep displacement. As the apparatus is sensitive to $\pm 2\mu$m, and the gauge length was ≈10mm, the maximum creep rate during this period was calculated to be 3×10^{-10} 1/s, which is about one-third that measured at first application of stress. Until transmission microscopy studies are completed on these specimens, our explanation of the creep observations are of necessity vague. As such modifications of the microstructure are expected in materials like silicon nitride, investigations of these processes will continue.

A summary of the steady state creep rate as a function of applied stress is shown in figure 4. The most complete set of data was collected at 1250°C; it shows the creep data fits a straight line with a slope of ≈3 for creep rates $<10^{-8}$ 1/s. A small increase in the slope is apparent at creep rates $>10^{-8}$ 1/s. Data collected at 1200°C lie roughly parallel to the data collected at 1250°C for creep rates $>10^{-9}$ 1/s. The data collected on the specimen that appeared to be affected by the phase transformation are also plotted on the graph (filled in squares). We note that the creep rate measurement made at 50 MPa is in line with the data collected at higher creep rates, whereas the creep rate measured at 30 MPa does not lie on the curve. Data collected at 1150°C seems to have slope that is less than that collected at the higher temperatures.

Creep rupture data representing the specimens tested to failure in the present study indicate that regardless of temperature or applied stress, the lifetime of the specimens can be correlated with the minimum creep rate for the entire range of failure times, figure 5. This finding is similar to that obtained for metals in which the failure time is an inverse function of the creep rate. As the failure time is related to a material property (i.e. the steady state creep rate), such curves have been used to develop new metallic alloys for high temperature application, and should be of similar value for ceramic materials. Unlike the curves obtained for metals, however, the curve shown in figure 5 has a slope with an absolute value of less than 1, which suggests that the critical strain criterion used to explain the creep rupture life of metals cannot be employed for this ceramic. Other ceramic materials studied by the authors have also been shown to have slopes with absolute values of less than 1. A microstructural analysis of the specimens that have been tested to date will be required for the development of a deeper understanding of the fracture process. Such studies are currently underway.

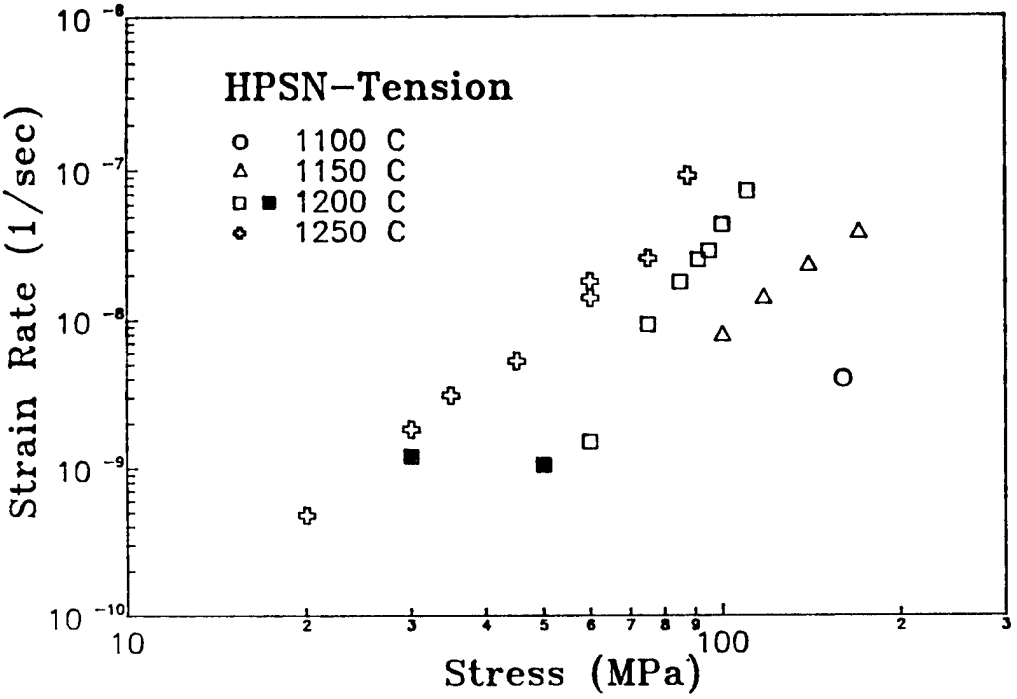

4. Summary of the steady state creep rate as a function of applied stress. The creep rate is observed to increase as the temperature is increased. The slope of the creep curve at 1250°C is ≈3. The two data points at 1200°C, given by the filled-in squares are from the creep curves in figure 3.

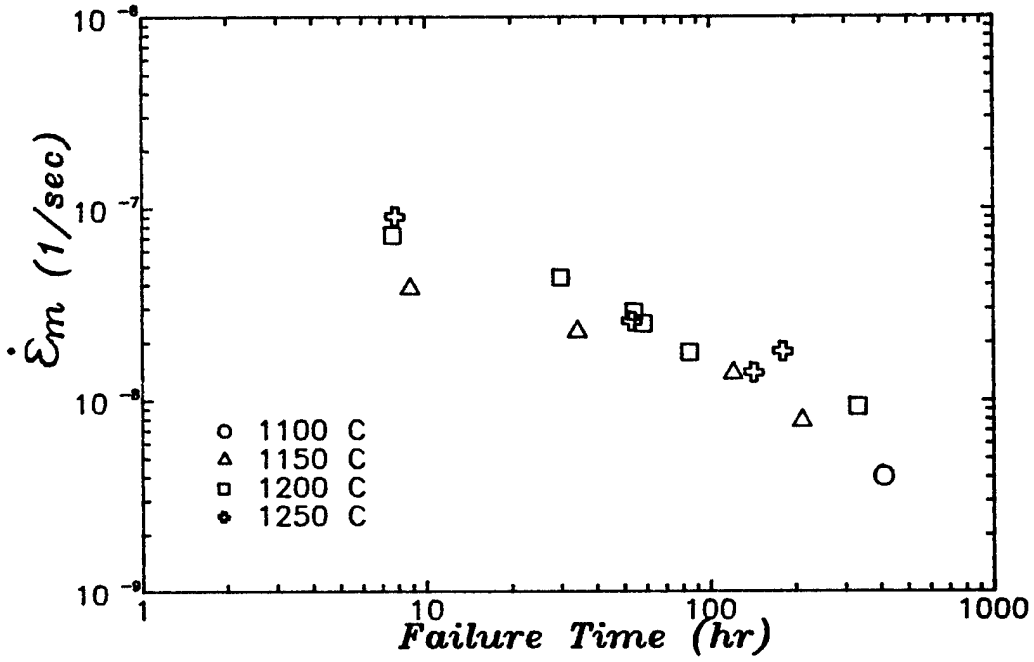

5. Creep rupture data presented in the form of a Monkman-Grant curve. Note that regardless of temperature, all of the data fall along a single curve.

Status of Milestones

341301 This milestone has been completed. A paper on the creep technique using laser measurements at elevated temperatures has been submitted and accepted for publication in the Journal of the American Ceramic Society.

341304 The Engineering Foundation on the subject of Structural Ceramics, was held in Palm Coast, FL on March 12-17, 1989.

All other milestones are on schedule (34102-34105).

Publications

1. D. F. Carroll and S. M. Wiederhorn, "A Technique for Tensile Creep Testing of Ceramics," J. Am. Ceram. Soc., Accepted.

2. T.-J. Chuang, D. F. Carroll and S. M. Wiederhorn, "Creep Rupture of a Metal-Ceramic Particulate Composite," Seventh International Conference on Fracture, pp. 2965-76 in Advances in Fracture Research, V.4, K. Salama, K. Ravi-Chandlerc D.M.R. Taplin and P. Rama Rao Eds., Pergamann Press, New York (1989).

3. S. M. Wiederhorn, "Design of Advanced Ceramics for Creep Resistance," Transactions of the Canadian Council on Advanced Ceramics, Design with Engineered Ceramics, held May 26-27, 1988, Toronto, Canada, published as part of the proceedings of the Conference.

4. D. F. Carroll and S. M. Wiederhorn, "High Temperature Creep Testing of Ceramics," Int. J. High Tech. Ceramics, 4, 227-241 (1988).

Fracture Toughness Determination of Thin Coatings

J. J. Wert and R. H. Parrish (Vanderbilt University)

Objective/scope

The goal of this program is to develop the scientific base and technology required to obtain the fracture toughness of thin coatings from microindentation.

Technical progress

During this reporting period Task 1 was completed and progress was made toward the completion of Task 2. Task 1 of this program was to conduct a literature review on indentation testing of ceramics. The review revealed many empirical models which help determine a parameter that can be related to the fracture toughness of a brittle material in bulk form. Most of the models consist of measuring a final crack length after indentation and relating this parameter to the applied load and the material's elastic modulus and hardness. There are a few models that are more analytically based. These deal with considering the stresses and strains during loading and the residual stresses after load removal. In the future, these models may prove to be of interest when correlated to fracture events on the load displacement diagrams obtained during indentation.

Task 2 of the program is to design and build a high load indentation apparatus to perform indentation fracture test on silicon, sapphire and zirconia. A previous testing apparatus used during the last reporting period was not capable of achieving the resolution required to record the fracture events on the load-displacement curves. The newly designed indentation fracture machine will be capable of loads between 10 grams and 10 kilograms. It has also been designed to have a low mass and a variable stiffness. It is expected that the machine will be completed by the end of April and indentation test underway by the first of June.

Task 3 requires performing preliminary tests on silicon and sapphire using the Mechanical Properties Microprobe (MPM). The MPM will be equipped with a high-load head in order to achieve the required loads for indentation fracture of most materials. Cooperation with HTML on the manufacture of the high-load head has been underway. All designs have been released to the manufacturers and many of the components are ready for assembly.

In order to increase the efficiency and to develop proper procedures in acquiring fracture data by the MPM, time has been spent running test samples on the MPM at HTML. This exercise will help avoid problems during the course of the project.

Status of milestones

341401	Literature review on the subject of indentation testing of ceramics.	Completed	2/28/89
341402	Build a high load indentation apparatus to perform indentation fracture tests on silicon, sapphire and zirconia.		9/15/89
341403	Preliminary tests on silicon and sapphire to be performed on the MPM.		3/30/89

Publications

None

3.5 NONDESTRUCTIVE EVALUATION DEVELOPMENT

Nondestructive Characterization
D. J. McGuire (Oak Ridge National Laboratory)

Objective/scope

The purpose of this program is to conduct nondestructive evaluation (NDE) development directed at identifying approaches for quantitative determination of conditions (including both properties and flaws) in ceramics that effect the structural performance. Those materials that have been seriously considered for application in advanced heat engines are all brittle materials whose fracture is affected by structural features with dimensions on the order of the dimensions of their microstructures. This work seeks to characterize those features using high-frequency ultrasonics and radiography to detect, size, and locate critical flaws and to measure nondestructively the elastic properties of the host material.

Technical progress

Ultrasonics - W. A. Simpson, Jr., and K. V. Cook

A special design, high numerical aperture ultrasonic transducer has been obtained for high-frequency surface wave evaluation of ceramic materials. This transducer is a 50-MHz, f/0.8 spherically focused unit which is capable of generating and detecting with high efficiency a radially propagating surface wave on typical ceramics. This wave is very sensitive to surface defects as well as those which lie within about one wavelength (~120 μm for alumina, silicon nitride, and silicon carbide) of the surface. In addition, the radial nature of the wave insures that cracks will be detected easily regardless of their orientation. Figure 1 is a black and white reproduction of a color display of the results obtained on an alumina coupon. The scale at the extreme right of the figure is a color chart which relates the amplitude of the ultrasonic signal to a particular color. The coupon was approximately 25 mm by 50 mm and contained a number of surface-breaking pits varying in diameter from about 50 to 150 μm and in depth from about 25 to 100 μm. No cracks were noted in a visual inspection of the part, but the ultrasonic results clearly show that the sample contained two large cracks. These cracks were subsequently located visually under high magnification and found to be extremely tight ($\leq$1 μm). The apparent width of the cracks in Fig. 1 is an artifact and is a measure of the diameter of the ultrasonic beam at the sample surface rather than of the true crack width.

Figure 1 also shows a number of pointlike indications scattered over the surface of the coupon. These are surface and near-surface voids, the former giving rise to the pits described above. All of the visual features were detected as well as numerous ones which originate from subsurface flaws. The gain reserve of the instrumentation indicated that surface-breaking voids as small as perhaps 25 μm should be detectable in this material.

Figure 1 also shows a periodic array of dark striae running horizontally across the sample from top to bottom. These were found to be grinding marks on the ceramic surface and could be detected visually only under extremely oblique illumination. Their amplitudes were measured under a microscope and found to be <10 μm.

Figure 2 shows the surface wave results obtained on a second coupon, which obviously contained three cracks. As before, these cracks were not detectable visually. The grinding marks for this sample run vertically through the figure.

We have examined 20 whisker-reinforced silicon nitride modulus of rupture (MOR) bars fabricated by HIPing. The bars consisted of two batches of ten, designated 2154C and 7X014. The former batch was prepared to improve homogeneity of the microstructure and to reduce the critical flaw size compared to the latter batch. We examined both batches with a 75-MHz, f/3 ultrasonic transducer which has been shown capable of detecting voids as small as about 20 μm in silicon nitride. Approximately three or four indications were found in each set, and these indications all occurred at or near the minimum detectable level, implying that the source was probably in the vicinity of 20 to 25 μm in diameter. The majority of bars in each set showed no detectable flaws. These bars are unquestionably among the cleanest that we have examined.

A back-surface ultrasonic reflectivity test was also performed on each bar in which an ultrasonic wave is transmitted through the bar and its amplitude digitized and displayed after reflection from the opposite face. This configuration is useful for detecting small cracks in the bars and will also delineate regions of inhomogeneity. Some variation was seen among the bars of a given set, but there were no obvious differences between sets. No cracks were detected in any of the bars.

A high-frequency surface wave examination of the bars, which would be most sensitive to surface-breaking and near-surface cracks, was not performed because of the very high apparent quality of the bars.

Since the intended differences between the two sets of MOR bars were related to the microstructures, we determined a material transfer curve for a representative specimen from each set. We have previously demonstrated that the transfer function is a very sensitive indicator of the microstructural state of the host material. The samples chosen were 2154C-10 and 7X014-10. The results obtained on 7X014-10 were representative of a typical fine-grained silicon nitride. The results on 2154C-10 were similar, except that the coefficient of linear attenuation (i.e., the slope of the attenuation versus frequency curve) was about 33% larger. If this result is characteristic of all the samples in the two groups, then the implication is that the microstructure of the 2154C set is slightly coarser than for the other set, or the 2154C set could contain significant numbers of scattering sites too small to be detected directly by the 75-MHz ultrasonic wave, e.g., a higher density of whiskers. A third possibility, of course, is that the observed differences are attributable to variables which we

have not yet identified in our studies. The first two conclusions are supported by our work in whisker-reinforced ceramics, however, where the presence of whisker clumps can be demonstrated either through direct high-frequency imaging or through their effect on the transfer curve.

The conclusion to be drawn from our study of the two sets of HIPed MOR bars is that both sets appear to be of very high quality with few discrete flaws, all of which are probably 25 μm or less in size. Destructive analysis on some of the bars would probably be required to determine the origin of the differences in the transfer curves of the two sample sets.

We continued our work on techniques to improve the ability to inspect ceramic parts nondestructively. One of the more important sample shapes, and one which is particularly troublesome to inspect ultrasonically because of the beam distortion induced by propagation through the surface curvature, is the cylinder. Unfortunately, many parts which we are requested to evaluate are basically cylindrical in shape, including many tensile specimens as well as ceramic wrist pins for automotive engines. The loss of sensitivity in these samples can be quite dramatic; although we can routinely detect voids as small as 25 μm at depths of 5 mm in planar samples of tetragonal phase zirconia, we have been unable to detect 100-μm voids at depths greater than about 0.5 mm in cylinders of zirconia having diameters of about 6 mm. However, since the inspection problems are caused by severe beam astigmatism induced by the surface curvature of the sample, it should be possible to correct for this condition in much the same way that astigmatic imaging is corrected in human vision; i.e., by using an aspherical transducer lens element consisting of a basic spherical surface with a superimposed cylindrical correction. We are investigating this approach using the beam distribution model which we developed previously.

Since the most useful transducer design for inspection of typical planar ceramics appears to be approximately 75 MHz f/3 (higher frequencies would theoretically give better resolution and sensitivity, but commercial designs for frequencies above 75 MHz require smaller piezoelectric elements, which mean greater f-ratios for a given focal length and ultimately yield less sensitivity for flaws in the range of sizes $\geq$25 μm), we are concentrating on the design of a 75-MHz, f/3 aspheric lens element. We are currently modifying the computer code of our beam distribution program to handle the nonspherical lens curvature. During this time, we are also calculating the distribution produced by a 75-MHz, f/3 spherical transducer in small diameter cylindrical specimens. These results will be compared with those of the aspheric transducer to assess the improvement obtained.

Although changes in the transducer lens design should improve our ability to inspect cylindrical (and other shape) ceramic specimens, we also require modifications to our scan system before more complex shapes can be efficiently handled. Our current inspection system is a commercial one which is primarily adapted to the inspection of planar

samples. We have previously designed modifications which allow us to mount and scan cylindrical specimens, but the data so obtained could not be acquired and stored by the system. It now appears that a suitable scan system for both planar and cylindrical samples can be built using small commercial stepping motor assemblies for a small fraction of the cost of our current system. We have obtained data from several vendors of such assemblies. Since peak detection and digitization of the ultrasonic signal are provided by our ultrasonic hardware, which is independent of the scan system, it appears that we would require only a relatively simple hardware and software interface to construct a complete system for the inspection of samples having both planar and cylindrical geometries. This approach is being investigated.

We are continuing to evaluate the shear wave field produced in ceramics by water-coupled transducers. This field has been almost entirely neglected in the literature, probably because there are apparently no models which can handle two-media propagation and mode conversion. However, we reported previously that our beam distribution model can treat the shear wave field as easily as the compressional wave field. We have examined the shear distribution produced inside alumina by a number of high-frequency transducers. The results are both startling and unpredictable. Although the shear wave intensity is less than the compressional wave intensity (at the respective foci) for some transducer configurations, the reverse is true for other designs. We have not been able to identify any particular transducer characteristic which guarantees the superiority of one field over the other, but some commercial designs would appear to be more sensitive if used at the shear wave focus than at the intended compressional wave focus. In addition, since the shear wave focus will always occur deeper in the specimen than the compressional wave focus and since the shear wavelength is about half that of the compressional wave for a given frequency, there could be considerable advantage in using the shear wave field for ceramic inspection. This is difficult to establish experimentally, however, since focusing on the same scatterer using both shear and compressional wave fields produces large changes in the required water column, which preferentially degrades the shear wave field because of losses in the water, while focusing the shear wave field on a deep flaw means that the scatterer is too deep for the compressional wave focus. For many of our MOR bar samples, however, the shear wave signal from the back surface of the bar is larger than that produced by the compressional wave, which cannot focus so deeply.

Radiography - B. E. Foster

Fabrication of the computerized X-ray tomography system at Scientific Measurement Systems, Inc. (SMS) in Austin, Texas, is proceeding. The purchase agreement includes several progress payment type milestones. Five milestones have been completed. They have included a design review; approval of major item drawings; fabrication of the image processing subsystem and fabrication of the array and back projection processor; receipt of major equipment items; and start of fabrication on the object positioning unit, specimen holder, collimator set, and calibration standards.

The hands-on training is progressing quite well. During the last session in November, I was successful in making several digital radiographs of a carbon-carbon composite, tomographs of a printed circuit board, and laminographs of a copper penny. During the last session in December, time was used learning how to manipulate, measure, and analyze prerecorded CT images. This training is early enough in the fabrication stage of our system to permit modifications (at no additional cost) that might be desired for customizing.

The installation (by SMS personnel) date for final acceptance at ORNL has been rescheduled for late April 1989. The reasons for this change in the installation date (originally February 15, 1989) are due to delays in receipt of associated detector items, redesign of the object positioning unit (this resulted in an improved system, i.e., capability to scan a 16-in.-diam sample instead of a 6-in.-diam sample), and the relocation of SMS into a larger facility (about double the original floor space).

Status of milestones

None.

Publications

W. A. Simpson, Jr., R. W. McClung, and D. R. Johnson, "Applications of Ultrasonics for Advanced Structural Ceramics," invited contribution to the *ASNT Handbook*, to be published.

W. A. Simpson, Jr., "Ultrasonic Techniques for Characterization of Advanced Structural Materials," presented at the WATTec '89, 16th Annual Technical Conference and Exhibition, Knoxville, Tennessee, February 14-17, 1989.

R. W. McClung and D. R. Johnson, "Nondestructive Examination and Characterization of Advanced Ceramics," presented at the ASM International, World Materials Congress, Chicago, Illinois, September 25-30, 1988.

W. A. Simpson, Jr. and R. W. McClung, "An Ultrasonic Evaluation of Silicon Carbide Whisker-Reinforced Ceramic Composites," submitted to *Materials Evaluation*.

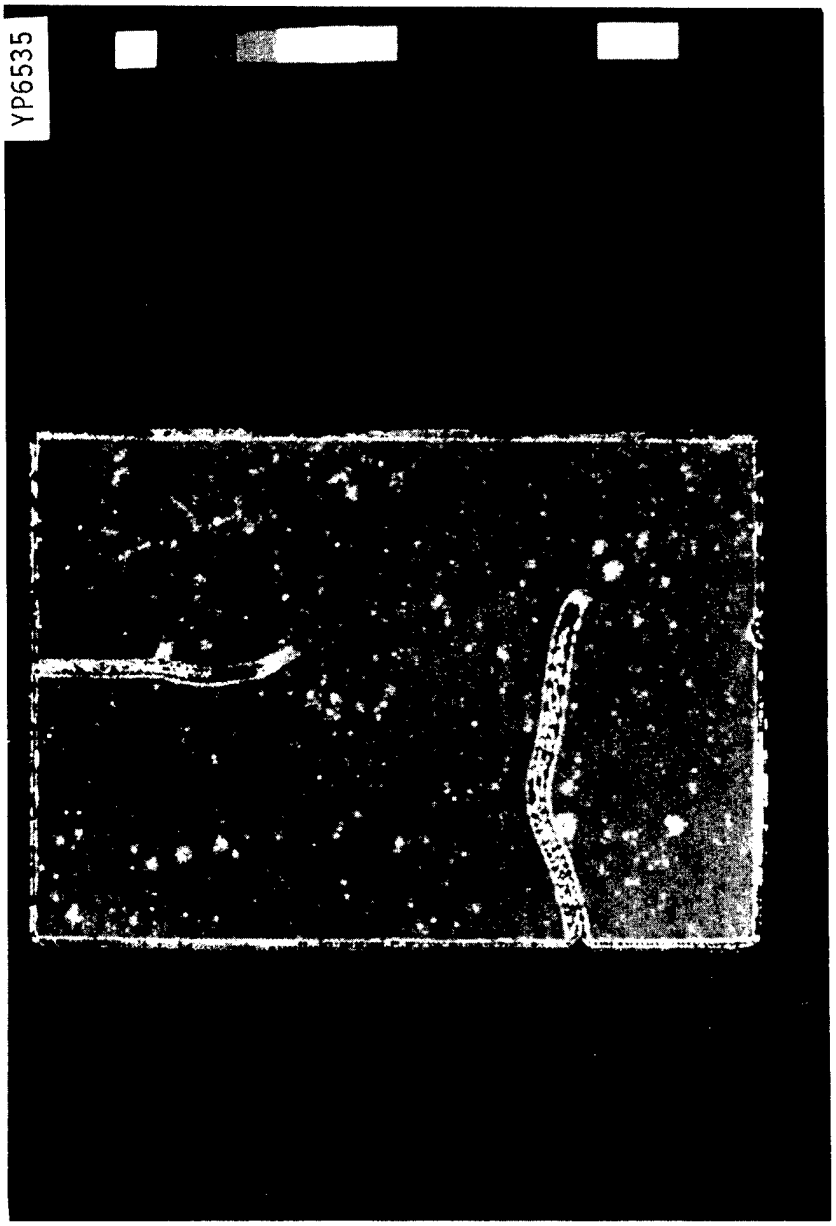

Fig. 1. Black and white reproduction of a color display showing the high-frequency ultrasonic surface wave detection of two cracks, voids, and grinding marks (horizontal striae) in an alumina coupon.

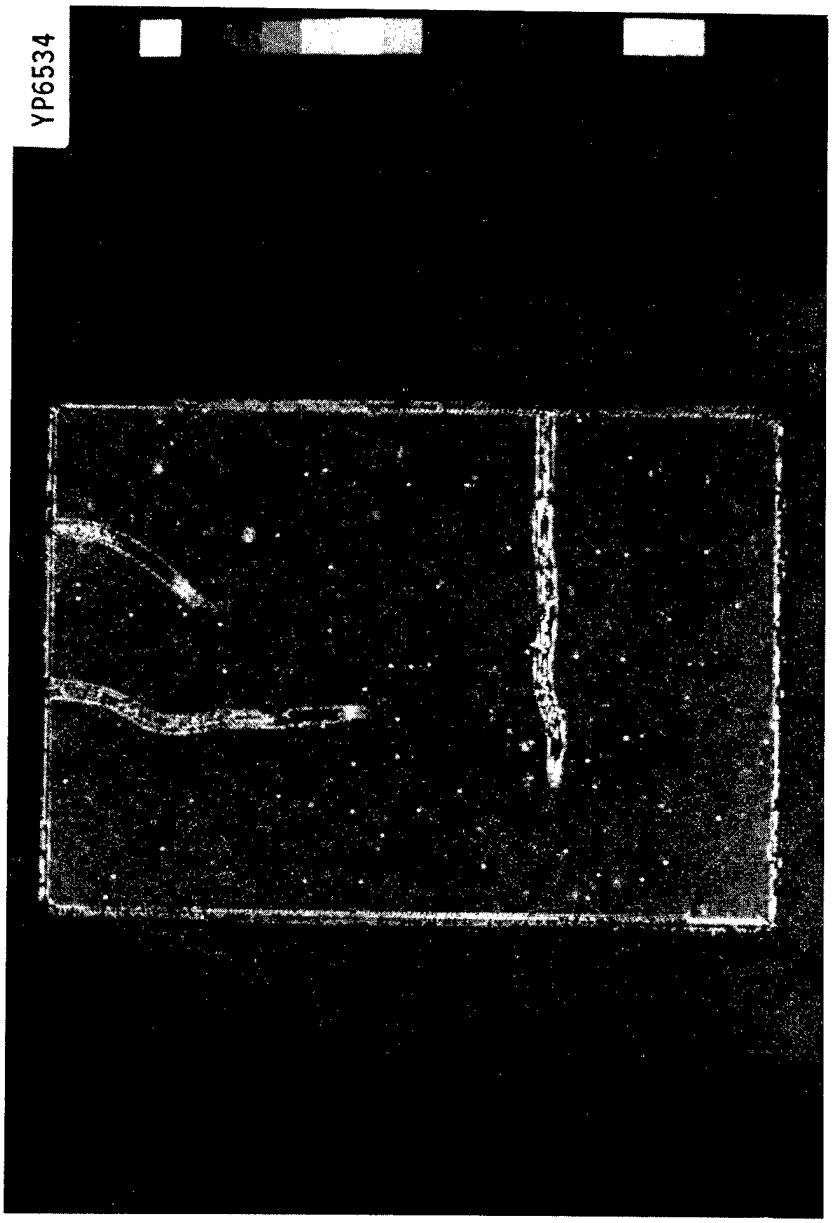

Fig. 2. Black and white reproduction of a color display showing the high-frequency ultrasonic surface wave detection of three cracks, voids, and grinding marks (vertical striae) in an alumina coupon.

Computed Tomography - W. A. Ellingson, H. P. Engel, M. W. Vannier, and H. C. Yeh (Argonne National Laboratory)

Objective/scope

The purpose of this program is to develop X-ray computed tomography (CT) imaging for application to structural ceramic materials. This technique has the potential for mapping short-range (<5 mm) and long-range (>5 mm) density variations, detecting and sizing high- and low-density inclusions, and detecting and sizing (within limits) cracks in green-state and densified ceramics. CT imaging is capable of interrogating the full volume of a component, and is non-contacting. It is also relatively insensitive to part shape and thus can be used to inspect components with complex shapes such as turbocharger rotors, rotor shrouds, and large individual turbine blades.

Technical progress

During the current reporting period, efforts were concentrated on developing a set of test phantoms with varying organic binder content, and determining the ability of X-ray CT scanners to detect and quantify these variations.

Description of test specimens

For this study, two specially made test specimens were obtained from the Garrett Ceramic Components Division of Allied-Signal Aerospace Company. The specimens were green-state, cold-pressed Si_3N_4 disks, 28.5 mm in diameter and 13 mm high with 6-mm-diam inserts, as shown in Fig. 1. The base material of each disk was Garrett's Si_3N_4 GN-10 injection-molding mix, which contains 15.5 wt.% organic binder and has a nominal theoretical density of 2.18 g/cm^3. The inserts contained known concentrations of organic binder material, ranging from 2 to 20 wt.%. Each individual insert was press-fit into a flat-bottom drilled hole so that a minimal air gap remained between the insert and the base material. The composition and density of each insert and the base material are given in Table 1.

Difficulties were encountered in fabricating the inserts with 2, 5, and 10 wt.% binder; they had exceptionally high porosity, and did not show the expected monotonic decrease in density with increasing binder content. However, an approximately linear relation between density and volume fraction of powder was observed for the inserts with 13.5 wt.% and higher binder concentrations.

X-ray computed tomography studies

During the production of the test specimens, microfocus contact X-ray images were obtained by Garrett Ceramic Components Division primarily as a quality check to see whether any cracks had been introduced into the specimens during fabrication and to assess the size of the gaps around the individual inserts. Since the density differences between

insert and base material can be as high as 13.3% (see Table 1), the X-ray film should detect most of these differences quite easily. Figures 2 and 3 are prints of the contact X-ray film images obtained by Garrett. Although the individual inserts can be seen quite easily, the contrast created by the gap between the inserts and the base material helps in visual detection. This observation is in line with earlier results obtained with real-time imaging.[1]

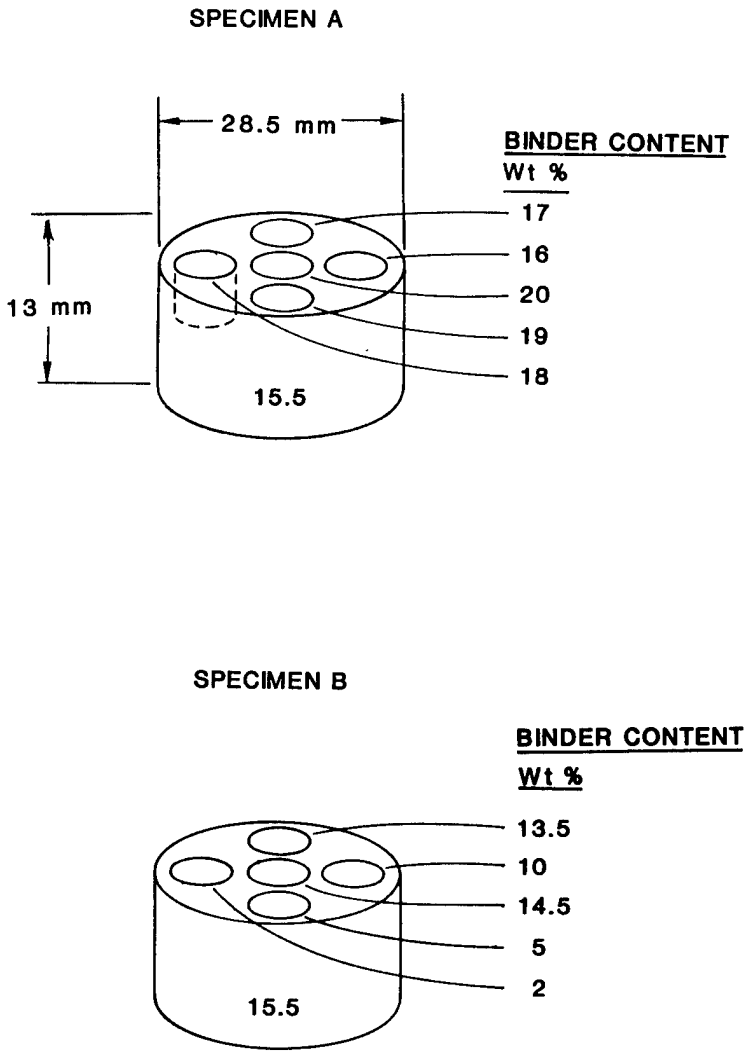

Fig. 1. Test Phantoms

Table 1. Characteristics of Test Specimen Components

Binder Content		Si_3N_4 Powder Content	Porosity	Density	Change in Density (%)[a]
wt. %	vol. %	(vol. %)	(vol. %)	(g/cm^3)	
2.0	4.1	56.3	39.6	1.92	11.93
5.0	10.2	53.8	36.0	1.89	13.30
10.0	21.9	55.1	23.0	2.04	6.42
13.5	34.1	61.1	4.8	2.36	8.26
14.5	36.2	59.6	4.2	2.33	6.88
15.5	38.2	59.0	2.8	2.18[b]	0.00
16.0	38.8	56.9	4.3	2.26	3.67
17.0	40.7	54.6	4.7	2.23	2.29
18.0	42.1	53.5	4.4	2.18	0.00
19.0	43.6	51.8	4.6	2.14	1.84
20.0	45.2	50.4	4.4	2.10	3.67

[a]Relative to that of the base material.
[b]Theoretically calculated.

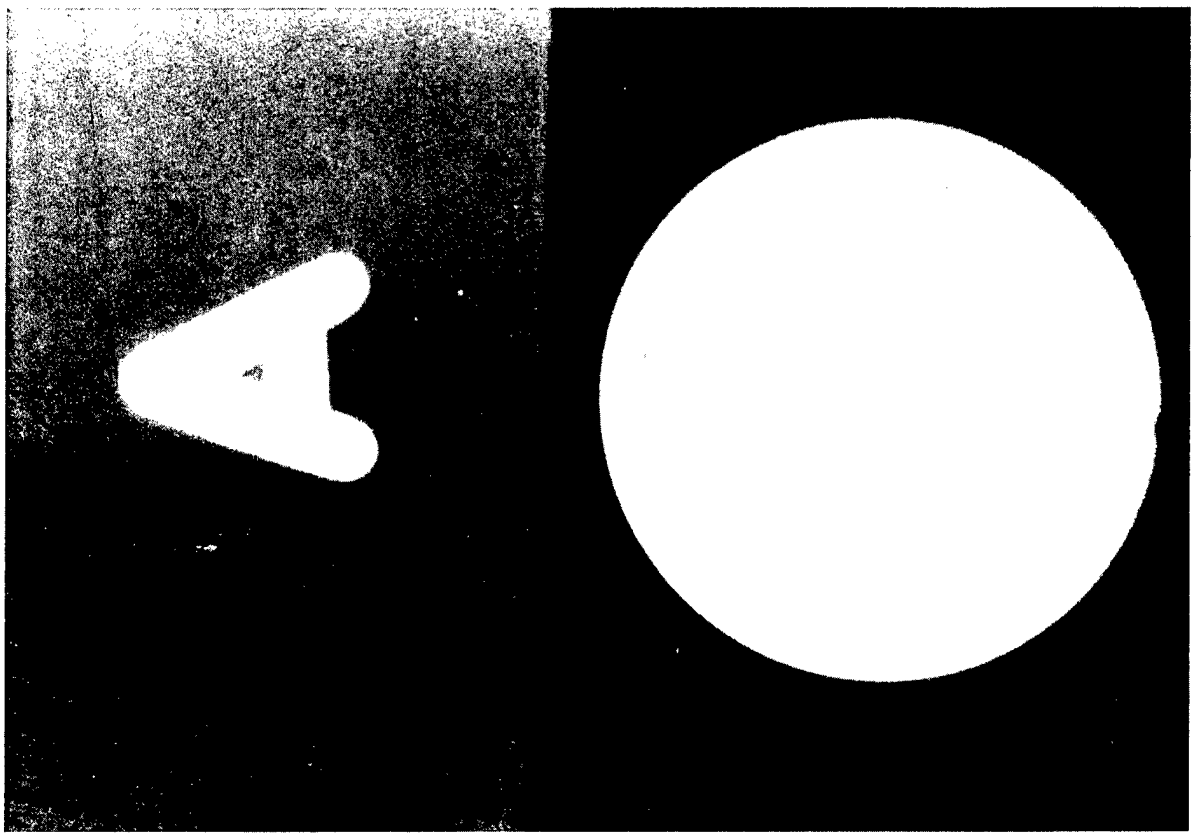

Fig. 2. Microfocus X-Ray Film Image (10-mm Focal Spot Size) of Specimen A.

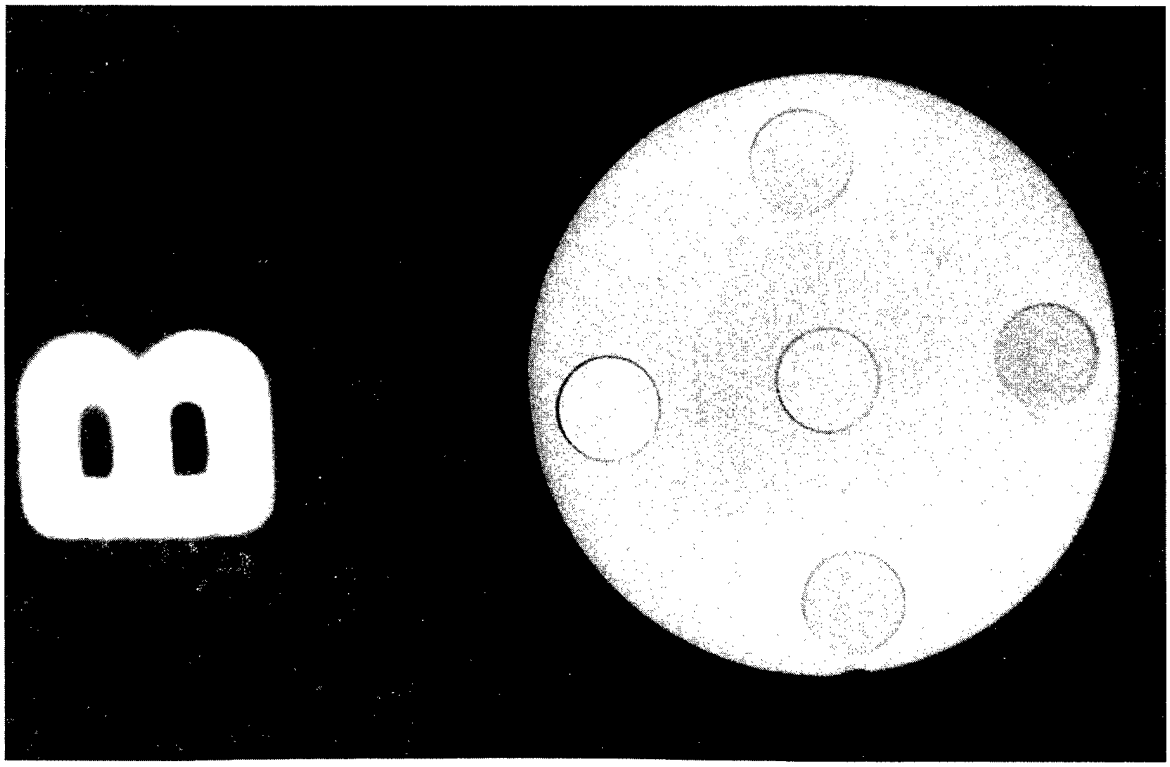

Fig. 3. Microfocus X-Ray Film Image (10-mm Focal Spot Size) of Specimen B.

It is generally accepted that X-ray CT is 10-100 times more sensitive to density variations than conventional film.[2] Initial X-ray CT tests were conducted with a GE 9800 medical CT scanner (140-kV X-ray head voltage) set up in an industrial environment. The scans were conducted in a single-energy mode. Figures 4 and 5 show poor-quality hard-copy prints of the resulting images; the sensitivity to differences in density is significantly better than in the film images.*

*Since we did not obtain the CT image data files, we could not determine the S/N ratios and therefore could not make quantitative comparisons with the film images.

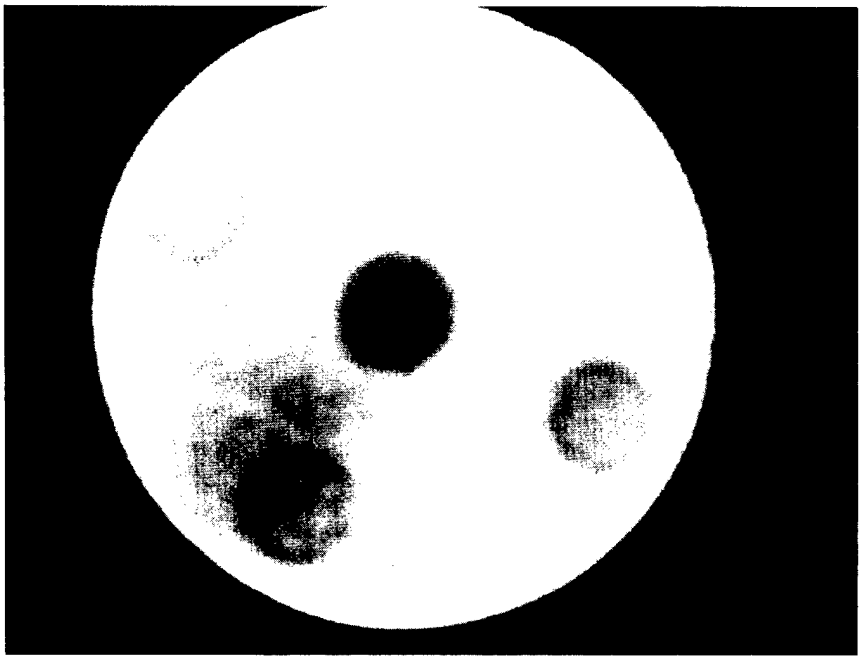

Fig. 4. X-Ray CT Image of Specimen A, Obtained from GE 9800 Machine.

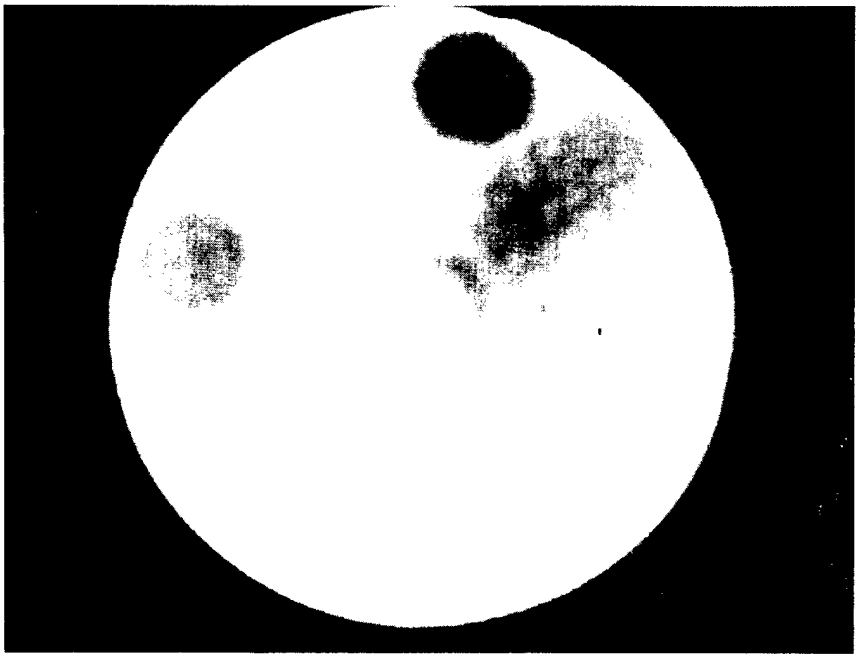

Fig. 5. X-Ray CT Image of Specimen B, Obtained from GE 9800 Machine.

We also conducted a set of tests with a Siemens DR-H medical CT scanner (125-kVp maximum X-ray head voltage) in a hospital environment. The machine was left calibrated on water and calcium, as earlier studies[2] had shown that this was a satisfactory calibration for green ceramics. We experienced significant difficulties in obtaining high-quality (i.e., high S/N ratio) images, in spite of various beam-hardening corrections[3] including an 80-mm-OD Teflon outer ring, a 50-mm-OD Perspex ring, and dual-energy[4,5] operation (at 85 and 125 kVp). We still do not fully understand the reasons for this difficulty. More difficulties were experienced with specimen B (which contained the inserts with 2, 5, and 10 wt.% binder) than with specimen A. The data for specimen A allowed a correlation to be obtained between Hounsfield units (CT number) and vol.% binder, as shown in Fig. 6. It is usually accepted that a detection sensitivity of 1-2% above noise can be achieved with X-ray CT. In the present case, this sensitivity is equivalent to 10-30 Hounsfield units, or a change of less than 1 wt.% in binder content.

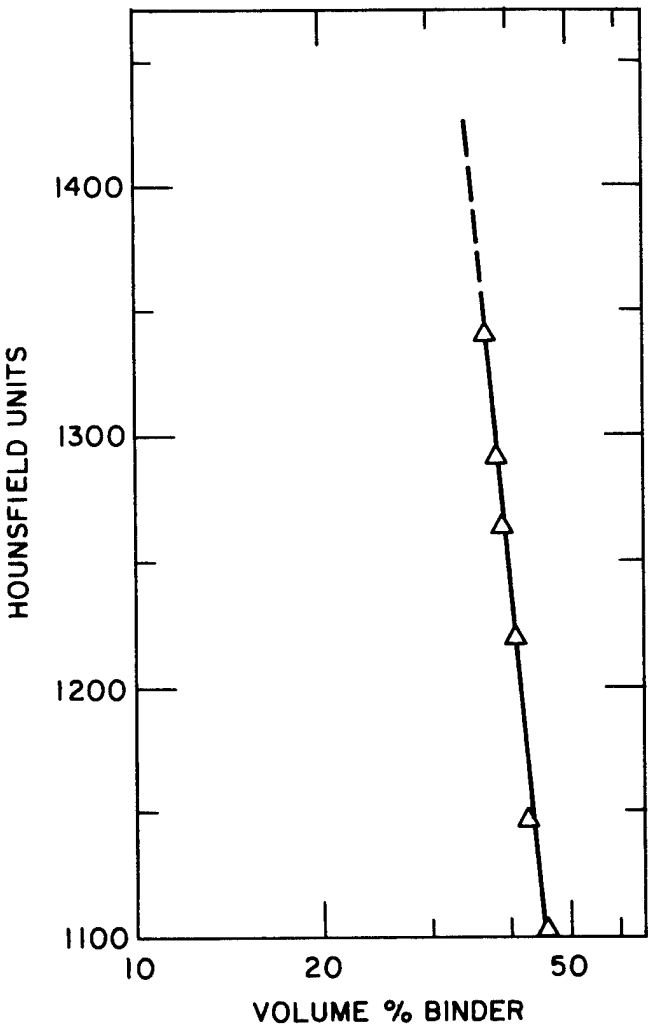

Fig. 6
Correlation Between X-Ray CT Number (Hounsfield Units) and Vol.% Binder for Specimen A.

We conducted an additional series of tests with these specimens on the X-ray CT scanner at NASA/Cape Canaveral. The source used in this case was ^{60}Co, which had an activity level of 81 Ci and yielded photons with an energy level of about 1 MeV. Theoretical optimum energy curves[6] for several materials are shown in Fig. 7. For a material in the density range of our specimens (2-2.5 g/cm^3), the optimum thickness would appear to be about 140-150 mm at a photon energy of 1 MeV. Since our specimens are only 28.5 mm in diameter, a photon energy in the 100-150 keV range could be expected to give optimum images. As noted earlier, in tests on polychromatic CT scanners at a 125-kV potential (with a tungsten target yielding ~60-65 keV photons) we obtained very poor images,[7] whereas in tests at 140 kV potential we obtained very good images. Very good images were also obtained with the ^{60}Co source, as shown in Fig. 8.

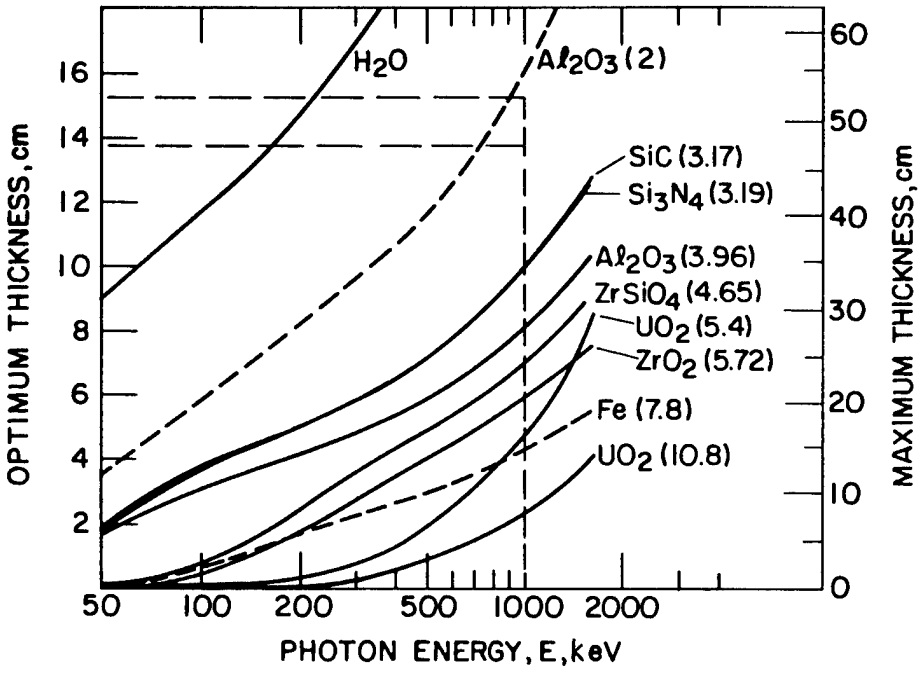

Fig. 7. Optimum and Maximum Thicknesses for Various Materials as a Function of Incident X-Ray Photon Energy. Numbers in brackets are the densities of the materials, in g/cm^3. (Adapted from Ref. 6.)

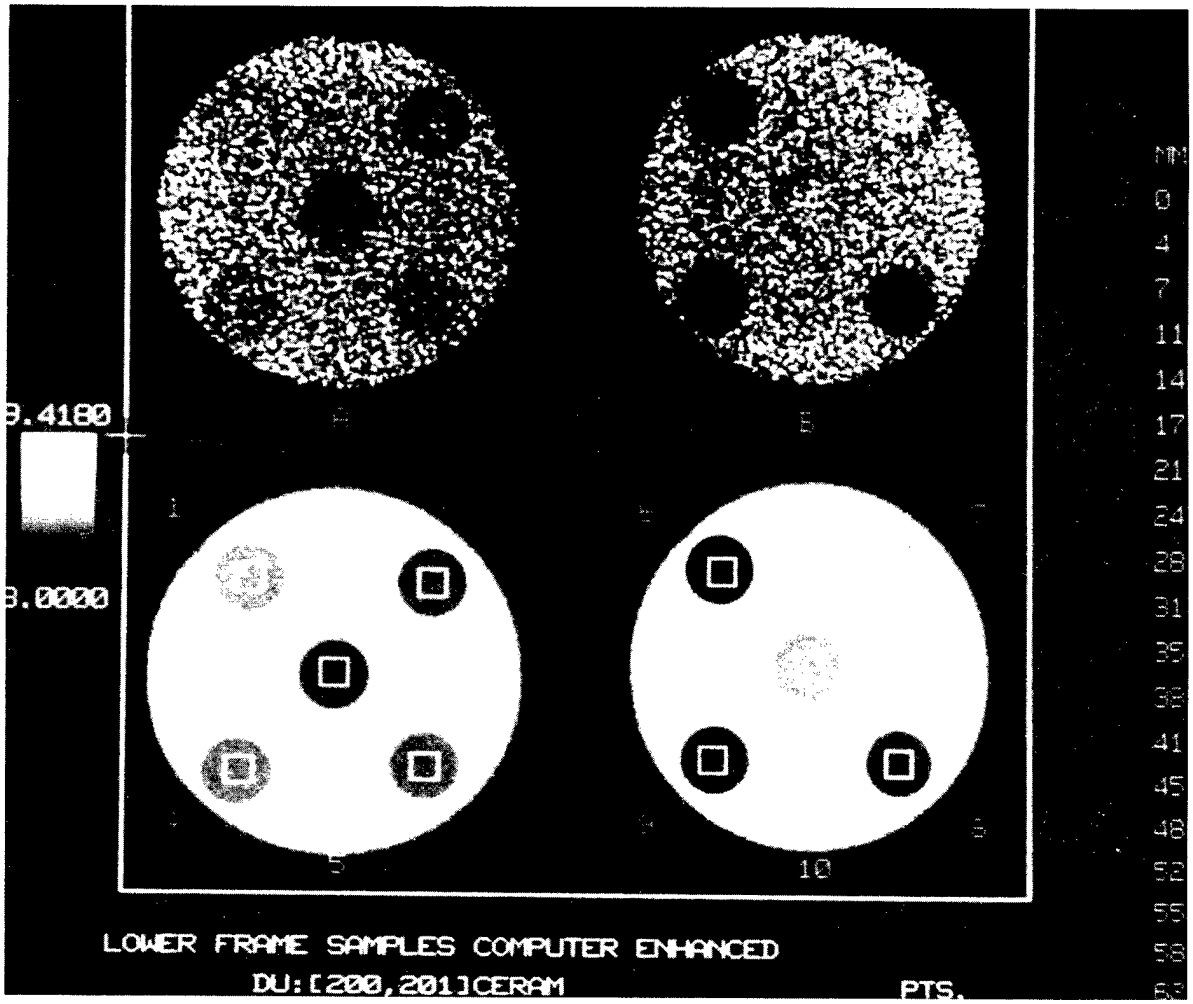

Fig. 8. ^{60}Co CT Scans of Si_3N_4 Test Samples A and B. Upper images are raw data images; lower images are digitally enhanced. The squares in the lower images show reg ions from which data were taken for a regression analysis.

By performing a regression analysis (see Fig. 9) on the image data obtained from the ^{60}Co scans, we obtained the following relationship between CT number and mass density ρ of the ceramic material:

$$\rho = -0.398 + 0.317 \text{ CT number}. \qquad (1)$$

The density of Si_3N_4 with 15.5 wt.% binder, calculated from Eq. (1), is 2.28 g/cm^3. This value seems much more reasonable than the theoretical density (2.18 g/cm^3) given in Table 1, in view of the density values for components with $\geq$ 13.5 wt.% binder. If organic content can be uniquely related to mass density, X-ray or gamma-ray CT may be a useful way to track organic content.

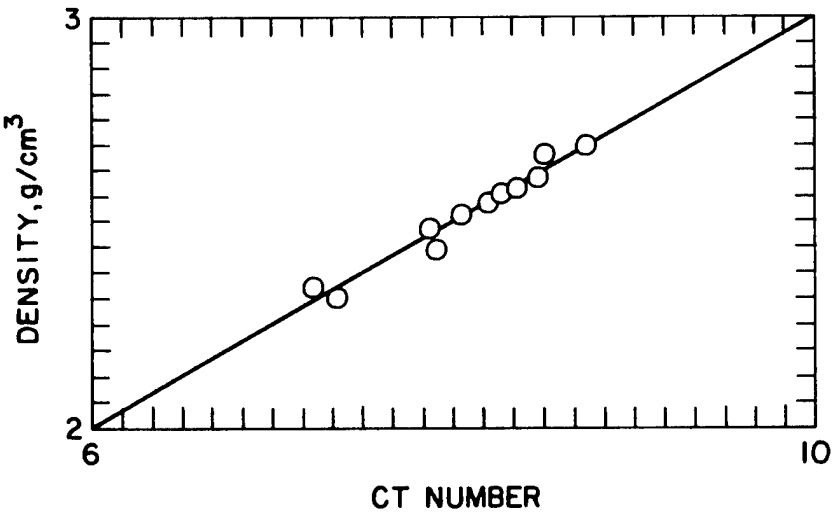

Fig. 9. Regression Analysis Relating Si_3N_4 Density to ^{60}Co Computed Tomography Data.

Status of Milestones

All milestones are on schedule.

References

1. W. D. Koenigsberg and J. T. Neil, "Ceramic Binder Removal Studies Using Projection Radiography," pp. 539-546 in Proceedings of Conference on Nondestructive Testing of High-Performance Ceramics, Aug. 25-27, 1987, American Ceramic Society, Westerville, OH, 1987.

2. W. A. Ellingson and M. W. Vannier, X-Ray Computed Tomography for Nondestructive Evaluation of Advanced Structural Ceramics, ANL-87-52, Argonne National Laboratory, Argonne, Ill., September 1988.

3. E. Segal and W. A. Ellingson, pp. 169-178 "Beam Hardening Correction Methods for Polychromatic X-Ray CT Scanners Used to Characterize Structural Ceramics," pp. 169-178 in Nondestructive Characterization of Materials II, eds. J. F. Bussiere et al., Plenum Press, New York, 1987.

4. R. T. Alvarez and A. Macovski, "Energy Selective Reconstructions in X-Ray Computed Tomography," Phys. Med. Biol. 21, 735-744 (1976).

5. A. J. Talbert, R. A. Brooks, and D. G. Morganthale, "Optimum Energies for Dual-Energy Computed Tomography," Phys. Med. Biol. 25, 261-269 (1980).

6. B. D. Sawicka and P. J. F. Palmer, "Applications of Computed Tomography to the Development of Advanced Ceramics," in Proceedings of the International Symposia on Fine Ceramics (ARITA '88), Arita, Saga, Japan, November 1988 (in press).

7. W. A. Ellingson, P. S. Wong, S. L. Dieckman, J. P. Pollinger, H. C. Yeh, and M. W. Vannier, "An Initial Comparison of X-Ray and NMR Computed Tomography for Detection of Organic Binder Distributions," in Proceedings of the American Ceramic Society 13th Annual Conference on Composites and Advanced Ceramics, Cocoa Beach, FL, January 1989 (in press).

Nuclear Magnetic Resonance Imaging - W. A. Ellingson, P. S. Wong, S. L. Dieckman, and J. P. Pollinger (Argonne National Laboratory)

Objective/scope

The objectives of this program are to (1) establish the feasibility of using NMR imaging systems to map distributions of organic binder/plasticizers (B/Ps), which are short-T_2 materials, in injection-molded green ceramics (with emphasis on Si_3N_4); (2) examine the potential of applying NMR spectroscopy to detect variations within and/or between batches of organic B/P that can affect process reliability; and (3) determine the sensitivity of NMR imaging methods to injection-molding process variables as manifested in distribution of the organic B/P.

Technical Progress

Preparation of injection-molded modulus-of-rupture test bars

During this reporting period, two different Si_3N_4* injection mixes were injection molded into test bars; both standard and nonstandard injection-molding parameters were used for each mix, resulting in four different combinations. A standard four-cavity die was used. A minimum of two sets of test bars (4 bars per set) with consistent quality were molded per mix/molding combination. The bars were visually inspected for flaws; the results are shown in Table I.

T_1 spectroscopic studies on samples containing various concentrations of organic binder/plasticizer

Five samples containing concentrations of 2, 5, 10, 15.5, and 20 wt.% organic B/P, respectively, in Si_3N_4 powder were used to study the effects of B/P concentration on T_1 values. The 7.1-T 300 AM Bruker spectrometer was used to estimate T_1 values with an inversion recovery pulse-sequence technique. T_1 values as a function of B/P concentration are shown in Fig. 1. The results indicate that T_1 increases as B/P concentration increases; this is probably due to the longer molecular correlation times $(\tau_c)^1$ observed in the samples containing >10 wt.% binder. The data were used in imaging studies to ensure adequate recovery delay times.

*GN-10 Si_3N_4 (Garrett Ceramic Components Division, Allied-Signal Aerospace Co., Torrance, CA).

Table I. Results of Visual Inspection of Injection-molded Modulus-of-Rupture Bars[a]

Group No.	Mix[b]	Molding Parameters[b]	Bar No.	Flaw Type	Location[c]	Severity[d]
1	S	S	1	Pits	A1	1
				Scratches	B1	1
				Flow lines	C1	1
			2	Flow lines	B1	1
			3	No defects		
			4	Flow lines	A1	1
2	N	S	21	Pits	A1	1
				Scratches	B1	1
			22	Flow lines	A1	1
				Scratches	D2	1
			23	Flow lines	A1	1
			24	No defects		
3	N	N	41	Flow lines	Entire Surface	3
			42			3
			43			3
			44			3
4	S	N	69	Flow Lines	Entire Surface	3
			70			3
			71			3
			72			3

[a]The following defects were present in all bars, except as noted, and are not listed above (see footnotes 3 and 4 for explanation of codes):

Flaw Type	Location	Severity
Flow lines	A1	0
Linear surface porosity	A1,A5	0
Surface porosity due to excess mold release agent	A1,A5	1
Scratches due to handling	Variable	0

[b]S = standard; N = nonstandard.

[c]Location codes:

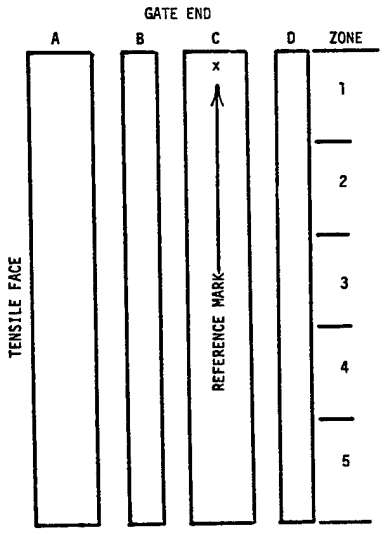

[d]Severity codes:
0 = noticeable at 30X mag.
1 = more than desirable.
2 = possible effect on properties.
3 = definite effect on properties.

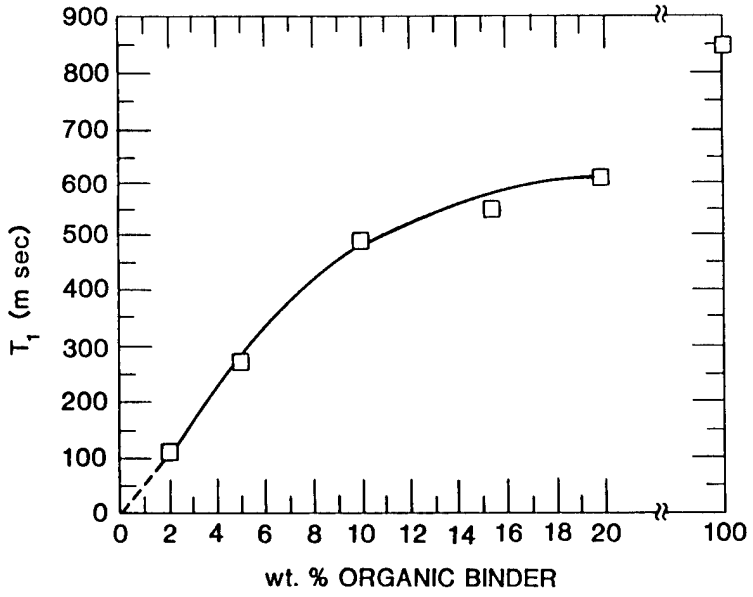

Fig. 1. Variation in T_1 with wt.% Organic B/P in Si_3N_4 Powder at 22°C.

T_2 spectroscopic studies on samples containing various concentrations of organic binder/plasticizer

The same samples used in the T_1 studies were used to study the effect of B/P concentration on T_2 values. The 7.1-T Bruker spectrometer was used to estimate T_2 values with a Hahn spin-echo pulse sequence at room temperature. A predelay time of 5 x T_1 was used for T_2 measurements to ensure that protons in each sample would relax to equilibrium before the application of the next pulse sequence. The T_2 values obtained in this manner are plotted against binder concentration in Fig. 2.

The results indicate that T_2 increases as B/P concentration increases up to 15.5 wt.%, but then decreases as B/P concentration increases further. It is not clear at present why the T_2 values peak at 15.5 wt.% B/P (the T_2 at that B/P concentration is 38% longer than the T_2 at 20 wt.%); however, it is interesting to note that 15.5 wt.% is the standard organic B/P concentration used in injection molding of Si_3N_4. It has been shown that advanced ceramic components exhibit the optimum formability and reliability at this B/P concentration. The observed variation in T_2 as a function of B/P concentration also (1) provides important information needed to interpret the S/N imaging intensity of samples containing different B/P concentrations and (2) suggests that back projection reconstruction is the appropriate imaging technique for quantitative measurement of B/P concentration by NMR imaging tomography.

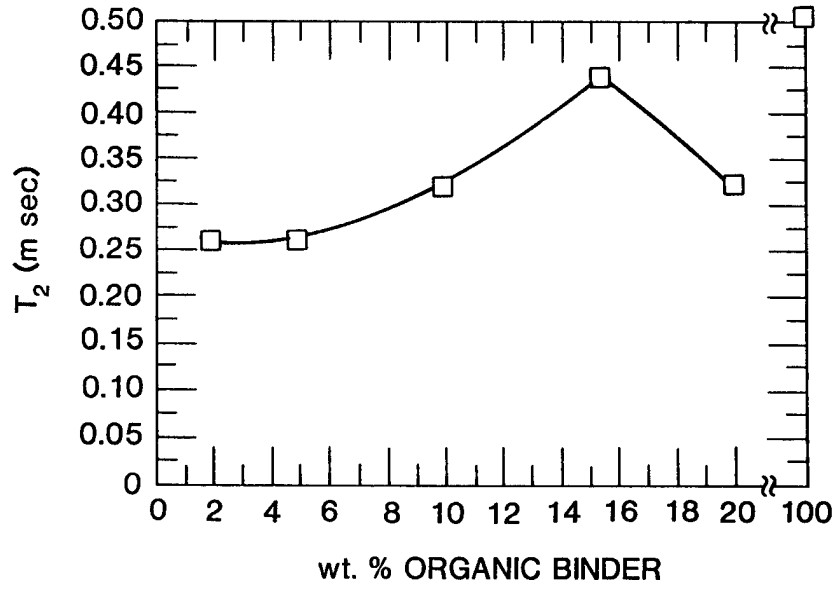

Fig. 2. Variation in T_2 with wt.% Organic B/P in Si_3N_4 Powder at 22°C.

T_2 spectroscopic studies on B/P alone and Si_3N_4 containing 15.5 wt.% binder/plasticizer, performed at 9.1 T

Two sets of samples (one of the organic B/P alone and one of pelletized GN-10 material) were studied at Massachusetts General Hospital with a 9.1-T Bruker spectrometer. These data will be compared with our 2.1-, 4.7-, and 7.1-T data to establish the influence of magnetic field strength, B_o, on relaxation effects. Also, during this reporting period, both Hahn spin-echo[2] and Carr-Purcell-Meiboom-Gill (CPMG)[3] pulse sequences were used to determine the T_2 values for B/P alone and Si_3N_4 containing 15.5 wt.% B/P at temperatures of 50 and 80°C. These data (see Table II) were used to investigate diffusion effects caused by elevated temperatures.

Table II. T_2 Values (ms) for B/P Alone and Si_3N_4 with 15.5 wt.% B/P, Measured with 9.1-T Spectrometer

Temp. (°C)	B/P Alone		Si_3N_4 + 15.5 wt.% B/P	
	Hahn	CPMG	Hahn	CPMG
50	19.2	31.2	0.50	1.23
80	104	234	0.98	2.30

At elevated temperature, the NMR relaxation time for the organic B/P sample may be subject to translational diffusion effects. These effects can be identified by using the CPMG pulse method. The higher T_2 values obtained at 50°C with the CPMG sequence, (i.e., 31.2 ms vs. 19.2 ms for the Hahn spin-echo sequence as shown in Table II) indicate that diffusion effects are present at elevated temperature. This finding suggests the need for a re-evaluation of the feasibility of using elevated-temperature NMR imaging to enhance the low intrinsic S/N ratio of these polymeric materials.

Effect of weighting functions on NMR signal amplitude

Before the raw NMR data acquired in the time domain are transformed into the frequency domain by Fourier transformation, it is the usual practice to multiply the time domain signal by a weighting function to optimize either the S/N ratio, resolution, or lineshape, depending on the type of results desired.[4] The applicability of the four most commonly used weighting functions to the imaging of solid-state organic B/P samples was investigated. These functions are exponential multiplication (EM), Gaussian multiplication (GM), double exponential multiplication (DM), and trapezoidal apodization function (TM). Initially, the effects of these weighting functions on free induction decay (FID) of the broad-linewidth, fast-decay organic B/P were studied, to identify the most promising functions for further investigation via imaging experiments.

The parameters used to acquire FID data were as follows: 85.54-MHz spectrometer frequency, 90° pulse width of 20 μsec, 20-kHz spectral width, 1024 data points of resolution, 32 scans/spectrum, 12-bit digitizer resolution, quadrature detection, and 3-sec recovery time (TR). Relative NMR signal amplitudes were normalized to that of the FID with no weighting function applied. The results (see Table III) indicate the following:

(1) Both the EM and GM weighting functions have no effect on the FID value of the organic B/P. This is because the line-broadening values used (±5 to ±50 Hz) in the EM and GM weighting functions are relatively small compared to the broad linewidth of the sample at room temperature, e.g., FWHM = 1024 Hz from this study.

(2) As the N1 value of the TM weighting function increases from 0 to 20, the relative Fourier-transformed signal amplitude decreases. Presumably, this decrease occurs because when the N1 parameter increases, the rising part of the TM function (see Fig. 3) becomes less steep; therefore, the early FID data points undergo less enhancement.

(3) As the DM parameter of the DM weighting function increases from 0 to 10, relative signal amplitude increases; this might be because when the DM parameter is higher, the DM function tends to have more impact on the early portion of the FID data (see Fig. 4). For our fast-decay organic B/P sample, the DM function will probably exhibit more significant effects on imaging as the DM parameter increases.

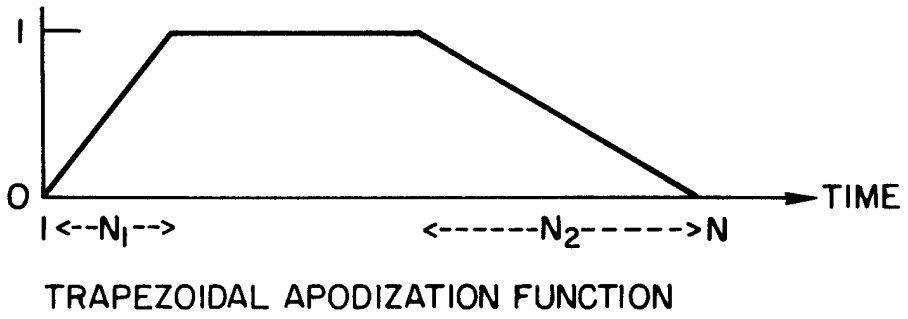

Fig. 3. A Trapezoidal Multiplication Weighting Function.

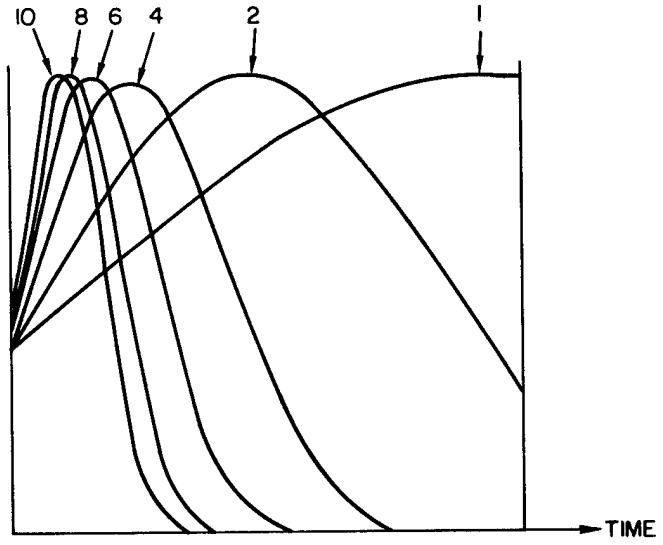

Fig. 4. A Plot of Double Exponential Multiplication (DM) Weighting Functions with Various DM Parameters.

On the basis of these preliminary studies, we decided to investigate the effects of the TM and DM weighting functions on B/P imaging. The weighting functions were applied to raw imaging data (before Fourier transformation) from an organic B/P phantom containing five drilled holes.

Effect of trapezoidal multiplication function on NMR imaging. Figure 5 shows the effects of TM weighting functions on a coronal (transaxial) image of the organic B/P phantom for values of N1,N2 ranging from 0 to 100. (An N1,N2 value of 0 indicates that no weighting function was applied.) The S/N ratio of each image (in gray

scale) was estimated by integrating the image intensity in the region of interest versus the adjacent noise level. Table IV shows the actual and normalized S/N ratios. The result indicates that the TM weighting function significantly changed the gray-scale intensity of the NMR image for this short-T_2 material. For example, a 26% higher S/N ratio was obtained with N1,N2 = 50 (image at upper right in Fig. 5) than with no TM function (image at upper left). This might be because the image obtained with N1,N2 = 50 has a linear apodization function applied from 0 to 1 in the early portion of data acquisition. Thus, some of the noise resulting from the pulse breakthough might have been minimized. As N1 increases further (from 50 to 75 to 100), the S/N ratio decreases, as observed in the previous FID study.

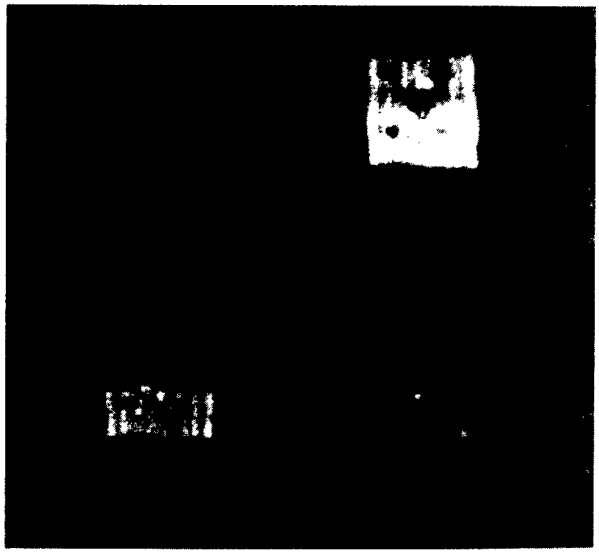

Fig. 5. Coronal Images of an Organic B/P Phantom after Use of TM Weighting Functions. (Upper left) N1,N2 = 0; (upper right) N1,N2 = 50; (lower left) N1,N2 = 75; (lower right) N1,N2 = 100.

Table IV. S/N Ratios for Images of Organic B/P Phantom, Obtained with TM Weighting Functions

	Value of TM Parameters N1 and N2			
	0	50	75	100
S/N	8.07	10.2	9.12	8.79
Normalized S/N[a]	1.00	1.26	1.13	1.09

[a]S/N normalized to that obtained with no weighting function (i.e., N1 = 0 = N2).

Effects of double exponential multiplication function on NMR imaging. Figure 6 shows the effects of DM weighting functions with DM parameters ranging from 0 to 6. The S/N ratios of the images (Table V) show a significant effect of the DM weighting function. For example, a 69% higher S/N ratio is achieved with DM = 3 than with DM = 0 (no weighting applied). However, too much enhancement by the DM weighting function can lead to peaks with negative valleys on each side and distortion of closely spaced lines. The images obtained with DM > 4 (Fig. 6) illustrate this problem. Figure 7 compares images obtained with no weighting function, the DM weighting function with DM = 3 and 4, and the TM weighting function with N1 = N2 = 50. The S/N ratios of these images are compared in Table VI.

The results indicate that with short-T_2 solid-state materials, consideration needs to be given to choosing an appropriate weighting function and associated parameters in order to enhance the intrinsic low S/N ratio characteristic of the samples.

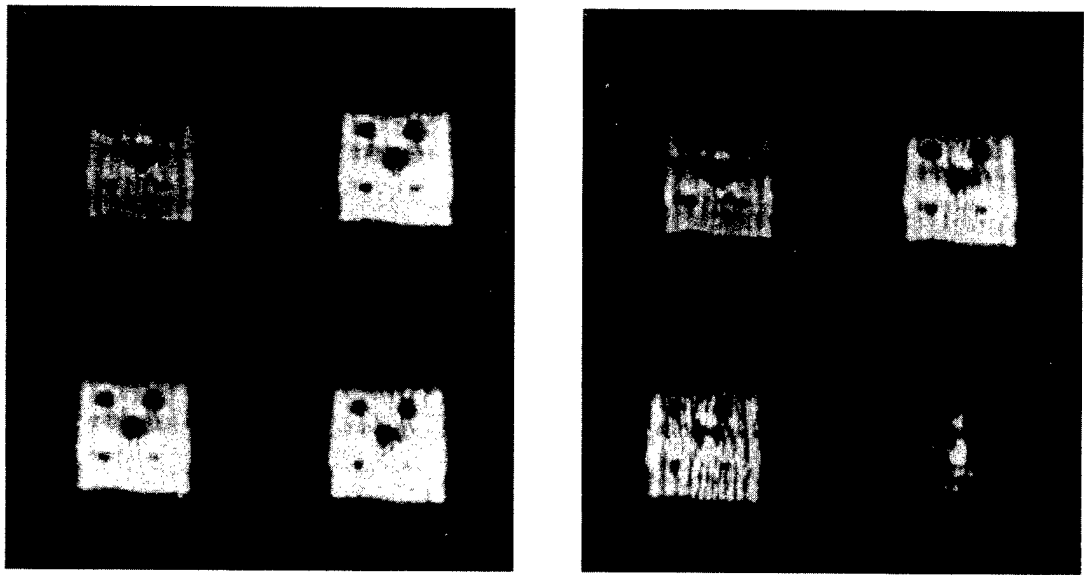

Fig. 6. Coronal Images of the Organic B/P Phantom Shown in Fig. 5 after Use of DM Weighting Functions. Left panel: (upper left) no weighting function; (upper right) DM = 2; (lower left) DM = 3; (lower right) DM = 4. Right panel: (upper left) DM = 3; (upper right) DM = 4; (lower left) DM = 5; (lower right) DM = 6.

Table V. S/N Ratios for Images of Organic B/P Phantom, Obtained with DM Weighting Functions

	Value of DM Parameter					
	0	2	3	4	5	6
S/N	8.07	9.85	13.7	11.3	6.86	4.37
Normalized S/N[a]	1.00	1.22	1.69	1.39	0.85	0.54

[a]S/N normalized to that obtained with no weighting function (i.e., DM parameter = 0).

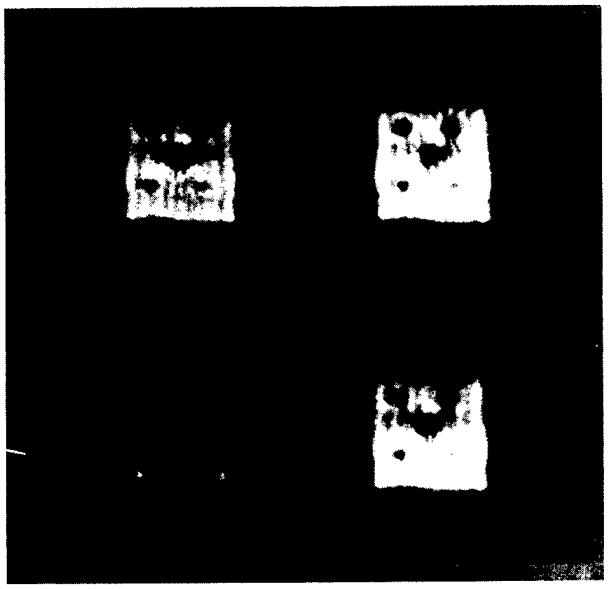

Fig. 7. Coronal Images of the Organic Binder Phantom Shown in Fig. 5 After Use of DM and TM Weighting Functions. (Upper left) DM = 3; (upper right) DM = 4; (lower left) no weighting function; (lower right) TM (N1 = 50 = N2).

Table VI. Comparison of S/N Ratios Obtained with TM and DM Weighting Functions

	No weighting function	TM (N1 = 50 = N2)	DM (DM = 3)	DM (DM = 4)
S/N	8.07	10.2	13.12	11.26
Normalized S/N[a]	1.00	1.26	1.69	1.39

[a]S/N normalized to that obtained with no weighting function.

Nuclear magnetic resonance imaging of modulus-of-rupture bars

Imaging experiments were conducted on the four groups of MOR test bars (4 bars/group) described above. A standard 2-D spin-warp spin-echo pulse sequence was used. The S/N ratios were calculated by integrating the region of interest (vs. background) in terms of gray-scale imaging intensity. The preliminary results, given in Table VII, showed variations in the integrated S/N ratios within the same group of MOR test bars; this might be due to variations in the B/P content within the regions imaged (~1.5 cm in height). The test bars will be returned to Garrett Ceramic Components Division for destructive evaluation to determine the content of polymeric organic B/P, so that correlations between NMR data and destructive analysis can begin.

Table VII. S/N Ratios for Images of Injection-molded Modulus-of-Rupture Bars

Group No.	Mix[a]	Molding Parameters[a]	Bar No.	S/N Ratio
1	S	S	1	11.99
			2	13.91
			3	10.56
			4	12.66
2	N	S	21	14.63
			22	15.69
			23	16.96
			24	15.93
3	N	N	41	12.18
			42	13.42
			43	13.07
			44	13.57
4	S	N	69	14.61
			70	15.14
			71	15.04
			72	11.21

[a]S = standard; N = nonstandard.

High-resolution solid-state NMR of organic binder/plasticizers

To determine the feasibility of using NMR to distinguish differences within and among B/P mixtures, high-resolution solid-state NMR spectroscopic techniques have been applied to several batches of soft-solid organic B/Ps. High-resolution (magic angle spinning) solid-state techniques improve the spectroscopic resolution significantly in both proton (^{1}H) and carbon (^{13}C) spectra.

One-pulse ^{1}H spectra acquired at ambient temperature without and with magic angle spinning are presented in Figs. 8a and b, respectively. With spinning, the linewidth at half maximum decreases from ~1300 Hz to ~120 Hz at 2.1 T. Additionally, the proton resonances of the methyls are partially resolved from the methylene resonances. A one-pulse ^{13}C spectrum acquired with magic angle spinning is presented in Fig. 9. The increased resolution allows integration and tentative assignment of the carbon resonances.

Status of milestones

All milestones are on schedule.

References

1. D. Shaw, *Fourier Transformation NMR Spectroscopy*, 2nd Edition, Elsevier, Oxford, 1984.

2. E. L. Hahn, "Spin Echoes," *Phys. Rev.* 80, 580-594 (1950).

3. S. Meiboom and P. Gill, Modified Spin Echo Method for Measuring Nuclear Relaxation Times," *Rev. Sci. Instrum.* 29, 688-691 (1958).

4. A. E. Derome, *Modern NMR Techniques for Chemistry Research*, Pergamon Press, New York, 1987.

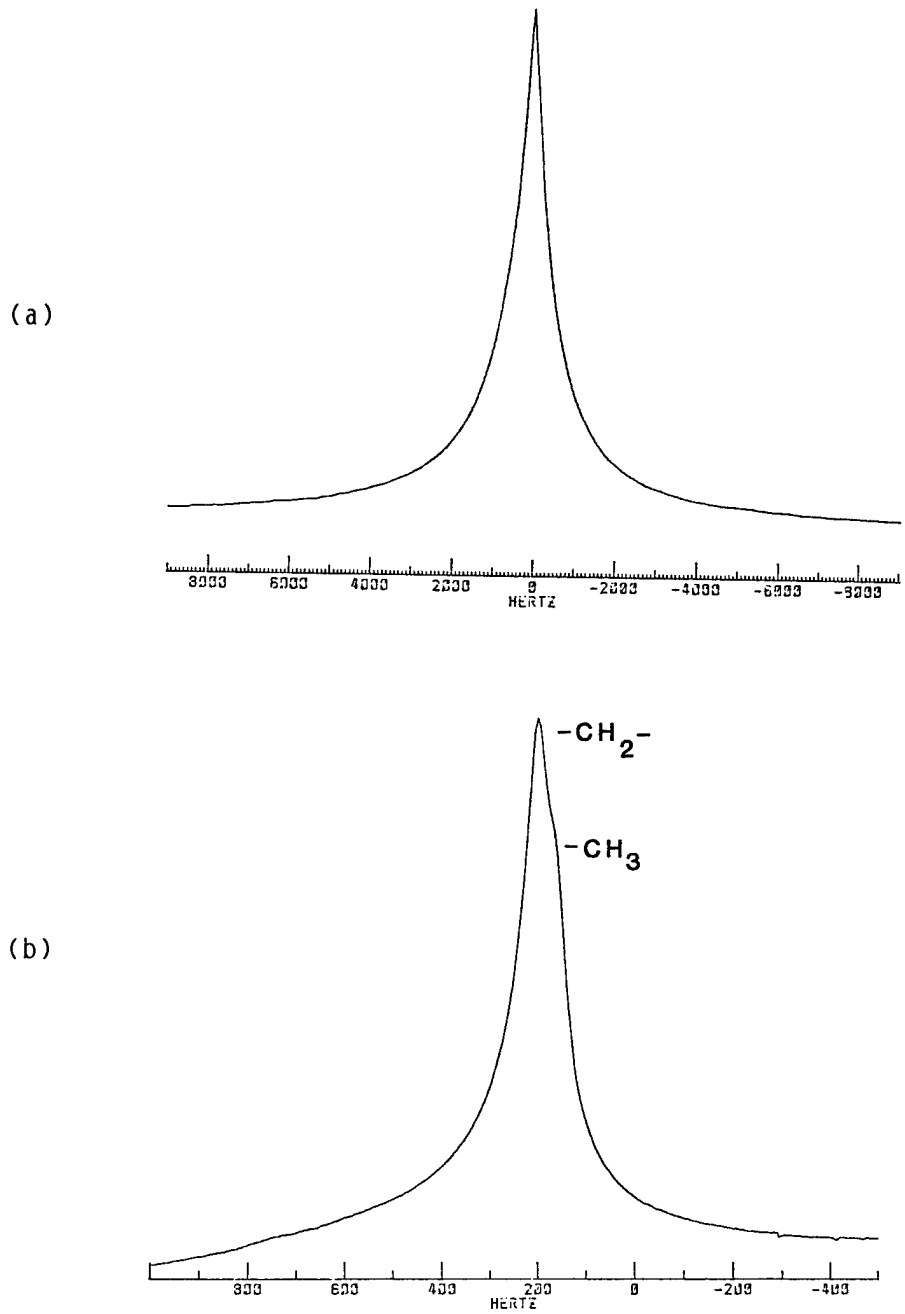

Fig. 8. One-Pulse Proton Spectrum of B/P Acquired at 2.1 T and Ambient Temperature (a) Without Spinning and (b) with a Magic Angle Spinning Rate of ~2500 Hz.

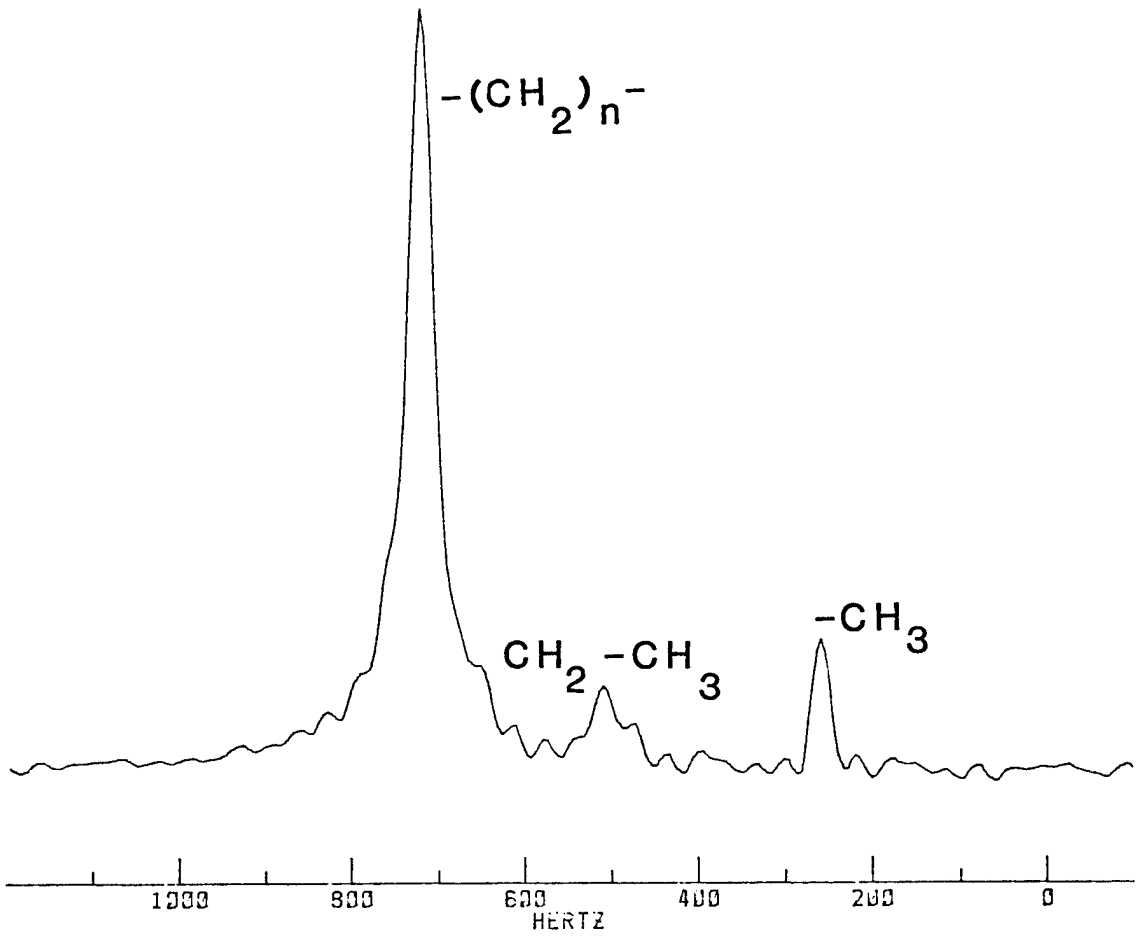

Fig. 9. One-Pulse Carbon (^{13}C) Spectrum of B/P Acquired at 2.1 T and Ambient Temperature with a Magic Angle Spinning Rate of ~2500 Hz.

Powder Characterization

O. O. Omatete, A. C. Young, and M. A. Janney (Oak Ridge National Laboratory)

Objective/scope

The objective of this research element is threefold: (1) to identify and characterize those aspects of the chemistry and physics of a ceramic powder/solvent interface that control processing; (2) to develop standard methods of analysis for item 1; and (3) to develop procedures for writing specifications for ceramic powders, to include any methods of analysis developed in the project.

Technical progress

Subcontracts

Three university subcontractors--Pennsylvania State, Rutgers and Wisconsin--have been selected and their contracts have now been signed. The kick-off meeting is scheduled for May 15-16, 1989.

In-house

The round robin measurement of electrophoretic mobility is one of the major tasks required in the subcontracts mentioned above. The need, therefore, arises for the establishment of a "benchmark" material for the mobility determinations. One set of potential materials is aqueous polystyrene latex suspensions from Interfacial Dynamics Corporation (IDC) of Portland, Oregon. Two of the IDC latexes, lot Nos. 2-112-9 and 10-36-23, were evaluated experimentally. The variation of their mobilities and of the specific conductances with pH were measured in KNO_3 and NaCl at several ionic strengths. Typical results are shown in Figs. 1 and 2 for the latex 2-112-19 in KNO_3.

In Fig. 1, the dashed lines show that the variation of latex mobility with pH at ionic strengths less than 0.01M does not conform to the expected behavior. Usually the absolute value of the latex mobility decreases with pH as the ionic strength increases as shown by the solid lines. In Fig. 2, however, the specific conductance shows the expected variation with pH at all ionic strengths.

Some preliminary results of ceramic surface characterization using gas chromatography have been obtained for alumina and silicon nitride powders. Table 1 shows the elution temperatures of several chemicals fed as probe molecules into columns packed with the two powders. The alumina RCHP DBM from Reynolds Chemicals was calcined at 800°C for 24 h before use, while the silicon nitride powder E-10 from Ube Chemicals was used as received.

Table 1 shows that all the probe molecules fed into the silicon nitride column eluted from it and all but the alcohols and pyridine eluted from the alumina column. Nonpolar and linear hydrocarbons show only slight interaction with alumina; their elution temperature varies with their molecular weights. Ketones with the high elution temperatures and the excessive tailing of their elution peaks show

strong interaction with the alumina surface. Alcohols and pyridine are so reactive that they may be permanently adsorbed by alumina in the temperature range tested. Differences were observed between the silicon nitride and the alumina columns; the elution temperatures of the ketones were higher in the alumina than in the nitride column. Also, the elution peaks and tails were quite different for the same probe molecules in the two columns. These differences could be used to characterize these powders.

As mentioned in an earlier report, Dr. Georges Guichon (an Oak Ridge National Laboratory distinguished scientist) and his coworkers in Analytical Chemistry Division are undertaking a similar study of attempting to characterize ceramic powders by gas chromatography. Using the data obtained from the previous powder dispersion studies, they have successfully constructed a surface-coated open tubular (SCOT) column with silica (SiO_2).

To pursue this research more vigorously, an order has been placed for a new sophisticated gas chromatograph system equipped with two detectors, an autoinjector and a computer data storage capability. It should be received in June 1989.

Table 1. Preliminary results of 2-112-19 in KNO_3

Chemicals[a]	Elution Temperature (°C) Al_2O_3[b]	Si_3N_4[c]
carbon disulfide	60	60
benzene	60	60
toluene	84	72
xylene	-	121
nonane	103	110
decane	124	135
undecane	146	159
dodecane	161	170
acetone	228	139
methyl-ethyl ketone	242	157
methyl-isobutyl ketone	243	183
2-butanone	-	165
ethyl ether	-	127
chloroform	-	66
methylene chloride	-	60
ethanol	n.e.[d]	-
propanol	n.e.	-
butanol	-	-
pyridine	n.e.	-

[a]Test solution: one drop of chemical in 10 mL CS_2, 2 μL per injection.

[b]Nonisothermal experiment: 60°C for 2 min, 8°C/min from 60 to 250°C and soaked for 4 min at the temperature.

[c]Experimental condition as for Al_2O_3 except final temperature was 300°C.

[d]No elution in the temperature range tested.

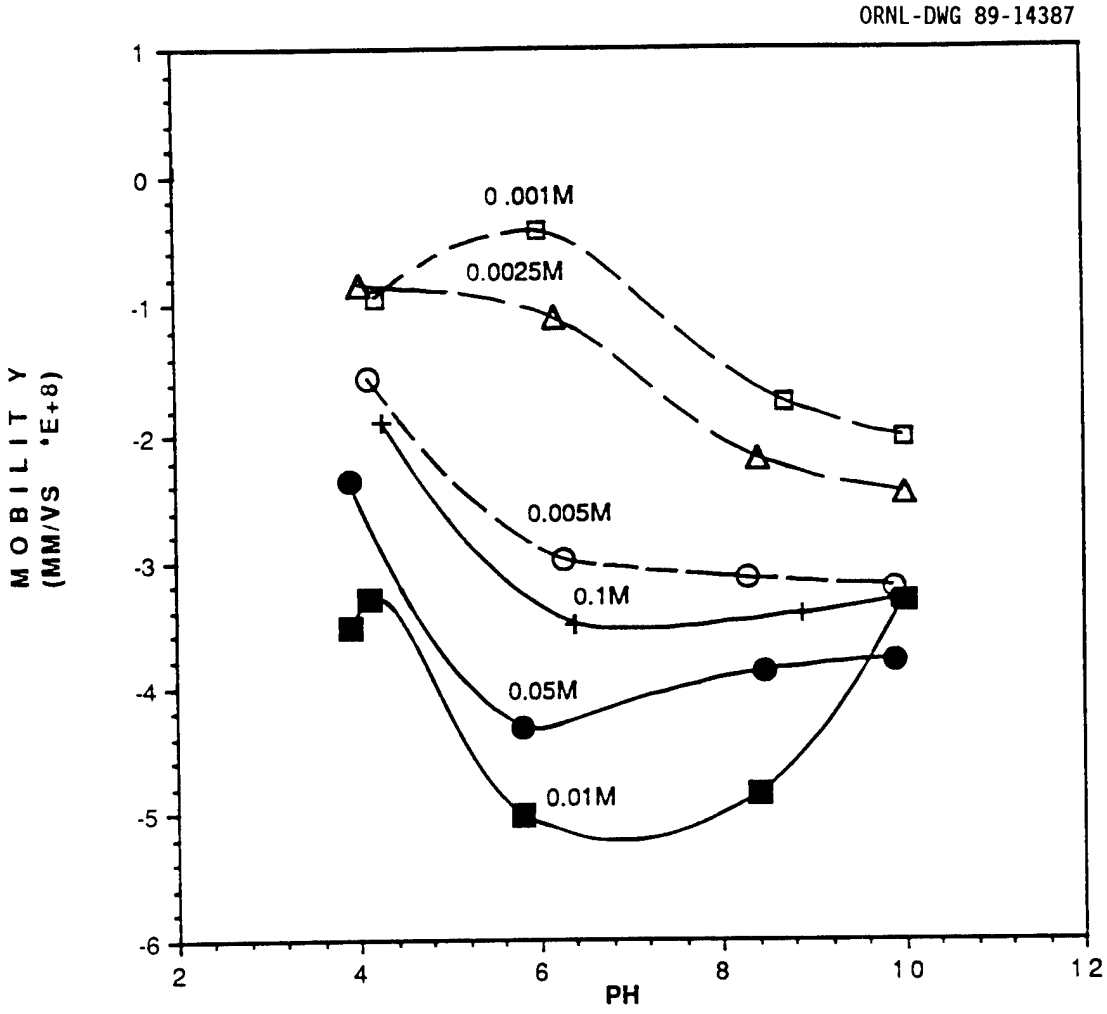

Fig. 1. Mobility of 2-112-19 in KNO_3.

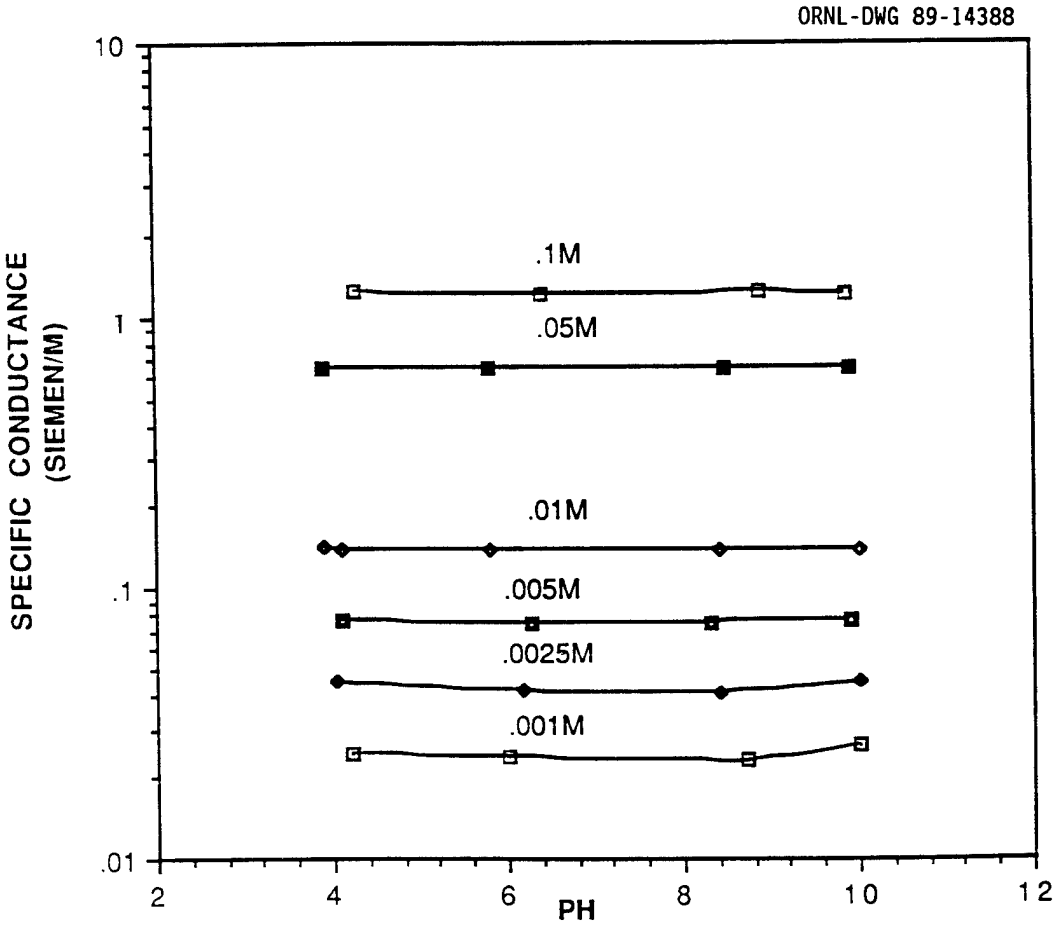

Fig. 2. Specific conductance of 2-112-19 in KNO_3.

4.0 TECHNOLOGY TRANSFER

4.1 TECHNOLOGY TRANSFER

4.1.1 Technology Transfer

Technology Transfer
D. R. Johnson (Oak Ridge National Laboratory)

Technology transfer in the Ceramic Technology Project is accomplished by a number of mechanisms including the following:

Trade shows - A portable display describing the program has been built and used at numerous national and international trade shows and technical meetings, most recently at the Society of Manufacturing Engineers Annual Conference and Exhibition on Advanced Ceramics, February 20-28, 1989, in Philadelphia.

Newsletter - A Ceramic Technology Newsletter is published regularly and sent to a large distribution.

Reports - Semiannual technical reports, which include contributions by all participants in the program, are published and sent to a large distribution. Informal bimonthly management and technical reports are distributed to the participants in the program. Open-literature reports are required of all research and development participants.

Direct Assistance - Direct assistance is provided to subcontractors in the program via access to unique characterization and testing facilities at the Oak Ridge National Laboratory.

Workshops - Topical workshops are held on subjects of vital concern to our community.

International Cooperation - Our program is actively involved in and supportive of the cooperative work being done by researchers in West Germany, Sweden, and the United States under an agreement with the International Energy Agency. That work, ultimately aimed at development of international standards includes physical, morphological, and microstructural characterization of ceramic powders and dense ceramic bodies, and mechanical characterization of dense ceramics. Detailed planning and procurement of ceramic powders and flexural test bars have been accomplished. Exchange of preliminary data on ceramic and powder characterization results has been started by those laboratories participating.

IEA ANNEX II Management

V. J. Tennery (Oak Ridge National Laboratory)

Objective/scope

The IEA Annex II agreement between the United States, the Federal Republic of Germany, and Sweden on structural ceramics is directed to cooperative research and development oriented to the identification and adoption of standardized methods for characterizing these materials. This agreement includes four subtasks: (1) information exchange, (2) ceramic powder characterization, (3) ceramic chemistry and structural characterization, and (4) ceramic mechanical property characterization. Each country is providing selected ceramic powders and sintered structural ceramics for use in the research work in Subtasks 2, 3, and 4 in all three participating countries. Participating laboratories in all three countries have agreed to share all resulting data with the purpose of using the knowledge gained from the work for developing standard measurement methods for characterizing ceramic powders and sintered structural ceramics.

The lack of such standard measurement methods has been an impediment to the evolution and development of structural ceramics, both from the point of view of the manufacturer and the user. This Annex II agreement was conceived to accelerate the development of standard methods for determining important properties of these evolving materials.

In the United States, many companies and their research staffs have contributed significant resources in performing the required measurements. In the United States, for example, in Subtask 2, 12 laboratories are participating; in Subtask 3, 7 laboratories are participating; and in Subtask 4, 8 laboratories are participating.

The research in Subtask 2 includes five ceramic powders which are being studied in this subtask. For Subtasks 3 and 4, three sintered ceramics are being studied, including one from each of the three countries. The ceramic from the United States is a silicon nitride, SNW-1000 from GTE-Wesgo, that from Germany is a hipped SiC from ESK Kempton, and that from Sweden is a silicon nitride from ASEA Cerama.

With the approaching conclusion of Annex II research, considerable discussion has been held in the United States relative to possible content of continued cooperative international research similar to that conducted under the Annex II agreement. Due to the different rates at which the research in Subtasks 2, 3, and 4 has progressed, the status of these discussions differs for each subtask. At the present time, mechanical properties research in Subtask 4 is nearest to completion, and therefore, in the United States, consideration of further research in this area is most mature. Research plans in the area of mechanical properties for an Annex III agreement were reviewed at the Executive Committee meeting held on November 30, 1988, in the United States. Results from the ceramic powder characterization research in Subtask 2 will be completed second, and it is planned to have future research plans finalized for cooperative ceramic powder characterization research by the middle of CY 1989. Results from sintered ceramic characterization in Subtask 3 will be available last, and it is not clear at this time if further research in this area will be supported as part of a

future international agreement. The status of the research in the three subtasks, powder characterization, sintered ceramic characterization, and mechanical properties within the United States relative to a possible Annex III agreement is discussed later in this report.

Technical progress

The major technical status changes since the last semiannual report will be reviewed briefly.

Subtask 2 - Ceramic Powder Characterization--A meeting to review all data and discuss possible future work was held on October 10 and 11, in Bertchesgaden, Federal Republic of Germany. At this meeting, A. Dragoo and S. Hsu of NIST distributed a draft copy of the data from all laboratories participating in Subtask 2. This document includes all data received to date resulting from work in the three countries on ceramic powder characterization, and includes data in both tabular and graphical form. This compilation includes all data for four of the powders studied, and is the largest assemblage of ceramic powder property results from a large number of laboratories ever completed. Results for the Toyasoda zirconia powder from Japan were not included, since these were covered in detail last November at the Orlando working group meeting.

During this meeting in Germany, it was agreed that the following schedule will be met for completing the work in Subtask 2 on ceramic powder characterization.

12/15/88 - All corrections in current data set due to S. Hsu, NIST.
4/30/89 - Part 1 of Final Report (Data Only) to printer (responsibility of S. Hsu).
6/1/89 - S. Hsu submits final revised Part 2 report to IEA Executive Committee for comment.
8/31/89 - Draft of final report to be distributed by NIST to participants.
12/15/89 - Part 2 of Final Report (Analysis and Recommendations) is published and distributed to participants.
12/15/89 - Statistical analysis of data started. (Optional as to completion; responsibility undetermined, but possibly NIST.)

Publication of Part 2 of the final report will officially conclude Subtask 2, and since this subtask will be the last component of the original work finished under the Annex, its completion will also officially conclude the work under the original work scope of Annex II. R. Neumann, senior person present representing the FRG, was quite emphatic that all research associated with the present Annex II research scope, including publication and distribution of the final reports, should be finished by the end of CY 1989.

The three national coordinators for Subtask 2 met on January 17 at the American Ceramic Society meeting in Cocoa Beach, Florida, and

further resolved final data needs from the NIST compilation provided at the Bertchesgaden meeting and reviewed recommendations for possible future work. Future work needs were considered in the three subject areas in the subtask, namely, (1) chemical characterization, (2) particle size distribution, and (3) other physical properties. These three areas are the responsibility of A. Dragoo, NIST (USA); H. Hausner, Technical University of Berlin (FRG); and R. Pompe, Swedish Silicate Institute (Sweden). At the 91st Annual Meeting of the American Ceramic Society, April 25, these three national coordinators will meet again to review their national positions on the state of ceramic powder characterization and the conclusions from this meeting will form the basis of the report and recommendation for possible future research due to the Executive Committee from S. Hsu by June 1, 1989.

The minutes of the Berchesgaden meeting were distributed by Dr. Boesch of EER, Inc. A meeting of possible future participants in powder characterization research from the U.S. will be held in Indianapolis on April 24. Steve Hsu and Alan Dragoo of the NIST are responsible for formulating these discussions into an inquiry to U.S. researchers who are potential participants in the follow-on research on characterization of ceramic powders. The response to this inquiry will form the basis for the U.S. position on future IEA based research in the area of ceramic powders. In addition, any changes or additions to the ceramic powder data compilation which NIST provided at Berchesgaden were completed. NIST is proceeding with getting the report into a final form for submission to ORNL for publication. The first portion, the data sets (Part 1 of this report), is scheduled to be provided to ORNL ready for publication by April 30, with Part 2 being provided to the Executive Committee by Steve Hsu by June 1.

Steve Hsu and Alan Dragoo of the NIST continued work on identifying candidate participants for possible follow on research on characterization of ceramic powders. The response to this inquiry will form the basis for the U.S. position on future IEA based research in the area of ceramic powders, and determine if DOE will support such future work. In addition, they continued work on the Subtask 2 report, which is due shortly to ORNL for publication. NIST is proceeding with getting the report into final form. The first portion of the report, the data sets (Part 1 of this report), is scheduled to be provided to ORNL ready for publication by April 30, with Part 2 being provided to the Executive Committee by Steve Hsu by June 1. The minutes of the national coordinator's meeting held in Cocoa Beach in January were received on March 9.

Subtask 3, Chemical Characterization of Sintered Ceramics--A letter was sent by V. J. Tennery (ORNL) in early December to all U.S. participants in Subtask 3 with a copy of the Swedish draft report for Subtask 3, requesting some additional details concerning the analysis techniques used and review comments by January 11, 1989. These were all received by the end of January, and a copy of the draft report including all U.S. modifications was sent to Dr. Hatcher in Sweden at the end of January.

In early February, a marked draft of the report was sent to Dr. Hatcher. A reply was received from Dr. Hatcher later that month agreeing with the suggestions, which included a distribution list for

the report in Sweden. It was agreed at the end of March that this report will also be published by ORNL, and that the final master of the report will be delivered to us at the end of April.

Subtask 4, Mechanical Properties of Ceramics--A final edited version of the fracture analysis report written in Germany was returned to Dr. Munz, along with the final version of the fractography analysis report written at ORNL. A research proposal describing future mechanical property research was prepared and distributed by ORNL. Information was solicited by ORNL and received from a number of U.S. industrial researchers to determine their interest and willingness to participate in the proposed follow-on mechanical property research including tensile and flexure strength measurements of ceramics and extensive strain gauging of specimens. A U.S. working group meeting was held in Dearborn, Michigan, on October 26 to discuss these plans. Eight industrial and two federal laboratories agreed to a research work scope including the ORNL proposal which was then presented to the members of the Executive Committee at the meeting on November 30. At this meeting, representatives of Germany presented a revised version of their proposal for future work, which was similar to the German proposal of October 1987. This new German proposal is being distributed to representatives of the 10 U.S. laboratories who previously agreed to the new U.S. proposal for comment by January 11.

At the Executive Committee meeting of November 30, it was agreed for efficiency reasons that any future research work will be conducted as new subtasks of Annex II, rather than pursue establishment of a new Annex III. Specifically, any mechanical property research will be organized and conducted as a new Subtask 5. Powder characterization or other work beyond the present research work scope will identified as subtasks above Subtask 5. It was also agreed that new countries will be offered entry as participants in new research under Annex II after the three presently participating countries agree on a research agenda. Countries interested in participating will possibly be invited to a workshop at which time the research plan will be presented for their consideration. It was agreed that new participating countries will not be given an option of proposing changes to the research agenda.

Opinions were solicited in the United States of the new German proposal distributed at the Las Vegas meeting at the end of November 1988. This included the response of the nine U.S. laboratories who had earlier agreed to accept the U.S. proposal and participate in additional research on mechanical properties as an extension (Subtask 5) of Annex II. The responses from these laboratories (eight industrial and one federal) (ORNL did not contribute to these opinions) favored the U.S. proposal because they felt that the tensile strength research coupled with the flexural strength measurements and use of strain gaged specimens would answer several critical questions presently complicating their attainment of the goal of high reliability strength measurements of structural ceramics.

A final version copy of the ORNL written fractography report was sent to Ms. Vierkorn-Rudolph of the KFA in Germany in December. Copies of this report were also sent to Dr. Hatcher and Dr. Pompe in Sweden in December for their information and comments. The German participants

contacted V. J. Tennery in January, and suggested that papers describing the results of Subtask 4 research be presented at the meeting of the European Ceramic Society in the Netherlands in June. It was decided, with DOE agreement to do so. During this period, correspondence with representatives of Japan who attended the IEA discussions at Las Vegas indicated that several researchers in Japan are anxiously waiting for a procedure to be identified for the Japanese ceramic community to become involved with the mechanical property research to be an extension of the present Annex II agreement. This contact was formalized via a letter from DOE Headquarters to a representative of MITI in Tokyo, in which Japan was asked to consider participating in the research outlined in the U.S. proposal.

The fractography and fracture analysis reports have been completed and are now in the publication process at ORNL. These reports should be ready for distribution by the middle of June. A meeting was held with Dr. D. Munz of Germany in Florida on March 15 to discuss the German position regarding follow on research in the area of mechanical properties. It appeared that little discussion had been held in Germany since last November when the U.S. proposal was presented at the Executive Committee meeting in Las Vegas. Munz agreed to meet with Neumann when he returned to Germany. During discussions with Munz at ORNL on March 20, it was agreed that he would try to clarify the German position as soon as possible. Recently, Dr. Munz has indicated that Germany is willing to include some level of tensile strength measurement research in future IEA Annex tasks. Several of the candidate U.S. participants in the future proposed structural ceramic research have expressed concern about the delay in starting the work. Some have indicated that if the research is not started reasonably soon, they can not be a participant. This was communicated to DOE headquarters personnel in mid-March, with the suggestion that the research be started unilaterally in the United States. The reply from DOE in a letter of March 28 indicated that the research could not be pursued with use of DOE funds for the foreseeable future. It therefore appears that further cooperative mechanical property research on structural ceramics under this annex may not occur.

Standard Reference Materials

A. L. Dragoo, S. G. Malghan, L. S. Lum, D. B. Minor, J. F. Kelly, and J. P. Cline (National Institute of Standards and Technology)

Objective/scope

Ceramics have been successfully employed in engines on a demonstration basis. The successful manufacture and use of ceramics in advanced engines depends on the development of reliable materials that will withstand high, rapidly varying thermal stress loads. Improvement in the characterization of ceramic starting powders is a critical factor in achieving reliable ceramic materials for engine applications. The production and utilization of such powders require characterization methods and property standards for quality assurance.

The objectives of the NBS program are (1) to assist with the division and distribution of five ceramic starting powders for an international round-robin on powder characterization; (2) to provide reliable data on physical (dimensional), chemical and phase characteristics of two silicon nitride powders: a reference and a test powder; and (3) to conduct statistical assessment and modeling of round-robin data. This program is directed toward a critical assessment of powder characterization methodology and toward establishment of a basis for the evaluation of fine powder precursors for ceramic processing. This work will examine and compare by a variety of statistical means the various measurement methodologies employed in the round-robin and the correlations among the various parameters and characteristics evaluated. The results of the round-robin are expected to provide the basis for identifying measurements for which Standard Reference Materials are needed and to provide property and statistical data which will serve the development of internationally accepted standards.

Technical progress

The technical progress covered in this report includes descriptions of work on the preparation of powder samples for the IEA/ANNEX II, Subtask 2, powder characterization round-robin and of the compilation and analysis of round-robin data.

Division, Distribution and Certification of Ceramic Starting Powders. This phase of the work is completed.

Powder Characterization. Characterization of powders for the Subtask 2 round-robin was completed during the previous reporting period. However, a statistical design study of the influence of sample preparation on particle size measurements by X-ray sedigraph is in progress as a part of another project on silicon nitride powder milling characterization. This study will contribute to the interpretation of the round-robin data and to the design of future round-robins intended to test sedigraph measurements.

Data Analysis. Since the IEA Subtask 2 meeting at Berchtesgaden, FGR, in October 1988, correction and final updating of all round-robin data for Subtask 2 was carried out. A new tabulation of the compiled data and summary statistics were prepared. Descriptions of the measurement methods were written. These are now being assembled into a manuscript for publication.

As agreed upon by the participants at Berchtesgaden, the technical leaders for Subtask 2 (H. Hausner, FGR; R. Pompe, Sweden; A. Dragoo) began the preparation of a report for the technical analysis of the data. Responsibilities for the various sections of the report were assigned as follows: (1) particle size measurements, Hausner; (2) specific surface area, permeametry and microscopy, Pompe; and (3) chemical and phase analyses, Dragoo. The technical leaders met at Coco Beach, FL, in January to plan the report and to establish guidelines for its preparation. The technical leaders agreed that the technical analyses will focus on evaluation and comparison of the measurement methods used for each property. The technical leaders will meet again at Indianapolis, IN, in April to exchange manuscripts and to discuss the report and their conclusions. The manuscript for the report is expected to be completed during the summer of 1989.

Status of milestone

Task 1. Subtask A and B are completed. Subtask C, intermediate milestones 411603 and 411604 are showing slippage due to larger than anticipated quantity of revisions and analysis.

ORNL/TM-11239

INTERNAL DISTRIBUTION

1-2. Central Research Library
3. Document Reference Section
4-5. Laboratory Records Department
6. Laboratory Records, ORNL RC
7. ORNL Patent Section
8-9. M&C Records Office
10. L. F. Allard, Jr.
11. B. R. Appleton
12. R. L. Beatty
13. P. F. Becher
14. T. M. Besmann
15. P. J. Blau
16. A. Bleier
17. E. E. Bloom
18. K. W. Boling
19. R. A. Bradley
20. C. R. Brinkman
21. V. R. Bullington
22. R. S. Carlsmith
23. P. T. Carlson
24. J. V. Cathcart
25. G. M. Caton
26. R. H. Cooper
27. S. A. David
28. J. H. DeVan
29. J. I. Federer
30. M. K. Ferber
31. W. Fulkerson
32. R. L. Graves
33. D. L. Greene
34. M. A. Janney
35-39. D. R. Johnson
40. R. R. Judkins
41. M. A. Karnitz
42. B. L. P. Keyes
43. H. D. Kimrey, Jr.
44. T. G. Kollie
45. T. B. Lindemer
46. K. C. Liu
47. E. L. Long, Jr.
48. W. D. Manly
49. R. W. McClung
50. D. L. McElroy
51. D. J. McGuire
52. J. R. Merriman
53. A. J. Moorhead
54. T. A. Nolan
55. J. L. Rich
56. C. R. Richmond
57. J. M. Robbins
58. M. W. Rosenthal
59. M. L. Santella
60. A. C. Schaffhauser
61. G. M. Slaughter
62. W. B. Snyder, Jr.
63. E. J. Soderstrom
64. D. P. Stinton
65. R. W. Swindeman
66. V. J. Tennery
67. T. N. Tiegs
68. J. R. Weir, Jr.
69. F. W. Wiffen
70. R. K. Williams
71. S. G. Winslow
72. C. S. Yust

EXTERNAL DISTRIBUTION

73. Donald F. Adams
University of Wyoming
Mechanical Engineering
Department
Laramie, WY 82071

74. Jane W. Adams
Corning Glass Works
SP-DV-21
Corning, NY 14831

75. J. Ahmad
Battelle Columbus
Laboratories
Engineering Mechanics
Department
505 King Avenue
Columbus, OH 43201-2693

76. Richard L. Allor
Ford Motor Company
Material Systems Reliability Division
20000 Rotunda Drive
P.O. Box 2053
Dearborn, MI 48121-2053

77. Richard T. Alpaugh
U.S. Department of Energy
Office of Transportation Systems
Forrestal Building CE-151
1000 Independence Avenue, SW.
Washington, DC 20585

78. Norman C. Anderson
Ceradyne, Inc.
Ceramic-to-Metal Division
3169 Redhill Avenue
Costa Mesa, CA 92626

79. H. Arbabi
Brunel University
Department of Materials Technology
Uxbridge Middlesex UB8 3PH
UNITED KINGDOM

80. V. S. Avva
NC A&T State University
Department of Mechanical Engineering
Greensboro, NC 27411

81. Kirit J. Bahnsali
U.S. Army Materials Technology Laboratory
SLCMT-EMM
405 Aresnal Street
Watertown, MA 02172

82. John M. Bailey
Caterpillar, Inc.
Research Department
Technical Center, Building L
P.O. Box 1875
Peoria, IL 61656-1875

83. Murray Bailey
NASA Lewis Research Center
21000 Brookpark Road, MS:77-6
Cleveland, OH 44135

84. R. R. Baker
Ceradyne, Inc.
3169 Red Hill Avenue
Costa Mesa, CA 92626

85. J. Gary Baldoni
GTE Laboratories, Inc.
40 Sylvan Road
Waltham, MA 02254

86. Dr. P. M. Barnard
Ruston Gas Turbines Limited
New Products Division
Firth Road
Lincoln LN6 7AA
ENGLAND

87. J. L. Bates
Battelle Pacific Northwest Laboratories
PSL/3000 Area
Richland, WA 99352

88. A. L. Bement, Jr.
TRW, Inc.
23555 Euclid Avenue
Cleveland, OH 44117

89. M. Bentele
Xamag, Inc.
259 Melville Avenue
Fairfield, CT 06430

90. Clifton G. Bergeron
University of Illinois
Department of Ceramic Engineering
204 Ceramic Building
105 South Goodwin Avenue
Urbana, IL 61801

91. Deane I. Biehler
Caterpillar, Inc.
Engineering and Research Materials
Technical Center, Building E
P.O. Box 1875
Peoria, IL 61656-1875

92. William D. Bjorndahl
TRW, Inc.
Materials Characterization and Chemical Analysis Department
Building 01, Room 2060
One Space Park
Redonda Beach, CA 90278

93. Dan Blake
Solar Energy Research Institute
1617 Cole Boulevard
Golden, CO 80401

94. Keith Blandford
Boride Products, Inc.
2879 Aero Park Drive
Traverse City, MI 49684

95. Paul N. Blumberg
Ricardo-ITI
415 East Plaza Drive
Westmont, IL 60559

96. Wolfgang D. G. Boecker
Carborundum Company
Niagara Falls R&D Center
P.O. Box 832
Niagara Falls, NY 14302

97. Tibor Bornemisza
Sundstrand Turbomach
Division of Sundstrand Corporation
4400 Ruffin Road
P.O. Box 85757
San Diego, CA 92138-5757

98. Han Juergen Bossmeyer
BMW Technologies, Inc.
Watermill Center
800 South Street
Waltham, MA 02154

99. J.A.M. Boulet
University of Tennessee
310 Perkins Hall
Knoxville, TN 37996

100. Steve Bradley
Signal UOP Research Center
50 UOP Plaza
Des Plaines, IL 60016

101. Raymond J. Bratton
Westinghouse Electric Corporation
R&D Center, 1310 Beulah Road
Pittsburgh, PA 15235

102. Catherine E. Brown
E. 1. DuPont de Nemours & Company
Experimental Station
Information Center E302/301
Wilmington, DE 19898

103. J. J. Brown
Virginia Polytechnic Institute and State University
Department of Materials Engineering
Blacksburg, VA 24061

104. S. L. Bruner
Ceramatec, Inc.
2425 South 900 West
Salt Lake City, UT 84119

105. W. Bryzik
U.S. Army Tank Automotive Command
R&D Center, Propulsion Systems Division
Warren, MI 48090

106. S. T. Buljan
GTE Laboratories, Inc.
40 Sylvan Road
Waltham, MA 02254

107. John M. Byrne, Jr.
PPG Industries, Inc.
Corporate Development Department
One PPG Place
Pittsburgh, PA 15272

108. Donald J. Campbell
Air Force Wright
Aeronautical Laboratory
AFWAL/POX
Wright-Patterson AFB, OH
45433

109. Larry E. Campbell
American Matrix, Inc.
118 Sherlake Drive
Knoxville, TN 37922

110. Roger Cannon
Rutgers University
Department of Ceramics
Bowser Road, P.O. Box 909
Piscataway, NJ 08855-0909

111. Harry W. Carpenter
19945 Acre Street
Northridge, CA 91324

112. David Carruthers
Allied-Signal Aerospace
Company
Garrett Auxiliary Power
Division
2739 East Washington Street
P.O. Box 5227
Phoenix, AZ 85010

113. Jere G. Castor
Allied-Signal Aerospace
Company
Garrett Auxiliary Power
Division
2739 East Washington Street
P.O. Box 5227
Phoenix, AZ 85010

114. En-sheng Chen
B&C Engineering Research
13906 Dentwood Drive
Houston, TX 77014

115. Albert A. Chesnes
U.S. Department of Energy
Office of Transportation
Systems
Forrestal Building CE-151,
5G-048
1000 Independence Avenue, SW
Washington, DC 20585

116. Frank Childs
EG&G, Inc.
Idaho National Engineering
Laboratory
P.O. Box 1625
Idaho Falls, ID 83415

117. Gilbert Y. Chin
Bell Telephone Laboratories
Research & Development
Murray Hill, NJ 07974

118. Melvin H. Chiogioji
U.S. Department of Energy
Office of Transportation
Systems
Forrestal Building CE-15
1000 Independence Avenue, SW
Washington, DC 20585

119. William J. Chmura
The Torrington Company
Corporate Research
59 Field Street
Torrington, CT 06790

120. Eugene V. Clark
Turbine Metal Technology, Inc.
7327 Elmo Street
Tujunga, CA 91042-2204

121. William L. Cleary
ORI, Inc.
1375 Piccard Drive
Rockville, MD 20850

122. Jack L. Clem
J. M. Huber Corporation
Carbon Black Division
P.O. Box 2831
Borger, TX 79008-2831

123. Harry E. Cook
Chrysler Motors Corporation
Automotive Research and
Technical Planning
1200 Chrysler Drive
Highland Park, MI 48288

124. Stephen Copley
University of Southern California
Materials Science Department
Los Angeles, CA 90089

125. John A. Coppola
Carborundum Company
Structural Ceramics Division
Building 91-2, P.O. Box 1054
Niagara Falls, NY 14302

126. Normand D. Corbin
Norton Company
Advanced Ceramics
Goddard Road
Northboro, MA 01532-1545

127. Charles H. Craig
Defense Technology Security Administration
400 Army-Navy Drive
Suite 300
Arlington, VA 22202

128. William J. Croft
U.S. Army Materials Technology Laboratory
405 Arsenal Street
Watertown, MA 02172

129. Gary M. Crosbie
1430 Culver Avenue
Dearborn, MI 48121

130. Floyd W. Crouse, Jr.
U.S. Department of Energy
Morgantown Energy Technology Center
P.O. Box 880
Morgantown, WV 26505

131. Raymond Cutler
Ceramatec, Inc.
2425 South 900 West
Salt Lake City, UT 84119

132. David A. Dalman
The Dow Chemical Company
Central Research, Organic Specialities Laboratory
1776 Building
Midland, MI 48674

133. James I. Dalton
Reynolds Metals Company
Metallurgy Laboratory
Fourth and Canal Streets
P.O. Box 27003
Richmond, VA 23261

134. Stephen C. Danforth
Rutgers University
Bowser Road, P.O. Box 909
Piscataway, NJ 08854

135. Robert F. Davis
North Carolina State University
Materials Engineering Department
232 Riddick Laboratory
Box 7907
Raleigh, NC 27695

136. Evelyn M. DeLiso
Corning Glass Works
Corning, NY 14831

137. J. Franklyn DeRidder
Omni Electro Motive, Inc.
12 Seely Hill Road
Newfield, NY 14867

138. Alan L. Dragoo
National Institute of Standards and Technology
Inorganic Materials Division
Gaithersburg, MD 20899

139. Keith F. Dufrane
Battelle Columbus Laboratories
505 King Avenue
Columbus, OH 43201

140. Edmund M. Dunn
GTE Laboratories, Inc.
40 Sylvan Road
Waltham, MA 02254

141. Jeremy D. Dunning
Indiana University
Industrial Research
Liaison Program
Bloomington, IN 47405

142. Dr. Sunil Dutta
NASA Lewis Research Center
21000 Brookpark Road
MS:49-3
Cleveland, OH 44135

143. Paul N. Dyer
Air Products and Chemicals,
Inc.
P.O. Box 538
Allentown, PA 18105

144. Robert J. Eagan
Sandia National Laboratories
Department 1840
P.O. Box 5800
Albuquerque, NM 87185

145. J. J. Eberhardt
U.S. Department of Energy
Energy Conversion and
Utilization Technologies
Program
Forrestal Building CE-12
1000 Independence Avenue, SW
Washington, DC 20585

146. William A. Ellingson
Argonne National Laboratory
9700 South Cass Avenue
Argonne, IL 60439

147. Charles D. Estes
U.S. Senate
Committee on Appropriations
SD-152 Dirksen Senate
Washington, DC 20510

148. John N. Eustis
U.S. Department of Energy
Office of Industrial
Programs
Forrestal Building CE-141
1000 Independence Avenue, SW
Washington, DC 20585

149. Peggy Evanich
National Aeronautics and
Space Administration
Energy Systems Office
Washington, DC 20546

150. Anthony G. Evans
University of California
College of Engineering
Santa Barbara, CA 93106

151. Robert C. Evans
NASA Lewis Research Center
Vehicular Gas Turbine and
Diesel Project Office
21000 Brookpark Road
MS:77-6
Cleveland, OH 44135

152. Katherine T. Faber
Ohio State University
Department of Ceramic
Engineering
2041 College Road
Columbus, OH 43210

153. John W. Fairbanks
U.S. Department of Energy
Office of Transportation
Systems
Forrestal Building CE-151,
5G-042
1000 Independence Avenue
Washington, DC 20585

154. Larry Farrell
Babcock and Wilcox
Old Forrest Road
Lynchburg, VA 24505

155. Rolf Fasth
Chem Systems, Inc.
303 South Broadway
Tarrytown, NY 10591

156. H. W. Foglesong
Dow Corning Corporation
3901 South Saginaw Road
Midland, MI 48686

157. Thomas F. Foltz
Avco Corporation
Special Materials Division
Two Industrial Avenue
Lowell, MA 01851

158. Robert G. Frank
Technology Assessment Group
10793 Bentley Pass Lane
Cincinnati, OH 45140

159. Douglas W. Freitag
LTV Aerospace and Defense Company
High Temperature Materials Research
P.O. Box 225907, MS:TH-85
Dallas, TX 75265

160. P. A. Gaydos
Battelle Columbus Laboratories
505 King Avenue
Columbus, OH 43201

161. George E. Gazza
U.S. Army Materials Technology Laboratory
Ceramics Research Division
405 Arsenal Street
Watertown, MA 02172

162. Charles M. Gilmore
The George Washington University
Department of Civil, Mechanical, and Environmental Engineering
Washington, DC 20052

163. Paul Glance
Concept Analysis
Dupont Automotive Development Bldg.
950 Stephenson Highway
Troy, MI 48007-7013

164. Fred M. Glaser
U.S. Department of Energy
Office of Fossil Energy
FE-14 GTN, Germantown GTN
Washington, DC 20545

165. Joseph W. Glatz
Naval Air Propulsion Test Center
Systems Technology Division
Box 7176, PE 34
Trenton, NJ 08628

166. W. M. Goldberger
Superior Graphite Company
2175 East Broad Street
Columbus, OH 43209

167. Stephen T. Gonczy
Signal UOP Research Center
Materials Science Department
50 UOP Plaza
Des Plaines, IL 60016

168. Robert J. Gottschall
U.S. Department of Energy
Office of Material Sciences
ER-131 GTN, Germantown GTN
MS:G-256
Washington, DC 20545

169. Dr. Earl Graham
Cleveland State University
Department of Chemical Engineering
Uclid Avenue at East 24th Street
Cleveland, OH 44115

170. Kenneth Green
Coors Ceramics Company
17750 West 32nd Street
Golden, CO 80401

171. Robert E. Green, Jr.
The Johns Hopkins University
Center for Nondestructive Evaluation
Maryland Hall 107
Baltimore, MD 21218

172. Lance E. Groseclose
General Motors Corporation
Allison Gas Turbine Division
P.O. Box 420
Indianapolis, IN 46206

173. T. D. Gulden
General Atomics
P.O. Box 81608
San Diego, CA 92138

174. P. Ulf Gummeson
Hoeganaes
River Road and Taylors Lane
Riverton, NJ 08077

175. Bimleshwar P. Gupta
Solar Energy Research Institute
Solar Heat Research Division
1617 Cole Boulevard
Golden, CO 80401

176. M. D. Gurney
NIPER
P.O. Box 2128
Bartlesville, OK 74005

177. John P. Gyeknyesi
NASA Lewis Research Center
2100 Brookpark Road
MS:49-7
Cleveland, OH 44135

178. J. J. Habeeb
Esso Petroleum Canada
Research Division
P.O. Box 3022
Sarina Ontario N7T 7MI
CANADA

179. H. T. Hahn
Pennsylvania State University
ESM Department
227 Hammond Building
University Park, PA 16802

180. Nabil S. Hakim
Detroit Diesel Corporation
13400 Outer Drive West
Detroit, MI 48239

181. John W. Halloran
CPS Superconductor Corporation
840 Memorial Drive
Cambridge, MA 02139

182. Friedrich Harbach
Asea Brown Boveri AG
Department Functional Ceramics
Eppelheimer Str. 82
D-6900 Heidelberg 1
WEST GERMANY

183. Kay Hardman-Rhyne
DARPA
1400 Wilson Boulevard
Arlington, VA 22209

184. R. A. Harmon
25 Schalren Drive
Latham, NY 12110

185. Stephen D. Hartline
Norton Company
Advanced Ceramics
Goddard Road
Northboro, MA 01532-1545

186. Michael H. Haselkorn
Caterpillar, Inc.
Engineering Research
Materials
Technical Center, Bldg. E
P.O. Box 1875
Peoria, IL 61656-1875

187. Willard E. Hauth
Dow Corning Corporation
Composite Development
Ceramics Program
3901 South Siginaw Road
Midland, MI 48640

188. Kevin L. Haynes
McDonnell Douglas
Astronautics Company
P.O. Box 516, MS:107/1
St. Louis, MO 63166

189. Norman L. Hecht
University of Dayton
Research Institute
300 College Park
Dayton, OH 45469-0001

190. S. S. Hecker
Los Alamos National
Laboratory
Material Science and
Technology Division
P.O. Box 1663
Los Alamos, NM 87545

191. Peter W. Heitman
General Motors Corporation
Allison Gas Turbine
Division
P.O. Box 420, W-5
Indianapolis, IN 46206

192. Richard L. Helferich
The Duriron Company, Inc.
P.O. Box 1145
Dayton, OH 45401

193. H. E. Helms
General Motors Corporation
Allison Gas Turbine
Division
P.O. Box 420
Indianapolis, IN 46206

194. Thomas L. Henson
GTE Products Corporation
Chemical & Metallurgical
Division
Hawes Street
Towanda, PA 18848-0504

195. Thomas P. Herbell
NASA Lewis Research Center
21000 Brookpark Road,
MS:49-3
Cleveland, OH 44135

196. Hendrick Heystek
Bureau of Mines
Tuscaloosa Research Center
P.O. Box L
University, AL 35486

197. Robert V. Hillery
General Electric Company
One Neumann Way
P.O. Box 156301
Cincinnati, OH 45215

198. Jonathan W. Hinton
Carborundum Company
Structural Ceramics
Division
P.O. Box 1054
Niagara Falls, NY 14302

199. Joe Homeny
University of Illinois
Department of Materials
Science and Engineering
Ceramics Building
105 South Goodwin Avenue
Urbana, IL 61801

200. A. T. Hopper
Battelle Columbus
Laboratories
Engineering Mechanics
Department
505 King Avenue
Columbus, OH 43201-2693

201. George Hsu
Jet Propulsion Laboratory
4800 Oak Grove Drive
MS:512-103
Pasadena, CA 91109

202. Shih Hsu
Digital Equipment
Corporation
77 Reed Road, HS:HL02-1/L8
Hudson, MA 01749

203. Stephen M. Hsu
National Institute of
Standards and Technology
Institute for Materials
Science and Engineering
Gaithersburg, MD 20899

204. Harold A. Huckins
Princeton Advanced
Technology, Inc.
56 Finley Road
Princeton, NJ 08540

205. Fred Huettic
Advanced Ceramic
Technology, Inc.
17 Deerfield Road
East Brunswick, NJ 08816

206. O. Richard Hughes
Celanese Research Company
86 Morris Avenue
Summit, NJ 07901

207. Joseph E. Hunter, Jr.
General Motors Corporation
Research Labs, Metallurgy
Dept.
12 Mile and Mound Roads
Warren, MI 48090-9055

208. Louis C. Ianniello
U.S. Department of Energy
Office of Materials Sciences
ER-13 GTN, Germantown GTN
Washington, DC 20545

209. Robert H. Insley
Champion Spark Plug Company
Ceramic Division
20000 Conner Avenue
Detroit, MI 48234

210. Curtis A. Johnson
General Electric Company
Ceramics Branch, Physical
Chemistry Laboratory
P.O. Box 8
Schenectady, NY 12301

211. Larry Johnson
Argonne National Laboratory
Center for Transportation
Research
Building 362
9700 South Cass Avenue
Argonne, IL 60439

212. L. A. Joo
Great Lakes Research
Corporation
P.O. Box 1031
Elizabethton, TN 37643

213. A. David Joseph
Sealed Power Corporation
100 Terrace Plaza
Muskegon, MI 49443

214. Debra Joslin
University of Tennessee
Metallurgical Engineering
Department
Knoxville, TN 37996

215. Dr. Adam Jostsons
Australian Nuclear Science
and Technology
Lucas Heights Research
Laboratories
New Illawarra Road
Lucas Heights New South
Wales
AUSTRALIA

216. Roy Kamo
Adiabatics, Inc.
630 South Mapleton
Columbus, IN 47201

217. Allan Katz
Air Force Wright
Aeronautical Laboratory
Metals and Ceramics
Division
Materials Laboratory
AFWAL/MLLM
Wright-Patterson AFB, OH
45433

218. R. N. Katz
U.S. Army Materials
Technology Laboratory
405 Arsenal Street
Watertown, MA 02172

219. Mr. Kawaguchi
Tokai Carbon
375 Park Avenue
Suite 3802
New York, NY 10152

220. Frederick L. Kennard, III
General Motors Corporation
AC Spark Plug Division
Dept. 32-24
1300 North Dort Highway
Flint, MI 48556

221. J. R. Kidwell
Allied-Signal Aerospace
Company
Garrett Auxiliary Power
Division
2739 East Washington Street
P.O. Box 5227
Phoenix, AZ 85010

222. Max Klein
Gas Research Institute
8600 West Bryn Mawr Avenue
Chicago, IL 60631

223. C. E. Knapp
Norton Company
8001 Daly Street
Niagara Falls Ontario L2G 6S2
CANADA

224. A. S. Kobayashi
University of Washington
Department of Mechanical
Engineering, MS:FU10
Seattle, WA 98195

225. rer. nat. Wolfgang Kollenberg
Projektleitung Material-
Rohstofforschung - PLR
Kernforschungsanlage Julich
GmbH
Postfach 1913
D-5170 Julich
WEST GERMANY

226. David M. Kotchick
Allied-Signal Aerospace
Company
AiResearch Los Angeles
Division
2525 West 190th Street
Torrance, CA 90509

227. Bruce Kramer
George Washington
University
Aerodynamic Center, Room T715
Washington, DC 20052

228. Saunders B. Kramer
U.S. Department of Energy
Office of Transportation
Systems
Forrestal Building CE-151
1000 Independence Avenue, SW
Washington, DC 20585

229. D. M. Kreiner
Allied-Signal Aerospace
Company
Garrett Auxiliary Power
Division
2739 East Washington Street
P.O. Box 5227
Phoenix, AZ 85010

230. A. S. Krieger
Radiation Science, Inc.
P.O. Box 293
Belmont, MA 02178

231. Pieter Krijgsman
Ceramic Design Int. Hold., Ltd.
P.O. Box 68
8050 AB Hattem
THE NETHERLANDS

232. Jack L'Amoreaux
11346 Gates Mill Drive
Knoxville, TN 37922

233. W. J. Lackey
Georgia Tech Research Institute
Energy and Materials Sciences Laboratory
Georgia Institute of Technology
Atlanta, GA 30332

234. Everett A. Lake
Air Force Wright Aeronautical Laboratory
AFWAL/POSL
Wright-Patterson AFB, OH 45433

235. Hari S. Lamba
General Motors Corporation
Electro-Motive Division
LaGrange, IL 60525

236. Manfred Langer
Volkswagen AG
Forschung-Neue Technologien Werkstofftechnologie
D-3180 Wolfsburg 1
WEST GERMANY

237. James Lankford
Southwest Research Institute
Department of Materials Sciences
6220 Culebra Road
P.O. Drawer 28510
San Antonio, TX 78284

238. David C. Larsen
Corning Glass Works
Materials Research Department
Sullivan Park, FR-51
Corning, NY 14831

239. Dr. S. K. Lau
Carborundum Company
Technology Division
P.O. Box 832
Niagara Falls, NY 14302

240. Harry A. Lawler
Carborundum Company
Niagara Falls R&D Center
P.O. Box 832
Niagara Falls, NY 14302

241. Alan Lawley
Drexel University
Materials Engineering
Philadelphia, PA 19104

242. Daniel Lee
Temescon
2850 7th Street
Berkeley, CA 94710

243. June-Gunn Lee
Korea Advanced Institute of Science and Technology
P.O. Box 131
Dong Dac Mun Seoul
KOREA

244. E. M. Lenoe
Air Force Office of Scientific Research
Office of Naval Research
Liaison Office, Far East
San Francisco, CA 96503

245. Stanley R. Levine
NASA Lewis Research Center
21000 Brookpark Road
Cleveland, OH 44135

246. David Lewis
Naval Research Laboratory
Materials Science and Technology Division
4555 Overlook Avenue, SW
Code 63-70
Washington, DC 20375

247. Bill Long
Babcock and Wilcox
P.O. Box 1260
Lynchburg, VA 24505

248. L. A. Lott
EG&G, Inc.
Idaho National Engineering Laboratory
P.O. Box 1625
Idaho Falls, ID 83415

249. Raouf O. Loutfy
Materials and Electrochemical Research Corporation
7960 South Kolb Road
Tuscon, AZ 85706

250. Bryan K. Luftglass
Chem Systems, Inc.
303 South Broadway
Tarrytown, NY 10591

251. Robert Lundberg
Swedish Institute for Silicate Research
Box 5403
S-402 29 Gothenburg
SWEDEN

252. Michael J. Lynch
General Electric Company
Medical Systems Group
P.O. Box 414, 7B-36
Milwaukee, WI 53201

253. Vincent L. Magnotta
Air Products and Chemicals, Inc.
Technical Diversification R&D Department
P.O. Box 538
Allentown, PA 18105

254. Tai-il Mah
Universal Energy Systems
4401 Dayton-Xenia Road
Dayton, OH 45432

255. L. Manes
Commission of the European Communities
Joint Research Centre
Ispra Establishment
1-21020 Ispra (Varese)
ITALY

256. Giel Marijnissen
Interturbine R&D
Research and Development
P.O. Box 4339
5944 ZG Arcen
THE NETHERLANDS

257. Gerald R. Martin
Fleetguard, Inc.
Cookeville, TN 38501

258. J. W. McCauley
U.S. Army Materials Technology Laboratory
SLCMT-OMM
405 Arsenal Street
Watertown, MA 02172-0001

259. Bryan J. McEntire
Norton Company
TRW Ceramics
Goddard Road
Northboro, MA 01532-1545

260. Thomas D. McGee
Iowa State University
Department of Materials Science and Engineering
Ames, IA 50011

261. H. Christopher McGowan
Advanced Ceramic Technology, Inc.
17 Deerfield Road
East Brunswick, NJ 08816

262. Malcolm G. McLaren
Rutgers University
Department of Ceramics
Busch Campus
Bowser Road, P.O. Box 909
Piscataway, NJ 08854

263. Arthur F. McLean
6225 North Camino Almonte
Tucson, AZ 85718

264. Brian L. Mehosky
British Petroleum
4440 Warrensville Center Road
Cleveland, OH 44128

265. Joseph J. Meindl
Reynolds International, Inc.
6603 West Broad Street
P.O. Box 27002
Richmond, VA 23261

266. D. Messier
U.S. Army Materials Technology Laboratory
DRXMR-MC
405 Arsenal Street
Watertown, MA 02172

267. Thomas N. Meyer
Aluminum Company of America
Alumina, Chemicals, and Ceramics Division
Alcoa Technical Center
Alcoa Center, PA 15069

268. Brad Miller
Norton Company
Advanced Ceramics
Goddard Road
Northboro, MA 01532-1545

269. Amar Mishra
Engelhard Corporation
CN-28
Menlo Park
Edison, NJ 08818

270. Bill Moehle
Ethyl Corporation
Ethyl Tower
451 Florida Avenue
Baton Rouge, LA 70801

271. Helen Moeller
Babcock and Wilcox
P.O. Box 11165
Lynchburg, VA 24506-1165

272. Frederick E. Moreno
Turbo Energy Systems, Inc.
2858 South Roosevelt
Tempe, AZ 85282

273. Peter E. D. Morgan
Rockwell International
Science Center
1049 Camino Dos Rios
P.O. Box 1085
Thousand Oaks, CA 91360

274. Lawrence M. Murphy
Solar Energy Research Institute
Thermal Systems Research Branch
1617 Cole Boulevard
Golden, CO 80401

275. Solomon Musikant
General Electric Company
Space Systems Division
P.O. Box 8555, MS:U-1219
Philadelphia, PA 19101

276. Pero Nannelli
Pennwalt Corporation
900 First Avenue
P.O. Box C
King of Prussia, PA 19406

277. William D. Nix
Stanford University
Department of Materials Science and Engineering
Stanford, CA 94305

278. Richard D. Nixdorf
American Matrix, Inc.
118 Sherlake Drive
Knoxville, TN 37922

279. S. D. Nunn
University of Michigan
Materials Science and Engineering
Ann Arbor, MI 48109

280. Brian M. O'Connor
The Lubrizol Corporation
29400 Lakeland Boulevard
Wickliffe, Oh 44092

281. W. Richard Ott
Alfred University
Center for Advanced Ceramic Technology
Alfred, NY 14802

282. William C. Owen
Sundstrand Turbomach
Division of Sunstrand Corporation
4400 Ruffin Road
P.O. Box 85757
San Diego, CA 92138-5757

283. Muktesh Paliwal
GTE Products Corporation
Hawes Street
Towanda, PA 18848-0504

284. Joseph E. Palko
General Electric Company
Gas Turbine Division
TTD Building, 55-113
Schenectady, NY 12345

285. Hayne Palmour, III
North Carolina State University
Engineering Research Services Division
2158 Burlington Engineering Labs
P.O. Box 5995
Raleigh, NC 27607

286. Joseph N. Panzarino
Norton Company
Advanced Ceramics
Goddard Road
Northboro, MA 01532-1545

287. Pellegrino Papa
Corning Glass Works
Corning Technical Products Division
Corning, NY 14831

288. R. H. Parrish
Vanderbilt University
Box 1621, Station B
Nashville, TN 37235

289. James G. Paschal
Reynolds Metals Company
P.O. Box 76154
Atlanta, GA 30358

290. Arvid E. Pasto
GTE Laboratories, Inc.
40 Sylvan Road
Waltham, MA 02254

291. James W. Patten
Cummins Engine Company, Inc.
Box 3005, Mail Code 50183
Columbus, IN 47202-3005

292. Timothy M. Pattison
Textron Lycoming
550 Main Street, MS:LSM1
Stratford, CT 06497

293. Robert A. Penty
Eastman Kodak Company
Manufacturing Technology Department, Apparatus Division
901 Elmgrove Road
Rochester, NY 14650

294. Gary R. Peterson
U.S. Department of Energy
Idaho Operations Office
785 D.O.E. Place
Idaho Falls, ID 83402

295. R. Byron Pipes
University of Delaware
Center for Composite Materials
2001 Spencer Laboratory
Newark, DE 19716

296. Bruce J. Pletka
Michigan Technological University
Department of Metallurgical Engineering
Houghton, MI 49931

297. Robert C. Pohanka
Office of Naval Research
800 North Quincy Street
Code 431
Arlington, VA 22217

298. J. P. Pollinger
Allied-Signal Aerospace Company
Garrett Ceramic Components Division
19800 South Van Ness Avenue
Torrance, CA 90509

299. Stephen C. Pred
ICD Group, Inc.
1100 Valley Brook Avenue
Lyndhurst, NJ 07071

300. Karl M. Prewo
United Technologies Corporation
Research Center
Silver Lane, MS:24
East Hartford, CT 06108

301. Hubert B. Probst
NASA Lewis Research Center
Materials Division
21000 Brookpark Road
MS:49-1
Cleveland, OH 44135

302. Joseph M. Proud
GTE Laboratories, Inc.
Materials Science Laboratory
40 Sylvan Road
Waltham, MA 02254

303. D. W. Prouse
Ceramatec, Inc.
2425 South 900 West
Salt Lake City, UT 84119

304. Carr Lane Quackenbush
Norton Company
Advanced Ceramics
Goddard Road
Northboro, MA 01532-1545

305. Brian Quigy
National Aeronautics and Space Administration
Energy Systems Office
Washington, DC 20546

306. George Quinn
U.S. Army Materials Technology Laboratory
405 Arsenal Street
Watertown, MA 02172

307. Dennis T. Quinto
Kennametal, Inc.
Phillip M. McKenna Laboratory
P.O. Box 639
Greensburg, PA 15601

308. S. Venkat Raman
Air Products and Chemicals, Inc.
Contract Research Department
P.O. Box 538
Allentown, PA 18105

309. Dennis Readey
Ohio State University
2041 College Road
Columbus, OH 43210

310. Robert R. Reeber
U.S. Army Research Office
P.O. Box 12211
Research Triangle Park, NC 27709

311. K. L. Reifsnider
Virginia Polytechnic Institute and State University
Department of Engineering Science and Mechanics
Blacksburg, VA 24061

312. Paul Rempes
Williams International
2280 West Maple Road
P.O. Box 200
Walled Lake, MI 48088

313. Theresa M. Resetar
U.S. Army Materials
Technology Laboratory
Materials Characterization
Center
ATTN:SLCMT-OMM
405 Arsenal Street
Watertown, MA 02172

314. K. T. Rhee
Rutgers University
College of Engineering
Bowser Road
P.O. Box 909
Piscataway, NJ 08854

315. Roy W. Rice
W. R. Grace and Company
7379 Route 32
Columbus, MD 21044

316. David W. Richerson
Ceramatec, Inc.
2425 South 900 West
Salt Lake City, UT 84119

317. Scott L. Richlen
U.S. Department of Energy
Office of Industrial Programs
Forrestal Building CE-141
1000 Independence Avenue, SW
Washington, DC 20585

318. Paul Rieth
Ferro Corporation
661 Willet Road
Buffalo, NY 14218-9990

319. Michael A. Rigdon
Institute for Defense
Analysis
1801 Beauregard Street
Alexandria, VA 22311

320. John E. Ritter, Jr.
University of Massachusetts
Mechanical Engineering
Department
Amherst, MA 01003

321. M. Rohr
DOE/ORO
Federal Office Building
P.O. Box 2001, MS:AMERD
Oak Ridge, TN 37831

322. Giulio A. Rossi
Norton Company
Advanced Ceramics
Goddard Road
Northboro, MA 01532-1545

323. Barry R. Rossing
Lanxide Corporation
Tralee Industrial Park
Newark, DE 19711

324. Donald W. Roy
Coors Ceramics Company
Research and Development
17750 West 32nd Street
Golden, CO 80401

325. Bruce Rubinger
Gobal
50 Milk Street, 15th Floor
Boston, MA 02109

326. Robert Ruh
Air Force Wright
Aeronautical Laboratory
Metals and Ceramics
Division
Materials Laboratory
AFWAL/MLLM
Wright-Patterson AFB,
OH 45433

327. Robert J. Russell, Sr.
Norton Company
Advanced Ceramics
Goddard Road
Northboro, MA 01532-1545

328. George P. Safol
Westinghouse Electric
Corporation
R&D Center
Pittsburgh, PA 15325

329. J. A. Salem
NASA Lewis Research Center
21000 Brookpark Road
Cleveland, OH 44135

330. J. Sankar
North Carolina A&T State University
Department of Mechanical Engineering
Greensboro, NC 27411

331. Maxine L. Savitz
Allied-Signal Aerospace Company
Garrett Ceramic Components Division
19800 South Van Ness Avenue
Torrance, CA 90509

332. Richard Schapery
Texas A&M University
Civil Engineering Department
College Station, TX 77843

333. Jim Schienle
Allied-Signal Aerospace Company
Garrett Auxiliary Power Division
2739 East Washington Street
P.O. Box 5227, MS:1302-2P
Phoenix, AZ 85010

334. Liselotte J. Schioler
Air Force Office of Scientific Research
Bolling AFB
Washington, DC 20332-6448

335. Richard A. Schmidt
Battelle Columbus Laboratories
Mechanics Section
505 King Avenue
Columbus, OH 43201-2693

336. Arnie Schneck
Deere & Company Technical Center
P.O. Box 128
Wood-Ridge, NJ 07075

337. Matthew Schreiner
ALANX Products L.P.
101 Lake Drive
Newark, DE 19702

338. John Schuldies
Industrial Ceramic Technology, Inc.
37 Enterprise Drive
Ann Arbor, MI 48103

339. R. B. Schulz
U.S. Department of Energy
Office of Transportation Systems
Forrestal Building CE-151, 5G-046
1000 Independence Avenue, SW
Washington, DC 20585

340. Wesley J. C. Schuster
Thermo Electron Corporation
Metals Division
115 Eames Street
P.O. Box 340
Wilmington, MA 01887

341. Murray A. Schwartz
Bureau of Mines
2401 Eye Street, NW
Washington, DC 20241

342. Douglas B. Schwarz
The Dow Chemical Company
52 Building
Midland, MI 48674

343. Thomas M. Sebestyen
U.S. Army Tank Automotive Command
AMSTA-RGRT
Warren, MI 48397-5000

344. Brian Seegmiller
Coors Ceramics Company
17750 West 32nd Street
Golden, CO 80401

345. S. G. Seshadri
Carborundum Company
Niagara Falls R&D Center
P.O. Box 832
Niagara Falls, NY 14302

346. Peter T. B. Shaffer
Advanced Refractory Technologies, Inc.
699 Hertel Avenue
Buffalo, NY 14207

347. Laurel M. Sheppard
Advanced Materials and Processes
Route 87
Metals Park, OH 44073

348. Dinesh K. Shetty
The University of Utah
Department of Materials Science and Engineering
Salt Lake City, UT 84112

349. Jack D. Sibold
Coors Ceramics Company
17750 West 32nd Street
Golden, CO 80401

350. Neal Sigmon
U.S. House of Representatives
Subcommittee on Interior and Related Events
Rayburn Building, Room B308
Washington, DC 20515

351. Dr. Richard Silberglitt
Quest Research Corporation
1651 Old Meadow Road
McLean, VA 22102

352. A. Sinha
North Carolina A&T State University
Department of Mechanical Engineering
Greensboro, NC 27411

353. Maurice J. Sinnott
University of Michigan
Chemical and Metallurgical Engineering
438 West Engineering Building
Ann Arbor, MI 48109-2136

354. S. R. Skaggs
Los Alamos National Laboratory
Program Office
P.O. Box 1663, MS:F-682
Los Alamos, NM 87545

355. J. Thomas Smith
GTE Laboratories, Inc.
40 Sylvan Road
Waltham, MA 02254

356. Jay R. Smyth
Allied-Signal Aerospace Company
Garrett Auxiliary Power Division
2739 East Washington Street
P.O. Box 5227,
MS:93-172/1302-2K
Phoenix, AZ 85010

357. Rafal Sobotowski
Carborundum Company
Research and Development
3092 Broadway Avenue
Cleveland, OH 44115

358. E. Solidum
Allied-Signal Aerospace Company
Garrett Ceramics Components Division
19800 South Van Ness Avenue
Torrance, CA 90509

359. Thomas M. Sopko
Lubrizol Enterprises, Inc.
29400 Lakeland Boulevard
Wickliffe, OH 44092

360. Richard. M. Spriggs
Alfred University
Center for Advanced Ceramic Technology
Alfred, NY 14802

361. M. Srinivasan
Carborundum Company
Niagara Falls R&D Center
P.O. Box 832
Niagara Falls, NY 14302

362. Gordon L. Starr
Cummins Engine Company, Inc.
Metallic/Ceramic Materials Department
Box 3005, Mail Code 50183
Columbus, IN 47202-3005

363. Harold L. Stocker
General Motors Corporation
Allison Gas Turbine Division
P.O. Box 420, T-23
Indianapolis, IN 46206

364. Paul D. Stone
The Dow Chemical Company
1801 Building
Midland, MI 48674

365. Roger Storm
Carborundum Company
Niagara Falls R&D Center
P.O. Box 832
Niagara Falls, NY 14302

366. E. E. Strain
Allied-Signal Aerospace Company
Garrett Auxiliary Power Division
2739 East Washington Street
P.O. Box 5227, MS:301-2N
Phoenix, AZ 85010

367. Thomas N. Strom
NASA Lewis Research Center
21000 Brookpark Road, 77-6
Cleveland, OH 44135

368. Jerry Strong
Albright & Wilson
P.O. Box 26229
Richmond, VA 23260

369. Richard Suddeth
Boeing Motor Airplane Company
P.O. Box 7730, MS:K-76-67
Wichita, KS 67277

370. Paul Sutor
Midwest Research Institute
425 Volker Boulevard
Kansas City, MO 64116

371. P. L. Sutton
U. S. Department of Energy
Office of Transportation Systems
Forrestal Building CE-151
1000 Independence Avenue, SW
Washington, DC 20585

372. J. J. Swab
U.S. Army Materials Technology Laboratory
Ceramics Research Division, SLCMT-EMC
405 Arsenal Street
Watertown, MA 02172

373. John W. Swain, Jr.
Kollmorgen Corporation
PCK Technology Division
15424 Garrison Lane
Southgate, MI 48195

374. Lewis Swank
Ford Motor Company
Material Systems Reliability Division
Room S-2023, SRL
20000 Rotunda Drive
P.O. Box 2053
Dearborn, MI 48121-2053

375. Truett Sweeting
Carborundum Company
Niagara Falls R&D Center
P.O. Box 832
Niagara Falls, NY 14302

376. Stephen R. Tan
ICI Advanced Materials
P.O. Box 11
The Heath, Runcorn Cheshire
WA7 4QE
ENGLAND

377. Anthony C. Taylor
U.S. House of Representatives
Committee on Science and Technology
Rayburn Building, Room 2321
Washington, DC 20515

378. Monika O. Ten Eyck
Carborundum Technical Ceramics GmbH
Nobelstrasse 6
D4050 Monchengladbach-Wickrath
WEST GERMANY

379. John K. Tien
Columbia University
1137 SW Mudd Building
New York, NY 10027

380. T. Y. Tien
University of Michigan
Materials and Metallurgical Engineering
Dow Building
Ann Arbor, MI 48109-2136

381. Julian M. Tishkoff
Air Force Office of Scientific Research
(AFOSR/WC) Bolling AFB
Washington, DC 20332

382. Louis E. Toth
National Science Foundation
Division of Materials Research
1800 G Street, NW
Washington, DC 20550

383. Richard E. Tressler
Pennsylvania State University
Ceramic Science and Engineering Department
201 Steidle Building
University Park, PA 16802

384. W. T. Tucker
General Electric Company
P.O. Box 8
Schenectady, NY 12301

385. Donald L. Vaccari
General Motors Corporation
Allison Gas Turbine Division
2001 South Tibbs Avenue
Indianapolis, IN 46241

386. Dr. ir. O. Van Der Biest
Katholieke Universiteit Leuven
Departement Metaalkunde en Toegepaste
de Croylaan 2
B-3030 Leuven
BELGIUM

387. Edward C. Van Reuth
Technology Strategies, Inc.
10722 Shingle Oak Court
Burke, VA 22015

388. V. Venkateswaran
Carborundum Company
Niagara Falls R&D Center
P.O. Box 832
Niagara Falls, NY 14302

389. Dr. K. E. Voss
Englehard Corporation
Research Department
Menlo Park, CN-28
Edison, NJ 08818

390. John B. Wachtman, Jr.
Rutgers University
Bowser Road
P.O. Box 909
Piscataway, NJ 08854

391. Harlan L. Watson
U.S. House of Representatives
Committee on Science and Technology
Rayburn Building, Suite 2321
Washington, DC 20515

392. John D. Watson
Broken Hill Proprietary Co., Ltd.
Melbourne Research Laboratories
245 Wellington Road
Mulgrave 3170 Victoria
AUSTRALIA

393. C. David Weiss
Caterpillar, Inc.
Engineering Research Materials
Technical Center
Building E, P.O. Box 1875
Peoria, IL 61656-1875

394. James J. Wert
Vanderbilt University
Box 1621, Station B
Nashville, TN 37235

395. Albert R. C. Westwood
Martin Marietta Laboratories
1450 South Rolling Road
Baltimore, MD 21227

396. Thomas J. Whalen
Ford Motor Company
Material Systems Reliability Division
Room S-2023, SRL
20000 Rotunda Drive
P.O. Box 2053
Dearborn, MI 48121-2053

397. Sheldon M. Wiederhorn
National Institute of Standards and Technology
Inorganic Materials Division
Gaithersburg, MD 20899

398. James C. Williams
General Electric Company
Engineering Materials Technology Labs.
One Neumann Way
Cincinnati, OH 45215-6301

399. Janette R. Williams
Kollmorgen Corporation
PCK Technology Division
322 L.I.E. South Service Road
Melville, NY 11747

400. Craig A. Willkens
Norton Company
Advanced Ceramics
Goddard Road
Northboro, MA 01532-1545

401. Roger R. Wills
TRW, Inc.
Valve Division
1455 East 185th Street
Cleveland, OH 44110

402. Jim M. Wimmer
Allied-Signal Aerospace Company
Garrett Auxiliary Power Division
2739 East Washington Street
P.O. Box 5227, MS:1302-2P
Phoenix, AZ 85010

403. David Wirth
Coors Ceramics Company
Technical Operations and Engineering
17750 West 32nd Street
Golden, CO 80401

404. Thomas J. Wissing
Eaton Corporation
Engineering & Research Center
26201 Northwestern Highway
P.O. Box 766
Southfield, MI 48037

405. Dale Wittmer
Southern Illinois University at Carbondale
Department of Mechanical Engineering and Energy Processes
Carbondale, IL 62901

406. Stanley M. Wolf
U.S. Department of Energy
Conservation and Renewable Energy
Forrestal Building CE-12
1000 Independence Avenue, SW
Washington, DC 20585

407. George W. Wolter
Howmet Turbine Components Corporation
Technical Center
699 Benston Road
Whitehall, MI 49461

408. James C. Wood
NASA Lewis Research Center
21000 Brookpark Road
MS:500-210
Cleveland, OH 44135

409. Roger P. Worthen
Eaton Corporation
Engineering and Research Center
26201 Northwestern Highway
P.O. Box 766
Southfield, MI 48076

410. Harry C. Yeh
Allied-Signal Aerospace Company
Garrett Ceramic Components Division
19800 South Van Ness Avenue
Torrance, CA 90509

411. Thomas M. Yonushonis
Cummins Engine Company, Inc.
Box 3005, Mail Code 50183
Columbus, IN 47202-3005

412. Don Zabierek
Air Force Wright Aeronautical Laboratory
AFWAL/POTC
Wright-Patterson AFB, OH 45433

413. Charles Zeh
U.S. Department of Energy
Morgantown Energy Technology Center
P.O. Box 880
Morgantown, WV 26505

414. Anne Marie Zerega
U.S. Department of Energy
Office of Transportation Systems
Forrestal Building CE-15
1000 Independence Avenue, SW
Washington, DC 20585

415. Martin Zlotnick
Nichols Research Corporation
8618 Westwood Center Drive
Suite 200
Vienna, VA 22180-2222

416. Klaus M. Zwilsky
National Materials
Advisory Board
National Research Council
2101 Constitution Avenue
Washington, DC 20418

417. Department of Energy
Oak Ridge Operations
Office
Assistant Manager for
Energy
Research and Development
P.O. Box 2001
Oak Ridge, TN 37831-8600

418-427. Department of Energy
Office of Scientific and
Technical Information
Office of Information
Services
P.O. Box 62
Oak Ridge, TN 37831

For distribution by microfiche
as shown in DOE/TIC-4500,
Distribution Category UC-95
(Energy Conservation).

☆U.S. GOVERNMENT PRINTING OFFICE 1989—648-199/00068